Spatio-Temporal Dynamics of Primary Lymphoid Follicles During Organogenesis and Lymphneogenesis

Dissertation

zur Erlangung des Doktorgrades
der Naturwissenschaften

vorgelegt beim Fachbereich Biologie
der Johann Wolfgang Goethe – Universität
in Frankfurt am Main

von
Tilo Beyer
aus Dresden

Frankfurt am Main 2007
(D F1)

Vom Fachbereich Biologie der Johann Wolfgang Goethe – Universität als Dissertation angenommen.

Dekan: Prof. Dr. Volker Müller
Gutachter: Prof. Dr. Anna Starzinski-Powitz
                            Prof. Dr. Jürgen Bereiter-Hahn / Dr. Michael Meyer-Hermann
Datum der Disputation: 07. April 2008

Kurzfassung

Die großen Fortschritte in der Biologie der letzten Jahre basieren im wesentlichen auf einer Zunahme experimenteller Daten. Zu großen Teilen steckt die Theoriebildung noch in den Kinderschuhen. In gewissen Bereichen, wie z.B. der Genetik oder der Evolutionsbiologie, werden zunehmend mathematische Modelle zur Auswertung experimenteller Befunde herangezogen. Der Nutzen theoretischer Biologie liegt dabei nicht nur in der Reproduktion von Experimenten, sondern auch in der Identifikation komplexer Zusammenhänge. Damit ist es möglich experimentell nicht direkt zugängliche Mechanismen und Fragestellungen zu untersuchen. Letztendlich führt dies zu Vorhersagen über Interaktionen eines komplexen Systems, die mit gezielt entwickelten Experimenten verifiziert werden können. Daraus folgend läßt sich der Informationsgewinn pro Experiment erhöhen und damit die Zahl der Experimente reduzieren, insbesondere im Hinblick auf Tierversuche ein erstrebenswertes Ziel. Die vorliegende Arbeit folgt dieser Philosophie in einem interdisziplinären Ansatz von Physik, Informatik und Biologie. Ziel ist es, die Genese von primären lymphoiden Follikeln zu verstehen. In einem ersten Schritt werden die vorhandenen Daten über zelluläre und molekulare Interaktionen verknüpft, um die grundlegenden Wechselwirkungen im primären Follikel zu identifizieren und ein geschlossenes Modell der Organogenese und Lymphneogenese sekundärer lymphatischer Gewebe zu erstellen. Der folgende Schritt ist die Untersuchung bisher unbekannter Mechanismen, die die Organisation der Follikel beeinflusst. Hierzu werden Experimente vorgeschlagen, die der Aufklärung grundlegender Wechselwirkungen und die Regulation der Genese sekundärer lymphatischer Gewebe dienen.

Primäre lymphoide Follikel   Primäre lymphoide Follikel sind Teil des Immunsystems, einem komplexen Netzwerk aus Molekülen, Zellen und spezialisierten Geweben [*Janeway and Travers*, 1997]. Zum Schutz vor Pathogenen besitzt das Immunsystem eines multizellulären Organismus verschiedene Möglichkeiten. Da primäre lymphoide Follikel nur in Säugetieren präsent sind, soll hier nur auf die Organisation des Säugetier-Immunsystems eingegangen werden.

Der erste und wirksamste Schutz sind physikalische Barrieren, auch wenn sie nicht unmittelbar Teil des Immunsystems sind. Die eigentlichen Teile des Immunsystems werden erst aktiv, wenn ein Pathogen in einen Organismus eingedrungen ist. Die erste innere Verteidigungslinie stellt das innate (angeborene) Immunsystem dar. Es besteht aus einer Reihe von Zellen und Molekülen die in Laufe der Evolution eine genetische vorprogrammierte Reaktion auf ein Pathogen erzeugen. Wirbeltieren – und damit auch Säugetieren – steht zusätzlich das adaptive (oder auch erworbene) Immunsystem zur Verfügung. Die Komponenten des adaptive Immunsystem unterliegen einer Art Mikroevolution. Dies bedeutet, dass die Fähigkeiten des Immunsystems durch die erfolgreiche Bekämpfung vorangegangener Pathogene bestimmt werden. Im allgemeinen erfolgt dadurch eine Anpassung an die spezifische Pathogenzusammensetzung der Umgebung eines Organismus. Zwei Zelltypen sind für die Funktion des adaptiven Immunsystems essentiell: B- und T-Lymphozyten. T-Zellen sind einerseits an der Bekämpfung intrazellulärer Pathogene, z.B. Viren, beteiligt und andererseits für die Regulierung des adaptiven Immunsystems verantwortlich, inklusive eines Großteils der B-Zell-abhängigen Immun-

antworten. Die Aufgabe der B-Zellen ist im wesentlichen die Produktion von Antikörpern, die der Bekämpfung von Pathogen in den Körperflüssigkeiten (Blut und Lymphe) dienen. In den meisten Vertebraten (wahrscheinlich mit Ausnahme der Klasse der Kieferlosen/Agnatha [*Du Pasquier*, 2005; *Kasahara et al.*, 2004]) ist das adaptive Immunsystem mit spezialisierten Gewebestrukturen assoziiert – den primären und sekundären lymphatischen Geweben. Die primären lymphatischen Gewebe sind hauptsächlich für die Erzeugung des initialen Repertoires an B- und T-Zellen verantwortlich [*Janeway and Travers*, 1997]. Dies heißt, es wird ein breites Spektrum an Zellen erzeugt, die jeweils verschiedenen molekulare Strukturen erkennen können, die nicht Teil des Organismus sind. Dies versetzt B- und T-Zellen in die Lage, körperfremde Moleküle zu erkennen, die in der Regel mit dem Eindringen von Pathogenen assoziiert sind.

Die sekundären lymphatischen Gewebe dienen als Filter [*Janeway and Travers*, 1997], in den potentielle körperfremde Moleküle (Antigene) einer großen Anzahl von Lymphozyten präsentiert werden. In der Tat befindet sich der größte Teil der Lymphozyten in diesen Geweben. Zu sekundären lymphatischen Geweben zählen die weiße Pulpa der Milz, Lymphknoten, Tonsillen und die Peyer'schen Plaques neben einigen wenigen anderen Geweben [*Fu and Chaplin*, 1999; *Janeway and Travers*, 1997]. Die sekundären lymphatischen Gewebe in Säugetieren zeigen eine charakteristische Morphologie. B- und T-Zellen kommen in getrennten Kompartimenten vor. Die B-Zellen formen zusammen mit follikulären dendritischen Zellen (follicular dendritic cells - FDC) das primäre lymphoide Follikel. Jedes sekundäre lymphatische Gewebe enthält bis zu mehreren Tausend dieser sphärisch geformten Follikel, die – weitgehenden unabhängig von Spezies und Gewebeart – eine Größe von einigen wenigen hundert Mikrometern erreichen (Tabelle 2.1). Zwischen den Follikeln befinden sich die T-Zone, die wie der Name bereits andeutet, im wesentlichen aus T-Zellen besteht, neben einer Reihe anderer Zellen des Immunsystems, Stützgewebe und Gefäßen. Im Blut zirkulierende Lymphozyten treten in sekundäre lymphatische Gewebe ein, indem sie durch die Wandungen der Blutgefäße transmigrieren [*Janeway and Travers*, 1997]. Anschließend wandern B- und T-Zellen in die zugehörigen Kompartimente ein, wo sie knapp einen Tag verweilen, bevor sie die sekundären lymphatischen Gewebe über die Lymphgefäße wieder verlassen (Abschnitt 2.4). Antigene werden unter anderem durch dendritische Zellen aus allen Teilen des Körpers über die Lymphgefäße in die sekundären lymphatischen Gefäße transportiert [*Ferguson et al.*, 2004; *Gretz et al.*, 1996]. Dies ermöglicht es den Lymphozyten, effektiv potentielle Pathogene zu erkennen und bei Bedarf eine adaptive Immunreaktion auszulösen. Die Rolle der primären lymphoiden Follikel hierbei ist zweifach. Zum ersten sind FDCs dazu prädestiniert B-Zellen Antigene zu präsentieren [*Szakal et al.*, 1988]. Sollte eine B-Zell-abhängige Immunreaktion ausgelöst werden, wird in den primären Follikeln eine sogenannte Keimzentrumsreaktion initiiert [*MacLennan*, 1994; *McHeyzer-Williams et al.*, 2001; *Tarlinton*, 1998]. Die zweite Funktion der Follikel ist dabei die Transformation in ein sekundäres lymphoides Follikel, das ein Keimzentrum enthält. In den Keimzentren spielen die FDCs eine wichtige Rolle bei der Affinitätsreifung, die durch Mikroevolutionsprozess zur Verbesserung der Antikörper der B-Zellen führt. Damit ist die Hauptaufgabe der primären lymphoiden Follikel die Bereitstellung der FDCs, die sowohl für die Initiierung als auch während der Keimzentrumsreaktion von essenzieller Bedeutung sind.

Kurz zusammengefasst besteht die Organogenese sekundärer lymphatische Gewebe aus drei Phasen [*Fu and Chaplin*, 1999; *Halleraker et al.*, 1994; *Hashi et al.*, 2001; *Nishikawa et al.*, 2003]. In der ersten wird das stromale Netzwerk aufgebaut und Immunzellen sind unorganisiert im Gewebe ver-

teilt. Dies stellt die Ausgangssituation für die Simulationen dar. In einer nächsten Phase werden die Gefäße reorganisiert und spezielle stromale Zelltypen induziert, die auch Chemokine ausschütten. Die Lymphozyten zeigen hierbei ein charakteristisches Muster, dass als B-Zell-Ring bekannt ist. Hierbei befinden sich die B-Zellen in einer Schale (in drei Dimensionen) bzw. (in einem zweidimensionalen Schnitt) um die T-Zone in der auch alle Gefäße zu finden sind. In der dritten und letzten Phase der Organogenese bilden sich FDCs im B-Zell-Ring aus unbekannten Vorläuferzellen durch ein Kontakt-signal der B-Zellen. Die FDCs produzieren das Chemokin CXCL13, dass den Rezeptor CXCR5 auf B-Zellen anspricht und diese so zur Chemotaxis in Richtung der FDCs veranlasst. Dies führt letzt-endlich zur Bildung primärer lymphoider Follikel. Während der normalen Organogenese sind statt Lymphozyten andere Zellen für die Organogenese verantwortlich. Dies sind 'lymphoid tissue indu-cer cells' die die Rolle von B-Zellen übernehmen und dendritische Zellen (nicht zu verwechseln mit FDCs), die sich im wesentlichen wie T-Zellen verhalten. Da die Organogenese mit experimentellen Mitteln sich soweit verzögern lässt, dass B- und T-Zellen selbst beteiligt sind, dienen sie im Rahmen der Arbeit als Synonyme für die anderen beiden Zelltypen.

Zielsetzung Ziel der Arbeit ist die Erstellung eines geschlossenen Modells der Genese von primären lymphoiden Follikeln. Es soll in der Lage sein, sowohl die Prozesse während der Organogenese als auch die Ergebnisse von genetischen Knockout-Experimenten zu beschreiben. Zwei Fragen stehen hierbei im Mittelpunkt: Wie wird die Größe eines Follikels reguliert? und Welche Mechanismen er-zeugen die Morphologie sekundärer lymphatischer Gewebe in einem Fließgleichgewicht von Lym-phozyten? Die erste Frage zielt auf die Beobachtung ab, dass lymphoide Follikel eine nahezu kon-stante Größe in allen Organismen und Geweben hat (Tabelle 2.1). Interessant ist, dass auch neu gene-rierte Follikel im Verlauf verschiedener Autoimmunerkrankungen die gleiche Größe aufweisen. Die Tatsache, dass Follikel während Autoimmunerkrankungen oder unter speziellen experimentellen Be-dingungen neu entstehen, wirft die Frage nach den Mechanismen der Organogenese und Lymphneo-genese auf. In der Vergangenheit sind bereits grundlegende Prozesse der Morphogenese entwickelt worden [*Meinhardt*, 1982]. Im allgemeinen sind eine lokale Anregung und eine langreichweitige In-hibierung für die Musterbildung in unterschiedlichsten Organismen verantwortlich. In dieser Arbeit sollen die zugehörigen zellulären und molekularen Prozesse in sekundären lymphatischen Geweben identifiziert werden. Dies ist besonders interessant im Hinblick auf einen bedeutenden Unterschied der Organogenese sekundärer lymphatischer Follikel. Das Gleichgewicht der Zellen im Gewebe wird nicht durch eine Balance von Wachstum und Tod der Zellen verursacht, sondern durch ein Fließ-gleichgewicht von ein- und austretenden Zellen. Von den Simulationen ausgehend sollen darüber Vorhersagen und geeignete Experimente erarbeitet werden, die zusätzliche Information zu den der Organogenese sekundärer lymphatische Gewebe zugrunde liegenden Prozesse liefern.

Das Modell Für die Simulation der Organogenese primärer lymphoider Follikel ist ein dreiteiliges Multiskalen-Modell entwickelt worden. Zellen werden als deformierbare Kugeln mit einer internen Dynamik in drei Dimensionen repräsentiert. Eine Stufe des Modells beinhaltet die interne Dynamik der Zellen. Dies sind zum Beispiel die Expressionslevel von Oberflächenmolekülen und allgemein der Phänotyp einer Zelle. Außerdem gehören interne Zeiten dazu, z.B. nach welcher Zeit eine Zelle diffe-renziert oder, im Fall der Lymphozyten-Migration, die Persistenzzeit. Die zweite Modellstufe erfasst

die kontaktabhängigen Zellinteraktionen, insbesondere die mechanischen Wechselwirkungen und aktiven Kräfte migrierender Zellen. Zur Definition eines Zellkontaktes dient die reguläre/Delaunay Triangulation bzw. die dazu duale Voronoi-Zerlegung (siehe nächster Absatz) [*Aurenhammer*, 1991; *Okabe et al.*, 2000]. Die Triangulation dient im Rahmen der Simulation zur Identifikation von Nachbarzellen und der Berechnung von Abständen und Kontaktflächen. Aus diesen Größen und einigen Zell-intrinsischen Eigenschaften werden die Kräfte berechnet, die eine Zelle selbst generiert, auf ihre Nachbarn ausübt und von ihren Nachbarn erfährt. Die mechanische Interaktion wird mit dem Modell von Johnson, Kendall und Roberts für adhäsive elastische Kugeln beschrieben [*Chu et al.*, 2005; *Johnson et al.*, 1971]. Für die während der Migration der Lymphozyten auftretenden Kräfte ist ein neues Modell auf der Basis experimenteller Daten [*de Bruyn*, 1946; *Lewis*, 1931; *Murray et al.*, 1992; *Wolf et al.*, 2003b] entwickelt worden. Die resultierenden Newtonschen Bewegungsgleichungen werden in der überdämpften Näherung gelöst [*Dallon and Othmer*, 2004; *Schaller and Meyer-Hermann*, 2005]. Die dritte Stufe des Modells beschreibt langreichweitige Wechselwirkungen durch diffundierende Signalmoleküle. Für die Simulation der primären lymphoiden Follikel ist besonders die Diffusion von Chemokinen von Interesse [*Cyster*, 2005]. Die Dynamik der Chemokine erfasst auch die Bewegung der Quellen – die stromalen Zellen – und die Bindung an die Rezeptoren der chemotaktisch aktiven Lymphozyten. Dadurch entsteht eine Reaktions-Diffusionsgleichung für jedes Chemokin. Das System der partiellen Differentialgleichungen wird auf einem Hintergrundgitter mittels einer Splitting-Methode gelöst (Abschnitt 5.6) [*Karlsen and Lie*, 1999; *Tyson et al.*, 1996].

Das Modell zeichnet sich durch die Verwendung der Voronoi-Zerlegung aus. Diese wird als Zerlegung C_n des Raumes definiert [*Aurenhammer*, 1991; *Okabe et al.*, 2000]:

$$\bigcup_n C_n = \mathbb{R}^3 \quad mit \quad C_n = \left\{ \mathbf{x} \in \mathbb{R}^3 : \|\mathbf{x} - \mathbf{c}_n\| - r_n^2 < \|\mathbf{x} - \mathbf{c}_m\| - r_m^2 \ \forall \ m \neq n \right\}. \tag{1}$$

Hierbei sind c_n die Positionen der Zellen mit Radius r_n. Dadurch wird eine von der Zellgröße r_n abhängige Einflußsphäre der Zellen n definiert. Daraus lassen sich die Kontaktflächen und Kontaktabstände zwischen den Zellen berechnen. Der dual Graph – die reguläre (oder auch gewichtete Delaunay) Triangulation – kennzeichnet die Nachbarschaftsbeziehungen zwischen Zellen [*Schaller and Meyer-Hermann*, 2005]. Für die praktische Anwendung wird die reguläre Triangulation genutzt. Dabei wurden im Rahmen der Arbeit eine Reihe neuer Algorithmen entworfen und implementiert, die die Simulation einer großen Zahl von Zellen auf einem parallelen Hochleistungsrechner erlauben [*Beyer et al.*, 2005]. Damit können realistische Zellzahlen für das Follikel ($10^4 - 10^5$ Zellen [*Liu et al.*, 1991]) simuliert werden. Alle relevanten Prozess wie Zellbewegung, Wachstum und Zelltod können durch entsprechende Operation auf die Triangulation abgebildet werden. Dadurch ist die reguläre Triangulation für jede Art von Partikelsimulationen auf parallelen Rechnerarchitekturen verfügbar geworden.

Ergebnisse Ein Resultat der Arbeit ist die Entwicklung eines neuen Modells für die Gewebe-Simulation vieler Zellen in drei Dimensionen. Auf einer regulären Triangulation aufbauend wird damit die Simulation hochdynamischer Gewebestrukturen möglich. Die Methode zeichnet sich insbesondere dadurch aus, dass die Zellen des untersuchten biologischen Systems schnell migrieren können. Diese schnelle Migration wurde für die durchgeführten Simulationen an aus 2-Photonen-

Imaging gewonnene Daten der B- und T-Zell-Migration angepasst [*Miller et al.*, 2002]. Damit konnte die Geschwindigkeitsverteilung dieser beiden Zelltypen erfolgreich mit zwei physikalischen Parametern pro Zelltyp beschrieben werden [*Beyer and Meyer-Hermann*, 2007b].

Für ein vollständiges Fließgleichgewicht der Lymphozyten sind Informationen über Zu- und Abfluss der Zellen nötig. Der Abfluss von Zellen ist noch recht spärlich experimentell untersucht. Jedoch scheint eine Blockade bestimmter Chemoattraktant-Rezeptoren (S1P$_1$ [*Matloubian et al.*, 2004]) den Abfluss zu blockieren, so dass in Ergänzung der restlichen experimentellen Daten ein Chemotaxis in Richtung einer Abflusszone für Zellen angenommen wurde. Diese Zone kann mit den efferenten lymphatischen Gefäßen identifiziert werden. Das so entstandene Modell ist in der Lage ein in Teilen korrektes Bild der Genese primärer lymphoider Follikel zu zeichnen. Es wurde gezeigt, dass zufällige gebildete Aggregate aus migrierenden B-Zellen in der Lage sind FDCs zu induzieren und die Follikelbildung einzuleiten. Dies führt im weiteren zur Separation von B- und T-Zellen in ein primäres Follikel und eine T-Zone. Für beide Lymphozytentypen stellt sich ein Fließgleichgewicht ein, dass eine realistische Größe beider Kompartimente erzeugt. Eine detaillierte Analyse offenbart jedoch eine wesentliche Unstimmigkeit mit experimentellen Daten. Das primäre lymphoid Follikel bildet sich direkt um die efferenten lymphatischen Gefäßen. Dies jedoch widerspricht den experimentellen Befunden. Efferente lymphatische Gefäße ebenso wie das lymphatische Endothel der sekundären lympatischen Gewebe sind im allgemeinen nur in der T-Zone aber nicht in den Follikeln zu finden [*Belisle and Sainte-Marie*, 1981a,b,c,d,e, 1990; *Belisle et al.*, 1982; *Sainte-Marie et al.*, 1981]. Dieses Problem lässt sich weder durch ein von den lymphatischen Gefäßen entfernt vorgeformtes Follikel lösen, noch durch die Variation der Entfernung zwischen Einfluss und Abfluss der Lymphozyten.

Ein erster Schritt zur Lösung der falschen relativen Position von Follikel und lymphatischen Endothel besteht darin die Lymphangiogenese negativ an die Entstehung von FDCs zu koppeln. Das heißt, dass die Generierung der FDCs eine Rückbildung des lymphatischen Endothels der Umgebung verursacht. Diese Vorhersage lässt sich experimentell überprüfen. Eine Möglichkeit ist die Beobachtung des lymphatischen Endothels während der Organogenese mit Markern wie LYVE-1, D6 und VEGFR-3 [*Hong et al.*, 2004]. Ebenso ist die Anwendung von Angiostatika (die möglicherweise auch die Bildung von Lymphgefäßen beeinflussen) während Rekonstituierungsexperimenten von Knockout-Mäusen denkbar, deren sekundäre lymphatische Gewebe nur unvollständig ausgebildet sind. Die nachträglich gebildeten Follikel sollten dann lymphatisches Endothel enthalten.

Die Dynamik des lymphatischen Endothels offenbart eine Reihe weitere Details der Follikelbildung. Zum ersten ist eine Chemotaxis in Richtung des Endothels (durch S1P [*Cyster*, 2005]) eher unwahrscheinlich, da es mit der Morphologie des Follikels interferiert, indem dessen Rand nicht mehr klar von der T-Zone separiert ist. Das gleiche Argument gilt in Bezug auf die chemotaktische Antwort von B-Zellen auf Chemokine der T-Zone. Letzteres wird bereits durch experimentelle Befunde gestützt [*Breitfeld et al.*, 2000; *Roy et al.*, 2002].

Da kein lymphatisches Endothel im Follikel vorhanden ist, stellt sich die Frage wie die B-Zellen das Follikel wieder verlassen. Wie oben angedeutet, ist eine Chemotaxis in Richtung des Endothels durch S1P nicht wahrscheinlich. Alternativ könnte eine Herunterregulierung der Antwort auf CXCL13 den B-Zellen ermöglichen, durch ungerichtete Migration das Follikel zu verlassen und am Rand des Follikels das lymphatische Endothel zum Austritt aus sekundären lymphatische Geweben zu nutzten. Die

Internalisierung des Chemokinrezeptors CXCR5 nach der Bindung des Chemokins CXCL13 erzeugt jedoch eine Instabilität der Form des Follikels, die nicht beobachtet wird. Daher sagt das Modell voraus, dass die Internalisierung von CXCR5 im Follikel eine untergeordnete Rolle spielt [*Beyer and Meyer-Hermann*, 2007b]. In der Tat ist die benötigte ungerichtete Migration der B-Zellen im Follikel auch ohne Internalisierung möglich. Der CXCL13-Gradient ist nur am Rand des Follikels wirksam. Damit besitzen B-Zellen die Möglichkeit zwischen Rand und Zentrum des Follikels zu zirkulieren, um das sekundäre lymphatische Gewebe zu verlassen.

Eine ungewollte Folge der Dynamik des lymphatischen Endothels ist eine Instabilität des Follikels, die zu einem steten Anwachsen der Follikelgröße führt [*Beyer and Meyer-Hermann*, 2007a]. Verschiedene Mechanismen zur negativen Regulation der Follikelgröße sind untersucht worden (u.a. CXCR5-Internalisierung). Als einzige verbleibende Möglichkeit, und damit zweite wesentliche Vorhersage des Modells, stellt sich eine negative Regulation heraus, die direkt die Generierung der FDCs beeinflusst. Das verantwortliche Signalmolekül muss diffundieren und hat eine recht kurze Lebensdauer von etwa 10 min bevor es entweder inaktiviert oder von anderen Zellen aufgenommen wird. Als Quelle des Signals kommen FDCs und folikuläre B-Zellen in Frage – auch wenn prinzipiell einige andere Quellen möglich, die jedoch nicht das Modellverhalten beeinflussen und daher so nicht unterscheidbar sind. Eine kritische Eigenschaft dieses negativ regulierenden Faktors ist, dass er die Differenzierung der FDCs aus ihren Vorläuferzellen inhibiert, jedoch keinen Einfluss auf bestehende FDCs hat. Die Konsequenz dieses Verhaltens des Signals ist, dass das Follikel aus zwei Zonen besteht. Am Rand des (durch B-Zellen definierten) Follikels befinden sich B-Zellen und lymphatisches Endothel aber keine FDCs, während das Zentrum FDCs enthält und frei von lymphatischen Endothel ist. Anhand bisheriger experimenteller Befunde über die Lokalisation des Endothels kann noch keine Aussage über die Richtigkeit dieser Vorhersage getroffen werden.

Die vollständige Genese der sekundären lymphatische Gewebe einschließlich der T-Zone und Gefäße benötigt eine Korrelation zwischen Gefäßen (Blutgefäße und lymphatisches Endothel) und den stromalen Zellen der T-Zone. Diese stromalen Zellen entwickeln sich im Modell durch Kontakt mit Lymphozyten aus stromalen Vorläuferzellen, die keine Chemokine produzieren. Dies erzeugt die korrekte Sequenz der Organogenese sekundärer lymphatischer Gewebe. Ausgehend von einem unorganisierten Zustand entsteht eine Zwischenstufe in der die B-Zellen eine Schale um die T-Zone bilden (in einem Schnitt als B-Zell-Ring sichtbar). In der B-Zell-Schale entstehen kurz darauf FDCs, die zu einer Symmetriebrechung führen. Dadurch verteilen sich die B-Zellen nicht mehr homogen um die T-Zone sondern formen langsam ein Follikel. Das Follikel wächst weiter bis die oben diskutierte negative Regulation der FDCs greift und die Follikelgröße stabilisiert. Ein wesentliches Ergebnis aus diesen Simulationen ist, dass die Schale/der Ring von B-Zellen um die T-Zone durch die Biomechanik der Zellmigration beeinflusst wird. In der Hauptsache sind die stärkeren Migrationskräfte der T-Zellen im Vergleich zu den B-Zellen verantwortlich, das letztere aus der T-Zone "herausgepresst" werden. Mit anderen Worten die Tatsache, dass T-Zellen sich schneller bewegen als B-Zellen und nicht differentielle Adhäsion oder verschiedene Chemokinrezeptor-Level sind für den B-Zell-Ring während der Organogenese verantwortlich.

Über die vorliegende Arbeit hinausgehend stellen die gewonnenen Erkenntnisse eine Basis für die Untersuchung ähnlich strukturierter Probleme der Biologie dar. Insbesondere die Mechanismen der

Organogenese können auf einen größeren Problemkreis angewendet werden. Denkbar sind Simulationen von Lymphozyten während Entzündungsreaktionen oder die Remodellierung von Knochensubstanz. Das Modell des primären lymphoiden Follikels selbst bildet eine geeignete Grundlage, um die Simulation einer Keimzentrumsreaktion durchzuführen und bestehende Modelle [*Beyer et al.*, 2002; *Meyer-Hermann and Beyer*, 2003; *Meyer-Hermann et al.*, 2001, 2006; *Meyer-Hermann and Maini*, 2005a] in eine physiologischen Umgebung einzubetten. Desweiteren kann die Entwicklung ektopischer Keimzentren im Verlauf einiger Immunerkrankungen (Abschnitt 2.6) auf dem Modell der Genese des primären lymphoiden Follikels aufbauen.

Abstract

Primary lymphoid follicles are structures which are important for adaptive immune responses in mammals. Within the follicles follicular dendritic cells (FDC) are maintained by constant stimuli provided by B cells. It is thought that the FDC are important for immune response. It is of interest to know how lymphoid follicles are regulated in order to understand their role in various autoimmune diseases in which these follicles are created ectopically. With the help of a tissue simulation relying on an agent-based cell model on top of a regular triangulation various scenarios suggested by the available experimental data have been investigated. In order to cope with the complexity in the simulation of immune tissue the regular triangulation has been implemented for the use on parallel computers. The algorithms for kinetic and dynamic regular triangulation have been created newly. Also the cell model underlying the simulation has been designed newly in many aspects. The simulations allowed to identify common factors that regulate the formation of lymphoid follicles normally during organogenesis in development and lymphneogenesis in the course of diseases. The generation of FDC from local stromal populations under the influence of B cell aggregates is shown to be possible with the given experimental parameters. The sequence of the organogenesis and lymphneogenesis can be described with regard to the morphology of the B and T zone. Tests for the stability of the primary lymphoid follicle system constraints the regulation of the B cell efflux. The required lymphatic vessels around the lymphoid follicle are shown to be negatively correlated with the FDC network. Moreover it is shown that the adjacent T zone consisting of its own stromal population and T cells has similar regulation principles. This easily explains the intermediate ring of B cells found around the T zone during development and certain signaling molecule deficiencies. A major result of this thesis is that the generation of FDC needs negative regulation while a number of other possible mechanisms is incompatible with the available experimental data. Moreover the observed microanatomy was brought into a functional relationship with data on the cellular level finally culminating in the proposal of new experiments that shed light on the dynamics of the primary lymphoid follicle. One conclusion is that the FDC directly or indirectly influence the angiogenesis and lymphangiogenesis processes in secondary lymphoid tissues. The work presented here may help to guide experiments with the help of computers in order to reduce the amount of experiments and design them in a way to maximize the amount of information about biological systems.

Contents

Chapter 1

Introduction and Motivation

Biology is still to a large extent an experimental and descriptive science. During recent years large efforts have been undertaken to introduce theoretical models in biology. One of the goals is to guide experiments by theoretical work in order to reduce the number of experiments and to increases their conclusiveness. Another very important aspect is to connect snapshots of the state of a biological system to its underlying dynamics by models and simulations. The thesis presented here is taking a step in this direction with an interdisciplinary approach that combines Physics, Informatics, and Biology. The organogenesis of lymphoid follicles is investigated using simulations based on a theoretical model of lymphoid tissue. The goal is to create a comprehensive picture of the experimental data and propose experiments which can shed light on the proposed mechanisms that are involved in the formation of lymphoid follicles during organogenesis and lymphneogenesis.

1.1   The immune system

The immune system is a complex network of molecules, cells, and tissues that protects an organism from pathogenic attacks [*Janeway and Travers*, 1997]. The majority of the immune function is provided by barriers – like the skin – that prevent pathogens from entering critical sites of the organism. The next line of defense in most multicellular organisms is the innate immune system. The innate part is entirely genetically encoded and provides more or less predetermined reactions to certain classes of pathogens. In addition vertebrates are equipped with an adaptive immune system. The capabilities of this system depend on the life history of the individual. It is set up around the birth of the organism by combinatorial variation of antigen receptor molecules. The repertoire of these molecules adapts to the specific pathogen load that the individual experiences throughout its life. The class of mammals has additional structures for the adaptive immune system which are the secondary lymphoid tissues. These tissues contain mainly B and T cells and numerous other immune cells in lower numbers. The co-localization of cells with immune function may help to increase the interaction frequency and therefore makes the immune reaction more efficient. Secondary lymphoid tissues contain subcompartments that are thought to host cells required for certain specific interactions of the adaptive immune system. One of these subcompartments is the primary lymphoid follicle.

1.2   The primary lymphoid follicle

The primary lymphoid follicle is a spherical structure of several hundred micrometer diameter. It can be found in healthy secondary lymphoid tissues like spleen, tonsils, lymph nodes, and Peyer's patches [*Fu and Chaplin*, 1999]. It is composed mainly of two cell types with different properties. One cell type are native B cells which are rather fast and motile cells of mostly spherical shape. These cells constantly enter and leave the secondary lymphoid tissue and consequently the primary lymphoid follicle. The second cell type are follicular dendritic cells (FDC). These cells are sessile and show an extensive branching that results in a tightly connected network of FDC residing in the follicle. FDC exhibit a dynamics in terms of their differentiation from their yet unknown progenitor cells. FDC are known to be generated upon stimuli produced by the B cells. They disappear when such signals are missing or blocked by experimental treatment. On the contrary, providing these signals outside secondary lymphoid tissues, either in the course of diseases or artifically by specific experimental conditions, FDC and lymphoid follicles can be generated ectopically.

The function of the primary lymphoid follicle is to maintain FDC network which has a unique function in the immune response. If some antigen is encountered it will be presented in its naive form by the FDC to B cells. The B cells start a germinal center reaction that converts the primary lymphoid follicle into a secondary lymphoid follicle with a different substructure [*MacLennan*, 1994; *McHeyzer-Williams et al.*, 2001; *Tarlinton*, 1998]. These structures are thought to be related to the function of the germinal center to adapt the antibody produced by B cells to the antigen. This results in the production of higher affinity antibody secreted by plasma B cells – a process known as affinity maturation. Additionally, most of the memory B cells can be shown to be produced in the course of a germinal center reaction. Thus the primary follicle is a precursor structure that is needed to perform the 'adaptive' action of the humoral immune response of the adaptive immune system.

1.3   Aim of this study

The central question inspiring this work is which mechanism is able to regulate the size of the follicle. It is worth to note that the size of the lymphoid follicles is practically independent of the species. The typical size of several hundred micrometer does not scale with the size of the secondary lymphoid tissue and remains almost constant from animals ranging from mice and rat to sheep and horses (see Table 2.1). The crucial difference to other systems that attracted the attention of theoretical biology investigating tissue organization and pattern formation is that the homeostasis of this system is not governed by a balance of growth and death of cells but by the migration of naive B cells and the differentiation of FDC. Even more striking the process of organogenesis can be delayed in experiment and artifically induced in tissues that normally do not develop primary lymphoid follicle ((Sec. 2.2.2) and (Sec. 2.5)). This suggests that the regulating mechanism is not based on the principles that determine the pattern formation for the organs during embryogenesis. It is likely that a local excitation process and a long-ranged inhibitory process [*Meinhardt*, 1982] account for the size regulation of the follicles. The subject of this study is to identify and test several mechanisms for the excitatory and inhibitory process qualitatively and quantitatively. The simulated mechanisms will be accompanied

by proposals of experiments that can give further insight into the formation of primary lymphoid follicles and validate the underlying model.

Finally, understanding the primary lymphoid follicle formation provides information on guiding principles in organogenesis and insight into the function of the immune system. The interplay of immune cells with stromal cells during organogenesis is critical to understand the lymphneogenesis of follicles and germinal center at sites of inflammation. This may help in the treatment of several autoimmune diseases and other diseases that can lead to ectopic follicle formation, i.e. the *de novo* generation of lymphoid tissue.

1.4   Methods used and developed in this work

The scope of this work is to simulate the formation of the primary lymphoid follicle using an agent-based tissue-simulation. The model is a multiscale model which consists of three levels that represent the interactions between cells. The first level deals with internal states of cells. These can be the direction of migration or the substances a cell produces. The second level are contact interactions. These are predominantly mechanical interactions due to elastic collisions, viscous forces from the surrounding, and forces generated by migrating cells. The contact interaction relies on the definition of cell contact based on regular triangulations [*Okabe et al.*, 2000]. The regular triangulation is an extension of the common Delaunay triangulation that can be used to define a neighborhood topology for spheres. The advantage of the regular triangulation compared to the normal Delaunay triangulation is that it can account for the different sizes of the cells in the primary lymphoid follicle system which allows to define an area of influence where a cell can make contact to other cells depending on its size. The mechanical description of cells on the second level is approximated by adhesive elastic spheres. The second level also accounts for the exchange of cell membrane bound signals that are coupled to the contact area between two cells. The contact surface is derived from the underlying regular triangulation via the dual graph known as Voronoi tessellation [*Okabe et al.*, 2000]. The third level of cell interaction takes into account long range interactions via diffusive substances. All these interaction levels couple to each other via the internal states which are influenced by contact interactions and the influence of diffusible substances.

The typical cell number in the follicle ranges from 10^4 to 10^5 cells ([*Liu et al.*, 1991] and estimate from diameter see (Sec. 2.2.1)). In order to deal with the large number of cells, algorithms have been developed to deal with regular triangulations on parallel computer architectures providing the necessary computing power. As a product of this work an implementation of parallel executable triangulator algorithms allowing for dynamic and kinetic changes to the regular triangulation has been created [*Beyer et al.*, 2005]. This allows to simulate the movement, growth, and death of cells by moving, inserting, and removing the corresponding vertices in the regular triangulation. Moreover, the algorithms developed and implemented throughout this work are in general feasible to be used for any particle simulation problem with large numbers of constituents that demand the usage of parallel computers. The usage of the Message Passing Interface standard (MPI) allows to use the program on most parallel architecture available nowadays.

1.5   Results

With the help of the performed simulations several boundary conditions could be derived governing the formation of primary lymphoid follicles. The model leads to a coherent description a large set of experiments and the proposal of new experiments that are targeted to a deeper understanding of the system using present experimental methods. An important result is that the microanatomy found in secondary lymphoid tissue is important to understand the size regulation of primary lymphoid follicles. The simulations point out the role of the efferent lymphatic vessels in shaping the lymphoid follicle and predicts that the lymphoid follicle is composed of two areas which are tightly connected: One contains only FDC and B cells. This area is engulfed by the second area made up by lymphatic endothelium and B cells. That implies that the vessel formation is inversely coupled to the generation of FDC suggesting that lymphangiogenic factors play a role in the primary lymphoid follicle system. Other mechanisms like the internalization of chemokine receptors and chemotaxis towards the lymphatic endothelium are shown to be irrelevant, to change the morphology, or even to destabilize the follicles.

The generation of FDC has been shown to be organized in such a way that rather small aggregates of B cells or specialized tissue inducer cells can initiate the formation of FDC to start the formation primary lymphoid follicle. This challenges the idea that a positive feedback loop acting between FDC and B cells is required for the follicle formation in the spleen [*Ansel et al.*, 2000] . In contrast it is suggested that the feedback loop is not relevant to understand the formation of primary lymphoid follicle. The results do not rule out the possibility of more complex interactions. However, they should then depend on a third player which has not been found up to now. Strikingly, a negative regulation of FDC generation is required to explain stable follicle sizes. It is suggested that the mediating molecule is diffusive and has a rather short lifetime in the order of 10 minutes. It may be produced by FDC directly or indirectly by B cells that are located in the follicles.

Regarding the environment of the primary lymphoid follicle it has been shown in the simulations that the adjacent T zone and the follicle can organize themselves without imposing a pre-structure. In order to do so a dynamics for the T zone is required. It is demonstrated that an interaction that is similar to the processes in the primary lymphoid follicle is sufficient to explain the formation of the T zone. The basic difference to the situation in the follicle is that T zone stroma and lymphatic endothelium are positively correlated implying that the T zones indirectly promote the lymphangiogenesis in this area. A similar mechanism should organize blood vessels in the T zone as the show an almost identical distribution compared to the lymphatic endothelium.

Overall the presented model framework is able to explain the guiding mechanisms behind the formation of primary lymphoid follicles and secondary lymphoid tissue. The new findings regarding the correlation of follicle formation and the structure of lymphatic vessels and the negative regulation of FDC generation may inspire new experiments to get a deeper insight in the organogenesis of secondary lymphoid tissue.

Chapter 2

The Primary Lymphoid Follicle

The goal of this chapter is to provide the context the primary lymphoid follicle is hosted in. The available experimental data on the primary lymphoid follicle (PLF) [1] is reviewed with focus on the correlation between signaling molecules and microanatomy of the PLF and adjacent structures. The differences and common basis of the PLF situated in different contexts is evaluated.

2.1 Overview of the Immune System

This section provides a general introduction to the location, organization, and function of the PLF in the immune system (IS). The relevant properties of the IS are briefly reviewed at first.

The IS is an ancient development in evolution [*Beutler*, 2004]. Many components of the IS can be found in insects, plants, fungi, and vertebrates. There exist two branches of the IS known as *adaptive immune system* (AIS) and *innate immune system* (IIS). The evolutionary older branch is the IIS which is still present in vertebrates and serves as the first line of defense against pathogens inside an organism. Its main executioner cells are granulocytes (neutrophils, eosinophils, and basophils) and macrophages that are programmed to attack and also phagocytose pathogens. The activation and response of the IIS is genetically determined and does not directly depend on infections previously encountered by the organism. Other IIS defense mechanisms are the production of protective molecules. Many of them are targeted to kill specific pathogens.

The focus of this work is the AIS [*Janeway and Travers*, 1997]. The AIS can be found in vertebrates – with the exception of a few very ancient species which show no or only incomplete AIS [*Du Pasquier*, 2005; *Kasahara et al.*, 2004]. In contrast to the IIS the performance of the AIS is not solely germline encoded and depends on the life history of the individual. There are two major types of cells providing the function of the AIS: T and B lymphocytes. Dendritic cells (DC) are another set of cells that are important for the function of the AIS by stimulating lymphocytes. Both lymphocyte types develop from blood stem cells. In mammals the process is taking place mostly in the bone marrow or the fetal liver before birth [*Janeway and Travers*, 1997]. In other species the cells are generated in other organs

---

[1] A list of abbreviations can be found on page 235.

like the liver in reptiles, amphibians, and some teleost fish, the kidneys in teleost fish, or the bursa of Fabricius in birds [*Zon*, 1995].

In contrast to the IIS the lymphocyte repertoire is diverse in the sense that lymphocytes form subsets which are composed of small populations of cells that are specific for a different set of antigens (Ag). This is achieved by the combinatorial assembly of the B cell receptor (BCR) of B cells and T cell receptor (TCR) of T cells during lymphocyte development. The major functional part of both receptors are immunoglobulins (Ig). These Ig are encoded by several genetic loci which can be combined and further modified to achieve a large number of different Ig from a relative low number of genes. The detailed process differs in the various species but basically the three Ig components termed V (variable), D (diverse), and J (joining) which are present in a number of variants each, are fused together. However, there are mammalian species like cows, sheep, pigs, and horses [*Griebel and Hein*, 1996; *Lanning et al.*, 2005; *Makala et al.*, 2002-2003] which probably use another strategy to diversify their lymphocyte repertoire. This is based on the observation that somatic hypermutation of Ig genes occurs independently of Ag in the ileal Peyers's patches of sheep (see (Sec. 2.1.5)). From this and other data it is assumed that the rearrangement of V, D, and J is very limited in these species generating a low combinatorial diversity of Ig which is then modified by somatic hypermutation and gene-conversion mechanisms to generate the diversity of Ig repertoire [*Eason et al.*, 2004; *Lanning et al.*, 2005]. Non-mammalian species can use yet other mechanisms like receptor editing and probably unidentified mechanisms to diversify their Ig repertoire [*Eason et al.*, 2004]. As the focus of this work is on SLT and lymphoid follicles which appear exclusively in mammals and birds [*Du Pasquier*, 2005] other vertebrate groups are not considered.

2.1.1 Primary lymphoid tissue

All cells of the immune system – i.e. leukocytes – are generated in the primary lymphoid tissue by hematopoietic stem cells (Fig. 2.1). The cells of the IIS like monocytes (macrophage progenitor), granulocytes, and dendritic cells are generated by the myeloid lineage that also generates the erythrocytes (red blood cells) and the megakaryocytes (platelet producer). The lymphoid lineage is the progenitor for lymphocytes, B and T lymphocytes, natural killer cells, and natural killer T cells. B lymphocytes (B cells) rearrange their Ig genes in the primary lymphoid tissue to form a functional BCR. B cells leave the tissue and migrate into the blood as matured B cells. Pro-T cells are generated in the bone marrow and then home to the thymus via the blood stream to complete their maturation program which includes the rearrangement of their Ig genes to form the TCR. The thymus itself is another primary lymphoid organ in which hematopoiesis does not occur, in contrast to the bone marrow. There are also T cells that do not need to mature in the thymus. However, these cells comprise only a minor fraction of lymphocytes and are not considered in this work. The same holds for natural killer and natural killer T cells.

The next four sections cover the *secondary lymphoid organs* in which the immune responses of the AIS are initiated. The tissue of these organs consists to a high degree of circulating lymphocytes that exit the blood stream. Within the SLT the lymphocytes can encounter Ag to initiate an immune response. Usually lymphocytes leave secondary lymphoid organs by entering the lymphatic system –
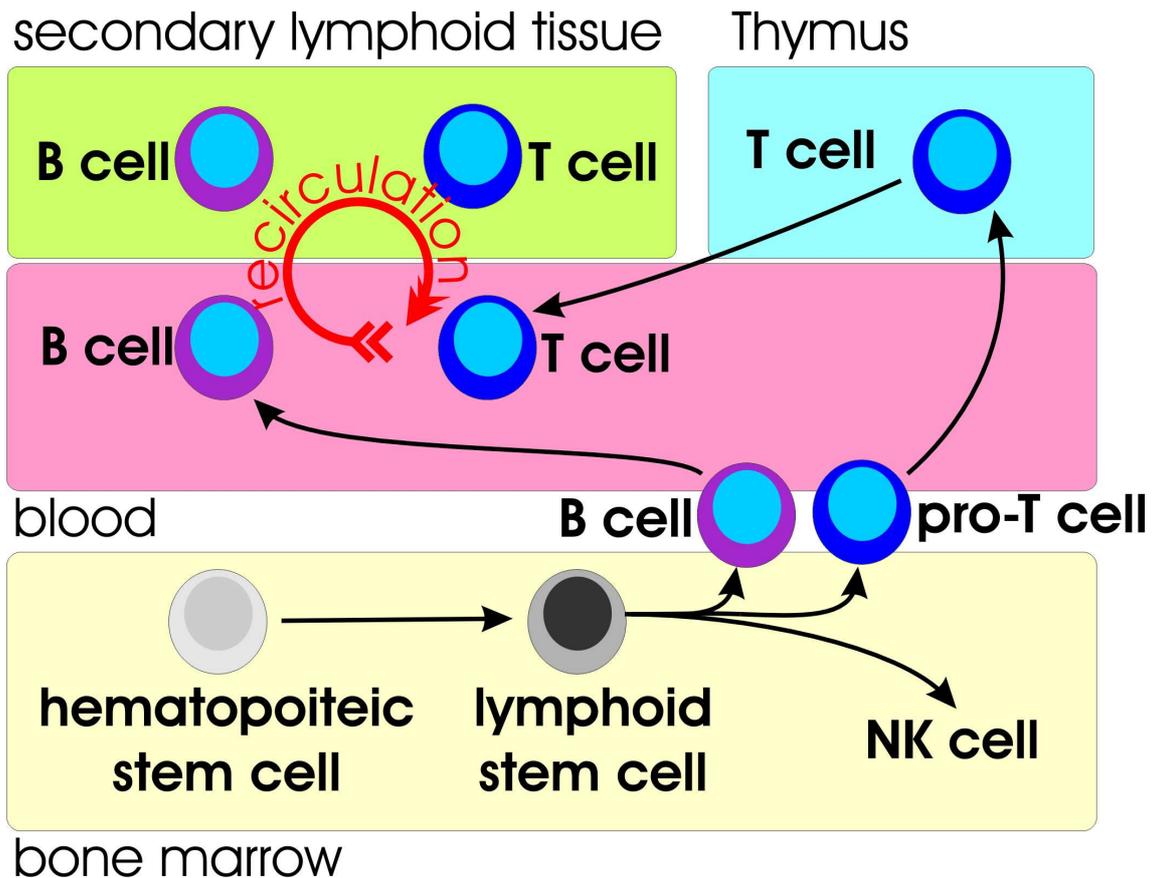
Figure 2.1: The circulation of lymphocytes between lymphoid tissues. B and T lymphocytes are generated in the bone marrow. B cells leave the bone marrow in a mature form while pro-T cells circulated through the blood to enter the thymus where they complete their maturation. The matured lymphocytes then circulate between the blood stream and SLT throughout their life time.

a second fluid transporting system, different from the vascular system – and reenter the blood stream via the thoracic duct (Fig. 2.2).

2.1.2 Secondary lymphoid tissue and the germinal center reaction

In this study the structure of interest is the primary lymphoid follicle (PLF). It is composed of follicular dendritic cells (FDC) and circulating B cells. The PLF can be found in every secondary lymphoid organ which are described in more detail in the following three sections. In this section a brief description of the major function of a PLF during an immune reaction will be given. The details of the PLF structure are discussed in (Sec. 2.2).

Upon stimulation with T-dependent Ag a germinal center reaction (GCR) is initiated during which a PLF is converted into a secondary lymphoid follicle (SLF) that harbors a germinal center (GC) [*Liu and Arpin*, 1997; *MacLennan*, 1994; *Tarlinton*, 1998]. These GC show a more developed structure than the PLF which can be identified on the basis of several B cell subtypes present in the GC. The classical GC has a dark zone composed of heavily proliferating B blasts (centroblasts). The adjacent
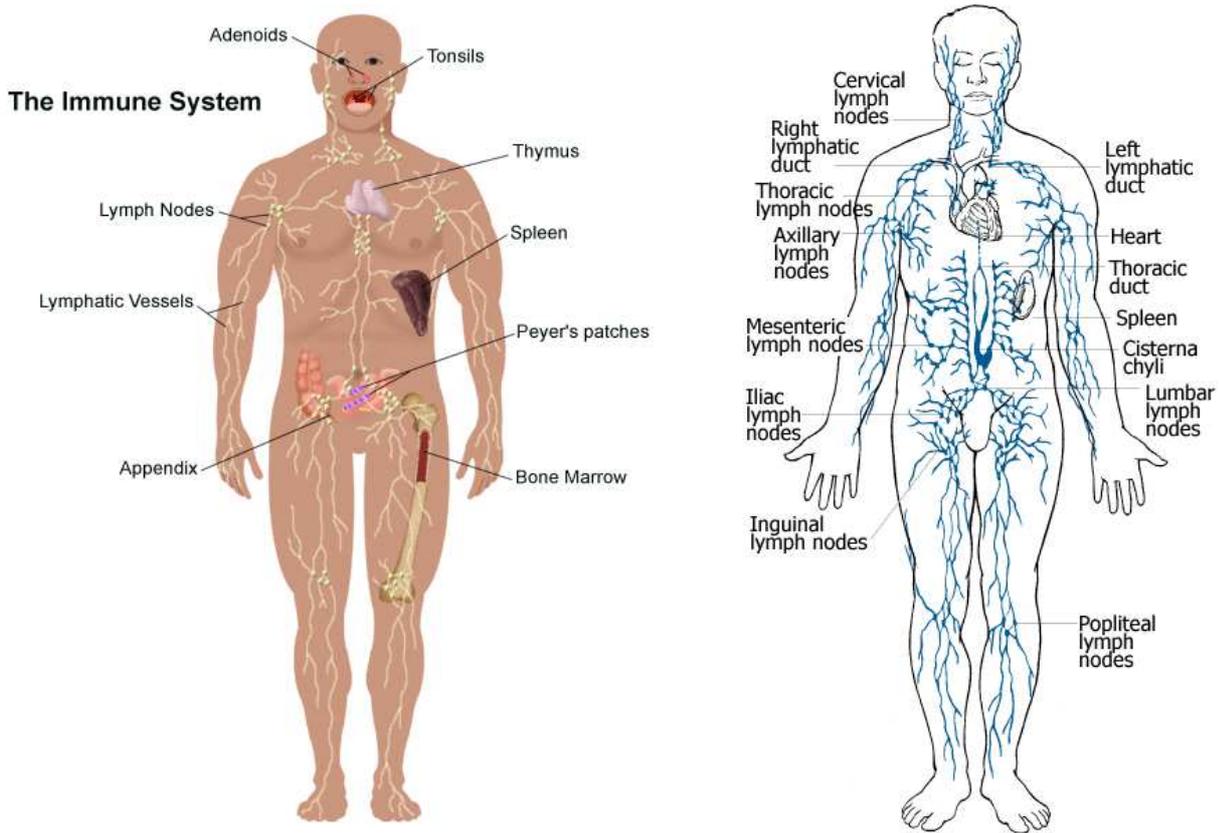
Figure 2.2: Primary and secondary lymphoid tissues of the human body. The lymph nodes are represented in groups like cervical (neck region), sacral (close to lower spine), mesenteric (close to the guts), inguinal (inner leg region), axillary and further groups. The lymphatic ducts close the circulation of lymphocytes providing them a route to go from the lymph fluid into the blood stream.

Source of left image: `http://www.ohsuhealth.com/images/gs/ei_0255.gif`

Source of right image: `http://home.thirdage.com/friendship/dreamchaser22/ lymphnodes.html`

light zone is in general crescent-shaped and covers one half of the dark zone. It is filled with smaller non-proliferating B cells termed centrocytes. The light zone itself is subdivided in a basal and apical light zone with the latter one being more distant from the dark zone and containing an additional T cell population. The GC is surrounded by the mantle zone which is in many cases asymmetrically covering the apical light zone only. The mantle zone is supposed to be the deformed PLF consisting of FDC and circulating naive B cells which have been pushed aside by the proliferative activity going on in the GC. Mantle zone and GC together form the SLF. The compartments of the GC are assumed to reflect the function that is executed by the B cells in this area. The centroblasts in the dark zone are proliferating and performing the somatic hypermutation of their Ig genes thus generating variations of their BCR. They differentiate then to centrocytes that move up to the basal light zone. The centrocytes are prone to die by apoptosis which can be stopped when centrocytes get into intimate contact with the Ag presenting FDC in the light zone. If the hypermutated BCR of the centrocytes recognizes the Ag, the centrocytes are temporarily rescued from apoptosis, i.e. the centrocytes are positively selected. If the recognition step fails the cells will undergo apoptosis and the remnants are removed by specialized macrophages sitting in the basal light zone. The positively selected centrocyte will proceed further to the apical light zone where T cells may perform a negative selection preventing the generation of

auto-antibodies. Furthermore, the T cells in this area provide differentiation signals that lead to the differentiation of the centrocyte into an antibody-producing plasma B cell or into a memory B cell. Theoretical [*Meyer-Hermann et al.*, 2006] as well as recent experimental studies [*Allen et al.*, 2007] point out the importance of limiting T cell help for the success of affinity maturation during the GCR. The formation of the GC is only temporary. The GCR stalls after a few weeks and the SLF transforms back into a PLF. The whole GCR leads to *affinity maturation* of BCR, which is the gradual increase of the binding of the antibody to the Ag presented on the FDC. In this context the function of the PLF is supposed to be the maintenance of the FDC network. The presence of the FDC before the onset of the GC reaction may allow the immune system to respond to lower Ag concentrations [*Kosco-Vilbois*, 2003]. Another function may be the preservation of the Ag in its native form for a long time possibly to induce protective memory [*Liu and Arpin*, 1997; *Liu et al.*, 1996; *Szakal et al.*, 1988]. Moreover, Ag is transported to the FDC in order to allow the naive B cells in the PLF to screen for pathogens [*Ferguson et al.*, 2004; *Gretz et al.*, 1996; *MacLennan*, 1994; *Szakal et al.*, 1988]. Thus the PLF represents an Ag filter within the lymphoid tissue structure that is part of the immune system in an inactive but 'ready for action' state.

2.1.3 Function and structure of the spleen

The spleen is the oldest known secondary lymphoid organ [*Du Pasquier*, 2005]. It can be found in basically all vertebrate species including its function in the immune system. The spleen has two morphologically and functionally different compartments: *red* and *white pulp* (Fig. 2.3) [*Janeway and Travers*, 1997]. The red pulp is responsible for the removal of senescent red blood cells and has no known direct impact on the immune function which is provided by the white pulp. The white pulp is formed around arterioles where lymphocytes are accumulating in an inner shell – the periarteriolar lymphoid sheath (PALS) – composed of DC and T cells mainly, and an outer shell enriched for B cells forming a B cell corona. The B cells are organized in PLF. In contrast to the other organs described below the spleen contains an additional B cell compartment separating the PLF from the red pulp which is the marginal zone. The B cells in this area are not circulating and are phenotypically different from the B cells found in the B cell follicles [*Pillai et al.*, 2005]. The B cell rich and T cell rich areas are called *B zone* and *T zone*, respectively. The basic structure of the splenic white pulp is also found in the other secondary lymphoid organs discussed below.

2.1.4 Function and structure of lymph nodes

Lymph nodes (LN) are only found in mammalian species [*Du Pasquier*, 2005]. They are small bags that extent from the lymphatic circulation [*Janeway and Travers*, 1997]. Lymph nodes contain additional blood vessels through which lymphocytes enter the lymphoid tissue. At the LN *afferent* lymphatic vessels terminate that transport body fluid (*lymph*) from the tissues. The lymph also contains cells like DC that transport Ag to the LN. The main function of LN is to filter the lymph for Ag and bring them together with lymphocytes from the blood stream.

The LN microarchitecture consists of three zones: cortex, paracortex, and medulla (Fig. 2.4). The
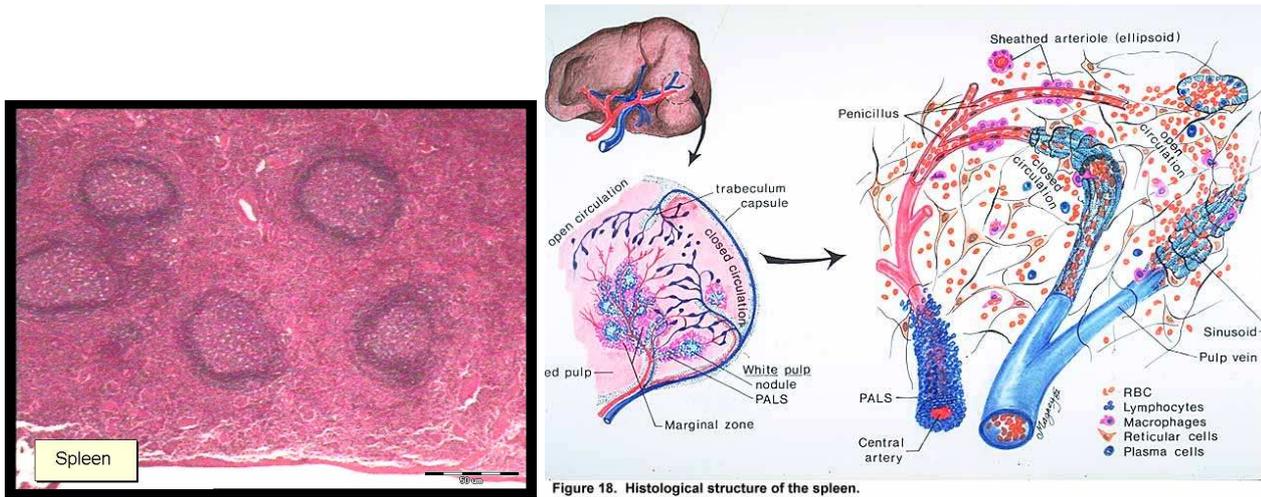
Figure 2.3: Micrograph of human splenic tissue stained with hematoxylin (left panel). The oval structures are lymphoid follicles all of them in the SLF stage with the dark rim representing the mantle zone and the brighter center the germinal center. The right panel shows a schematic representation of the spleen structures. The term nodule refers to the term lymphoid follicle used throughout this work.

Source of left image: `http://www.technion.ac.il/~mdcourse/274203/slides/Lymphatic_Organs/19-Spleen.jpg`

Source of right image: `http://www.mednote.co.kr/images/spleen.jpg`

cortex is enriched for B cells that form follicles (Sec. 2.2) similar to those found in the spleen. The paracortex contains mostly T cells and DC and therefore makes up the T zone of LN. Also the majority of blood vessels is situated in this area. The venules in the T zone come in a specialized form which in most species is visible by a layer of thick endothelial cells with a cuboid shape. Therefore these venules are called *high endothelial venules* (HEV) [*Yamaguchi and Schoefl*, 1983]. Lymphocytes transmigrate from the blood stream through the HEV to enter the lymphoid tissues. In some exceptional cases lymphocytes may also leave via HEV as it is observed in pigs [*Binns and Licence*, 1990]. The medulla of the LN contains all cell types and a high amount of lymphatic endothelium. The lymphocytes form finger-like *medullary cords* in a labyrinthic structure of lymphatic sinuses [*von Andrian and Mempel*, 2003; *Belisle and Sainte-Marie*, 1981d]. The latter one increase in density towards one side of the LN culminating in the *hilum* where lymphocytes finally enter the *efferent* lymphatic vessel to continue their circulation. Together the LN has a similar generic structure as the white pulp of the spleen but has additional substructures and a more sophisticated transport system for cells.

2.1.5   Other secondary lymphoid tissue

There are various other SLT which exhibit less organization compared to LN and spleen [*Janeway and Travers*, 1997]. These tissues form beneath endothelial tissues at various places. The largest one are the *Peyer's patches* (PP) – named after the swiss physician Johann Conrad Peyer – that form several long and flat lymphoid tissues along the walls of the small intestine. They are part of the *gut-associated lymphoid tissues* (GALT) to which also the appendix belongs. All tissues of this type are summarized under the term *mucosa-associated lymphoid tissue* (MALT). Other examples for MALT
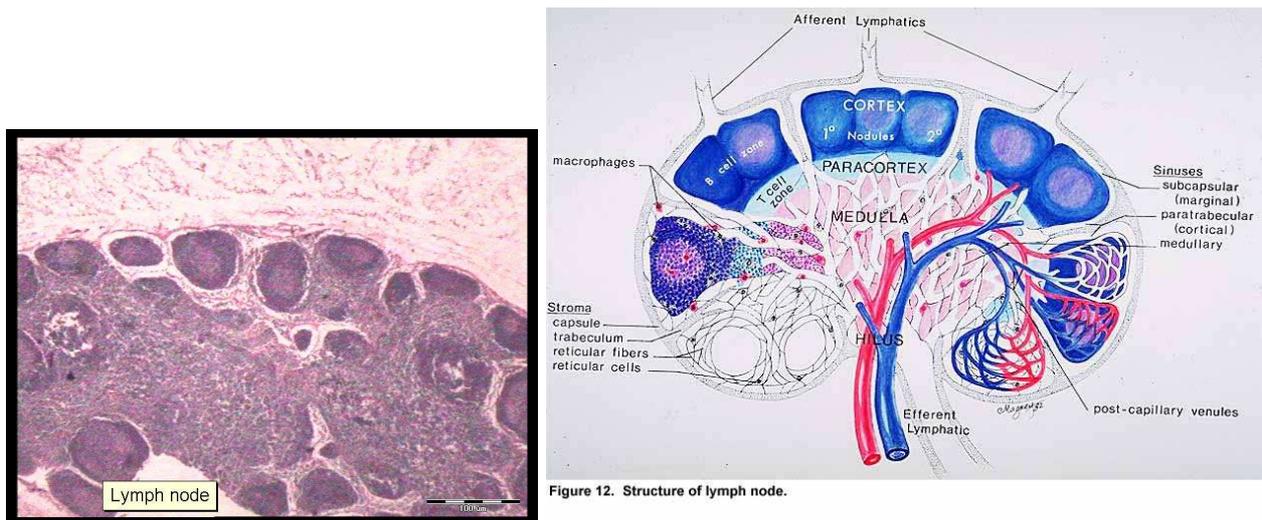
Figure 2.4: Micrograph of a human lymph node staining with hematoxylin (left). The round structures are lymphoid follicles. Follicles with a bright center are SLF with a GC inside. The right panel shows a schematic view of a LN. The termini 1 and 2 nodules refer to PLF and SLF, respectively. Post-capillary venules are in many cases specialized into HEV (not shown in the picture).

Source of left image: `http://www.technion.ac.il/~mdcourse/274203/slides/Lymphatic_Organs/6-Lymph node.jpg`

Source of right image: `http://www.mednote.co.kr/images/lymphnode.jpg`

are the tonsils providing immune functions that protect against invaders entering through the mucous membranes of the mouth.

The characteristic structure of MALT is a specialized epithelium that transports Ag via so-called M-cells to an assembly of B cell follicles situated below the epithelium (Fig. 2.5) [*Fukuyama et al.*, 2002; *Pabst et al.*, 2005; *Yamanaka et al.*, 2001]. These follicles are surrounded on one side by T cells forming the T zone of MALT. Similar to LN, lymphocytes enter the MALT via HEV in the T zone. To complete the analogy, efferent lymphatic vessels (ELV) in the vicinity collect the lymphocytes and transport them back to the thoracic duct [*Janeway and Travers*, 1997].

The PP are collections of follicles in the mucosa of the small intestine. There exists also isolated lymphoid follicles (ILF) in the intestine [*McDonald et al.*, 2005; *Pabst et al.*, 2005]. These are different in the cellular composition compared to PP or LN as they contain about one fourth non-B, non-T cells which are not present in the other SLT. Those non-lymphocyte immune cell contributions in SLT will not be considered in this thesis.

Peyer's patches as primary lymphoid tissue   The characterization of some GALT to be SLT is not clear. There is some evidence that the function of these lymphoid tissues is of primary nature. The question remains if those follicles are based on the same organization principles as in PP with clear secondary function.

Some of the PP in species like cows, sheep, and pigs may belong to primary lymphoid tissue after birth [*Griebel and Hein*, 1996; *Makala et al.*, 2002-2003; *Nicander et al.*, 1991]. In these animals a large continuous PP extends along the terminal end of the intestine (ileum) around birth and involutes
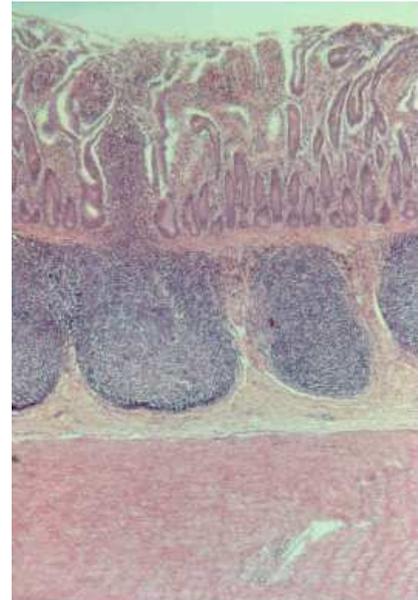
Figure 2.5: Micrograph of a Peyer's patch from a cat stained with hematoxylin. The gut lumen is in the upper part of the image. The folded structure is the epithelium. Follicles show up as blue roundish structures. The extension of the large follicle on the left into the epithelium is the specialized epithelium associated with the follicle where M-cells are located.
Source of image: `http://oregonstate.edu/~hanba/Projector Slides/`
`Projector Slides/Duodenum Peyers Patch Type II Lymph Nodules Cat-1.jpg`

in most of the species early in life like the thymus does [*Janeway and Travers*, 1997]. Recent work indicates that the maturation of B cells and possibly also their generation can happen in ileal PP as in the bursa of Fabricius in birds whereas the jejunal PP (beginning of the small intestine) is similar to a normal SLT [*Griebel and Hein*, 1996; *Makala et al.*, 2002-2003; *Nicander et al.*, 1991]. The PP in the ileum of sheep have been shown to contain B cells that somatically hypermutate their Ig genes independent of Ag – this process occurs even before birth [*Griebel and Hein*, 1996]. These follicles seem to build up the B cell repertoire in some species. This process may be unspecifically initiated by the intestinal microflora [*Yamanaka et al.*, 2003] and is independent of T cell help [*Lanning et al.*, 2005]. Furthermore, it seems that these PP structures are converted gradually into SLT.

The presumed primary lymphoid tissue function correlates with prenatal maturation of a large single ileal PP [*Griebel and Hein*, 1996; *Makala et al.*, 2002-2003; *Nicander et al.*, 1991]. In contrast, animals that do not have this PP type, exhibit randomly distributed spots of PP tissue along the ileum which matures postnatally. The PP in the jejunum develops after birth in all species [*Griebel and Hein*, 1996; *Makala et al.*, 2002-2003]. There is also a morphologic difference between the two PP types. The ileal follicles developing prenatally have basically no T zone between large follicles. Instead the follicles are separated by loose connective tissue. The FDC inside the follicles are morphologically distinct from FDC seen in classical GC albeit there are kinds of dark and light zone which – in contrast to normal mammalian GC – are concentrically organized with a high mitotic rate in the outer region much like in GC of chicken [*Griebel and Hein*, 1996; *Makala et al.*, 2002-2003; *Olah and Glick*, 1979; *Romppanen*, 1981; *Yasuda et al.*, 2003, 1998]. When these ileal PP are exposed to foreign Ag the morphology develops into classical GC [*Griebel and Hein*, 1996] while their primary function seem to depend on the microbial flora [*Yamanaka et al.*, 2003]. Also mature lymphocytes seem not to circulate through the prenatally developing ileal PP before they convert into SLT indicating once more that this PP may function as primary lymphoid tissue [*Griebel and Hein*, 1996]. Note, that there exist also B cell-follicles in the mucosa of the large intestine. However, those are more or less ignored in the literature and there is not much known about structure and function of these follicles [*Griebel and Hein*, 1996]. Thus they will not be covered in this thesis. However, it is assumed

that the organogenesis of the lymphoid follicles with primary function follows the same principles as those which belong to SLT right form the beginning except that lymphocyte migration is likely to be regulated in a different way [*Griebel and Hein*, 1996].

Appendix as primary lymphoid tissue   In rabbits a part of lymphoid tissue with primary function is located in the appendix [*Dasso et al.*, 2000]. Comparison with the avian bursa and human appendix show that the follicles in the rabbit appendix are much like the ones of chicken – including the fact that gene conversion happens together with somatic hypermutation processes. The more circular shape of dark and light zone in the rabbit are similar to the case of chicken [*Griebel and Hein*, 1996; *Makala et al.*, 2002-2003; *Olah and Glick*, 1979; *Romppanen*, 1981; *Yasuda et al.*, 2003, 1998]. Although the follicles of all species have a similar shape and size distribution behavior, the lymphoid tissues in the appendix of human and rabbits share the property of T zones and maturation after birth. This may indicate that the lymphoid tissue in the rabbit appendix is of mixed function while the avian bursa and the human appendix are of pure primary and secondary lymphoid tissue, respectively.

Taken together the follicles in GALT may have primary function. This may occur at least around the birth of the animal. Later on the follicles may be transformed into follicles with typical SLT function of filtering Ag and the ability to host classical GC. One may conclude that the development of those lymphoid follicles follows the same principles as the PLF of the spleen or LN despite a period of primary function.

2.2 *Lymphoid Follicle Structure*

In general the lymphoid organ structure depends on continued signaling and changes significantly upon immune reaction-induced or artificially-induced modulations (discussed in detail in (Sec. 2.2.2)). The overall organization is that the stroma in the B and T zone, respectively, attracts the proper lymphocyte population by specific chemokines (Fig. 2.6) [*Cyster*, 2005; *Moser and Loetscher*, 2001]. Follicular dendritic cells produce the chemokine CXCL13 [*Gunn et al.*, 1998; *Vissers et al.*, 2001] attracting B cells via the CXCR5 receptor [*Forster et al.*, 1996; *Gunn et al.*, 1998; *Legler et al.*, 1998]. The stromal compartment of the adjacent T zone and the HEV in LN and PP produce CCL21 [*Cyster*, 2005; *Okada et al.*, 2002; *Rangel-Moreno et al.*, 2005; *Willimann et al.*, 1998; *Yoshida et al.*, 1998]. In humans – and probably other species – however CCL21 seems to absent from HEV and is only found on stromal cells in the T zones [*Manzo et al.*, 2005]. The stroma is composed of fibroblastic reticular cells (FRC) (Sec. 2.2.4). Additionally, DC in the T zone produce CCL19 [*Ngo et al.*, 1998; *Vissers et al.*, 2001] and possibly CCL21 [*Willimann et al.*, 1998]. Both chemokines attract T cells via the CCR7 receptor [*Kim et al.*, 1998; *Willimann et al.*, 1998; *Yoshida et al.*, 1998]. The picture is, however, more involved because CCL19 and CCL21 attract B cells via CCR7 as well [*Kim et al.*, 1998; *Yoshida et al.*, 1998]. Details of the lymphoid tissue architecture are discussed in the following sections.
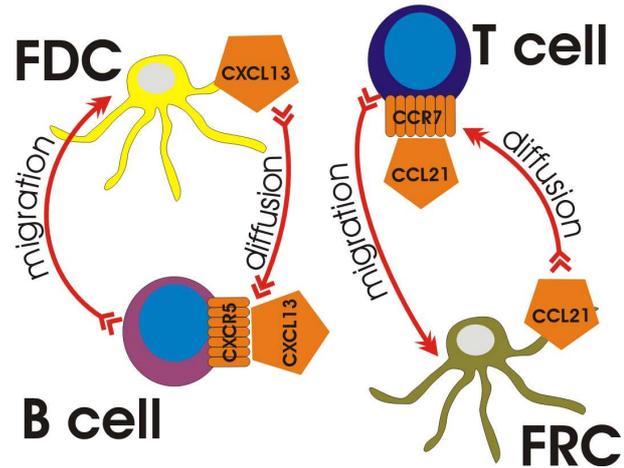
Figure 2.6: Basic processes found in SLT. Stromal cells of the T zone (FRC) attract T cells via diffusible chemokines named CCL21. In a similar manner FDC of the follicle attract B cells via the chemokine CXCL13.

2.2.1 Morphology

The morphology is the main feature of the PLF that is studied in this work. The knowledge of the detailed structure is therefore crucial to judge the results of the simulations.

The lymphoid follicle is basically a spherical or ovoid structure of several hundred micrometer diameter (Table 2.1). The stromal component is made of FDC which form a dense network that harbors the circulating naive B cells. The FDC engulf B cells, although this might be only the case for the matured FDC in GC engulfing the GC B cells [*Clark et al.*, 1992; *Kosco et al.*, 1988; *Tsunoda et al.*, 1997]. Histologically, the FDC are identified using the molecules CD35 and CD21 which are the complement receptors 1 and 2, respectively. These are common to most FDC despite difference on the ultrastructure of FDC in PLF and GC [*Szakal et al.*, 1985]. Other markers are BP-3, WP1 – which is shared with FRC, the mouse antibodies FDC-M1, FDC-M2, intercellular adhesion molecule (ICAM)-1, vascular adhesion molecule (VCAM)-1, and mucosal addressin-cell adhesion molecule (MAdCAM)-1 [*Clark et al.*, 1992; *Cyster et al.*, 2000; *Kosco et al.*, 1992]. The functional definition of FDC is the capability of trapping immune complexes [*Haberman and Shlomchik*, 2003; *Szakal et al.*, 1985, 1988], i.e. the unique property of FDC to bear unprocessed Ag in the form of immune complexes on their surface. The markers mentioned above are not strictly correlated to each other. For example the network stained for BP-3 is broader than the one stained for CD21/CD35. This is in accordance with the observation that more IC get trapped in the center of FDC networks [*Cyster et al.*, 2000] which correlates with the expression of CD35 (e.g. [*Fu and Chaplin*, 1999; *Fu et al.*, 1998; *Kasajima-Akatsuka and Maeda*, 2006; *Muller et al.*, 2003]). The PLF has therefore two regions: One with all mentioned markers of FDC present and a periphery where some makers are missing. In this sense the stromal cells at the periphery of PLF cannot be termed FDC with respect to the expressed molecules. However, CXCL13 that guides the B cell migration is expressed strongly in both regions. There are other indicators of a non-uniform FDC population that are discussed in more detail in (Sec. 2.2.3).

species	size [μm]	follicle	reference
mouse	100x200	PLF	[*Garside et al.*, 1998; *Katakai et al.*, 2003, 2004b; *McDonald et al.*, 2005; *Pabst et al.*, 2005]
mouse	100–250	GC	[*Allen et al.*, 2004]
mouse	150–500	SLF	[*Allen et al.*, 2004; *Garside et al.*, 1998; *Katakai et al.*, 2004a, 2003]
mouse (gastritis)	100–500	ectopic SLF	[*Katakai et al.*, 2003]
rat	70–100		[*Ushiki et al.*, 1995]
rat	400–600	SLF	[*Bhalla et al.*, 1981; *Ohtani et al.*, 2003]
sheep	250–400	PLF	[*Halleraker et al.*, 1994]
sheep	300x700–500x750	GC	[*Halleraker et al.*, 1994]
human	150–350	PLF	[*Brachtel et al.*, 1996; *Kasajima-Akatsuka and Maeda*, 2006]
human	150–350	GC	[*Armengol et al.*, 2001; *Brachtel et al.*, 1996]
human	500x600	GC	[*Kasajima-Akatsuka and Maeda*, 2006]
human	200–450	SLF	[*Armengol et al.*, 2001]
human	330x430–600x700	SLF	[*Kasajima-Akatsuka and Maeda*, 2006]
human (synovitis)	350x550	ectopic SLF	[*Lindhout et al.*, 1999]
pig	300	unknown	[*Belz*, 1998]
horse	150–500	SLF	[*Kumar and Timoney*, 2006]
chicken	100–200	GC	[*Romppanen*, 1981; *Yasuda et al.*, 2003]

Table 2.1: The size of PLF and SLF from various species. The shapes are ovoid in many cases and the width and length are given (width 'x' length). In other case only the range of the maximal diameter is known (from '–' to). For most of the values it is not sure that they represent the maximal extensions of the follicle.

2.2.2   Molecular signaling in lymphoid follicles

In general molecular signaling concerns four questions: Which molecule produced by whom acts how on which target cell? The how implies the question if the signal is just inductive to a property or is it required to be given constitutively. Many experiments have been done in the past to identify the regulation network that leads to the formation of PLF. By cutting off certain parts, the network has been reconstructed partly.

Disruption of signaling by knockouts   Knockout and blocking antibody experiments in mice provide some details on the molecular requirements of lymphoid follicle formation (Table 2.2). This type of studies reveals some differences between the different lymphoid tissues but in general the requirements are quite similar [*Fu and Chaplin*, 1999; *Muller et al.*, 2003; *Tumanov et al.*, 2003]. The molecules involved on one side are members of the tumor necrosis factor superfamily (TNF superfamily) (Fig. 2.7): These members are TNF-α, lymphotoxin α (LTα), and LTβ. The latter two become functional in the homotrimeric form LTα_3 and the heterotrimeric form LT$\alpha_1\beta_2$. On the other side are the receptors TNFR-I and LTβR while another receptor TNFR-II seems to have no role in PLF formation. From the binding data of TNF-α and LTα_3 to the shared receptors TNFR-I and
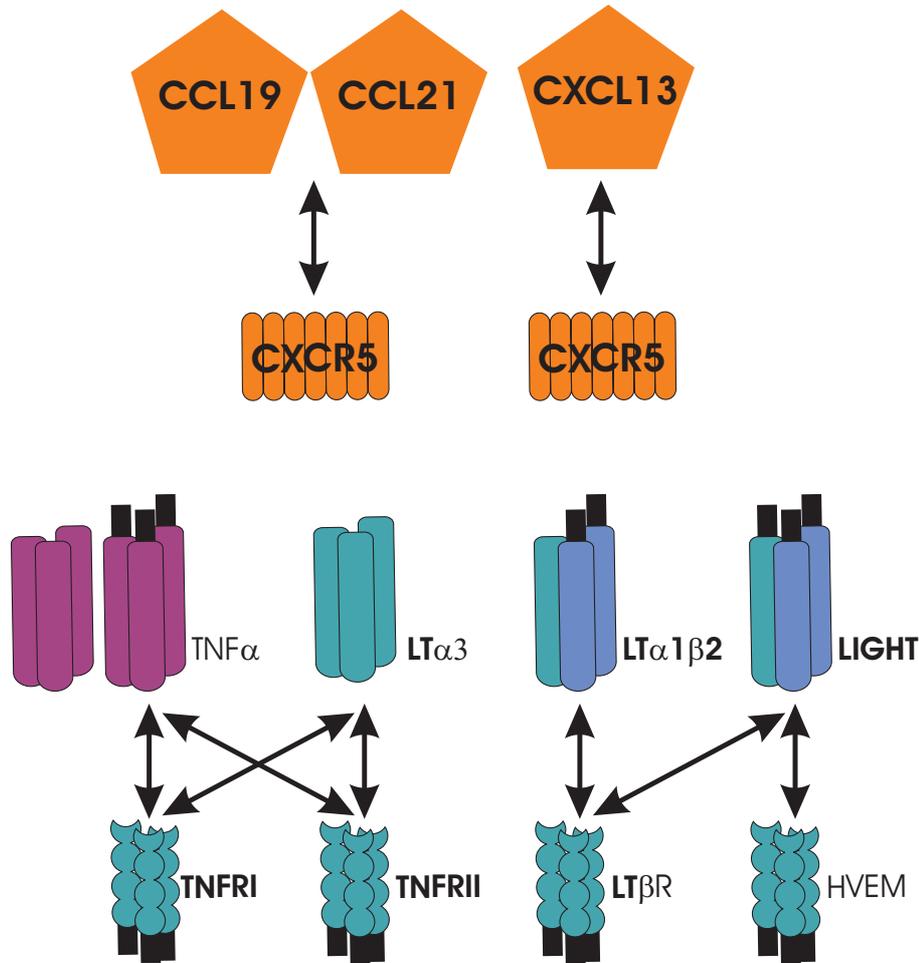
Figure 2.7: Molecular interactions relevant for the lymphoid follicle. The upper panel shows the chemokine interactions relevant for the follicle. The lower panels shows the members of the TNF superfamily and the corresponding receptors. The ligands are functional in their trimeric form. Monomeric forms are usually not effective triggering the receptor. The receptor TNFR-II does not play a role in the PLF system while the function of HVEM (herpes virus entry mediator) in the SLT context has not been clarified yet. TNF-α exists in membrane-bound and soluble form. LTα_3 exists as soluble form. LT$\alpha_1\beta_2$ and LIGHT come both in the membrane-bound form.

TNFR-II one might expect a functional redundancy of the two ligands [*Fu and Chaplin*, 1999; *Muller et al.*, 2003]. There is only the little difference that TNF-α comes in a membrane-bound and a soluble form (by cleavage of the membrane-TNF-α) while LTα_3 comes soluble only. It seems that the soluble form of TNF-α prefers to stimulate TNFR-I while the membrane-bound form is more efficient to activate TNFR-II [*Grell et al.*, 1995] suggesting that the soluble form of TNF-α is more import for PLF formation. LT$\alpha_1\beta_2$ is always membrane-bound and has its own receptor LTβR which does not bind TNF-α or LTα_3. Also LT$\alpha_1\beta_2$ does not bind to TNFR-I or TNFR-II. The LTβR receptor is used by another ligand named LIGHT. All these molecules but LIGHT are required for the normal follicle structure. Additionally, TNF-α is required for FDC formation. When FDC fail to form PLF are also absent pointing out the importance of this cell type in the development. The monomer LTα is expressed by T cells, especially CD4 T helper cells, and activated B and NK cells [*Fu et al.*, 1998]. B cells and T cells constitutively express low levels of LT$\alpha_1\beta_2$ independent of activation events [*Luther*

et al., 2002]. The data indicate that LTα on B cells is required for the normal formation of splenic development including FDC and GC formation while other sources are not relevant [*Fu et al.*, 1998]. Further studies revealed that LTα-deficient animals have no LN, PP, and no GC in the spleen [*Matsumoto et al.*, 1996; *Tumanov et al.*, 2003]. There is also no doubt that B cells are indispensable for FDC formation [*Fu and Chaplin*, 1999]. From the data about FDC generation in GC upon immunization, it seems that the induction of SLF may be due to increased levels of LT$\alpha_1\beta_2$ and TNF-α upon activation even when the base levels are insufficient to induce PLF [*Fu and Chaplin*, 1999; *Muller et al.*, 2003; *Tumanov et al.*, 2003]. This implies that the formation of GC is not strictly dependent on the presence of PLF.

One has to take care not to interpret the genetic knockout experiments to strictly. A recent study using a different knockout-strategy for TNF-α resulted in a different phenotype compared to the 'conventional' knockout [*Kuprash et al.*, 2005; *Pasparakis et al.*, 1997]. The conventional study [*Pasparakis et al.*, 1997] found PP in TNF-α-deficient mice which show that B cells separated from T cells but do not form PLF, instead B cells appear as ring around the T zone[2]. Also FDC and GC are missing. Another knockout approach for a TNF-α-deficiency lead to the complete disruption of PP formation [*Kuprash et al.*, 2005]. That indicates that different knockout strategies may not all lead to the complete suppression of the gene product. Seemingly identical phenotypes to the more complete knockout have been observed by generating knockouts for TNFR-I or injection of a blocking TNFR-I-Ig supporting that the 'conventional' knockout could not completely block this interaction either by remaining TNF-α or – more likely – by the alternative ligand LTα_3. Also of interest is the fact that the knockout of LTα reduces the TNF-α levels [*Fu and Chaplin*, 1999; *Pasparakis et al.*, 2000]. Compensating this loss by transgenic expression of TNF-α can partially restore the defects caused by LT$\alpha^{-/-}$, namely the B/T separation but not follicle formation [*Fu and Chaplin*, 1999].

The total knockout of TNF-α and all lymphotoxin loci results in additive effects compared to TNF-$\alpha^{-/-}$ and LT$\alpha^{-/-}$ mice [*Kuprash et al.*, 2002]. There are no additional qualitative differences except for a slightly more severely disturbed splenic architecture. This suggests that these molecules are required (but of course not necessarily sufficient) for a normal lymphoid tissue organogenesis and that these molecules have partly redundant functions.

Blocking of lymphotoxin signals by antibodies Blocking of the LT$\alpha_1\beta_2$ signals using an LT$\alpha_1\beta_2$-Ig fusion protein during development results in the loss of follicles and B/T segregation in the white pulp [*Fu and Chaplin*, 1999; *Wang et al.*, 2001b]. Later treatment after completed splenic development results only in the loss of follicles and FDC. FRC are also strongly reduced following a deficiency of TNF-α or TNFR-I and are lacking completely in the absence of LTα or LTβ as shown by BP-3 staining [*Ngo et al.*, 1999]. Consistently, blocking LT$\alpha_1\beta_2$ by fusion protein or antibody disrupted the BP-3$^+$ network. In LN blocking via LTβR-Ig results in the loss of PLF and the formation of a ring of B cells around the T zone thus maintaining the B/T segregation [*Rennert et al.*, 1997]. Loss of FDC due to blockade of LT$\alpha_1\beta_2$ in spleen and LN occurs within a few days [*Gommerman et al.*, 2002; *Huber et al.*, 2005; *Mackay and Browning*, 1998; *Wang et al.*, 2001b]. Blocking with a TNFR-I-Ig is less effective. Recovery from the PLF disruption in the spleen takes 2–3 weeks [*Gommerman et al.*,

---

[2]The ring appears in 2D slices while in 3D the B cells form a shell around the T cells.

deficiency	Spleen		lymph nodes			Peyer's patches	
	B/T	GC	MLN	PLN	GC	PP	GC
$LT\alpha^{-/-}$ or $LT\beta R^{-/-}$	no[a]	no	no[b]	no	ND	no	ND
$LT\alpha^{-/-}$ and TNF-α-tg	ring	ND	ND	ND	ND	ND	ND
$LT\alpha^{-/-}$ and TRANCE-tg	ND	ND	no	no	ND	no	ND
$LT\alpha^{-/-}$ and anti-LTβR at day 12–17	ND	ND	yes	yes	ND	no	ND
$LT\beta^{-/-}$	ring*	no	yes*	no	yes	no	ND
LTβR-Ig	ring*	no	yes	no	ND	no	ND
TNF-$\alpha^{-/-}$ or TNFR-I$^{-/-}$	ring	no	disordered	yes	yes	partial	no
TNF-$\alpha^{-/-}$	ring	ND	yes	yes	yes	no	ND
TNFR-I$^{-/-}$	ring	no	yes	yes	yes	yes	no
TNFR-II$^{-/-}$	PLF	yes	yes	yes	yes	yes	yes
TNF-$\alpha^{-/-}$	ring	ND	yes	yes	yes	no	ND
TNFR-I$^{-/-}$	ring	no	yes	yes	yes	yes	no
TNFR-I-Ig	partial ring	ND	yes	yes	ND	yes	ND
$LT\beta^{-/-}$ and TNFR-I$^{-/-}$	ring*	no	no	no	ND	no	ND
$LT\beta^{-/-}$ and TNF-$\alpha^{-/-}$	ring*	no	yes	no	yes*	no	ND
$LT\alpha^{-/-}$ and $LT\beta^{-/-}$ and TNF-$\alpha^{-/-}$	no	no	no	no	ND	no	ND
B cell $LT\beta^{-/-}$	some PLF	some	yes	yes	yes	yes	yes
T and B cell $LT\beta^{-/-}$	ring*	no	yes	yes	yes	yes	yes
T cell $LT\beta^{-/-}$	PLF	yes	yes	yes	yes	yes	yes
SCID	ring†	ND	yes	yes	ND	yes	ND
LIGHT$^{-/-}$	PLF	yes	yes	yes	yes	yes	yes
LIGHT$^{-/-}$ and $LT\beta^{-/-}$	ring*	no	yes*	no	no	no	ND
LIGHT-tg and $LT\alpha^{-/-}$	PLF*	yes*	no	no	yes*	no	ND
CXCL13$^{-/-}$ or CXCR5$^{-/-}$	ring	yes	ring[d]	ring[d]	yes	ring*	yes
plt/plt or CCR7$^{-/-}$	PLF*	yes	yes[e]	yes[e]	yes	yes[e]	yes
CXCR5$^{-/-}$ and CCR7$^{-/-}$	no	ND	disordered	no	ND	disorded	ND
IL-7R$\alpha^{-/-}$	ND	ND	yes	yes	yes	no	ND
IL-7R$\alpha^{-/-}$ and CXCL13$^{-/-}$	ND	ND	no	no	ND	ND	ND
TRANCE$^{-/-}$	ring[c]	yes	no	no	ND	yes	ND
TRANCE-R$^{-/-}$	PLF	yes	no	no	ND	yes	ND

Table 2.2: Based on several reviews [*Fu and Chaplin*, 1999; *Muller et al.*, 2003; *Tumanov et al.*, 2003] and the articles cited in this section the effects of lymphotoxin on the presence of different lymphoid tissues are summarized. Basically all deficiencies cause a reduction in number or size of the indicated structures. The absence might not be 100% as there can exist animals which exceptionally show the presence of the indicated structures at very low numbers [*Fu and Chaplin*, 1999]. In this table the existence of GC implies the formation of FDC in these GC. However, some authors call PNA$^+$ clusters of B cells GC without detecting FDC. These cases are not incorporated here. (B/T = segregation of B and T cells, ND = not determined/not possible, MLN = mesenteric lymph nodes, PLN = peripheral lymph nodes, ring = B cells form a ring around the T zone, *plt/plt* is a mutation that causes a lack of CCL19 and CCL21 except the long CCL21 isoform is expressed on lymphatic vessels)

* impaired, reduced, or only partially present; †splenocyte injection demonstrates a preformed ring structure [*Gonzalez et al.*, 1998]; [a] the $LT\alpha^{-/-}$ has been shown to have a concomitant deficiency for TNF-α [*Pasparakis et al.*, 2000]; [b] occasionally MLN are present with apparently normal structure [*Fu and Chaplin*, 1999]; [c] in ~ 30% of the cases normal splenic structure with PLF observed [*Kim et al.*, 2000; *Muller et al.*, 2003]; [d] also normal PLF are reported for CXCR5$^{-/-}$ [*Forster et al.*, 1996; *Voigt et al.*, 2000]; [e] reduced T cell number in these organs, increased T cell number in peripheral blood, spleen, and bone marrow [*Muller et al.*, 2003]

2002; *Huber et al.*, 2005]. However, one of the studies suggests that there is no recovery in the LN within 3 months [*Gommerman et al.*, 2002]. The different responses seen in TNFR-I-Ig and LTβR-Ig treatment is a result of developmentally different influences of TNF-α and LT$\alpha_1\beta_2$ with the former one mainly involved in the induction of FDC only whereas LT$\alpha_1\beta_2$ is required for both induction and maintenance [*Fu and Chaplin*, 1999; *Mackay and Browning*, 1998; *Wang et al.*, 2001b].

Comparing the blockade of LTβ by antibodies with the selective deletion of B cell LTβ there are some splenic FDC left in the latter case [*Tumanov et al.*, 2002]. This suggests that there is another source of LT$\alpha_1\beta_2$ that can initiate FDC, possibly T cells. However, why is the T zone in the normal spleen completely void of FDC? Although the picture is not absolutely consistent, summing up one can say that B cells are the primary source of LT$\alpha_1\beta_2$ which is needed to generate and maintain FDC.

Bone marrow and cell transfer experiments A large set of experiments uses transfers bone marrow or lymphocytes from or to animals deficient for the molecules mentioned above to separate the molecules impact around the time of organogenesis from the inherent defects of lymphocytes. Such experiments show that lymphocytes from LT$\alpha^{-/-}$ mice transfered into normal recipients migrate properly to the lymphoid tissues demonstrating that the defects seen in LTα-deficiencies are developmental and not a failure of lymphocyte migration [*Fu and Chaplin*, 1999; *Fu et al.*, 1997]. Also PLF and FDC remain detectable in these mice for a short time and get lost only on the long run leading to the ring structure of B and T cells [*Fu et al.*, 1997].

The short term reconstitution of SCID[3] mice with LT$\alpha^{-/-}$ lymphocytes show an apparently normal segregation of B and T cells with the formation of follicle-like structures without typical FDC marker, i.e. the B and T cells home to areas as if B and T zone would be present [*Gonzalez et al.*, 1998]. This structure appears within one day. However, the apparently normal segregation can be prevented by injection of LTβR-Ig and suggesting that other cells than lymphocytes can be sources for LTα during development [*Fu and Chaplin*, 1999; *Gonzalez et al.*, 1998; *Muller et al.*, 2003]. Upon long term reconstitution of SCID mice with LT$\alpha^{-/-}$ lymphocytes, the B cells organize ring-like around the T zone. This indicates that the unknown LTα-source has to signal constantly as the splenic structure gets lost after signal transfer while it is clear that the structure had been established during development. It may further indicate that there exist follicle-like structures with immature FDC producing CXCL13 and some non-lymphocyte cell providing LT$\alpha_1\beta_2$ – possibly lymphoid tissue inducer cells (LTIC) (Sec. 2.5). However, the LTIC usually disappear around birth [*Yoshida et al.*, 1999] challenging this interpretation. It may also be that the reorganization of CXCL13 expressing immature FDC into follicle-like aggregates is completed in less than one day. A recent work identified a ring-like pattern of CXCL13-expressing cells in SCID mice in the absence of lymphocytes which may serve as cellular source for this redistribution [*Cupedo et al.*, 2004b]. The initial CXCL13-expression may be promoted by LTIC [*Mebius et al.*, 1997]. Long term reconstitution experiments of LT$\alpha^{-/-}$ mice with normal bone marrow can restore white pulp structure containing PLF although B/T segregation remains incomplete 6 weeks after transfer [*Fu et al.*, 1997; *Matsumoto et al.*, 1997; *Tkachuk et al.*, 1998]. In full consequence the segregation of T and B cells in distinct areas requires constant signals

---

[3]Severe Combined Immunodeficiency (SCID) is a mutation that causes the lack of a functional immune system and the absence of B and T cells.

of LTα.

TNFR-I$^{-/-}$ show a disturbance of the splenic structure similar to LT$\alpha^{-/-}$. In contrast to the LT$\alpha^{-/-}$ situation, bone marrow transfer cannot recover normal splenic architecture including the absence of GC formation [*Matsumoto et al.*, 1997; *Tkachuk et al.*, 1998] because TNFR-I is needed by stromal populations which are not transfered with the bone marrow. More detailed transfer experiments confirmed that LTβR is required to be expressed on stromal cells to allow FDC formation whereas LTβ and TNF-α is required to be provided by B cells [*Endres et al.*, 1999; *Wang et al.*, 2001b]. To a limited extent TNF-α from other sources like T cells can substitute the B cell-derived TNF-α most likely because TNF-α diffuses in contrast to the membrane-bound LT$\alpha_1\beta_2$ [*Wang et al.*, 2001b].

However, there seems to be a striking difference between the spleen and other lymphoid tissues [*Fu and Chaplin*, 1999; *Tumanov et al.*, 2003]. The white pulp development relies on lymphocytes while LN and PP are dependent on LTIC (Sec. 2.5) which are present in a larger fraction only before or around birth and vanish thereafter [*Yoshida et al.*, 1999]. This is supported by the fact that the selective inactivation of LTβ on B and/or T cells does not impair the development of the LN and PP while the complete knockout of LTβ does. Moreover the SLF in MLN can develop in the absence of LTβ on B cells [*Tumanov et al.*, 2003]. This implies that other signals like TNF-α or LTα_3 are sufficient for the development of FDC in MLN pointing out the different molecular requirements of SLT.

Chemokines   So far the molecular requirements for structural features of SLT have been discussed. This is mostly related to the presence of FDC which can be interpreted as a failure of FDC differentiation. In order to get a mechanistic interpretation for the lymphocytes the homing chemokines regulating their localization in SLT should be considered. Of note, the effects of chemokines can have a stronger dosage effect than the other molecules, i.e. the concentrations used *in vitro* may be not relevant for the situation *in vivo* thus generating artificial cell behavior. In a similar manner to the effects of the members of TNF superfamily, deficiencies for the chemokines or their receptors provide information about relationships between the two classes of signaling pathways in SLT.

In the absence of TNF-α or TNFR-I splenic CXCL13 levels are decreased [*Ngo et al.*, 1999]. The expression of CCL21 is slightly reduced. Deficiencies of LTα or LTβ cause not only the lack of PLF and FDC but also a severe reduction of CXCL13 levels in the spleen. Also B and T zone are not clearly separated. The T zone is almost completely lost when mice are double-deficient for LTα and LTβ or LTα and TNF-α. Also the levels of CCL21 are reduced strongly. In all the variants of deficiencies CCL19 is reduced albeit less severe than CCL21 in each case. This suggests that the effects promoted by members of the TNF superfamily are not only affecting the presence of FDC but also on the expression of chemokines in both the B and the T zone of SLT.

By blocking LT$\alpha_1\beta_2$ with a soluble LTβR-Ig fusion protein it is possible to separate the requirement for constitutive expression from the transient influence during organogenesis [*Fu and Chaplin*, 1999]. The levels of CXCL13 in the spleen are decreased slowly over weeks. Also CCL21 is slightly reduced but seemingly not consistent. The contribution of the related LIGHT molecule could be shown to be low despite its ability to utilize the same as LT$\alpha_1\beta_2$. A specific deficiency for LTβ on B and/or T cells cannot substantially reduce the CXCL13 levels in SLT [*Tumanov et al.*, 2003] except in the spleen

[*Ngo et al.*, 1999]. Similar CCL19 and CCL21 are widely independent of $LT\alpha_1\beta_2$ on lymphocytes once more with the exception of the spleen. Strikingly, $LT\alpha_1\beta_2$ on T cells can be stimulated *in vitro* by various cytokines including CCL19, CCL21, IL-4, IL-7, and IL-15 [*Cyster*, 2005; *Luther et al.*, 2002; *Tumanov et al.*, 2003]. This opens the possibility of a positive feedback in which T cells stimulate stromal cells in the splenic T zone to produce CCL21 (and maybe IL-7) via $LT\alpha_1\beta_2$. The increased CCL21 in turn enhances the signaling to the stromal cells by attracting further T cells and increasing the expression of $LT\alpha_1\beta_2$ on the surface of the T cell by IL-7 and CCL21. However, other studies failed to demonstrate increased $LT\alpha_1\beta_2$ expression of naive T cells in LN directly [*Luther et al.*, 2002]. This may be explained by the high levels of CCL21. The $LT\alpha_1\beta_2$ induction by CCL21 starts at 1 nM and may be far beyond the optimum at CCL21 concentrations of several 100 nM found in SLT which may even negatively regulate $LT\alpha_1\beta_2$ on T cells [*Luther et al.*, 2002]. This idea is consistent with the results of the knockout experiments, i.e. the expression of chemokines in the T zone is not dependent on constitutive $LT\alpha_1\beta_2$ signaling by lymphocytes but depends on other cells during a developmental time window.

The coupling of constitutive $LT\alpha_1\beta_2$ expression in the spleen and the CXCL13 levels there suggest the presence of a positive feedback loop between $LT\alpha_1\beta_2$ and CXCL13 [*Ansel et al.*, 2000]. The ligation of B cell CXCR5 via CXCL13 induces enhance surface expression of $LT\alpha_1\beta_2$ which in turn stimulates CXCL13 production of FDC by signaling through $LT\beta R$ (Fig. 2.8). However, B cells also express basal $LT\alpha_1\beta_2$ levels independent of CXCL13 [*Cyster*, 2005]. The induction of $LT\alpha_1\beta_2$ on B cells requires CXCL13 concentrations of about 10 nM [*Luther et al.*, 2002]. This is in the range of measured CXCL13 concentrations in SLT [*Luther et al.*, 2002]. Such, in contrast to the situation in the T zone between $LT\alpha_1\beta_2$ on T cells and CCL21 on the T zone stromal cells, the concentration of CXCL13 in the spleen renders the positive feedback loop functional. When the feedback loop is shut off in an animal deficient for CXCR5, the formation of PLF is prevented and a ring-shaped B cell area surrounding the T zone appears in SLT [*Ansel et al.*, 2000; *Gonzalez et al.*, 1998; *Voigt et al.*, 2000]. Although the lack of CXCR5 does not prevent the formation of GC and FDC upon immunization [*Ansel et al.*, 2000; *Voigt et al.*, 2000]. However, it is not clear if the GC structure remains unaffected, e.g. if dark and light zone in these GC are absent [*Voigt et al.*, 2000] or not [*Allen et al.*, 2004]. The generation of the FDC during a GC is most likely a result of the high levels of $LT\alpha_1\beta_2$ on GC B cells which is a result of their Ag-activation and independent of CXCL13 [*Ansel et al.*, 2000; *Fu et al.*, 1998; *Muller et al.*, 2003] making the feedback loop dispensable. However, one should take into account that the lack of CXCR5 also prevents the B cells from homing properly [*Reif et al.*, 2002] such that the observed effects may be related to a migration failure instead of a signaling failure in the $LT\alpha_1\beta_2$ path.

In the spleen of TNF-$\alpha^{-/-}$ mice CD35 staining can be observed in a ring surrounding the B cell area which itself forms a ring around the T zone [*Mandik-Nayak et al.*, 2001]. CD35 is one of the FDC marker and therefore may indicate the presence of FDC or FDC-like cells not forming PLF with the B cells which is similar to the situation in CXCR5$^{-/-}$ mice [*Voigt et al.*, 2000]. Treating the TNF-$\alpha^{-/-}$ animals with an TNFR-I-agonist restores the normal clustering of CD35$^+$ FDC into PLF [*Mandik-Nayak et al.*, 2001]. The treatment increases the CXCL13 levels but strikingly reduces the levels of CCL19 and CCL21 by a factor of 2. The conclusion is that TNF-α may be required to induce sufficiently high CXCL13 levels on FDC such that B cells are attracted by CXCL13 and overcome

their response to the chemokines CCL19 and CCL21. It seems if CCL19 and CCL21 act dominantly (as strongly indicated by the CXCR5$^{-/-}$ case) the formation of follicles is prevented and a ring-shaped B cell area remains. Moreover an intermediate ring-structure prior to the formation of PLF seems to be a required step during normal organogenesis (Sec. 2.5). The ring may be formed simply by the exclusion of B cells from the T zone due to a low response to CCR7 compared to T cells as suggested by the receptor levels [*Okada et al.*, 2002]. This concept is supported by the observation that reduced expression of CCR7 on T cells can lead to T cell exclusion from the T zone [*Randolph et al.*, 1999; *Reif et al.*, 2002] as suggested for B cells. Similarly, B cell exclusion from the PLF upon Ag-stimulus may be attributed to CCR7 upregulation [*Breitfeld et al.*, 2000; *Cyster*, 2005; *Roy et al.*, 2002] which is possibly accompanied by a decreased CXCL13-responsiveness [*Casamayor-Palleja et al.*, 2002]. Thus not only presence or absence of chemokines determines their effect on lymphocytes but also there absolute concentrations (to become functional) and relative concentrations (to determine which is dominant) (see also (Sec. 3.3)).

CXCL13 expression in most lymphoid organs is reduced when B cells are deficient for LT$\alpha_1\beta_2$ [*Cyster*, 2005]. In complete LT$\alpha_1\beta_2$ or TNF-α knockout CXCL13 expression is reduced by a factor 20 in LT$\alpha_1\beta_2$-deficient and 3–4 in TNF-α-deficient animals, respectively. Surprisingly, in the spleen CCL19 and CCL21 depend partly on the presence of LT$\alpha_1\beta_2$ on B cells as well [*Ngo et al.*, 1999] whereas this does not occur in LN [*Cyster*, 2005]. Presumably the LTIC are responsible for these chemokines in LN instead of B cells. This may happen only during a developmental time window as LTIC are replaced by lymphocytes even before the SLT development is completed (Sec. 2.5). Additionally, the absence of LT$\alpha_1\beta_2$ or TNF-α causes lack of stromal networks, all FDC markers, and loss of BP-3 in the T zone.

Other secondary lymphoid organs such as nasal-associated lymphoid tissue (NALT) develop independently of lymphotoxins [*Fukuyama et al.*, 2002; *Rangel-Moreno et al.*, 2005; *Tumanov et al.*, 2003]. Consequently deficiencies for CCL19, CCL21, and CXCL13 do not prevent the development of NALT structure but impair the formation of the proper microarchitecture [*Rangel-Moreno et al.*, 2005]. Like in the other tissues, NALT in LT$\alpha^{-/-}$ animals do not produce CXCL13 and have reduced CCL21 levels. Interestingly, CCL19 levels are reduced in CXCL13-deficient mice whereas CCL21 remains unchanged. Possibly CCL21 is under the control of other lymphotoxins like LIGHT. Moreover, LTβ and TNF-α are also reduced in the NALT of CXCL13$^{-/-}$ and LT$\alpha^{-/-}$ mice. Although ER-TR7$^+$ fibroblasts can be seen in all type of deficiencies the formation of networks of these cells is only unaffected in deficiencies for CCL19 and/or CCL21. This is consistent with the culture observations made by another group [*Katakai et al.*, 2004b] (Sec. 2.2.4). The NALT development strengthens the notion that CXCL13 is correlated with LTα-dependent signaling while CCL19 and CCL21 are widely independent. It also shows again that LTα, LTβ, and TNF-α can influence the stromal cells of the T zone by changing their behavior with respect to the formation of networks.

Additional chemokines besides CXCL13 can be produced by FDC such as IL-15 [*Husson et al.*, 2000; *Park et al.*, 2004] and IL-6 [*Clark et al.*, 1992; *Huber et al.*, 2005; *Husson et al.*, 2000; *Kim et al.*, 1994; *Park and Choi*, 2005]. Both are chemotactic for lymphocytes [*Nieto et al.*, 1997; *Weissenbach et al.*, 2004]. If they play a role in the formation of PLF or their dependence on the signals by TNF-α and LT$\alpha_1\beta_2$ is not known.
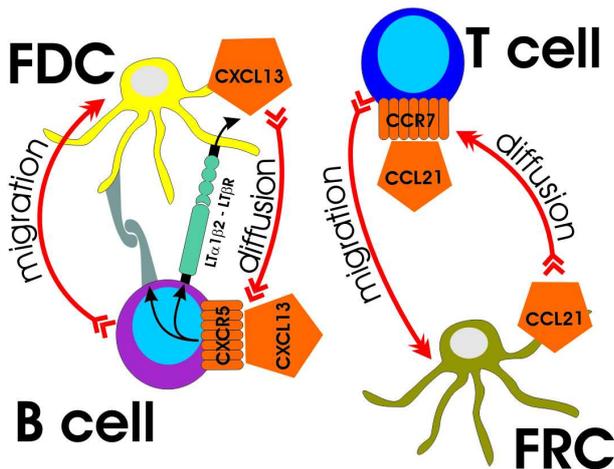
Figure 2.8: Positive feedback loop. The stimulation of B cells with CXCL13 causes them to upregulate $LT\alpha_1\beta_2$ and adhesion receptors on their membrane. This allows intimate contact with FDC and the stimulation of $LT\beta R$ via $LT\alpha_1\beta_2$ induces increased CXCL13 production. For the corresponding FRC - T cell system nothing similar has been reported leaving CCL21 expression and T cell responses independent of each other.

Considering the data from knockout, antibody blocking, and cell transfer experiments for TNF-α and $LT\alpha_1\beta_2$ it is clear that the chemokines CCL19, CCL21, and CXCL13 depend on the presence of these signals and the corresponding receptors on stromal cells including FDC. However, the cellular source for the signals is not clear. In the spleen B cells seem to be at least in part responsible for this function while for LN, and MALT B cells seem to have no influence. The signaling function may be attributed to LTIC during a developmental time window discussed in more detail in Sec. 2.5.

Gene expression in lymphoid tissue Direct observation of gene expression patterns in the stromal compartment of the splenic white pulp could not identify many differences in animals that are deficient for either TNF-α or $LT\alpha_1\beta_2$ compared to normal mice [*Shakhov et al.*, 2000; *Shakhov and Nedospasov*, 2001]. A major difference that can be observed is the reduction of BP-3 when $LT\alpha_1\beta_2$ but not when TNF-α is lacking. Using immmunohistochemistry, BP-3 in $LT\alpha_1\beta_2^{-/-}$ has been shown to be below detection level in B and T zone while in TNF-$\alpha^{-/-}$ it is detectable but reduced strongly. The difference in the mRNA and protein results for TNF-$\alpha^{-/-}$ may be due to post-translational mechanisms but that has not been investigated in detail yet. The chemokines CXCL13, CCL19, and CCL21 are reduced in $LT\alpha_1\beta_2^{-/-}$ mice while TNF-α deficiency causes only the loss of CXCL13 [*Shakhov et al.*, 2000; *Shakhov and Nedospasov*, 2001]. The authors of the study identified a few more molecules whose expression levels are reduced. However, there is no study shedding any light on their function in lymphoid organogenesis. An interesting observation is that the defects induced by TNF-$\alpha^{-/-}$ are all seen in $LT\alpha_1\beta_2^{-/-}$ as well and that the deficiency for $LT\alpha$ (which implies the lack of $LT\alpha_1\beta_2$) has the most severe effects on mRNA expression patterns. A similar work identified genes differently expressed before and after $LT\beta R$-Ig treatment [*Huber et al.*, 2005]. The only molecule identified in these studies that is known to be involved in organogenesis is CXCL13 which is reduced by two orders of magnitude upon fusion protein treatment. Like in the gene expression study of knockout mice other molecules have no known effect in PLF formation. Comparison with $LT\beta R^{-/-}$, TNF-$\alpha^{-/-}$, and TNFR-I$^{-/-}$ gives the same results with a smaller reduction of gene expression for the latter two cases. TNFR-II$^{-/-}$ had no effects consistent with the observation that it is not involved in PLF, FDC, or GC formation. The results of those studies confirm the dependency of splenic chemokine expression on $LT\alpha_1\beta_2$ and TNF-α. The results are extended in so far as CCL19 and CCL21 appear independent on TNF-α.

2.2.3 Follicular dendritic cells

The two major questions about FDC are: Which are the precursors of these cells and how are these precursors induced to differentiate to FDC? The latter question has been in part answered by the data of the former section elucidating the requirement for $LT\alpha_1\beta_2$ and TNF-α from some source and the presence of the corresponding receptors.

The observed slow replacement of FDC by migratory precursors and inefficient seeding by bone marrow-derived cells argues against hematopoietic origin of FDC [*Cyster et al.*, 2000]. The most common notion is that FDC are derived from stromal cells which are possibly related to the stromal cells seen in the T zone. Comparative reviews supporting the mesenchymal origin of FDC can be found in [*van Nierop and de Groot*, 2002]. A first indication of the mesenchymal origin is the morphology of FDC which is much different from the more or less spherical lymphocytes thus speaking against a hematopoietic origin of FDC. An FDC is composed of a soma of several micrometer diameter [*Suzuki et al.*, 2001; *Tsunoda et al.*, 1999] with 6–10 sometimes up to 15 dendrites of 15–20 μm length [*Szakal et al.*, 1985]. Occasionally, FDC show several cell bodies which are connected by cytoplasmatic bridges [*Szakal et al.*, 1985]. In culture the FDC become flattened with the soma reaching 50 μm diameter and the dendrites extending up to 150 μm [*Lindhout et al.*, 1999].

The evidence for the relation of FDC to the FRC of the T zone is given by shared markers [*Bofill et al.*, 2000]. There exists a gradual decrease of the fibroblast marker ASO-2 from the T zone to the heart of a GC with an overlap of CD21 and ASO-2 at the border. The change is accompanied by a gradual morphologic change from the 'classical fibroblastic' to the typical FDC morphology [*Szakal et al.*, 1985]. A similar change of marker expression has been observed in the PLF although a few intermediate steps are missing [*Bofill et al.*, 2000]. Five subsets of FDC/FRC markers have been identified (Table 2.3). The co-localization with the different lymphocyte subsets in the areas of the PLF and SLF lead the authors [*Bofill et al.*, 2000] to the conclusion that a constant differentiation signal is required to maintain the FDC state and prevent the back-differentiation to FRC. In addition the stromal cell marker BP-3 has been found to co-stain with some CD35$^+$ cells and can be found around the PLF border and even in the center of the follicle [*Ngo et al.*, 1999] strengthening the notion of the stromal origin of FDC. Another support for the local differentiation relying on constant stimuli is the fact that FDC rapidly loose many of there characteristic markers when brought into culture ([*Chang et al.*, 2003; *Clark et al.*, 1992; *Tsunoda et al.*, 1997] and references therein). Also additional markers with gradual transitions have been investigated like CD35 (strongest in apical light zone of GC) and CXCL13 being stronger in the GC than in the mantle. Some authors [*Chang et al.*, 2003] suggest an increased 'FDC-ness' by acquiring expression of CXCL13 followed by CD21,CD35 and finally CD23 from the immature to the most mature state. Other markers which are different in culture and *in vivo* are summarized in (Table 2.4). The loss of typical FDC markers in culture conditions is in parts reversible. Expression of ICAM-1 in culture could be initiated by IFN-γ, TNF-α, and other cytokines. VCAM-1 can be induced by IFN-γ and IL-4. It seems that VCAM-1 is only induced on FDC in the GC but not in FDC found in PLF [*Balogh et al.*, 2002]. Additionally MAdCAM can be induced on FDC. *In vivo* MAdCAM expression is broader than VCAM-1 resulting in a MAdCAM$^+$ VCAM-1$^-$ ring of 30-50 μm thickness in the SLF, i.e. at least two FDC subtypes can be distinguished in this way [*Balogh et al.*, 2002]. A recent study of FDC-development performed on

subtype	ASO-2	RFD3	CD23	Vitronectin	IgM	localization
Type 1	90–100%	40–90%	90–100%	0	0	PLF
Type 2	90–100%	10–40%	0	0	0	SLF (MNZ)
Type 3	< 10%	90–100%	0	0	0	SLF (DZ)
Type 4	0	90–100%	0	40–90%	40–90%	SLF (BLZ in tonsil, appendix not LN, spleen)
Type 5	< 10%	90–100%	90–100%	40–90%	40–90%	PLF/SLF (center/ALZ)
Type 6	40–90%	90–100%	90–100%	40–90%	40–90%	after GCR

Table 2.3: The FDC subtypes identified in [*Bofill et al.*, 2000] based on the expression of the indicated markers. The common marker of these FDC are CD21 (short isoform) and DRC-I (long isoform of CD21). IgM and vitronectin are not produced by FDC but are found associated with FDC. There is a gradual transition between the FDC subtypes in the PLF and SLF.

archived specimen of human LN [*Kasajima-Akatsuka and Maeda*, 2006] supports the idea of local FDC differentiation by the fact that FDC seem to acquire more and more markers that are lost in reverse sequence in the culture experiments. The study supports and extends the 'FDC-ness' picture to several other markers not investigated in previous studies.

Some studies indicate the ability of cultured FDC to divide every 3 to 4 days [*Clark et al.*, 1992; *Kim et al.*, 1994; *Tsunoda et al.*, 1997]. It is not clear if this happens at significant levels *in vivo* in the PLF and will therefore not be taken into account in this study.

The adhesion of B cells to FDC in culture is very strong and FDC are engulfing the B cells – a process called emperipolesis – making it hard separating FDC from lymphocytes [*Clark et al.*, 1992; *Kim et al.*, 1994; *Tsunoda et al.*, 1997, 1992] and raising the question how B cells move in the PLF considering the migration data available (Sec. 3). However, the emperipolesis of B cells might be an experimental bias as the FDC isolated for culturing are mostly from the strong adherent subtype of population found in GC [*Clark et al.*, 1992; *Kim et al.*, 1994; *Tsunoda et al.*, 1997]. In support of this most recent data from two-photon imaging of GC demonstrate that almost all lymphocytes are highly mobile among the FDC network [*Allen et al.*, 2007; *Schwickert et al.*, 2007]. In the mantle zone of GC, FDC do not show emperipolesis of B cells making it hard to isolate FDC from the tissue [*Tsunoda et al.*, 1992]. The morphology of cultured FDC changes, finally adopting a flat adherent FDC losing all contact to all engulfed co-cultured lymphocytes [*Tsunoda et al.*, 1997]. The cultured FDC are also proliferating with the marked difference that dividing cells produce ECM while the non-proliferating subpopulations does not produce ECM. The latter point has been observed *in vivo* indirectly (see also (Sec. 2.3.1)) by investigating the developmental changes in sheep fetuses [*Halleraker et al.*, 1994]. During development the PLF do not just increase in size but also loose ECM fibers that are present in the initial stages. Morphologically immature FDC are still attached to ECM suggesting that the differentiation from FRC to FDC is accompanied by the loss of the ability to produce ECM or alternatively by an increase of ECM degradation abilities.

FDC express several adhesion molecules. Among them are: CD11b, CD15s, CD22, CD29, CD40, CD49c, CD49e, CD49f, CD50, CD54, CD80, CD106 [*Clark et al.*, 1992; *Ogata et al.*, 1996; *Suzuki et al.*, 2001; *Tsunoda et al.*, 1997]. These are not present on all FDC subtypes and further strengthen

Table 2.4: FDC markers reproduced from [*Clark et al.*, 1992]. The comparison with normal DC shows little coincidence suggesting that FDC are not derived from DC. Interestingly, CD45RO – a marker for cells of hematopoietic origin – is missing indicating that FDC are not derived from the hematopoietic lineage. Strength of expression above background levels is indicated by the number of '+'. Discrepancies in literature are indicated by +/−. (+sub = low expression, ND = not determined)

marker	cultured FDC	*in vivo* FDC	DC
Myeloid-associated			
CD14	+	+	-
CD11b	+	+	-
CD11c	-	-	++
CD32	-	+/-	-
CD33	-	-	ND
CD35	+sub	+	-
B cell-associated			
CD19	-	+/-	-
CD20	-	+/-	-
CD21	+/-	+	-
CD22	-	-	-
CD23	+sub	+/-	-
CD24	-	+/-	-
CD37	-	+	-
CD38	+sub	+/-	ND
CD73	++	++	ND
CD74	+sub	+	+
Adhesion molecules			
CD18	-	-	-
CD29	+	++	++
CD54	++	++	++
CD49d	+	+/-	ND
CD106	++	++	ND
CD44	+sub	-	ND

the notion of a gradual differentiation of FDC. The possible interactions of the adhesion molecules found on FDC with the ECM are:

- CD49c + CD29 ↔ fibronectin, laminin, collagen

- CD49e + CD29 ↔ fibronectin

- CD49f + CD29 ↔ laminin

For the interaction of FDC with B cells following pairs have to be considered:

- CD11b (CR3) ↔ CD54 (ICAM-1)

- CD15s(sialyl-lewis-X) ↔ CD62L (L-selectin)

- CD50 (ICAM-3) ↔ CD11a/18 (LFA-1)

- CD54 (ICAM-1) ↔ CD11a/18 (LFA-1)

- CD106 (VCAM-1) ↔ CD49d/29 (VLA-4)

To asses which molecules may affect FDC behavior and phenotype, the cytokine receptor expression

pattern has been investigated [*Yamada et al.*, 1997]. The receptors identified according to the subtype distribution (Table 2.3) are:

- Type 1, Type 2, Type 3: GM-CSF Rα, IL-4R, IL-6R

- Type 4: GM-CSF Rα, TNFR-I, IL-1R-II, IL-2Rβ, IL-4R, IL-6R

- Type 5: GM-CSF Rα, TGFβ-R-II, TNFR-I, IL-1R-II, IL-2Rβ, IL-4R, IL-6R

The failure to identify the TNFR-I receptor on the first three subtypes is puzzling in view of the dependency of FDC development on TNF-α (Sec. 2.2.2) (the receptor LTβR has not been investigated in that experiment).

Effect of TNF superfamily members on FDC The effects of TNF-α and LT$\alpha_1\beta_2$ have been assessed directly by studies of cultured FDC that where freshly isolated from human tonsils [*Husson et al.*, 2000]. TNF-α and LT$\alpha_1\beta_2$ are able to induce increased VCAM-1 levels although to a lesser extent for LT$\alpha_1\beta_2$. ICAM-1 can be enhanced as well by these molecules. FDC express RNA of CXCL12 and IL-8. Both cytokines can act as chemoattractants [*Cyster*, 2005; *Moser and Loetscher*, 2001; *Wilkinson and Newman*, 1992]. IL-8 is enhanced in the presence of TNF-α or LT$\alpha_1\beta_2$ while CXCL12 is suppressed, again with TNF-α being more effective. Interestingly, this study could detect CXCL13 mRNA but not the protein, raising the question how much of the FDC properties remained in the cultured cells when CXCL13 is not expressed in a functional form. Another effect of TNF-α is to induce proliferation of FDC consistent with the previous observation of cultured FDC [*Clark et al.*, 1992; *Kim et al.*, 1994; *Tsunoda et al.*, 1997].

There is a partially successful attempt to induce the FDC phenotype on stromal cells in culture. Fibroblast-like synoviocytes (FLS) were cultured in the presence of TNF-α [*Lindhout et al.*, 1999]. These cells have been taken from patients with and without rheumatoid arthritis (Sec. 2.6), i.e. ectopic follicles are only present in the first group. The FDC phenotype was confirmed by increased expression of CD55, ICAM-1, VCAM-1, and DRC-1 and the morphological changes specific for FDC although the FDC phenotype is incomplete. Unstimulated FLS expressed the marker ASO-2 which is a hallmark of fibroblasts (and FRC) further supporting the concept of gradual differentiation from stromal cells [*Bofill et al.*, 2000]. Studying the molecular requirements for the FDC-like properties of FLS revealed that LTβR is expressed by these cells [*Braun et al.*, 2004]. Consequently, LT$\alpha_1\beta_2$ can induce the expression of several molecules like IL-1, IL-6, ICAM-1, VCAM-1, TNF-α, and the matrix metalloproteinases MMP-1 and MMP-3. However, neither morphologic changes nor the expression of CCL21 or CXCL13 have been observed in the LT$\alpha_1\beta_2$-treated cultured FLS. Chemokines that where induced are CCL2, CCL5, and CXCL8 that attract monocytes, T cells, and neutrophils, respectively [*Moser and Loetscher*, 2001; *Moser et al.*, 2004]. The lack of the homeostatic chemokines CCL21 and CXCL13 challenges the view that FDC derive from local stromal cells. This may be related to different requirements for the stimulus as TNF-α is able to induce at least part of the phenotypic changes although the chemokine expression has not been investigated in the first study [*Lindhout et al.*, 1999]. Interestingly, the LT$\alpha_1\beta_2$ response has been shown to be bell-shaped with decreasing effect at high doses possibly explaining the different outcomes of these experiments.

Other possibilities for the origin of FDC   A recent study could not identify a clear relationship between FRC and FDC based on newly developed markers [*Balogh et al.*, 2004]. These markers stained FRC and FDC separately and the developmental sequence did not reveal a correlation between the two cell types, i.e. no overlapping expression was found.

Another study that uses bone marrow transfer into SCID mice identified donor-derived FDC [*Kapasi et al.*, 1998]. FDC in follicles were either of donor or of host type although some show mixed FDC origin. However, it could be that the bone marrow transfer experiment also transfers stromal cells that repopulate the lymphoid tissue in SCID mice thereby not ruling out the stromal origin of FDC.

TNFR-I knockouts and mice given injections of a blocking TNFR-I-Ig show signs of what appears to be an immature FDC or FDC precursor around splenic follicles suggesting migrative FDC progenitors [*Kuprash et al.*, 2005]. Similar conclusions have been drawn from FDC marker staining in TNF-$\alpha^{-/-}$ and TNFR-I$^{-/-}$ mice [*Pasparakis et al.*, 2000]. More support for the immigration of FDC precursor instead of local differentiation comes from the expression pattern of TuJ1, a microtubule-related protein [*Lee et al.*, 2005]. The broad distribution with single positive cells scattered around SLF may indicate migratory activity of FDC. This has some support from a LTβR-Ig treatment study [*Gommerman et al.*, 2002]. It has been observed that after the treatment is stopped by removing the antibody the recovery of FDC networks causes an initially diffuse distribution of FDC before formation of a compact follicle.

In chicken the precursor of FDC are not stromal cells but are attributed to ellipsoid associated cells which are thought to be some chicken analog for DC found in mammals [*Gallego et al.*, 1997]. This may indicate that the precursor in mammals is not of mesenchymal origin or that the FDC of chicken have rather different properties and are a result of co-evolution but otherwise unrelated to mammalian FDC.

It may finally turn out that FDC are of heterogeneous origin that can develop from hematopoietic and stromal precursors [*Crivellato et al.*, 2004; *Cyster et al.*, 2000]. This may favor the view that FDC are a transient state of cells and not the terminal differentiated form of some cell type.

Conclusions about the origin of FDC   The conclusion drawn from the experimental situation is that FDC are most probably derived from stromal cells like FRC. The typical features of FDC with respect to their markers and cellular morphology is a transient feature that is induced by TNF-α and LT$\alpha_1\beta_2$. The maintenance of the FDC phenotype requires at least the constitutive presence of LT$\alpha_1\beta_2$. Considering the different expression patterns of markers on cells that are considered to be FDC it is assumed that the property to be an FDC is not the state of differentiation of a progenitor cell but more a kind of activation state of stromal cells.

2.2.4 Fibroblastic reticular cells

The fibroblastic reticular cell (FRC) forms the stromal backbone of lymphoid tissue, especially the T zone [*Bairati et al.*, 1964; *Clark*, 1962; *Crivellato and Mallardi*, 1997; *Crivellato et al.*, 2004; *Downey*, 1922; *Moe*, 1963]. FRC have not yet attracted as much attention as FDC. In marked contrast

to other fibroblast cell lines in connective tissue these cells are not embedded in the ECM but are ensheathing fibers made of ECM proteins [*Gretz et al.*, 1996]. It appears that the reticular network is also dependent on the contact with immune cells much like the FDC [*Katakai et al.*, 2004b]. The FRC phenotype can be identified by ER-TR7, gp38, VCAM-1 [*Katakai et al.*, 2004b]. The adhesion to resting T cells from the LN is weak. Co-culturing FRC with T cells induces the formation of an ER-TR7$^+$ network suggesting that ER-TR7 is a protein found in ECM fibers (up to now the protein stained by the ER-TR7 antigen has not been identified). The effect seems to be mediated partially by TNF-α which can also induce proliferation of cultured FRC. This may be related to the TNF-α-induced proliferation of cultured FDC [*Clark et al.*, 1992; *Husson et al.*, 2000; *Kim et al.*, 1994; *Tsunoda et al.*, 1997]. TNF-α also induces the expression of ICAM-1 and increases the formerly low chemokine production of CCL4, CCL5, CCL20, and CXCL10. The chemokines CCL2, CXCL12, and CX3CL1 are produced in culture without a stimulus. Note, that CCL21 could not be found in cultured FRC implying that either other stimuli are required or another stromal population is responsible for the production of CCL21 in the T zone of lymphoid tissue. Additionally, FRC express IL-6, IL-7, and IL-15 with the latter two being able to stimulate LT$\alpha_1\beta_2$ on T cells [*Cyster*, 2005; *Luther et al.*, 2002; *Tumanov et al.*, 2003] and IL-6 and IL-15 having chemotactic effects [*Clark et al.*, 1992; *Huber et al.*, 2005; *Husson et al.*, 2000; *Kim et al.*, 1994; *Park and Choi*, 2005; *Park et al.*, 2004]. Similar effects compared to TNF-α on cultured FRC are promoted by LTα [*Katakai et al.*, 2004b] most likely explained by the fact that the soluble homotrimer LTα_3 uses the same receptors as TNF-α, namely TNFR-I and TNFR-II. The presence of LT$\alpha_1\beta_2$ alone has no effect on FRC however when it acts synergistically with TNF-α or LTα it dramatically enhances ER-TR7$^+$ network formation and proliferation of FRC leading to the complete construction of a reticular network in culture. The fibers are rich for fibronectin and laminin beside the unknown ER-TR7 component. The fiber formation includes the formation of a conduit system [*Gretz et al.*, 1996, 2000; *Nolte et al.*, 2003; *Sixt et al.*, 2005]. The conduit system is a network of small open channels formed by ECM. The hollow fibers themselves are enwrapped by FRC. When the culture experiments are done with a 3D environment for FRC a conduit-like system can be established [*Katakai et al.*, 2004b]. Thus the correct formation of the reticular fibers and FRC in the LN depends on the intimate contact with immune cells as LT$\alpha_1\beta_2$ exists membrane-bound only. Reports indicate that the same principles for reticular network formation apply to the spleen [*Nolte et al.*, 2003]. The presence of reticular networks in lymphneogenesis (Sec. 2.6) [*Katakai et al.*, 2003] suggest that FRC networks can be generated *de novo* in various connective tissues. In the spleen the formation of the network is independent of LTα [*Nolte et al.*, 2003] suggesting that TNF-α is sufficient to set up the conduit system in the spleen. This is again an example of different molecular requirements for the formation of SLT with respect to the members of the TNF superfamily (Sec. 2.2.2). Considering the presented experimental data it is not clear in detail what causes the CCL21 expression in the T zone and which stromal cells are responsible for it. Thus, the development of FRC remains inconclusive except for the induction of the reticular network and the conduit system by TNF-α, LTα_3, and LT$\alpha_1\beta_2$.

2.3   Lymphoid Follicle Environment

This section considers the environment of the PLF. Formally, FRC belong to this section but won't be discussed here as they have been presented in detail in the previous sections. The remaining structures of the lymphoid tissue are the extracellular matrix (Sec. 2.3.1), the blood vascularization (Sec. 2.3.2), and the lymphatic vessels (Sec. 2.3.3).

2.3.1   Reticular network and extracellular matrix

The ECM does not only act as mechanical backbone of connective tissue but is also important for the migration of lymphocytes (Sec. 3.2). Therefore the location and composition of the ECM is important. There is a bias in the presence of ECM fibers in the follicle areas and the T zone. Various studies indicate that the PLF contain only a sparse ECM network and SLF are more or less completely devoid of ECM proteins ([*Castanos-Velez et al.*, 1995; *Katakai et al.*, 2004b; *Liakka and Autio-Harmainen*, 1992; *Maatta et al.*, 2004; *Ohtani et al.*, 1991; *Ohtsuka et al.*, 1992; *Satoh et al.*, 1997; *Ushiki et al.*, 1995] and references therein). In general the ECM fibers are also thicker in the T zone while the few fibers in the PLF are rather thin [*Ohtani et al.*, 1991; *Ushiki et al.*, 1995]. The T zone contains ECM fibers like collagen of type I and III [*Castanos-Velez et al.*, 1995; *Sixt et al.*, 2005; *Wolf et al.*, 2003b], fibronectin [*Castanos-Velez et al.*, 1995; *Liakka and Autio-Harmainen*, 1992], tenascin [*Castanos-Velez et al.*, 1995; *Liakka and Autio-Harmainen*, 1992], and lower amounts of collagen IV [*Castanos-Velez et al.*, 1995; *Maatta et al.*, 2004] and laminin [*Castanos-Velez et al.*, 1995; *Maatta et al.*, 2004; *Sixt et al.*, 2005]. Interestingly there is an accumulation of fibers composed of collagen I,III, and IV, fibronectin, laminin, vitronectin, and tenascin between T zone and the follicular areas [*Castanos-Velez et al.*, 1995; *Katakai et al.*, 2004a]. It is not clear if this is a result of mechanical interaction – B cells may push the ECM in the PLF aside – or an effect of increased ECM production at this site. Experimentally, the latter possibility is supported (see below [*Thomazy et al.*, 2003]). The PLF contains some ECM fibers of collagen I and III, and small amounts of fibronectin and vitronectin [*Castanos-Velez et al.*, 1995; *Liakka and Autio-Harmainen*, 1992]. These few proteins are correlated with vessels passing through the PLF [*Kaldjian et al.*, 2001; *Katakai et al.*, 2004a]. In SLF the mantle zone is virtually lacking all ECM fibers while the GC has some vitronectin present in the apical light zone [*Castanos-Velez et al.*, 1995]. A similar pattern can be observed for the proteoglycans, another component of the ECM fibers [*Kaldjian et al.*, 2001]. The ECM fibers themselves seem to have an organized structure of their components with a core composed of collagen III and fibronectin surrounded by layers of tenascin and laminin [*Kaldjian et al.*, 2001; *Sixt et al.*, 2005]. However, fibronectin may also be present on the outer surface of the FRC ensheathing the ECM fibers (Sec. 2.2.4).

The distribution of integrins corresponding to the ECM components has demonstrated that the mantle zone of SLF does not contain any integrin subunit of the types $\beta_1, \beta_3, \beta_4, \alpha_1, \alpha_2, \alpha_3, \alpha_4, \alpha_5, \alpha_6, \alpha_{\mathrm{IIb}}, \alpha_{\mathrm{V}}$ [*Castanos-Velez et al.*, 1995]. In general, the integrin distribution matches the presence of the ECM components the integrins can bind to (Table 2.5). The T zone contains lymphocytes expressing the β_1 and α_4 subunits binding to VCAM-1 and fibronectin. At the border of follicle and T zone only β_1 out of the integrin subunits listed before has been identified. However, there exist difference between

ECM component	integrin
collagen	$\alpha_1\beta_1$, $\alpha_2\beta_1$, $\alpha_3\beta_1$
laminin	$\alpha_1\beta_1$, $\alpha_2\beta_1$, $\alpha_3\beta_1$, $\alpha_6\beta_1$
fibronectin	$\alpha_3\beta_1$, $\alpha_4\beta_1$, $\alpha_5\beta_1$, $\alpha_V\beta_1$, $\alpha_{IIb}\beta_3$, $\alpha_V\beta_3$
vitronectin	$\alpha_V\beta_3$, $\alpha_V\beta_5$
thrombospondin	$\alpha_4\beta_1$, $\alpha_5\beta_1$, $\alpha_V\beta_3$
tenascin	$\alpha_V\beta_3$

Table 2.5: The correspondence between integrin subunit and ECM component [*Castanos-Velez et al.*, 1995].

species as monkeys show β_1 integrin subunit expression in the GC in contrast to humans [*Castanos-Velez et al.*, 1995]. The question remains if the lymphocytes adapt to the ECM components or the integrin expression pattern of the lymphocytes guides them to their subcompartments.

Consistent with the ECM pattern the expression of transglutaminase (TG) – a protein that mediates ECM production and integrin adhesion – has been found to be largely absent from follicles while it is strong on FRC [*Thomazy et al.*, 2003]. Immediately around the follicle TG staining is strong on lymphatic endothelial cells but low on FRC. The TG levels of the latter increase when the PLF is tranformed into a GC-containing SLF. *In vitro* experiments show that IL-4 may be responsible for the increased TG levels. Other cytokines that induce TG are IL-1, IL-6, TNF-α, and IFN-γ. This already indicates that the ECM pattern is not static. Studies in sheep demonstrated that immature PLF forming in a fetus contain high numbers of reticular fibers [*Halleraker et al.*, 1994; *Nicander et al.*, 1991]. These fibers are vanishing with age while at the same time immature FDC can be seen that show typical ultrastructural features while they are still covered with ECM fibers. The loss of ECM may be directly related to the formation of FDC which show increased expression of MMP (Sec. 2.2.3) degrading the ECM. This may have an effect on the migration of lymphocytes by changing the adhesive and mechanical properties of the environment.

The stromal background of the lymph node is mainly provided by the reticular network formed by the FRC [*Bairati et al.*, 1964; *Clark*, 1962; *Crivellato and Mallardi*, 1997; *Crivellato et al.*, 2004; *Downey*, 1922; *Gretz et al.*, 1996; *Moe*, 1963]. These cells ensheath the ECM fibers and almost completely prevent the direct contact of lymphocytes with the ECM proteins challenging the correlation with the integrin distribution cited above (see also next passage). The abundant fibers in the T zone have a typical spacing of 5–20 μm thus only a small region of the lymphocyte surface has contact to the reticular network [*Gretz et al.*, 1996; *Kaldjian et al.*, 2001]. This also causes the lymphocytes to adopt a more spherical shape compared to other situations [*Friedl et al.*, 2001; *Friedl and Brocker*, 2000]. There is a preferred direction of fibers from the HEV towards the subcapsular sinus ((Fig. 2.4), right panel). However, this seems not to induce a preferred direction of migration as shown by direct imaging in contrast to the *in vitro* results of cell migration (Sec. 3.2.1). FRC have also been show to bind CCL21 *in vivo* thus providing a migrative substrate for lymphocytes [*Nolte et al.*, 2003].

The combination of ECM fibers wrapped by FRC forms the basic structure for the conduit system [*Chen and Weiss*, 1972; *Gretz et al.*, 1996; *Rinehart*, 1930]. It has been shown that the reticular fibers are hollow structures that allow selected small molecules to move with a bulk flow within them

[*Gretz et al.*, 2000; *Nolte et al.*, 2003; *Sixt et al.*, 2005]. The general direction is from the subcapsular sinus to the T zone and HEV [*Crivellato and Mallardi*, 1997; *Sixt et al.*, 2005]. Interestingly, the FRC provide openings directed to FDC at the border of PLF that may be suited for transporting Ag to the FDC to induce a GCR [*Crivellato and Mallardi*, 1997]. Despite the fact that FRC wrap most of the surface of reticular fibers [*Gretz et al.*, 1996, 2000; *Nolte et al.*, 2003; *Sixt et al.*, 2005] there is sufficient contact between ECM and DC but not between lymphocytes and ECM [*Sixt et al.*, 2005]. It is possible that DC uptake Ag from the conduit system directly in a similar manner as FDC are supplied with Ag by the conduit system. The conduit system exists both in LN [*Gretz et al.*, 2000; *Kaldjian et al.*, 2001; *Nolte et al.*, 2003; *Sixt et al.*, 2005] and spleen [*Crivellato et al.*, 2004] but has not been reported for any MALT type yet while it has been found in ectopically generated lymphoid tissue [*Cupedo et al.*, 2004a] suggesting that it may be present in the MALT as well. This immediately raises the question if the structure of the ECM in SLT serves primarily for the transport of fluids or as substrate for lymphocyte migration. As the question remains open and the *intravital* imaging of lymphocytes (Sec. 3.2.1) suggests that the ECM composition may be less important for the positioning of lymphocytes than chemokines. The ECM is therefor not considered explicitly in the model (Sec. 5).

Follicle encapsulation   The shape of a follicle could in principle be determined by preformed structures of the underlying connective tissue. The increased ECM density around the follicle [*Castanos-Velez et al.*, 1995; *Katakai et al.*, 2004a] may indicate a capsule that determines shape and size of the follicle. Indeed, the GC of chicken is separated from the surrounding tissue by a layer of reticular cells [*Olah and Glick*, 1979; *Romppanen*, 1981; *Yasuda et al.*, 2003, 1998]. The presence of a GC determines if this capsule is closed or partly open. The follicles with closed capsule are also usually larger [*Olah and Glick*, 1979]. The GC of chicken lacks a mantle zone containing lymphocytes suggesting that PLF do not exist in birds. Of note the morphology of the GC is also different [*Olah and Glick*, 1979; *Yasuda et al.*, 1998]: The center is filled with large lymphoblasts which seem to be similar to centrocytes. The outer layer is composed of rapidly dividing smaller lymphoblasts seemingly similar to centroblasts. Thus a slice of the chicken GC exhibits a ring shaped pattern with a dark zone surrounding a light zone. In the light zone a cell type sharing structural and functional properties of FDC can be found.

There may exist a separating structure between T and B zone in mammals as well as indicated by the identification of a 'cortical ridge' [*Katakai et al.*, 2004a]. This is a small zone at the T/B border of follicles enriched for reticular fibers and vessels, especially HEV. The cortical ridge seem to scale with the size of the follicle it is surrounding. Also the zone has a higher frequency of CD11c^{+} DC which are involved in the activation of T and B cells to initiate a GCR [*Banchereau and Steinman*, 1998; *Dubois et al.*, 2001; *Fillatreau and Gray*, 2003; *Kaser et al.*, 2000, 1999; *Mempel et al.*, 2004; *Miller et al.*, 2004; *Schaniel et al.*, 1998; *Stoll et al.*, 2002]. The DC localization may be attributed to preferred adhesion of these cells in the cortical ridge as shown by *in vitro* assays [*Katakai et al.*, 2004a]. Conceptually, this increases the frequency of DC contacts with T cells entering through the numerous HEV in this area. However, with certain immunization protocols the cortical ridge structure disappeared. Other studies indicate that at least the lymphoid follicle border is enriched for ECM fibers not necessarily forming a separating structure ([*Castanos-Velez et al.*, 1995; *Satoh*

et al., 1997; *Ushiki et al.*, 1995] and references in [*Ohtsuka et al.*, 1992]). It is also discussed that these structures surrounding the follicle are involved in guiding lymphocytes to the medullary cords providing a route to exit the LN [*von Andrian and Mempel*, 2003; *Fu and Chaplin*, 1999]. Looking at older data the cortical ridge may be just a result at which angle the LN is sliced for preparation. The cortical ridge structures seem to be related to the deep cortical unit discussed about 25 years ago [*Belisle and Sainte-Marie*, 1981a,b,c,d,e, 1990; *Belisle et al.*, 1982; *Sainte-Marie et al.*, 1981]. The unit is discussed in slight more detail in the next section (Sec. 2.3.2).

In other mammalian species like sheep there exist follicles which have a capsule that is more similar to the case of chickens [*Belz and Heath*, 1995; *Halleraker et al.*, 1994; *Nicander et al.*, 1991]. The capsule-like structure consist of several layers of concentrically arranged FRC alternating with layers of ECM fibers around SLF. PLF have an incomplete capsule consisting of a single discontinuous layer of fibers and FRC. The capsule is less developed in LN [*Halleraker et al.*, 1994] but almost bird-like in ileal PP [*Nicander et al.*, 1991]. This may be related to the low B cell flux observed in those PLF [*Griebel and Hein*, 1996] that are considered to have primary immune function in ileal PP (Sec. 2.1.5). In the tonsil of pigs a capsule-like structure has been observed to engulf the dark zone of SLF while the mantle zone is not bounded by ECM and/or FRC layers [*Belz*, 1998]. Thus a separating structure between B and T zone of SLT which suppresses lymphocyte migration may exist in some species. The existence of species that form structurally almost identical compartments in SLT indicates that a capsule is not required to understand the formation of PLF. The capsule may be just a phenomenon that occurs as additional modification of the environment after the follicle has been formed.

2.3.2 High endothelial venules

To understand the immigration of lymphocytes into SLT one needs to now the different responsible structures in the spleen and other SLT. High endothelial venules exist in LN and MALT [*Janeway and Travers*, 1997]. The endothelium of these blood vessels is specialized to allow for a high frequency of transmigrating lymphocytes. The transmigration is regulated by chemokines like CCL19, CCL21, CXCL12, and CXCL13 [*Cyster*, 2005; *Okada et al.*, 2002] that initiate the firm adhesion of rolling lymphocytes by triggering integrin adhesion [*Cyster*, 1999, 2005; *Kim*, 2005; *Samstag et al.*, 2003]. Adhesion to HEV is mediated by molecules like PNAd, MAdCAM, and ICAM-1 that are partly specific for the corresponding SLT and certain B and T cell subsets [*Mebius et al.*, 1997; *Rennert et al.*, 1997]. However, the different expression pattern of these adhesion molecules seems not to represent a functional difference of HEV [*Rennert et al.*, 1997].

The generation of HEV seems to have similar dependencies on lymphotoxin and TNF-α like the other lymphoid structures have and the typical adhesion marker appear only in the presence of these signals [*von Andrian and Mempel*, 2003; *Cupedo et al.*, 2004c; *Drayton et al.*, 2003; *Rennert et al.*, 1997]. The HEV show a characteristic pattern by forming a network around follicles while only few capillaries are penetrating PLF [*Azzali and Arcari*, 2000; *Azzali et al.*, 2002; *Belisle and Sainte-Marie*, 1990; *Bhalla et al.*, 1981; *Ekino et al.*, 1979; *Herman et al.*, 1972; *Sainte-Marie et al.*, 1984]. In contrast, blood vessels in the T zone form a dense meshwork. Also GC can have a rich vascularization [*Azzali et al.*, 2002] which seems to develop rapidly after immunization and vanishes when the SLF

transforms back into an PLF [*Herman et al.*, 1972]. The HEV in LN are found close to lymphatic vessels forming gaps of less than 10 μm between the two vessel types. The gaps are densely filled with lymphocytes [*Ohtani et al.*, 2003, 1986]. Of note, a series of studies found out that the T zone has a substructure – the so-called deep cortical units [*Belisle and Sainte-Marie*, 1981a,b,c,d,e, 1990; *Belisle et al.*, 1982; *Sainte-Marie et al.*, 1981]. The T zone is not a continuous and homogeneous layer of cells in the LN. The deep cortical units are semispherical in shape and are located beneath 2–6 associated follicles. They extend into the medulla of the LN. The typical size is around 1 millimeter. A deep cortical unit is divided into two parts: A vessel and ECM rich periphery and a center densely filled with lymphocytes. Thus in many structural aspects the deep cortical units are similar to PLF.

HEV do not exist in the spleen. Direct observation by *intravital* microscopy have revealed that the central arteriole supports smaller vessels – termed pulsating vessel – which end up in channels that are probably formed by ECM and are not lined by endothelial cells – the terminal vessels [*Grayson et al.*, 2003]. T cells enter the white pulp of the spleen through these vessels. In contrast to the requirements for specific adhesive interactions of lymphocytes to enter through HEV, the entry into the spleen is unaffected when these interactions are blocked [*Grayson et al.*, 2003]. Previous expectations that lymphocytes enter through the red pulp and the marginal zone [*Crivellato et al.*, 2004; *Cyster*, 2005; *van Ewijk and Nieuwenhuis*, 1985; *Pellas and Weiss*, 1990b; *Schmidt et al.*, 1985, 1988] could not be confirmed by the direct observation of lymphocytes [*Grayson et al.*, 2003]. Despite not being HEV in terms of adhesive and structural features, the blood vessels in the spleen rarely enter the follicle and are forming a network around it [*Pellas and Weiss*, 1990a; *Schmidt et al.*, 1985, 1988].

The general picture developed in this section is that lymphocytes enter SLT in the T zone either directly through HEV or indirectly using other structures in the case of the spleen. This implies that B cells enter in the T zone before they migrate into the PLF.

2.3.3 Lymphatic vessels

To achieve a flow equilibrium of lymphocytes through SLT the exit routes are equally important to the entry routes. However, the experimental data is rather small and has increased only slowly during the past few years. It is commonly thought that the lymphatic sinuses are sites that guide lymphocytes to leave LN [*Cyster*, 2005]. The sinuses merge with the ELV exiting the LN and therefore are considered to belong to the efferent lymphatic system throughout this work. However, one has to note that there are smaller ELV (3 μm diameter) that may be only suited for fluid transport as can be seen in the spleen [*Alexandre-Pires et al.*, 2003].

The most extensive studies of the lymphatic vascularization has been performed in the nice work of Azzali et al. on PP of various species [*Azzali*, 2003; *Azzali and Arcari*, 2000; *Azzali et al.*, 2002]. The corrosion cast can visualize the vessel network independent of other tissue structures. In this technique colored latex is injected into the vessels. After fixation and polymerization the remaining tissue is removed by hydrochloric acid. However, this makes the detailed correlation of the vessel distribution with the PP microarchitecture particular difficult. The lymphatic vessels are surrounding the follicle and form a half-open basket around it. The typical diameter of the vessels around the

top is 50–60 μm, 60–90 μm in the interfollicular area, and 120–180 μm for the vessels beneath the lymphoid follicles collecting the lymph. The latter two vessel types are frequently found to contain transmigrating lymphocytes and are filled with lymphocytes. Generally, the number of lymphatic vessels is higher than that of blood vessels [*Azzali et al.*, 2002]. The basket-like pattern is also found in the tonsils of pigs [*Belz*, 1998]. Interestingly, the ELV are quite big compared to HEV which have an average size of about 28 μm in LN and PP [*Grayson et al.*, 2003]. The terminal vessels of the spleen are even smaller with about 12 μm diameter [*Grayson et al.*, 2003] while the central arteriole ranges from 75 to 250 μm [*Alexandre-Pires et al.*, 2003]. A review [*Azzali*, 2003] shows that the overall pattern – lymphatic vessels around but not inside follicles – appears in PP, ILF, appendix, and tonsils, i.e. all types of MALT.

Older microanatomical studies demonstrate that – as explained above for the PP – the ELV exhibit the basket-like shape of these vessels around the follicles of other SLT [*Belisle and Sainte-Marie*, 1990; *Belz and Heath*, 1995; *Drinker et al.*, 1933; *van Ewijk and van der Kwast*, 1980; *Ohtani et al.*, 2003, 1986; *Pellas and Weiss*, 1990a]. Dependent on the species this basket consists of a network of anastomosing vessels or flattened vessels that form an almost continuous shell around the basal part of the follicle [*Belz and Heath*, 1995; *Ohtani et al.*, 1986]. In general the part located away from the adjacent T zone is free of vessels and in many cases the ELV form a crown around this part of the follicles [*Azzali*, 2003; *Azzali and Arcari*, 2000; *Azzali et al.*, 2002; *Ohtani et al.*, 1986]. The walls of the lymphatic vessel can have openings in the vicinity of the follicles [*Drinker et al.*, 1933; *Ohtani et al.*, 1991]. Of interest the mentioned ELV pattern is also observed in the bursa of chicken [*Ekino et al.*, 1979]. There it has been shown that the vessels close to follicle are filled with lymphocyte populations that resemble that of the adjacent follicle [*Ekino et al.*, 1979]. All this data indicates that the lymphatic vessels are indeed designed to permit the emigration of lymphocytes from SLT and especially from the PLF.

In contrast to the other tissues LN have also an afferent lymphatic vascularization that partly continues into the efferent lymphatic vascularization [*Ohtani et al.*, 2003]. Via this path lymph fluid and DC arrive at the LN both of which bring Ag into contact with lymphocytes. The lymph itself may be filtered and transported to the follicles via the conduit system described previously (Sec. 2.3.1). The afferent lymphatic system is required to maintain HEV and maintain the LN ability to recruit lymphocytes from the blood [*von Andrian and Mempel*, 2003; *Hendriks and Eestermans*, 1983] which indicates that the $LT\alpha_1\beta_2$ expression of lymphocytes in the LN depends on the support by the afferent lymphatics.

The amount of recent studies about the lymphatic system suffers from the lack of specific markers for lymphatic endothelium cells (LEC). Among the few markers are D6 (β-chemokine receptor) [*Hong et al.*, 2004; *Nibbs et al.*, 2001], LYVE-1 (an endocytic receptor for hyaluronan) [*Garrafa et al.*, 2006; *Hong et al.*, 2004; *Prevo et al.*, 2001; *Tammela et al.*, 2005], and VEGFR-3 (vascular endothelial growth factor receptor-3) [*Garrafa et al.*, 2006; *Hong et al.*, 2004; *Makinen et al.*, 2001]. Culture experiments show that LEC are widely similar to blood endothelial cells (BEC) using just another growth factor namely VEGF-C utilizing the receptor VEGFR-3 [*Garrafa et al.*, 2006; *Ng et al.*, 2004; *Tammela et al.*, 2005]. Another growth factor VEGF-D [*Hong et al.*, 2004; *Tammela et al.*, 2005] seems not to be absolutely required [*Baldwin et al.*, 2005]. The source for VEGF-C in

tissue can be DC with the MHC II-negative subset expressing the receptor VEGFR-3 at the same time [*Hamrah et al.*, 2003]. One of the upregulating factors for VEGF-C is TNF-α [*Hamrah et al.*, 2003; *Kerjaschki*, 2005]. Macrophages can also produce VEGF-C [*Kerjaschki*, 2005]. Even more important macrophages have been shown to transdifferentiate into LEC – a notion that is supported by the fact that macrophages express VEGFR-3 [*Kerjaschki*, 2005]. This together suggests that the lymphatics in SLT can be influenced directly or indirectly by lymphocytes via TNF-α.

A recent study identified a new mannose receptor on lymphatic endothelium [*Irjala et al.*, 2001]. This receptor is almost exclusively found on the lymphatic vessels of LN and binds CD62L. The interaction of lymphocyte CD62L with the new mannose receptor on the ELV mediates the binding of the lymphocytes enabling the exit from the LN. In contrast to the requirement for shear forces for effective CD62L binding in the blood stream and subsequent transmigration through HEV, the new receptor acts independently of shear forces [*Irjala et al.*, 2001]. Even more striking shear forces prevent efficient binding to lymphatic endothelium. The interesting question is whether this receptor is found on the HEV of LN in pigs which are the primary route for lymphocyte egress in these animals [*Binns and Licence*, 1990]. It has been shown that lymphocytes from pigs injected into sheep take the 'normal' route through ELV while sheep lymphocytes injected into pigs take the HEV route suggesting that the exit of lymphocytes is determined by the vessels and not by lymphocytes themselves [*Binns and Licence*, 1990]. This strengthens the notion that the lymphatic vessels inside the SLT are involved in the exit of lymphocytes from SLT providing they have the proper phenotype.

Altogether the lymphatic sinuses serve as exit routes for lymphocytes in SLT. For simplicity, and considering their function, they are collected in the term ELV. Structurally, the ELV form a network around the B zone and are well represented in the T zone such that B cells have to leave the PLF first in order to exit from SLT.

2.4   Homeostasis - migratory transit of lymphocytes

Lymphocytes are circulating through SLT by leaving the blood vessels, home to the proper zone, and leave the tissue again to enter the ELV thus forming a flow equilibrium. The overall transit time for T cells from blood to efferent lymph is in the order of 24–36 hours [*Young et al.*, 2000]. Others sources report shorter times of 12–18 hours [*Binns and Licence*, 1990; *Cyster*, 2005; *van Ewijk and van der Kwast*, 1980]. The differences may be related to which type of SLT the lymphocytes are passing during a transit cycle. Detailed evaluations of lymphocyte traffic through sheep LN revealed typical transit times for T and B cells to be in the order of 12 hours and minimal transit times of 4–5 hours [*Srikusalanukul et al.*, 2002]. Previous studies indicated typical transit times of about 24 hours for lymphocytes traveling from the blood to enter efferent lymph via LN [*von Andrian and Mempel*, 2003; *Cyster*, 2005; *van Ewijk and van der Kwast*, 1980; *Lo et al.*, 2005; *Seabrook et al.*, 1999; *Srikusalanukul et al.*, 2002; *Young*, 1999; *Young et al.*, 2000] while several older studies revealed shorter times of 3–6 and 8 hours for T and B cells, respectively, in the spleen [*Pellas and Weiss*, 1990a,b; *Young*, 1999].

The typical number of lymphocytes traveling through 1 gram ($\sim 2 \cdot 10^9$ cells) of LN tissue has been

measured to be $3 \cdot 10^7$ cells per hour with about 85% entering the LN through HEV and the rest being generated inside the LN or entering via the afferent lymphatic vessels [*Young*, 1999]. Further estimates yield that about half of the lymphocytes passing the blood vessels through a LN are entering the lymphoid tissue. The ratio of B to T cells is in the range of 1:2 to 2:3 [*Sacca et al.*, 1998; *Young*, 1999].

More T than B cells enter the tissue and B cells stay longer inside the tissue in average. The latter fact may be easily explained by the longer route the B cells have to take across the T zone to reach the PLF (Sec. 2.3.2 and Sec. 2.3.3) and the lower migration speed of B cells [*Gunzer et al.*, 2004; *Miller et al.*, 2003, 2002; *Okada et al.*, 2005; *Wei et al.*, 2003].

2.4.1 Migration into secondary lymphatic organs

There are several distinct combinations of chemokine and adhesion receptors requirements for lymphocytes to enter different SLT. The chemokine receptors CXCR4 is required for the entrance to LN and PP [*Okada et al.*, 2002]. The corresponding chemokine CXCL12 is expressed by HEV both in LN and PP. Additionally, CXCL12 is strongly expressed in the medullary cords possibly guiding the exit of lymphocytes from the LN (see next section). CCR7 the receptor for the chemokines CCL19 and CCL21 is recruiting T cells into LN and PP whereas B cells do not require CCR7 to enter PP. These requirements can be tested by either knockout experiments for receptors or pretreatment with chemokine (which downregulates the receptor (Sec. 3.3)). Interestingly, neither CXCR4 nor CCR7 are required for B cells to enter the spleen [*Okada et al.*, 2002]. B cells are recruited to PP mainly by CXCR5 through CXCL13-expressing HEV found only in the follicles of PP [*Okada et al.*, 2002]. In contrast those CXCL13$^+$ vessels could not be observed in LN. Consequently, CXCR5 deficiency does not alter the recruitment of lymphocytes to LN but B cell entrance of PP is strongly reduced. In the spleen T cell recruitment is tributed to CCR7 and B cell entry is related to CXCR5 and CCR7 [*Cyster*, 2005; *Muller et al.*, 2003]. The requirements for NALT lymphocyte recruitment seem to differ as CXCL13$^{-/-}$ show a severe reduction of T cell entrance compared to deficiencies in the chemokines CCL19 and CCL21 that leave T cell numbers almost unchanged [*Rangel-Moreno et al.*, 2005]. Thus NALT may preferentially recruit a CXCR5$^+$CCR7$^-$ subset of T cells.

The requirement for adhesion receptors is less specific. The transmigration process mediated by HEV (Sec. 2.3.2) depends on the presence of the proper integrins, selectins, and their receptors [*Cyster*, 1999, 2005; *Kim*, 2005; *Samstag et al.*, 2003]. Only the entrance of the spleen is widely independent of integrins. It may be concluded that the composition of lymphocyte subpopulations differs in the various SLT while it is assumed that the guiding processes for the structure formation in the process of organogenesis remains unaffected.

2.4.2 Lymphoid organ egress

There are not many studies concentrating on the question how the exit of lymphocytes from SLT is regulated. The situation is similar to the lack of studies about the lymphatic vessel system (Sec. 2.3.3)

involved in this process.

A set of experiments could demonstrate that certain integrins (α_4- and β_2-integrins) are required for the entry of lymphocytes but are dispensable for the exit [*Lo et al.*, 2005]. Inhibiting the Gα_i signaling – which is part of the signaling cascade of chemokine receptors – reduces the efficiency of LN egress of lymphocytes. Several experimental studies identified the sphingosine-1-phosphate receptor 1 (S1P$_1$) and its ligand sphingosine 1 (S1P) to be relevant [*Cyster*, 2005; *Lo et al.*, 2005; *Matloubian et al.*, 2004; *Sallusto and Mackay*, 2004]. S1P is present in high concentration of 100–400 nM in the blood and other body fluids ([*Schwab et al.*, 2005] and references in [*Cyster*, 2005; *Lo et al.*, 2005; *Matloubian et al.*, 2004; *Rosen and Goetzl*, 2005]). It is a lipid that can induce chemotactic responses. Treating mice with the drug FTY720 – whose phosphorylated form is an S1P agonist – causes the downregulation of S1P$_1$ on lymphocytes and the accumulation of lymphocytes in secondary lymphoid organs. After cells enter the SLT they downregulate S1P$_1$ for 1–2 days by downregulation of S1P$_1$ mRNA. A faster desensitization mechanism comparable to that of chemokine receptors (Sec. 3.3) is by the internalization of S1P$_1$ within 45 minutes exposure to S1P at blood level concentrations [*Lo et al.*, 2005]. The reduction of S1P$_1$ levels is restored partially within 1.5 hours and fully after around 4 hours. On the other side when cells are deficient for S1P$_1$ they accumulate in the lymphoid tissues similarly to the FTY720 drug treatment [*Matloubian et al.*, 2004]. Considering the transit times of lymphocytes through SLT (Sec. 2.4) the downregulation of S1P$_1$ mRNA seems not to be the major mechanism that keeps the cells inside the tissue as the corresponding time for S1P$_1$ reexpression is to long.

S1P can modulate the chemotactic responses of cells to other chemokines either by enhancing [*Kim*, 2005; *Rosen and Goetzl*, 2005; *Yopp et al.*, 2005] or reducing the sensitivity in a dose-dependent manner [*Dorsam et al.*, 2003]. If B cells overexpress S1P$_1$ they relocate from the splenic PLF to the red pulp. This relocation can be abrogated by treating the mice with FTY720. On the contrary, T cells are not affected in their localization by S1P$_1$ overexpression. Thus the effect of S1P inhibition might not be directly related to its own chemotactic activity but by changing the overall migratory behavior of lymphocytes. Yet another option for the effects of S1P is offered by the fact that S1P can modulate the permeability of the endothelium of vessels directly regulating the transmigration of lymphocytes [*Rosen and Goetzl*, 2005; *Wei et al.*, 2005; *Yopp et al.*, 2005]. However, this seems not to explain the requirement of the receptor S1P$_1$ on lymphocytes for the egress from SLT [*Matloubian et al.*, 2004; *Wei et al.*, 2005]. Direct observations of S1P-related drugs revealed that T lymphocytes are prevented from entering the lymphatic vessels when S1P agonists are stimulating the endothelial cells as noticed by empty vessels [*Wei et al.*, 2005]. The migration of the cells remains basically unaffected by the treatment.

S1P itself can be upregulated by TNF-α [*Rosen and Goetzl*, 2005]. One of the major source for S1P are endothelial cells. It is rapidly degraded in tissues by the S1P lyase [*Rosen and Goetzl*, 2005; *Schwab et al.*, 2005]. S1P also can get inactivated by the abundant presence of lipid-phosphate-phosphohydrolases on the cell surfaces. This leads to tissue concentrations of 5–20 nM which is in the range of chemotactic activity but does not induce significant internalization of S1P$_1$ [*Dorsam et al.*, 2003; *Rosen and Goetzl*, 2005; *Schwab et al.*, 2005]. By blocking the lyases, S1P levels can be enhanced in tissues [*Schwab et al.*, 2005]. This leads to the downregulation of S1P$_1$ on lymphocytes

and the trapping of the cells in lymphoid tissues similar to the effect mediated by FTY720.

In LN the exit of lymphocytes may also depend on CXCL12 expressed in the medullary cords [*Okada et al.*, 2002]. The chemokine may attract the lymphocytes from the cortex to enter the ELV present in this area [*von Andrian and Mempel*, 2003; *Fu and Chaplin*, 1999].

The egress of T cells from peripheral tissue by entering the afferent lymphatic vessels is guided by CCL21 expressed on LEC [*Bromley et al.*, 2005; *Randolph et al.*, 2005]. Another study showed that a deficiency of CCR7 reduced the number of T cells that enter the afferent lymphatic vasculature [*Debes et al.*, 2005]. This raises the question if CCL21 could do the same in secondary lymphoid organs to guide lymphocytes into the efferent lymphatic system. Also the other CCR7 ligand CCL19 might promote this function as CCL19 can be present on LEC as well [*von Andrian and Mempel*, 2003]. Note, that the expression of CCL21 on lymphatic vessels in mice does not depend on $LT\alpha_1\beta_2$ as the stromal expression in the T zone does due to a different isoform of CCL21 [*Cyster*, 2005; *Luther et al.*, 2000]. If $LT\alpha_1\beta_2$-independence of CCL21 on lymphatic vessels is true for other mammals is not clear as for example humans lack the corresponding long isoform of CCL21 [*von Andrian and Mempel*, 2003].

Another molecule that may influence the egress of lymphocytes from lymphoid tissues is $IFN\alpha$ [*Hein and Supersaxo*, 1988; *Kalaaji et al.*, 1988]. Increased $IFN\alpha$ levels reduce the amount of lymphocytes in the ELV while immigration is seemingly unaffected, i.e. $IFN\alpha$ is reducing the outflux of lymphocytes from SLT. A possible explanation for this effect might be the observation that $IFN\alpha$ can increase the chemotaxis of B cells [*Badr et al.*, 2005] (Sec. 3.3). Thus B cells are insensitive for a re-balance of their chemotactic response by increasing $S1P_1$ levels and the cells get trapped in the PLF by the ongoing CXCL13 response.

The direct *in vivo* data on the migration pattern of lymphocytes in LN [*Gunzer et al.*, 2004; *Miller et al.*, 2003, 2002; *Okada et al.*, 2005; *Wei et al.*, 2003] suggests that chemotaxis may not play a role at all and that random migration permits the lymphocytes to leave the tissue via the ELV. The dependence on chemokine receptors could be that the chemokinetic effect mediated by these receptors reduces the random migration as well and thus reduces the transmigration of lymphocytes into the lumen of lymphatic vessels.

In the spleen the egress of lymphocytes is supposed to occur via migration to the red pulp [*Cyster*, 2005]. Several other groups suggest, based on the lymphatic vascularization of the white pulp, that lymphocytes leave the white pulp primarily though ELV like in the other SLT.

As already pointed out the data on the lymphocyte exit from SLT is less settled compared to the entry via HEV. It is not clear if chemotaxis plays a significant role or not. It seems however that S1P and its receptor $S1P_1$ on lymphocytes are involved in regulating the egress of lymphocytes although the detailed mechanism is not known.

2.5   *Organogenesis of Primary Lymphoid Follicles*

Organogenesis of SLT is the process of formation and structuring of tissue to perform immune functions. This section shall not cover the whole process. Only the steps involving lymphocytes and related cells are considered. The prestructures like primordial lymph sacs [*Cupedo et al.*, 2004c; *Kim et al.*, 2000] or the spleen before white pulp formation is not considered here. The data available for lymphoid tissue organogenesis are mostly for PP and LN of mice. The spleen is almost not investigated in this context. There are some morphologic studies on other mammalian species as well. Indirect information on the single processes can be drawn also from the knock-out and bone marrow transfer experiments discussed previously (Sec. 2.2.2).

With the help of the injection of LTβR-Ig that blocks the correct signaling along the LT$\alpha_1\beta_2$-LTβR path the sequence of organogenesis of various SLT can be determined in mice [*Fu and Chaplin*, 1999; *Nishikawa et al.*, 2003; *Rennert et al.*, 1997]. First, around day 12 of gestation, MLN, sacral, and cervical LN are formed [4]. Until gestational day 16 axillary and inguinal LN are generated. Popliteal LN are the last LN formed until day 18. Peyer's patches as the last SLT in the sequence are completed around birth. However, some LN types do not require LTβR and therefore cannot be blocked by LTβR-Ig. These LN are some cervical, sacral, and lumbar LN in addition to MLN. This raises the question when these LN are really generated. Further experiments showed that this set of LN does depend on the gene for LTα but not on those for LTβ, TNF-α, TNFR-I, TNFR-II, and LTβR[*Rennert et al.*, 1997] suggesting the existence of additional receptors that may bind LTα_3 and are sufficient to induce these LN. Also unidentified gene products of LTα may exist acting on unknown receptors. The requirement for LT$\alpha_1\beta_2$ in the formation of LN and PP is restricted to a developmental time window as indicated by the fact that the later injection of LTβR-Ig does not destroy the LN or PP – but of course influences the microarchitecture (Sec. 2.2.2).

2.5.1   Peyer's patch development

The most detailed studies on SLT development are about PP in mice [*Finke*, 2005; *Fu and Chaplin*, 1999; *Muller et al.*, 2003; *Nishikawa et al.*, 2003]. The PP has also the favorable property to be the SLT with the lowest grade of complexity, i.e. there are no prestructures except for the epithelial layers which are not directly involved in the process of organogenesis of the lymphoid tissue. The two cell types dominating in SLT organogenesis are lymphoid tissue inducer cells (LTIC) and lymphoid tissue organizing cells (LTOC) [*Cupedo et al.*, 2004c; *Honda et al.*, 2001; *Nishikawa et al.*, 2003]. LTIC are of hematopoietic origin as indicated by the CD45 marker while LTOC are of mesenchymal origin. The LTIC are characterized as CD3$^-$CD4$^+$IL-7R$^+$ cells and are likely to be generated in the fetal liver and not in the bone marrow [*Mebius et al.*, 2001, 1997; *Yoshida et al.*, 1999]. Due to their mesenchymal nature it seems likely that LTOC are derived from local stromal cell populations [*Nishikawa et al.*, 2003] and therefore directly related to FRC and FDC. The detailed histochemistry of the two cell types is summarized in (Table 2.6).

---

[4]Location of the LN types is shown in (Fig. 2.4), right panel.

The first step of PP formation seems to be MAdCAM expression on venous endothelial cells along the intestine as early as day 9.5 of gestation [*Hashi et al.*, 2001]. The expression pattern starts as homogeneous distribution in the PP anlagen and rearranges in a network pattern until day 17.5, eventually indicating the formation of HEV. At the same time CCL21 expression can be observed for the first time [*Honda et al.*, 2001]. The first signs of internal structure in the PP anlagen is the formation of an irregular cluster of LTIC and LTOC at day 15 which subsequently splits up into several compartments [*Fu and Chaplin*, 1999; *Hashi et al.*, 2001; *Yoshida et al.*, 1999, 2002]. The first cells that immigrate into PP anlagen after the LTIC are CD11c$^+$ DC [*Hashi et al.*, 2001; *Yoshida et al.*, 1999]. It is also possible that the CD11c$^+$ DC are a result of the differentiation of LTIC as shown by *in vitro* culturing [*Finke*, 2005; *Muller et al.*, 2003]. The DC accumulate at the periphery of the developing PP [*Hashi et al.*, 2001; *Yoshida et al.*, 1999]. 2 days after birth several follicle-like structures are formed [*Hashi et al.*, 2001]. Their centers are composed of LTIC surrounded by CCR7$^+$CXCR5$^-$CD11c$^+$ DC. The ECM is also structured with the expression of VCAM-1 correlating with DC localization. MAdCAM expression correlates with the VCAM-1 pattern with a delayed dynamics finally ending up with an exclusive expression on HEV surrounding the follicles.

Lymphocytes enter PP around birth. They distribute homogeneously at the beginning, consistent with the yet homogeneous vascular pattern demarcated by MAdCAM. Following the reorganization of MAdCAM expression, B cells relocate to the follicles and demonstrate a distribution similar to the LTIC. T cells remain outside the follicles occupying a larger area than the DC. In later stages DC evenly redistribute in the T cell occupied zone. As expected by the late entry of lymphocytes the compartmentalization occurs also in SCID mice with just smaller follicles [*Hashi et al.*, 2001]. A similar process may happen in the spleen as indicated by the follicle-like pattern which is highlighted when LT$\alpha^{-/-}$ lymphocytes are injected into SCID mice [*Gonzalez et al.*, 1998].

The molecular mechanism behind the organogenesis process involve additional molecules that have not yet been discussed (Sec. 2.2.2). IL-7 and its receptor IL-7Rα play a major role in the initial stages of PP organogenesis. Stimulation of IL-7Rα on LTIC leads to the expression of LT$\alpha_1\beta_2$ [*Finke*, 2005; *Honda et al.*, 2001; *Kim et al.*, 2000; *Luther et al.*, 2003; *Muller et al.*, 2003; *Nishikawa et al.*, 2003; *Yoshida et al.*, 1999, 2002]. Like in the positive feedback loop in the spleen between FDC derived CXCL13 and B cell LT$\alpha_1\beta_2$ [*Ansel et al.*, 2000], LT$\alpha_1\beta_2$ on LTIC stimulates LTβR on LTOC inducing the latter ones to produce CXCL13, CCL19, CCL21 and IL-7 and to express ICAM-1 and VCAM-1 [*Honda et al.*, 2001; *Muller et al.*, 2003; *Nishikawa et al.*, 2003]. This sets up a feedback-loop between IL-7 and LT$\alpha_1\beta_2$ different from the splenic feedback loop made up by CXCL13 and LT$\alpha_1\beta_2$. In contrast the FDC-B-cell positive feedback loop, CXCL13 cannot upregulate LT$\alpha_1\beta_2$ on LTIC [*Luther et al.*, 2003; *Yoshida et al.*, 2002]. In addition, IL-7 is only one of the molecules that can induce LT$\alpha_1\beta_2$ on LTIC, others are TRANCE (TNF-related activation-induced cytokine) and TNF-α [*Luther et al.*, 2003; *Muller et al.*, 2003; *Nishikawa et al.*, 2003; *Yoshida et al.*, 2002]. Current evidence suggest that signals either via LTβR of IL-7Rα are initiating the development of PP [*Honda et al.*, 2001; *Yoshida et al.*, 1999]. In IL-7Rα-deficient mice PP anlagen do not form while in IL-7$^{-/-}$ mice PP are formed demonstrating that there is another ligand for IL-7Rα [*Nishikawa et al.*, 2003; *Yoshida et al.*, 1999]. The induction of PP seems not to be strictly regulated during development as size and position of the anlagen varies among individuals. Some authors suggest that a reaction-diffusion system of IL-7 or the other IL-7Rα-ligand is responsible for the positioning of the PP [*Honda et al.*,

	LTIC	LTOC
marker	CD45$^+$ CD4$^+$ CD3$^-$	
adhesion	$\alpha_4\beta_7$ $\alpha_4\beta_1$ ICAM-1	VCAM-1 ICAM-1 MAdCAM-1
signals	IL-7Rα LT$\alpha_1\beta_2$ TRANCE TRANCE-R	IL-7 LTβR
migration	CXCR4 CCR7 CXCR5	CXCL12 CCL19 CCL21 CXCL13

Table 2.6: The marker identifying the two main cell populations involved in PP and LN organization. Data is taken from [*Cupedo et al.*, 2004c; *Finke*, 2005; *Hashi et al.*, 2001; *Honda et al.*, 2001; *Kim et al.*, 2000; *Luther et al.*, 2003; *Mebius et al.*, 1997; *Muller et al.*, 2003; *Nishikawa et al.*, 2003; *Yoshida et al.*, 1999, 2002]. It has been show that CXCR4, CXCR5, and CCR7 are functional.

2001; *Nishikawa et al.*, 2003]. However, the size of the fetuses of mammalian species (all are known to have PP) is by far too large to allow this mechanism to work. A fact that counts strong as the PP are formed around birth when the organism is already quite large. A simple estimate of the characteristic time required to cover 1 cm by diffusion is in the order of 1 week (diffusion constant $D = 100\mu m^2 s^{-1}$ [*Randolph et al.*, 2005]). It is unlikely that such a gradient is stable over that time. For animals where this distance is 10 cm the time is in the order of 100 weeks exceeding the time of development.

Analogously to the injection of LTβR-Ig described at the beginning the time window for PP development in mice can be determined by anti-IL-7Rα to be at day 12 to 14 of gestation starting with the PP of the jejunum and proceeding to the PP in the ileum [*Nishikawa et al.*, 2003; *Yoshida et al.*, 1999]. The requirement for LT$\alpha_1\beta_2$ exceeds that of IL-7Rα-signals as its inhibition can lead to defects after this time window indicating that the maintenance of the PP structure depends on continuous LT$\alpha_1\beta_2$-signaling as already suggested by the molecular requirements cited above (Sec. 2.2.2). Furthermore, the induction of LT$\alpha_1\beta_2$ on LTIC seems to be differently regulated compared to B cells. In contrast to the constitutive presence of CXCL13 in the case of B cells ongoing exposure to IL-7 is not required – as shown by blocking with anti-IL-7Rα. However, LTIC seem to be the only source for LT$\alpha_1\beta_2$ at this time point as lymphocytes as alternative source immigrate only at later time points pointing out that LT$\alpha_1\beta_2$ expression remains high on LTIC without IL-7 stimulus. Interestingly, the administration of a LT$\alpha_1\beta_2$-substitute cannot restore PP formation in LT$\alpha^{-/-}$ mice while it is sufficient for the generation of LN [*Nishikawa et al.*, 2003] suggesting a role for LTα_3 in PP formation.

Although not studied in that much detail, the PP development of species like sheep [*Halleraker et al.*, 1994; *Nicander et al.*, 1991], goat [*Nicander et al.*, 1991], and pig [*Makala et al.*, 2000] confirmed the developmental steps described for the mouse. In the first two mentioned species the ileal PP with presumed primary lymphoid tissue function (Sec. 2.1.5) have been investigated. The PP development is completed before birth. In the pig the development of the jejunal PP completes only after birth [*Makala et al.*, 2000] like the PP in the case of mice.

In summary, the steps in PP organogenesis are:

- formation of vessels and expression of adhesion molecules

- unorganized aggregate of a LT$\alpha_1\beta_2$ source (LTIC)

- induction of homeostatic chemokines CCL21 and CXCL13

- DC enter the site and form a peripheral ring

- immigration of lymphocytes

- transformation of the ring into a follicular pattern with LTIC in the center and DC at the periphery

- B cells home to follicles and T cells occupy the remaining tissue, DC distribute homogeneously in the T zone

Development of other MALT   The isolated lymphoid follicles (ILF) found along the intestine are different from PP including their developmental steps. They depend on the presence of B cells but not on LTIC [*McDonald et al.*, 2005]. More precisely immature ILF – which are just B cell aggregates – form in the presence of some LTα-source (lymphocytes or LTIC) but the progression to mature ILF with the typical lymphoid microarchitecture requires LTα on B cells but not on other cell types. This suggests that ILF are no true SLT but *tertiary* lymphoid tissue. This tissue type requires an immune reaction for their organization (Sec. 2.5.4) and the follicles develop directly as SLF including a GC. They are either induced artificially (Sec. 2.5.4) or during diseases (Sec. 2.6). However, in the case of ILF the GC may be atypical and not dependent on adaptive immune responses [*McDonald et al.*, 2005]. Some evidence indicates that ILF are initiated by innate immune responses.

NALT development occurs around birth. It gradually develops the typical secondary lymphoid structure within a few weeks after birth [*Ying et al.*, 2005]. The levels of CCL21 appear first on lymphatic vessels at day 4 after birth and appear on HEV from day 21 on. In contrast to LN CCL21 does not appear on stromal cells. CXCL13 can be detected from day 7 on homogeneously distributed throughout the NALT reaching its normal compartmentalization after two more weeks. The chemokine expression depends on LTα and is largely reduced but present in LT$\beta^{-/-}$ mice. Even though NALT is morphologically very similar to PP its development is IL-7 independent and the accumulation of DC does not require LTα. Albeit LTIC can be found at the sites of NALT formation [*Fukuyama et al.*, 2002].

To conclude, PP is representative for the development of MALT despite the slightly different molecular and cellular requirements (Sec. 2.2.2 and Sec. 2.5).

2.5.2   Lymph node development

The development of LN is largely analog to PP [*Mebius et al.*, 1997; *Nishikawa et al.*, 2003]. It seems however that TRANCE and TRANCE-R are required (see (Table 2.2) and reference there) while IL-7 and IL-7Rα are dispensable for LN development [*Finke*, 2005; *Kim et al.*, 2000; *Muller et al.*, 2003; *Nishikawa et al.*, 2003; *Yoshida et al.*, 2002]. Another difference is that LTIC may be activated to express LT$\alpha_1\beta_2$ after migration to the LN anlagen while it is likely that LTIC get activated before entering the PP anlagen [*Luther et al.*, 2003].

TRANCE has been found to be expressed by LTIC together with its receptor TRANCE-R [*Kim et al.*, 2000]. TRANCE can be found in LN anlagen but not in the developing PP [*Yoshida et al.*, 2002]. The signaling via TRANCE-R on LTIC can induce high levels of $LT\alpha_1\beta_2$ on LTIC suggesting that clusters of LTIC generate $LT\alpha_1\beta_2$-signals transmitted to $LT\beta R^+$ mesenchymal cells [*Finke*, 2005; *Kim et al.*, 2000; *Muller et al.*, 2003; *Yoshida et al.*, 2002]. The mesenchymal cells are likely to be similar to the LTOC seen in PP anlagen. However, $TRANCE^{-/-}$ mice treated with anti-LTβR to substitute for the missing $LT\alpha_1\beta_2$ signal cannot restore LN formation. This suggests that TRANCE has an additional effect besides upregulation of $LT\alpha_1\beta_2$ on LTIC [*Muller et al.*, 2003]. Moreover the LN development is partially restored by injecting IL-7, i.e. LN show up but there is no B/T segregation [*Muller et al.*, 2003; *Yoshida et al.*, 2002]. That indicates that the LTIC in PP and LN development are the same but are differently regulated during organogenesis, i.e. TRANCE for LN and IL-7 for PP [*Yoshida et al.*, 2002]. Furthermore one can conclude that IL-7 will have additional effects on LTIC in addition $LT\alpha_1\beta_2$ upregulation as it is the case for TRANCE. The requirement for TRANCE in LN development seems not be apply to all LN as some cervical LN can develop partly in its absence forming a ring structure of B and T zone [*Kim et al.*, 2000]. Transgenic TRANCE-overexpression on B and T cells in $TRANCE^{-/-}$ can restore LN formation with only slightly disturbed PLF structure [*Kim et al.*, 2000]. This sets in question the role of LTIC in the formation of the LN structure. Even more puzzling, the disruption of the $LT\alpha_1\beta_2$ pathway has been shown to prevent the formation of specific LN types dependent on the time of administration of blocking antibodies [*Fu and Chaplin*, 1999; *Nishikawa et al.*, 2003; *Rennert et al.*, 1997]. This implies a time window for the formation of the various LN types. The candidate for $LT\alpha_1\beta_2$ in developing LN are TRANCE-stimulated LTIC. As previously said $LT\alpha_1\beta_2$ cannot restore the LN of $TRANCE^{-/-}$ animals indicating that TRANCE has another effect that supports LN formation. However, this interpretation does not explain the success of TRANCE-expressing lymphocytes in restoring LN formation because they appear at a later time point in LN development (see below) than the critical time points indicated by the LTβR-Ig treatment. It is unlikely that the time window of LN development is open to allow the TRANCE-expressing B cells to take over the function of LTIC by providing critical signals or supporting the LTIC with the TRANCE signal.

In mice, LN development starts at day 10.5 of gestation with the budding of larger veins which establishes a primordial lymph sac [*Cupedo et al.*, 2004c; *Kim et al.*, 2000]. Like in PP development MAdCAM expression on venous endothelial cells may precede this development [*Hashi et al.*, 2001]. Mesenchymal connective tissue invaginates into the lumen of the growing lymph sac [*Kim et al.*, 2000]. The primordial LN are formed by a cellular reticula surrounded by endothelial cells from the lymph vessels. The accumulation of LTIC in the various LN anlagen takes place from day 12.5 to day 13.5 starting from the anterior region proceeding in posterior direction [*Yoshida et al.*, 2002]. This step is independent of $LT\alpha_1\beta_2$ and may be the additional effect of TRANCE mentioned above. Lymphocytes do not enter before day 16.5 and proper HEV appear even later. The endothelial cells differentiate partly to LEC providing the basis for the formation of afferent and ELV. At this time both endothelial cells express the marker LYVE-I. Only later the marker is restricted to lymphatic endothelium. The LTOC can be seen to polarize in the LN anlagen with ICAM-1$^+$ VCAM$^+$ MAdCAM$^+$ concentrating in the outer edge of the forming LN [*Cupedo et al.*, 2004c]. The LTOC in the central region lack MAdCAM expression and have lower levels of the two other adhesion molecules. Both populations

express mRNA for CCL19, CCL21, and CXCL13 with higher levels in the MAdCAM$^+$ population. However, the MAdCAM$^-$ population has higher levels of LTβR. The MAdCAM$^-$ LTOC occur in higher numbers in MLN possibly explaining why MLN resist many knockout attempts because the LTOC may be more sensitive to low levels of LT$\alpha_1\beta_2$ [*Cupedo et al.*, 2004c]. In the developing LN – but not after complete formation – TRANCE is expressed on LTOC [*Kim et al.*, 2000]. The existence of two LTOC populations raises the question whether they are distinct prior to LN development or dynamically generated by the LTIC and LT$\alpha_1\beta_2$. In both cases the question is why they form the circular pattern. The dynamic induction by LTIC seems questionable. There are no known LTIC subpopulations that could have different effects on a homogeneous LTOC populations.cannot explain the difference in the expression of adhesion molecules because the population of LTIC is seemingly homogeneous. This applies especially to the chemokine receptors. Even more both LTOC populations have the same chemokine profile which therefore could not lead to a generation and separation of LTOC subpopulations. However, the populations may differ in their expression of not yet investigated chemokines.

The postnatal stages of LN development in mice start without apparent lymphocyte organization where B cells are scattered throughout the LN while T cells are absent [*Cupedo et al.*, 2004b; *Mebius et al.*, 1997]. T cells enter the LN around 2 days after birth which causes the B cells to localize to the outer cortex and to form a ring at day 4. At day 7 the first B cell clusters appear accompanied by FDC generation finally leading to PLF formation. The B cell accumulation in the outer cortex is correlated with increased CXCL13 mRNA [*Cupedo et al.*, 2004b]. The cells required for the induction of CXCL13 can be shown to be LTIC which respond chemotactically to CXCL13 from day 0 on. The CXCL13 mRNA expression increases the following days and is correlated with the position of the B cells. The ring formation at day 4 is independent of CXCL13 as can be clearly observed in CXCL13$^{-/-}$ mice. In normal mice the B cells increase their CXCR5 levels and consequently their chemotactic response to CXCL13 from zero-level at day 0 to normal levels at day 4. The surface levels of LT$\alpha_1\beta_2$ raise in the same manner. It should be noted that CXCL13 protein is not detected before day 10 in contrast to CCL21 which becomes apparent from day 1–2. The undetectable CXCL13 protein levels at early stages may not be relevant for the initial B/T segregation by chemotaxis but one may hypothesize that it is already responsible for the increase of LT$\alpha_1\beta_2$ on B cells (which is however unlikely, see below). SCID mice show a similar behavior but do not form follicles. The B cell ring observed in normal mice is replaced by a ring-like CXCL13 pattern in the SCID mouse. This suggests that the initial CXCL13 levels are induced by other cells than B cells but the formation of follicular CXCL13 patterns requires B cells. Here may be the point where the positive feedback loop between CXCL13 and LT$\alpha_1\beta_2$ [*Ansel et al.*, 2000] comes in. The low initial CXCL13 levels may start the feedback loop leading to increased LT$\alpha_1\beta_2$ and finally to increased CXCL13. CXCL13 is then strong enough to induce chemotaxis in B cells to dominate their response to CCL21 and thus to induce aggregation of B cells and PLF formation. However, the *in vitro* data about LT$\alpha_1\beta_2$ induction shows that high CXCL13 levels (10 nM) are required to efficiently induce LT$\alpha_1\beta_2$ on B cells [*Luther et al.*, 2002]. This concentration is already optimal for chemotaxis [*Gunn et al.*, 1998; *Legler et al.*, 1998] leaving open the question why B cells increase LT$\alpha_1\beta_2$ levels prior to their chemotactic response in the postnatal stages of LN development.

The overall picture of LN organogenesis corresponds to the developmental stages in PP organogenesis

[*Hashi et al.*, 2001] although vascular dynamics and DC distributions have not been investigated in LN.

The development of human LN has been studied recently by screening tissues from archived autopsy material [*Kasajima-Akatsuka and Maeda*, 2006]. The sequence for mice could not be identified completely most likely due to a lack of specimen. The time at which lymphocytes enter for the first time and the presence of LTIC could not be determined. The initial stage in human LN development is an unstructured LN filled with stromal cells, blood vessels and some lymphocytes. The next stage shows already the cortical, paracortical, and medullary structure with the paracortex enriched for T cells and B cells which form the cortical ring-structure around the T zone. The PLF development spans several weeks in which small unorganized B cell aggregates with CNA.42-positive cells enlarge and transform into fully grown follicles. It seems that there is a hierarchy of FDC development with the new CNA.42 marker as the first evidence for FDC generation – possibly a marker of FDC precursor. The maturation states of FDC according to the markers appearing during development resemble the 'FDC-ness' picture (Sec. 2.2.3):

- early FDC (and possibly FDC precursors in B cell aggregates): CNA.42, CD21 (long isoform)

- immature FDC (FDC in follicle-like B cell aggregates): CD21, CD35, NGFR

- mature FDC (PLF): CD23, X-11

- activated FDC (in the light zone of GC): CD55, VCAM-1, S100α

It is likely that this hierarchy is valid for all FDC even though being proven for LN only.

2.5.3 Splenic development

The spleen is the only SLT that is common to all vertebrates [*Du Pasquier*, 2005] yet the data on its embryonal development are rare. The primordium of the spleen is formed in mice around day 10.5 of gestation with MAdCAM expression on venous endothelial cells – which seems to be a generic feature during embryogenesis [*Hashi et al.*, 2001]. Note, that the spleen is not purely an organ with SLT function thus it develops even in the complete absence of immune function, e.g. in TNF-$\alpha^{-/-}$ and LT$\alpha^{-/-}$ the spleen is still present, despite the absence of LN and MALT, just the white pulp is not properly developed. In the mouse spleen the first FDC marker FDC-M1 appears postnatal at day 3 as a rim at the white pulp periphery [*Balogh et al.*, 2001]. Clustering of these cells starts around day 7 together with the first cells expressing CD21 and CD35. On day 10 expression of FDC-M2 appears. 14 days postnatal the adult microarchitecture of the splenic white pulp is established. This development is unaltered when mice are irradiated at day 3 thus substantially reducing cells of hematopoietic origin. The questions raised by this experiment are: What is the source of the LT$\alpha_1\beta_2$ signal and/or TNF-α signal? Are the few remaining B cells sufficient to support FDC or do FDC undergo a fixed differentiation program even in the absence of the signals once it has been started?

Using a novel set of markers IBL-10 and IBL-11 the developmental dynamic of fibroblast cells in the spleen of mice has been studied [*Balogh et al.*, 2004]. In the fully developed spleen IBL-10 was found to stain the white pulp with a preference for B cell follicles and the highest expression found at

the follicle border. IBL-11 is restricted to the T zone of the white pulp. Transfer experiments of bone marrow into SCID mice shows that the IBL-10 expression depends on lymphocytes while IBL-11 is independent of it. Interestingly, the IBL-10 staining in the PLF does not coincide with CD21 or CD35 suggesting that FDC do not express the corresponding marker. The first step in development of the white pulp is seen at day 1 after birth as an accumulation of IBL-10$^+$ cells around the central arteriole. B cells also form an aggregate in this region. Between day 3–5 B cells rearrange to form a ring that is shifted away from the central arteriole by an accumulation of immigrating T cells. At day 7 the first IBL-11$^+$ fibroblasts appear at the periphery of the developing white pulp. The B cells from small aggregates within the ring surrounding the T cells. By day 10 follicles are clearly visible staining strongly for IBL-10 with a strongest staining at the follicle periphery. IBL-11 becomes restricted to the T zone.

Interestingly, the production of the T zone chemokines CCL19 and CCL21 in the spleen seem to depend on the LT$\alpha_1\beta_2$-level on B cells [*Ngo et al.*, 2001]. This is in sharp contrast to the case of LN were these chemokines are independent of B cells. In both cases these chemokines do not depend on T cells. Further experiments suggest a developmental time window for the B cell affecting CCL21 levels in the spleen. Lymphocyte-deficient adult mice reconstituted with normal bone marrow do not increase CCL21 but CXCL13 in the spleen. This suggests that B cells play the role of LTIC in splenic development in organizing the white pulp structure. That is further supported by experiments injecting LT$\alpha_1\beta_2$-transgenic B cells into LTα-deficient recipients immediately after birth restoring most of splenic but not LN or PP structure. Furthermore, this is consistent with the observation that most of the LN and PP development occurs before birth whereas the white pulp develops after birth. Interestingly, the transgenic expression of LT$\alpha_1\beta_2$ on B cells prevents the proper formation of PLF by inducing follicles that are less sharp delineated. The CXCL13 levels remain normal suggesting that the positive feedback loop may be responsible for the sharp border of normal follicles [*Ngo et al.*, 2001]. However, experiments with SCID mice suggest that other cell types (probably LTIC) contribute to the splenic white pulp microarchitecture as well [*Gonzalez et al.*, 1998]. Even in the absence of lymphocytes, injected B cells and T cells home to compartments that can be considered as PLF and T zone, respectively, but are apparently formed by other cell populations. Thus LTIC may contribute to splenic white pulp development as further indicated by the knockout of TRANCE – a molecule that is related to LN development (Sec. 2.5.2) – that interferes with the formation of PLF in the spleen [*Kim et al.*, 2000]. TRANCE is found on LTIC but not on lymphocytes suggesting that even in normal animals LTIC can organize white pulp structure in addition to B cells as it has been already suggested by the prestructures found in the spleen of SCID mice [*Gonzalez et al.*, 1998]. Following this, the possibility to restore splenic organization by wildtype lymphocytes at any later time point may be reinterpreted as tertiary lymphoid tissue generation and not as restoration of the normal development. Thus, like in LN and PP, splenic SLT structure would be predominantely organized by LTIC in a healthy individual.

It is possible that LTIC survive as a minor population in adults [*Lane et al.*, 2005]. There they may be involved in the activation of T cells. Although the adult LTIC express additional T cell activating molecules like OX40L and CD30L these cells retain their expression of LT$\alpha_1\beta_2$ and TRANCE. Thus there may be a factor that maintains the lymphoid tissue architecture in adults and probably is responsible for the maintenance of organization of secondary lymphoid organs in SCID mice.

2.5.4 Lymphneogenesis

The major difference of lymphneogenesis and organogenesis seems to be that only lymphocytes are mediating the organization of the SLT structure in these *tertiary* lymphoid tissues. Therefore the development is mostly similar to the case of spleen. The principles may be the same however it appears that the thresholds are larger thus generating ectopic lymphoid tissue only when higher than background levels of $LT\alpha_1\beta_2$ are present.

Ectopic expression of molecules   Lymphneogenesis does not only occur during diseases (see next section) but is frequently induced artificially (reviewed in [*Hjelmstrom*, 2001]). A widely used approach is the rat insulin promoter-driven (RIP-driven) expression of various molecules which causes the expression of the designated molecule by beta cells of the pancreatic islets, and on some cells in the kidney. One approach ectopically expresses $LT\alpha$ (RIP-$LT\alpha$ mouse) [*Kratz et al.*, 1996; *Sacca et al.*, 1998]. This causes infiltration of pancreatic islets and kidneys by lymphocytes with a dominance of B cells. The typical lymphoid structure like FDC, HEV, and a LN-like microarchitecture can be found. These structures are functional in hosting an immune response including the formation of GC [*Kratz et al.*, 1996]. There are also hints that angiogenesis is induced by $LT\alpha$ [*Kratz et al.*, 1996]. The infiltrates even appear in mice deficient for TNFR-II and $LT\beta$ but not in a TNFR-I-deficiency [*Sacca et al.*, 1998]. It seems that $LT\alpha_3$ is sufficient to induce ectopic lymphoid tissue formation in these organs. Also RIP-$LT\beta$ alone does not induce lymphoid neogenesis [*Drayton et al.*, 2003]. The structure of the infiltrates in RIP-$LT\alpha_1\beta_2$ mice is similar to the ones seen in normal SLT [*Drayton et al.*, 2003]. The levels of the chemokines CCL19, CCL21, and CXCL13 seen in RIP-$LT\alpha_1\beta_2$ infiltrates are higher than for RIP-$LT\alpha$ infiltrates indicating a difference in the signaling efficiency of the two lymphotoxin trimers. This may also explain the differences seen in certain lymphotoxin-knockouts (Sec. 2.2.2) if one assumes that the relative contribution of $LT\alpha_1\beta_2$ and $LT\alpha_3$ differs in the various SLT.

Ectopic expression of CCL19 in RIP-CCL19 mice causes small infiltrates of lymphocytes with poor organization [*Luther et al.*, 2002]. CCL21 induces better organized infiltrates of larger size. In both cases networks of $gp38^+BP-3^+ER-TR7^+$ FRC form with higher network organization in the case of CCL21 [*Fan et al.*, 2000; *Luther et al.*, 2002]. Of note, in none of the two cases CXCL13-expression or FDC-specific marker are found [*Luther et al.*, 2002]. Using the $LT\alpha_1\beta_2$-blocking fusion protein $LT\beta$R-Ig the stromal network can be disrupted. Similar the occasional formation of HEV with typical adhesion molecules like PNAd and MAdCAM is strongly reduced. Interestingly, DC and T cells were located close to the CCL21-expressing pancreatic islet cells with B cells surrounding them [*Fan et al.*, 2000; *Luther et al.*, 2002] a morphology similar to that observed in various lymphotoxin-modulating experiments with intact B/T segregation but disturbed PLF formation (Sec. 2.2.2). This picture is inverted in RIP-CXCL13 mice where B cells surround the CXCL13 expressing stromal cells of the pancreas whereas T cells and DC accumulate around the B cells [*Luther et al.*, 2000]. The RIP-CXCL13 infiltrates also show an extensive $BP-3^+$ network. Again FDC could not be detected in the infiltrate whereas CCL21 expression is induced. Using RIP-CXCL13 on a background of $LT\alpha^{-/-}$ or $TNFR-I^{-/-}$ shows that only in the $LT\alpha^{-/-}$ case the infiltrate size is reduced. This correlates with a failure in the recruitment of T cells indicating that the CCL21 expression seen before depends on

$LT\alpha_1\beta_2$ but not on the TNFR-I ligands $LT\alpha_3$ or TNF-α. Staining methods show that the BP-3$^+$ network and CCL21 are disrupted on the $LT\alpha^{-/-}$ background. A similar effect can be generated using $LT\beta R$-Ig supporting the concept that $LT\alpha_1\beta_2$ is required for CCL21 expression in lymphoid neogenesis. Looking on the data for FRC (Sec. 2.2.4) it would be interesting if the marker ER-TR7 has a similar behavior possibly relating FRC to CCL21 expression despite that the culture experiments failed to show this [*Katakai et al.*, 2004b]. Ectopic CXCL12 expression causes the immigration of naive B cells while T cells are virtually absent from the infiltrates [*Luther et al.*, 2002] demonstrating that a pure accumulation of B cells is not able to induce SLT-like structures.

The results of this section show that the ectopic generation of lymphoid tissue by various molecules can induce the features of normal SLT at least in part. The morphology relies mainly on the signaling via $LT\alpha_1\beta_2$. Of note, except for direct ectopic expression of $LT\alpha$ or $LT\alpha_1\beta_2$ none of the molecules is able to induce FDC. This suggests that the threshold for generating FDC at these sites is quite high. Moreover, the positive feedback loop seems not to work properly because CXCL13 is not able to induce FDC despite it has been shown to upregulate $LT\alpha_1\beta_2$ on B cells [*Ansel et al.*, 2000]. This may also be interpreted in the sense that FDC precursor are not present and additional factors are required to ensure that FDC precursors home to sites of ectopic lymphoid tissue formation and SLT.

Injection of cell populations   Instead of ectopic expression under the control of RIP, injection of LTIC can be used to induce lymphneogenesis. For this purpose LTIC are extracted from the LN of newborn mice [*Cupedo et al.*, 2004a]. Injection into the skin of adult mice could induce unorganized lymphocyte infiltrates even on a $LT\alpha^{-/-}$ background. In normal adult mice immunization protocols can induce the full lymphoid tissue architecture with segregated B and T cell areas and the formation of FDC-containing follicles. The presence of HEV and a reticular network has been demonstrated. Interestingly, the lymphatic endothelium and HEV in these structures and some stromal cells were made up from the donor cells while all cells of hematopoietic origin are host derived (i.e. the injected LTIC are not detectable after a certain amount of time). In contrast cells isolated form the LN of adults mice could not induce infiltrates in adult mice. Injection of unsorted LN extracts from young mice into the skin of newborn mice induce fully organized lymphoid structures with segregated B and T zones and PLF. This process requires $LT\alpha$ but not TNFR-I in contrast to previous data that linked the presence of FDC to TNFR-I (Sec. 2.2.2). Interestingly, the FDC in the induced PLF are donor-derived. All this strongly suggests that a developmental time window exists that allows to form fully organized lymphoid tissue structures. The difference between young and adult mice may be the level of IL-7 and/or TRANCE (see Sec. 2.5.1 and Sec. 2.5.2) that induce high levels of $LT\alpha_1\beta_2$ on the LTIC which are transferred with the LN extract. This is further supported by the observation that immunization can organize the unorganized infiltrates in adult mice most probably due to elevated $LT\alpha_1\beta_2$ levels on Ag-activated B cells. The ability of the unsorted LN extract to induce the complete lymphoid tissue architecture may be interpreted such that the stromal cells delivered with the extract have a low $LT\alpha_1\beta_2$ signal threshold that enables them to become FDC without the need for high $LT\alpha_1\beta_2$ levels of Ag activated lymphocytes.

Injecting transgenic cells   Another artificial induction of lymphoid tissue can be done using an approach similar to RIP-LTα by injecting LTα-bearing tumor cells into the skin of mice [*Kim et al.*, 2004b]. The local production of LTα attracts B cells to form follicles at the edge but not within the tumor. The follicles are most likely PLF as indicated by the absence of proliferation markers which are expected when GC would have been formed. The central area of the B cell follicle contains an FDC network which lacks a few of the typical markers like CD35 (compare with the FDC type hierarchy (Sec. 2.2.3 and Sec. 2.5.2). HEV can be found as well. Injecting the LTα^+ tumor cells into SCID mice induces FDC at various developmental stages (according to the FDC hierarchy). Notably, the different FDC stages do not mix but are homogeneous within one FDC cluster. The SCID model demonstrates that FDC can develop in the complete absence of lymphocytes solely on the basis of the presence of LTα. However, this result has to be taken with care as the used tumor cell line J558L is derived from lymphocytes and may express some molecules that are generically present on all lymphocytes. Also CD4$^+$CD3$^-$CD11c$^+$ cells accumulate in the tumor which might be related to LTIC [*Kim et al.*, 2004b] thus substituting the missing lymphocytes. Another interesting result for normal mice is that no GC could be induced in the tumor while a normal GCR is detected in the spleen suggesting that the PLF around the tumor are not fully functional.

Artificial lymphoid tissue in culture   Recent attempts to engineer lymphoid tissue in culture are similar to lymphneogenesis [*Suematsu and Watanabe*, 2004]. The stromal cell type used is the thymus-derived TEL-2 lineage expressing LTβR and VCAM-1 but not the chemokines CCL19, CCL21, CXCL13 or the adhesion molecule ICAM-1. The cells are cultured on a collagenous 3D scaffold after transfecting them with genes for LTα. Infiltrates of T and B cells form small clusters with FDC-like cells. The whole process produces better organized structures when Ag-activated CD11c$^+$ DC are added. This again stresses that immune reactions can help to set up the SLT microstructure. Overall the artificial tissue constituted a structure similar to SLT including the formation of GC. Also the formation of HEV could be observed. The created organoids can be transplanted into mice retaining their function in an immune response. Of interest this study demonstrates that DC have an influence on the formation of lymphoid tissue although they are not strictly required. This influence may be beyond lymphocyte activation by Ag.

Tertiary lymphoid tissue under normal conditions   Normal immune reactions lead to the swelling of LN due to lymphocyte immigration and GC formation. In the medulla of LN the reticular network is remodeled and small nodules appear composed of segregated T and B cells enclosed by a single layer of FRC [*Herman et al.*, 1972; *Katakai et al.*, 2004b]. This may indicate that even in LN something like an ectopic follicle can be formed suggesting that lymphneogenesis is a process occurring normally in infected but otherwise healthy individuals. This is confirmed by the high frequency of SLF in the thymus of healthy dogs [*Ploemen et al.*, 2003] and the presence of ILF in mice [*McDonald et al.*, 2005] which both are assumed to be of tertiary nature.

2.6 Diseases involving Lymphoid Follicles

On one hand lymphneogenesis is observed in many autoimmune disease and on the other hand infections like HIV can disrupt the proper formation of follicles. A recent review [*Weyand et al.*, 2001] provides a nice overview of the state of research about ectopic follicle formation and connecting it to the artifically induced lymphoid aggregates discussed in the previous section.

Chronic arthritis In chronic inflammations in the context of arthritis ectopic GC can be found in synovial membranes [*Hjelmstrom*, 2001; *Kang et al.*, 2002; *Magalhaes et al.*, 2002; *Manzo et al.*, 2005; *Shi et al.*, 2001; *Takemura et al.*, 2001; *Wagner et al.*, 1998; *Weyand et al.*, 2000, 2001]. The FDC express CXCL13 like in common GC suggesting lymphneogenesis in the synovium. It has been shown that the GC forming in the synovial tissue during rheumatoid arthritis are fully functional and produce affinity maturated auto-antibodies against the Fc part of IgG [*Magalhaes et al.*, 2002]. The GC is accompanied by a T zone with CCL21 expression [*Manzo et al.*, 2005]. A key morphological data is the activation of fibroblasts to express the FDC phenotype supporting the notion of FDC being derived from local stromal cells [*Magalhaes et al.*, 2002]. However, the production of CXCL13 does not correlate with the presence of FDC defined by CD21 expression [*Manzo et al.*, 2005]. The expression of CXCL13 is required and sufficient for the formation of lymphoid aggregates but it is not sufficient for the formation of B cell follicles in the infiltrates. Similar CCL21 expression can be found in the absence of B/T segregation and follicles. Together the data indicates that the B and T cell infiltrates are unorganized in the absence of an immune reaction despite the expression of CXCL13 and CCL21, i.e. PLF are never observed [*Takemura et al.*, 2001]. When a GC is formed the T cells separate from the follicle and the typical lymphoid tissue morphology appears. In the latter case an increased expression of CXCL13 and CCL21 can be found [*Takemura et al.*, 2001] suggesting a chemokine threshold for the formation of B cell clusters and mature FDC. This situation resembles the injection experiment discussed in (Sec. 2.5.4).

The development of GC in the synovium seems to be dependent on CD8 T cells which stimulate B cells and induce TNF-α production to form ectopic GC [*Kang et al.*, 2002; *Wagner et al.*, 1998; *Weyand et al.*, 2000, 2001]. It seems that these CD8 T cells are a major source of LTβ [*Kang et al.*, 2002]. Depletion of these T cells causes the loss of FDC in the ectopic GC despite the identification of LT$\alpha_1\beta_2$ on the corresponding mantle zone B cells [*Kang et al.*, 2002; *Takemura et al.*, 2001; *Wagner et al.*, 1998]. This may be correlated to the not yet understood loss of LTβ on B cells in the infiltrates without GC [*Takemura et al.*, 2001]. The recruited T cells seem to be specific for the Ag presented in the GC and are found around the SLF and rarely in the ectopic GC itself [*Kang et al.*, 2002]. Interestingly, these CD8 T cells seem to perform B helper functions as they express the B cell activating molecule CD154 (CD40L) [*Kang et al.*, 2002; *Wagner et al.*, 1998]. Also typical for these T cells is the production of IFN-γ which is unusual for normal GC [*Kang et al.*, 2002]. Overall how the CD8 T cells influence the lymphneogenesis during autoimmune diseases remains an open question but they may induce the formation by providing signals via LTβ.

Thyroid autoimmune disease   Hashimoto's thyroiditis and Graves's disease are autoimmune thyroid diseases accompanied by the formation of SLF in the thymus. It has been shown that these ectopic GC are fully functional and resemble all structures typically found in SLF [*Armengol et al.*, 2001]. The presence of FDC and a mantle zone have been confirmed as well. The SLF in Hashimoto's thyroiditis where found to be large and similar to tonsillar SLF while the follicles found in Graves's disease are smaller and more like SLF in LN. It seems that the follicle formation in Graves's disease does not involve CXCL13. These two examples indicate that even the ectopic follicle formation may have differences in the detailed molecular signaling like it is the case for the various SLT (Sec. 2.2.2).

Other ectopic lymphoid follicle formation   The formation of ectopic lymphoid follicles implies in most cases the development of GC. Examples are GC forming in oral mucosal tissue aside from tonsils correlated with lesions close to amalgam-fillings [*Larsson and Warfvinge*, 1998]. In patients with multiple sclerosis ectopic GC can be found. In a mouse model it has been shown that these GC are fully functional ([*Magliozzi et al.*, 2004] and reference therein). Another example for ectopic lymphoid tissue formation is autoimmune gastritis [*Katakai et al.*, 2003]. A couple of other chronic inflammations/autoimmune diseases are reviewed in [*Hjelmstrom*, 2001].

HIV infection   During HIV infection FDC become a major reservoir of the virus ([*Smith-Franklin et al.*, 2002] and references therein and references in [*Estes et al.*, 2002; *Paiva et al.*, 1996]). CD4 is one of the receptors enabling entry of HIV-2 to T cells via binding through gp120 to CD4. CD4 also serves as chemokine receptor for IL-16 [*Cruikshank et al.*, 1994]. The binding of gp120 causes also modulation of chemotactic responses to other chemokines like CXCL12 and CCL4 [*Van Drenth et al.*, 2000] (Sec. 3.3). The subtype HIV-1 utilizes CCR5 and CXCR4 for entry to cells (references in [*Estes et al.*, 2002; *Vicente-Manzanares and Sanchez-Madrid*, 2004]. Factors present on the membrane of FDC are able to stimulate the upregulation of surface CXCR4 on T cells [*Estes et al.*, 2002] making these cells more susceptible to HIV infection by viruses hosted on FDC. The mechanism has been shown *in vitro* and *in vivo* for the subtype of T cells found in GC.

The maintenance of HIV on FDC requires the presence of specific antibody [*Smith-Franklin et al.*, 2002] suggesting that a GCR is taking place before FDC serve as 'effective' HIV reservoir. Another unfavorable property of FDC is that they preserve the HIV infectivity by reducing the loss of gp120, the molecules that is required by the virus to enter T cells.

The HIV infection induce morphologic changes in the LF leading to fragmentation of LN follicles [*Paiva et al.*, 1996]. This results in shape changes of GC with lymphocytes forming small clusters inside the GC. The outbreak of AIDS is correlated with the further destruction of follicles leading to their involution and finally a diffuse pattern with increased vessel numbers and fibrous tissue and a decreased lymphocyte content. This leads to severe defects in humoral immune responses explaining part of the effect of AIDS progression.

Conclusions on lymphneogenesis   Taken together lymphneogenesis is a phenomenon that occurs quite frequently in various diseases. The organization of the lymphocyte infiltrates depends on an

ongoing immune reaction, i.e. the formation of GC. Although these aggregates are most probably not the reason of the disease their formation may increases the damage to the tissue. Thus for autoimmune diseases the suppression of lymphneogenesis seems to be favorable. The understanding of the PLF formation is an important step towards this issue. Considering HIV infection the destruction of follicles – and especially the loss of FDC – in SLT may be an approach to fight against the infection as FDC have a couple of effects that make T cells susceptible for the virus. Also the HI-virus would loose FDC as hosts to hide from the immune system.

2.7 Summary of experimental data

First of all the PLF is a structure that helps the immune system to filter Ag collected from various sites where Ag may enter the organism. The concentration of B cells helps to quickly induce a specific immune reaction. The formation of GC leading to affinity maturation and B cell memory formation relies on FDC which are maintained by PLF. Although FDC in GC can be induced without the presence of PLF it is reasonable to assume that the FDC present in the PLF may speed up the reaction and lower the sensitivity threshold for the induction of GC reactions.

The organogenesis leading to the formation of PLF relies mainly on $LT\alpha_1\beta_2$ and TNF-α. Whereby $LT\alpha_1\beta_2$ is delivered by B cells in the spleen and by LTIC in basically all other SLT during development. TNF-α can be provided by other cell types in addition to B cells and LTIC which is related to the possibility of diffusion of TNF-α while $LT\alpha_1\beta_2$ comes only in a membrane-bound form. $LT\alpha_1\beta_2$ is required for induction of the homeostatic chemokines CCL19 and CCL21 acting on T cells. The chemokine CXCL13 acting on B cells requires TNF-α. Moreover, $LT\alpha_1\beta_2$ and TNF-α are both required for the generation of FDC and consequently for the organization of PLF. The progenitor cells for FDC are still unknown. However, the majority of data suggest a stromal origin. The necessity to have a constant stimulus of $LT\alpha_1\beta_2$ to maintain FDC inspired the view used in the present thesis that FDC are a kind of 'activated' state of stromal cells. This is further supported by the experimental data that describes different FDC subpopulations with increased amount of marker expression suggesting a hierarchy of 'FDC-ness' or higher 'activation levels'.

It is important to note that the experimental data on the molecular requirements for the structure of SLT are not consistent. There are a number of observations that need interpretation:

- The fact that the CXCL13 expression in PLF depends on $LT\alpha_1\beta_2$ of B cells in the spleen but not in LN raises the question how relevant the positive feedback loop between CXCL13 and $LT\alpha_1\beta_2$ really is or whether a similar loop between other molecular players exists.

- The T zone structure depends on B cell $LT\alpha_1\beta_2$ in the spleen but not in LN. This seems to be related to the contribution of LTIC in LN development which suggests a time window which is not consistent with the late reconstruction of the T zone chemokine CCL21 by administering $LT\alpha_1\beta_2$ to $LT\alpha_1\beta_2^{-/-}$ mice. The B cell/T cell segregation remains incomplete after the reconstruction suggesting that the T zone has a certain plasticity that may decline with age.

- CCL21 in the T zone depends on $LT\alpha_1\beta_2$ as well but FDC do not develop in this area. TNF-

α cannot serve as an explanation because TNF-α from T cells is sufficient to induce FDC in the PLF but obviously not in the T zone.

- The structure of the spleen seems to develop in dependence of B cell LT$\alpha_1\beta_2$. However, the presence of CXCL13 in SCID mice suggests that either non-FDC cells are expressing CXCL13 or other cells can provide LT$\alpha_1\beta_2$. Probably in the absence of B cells LTIC can take over the organization of the white pulp in SCID mice.

- The formation of the T zone is LT$\alpha_1\beta_2$ dependent (to generate B/T segregation) while culture experiments suggested that TNF-α is responsible for the FRC network formation. The gene expression data agree with the former dependency, i.e. CCL21 expression depends on LT$\alpha_1\beta_2$ but not on TNF-α. Is the network formation a prerequisite for the formation of FDC? But why fails LT$\alpha_1\beta_2$ to induce CCL21 in the culture experiment? Why shows TNF-α and LT$\alpha_1\beta_2$ treatment of cultured cells no differences in the expressed molecules that are related to the FRC/FDC phenotypes?

- Ag activated B cells can induce ectopic GC containing FDC presumably by high LT$\alpha_1\beta_2$ levels. In contrast, ectopic expression of CXCL13 cannot induce FDC despite the positive feedback loop that should lead to high LT$\alpha_1\beta_2$ levels on B cells when CXCL13 ligates to CXCR5. This may be explained by receptor internalization induced by too high CXCL13 concentrations upon ectopic expression compared to the normal physiologic situation (Sec. 3.3).

- LT$\alpha_1\beta_2$ has been shown to induce IL-1, IL-6, and TNF-α in cultured FDC-like cells. These three molecules are able to stimulate transglutaminase, i.e. promote ECM production by those FDC. However, the molecules are also stimulating MMP. From the fact that PLF are practically void of ECM it is clear that ECM degradation dominates raising the question which effect the transglutaminase has *in vivo*.

- TRANCE has been shown to be required for LN development. Yet transgenic TRANCE expression on B and T lymphocytes can restore LN development in TRANCE$^{-/-}$ mice. These TRANCE expressing cells appear only after birth and after the initiation of LN development. This raises the question what cell type delivers the TRANCE signal during the first stages of LN development when B and T cells are not yet present.

Finally, the pattern of vessels in SLT has not been explained by any study. The most striking feature that HEV, ELV, and also the ECM are absent from the PLF while the T zone is rich in all of these three structures remains unexplained. The results presented in this thesis will shed some light on this subject and propose experiments to engage the vessel distribution of ELV experimentally.

Chapter 3

Cell Movement and Migration

The pattern formation in the PLF system is a result of fast migrating lymphocytes in a flow equilibrium. The former chapter (Sec. 2) provided the information about the key molecules that are required for certain anatomical structures and expression of molecules related to the stromal cell phenotypes. However nothing has been said yet about the question how these regulatory factors translate into morphological patterns. Therefore it is of utmost importance to understand how cells migrate and consequently how migration is regulated by the key molecules involved in the organogenesis of SLT. This can be rephrased by asking how chemotaxis is regulated and how the physics of cell migration and force generation maps on the biological cell behavior.

3.1 Mechanics and Migration of Cells - Molecular Structures

To understand the mechanical response and the active motion of cells three major components are needed: cell membrane, cytoplasm, and cytoskeleton [*Zhu et al.*, 2000]. The cell membrane can be considered as flexible two-dimensional object. Most of its mechanical properties are connected to the underlying cortical shell. It consists of actin and intermediate filaments that are tightly connected to the lipid bilayer forming the cell membrane. The cytoplasm is basically a viscous fluid phase under pressure bounded by the cell membrane. In contrast to plant cells the cytoplasm in animal cells is generally under low pressure thus the cytoskeleton of a cell is the predominant part for the mechanical response of the cells. The cytoskeleton is formed by three distinct components (Fig. 3.1) (an overview about can be found in [*Zhu et al.*, 2000]).

- Microtubules: These are hollow cylinders of about 25 nm diameter and several μm in length. The centralized organization of microtubules radiating outwards from an area close to the nucleus primes this part of the cytoskeleton for transporting organelles and proteins through the cell. Microtubules serve also as structural support and force generators due to their polymerization dynamics. Motor proteins can also shift microtubules along each other similar to the actin-myosin pair. For instance, these forces lead to the chromosome separation during cell division.

- Microfilaments: These are formed by polymerization of the protein actin. They can assemble to filaments of considerable thickness – even thicker than microtubules – and can resist stretching and compression. The filaments exhibit dynamic redistributions by polymerization and de-polymerization. When forces are exerted on certain cell types, actin is forming stress fibers within minutes. Microfilaments are thought to be the major driving force during cell migration. Actin filaments are also responsible for active deformations of the cell membrane by forming microvilli, protrusions, and pseudopods.

- Intermediate filaments: Their typical thickness of 9-11 nm is in between actin filaments and microtubule. They are highly resistive to stretching when large strain is applied [*Stamenovic and Ingber*, 2002; *Wang et al.*, 2002b]. Intermediate filaments form a tight network throughout the cell body concentrating around the nucleus. Recent results show that they might be actively involved in migration [*Brown et al.*, 2001; *Helfand et al.*, 2003]. Intermediate filaments can also connect cells to other cells via desmosomes and the ECM via hemidesmosomes.

In addition to these components myosin II plays an important role [*Zhu et al.*, 2000]. It can shift actin filaments along each others thus generating contractile forces. Experimental evidence indicates that also the cell nucleus plays an important role in the cell mechanics [*Maniotis et al.*, 1997]. It is usually stiffer than the remaining cell body. Intermediate filaments are connecting the nucleus tightly with the other parts of the cytoskeleton and the cell membrane which influences its mechanical properties.

The basic morphology of a migrating lymphocyte is characterized by three parts [*Friedl and Brocker*, 2000; *Galbraith and Sheetz*, 1998; *Lauffenburger and Horwitz*, 1996; *Mitchison and Cramer*, 1996; *Samstag et al.*, 2003; *Serrador et al.*, 1999; *Vicente-Manzanares and Sanchez-Madrid*, 2004; *Webb et al.*, 2002; *Wolf et al.*, 2003b]. At the front of the cell is the leading edge consisting of one or more membrane protrusions generated by the polymerization dynamics of the actin network located there. It is followed by the round main cell body with the nucleus. The rear is formed by the trailing edge which consists of a narrow, cytoplasmatic, backward directed extension called 'uropod'. The leading edge is rich in chemokine receptors, adhesion molecules, actin, and actin-related proteins. Towards the rear between uropod and main cell body the microtubule organizing center (MTOC) is located. From the MTOC the microtubule network is radiating outwards to reduce the mechanical stiffness of the cell allowing for larger cell deformations. Some intercellular adhesion molecules are concentrated in the uropod. The enrichment of myosin II in the uropod may indicate that the driving forces are generated in this region (Sec. 3.2.2). In the case of T cells TCRs are also found at the trailing edge allowing Ag presenting cells to initiate contact from the back of the cell. Several studies indicate that the intermediate filament network is also retracted into the uropod [*Brown et al.*, 2001; *Vicente-Manzanares and Sanchez-Madrid*, 2004] probably for the same reason as the microtubules, i.e. to increase the flexibility of the cell.

As a conclusion one can say that the phenomena coupled to cell migration and deformation are known quite well. However, the mechanisms underlying it and especially models that can be used in simulations are still not known sufficiently well (see also (Sec. 5.1.1)).
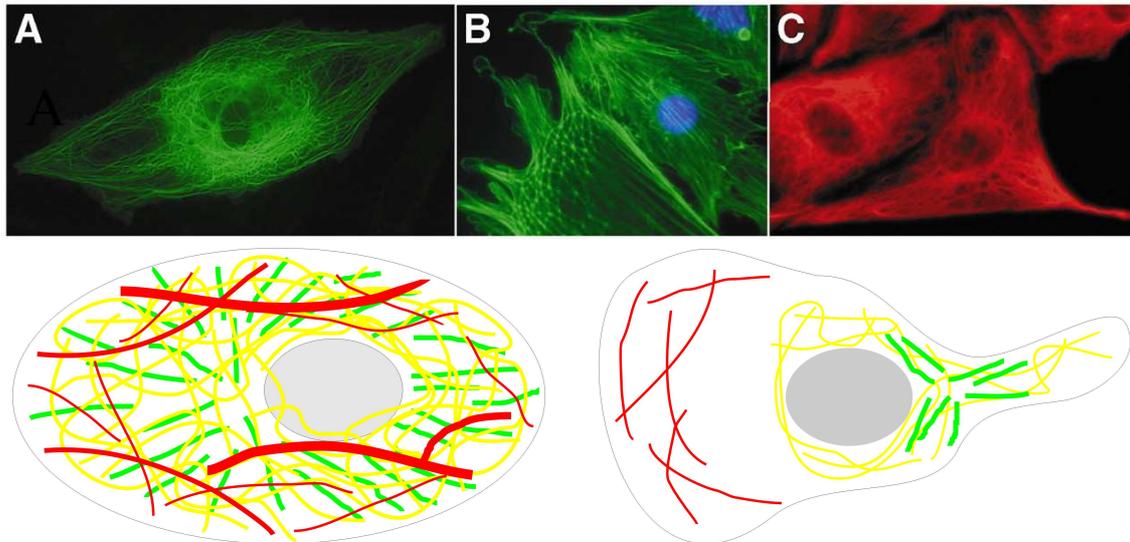
Figure 3.1: The cell cytoskeleton. The top panel shows the fluorescence marked components of the cytoskeleton: microtubules (A), microfilaments (B), and intermediate filaments (C). The lower left panels shows a schematic representation of the cytoskeletal components. The microtubules (green) radiate outwards from an area close to the nucleus (small ellipse). The microfilaments (red) form long stress fibers of various thickness sometimes crossing the whole cell. The intermediate filaments (yellow) form a extensive network which is denser around the nucleus. In the lower right panel the cytoskeleton of a migrating lymphocyte is shown. The marked differences to that of stromal cells is that the microtubules and intermediate filaments are retracted in a narrow region which forms the uropod while the microfilaments concentrate on the opposite end of the cell that forms the leading edge of the migrating lymphocyte.

Source for upper panel: `http://jcs.biologists.org/cgi/content/full/116/7/1157/FIG3`

3.2 Mechanics of Migration

Several basic mechanisms are discussed in order to explain active migration of cells (reviewed in [*Friedl et al.*, 2001; *Friedl and Brocker*, 2000]). *Actin polymerization* is considered to be the dominant mechanism of force generation in migrating cells. Actin comes in two forms, soluble actin monomers and polymerized as microfilaments. The polymerization of actin to microfilaments is a polarized process that takes place only on one end of the polymer while the other end is prone to depolymerization. The growth of the filaments generates a branching actin network that has a certain stiffness able to mechanically support membrane protrusions and pseudopod growth. The actin polymerization also extents these structures by elongation of the microfilaments just beneath the membrane.

Myosin sliding might not only take place in muscle cells but also in every other migrating cell. The filaments of the myosin-II are cross-linked with actin thus stabilizing the microfilaments structure and generate contractile forces. This may be the cause for the retraction of the rear of a cell during migration. Experimental show that cells can migrate in the absence of functional myosin-II, however at significant lower speed.

The *cortical expansion model* explains pseudopod formation by locally increased pressure of the cytoplasm induced by ion influx at the leading edge of cells. Additionally, hydrostatic pressure induced

by cell contraction at the uropod may squeeze the cell forward. Although the actin cytoskeleton reorganizes during these processes it plays a different role than in the actin polymerization model as it is not generating the forces that drive the cell forward.

3.2.1   Three step model of cell migration

The mechanisms of cell migration have been studied mostly with fibroblast on 2D substrates. That lead to the formulation of the three-step model of *mesenchymal migration* [*Entschladen et al.*, 2000; *Friedl et al.*, 2001; *Friedl and Brocker*, 2000; *Galbraith and Sheetz*, 1998; *Lauffenburger and Horwitz*, 1996; *Mitchison and Cramer*, 1996; *Webb et al.*, 2002].

The first step is the firm adhesion of one or more protrusions to the substrate (Fig. 3.2). The pseudopod formation at the leading edge of a cell is dependent on actin polymerization which is also the cause of the ruffling of fillipodia preceding the pseudopod formation. The firm adhesion is mediated by adhesion molecules like members of the integrin family leading to the formation of focal adhesions. The formation of these contacts can take 10 to 20 minutes. Upon attachment the integrins provide signals to the interior of the cell finally leading to actin polymerization and the formation of stress fibers. The second step is the formation of a force gradient acting on the focal adhesions at the leading edge and the adhesive bonds to the substrate at the trailing edge. The stress applied to the focal adhesions induces signals that strengthen the actin polymerization and the adhesion. That in turn increases the force acting on the leading edge enlarging the force gradient in the direction of cell movement. The final step in the migration model is the detachment of the rear of the cell from the substrate. This can happen by two mechanisms, the cleavage of integrin molecules or the anchoring structures in the cell or the affinity modulation of integrins. In the latter case integrin unbind from the substrate and are transported to the leading edge by integrin-coated membrane vesicles [*Palecek et al.*, 1998; *Pierini et al.*, 2000]. This process can transport the equivalent of the cell surface in 4–8 minutes along the cell length.

When fibroblast cell migration is studied in 3D ECM-models all three steps seem to be similar to the 2D substrate. A difference lies in the morphology of the leading edge which is no longer flat by shows several cylindrical protrusions [*Friedl and Brocker*, 2000]. Also the overall morphology of the cell is more bi- or tripolar compared to the spread shape in 2D. Likewise in 3D contact guidance is of importance. Cell migration in ECM follows fibers and passes through larger gaps thus minimizing the resistance felt by the ECM. In contrast, *intravital* imaging by two-photon microscopy revealed that for tumor cells the migration pattern is quite different from 2D and 3D *in vitro* experiments [*Condeelis and Segall*, 2003]. First of all the velocities in tissue are one order of magnitude higher. Second – and more importantly – the cells *in vivo* show a persistent linear motion compared to the random walk in culture presumably guided by ECM fibers. There exist also tumor cells with a highly non-linear migration pattern in the absence of ECM when cells are crawling directly over each other [*Condeelis and Segall*, 2003].

The adhesion-dependence of mesenchymal migration is such that at low and high adhesion cells are slow either by the lack of force transmission to the substrate at the leading edge or the resistance
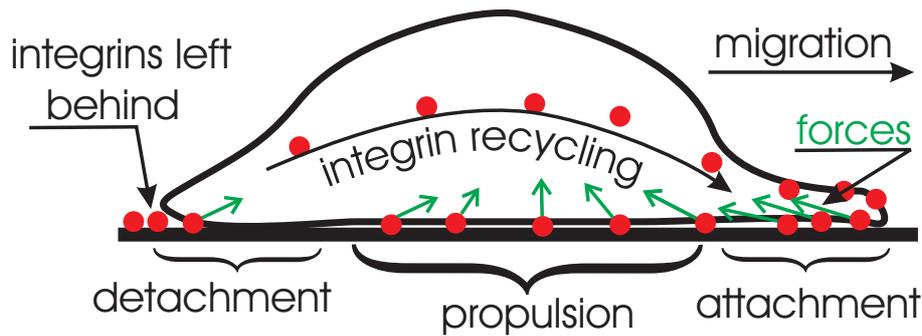
Figure 3.2: Three step model of cell migration. The cell moves from the left to the right by forming protrusions at its leading edge that attach to the substrate via integrins (red dots). Using these as anchors the cell propulses itself by exerting forces (green arrows, a more detailed picture of the force generation can be found in Fig. 3.4) on these contacts generated by the dynamics of the cytoskeleton. The rear of the cell detaches from the substrate by either cleaving the integrins, leaving them behind, or by modulating their affinity and keeping them in the cell membrane. The integrins at the rear may be transported along the membrane or with the help of vesicles to the leading edge of the cell.

due to sticking to the substrate at the rear [*Friedl et al.*, 2001; *Palecek et al.*, 1998]. In a range of medium adhesion cells show their maximum motility. A variant of focal adhesions are focal contacts that are smaller and consequently form faster which are involved in the migration of leukocytes. Thus the fibroblast picture of migration may fit to some extent to the migration of lymphocytes as well. However, it is not confirmed whether the environment of the PLF supports this type of migration or not (Sec. 2.3.1).

Migration of leukocytes   The dominant population of the PLF system are not fibroblast-like cells but lymphocytes which belong to the group of leukocytes. They use the amoeboid migration mechanism which is different from mesenchymal migration in several aspects [*Entschladen et al.*, 2000; *Friedl et al.*, 2001; *Friedl and Brocker*, 2000]. A difference is for example in the dynamics of the adhesion molecules. In mesenchymal migration the integrins are capped and leave a track of remaining adhesion receptors behind the migrating cell. Leukocytes do not need to cap their adhesion molecules thus taking their adhesion receptors with them. The morphology of amoeboid migration is also different as leukocytes polarize in response to any locomotory stimulus. The cell body and uropod are rather stiff compared to the leading edge thus stabilizing the polarized morphology. The traction forces of these cells is about one order of magnitude lower compared to fibroblasts estimated to be in the range of 30 nN for neutrophils [*Friedl et al.*, 2001; *Lauffenburger and Horwitz*, 1996]. At the same time neutrophils are one order of magnitude faster reaching velocities of $10\,\mu\mathrm{m\,min^{-1}}$ with peak velocities of $30\,\mu\mathrm{m\,min^{-1}}$ [*Ehrengruber et al.*, 1996; *Friedl et al.*, 2001]. The response to external stimuli is very fast raising actin polymerization within 15 s after a chemotactic trigger and falling back to base levels within 3–10 s after removal of the chemoattractant [*Albrecht and Petty*, 1998; *Friedl et al.*, 2001]. Certain experiments suggest that leukocytes move on 2D substrates much like fibroblast while this picture changes in 3D demonstrated by the migration on ECM which can occur independent of adhesion [*Friedl and Brocker*, 2000]. It seems that in this case bio-physical contacts replace the function of adhesion molecules providing the anchorage to transmit traction forces
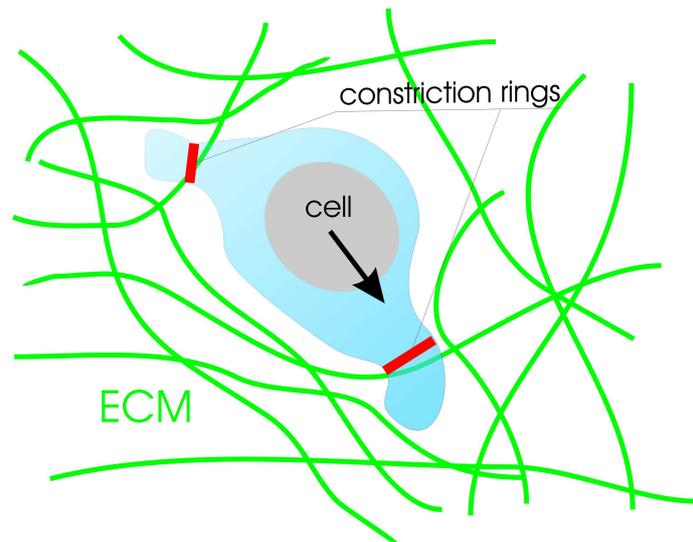
Figure 3.3: Schematic representation of a migrating lymphocytes. The lymphocyte forms constriction rings (red) along its cells body that allow the cell to squeeze through gaps in the ECM (green lines).

[*Haston and Shields*, 1984]. This interaction is provided by bleb-like structures expanding in between the ECM fibers. Even the formation of focal contacts and stress fibers is suppressed and the cortical actin is diffusely distributed. The anchors can by provided by lateral protrusion hooking in the ECM. Another frequently observed structure are constriction rings [*Bornens et al.*, 1989; *Lewis*, 1931; *Murray et al.*, 1992; *Wolf et al.*, 2003b] that are pressed against gaps in the ECM and support the flow of the cytoplasm though the gap when the rear of the cell contracts [*de Bruyn*, 1946] (Fig. 3.3). In contrast to the mesenchymal migration mode the matrix is not modified by degradation using matrix metalloproteinases [*Wolf et al.*, 2003b]. The adhesion-independent properties of leukocyte migration may be dominant considering the lack of ECM in the PLF (Sec. 2.3.1).

In T cells the MTOC is formed as a rod-like shaft bearing basically all microtubules [*Ratner et al.*, 1997]. Therfore, it seems that the microtubules play no active role in migration – except the MTOC's role for defining the polarity – and are moved 'out of the way' to increase the deformability of the cell. However, other experiments indicate that the microtubules may be involved in controlling the actin-myosin interaction in the cell [*Bornens et al.*, 1989]. The microtubule retraction is reversible which plays a role when T cells make cognate contacts with Ag presenting cells where the microtubules are required to support the transport of proteins and organelles [*Bornens et al.*, 1989; *Meyer-Hermann and Maini*, 2005b]. The microfilaments are concentrated in one or more lamellipodia at the leading edge of the cell. The typical shape of lymphocytes requires contact to the ECM, without it the cells remain in a spherical shape which is typical for the situation in lymphoid tissue due to the large gaps in the ECM (Sec. 2.3). Overall, this suggests that the mesenchymal migration type does not fit very well for lymphocytes. Probably this is directly related to the less organized cytoskeleton of lymphocytes (no stress fibers).

Interestingly, fibroblasts use a more amoeboid type of migration in the presence of the chemokine IL-8. Then the formation of focal adhesions is lacking [*Friedl and Brocker*, 2000]. Likewise tumor cells can switch between the mesenchymal and amoeboid migration mode when matrix metalloproteinases are blocked [*Niggemann et al.*, 2004; *Sahai and Marshall*, 2003; *Wolf et al.*, 2003a] raising the question if leukocytes could do something similar enabling them to use mesenchymal migration [*Samstag et al.*, 2003]. The switch to amoeboid migration in tumor cells is correlated with a change of

morphology from a constitutive elongated spindle-shape to a less polarized, more ellipsoidal, flexible morphodynamics exhibiting constriction rings in order to pass narrow gaps in the ECM instead of dissolving the ECM [*Wolf et al.*, 2003a]. The formation of constriction rings may occur quite often in the T zone of the SLT where ECM is present. However, there are relatively large gaps between the ECM fibers in this region (Sec. 2.3.1).

Intravital imaging of lymphocyte movement in excised LN have broadened the view on migration very recently. Two-photon microscopy experiments could show lymphocytes and the natural ECM together [*Grayson et al.*, 2003; *Gunzer et al.*, 2004; *Miller et al.*, 2003, 2002; *Okada et al.*, 2005; *Wei et al.*, 2003]. The sparse network of reticular fibers (Sec. 2.3.1) forms the substrate of cell migration in LN. Migrating cells collide with other cells but cause them to move only a few micrometers, i.e. the Brownian-like motion induced by other cells is small compared to the active migration [*Wei et al.*, 2003]. T cells are shown to have a 2 minute-cycle between two phases of migration [*Miller et al.*, 2003, 2002; *Wei et al.*, 2003]: An elongated phase with a compact triangular morphology during movement which is alternating with the resting phase in which the cells are balling up. The distance traveled in one cycle is about $20\,\mu$m with peak velocities of $25\,\mu$m min^{-1}. The mean velocity of the cells is about $12\,\mu$m min^{-1}. The migration pattern is amoeboid during the elongated phase with a leading edge followed by the cell body and the trailing edge/uropod. The direction of motion is fairly constant over one cycle, sometimes even over several cycles. However, there is a high probability that the direction of motion changes after each balling-up of the T cell realized by forming a new leading edge instead of turning of the cell. On the long term the migration of T cells appears to be a random walk with a diffusion coefficient of 67μm min^{-2}. B cells show a slightly different behavior. They are slower with $6\,\mu$m min^{-1} and change direction more frequently probing their environment using amoeboid-like cell extensions. On the long run the migration is again a random walk with a diffusion coefficient of about $12\,\mu$m min^{-2}.

Up to now *intravital* studies showing migration of lymphocytes directed by chemotaxis are rare. The imaging data fails to detect gradient-responses even at the boundary of PLF [*Wei et al.*, 2003]. The separation of lymphocytes seems to be mediated by temporal sensing, i.e. lymphocytes reverse their direction when they enter the 'wrong' compartments [*Wei et al.*, 2003]. Thus, it seems that chemokines act mainly as factors presented on surfaces rather than soluble factors. This indicates a haptotaxis mechanism of chemokines bound to the ECM. Chemokine receptors are preferentially located at the leading edge at a 10:1 ratio or higher independent of the presence of chemokines [*Nieto et al.*, 1997; *Pelletier et al.*, 2000]. It seems that, once they started migrating and have polarized, cells maintain their direction even in the absence of the gradient [*Pelletier et al.*, 2000] explaining the persistence of the migration direction during the elongated phase of T cell migration discussed above. This may also provide an alternative explanation of the apparent temporal sensing mechanism seen in the PLF. The gradient of the chemokine may be detected during a certain phase of migration and is then ignored for a certain period contrasting with a true temporal sensing by comparing concentrations along the path of migration as it has been shown for neutrophils [*Albrecht and Petty*, 1998]. Thus chemotaxis seems to play a role in the cell migration in SLT but the mode in which gradient guidance is realized may look different from the picture that results from *in vitro* experiments. It is also possible that the high density of cells in the *intravital* imaging approach compared to the *in vitro* experiments is the crucial difference.

3.2.2 Force generation

The force generation of migrating cells has been of great interest in the past years and is required as input for the simulation of cell migration. The experimental studies concentrate on the actin polymerization dynamics and force generation during cell migration on 2D substrates [*Balaban et al.*, 2001; *Burton et al.*, 1999; *Galbraith and Sheetz*, 1999; *Oliver et al.*, 1999]. A method to determine these forces is to plate fibroblasts on elastic substrates measuring the deformation of the substrate during cell migration. With the help of known mechanical properties of the substrate the forces can be calculated. The stress applied at the cell's contacts to the substrate are in the range of 5.5 nNμm^{-2} [*Balaban et al.*, 2001] to 80–130 nNμm^{-2} [*Burton et al.*, 1999]. The forces are exerted in all directions with a center located in front of the nucleus (Fig. 3.4) [*Burton et al.*, 1999; *Schwarz et al.*, 2002]. These traction forces reach 200 nN in the case of fibroblasts while the net force is in the order of 10-30 nN. The strongest forces are generated predominantly perpendicular to the direction of motion [*Burton et al.*, 1999].

Similar measurements for keratocytes showed forces in the order of 45 nN with a net propulsive force of 10 nN exhibiting the same pattern of traction forces like fibroblasts [*Galbraith and Sheetz*, 1999; *Oliver et al.*, 1999]. These experiments demonstrated that a myosin-dense region close to the cell nucleus is the dominant force generator. In contrast, the leading edge produces substantially smaller forces which are only sufficient to explore the environment prior to the formation of focal contacts.

The traction force pattern for *Dictyostelium discoideum* exhibits a cyclic behavior [*Uchida et al.*, 2003]. There is a retraction phase similar to fibroblast where large contracting forces act perpendicular to the direction of motion which shortens the shape of the cell. This phase interchanges periodically with a time constant of 70 ± 28 s with an extension phase that shows contractile force parallel to the migration direction elongating the cell again. Further studies demonstrated that the extension phase is independent of myosin II while the retraction phase requires it. Cells deficient in myosin II still cycle between the two phases morphologically but do not produce the corresponding forces in the retraction phase. Also the cells move significantly slower. The authors [*Uchida et al.*, 2003] and others [*Samstag et al.*, 2003] concluded that myosin II causes contraction of the rear of the cell thus pushing its leading edge forward. From the morphology point of view the case of *Dictyostelium discoideum* is closest to lymphocytes [*Friedl et al.*, 2001]. However, fibroblasts and keratocytes provide an estimate for the typical forces occurring during cell migration.

Shape oscillations Neutrophils are another cell type that has been extensively studied with regard to their migration behavior. It seems that the mechanisms for migration of neutrophils is different from the fibroblast – generally called *amoeboid migration* in contrast to *mesenchymal migration* of fibroblast-like cells. There have been studies that the shape oscillates with periods of roughly one minute ([*Ehrengruber et al.*, 1996] and references therein). This coincides with the frequency of directional changes in these cells. Thus the shape oscillation seem to be directly related to the persistence time of neutrophils. Detailed studies on *Dictyostelium discoideum* cells demonstrated that the shape change and oscillations are not random but a result of oscillatory waves resulting from the actin polymerization dynamics [*Killich et al.*, 1993]. It has also been shown that the formation of
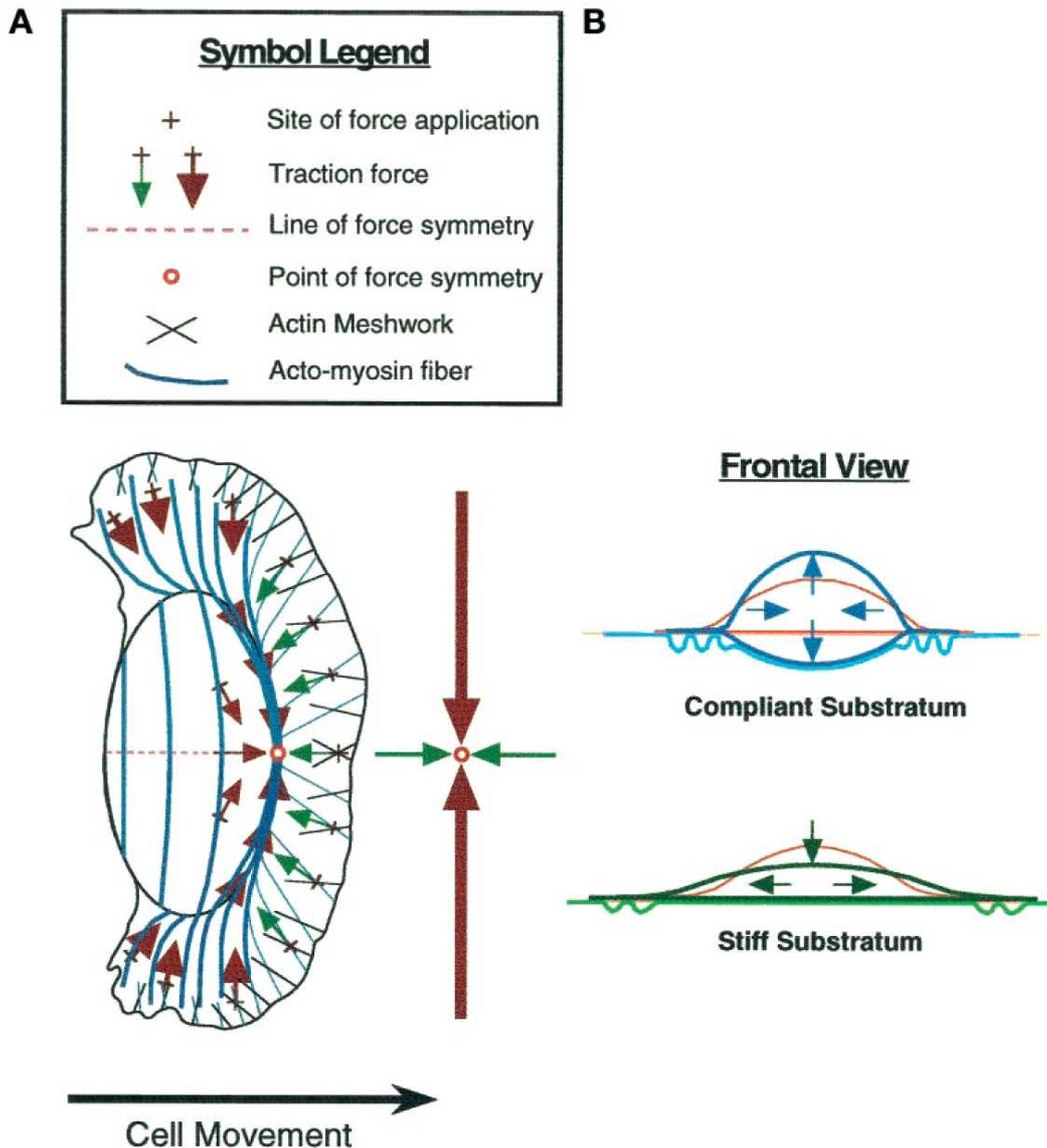
Figure 3.4: The traction force pattern of a migrating keratocyte. The picture has been taken from [*Burton et al.*, 1999]. The traction forces are predominantly acting perpendicular to the direction of motion. The center of all force vectors lie slightly in front of the nucleus.

pseudopods is not a random process but follows the same principle as the shape oscillations. Later work proposed that the actin dynamics follows self-organized reaction-diffusion waves providing the basis for the observed shape changes [*Vicker*, 2002a,b]. Looking on the cycling behavior of T cells [*Miller et al.*, 2002; *Wei et al.*, 2003] it seems that leukocytes generally show this type of oscillatory shape changes. Thus the traction force pattern may be similar to *Dictyostelium discoideum* because the morphology of cycling is similar to that observed for neutrophils and T cells.

Constriction Rings   A characteristic property of lymphocyte migration is the constriction ring [*Bornens et al.*, 1989; *Lewis*, 1931; *Murray et al.*, 1992; *Wolf et al.*, 2003b]. A constriction ring has a diameter of ~ 4/5 of the lymphoblast diameter [*Bornens et al.*, 1989]. The ring separates the cytoplasm

in an organelle-free and organelle-containing part. Cytoplasm flows from the ring towards the pole of the organelle-free part causing membrane activity by inducing the formation of protrusions. The only larger structure in this area is the centrosome.

When microtubules are disrupted by drug treatment the constriction ring is narrowed to $\sim 1/5$ of the cell diameter. This has the additional consequence of permitting a forth-and-back oscillation of the constricting ring between the two ends of the cell within 2.5 to 4.5 minutes resulting in an average speed of about $0.1\,\mu$ms^{-1}. Additionally, increased membrane activity is taking place on the cell's pole opposite to the ring of the treated cell. When microfilaments are disrupted the cell looses its overall spherical shape looking like the Greek letter ϕ – a spherical cell body with two opposing, long and thin extensions of unequal length. Disrupting both – microtubules and microfilaments – the cells remains spherical and exhibits blebbing of the cell membrane. On the contrary enhancing the microtubule formation by drug treatment also causes an elongated cell shape quite similar to the absence of microfilaments.

Myosin is also involved in the shape changes. In untreated cells myosin is uniformly distributed with a slightly higher concentration in the cortical shell. Disrupting the microtubules causes a relocation to the plasma membrane as ring or a tight cap. When the microfilaments are destroyed myosin distributes in the long extensions of the cell that are formed. Microfilaments are present asymmetrically around the constriction ring with an accumulation towards one cell pole. The free actin is homogeneously distributed.

The conclusion from the organization and behavior of the cytoskeletal elements is that the constriction ring is the site of force generation leading to forward protrusion and cytoplasmatic flow [*Bornens et al.*, 1989]. Without microfilaments myosin is exclusively associated with the ring. The ring oscillation involves an assembly-disassembly cycle recruiting myosin from the cap to the ring, transport across the cell and relocation in a new cap at the other side of the cell. The results suggest that microtubules control the distribution of myosin and guide the cytoplasmatic flow towards the active membrane. Finally, the microtubules enforce an acto-myosin system with unidirectional activity thereby maintaining the cell polarity. This might explain the recent two-photon imaging data that T cells tend to maintain their direction of motion for quite some time [*Wei et al.*, 2003]. How the association of myosin with chemokine receptors like CXCR4 fits into this picture remains unclear [*Rey et al.*, 2002]. There exists a model for the oscillations caused by microtubule disruption in lymphoblasts based solely on actin polymerization dynamics [*Guyader and Hyver*, 1997]. The shape change when the microfilaments are disrupted have been investigated in more detail for fibroblasts experimentally and theoretically as well [*Iglic et al.*, 2001]. The basic idea behind the theory applied to the ϕ shape is that the cortical shell is under stress trying to minimize the elastic energy and apparent cell surface when spanned along the microtubular rod. However, this study has been performed on fibroblasts which show the same elongated ϕ shape. The long arms where made of a microtubules rod. Disrupting the microtubules in addition caused the same spherical structure with a blebbing surface like the lymphoblasts. However, no constriction ring could be observed.

Intermediate filaments are also involved in the cell migration processes. Upon initiation by migration, for instance by chemotactic factors, intermediate filaments aggregate in the uropod of T cells [*Brown et al.*, 2001] like microtubules in the MTOC. Usually these filaments limit the deformability of cells.

Relocation of intermediate filaments may provide a mechanism to increase the flexibility of the cell enabling to migrate through narrow corridors as observed during transendothelial migration.

Observing the constriction ring on moving lymphocytes reveals a wave-like motion passing down the length of the cell [*Haston and Shields*, 1984] as observed when disrupting microtubules [*Bornens et al.*, 1989]. The basic difference is that the ring is fixed and the cell moves through the ring within 16–80 s (mean 30 s) [*Haston and Shields*, 1984]. This has been described first by Lewis [*Lewis*, 1931]. Detailed studies show that bleb-like structures fix the constriction ring with respect to collagen matrices [*Haston and Shields*, 1984]. The cytoplasm in the blebs does not join the cytoplasm squeezing through the ring during migration. These experiments showed a similar behavior for B cells.

One still has to take care of transferring data collected with neutrophils to lymphocytes despite both belonging to the leukocyte class of cells [*Entschladen and Zanker*, 2000]. Microtubule disruption induces increased T cell migration by initiating more cells of a population to migrate, increasing the velocity, and prolonging the period of motion. In contrast to the MTOC of T cells [*Bornens et al.*, 1989], microtubules in neutrophils are located close to the leading edge even that it is less organized (references in [*Entschladen and Zanker*, 2000]). A possible explanation for all these differences is that neutrophils are not able to proliferate and do no longer require a organized microtubule system in contrast to T cells [*Entschladen and Zanker*, 2000]. Thus, the formation of the MTOC can be omitted to allow a high flexibility of the neutrophil. Another striking difference is that chemotactic responses of T cells do not change the average speed of migration while neutrophils significantly speed up by a factor 2 to 3 [*Entschladen and Zanker*, 2000]. This is due to different internal signaling pathways. An interesting consequence is that the ability of chemokines to induce migration, i.e. chemokinesis, can occur independently from the induction of guided motion, i.e. chemotaxis.

In summary the lymphocytes adapt their cytoskeleton to a state that allows for a high deformation of the cell shape. The migration of the cells may be more a flow of cytoplasm that is generated by contraction of cytoskeletal elements than the complex dynamics of the three step model derived from result on fibroblasts migrating on 2D substrates.

3.3 *Chemotaxis*

Chemotaxis is the directed migration of a cell upwards or downwards a gradient of some substance called chemoattractant or chemorepellent, respectively. Chemorepellents will not be discussed in the following as they have not been shown to be involved in the lymphocyte migration in the PLF system.

The dominant group of chemoattractants for lymphocytes are *chemokines (chemoattractant cytokines)* [*Moser et al.*, 2004; *Sallusto and Mackay*, 2004]. These are small proteins of about 100 amino acids size. Other chemoattractants like lipids have not been shown to play a role for the migration of lymphocytes in lymphoid tissue with the exception of S1P (Sec. 2.4.2). Chemokines constitute their function *in vivo* when they are bound to glycosaminoglycans (GAG) connected to the ECM while soluble chemokines are hardly detectable [*Hoogewerf et al.*, 1997; *Moser et al.*, 2004; *Pelletier et al.*,

2000; *Proudfoot et al.*, 2003; *Weissenbach et al.*, 2004]. Cells can detect chemokines in their GAG-bound or unbound form using their chemokine receptors. Of note, one-to-one relationships between chemokines and their receptors are rare. Mostly a chemokine uses several receptors and in the same manner a receptor can bind various chemokines (reviewed in [*Moser et al.*, 2004]).

Sensing of chemokines   Temporal gradient sensing has been demonstrated for neutrophils [*Albrecht and Petty*, 1998]. The molecular basis is an oscillation of the signal transduction system with a period of 10 s. When the concentration of the chemoattractant is lowered homogeneously the cell reverses its direction. The change of direction is usually performed by initiating a new lamellipodium in the new direction of migration rather than a rotation of the cell. Increasing the concentration does not change the direction of locomotion implying that the effect can guide a cell upwards a concentration gradient.

Direct spatial gradient detection by eukaryotic cells has been demonstrated [*Parent and Devreotes*, 1999]. Several models for this process have been proposed [*Levchenko and Iglesias*, 2002; *Parent and Devreotes*, 1999]. The cell's sensitivity depends on the steepness of the gradient – 2% difference between front and rear are sufficient – and is much less dependent on the total concentration of the chemoattractant.

The dependency of chemotaxis on the concentration *in vitro* is in general bell-shaped in terms of the efficiency of the induction of cell migration, i.e. chemokinesis. This behavior was confirmed for the chemokines acting in the SLT with a typical maximum around 10–200 nM (e.g. [*Bardi et al.*, 2001; *Bernardini et al.*, 1998; *Cruikshank et al.*, 1994; *Kim et al.*, 1998; *Matloubian et al.*, 2004; *Willimann et al.*, 1998; *Yopp et al.*, 2005; *Yoshida et al.*, 1998]). Also there is a threshold below which cells do not respond to a chemoattractant. The typical threshold is about 1 nM [*Kim et al.*, 1998; *Tomhave et al.*, 1994; *Yoshida et al.*, 1998] but values of 30 nM have been reported as well [*Willimann et al.*, 1998]. Typical values for the half maximal response (EC$_{50}$) for neutrophil chemoattractants are approximately 1 nM which is close to the K_d of these chemoattractants [*Tomhave et al.*, 1994]. The K_d values for other chemokines like CCL19, CXCL12, CCL5, or IL-8 are in a similar range [*Lin et al.*, 2004; *Pelletier et al.*, 2000; *Slimani et al.*, 2003; *Yoshida et al.*, 1998] as well as the EC$_{50}$ thresholds for the leukocyte responses to these chemokines [*Kim et al.*, 1998]. For the specific combination of CXCL13 and CXCR5 guiding the B cell migration in PLF the response starts at concentrations of about 10 nM and drops to zero again at 1 μM [*Gunn et al.*, 1998]. In the T zone of lymphoid tissue CCL21 attracts lymphocytes via CCR7 although a relatively high concentration of 100 nM is required for optimal responses [*Willimann et al.*, 1998]. Typical concentrations found for CCL21 are in the range of 1 μM [*Luther et al.*, 2002]. The other CCR7 ligand CCL19 can be found in a 100-fold lower concentration in tissue.

The overall data on chemotaxis prompts the question what eucaryotic cells sense *in vivo*. It seems that gradient sensing works only when the cell first contacts the chemoattractant and starts migrating. The signal seems to be redundant once the cell polarizes and temporal sensing becomes relevant. This view is supported by the fact that the cells detect ECM-bound chemokines which may generate a more uniform distribution in the tissue thus only gradients at the edges of an area defined by chemokines are important [*Pelletier et al.*, 2000; *Wei et al.*, 2003]. The results of the simulations show that this mode

of migration is more consistent than persistent gradient sensing by cells (Sec. 6). However, the *in vivo* results that cells turn at the PLF border may be equally explained in another way. The gradients of the chemokines are shallower in the center of an area defined by chemokines [*Okada et al.*, 2005]. Thus the threshold of detection of gradients defines where cells are able to perform chemotaxis (Sec. 6).

Regulation of chemotaxis   The chemotactic responses of cells can be regulated on many levels. First, the expression of the corresponding receptors can be regulated on the genetic level. Also modification of the receptor activity including internalization is relevant. Effects on the genetic level are not considered for the PLF system due to the long characteristic times associated with it (up to several days, e.g. [*Lo et al.*, 2005]).

The internalization of the chemokine receptors seems not to be critically important for robust chemotactic responses of cells [*Arai et al.*, 1997; *Moser et al.*, 2004; *Neel et al.*, 2005]. It seems that this mechanism is required to redistribute the receptors on the cell surface allowing the cell to sense the direction of gradients [*Moser et al.*, 2004]. Studies on neutrophils also showed that the desensitization of the chemoattractant receptors occurs usually when high concentrations of the chemoattractant are given [*Tomhave et al.*, 1994]. One mode of desensitization is the internalization of the chemokine receptor. In line with the dependence on high concentrations it has been shown that for chemotactic responses at low or medium concentration do not critically depend on whether internalization occurs or not [*Arai et al.*, 1997; *Bardi et al.*, 2001; *Moser et al.*, 2004; *Neel et al.*, 2005]. Interestingly, CCL21 does not induce the internalization of CCR7 in contrast to CCL19 which causes the downregulation of this chemokine receptor. That indeed raises the question which mechanism causes the cross-desensitization between CCL19 and CCL21 reported in an older study [*Willimann et al.*, 1998]. It is also a general observation that different ligands of the same receptor cause different internalization levels [*Neel et al.*, 2005]. It seems more plausible to assume that the ligand effects the recycling of the receptor rather than the internalization rate (as it is suggested by the equation (Eq. 5.49) in (Sec. 5.5)). Even more striking the internalization seems to be subject to regulation by factors other than chemokines. For instance IFNα can enhance the chemotactic response of B cells by decreasing the chemokine receptor internalization [*Badr et al.*, 2005]. The fact that IFNα does not interfere with the spontaneous internalization, i.e. the background level of receptor internalization in the absence of the ligand, suggests that not the internalization process itself but the recycling of the receptor is changed.

Of note, some experiments fail to detect CXCL12 and CXCL13 responses of naive B cells freshly isolated from tonsils [*Roy et al.*, 2002]. Thus, the presence of chemokine receptors CXCR4 and CXCR5 is necessary but not sufficient to cause chemotaxis of naive B cells. B cells from the GC show a similar behavior [*Bleul et al.*, 1998; *Casamayor-Palleja et al.*, 2002; *Roy et al.*, 2002]. Most likely the suppression of its function is mediate by a desensitization mechanism either by internalization or cross-desensitization (see below). This has to be taken into account in the interpretation of experimental data. The demonstration of a chemokine receptor on a certain cell type does not necessarily imply a function in chemotaxis for the same cells.

The importance of this may be demonstrated by the response of B cells towards CCL21. The surface CCR7 level on freshly isolated B cells is undetectable [*Casamayor-Palleja et al.*, 2002]. The protein

can be identified in the cytoplasm and is brought to the surface in CCL21-free culture suggesting receptor internalization by exposure to CCL21 or CCL19. Freshly isolated lymphocytes also show little attraction to CCL19 [*Yoshida et al.*, 1998] suggesting an internalization mechanism for T cells as well although the CCR7 levels have not been investigated in detail. Internalization may explain why, despite the presence of CCL21 in the T zone and the receptor CCR7 on lymphocytes, no chemotaxis can be observed in the T zone [*Wei et al.*, 2003].

Complex responses to multiple chemokines   In several systems cross-talks between different chemokines/chemokine receptors were observed [*Moser et al.*, 2004]. CD4 T cells chemotax in response to IL-16 [*Cruikshank et al.*, 1994]. This can block chemotaxis in response to CXCL12 without downregulating the corresponding receptor CXCR4 [*Van Drenth et al.*, 2000]. The blocking takes 10–15 minutes and reaches maximum after 1 hour. Conversely, CXCL12 cannot block chemotaxis in response to IL-16. The same authors reported reciprocal blocking of chemokine response between IL-16 and CCL4 (MIP-1β). A cross-desensitization has been reported for CXCL12 blocking the CCL19 response of lymphocytes while CCL19 cannot block CXCL12 [*Kim et al.*, 1998]. As expected, cross-desensitization occurs when chemokine use the same receptor as was shown for CCL19 and CCL21 [*Willimann et al.*, 1998].

Not in all cases the effect of the presence of multiple chemoattractants is the block of all but one response. It is also possible that the cell computes a vector sum of the incoming signals to determine an average direction of multiple chemoattractants [*Foxman et al.*, 1999]. However, the speed of the cell does not change. The integrated response influences the direction only. A difference occurs when those multiple signals are given in some sequential order. Then the direction is dominated by the newer chemoattractant even if it is presented in lower concentrations and/or gradients [*Foxman et al.*, 1999]. An explanation for this behavior would be the desensitization of receptors for instance by internalization (see above and [*Bardi et al.*, 2001]). Another explanation is provided by a work on neutrophils identifying two signaling pathways for two different chemoattractant receptors indicating that a hierarchy of chemoattractants exist [*Heit et al.*, 2002]. The hierarchy levels are named 'target' and 'intermediary' chemoattractants. When concurrent signals of members from one group only are provided the cell responds by computing the vector sum otherwise the target chemoattractants are preferred. Yet the blocking of intermediary chemoattractants by a target chemoattractant can be incomplete [*Tomhave et al.*, 1994]. Interestingly, the presence of an intermediary chemoattractant can enhance chemotaxis to a target chemoattractant allowing the cell to respond to lower concentrations than with the target chemoattractant alone.

Which type of response results from multiple signals may rely on the signaling cascade, i.e. which receptors share or use a concurring cascade to induce directed cell migration. The data available on the chemokines CXCL12, CCL19, CCL21, CXCL13, and possible S1P important for the PLF system are not conclusive and do not allow the determination of a signaling hierarchy. Some evidence is provided by studying the behavior of Ag-activated cells. Newly activated naive B cells upregulate there CCR7-levels by a factor of two to three consequently enhancing their response to CCL19/CCL21 which then balances their CXCL13 response such that the migrate to the border of the PLF with the T zone [*Breitfeld et al.*, 2000; *Casamayor-Palleja et al.*, 2002; *Cyster*, 2005; *Muller et al.*, 2003; *Okada*

et al., 2005; *Reif et al.*, 2002; *Roy et al.*, 2002]. When either CXCR5 is overexpressed or CCR7 is lacking B cells fail to relocate to the follicle border upon Ag-stimulation and remain in the follicle [*Reif et al.*, 2002]. Similar if CCR7 is overexpressed by genetic manipulations the B cells locate at the border without Ag and are moving farther into the T zone as expected considering the higher CCR7 levels upon Ag-stimulation. Reversely, activated T cells upregulate the response to CXCL13 relocating to the follicle border as well [*Ansel et al.*, 1999; *Breitfeld et al.*, 2000; *Cyster*, 2005; *Fillatreau and Gray*, 2003]. The fact that different chemokine receptor levels can affect the localization of lymphocytes bases on the distribution of chemoattractants that extends beyond the location of the sources. Direct measurements suggest that the effective range of the gradients is 80–140 *μm* beyond the corresponding target zone [*Okada et al.*, 2005]. Detectable gradients go even further reaching 150–200 *μm*. However, the gradients or concentrations are seemingly not strong enough to induce chemotaxis at this range. Overall it is suggested that the relevant chemokines in the PLF system have the same hierarchy level (assumed to be intermediary) and thus chemotactic responses of lymphocytes are the result of computing the vector sum of concurrent chemokine signals.

Crosstalk with TNF-α Some of the molecules of the TNF superfamily involved in the organization of follicles (Sec. 2.2.2) have also some effects on lymphocytes directly. For example, TNF-α ligating TNFR-II can enhance the migratory response of B cells and possibly act as chemotactic factor [*Corcione et al.*, 1997]. Naive B cells can produce TNF-α on their own and release it when stimulated. This has some importance for the generation of FDC which are another source of TNF-α [*Braun et al.*, 2004; *Corcione et al.*, 1997] (however, another study failed to show TNF-α production by FDC [*Yamada et al.*, 1997]). In conclusion, the effect of TNF-$\alpha^{-/-}$ may not only be the regulation of stromal differentiation and CXCL13 production but also a direct modulation of B cell responses to chemokines.

TNF-α can bind to ECM and increase the adhesion of T cells to fibronectin. This requires the stimulation of T cells by CXCL12 or CCL5. Furthermore TNF-α is required to be bound to fibronectin [*Franitza et al.*, 2000]. The final effect of TNF-α on migration in this context is a reduction of the time of active migration and not a modulation of speed or directionality. The mechanism might be affinity modulation of β_1 integrins. This effect of TNF-α on T cell migration may prolong the time that T cells stay in the T zone but will not be considered as it seems not to be relevant to understand the organogenesis itself.

3.4 *Final remarks on cell migration*

Cell migration is a field that gained much attention, both on the experimental and the theoretical side. Yet the results are too broad-ranged to allow for a clear decision how cells migrate in the PLF environment. The complex interplay of chemokines and chemokine receptors remains unknown. Such the influence of the major chemokines CCL19, CCL21, and CXCL13, and the chemoattractant S1P may differ from the *in vitro* results demonstrating the activity of each of those chemokines in mainly non-physiologic conditions. Effects like the sensitivity threshold for chemoattractants, saturation and

internalization of receptors, and cross-desensitization may play a role but are not sufficiently determined for the case of the PLF and are therefore varied in the simulations to a certain extent to put some constraints on these parameters (Sec. 6).

Chapter 4

Regular Triangulation and Voronoi Tessellation

This chapter covers the basic geometric structure underlying the tissue model used in this work. The general properties of regular triangulations and its dual graph the Voronoi tessellation [*Aurenhammer*, 1987; *Okabe et al.*, 2000] are discussed. The regular triangulation serves as basis to identify neighbor cells. The dual Voronoi tessellation is used to determine cell contact surfaces and cell volumes [*Meineke et al.*, 2001; *Schaller*, 2006; *Schaller and Meyer-Hermann*, 2005]. The algorithms for dynamic and kinetic regular triangulations will be presented as well as the newly created parallel algorithms [*Beyer et al.*, 2005]. The update procedures for the regular triangulation account for the changing geometry of migrating cells changing their relative position, contact surfaces and volumes. The chapter will close with a semi-experimental part discussing the efficiency of the implementation of 3D dynamic and kinetic regular triangulation algorithms and demonstrating its suitability for tissue simulations with large numbers of cells.

4.1   Definition of Delaunay and regular triangulations

The basic geometric structure used for cell modeling is the *regular* triangulation [*Edelsbrunner and Shah*, 1996; *Ferrez*, 2001; *Okabe et al.*, 2000]. It is a natural extension of the Delaunay triangulation and therefore also known as *weighted* Delaunay triangulation. For clearness of the definitions the notation for all geometric objects used throughout this chapter are given first. The definitions are restricted to the three dimensional case but can be extended to any dimension.

Definition 1 *Let* $\mathbf{p} \in \mathbb{R}^3$ *define a* point. *The pair* $P = \left(\mathbf{p}, w_p\right) \in \mathbb{R}^3 \times \mathbb{R}$ *is called a* vertex. w_p *is called* weight *of the vertex P.*

For simplicity the vertices of the set $\mathcal{V}$ (see below) are restricted to be $P \in \mathbb{R}^3 \times \mathbb{R}^+$. Thus the weight of the vertex can be interpreted as a sphere with radius $\sqrt{w_p}$. This allows vertices to represent cells as spheres in a regular triangulation. Note, that the restriction to positive weights is not appropriate for orthospheres (see below).

Definition 2 *A simplex σ is the convex hull of $d + 1$ points $\mathbf{v}_i \in \mathbb{R}^d$ in a space of dimension d. More general a* k-simplex Δ_S *is the convex hull of $k + 1$ affinely independent points $\mathbf{u}_i \in S \subset \mathbb{R}^d$.*

In the present case $d = 3$ the term simplex (or 3-simplex) is a synonym for a *tetrahedron*. To simplify the notation the points of a simplex $\sigma_{\langle P_1, P_2, P_3, P_4 \rangle}$ will be noted by the vertices with the corresponding coordinates $\mathbf{p}_i$, $i = 1, 2, 3, 4$. Another simplification of notation is

Definition 3 *An* edge *(1-simplex)* $\langle P_1, P_2 \rangle$ *is the line connecting the points $\mathbf{p}_1$ and $\mathbf{p}_2$. A* face *(2-simplex)* $\langle P_1, P_2, P_3 \rangle$ *is the triangle formed by $\mathbf{p}_i$, $i = 1, 2, 3$.*

Like for simplices the points forming the edges and faces, respectively, are referred to by the corresponding vertices. The vertices/points forming an edge, face, or simplex are called endpoints of these objects. As stated in definition 2 it is assumed that all point configurations are affinely independent. This is also known as the *general position assumption* [*Mücke*, 1998], i.e. in the three dimensional case

1. no two points are identical,

2. no three points are collinear,

3. no four points are coplanar.

The first condition implies that even two vertices with different weights but identical coordinates are not allowed which would correspond to two cells with one engulfing the other.

Furthermore, the *opposing vertex* of a simplex with respect to a face is the fourth vertex of the simplex, e.g. for the simplex $\sigma_{\langle A,B,C,D \rangle}$ the vertex D is opposite to the face $\langle A, B, C \rangle$. The side of the face pointing towards its opposing vertex is called *inwards* the other side is called *outwards*. Note, that this definition is context-dependent as it depends on the simplex under consideration.

The definition of a triangulation follows previous work [*Edelsbrunner and Shah*, 1996]

Definition 4 *A triangulation $\mathcal{T}(\mathcal{V})$ of a finite point set $\mathcal{V}$ is a set of simplices (also called* simplicial cell complex *[Edelsbrunner and Shah, 1996]) such that for a k-simplex Δ_S:*

(i) If $\Delta_S \in \mathcal{T}$ then $\Delta_{S'} \in \mathcal{T}$ for all $S' \subseteq S$

(ii) If Δ_S, $\Delta_{S'} \in \mathcal{T}$ then $\Delta_S \cap \Delta_{S'} = \Delta_{S \cap S'}$.

Additionally, all vertices of $\mathcal{V}$ are 0-simplices of $\mathcal{T}$ and the pointwise union of the triangulation $\mathcal{T}$ is the convex hull of the vertex set $\mathcal{V}$.

The first condition given in the definition above implies that the edges and faces of the simplices in the triangulation $\mathcal{T}$ are also part of the triangulation. Condition (ii) states that the intersection of two k-simplices of $\mathcal{T}$ is either empty or another k-simplex, i.e. the intersection of two tetrahedra is empty, a vertex, an edge, or a face. The second condition also implies that two non-identical simplices (tetrahedra) do not overlap. Practically, the non-overlapping property can be easily computed for two simplices with a common face by using the orientation property of a simplex. The orientation of a

simplex $\sigma_{\langle A,B,C,D \rangle}$ is given by the sign of the determinant [1]

$$
O(A, B, C, D) \overset{\text{def}}{=}
\begin{vmatrix}
a_x & a_y & a_z & 1 \\
b_x & b_y & b_z & 1 \\
c_x & c_y & c_z & 1 \\
d_x & d_y & d_z & 1
\end{vmatrix}
=
\begin{vmatrix}
a_x - d_x & a_y - d_y & a_z - d_z \\
b_x - d_x & b_y - d_y & b_z - d_z \\
c_x - d_x & c_y - d_y & c_z - d_z
\end{vmatrix},
\tag{4.1}
$$

with $a_x, a_y, \ldots$ being the components of the point vectors $\mathbf{a}, \mathbf{b}, \mathbf{c}$, and $\mathbf{d}$. Two simplices $\sigma_{\langle V_1,V_2,V_3,V_4 \rangle}$ and $\sigma'_{\langle V_1,V_2,V_3,V_5 \rangle}$ are non-overlapping if $O(V_1, V_2, V_3, V_4) \cdot O(V_1, V_2, V_3, V_5) < 0$, i.e. the vertices V_4 and V_5 are on opposite sides of the common face $\langle V_1, V_2, V_3 \rangle$ of the simplices. The sign-evaluation of the determinant (Eq. 4.1) is also called orientation *primitive* or *predicate*. Similar the determinant used to calculate the orthosphere criterion given below (Eq. 4.2) is also known as orthosphere primitive or predicate.

The regular triangulation is a special case of a triangulation. This requires the definition of the power distance and the orthosphere:

Definition 5 *The* power distance *of two vertices U, V is given by $\rho(U, V) = \|\mathbf{u} - \mathbf{v}\|^2 - w_u - w_v$.*

Thereby $\|.\|$ denoting the euclidian distance in $\mathbb{R}^3$. With the help of the power distance the orthosphere of a simplex can be defined.

Definition 6 *The orthosphere M of a simplex $\sigma_{\langle V_1,V_2,V_3,V_4 \rangle}$ is defined as the solution $M = (\mathbf{m}, w_m)$ of the equations $\rho(V_i, M) = 0$, $\forall i = 1, 2, 3, 4$.*

In case that the weight w_m of the orthosphere is positive it can be interpreted as a sphere such that the tangential planes of M at the intersecting points of the spheres representing the vertex weights w_i are orthogonal to the tangential planes of these spheres (Fig. 4.1). Note, that even when all vertices V_i have a positive weight the orthosphere M can still have a negative weight and the radius is given by $\sqrt{|w_m|}$.

Finally, the regular triangulation can be defined.

Definition 7 *A triangulation $\mathcal{D}(\mathcal{V})$ is called* regular triangulation *or* weighted Delaunay triangulation *when all simplices fulfill the orthosphere criterion that is, no vertex lies inside the orthosphere of a simplex.*

The emptiness of the orthosphere can be tested by calculating the power distance of a vertex $V = (\mathbf{v}, w_v)$ to the orthosphere M. The orthosphere criterion states that $\rho(V, M) \geq 0$, $\forall \; V \in \mathcal{V}$. With the general position assumption $\rho(V, M) > 0$ holds for all vertices that do not define the orthosphere M itself (for which $\rho(V, M) = 0$). In practice it is not necessary to compute the sphere M directly. Instead the relation of Delaunay triangulations to convex hulls is used [*Brown*, 1979]. Under the *lifting map* transformation $\mathrm{LM} : V \in \mathbb{R}^3 \times \mathbb{R} \mapsto V^+ \in \mathbb{R}^4$ with $\mathrm{LM}(V) = V^+ = \left(\mathbf{v}, \|\mathbf{v}\|^2 - w_v\right) = \left(v_x, v_y, v_z, v_x^2 + v_y^2 + v_z^2 - w_v\right)$ the regular triangulation becomes the projection of the lower convex hull

---

[1]To achieve a consistent notation all functions that rely on points will have vertices as arguments while ignoring their weights as in (Eq. 4.1). The convention is that these functions may also take point arguments. That is useful to separate between vertices representing the applications objects – which are biological cells in this work – from points that are only geometrically relevant and lack the weight property.

Figure 4.1: The orthocircle M (red circle) of the simplex $\sigma_{\langle A,B,C \rangle}$ perpendicularly intersects all circles associated with the vertices A, B, C as indicated by the dashed lines. The weight of each vertex is represented as the radius $\sqrt{w}$ of the circles. A vertex V violates the orthosphere if the point where the tangent from the center of M to the circle of the vertex (tangent in green, circle in blue) is located inside the sphere representing the weight of the orthocircle M.
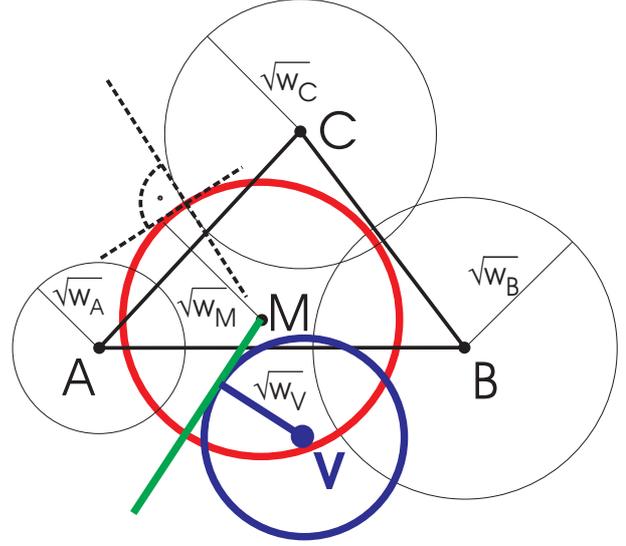
Figure 4.2: Definition of a Delaunay triangulation. All triangles of the Delaunay triangulation have empty orthocircles (which are the same as the circumcircles in the Delaunay case) as shown for the simplex $\sigma_{\langle V_1,V_2,V_3 \rangle}$ and the vertex U lying outside the orthocircle (red).
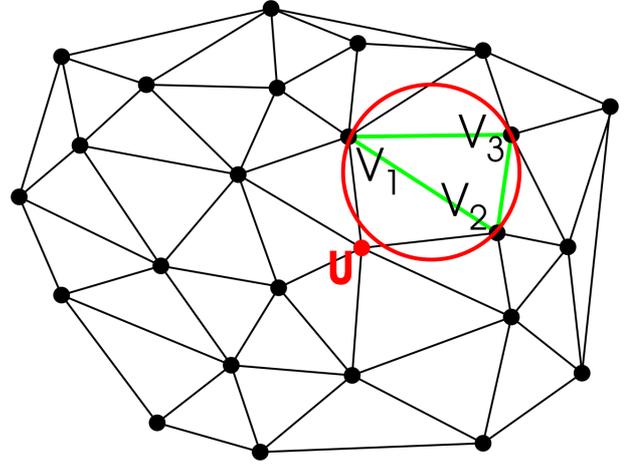
of the lifted point set $\mathcal{V}^+ = \text{LM}\,(\mathcal{V})$ into $\mathbb{R}^3$. The empty orthosphere criterion in $\mathbb{R}^3$ translates into an orientation criterion in $\mathbb{R}^4$. Thus, for four vertices A, B, C, and D of a simplex $\sigma_{\langle A,B,C,D \rangle}$ the orientation primitive for the lifted vertices A^+, B^+, C^+ and D^+ with a vertex V^+ in question is performed by calculating the sign of the determinant

$$S\,(A, B, C, D, V) \overset{\text{def}}{=} \begin{vmatrix} a_x - v_x & a_y - v_y & a_z - v_z & \left(\|\mathbf{a}\|^2 - w_a\right) - \left(\|\mathbf{v}\|^2 - w_v\right) \\ b_x - v_x & b_y - v_y & b_z - v_z & \left(\|\mathbf{b}\|^2 - w_b\right) - \left(\|\mathbf{v}\|^2 - w_v\right) \\ c_x - v_x & c_y - v_y & c_z - v_z & \left(\|\mathbf{c}\|^2 - w_c\right) - \left(\|\mathbf{v}\|^2 - w_v\right) \\ d_x - v_x & d_y - v_y & d_z - v_z & \left(\|\mathbf{d}\|^2 - w_d\right) - \left(\|\mathbf{v}\|^2 - w_v\right) \end{vmatrix} \tag{4.2}$$

$$= \begin{vmatrix} a_x - v_x & a_y - v_y & a_z - v_z & \|\mathbf{a} - \mathbf{v}\|^2 - w_a + w_v \\ b_x - v_x & b_y - v_y & b_z - v_z & \|\mathbf{b} - \mathbf{v}\|^2 - w_b + w_v \\ c_x - v_x & c_y - v_y & c_z - v_z & \|\mathbf{c} - \mathbf{v}\|^2 - w_c + w_v \\ d_x - v_x & d_y - v_y & d_z - v_z & \|\mathbf{d} - \mathbf{v}\|^2 - w_d + w_v \end{vmatrix} \tag{4.3}$$

which is equal to the orthosphere primitive in three dimensions. If $S\,(A, B, C, D, V) < 0$ than V lies in the orthosphere of the simplex $\sigma_{\langle A,B,C,D \rangle}$.
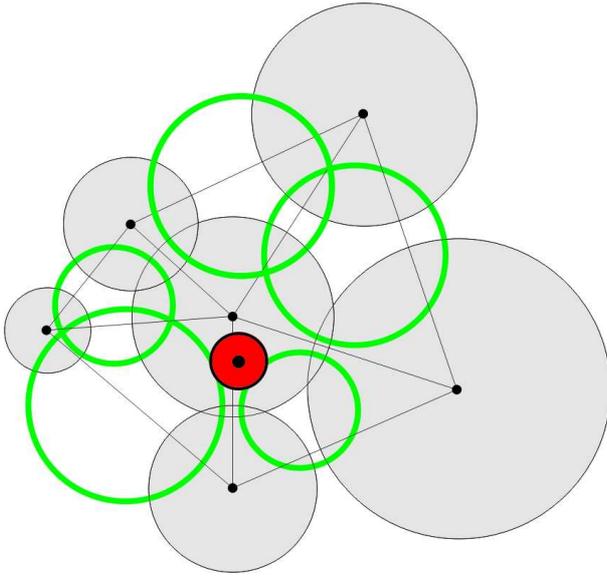
Figure 4.3: Redundant vertex. The vertex indicated by the red disk is redundant because it lies outside of all orthocircles according to the definition in Fig. 4.1 (green) of all simplices formed by the surrounding vertices indicated as grey disks. Thus, the redundant vertex is not endpoint of any simplex and the structure of the triangulation does not change if this vertex is present or not.

The usual Delaunay triangulation is a special case of regular triangulations with all vertex weights $w_v = 0$ (Fig. 4.2). It is also recovered by having all vertex weights w_v equal but non-zero. In this case the power distance $\rho(.,.)$ collapses to the usual euclidian distance squared and some constant offset. Also, it can be seen from the lifted map LM that all vertices in the lifted map are shifted by a constant amount. By a simple shift in the fourth coordinate this case can be transformed back to the case $w_v = 0$. Finally, the corresponding terms in the determinant $S(A, B, C, D, V)$ just cancel.

In contrast to the usual Delaunay triangulation a regular triangulation can have vertices $\{V_i\}$ which are not endpoints of any simplex. That is that the triangulation is the same with and without these vertices $\mathcal{D}(\mathcal{V}\backslash\{V_i\}) = \mathcal{D}(\mathcal{V})$. Such vertices are called *redundant vertices* (Fig. 4.3).

Additional terminology   Two vertices that are connected by an edge, i.e. they are endpoints of at least one common simplex, are called *neighbor vertices*. If two simplices share a common face they are said to be *adjacent* to each other or *neighbor simplices*. The simplices which have at least one face not shared with other simplices are called *outer simplices*. The union of these faces forms a polyhedra that bounds the convex hull of the vertex set $\mathcal{V}$.

For the algorithms it is important to introduce another definitions.

Definition 8 *Vertices lying inside an orthosphere are* violating *the orthosphere or the corresponding simplex. A simplex is called* locally regular *if the orthosphere criterion is fulfilled with the vertices of its adjacent simplices, otherwise it is called* locally non-regular *or* invalid*. A simplex is called* globally regular *if no vertex violates the orthosphere criterion, otherwise it is* globally non-regular*.

Note, that from the property that all simplices are locally regular it follows that the triangulation is regular while it is not necessary that a locally regular simplex is globally regular in a non-regular triangulation.
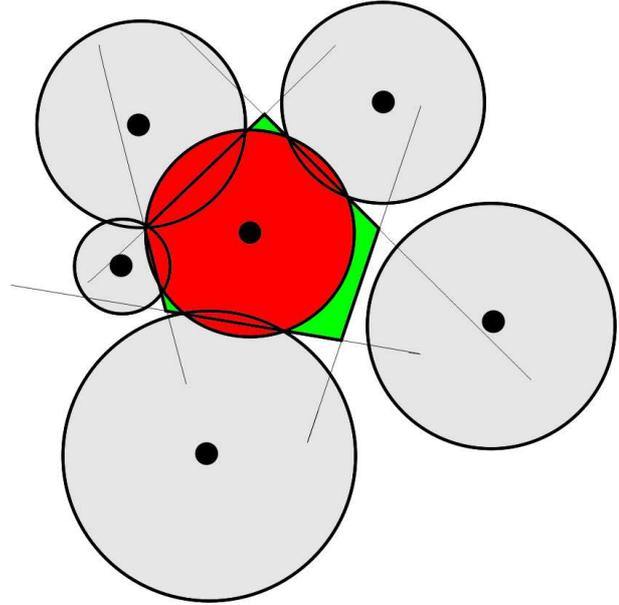
Figure 4.4: The Voronoi tessellation is the dual graph of the regular triangulation. Here it is shown for the vertex indicated by the red disk. The neighbor vertices are marked as grey disks. The Voronoi cell is a polygon shown in green.

4.1.1 Voronoi tessellations

There exists a dual graph of the Delaunay triangulation which is known as *Voronoi tessellation*

Definition 9 *A* Voronoi tessellation *is a subdivision* $\{C_n\}$ *of space such that*

$$\bigcup_n C_n = \mathbb{R}^3 \quad with \quad C_n = \left\{ \mathbf{x} \in \mathbb{R}^3 : \|\mathbf{x} - \mathbf{v}_n\| < \|\mathbf{x} - \mathbf{v}_m\| \ \forall \ m \neq n \right\}. \tag{4.4}$$

The points $\mathbf{v} \in \mathcal{V}$ *are called the generators. The* C_n *are called* Voronoi cells.

The Voronoi cells are polyhedra in three dimensions. The duality of the Delaunay triangulation and the Voronoi tessellation is shown in (Fig. 4.4). Each face of the Voronoi cell polyhedra corresponds to an edge between the vertices being the generators of those two cells. There is the additional property that the center of the circumsphere of the simplices of the Delaunay triangulation are the endpoints of the polyhedra forming the Voronoi cells (Fig. 4.4).

There is also a more general form of Voronoi tessellations that is the corresponding dual graph for regular triangulations. The Voronoi cells of this type are also called *Laguerre cells* and the tessellation is called a weighted Voronoi tessellation. A similar definition as for the standard Voronoi tessellation holds.

Definition 10 *A* weighted Voronoi tessellation *is a subdivision* $\{C_n\}$ *of space such that*

$$\bigcup_n C_n = \mathbb{R}^3 \quad with \quad C_n = \left\{ \mathbf{x} \in \mathbb{R}^3 : \|\mathbf{x} - \mathbf{v}_n\| - w_{v_n} < \|\mathbf{x} - \mathbf{v}_m\| - w_{v_m} \ \forall \ m \neq n \right\} \tag{4.5}$$

$$= \left\{ \mathbf{x} \in \mathbb{R}^3 : \rho(X, V_n) < \rho(X, V_m) \ with \ X = (\mathbf{x}, 0) \ \forall \ m \neq n \right\}. \tag{4.6}$$

The vertices $V \in \mathcal{V}$ *are called the generators. The* C_n *are called* Voronoi cells *or* Laguerre cells.

The duality between the weighted Voronoi tessellation and the regular triangulation is similar to the simple Voronoi/Delaunay case. Instead of circumspheres the centers of the orthospheres of the simplices are the endpoints of the Laguerre cells (Fig. 4.4). The redundant vertices occurring in regular

triangulations are the generators of the weighted Voronoi tessellation with empty Laguerre cells.

Computing the weighted Voronoi tessellation from a regular triangulation For applications mainly three properties of the weighted Voronoi tessellation are needed. These are the volume of the Laguerre cell, the area of the face between two cells, and the distance between a face of the cell and its generating vertex. The face of a Laguerre cells has the favorable that it lies in the same plane as the intersection circle of the two overlapping spheres. Following previous work [*Okabe et al.*, 2000; *Schaller and Meyer-Hermann*, 2004] the way how to compute the properties is described.

Let V be the vertex that is the generator of the Laguerre cell under consideration, further let $\{U_n\}$ be the neighbor vertices of V. Then one computes the centers of the orthospheres $\{\mathbf{m}\}$ of all simplices $\{\sigma_{\langle V,A,B,C\rangle}\}$, $A, B, C \in \{U_n\}$ with the endpoint V. This can be computed by solving the equations for the orthosphere $M = (\mathbf{m}, w_m)$

$$\rho(V, M) = 0 = \|\mathbf{v} - \mathbf{m}\|^2 - w_v - w_m \tag{4.7}$$

$$\rho(A, M) = 0 = \|\mathbf{a} - \mathbf{m}\|^2 - w_a - w_m \tag{4.8}$$

$$\rho(B, M) = 0 = \|\mathbf{b} - \mathbf{m}\|^2 - w_b - w_m \tag{4.9}$$

$$\rho(C, M) = 0 = \|\mathbf{c} - \mathbf{m}\|^2 - w_c - w_m \tag{4.10}$$

The equation system can be transformed into

$$w_v + w_m = \|v\|^2 - 2\mathbf{v} \cdot \mathbf{m} + \|m\|^2 \tag{4.11}$$

$$w_a + w_m = \|a\|^2 - 2\mathbf{a} \cdot \mathbf{m} + \|m\|^2 \tag{4.12}$$

$$w_b + w_m = \|b\|^2 - 2\mathbf{b} \cdot \mathbf{m} + \|m\|^2 \tag{4.13}$$

$$w_c + w_m = \|c\|^2 - 2\mathbf{c} \cdot \mathbf{m} + \|m\|^2 . \tag{4.14}$$

By subtraction of the first line from the other three equations one yields a reduced linear system for the orthosphere center $\mathbf{m}$

$$w_a - w_v = \|a\|^2 - \|v\|^2 + 2(\mathbf{v} - \mathbf{a}) \cdot \mathbf{m} \tag{4.15}$$

$$w_b - w_v = \|b\|^2 - \|v\|^2 + 2(\mathbf{v} - \mathbf{b}) \cdot \mathbf{m} \tag{4.16}$$

$$w_c - w_v = \|c\|^2 - \|v\|^2 + 2(\mathbf{v} - \mathbf{c}) \cdot \mathbf{m} \tag{4.17}$$

This can be read as linear system of the type

$$\mathbf{d} = 2A\,\mathbf{m} \tag{4.18}$$

with

$$\mathbf{d} = \begin{pmatrix} \|v\|^2 - \|a\|^2 + w_a - w_v \\ \|v\|^2 - \|b\|^2 + w_b - w_v \\ \|v\|^2 - \|c\|^2 + w_c - w_v \end{pmatrix} = \begin{pmatrix} \rho(V, 0) - \rho(A, 0) \\ \rho(V, 0) - \rho(B, 0) \\ \rho(V, 0) - \rho(C, 0) \end{pmatrix} \tag{4.19}$$

and

$$A = \begin{pmatrix} v_x - a_x & v_y - a_y & v_z - a_z \\ v_x - b_x & v_y - b_y & v_z - b_z \\ v_x - c_x & v_y - c_y & v_z - c_z \end{pmatrix}. \tag{4.20}$$

The orthosphere center is then quickly computed via

$$\mathbf{m} = \frac{1}{2} A^{-1} \mathbf{d}. \tag{4.21}$$

The center of the orthosphere of a simplex $\sigma_{\langle A,B,C,D \rangle}$ will be denoted by $\mathbf{m}_{\langle A,B,C,D \rangle}$ in the following.

The distance of the generator V to the plane of a face of its Laguerre cell is given by

$$\rho(V, P) = 0 \quad \text{and} \quad \rho(U, P) = 0 \tag{4.22}$$

on a line connecting the generator V with its neighbor vertex U such that

$$P = (\mathbf{p}, 0) = (\mathbf{v} + \lambda[\mathbf{u} - \mathbf{v}], 0). \tag{4.23}$$

Solving the equation (Eq. 4.22) for the variable λ from (Eq. 4.23) gives the distance dist_{VU} of the Vertex V of the Voronoi face with the vertex U

$$\text{dist}_{VU} = \frac{1}{2} \|\mathbf{u} - \mathbf{v}\| \left(1 + \frac{w_v - w_u}{\|\mathbf{u} - \mathbf{v}\|^2} \right). \tag{4.24}$$

The area area_{VU} of a face of the Laguerre cell between the vertices V and U can be decomposed into a sum of triangular areas. These triangles are formed by the vertex V and the orthosphere centers of two simplices $\sigma_{\langle V,U,A_i,A_{i+1} \rangle}$ and $\sigma_{\langle V,U,A_i,A_{i+2} \rangle}$ $(A_i \in \{U_n\})$ with the common face $\langle V, U, A_i \rangle$.

$$\text{area}_{VU} = \frac{1}{2} \left| \sum_i (\mathbf{m}_{\langle V,U,A_i,A_{i+1} \rangle} - \mathbf{q}) \times (\mathbf{m}_{\langle V,U,A_i,A_{i+2} \rangle} - \mathbf{q}) \right| \quad \text{with} \quad \mathbf{q} = \mathbf{v} + \text{dist}_{UV} \frac{\mathbf{u} - \mathbf{v}}{\|\mathbf{u} - \mathbf{v}\|} \tag{4.25}$$

The summation using the cross product of vectors has the nice property to work also in the case where the point $\mathbf{p}$ is not located within the face.

Finally, the volume of a Laguerre cell can be calculated by subdividing it into pyramids and summing up their volume. Each pyramid is formed by a face of the cell as basis and the vertex V as tip. The volume is then given by

$$\text{vol}_V = \frac{1}{3} \sum_{\{U_n\}} \text{area}_{VU_n} \text{dist}_{VU_n}. \tag{4.26}$$

4.2   Construction algorithms

There exists a variety of algorithms to construct Delaunay triangulations in two dimensions. However, with few exceptions most cannot be generalized to three or more dimensions. There exist basically three algorithms that can construct Delaunay triangulations in three dimensions. All of them can be generalized to be used for regular triangulations.

Flip algorithm   The first algorithm is known as *flip algorithm* [*Lawson*, 1972]. First invented for two dimensions it has been extended to three and higher dimensions [*Joe*, 1989, 1991] and regular triangulations [*Edelsbrunner and Shah*, 1996]. The algorithm is based on elementary topological
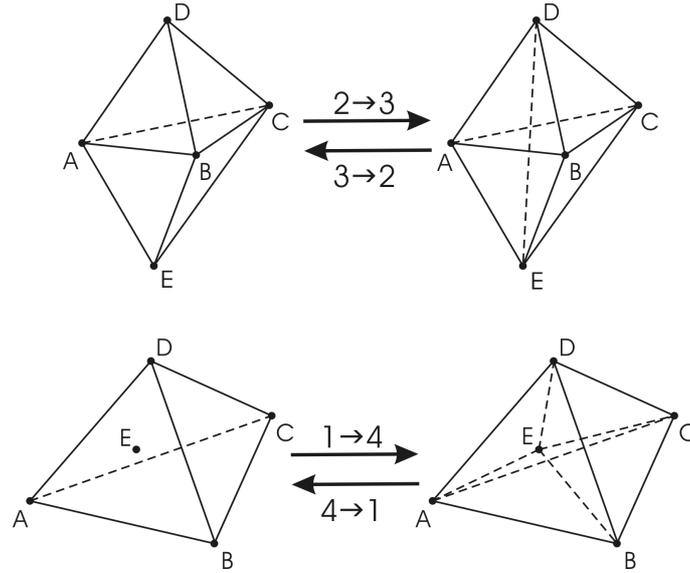
Figure 4.5: The four basic flips in regular triangulations. The Flip $\mathcal{F}_{2\leftarrow 3}$ replaces the two simplices $\langle A, B, C, D\rangle$ and $\langle A, B, C, E\rangle$ by three simplices $\langle A, B, D, E\rangle$, $\langle B, C, D, E\rangle$, and $\langle A, C, D, E\rangle$. Flip $\mathcal{F}_{3\leftarrow 2}$ reverses this operation. Similar the flip $\mathcal{F}_{1\leftarrow 4}$ inserts the vertex E into a simplex $\langle A, B, C, D\rangle$ by forming the four simplices $\langle A, B, C, E\rangle$, $\langle B, C, D, E\rangle$, $\langle A, B, D, E\rangle$, and $\langle A, C, D, E\rangle$. The inverse operation removing a vertex is done by the flip $\mathcal{F}_{4\leftarrow 1}$.

transformations called *flips*. This transformation replace a simplex configuration containing five vertices (in three dimensions) by an alternative simplex configuration. In three dimensions there are two pairs of transformations namely (Fig. 4.5)

- Flip $\mathcal{F}_{2\leftarrow 3}$ and its inverse $\mathcal{F}_{3\leftarrow 2}$. It replaces the common face $\langle A, B, C\rangle$ between two simplices by an edge connecting the opposing vertices of the two simplices. This transformation requires the five vertices A, B, C, D, E to be in a convex configuration, i.e. all vertices are on the border of their convex hull. The flip $\mathcal{F}_{2\leftarrow 3}$ is applied to the simplices $\sigma_{\langle A,B,C,D\rangle}$ and $\sigma_{\langle A,B,C,E\rangle}$ when $S(A, B, C, D, E) < 0$ provided that $O(A, B, C, D) > 0$. If $S(A, B, C, D, E) > 0$ then the reverse operation results in the three simplices $\sigma_{\langle A,B,D,E\rangle}$, $\sigma_{\langle A,C,D,E\rangle}$, and $\sigma_{\langle B,C,D,E\rangle}$.

- Flip $\mathcal{F}_{1\leftarrow 4}$ splits a simplex $\sigma_{\langle A,B,C,D\rangle}$ having a vertex E in its interior into four simplices around the vertex E. If $S(A, B, C, D, E) < 0$ then flip $\mathcal{F}_{1\leftarrow 4}$ results in the four simplices $\sigma_{\langle A,B,C,E\rangle}$, $\sigma_{\langle A,B,D,E\rangle}$, $\sigma_{\langle A,C,D,E\rangle}$, and $\sigma_{\langle B,C,D,E\rangle}$. The reverse transformation flip $\mathcal{F}_{4\leftarrow 1}$ is applied when $S(A, B, C, D, E) > 0$. Note, that in Delaunay triangulations the latter operation never occurs since it would produce a redundant vertex which exists only in true regular triangulations.

The flip operations are performed when the simplices are locally non-regular and in the proper topological configuration (compare (Sec. 4.3.3)). In the case of flip $\mathcal{F}_{3\leftarrow 2}$ that is realized by checking $S(A, B, E, D, C) < 0$ instead of $S(A, B, C, D, E) > 0$. Thus the sign of the orthosphere criterion changes as the argument sequence is changed and every flip is indicated by finding configurations of five vertices with $S(.,.,.,.,.) < 0$.

The whole algorithm works as follows

- Generate a list $\mathcal{S}$ of all simplices.

- For all simplices σ check the local regularity property.

- If the simplex σ is locally non-regular identify the simplex configuration and apply the required flip if possible (note non-flippable configurations (Sec. 4.3.3)). Store the resulting simplices in the list $\mathcal{S}$. Note, the flip operation does not necessarily create regular simplices it generates just *locally* regular simplices.

- Remove the simplex σ from the list $\mathcal{S}$.

- The algorithm terminates when the simplex list $\mathcal{S}$ is empty, that is when the triangulation has become regular.

The algorithm will always terminate as even in the case of non-flippable configurations the participating simplices are removed from $\mathcal{S}$. In most but not all cases such configurations are solved later when adjacent simplices are changed by flips unless special algorithms have to be applied (Sec. 4.3.3).

Using the flip algorithm for constructing the regular triangulation works as follows. At first an artificial simplex σ_{init} is constructed by adding four artificial vertices to the vertex set $\mathcal{V}$. These vertices have to be calculated such that the simplex σ_{init} covers the convex hull of the vertex set $\mathcal{V}$ entirely. The first vertex of $\mathcal{V}$ is inserted by using flip $\mathcal{F}_{1\to4}$. For short let $\mathcal{T}_n = \mathcal{T}(\mathcal{V}_n)$ denote the triangulation after inserting n vertices $V \in \mathcal{V}_n \subset \mathcal{V}$. For adding the remaining vertices V_n one has to determine which simplex contains the vertex before applying flip $\mathcal{F}_{1\to4}$. This can be done by the simplex walk (Fig. 4.6). One starts at some arbitrary simplex $\sigma_1 \in \mathcal{T}_n$. Then for each face $\langle A, B, C \rangle$ the side on which V_n lies is computed. This is similar to the check for the non-overlapping property of simplices: $\text{O}(A, B, C, D) * \text{O}(A, B, C, V) < 0$. If V_n lies on the opposite side then one 'walks' to the simplex adjacent to σ_1 and repeats this step until a simplex is reached where the vertex is located inside, i.e. $\text{O}(A, B, C, D) * \text{O}(A, B, C, V) > 0$ for all faces. If the vertex violates the orthosphere of that simplex the flip $\mathcal{F}_{1\to4}$ is applied (Fig. 4.6). The vertex is redundant otherwise. When all vertices are inserted, the triangulation $\mathcal{T}$ is not necessarily regular as the orthospheres of simplices adjacent to newly inserted simplices might be violated by the inserted vertices V_n. To transform it into a regular triangulation flips are applied. However, in contrast to the two dimensional case this may fail in higher dimensions or with even in two dimensions with non-zero vertex weights by the presence of non-flippable configurations [*Edelsbrunner and Shah*, 1996]. A solution is to sort the elementary topological transformations according to a certain scheme [*Joe*, 1989, 1991]. This has the unfavorable consequence of increasing the computational complexity of the code. Another possibility is to transform each intermediate triangulation $\mathcal{T}_n$ into a regular by applying flips before inserting the next vertex via flip $\mathcal{F}_{1\to4}$ [*Edelsbrunner and Shah*, 1996].

Incremental Insertion   A second method is the Bowyer-Watson method [*Bowyer*, 1981; *Watson*, 1981]. It starts the same way as the flip algorithm and also uses the simplex walk to localize the simplex σ that contains the vertex V (Fig. 4.6). Instead of applying the flip $\mathcal{F}_{1\to4}$ all simplices $\sigma_{\langle A_i, B_i, C_i, D_i \rangle}$ are collected for which $\text{S}(A_i, B_i, C_i, D_i, V) < 0$. This is done by checking the adjacent simplices of the simplex σ first. If V violates their orthospheres they are stored in a list $\mathcal{L}$. Then one checks the orthosphere of every neighbor simplex σ' of simplices $\sigma_{\mathcal{L}} \in \mathcal{L}$. If V violates the orthosphere of σ' it is also stored in $\mathcal{L}$. This continues until all neighbor simplices of the simplices $\mathcal{L}$ are tested and
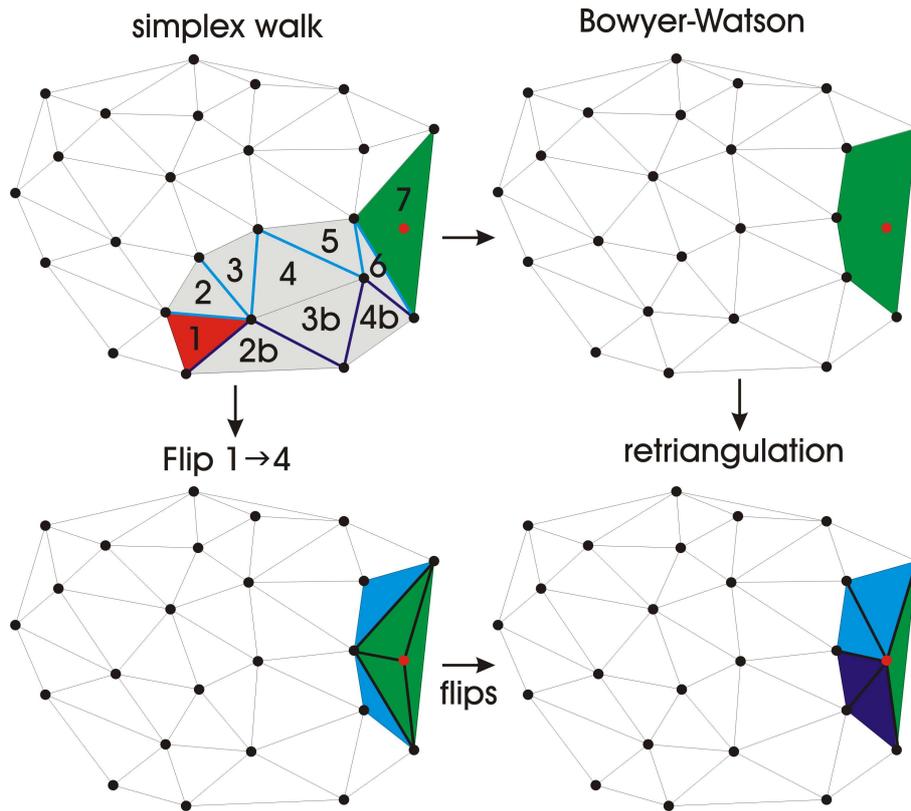
Figure 4.6: The simplex walk and insertion algorithms. In order to locate the simplex in which the vertex lies one can start with some simplex and computes the face of the simplex that is oriented towards the vertex. For the simplex adjacent to this face the orientation step is repeated until the simplex the vertex is located in is found. Note, that more than one face can be oriented towards the vertex, such that there are several ways to find the simplex. In both insertion algorithms the simplex in which the vertex lies. This simplex is converted to four simplices using Flip $\mathcal{F}_{1\to4}$ (which in 2D is a flip from 1 to 3 triangles). Then the other flip operations are applied to make the triangulation regular. The Bowyer-Watson algorithm first collects all simplices whose orthospheres are violated by the vertex to be inserted and replace them by a star-shaped region which is regular.

until only valid simplices with respect to V remain. The union of the simplices forms a polyhedra bounded by triangular faces. The interior of the polyhedra is replaced by a star-shaped triangulation forming simplices out of the triangular face and the vertex V. The resulting triangulation is a regular triangulation. This method is basically a non-elementary transformation of a regular triangulation and replaces the application of flip $\mathcal{F}_{1\to4}$ followed by other elementary topological transformations. Note, in the case that the vertex V is redundant it will not invalidate any simplex, i.e. $\mathcal{L} = \emptyset$ thus no changes are done to the triangulation .

Incremental Construction The third method is fundamentally different from the two described above. It does not compute a sequence of triangulations adding each vertex incrementally. Instead the full set $\mathcal{V}$ of vertices is used and any simplex constructed is already part of the final regular triangulation. There is more than one possibility to compute the triangulation in this way which basically differ in the details of the underlying computations to be done. Here, only the method that is used in this work is presented. The term *incremental construction* will serve as synonym for

Figure 4.7: Incremental construction. The basic step of the incremental construction is that the faces stored in the AFL (shown in blue) are expanded into simplices of the final triangulation by minimizing the signed Delaunay distance (SD). The new faces created by the simplex are stored in the AFL while faces present in the AFL are removed from it. The search for the vertex can be limited to one half space as indicated by the dashed line. The algorithms can be improved using a grid (bright blue lines) in order to keep the vertex search local.
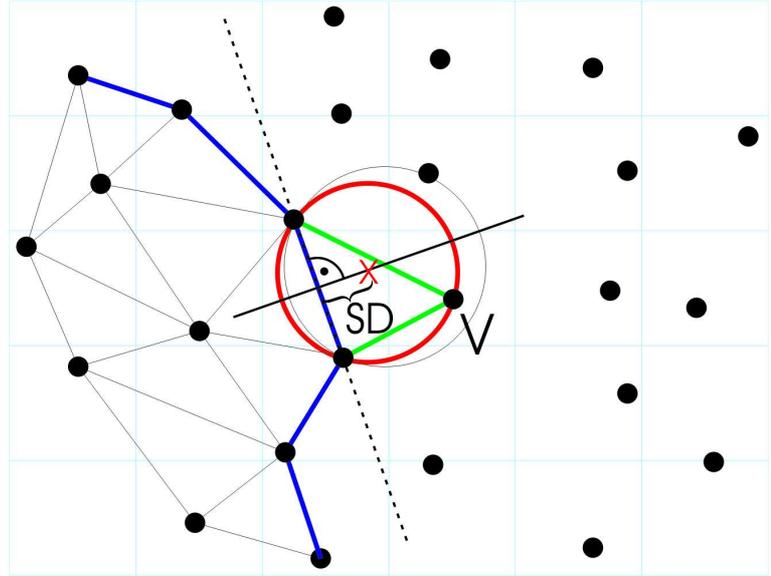
the algorithm described in the following. First, the case of a Delaunay triangulation will be given. The newly derived extension to regular triangulations [*Beyer et al.*, 2005] is described in the next paragraph.

Given a set $\mathcal{V}$ of vertices the algorithm starts to compute an initial simplex. For clarity the computation of the initial simplex will be given later. The faces of the initial simplex are stored in a list called *active face list* (AFL). Additionally, an orientation is assigned to each of the faces that is defined as *outwards*. The orientation defines in which half space the opposing vertex of the generating simplex is located which is defined as *inwards*. For each face $\langle A, B, C \rangle$ a fourth vertex V from the outward half space is calculated such that the four vertices form a regular simplex of the final triangulation (Fig. 4.7). The criterion for the vertex V to be checked is that it minimizes the *signed Delaunay distance* with respect to the face $\langle A, B, C \rangle$ [*Cignoni et al.*, 1993; *Teng et al.*, 1993].

Definition 11 *The* signed Delaunay distance S*D of a vertex D with respect to a face $\langle A, B, C \rangle$ is given by*

$$\mathrm{SD}\,(\mathbf{d}) \stackrel{\text{def}}{=} (\mathbf{m}\,(\mathbf{d}) - \mathbf{m}_{\langle A,B,C \rangle}) \cdot \frac{(\mathbf{a} - \mathbf{b}) \times (\mathbf{a} - \mathbf{c})}{\|(\mathbf{a} - \mathbf{b}) \times (\mathbf{a} - \mathbf{c})\|} \tag{4.27}$$

with $\mathbf{m}_{\langle A,B,C \rangle}$ being the center of the orthosphere of the face and $\mathbf{m}\,(D)$ the center of the orthosphere of the four vertices A, B, C, D.

The orthosphere of a face is defined such that the center is located in the same plane as the face. This is also the orthosphere with the minimal weight. The definition solves the ambiguity of the three equations

$$\rho(A, M_{\langle A,B,C \rangle}) = 0 \tag{4.28}$$
$$\rho(B, M_{\langle A,B,C \rangle}) = 0 \tag{4.29}$$
$$\rho(C, M_{\langle A,B,C \rangle}) = 0 \tag{4.30}$$

for the four variables of $M_{\langle A,B,C \rangle}$ (which are three for the coordinates $\mathbf{m}_{\langle A,B,C \rangle}$ and one for the weight $w_{m_{\langle A,B,C \rangle}}$).

When a new simplex is found by minimizing the signed Delaunay distance (Eq. 4.27) all faces are stored in the AFL if they are not yet stored in the AFL. If a face is already present in the AFL then it will be removed as it indicates that two simplices are constructed out of the same face. This in turn means that two adjacent simplices sharing the common face are already constructed and the face is no longer needed to construct any further simplex. There is a special case for outer simplices. They have one or more faces which cannot be expanded into regular simplices, i.e there are no vertices in the outward half space to form a simplex. In that case the face is also removed from the AFL. The triangulation has been constructed completely when the AFL is empty.

In order to find the initial simplex for Delaunay triangulations one has to perform the following steps:

1. Given a vertex V_1 find a second vertex V_2 with minimal distance $\|\mathbf{v}_1 - \mathbf{v}_2\|$ to V_1.

2. Starting from the edge $\langle V_1, V_2 \rangle$ the vertex V_3 minimizing the Delaunay distance $\text{SD}(\mathbf{V}_3)$ (with $\mathbf{m}_{\langle A,B,C \rangle}$ in equation (Eq. 4.27) replaced by the 1-dimensional orthosphere $\mathbf{m}_{\langle V_1,V_2 \rangle} = \mathbf{v}_1 + \frac{1}{2}\left(1 + \frac{w_{V_1} - w_{V_2}}{\|\mathbf{v}_2 - \mathbf{v}_1\|}\right)(\mathbf{v}_2 - \mathbf{v}_1))$ has to be found resulting in the initial face $\langle V_1, V_2, V_3 \rangle$.

3. The start simplex $\sigma_{\langle V_1,V_2,V_3 \rangle}$ can be found be minimizing the Delaunay distance (Eq. 4.27) for the vertex V_4 without restricting the search for vertices to one half space like in the iterated step of the algorithm above.

The algorithm in its naive form has a high complexity as both the minimization procedure and the comparison of faces in the AFL are operations of linear complexity, i.e. checking all vertices and all faces for every simplex to be created. The comparison of faces can be made a constant time operation by using hash maps. The vertex search can be speeded up by using bucketing techniques like uniform grids [*Asano et al.*, 1985] to quickly localize a vertex in question. In more detail one has to do the following steps:

- Create a uniform grid and assign vertices to boxes of the grid containing the vertex.

- Compute the orthosphere $\mathbf{m}_{\langle A,B,C \rangle}$ of the face $\langle A, B, C \rangle$.

- Calculate all boxes that intersect with the orthosphere and collect all their vertices in a list $\mathcal{L}$.

- If $\mathcal{L} = \emptyset$ increase the search radius taking more boxes into account until $\mathcal{L} \neq \emptyset$.

- Minimize the signed Delaunay distance of these vertices.

- Compute the orthosphere $\mathbf{m}(\mathbf{D})$ of the vertex minimizing the signed Delaunay distance.

- Calculate all boxes intersection with the orthosphere around $\mathbf{m}(\mathbf{D})$ and collect all vertices $V \notin \mathcal{L}$ in a new list $\mathcal{L}^{(1)}$.

- Repeat the minimization procedure if necessary, i.e. until $\mathcal{L}^{(1)} = \emptyset$

For the kinetic routine (Sec. 4.3.3) it is necessary to have artificial vertices that where introduced with the flip algorithm mentioned above. It is not useful to treat those vertices with the uniform grid because of their special position far away from the vertex set. Instead they are included in the minimization of the signed Delaunay distance when the search for vertices exceeds the grid by a certain amount or no candidates for the expansion of a face were found on the grid ($\mathcal{L} = \emptyset$).

Incremental Construction - Extension to regular triangulations   For the generalization of the method to the case of regular triangulations the efficient calculation of the signed Delaunay distance generalized to regular triangulations is presented. It is mostly following previous work [*Teng et al.*, 1993].

The signed Delaunay distance $SD(D)$ of a vertex $D = (\mathbf{d}, w_d)$ with respect to the face $\langle A, B, C \rangle$ is defined similar to the Delaunay case (Eq. 4.27) as:

$$SD(D) \overset{\text{def}}{=} [\mathbf{m}(D) - \mathbf{m}_{\langle A,B,C \rangle}] \cdot \frac{(\mathbf{a} - \mathbf{b}) \times (\mathbf{a} - \mathbf{c})}{\|(\mathbf{a} - \mathbf{b}) \times (\mathbf{a} - \mathbf{c})\|} \, . \tag{4.31}$$

Note, that the argument is now a vertex instead of a point. The Delaunay case is still covered when all vertex weights are equal. To get a useful expression for evaluating $SD(D)$ rewrite the orthosphere equation $S(A, B, C, D, \mathbf{m}(D)) = 0$ (Eq. 4.2) in matrix form to get $\mathbf{m}(D)$ following [*Teng et al.*, 1993]:

$$\begin{bmatrix} 1 & a_x & a_y & a_z \\ 1 & b_x & b_y & b_z \\ 1 & c_x & c_y & c_z \\ 1 & d_x & d_y & d_z \end{bmatrix} \begin{bmatrix} \|\mathbf{m}(D)\|^2 - w_m \\ -2m_x(D) \\ -2m_y(D) \\ -2m_z(D) \end{bmatrix} = - \begin{bmatrix} \|\mathbf{a}\|^2 - w_a \\ \|\mathbf{b}\|^2 - w_b \\ \|\mathbf{c}\|^2 - w_c \\ \|\mathbf{d}\|^2 - w_d \end{bmatrix} \tag{4.32}$$

Subtracting the first row from the others rows gives

$$\begin{bmatrix} b_x - a_x & b_y - a_y & b_z - a_z \\ c_x - a_x & c_y - a_y & c_z - a_z \\ d_x - a_x & d_y - a_y & d_z - a_z \end{bmatrix} \begin{bmatrix} -2m_x(D) \\ -2m_y(D) \\ -2m_z(D) \end{bmatrix} = - \begin{bmatrix} \|\mathbf{b}\|^2 - \|\mathbf{a}\|^2 - w_b + w_a \\ \|\mathbf{c}\|^2 - \|\mathbf{a}\|^2 - w_c + w_a \\ \|\mathbf{d}\|^2 - \|\mathbf{a}\|^2 - w_d + w_a \end{bmatrix} \, . \tag{4.33}$$

Now write the equations in the form $M^T [-2\mathbf{m}(D)] = -\boldsymbol{\alpha}$ with

$$M = \begin{bmatrix} b_x - a_x & c_x - a_x & d_x - a_x \\ b_y - a_y & c_y - a_y & d_y - a_y \\ b_z - a_z & c_z - a_z & d_z - a_z \end{bmatrix} \quad \text{and} \quad \boldsymbol{\alpha} = \begin{bmatrix} \|\mathbf{b}\|^2 - \|\mathbf{a}\|^2 - w_b + w_a \\ \|\mathbf{c}\|^2 - \|\mathbf{a}\|^2 - w_c + w_a \\ \|\mathbf{d}\|^2 - \|\mathbf{a}\|^2 - w_d + w_a \end{bmatrix} \, .$$

By finding a *QR*-decomposition [*Steward*, 1973] of the matrix M into an upper triangular matrix R and an orthogonal matrix $Q = [\mathbf{q}_1, \mathbf{q}_2, \mathbf{q}_3]$ with the orthonormal column vectors $\mathbf{q}_i$ one yields:

$$M = \begin{bmatrix} b_x - a_x & c_x - a_x & d_x - a_x \\ b_y - a_y & c_y - a_y & d_y - a_y \\ b_z - a_z & c_z - a_z & d_z - a_z \end{bmatrix} = QR = \begin{bmatrix} q_{11} & q_{12} & q_{31} \\ q_{12} & q_{22} & q_{32} \\ q_{13} & q_{23} & q_{33} \end{bmatrix} \begin{bmatrix} r_{11} & r_{12} & r_{13} \\ 0 & r_{22} & r_{23} \\ 0 & 0 & r_{33} \end{bmatrix} \, . \tag{4.34}$$

The left hand side of the equation can be written as

$$M^T [-2\mathbf{m}(D)] = R^T \left[-2Q^T \mathbf{m}(D) \right] = R^T \boldsymbol{\mu} \tag{4.35}$$

with $\boldsymbol{\mu} = -2Q^T \mathbf{m}(D)$. The vectors $\mathbf{q}_1$ and $\mathbf{q}_2$ can be chosen in the affine plane containing the face $\langle A, B, C \rangle$. Consequently, only $\mathbf{q}_3$ depends on the vertex D.

When comparing M with (Eq. 4.1) one can see that $\det(M) = -O(A, B, C, D)$, hence $O(A, B, C, D) = -r_{11} r_{22} r_{33}$ when the QR decomposition is used. Therefore the sign of the determinant of the matrix R will give the orientation of the simplex formed by the face $\langle A, B, C \rangle$ and the vertex D.

Now one can rewrite the expression for the center of the orthosphere $\mathbf{m}(D)$ using eq. 4.35 with only μ_z depending on the vertex D:

$$\mathbf{m}(D) = -\frac{1}{2}\left(\mu_x\mathbf{q}_1 + \mu_y\mathbf{q}_2 + \mu_z\mathbf{q}_3\right) . \tag{4.36}$$

The center of the orthosphere of the face $\langle A, B, C\rangle$ is then given by

$$\mathbf{m}_{\langle A,B,C\rangle} = -\frac{1}{2}\left(\mu_x\mathbf{q}_1 + \mu_y\mathbf{q}_2\right) + (\mathbf{q}_3 \cdot \mathbf{a})\,\mathbf{q}_3 . \tag{4.37}$$

Taking into account that:

$$\frac{(\mathbf{a} - \mathbf{b}) \times (\mathbf{a} - \mathbf{c})}{\|(\mathbf{a} - \mathbf{b}) \times (\mathbf{a} - \mathbf{c})\|} = \operatorname{sign}(r_{11}r_{22}r_{33})\,\mathbf{q}_3 , \tag{4.38}$$

this yields another form of the signed Delaunay distance

$$\mathrm{SD}(D) = -\operatorname{sign}(r_{11}r_{22}r_{33})\left(\frac{\mu_z}{2} + \mathbf{q}_3 \cdot \mathbf{a}\right) . \tag{4.39}$$

To find a vertex D, which expands the face $\langle A, B, C\rangle$, the *QR* decomposition for this face is performed only once giving the three vectors $\mathbf{q}_1, \mathbf{q}_2, \mathbf{q}_3$ and the components r_{11}, r_{12}, r_{22}. Now the signed Delaunay distance is evaluated by computing r_{33} to get the orientation primitive and μ_z for the orthosphere primitive.

The extension of the incremental construction to regular triangulations uses the minimization of (Eq. 4.39) for each face in the AFL. There are two other modifications needed. First, redundant vertices have to be detected. Basically all vertices that are not used to construct the regular triangulation, i.e. the AFL gets empty but vertices are not part of simplices, are redundant vertices. This will slightly change when performing the algorithm in parallel (Sec. 4.4.2).

The second change is the construction of the initial simplex which suffers from the existence of redundant vertices. For example if one starts the procedure given in the former paragraph with a vertex that turns out to be redundant in the final triangulation the construction algorithm will not only produce the wrong result but is most likely prohibited from terminating because overlapping simplices can be generated which result in an infinite sequence of new faces in the AFL. The solution of the problem makes use of the lifting map (Sec. 4.1). The regular triangulation relates to the convex hull [*Brown*, 1979] by the lifted map $V \in \mathcal{V} \subset \mathbb{R}^3 \times \mathbb{R} \mapsto V^+ = \left(\mathbf{v}, \|\mathbf{v}\|^2 - w_v\right) = \left(v_x, v_y, v_z, \|\mathbf{v}\|^2 - w_v\right) \in \mathbb{R}^4$. This translates the incremental construction into a gift-wrapping algorithm for convex hulls. In the case of equal weights all vertices lie on a paraboloid in $\mathbb{R}^4$. With different weights w_v lifted vertices V^+ are shifted below or above (in the case of negative weights) the paraboloid.

The starting simplex is then found as follows (fig. 4.18, right panel) (Fig. 4.8):

- The tangential hyper plane $T_V M$ of the paraboloid in $\mathbb{R}^4$ generated by the lifting map is calculated for an arbitrary vertex V. The tangential plane through the point $V^+ = \left(\mathbf{v}, \|\mathbf{v}\|^2 - w_v\right) \in \mathbb{R}^4$ is given by its normal T

$$T = \frac{1}{\sqrt{4\|\mathbf{v}\|^2 + 1}}\,(2\mathbf{v}, -1) . \tag{4.40}$$

Figure 4.8: The two-dimensional lifted map of a one-dimensional regular triangulation demonstrating how to find a starting vertex for the incremental construction. The paraboloid of a standard Delaunay triangulation is shown as reference. The vertices are shifted downwards (assuming positive weights). Starting the algorithm with the (lifted) vertex V^+ one finds the tangential plane $T_V M$ (dashed line) with normal vector T. The tangential plane $T_V M$ is shifted along T until no vertex is on its positive side (defined by T) thus finding the vertex U^+ as start vertex and the shifted plane $T_V M^\star$ (full line). To get the initial simplex (edge in the example) one searches for the vertex W^+ which minimizes the angle α between the shifted plane $T_V M^\star$ and the line connecting the start vertex U^+ with itself resulting in the plane $T_V M'$ (dashed dotted line). Open circles denote redundant vertices of the triangulation.
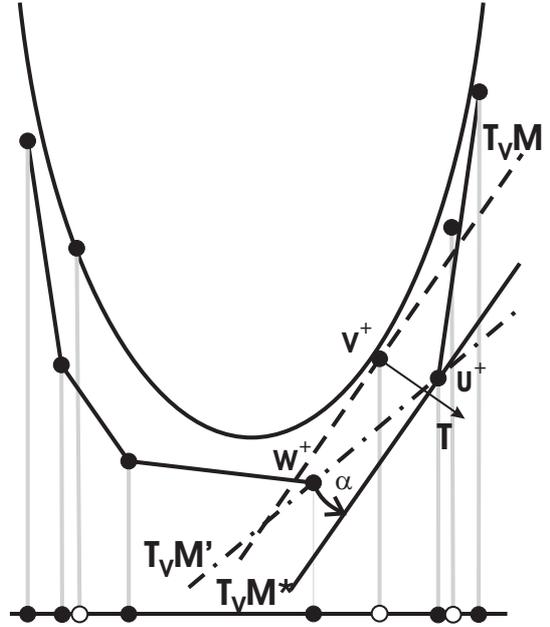
If no lifted vertex D^+ lies on the positive side of the tangential hyper plane $T_V M$, i.e. if

$$T \cdot (D^+ - V^+) = \mathbf{t} \cdot (\mathbf{d} - \mathbf{v}) - \left(\|\mathbf{d}\|^2 - \|\mathbf{v}\|^2 - w_d + w_v \right) < 0 \quad \forall \quad D^+ \in \mathcal{V}^+ , \tag{4.41}$$

then the vertex is not redundant. Note, that $T \cdot (D^+ - V^+) > 0$ does not necessarily mean that the vertex is redundant. In the case of redundancy the tangential hyper plane $T_V M$ is parallel shifted into the point D^+ and the search is repeated until a proper vertex U^+ and the shifted hyperplane $T_V M^*$ is found (Fig. 4.8).

- From U^+ the initial edge is computed by searching for the vertex W^+ which minimizes the angle α:

$$\cos \alpha = \frac{T \cdot (W^+ - U^+)}{\|W^+ - U^+\|_4} \tag{4.42}$$

  (with $\|.\|_4$ being the Euclidian norm in $\mathbb{R}^4$). In $\mathbb{R}^3$ the initial edge is then given by $\langle U, W \rangle$.

- To find the first face of the initial simplex one 'tilts' the tangential hyper plane $T_V M$ into a hyper plane $T_V' M$ containing the edge so that the normal T' becomes

$$T' = \frac{N}{\|N\|_4} \quad \text{with} \quad N = T - (W^+ - U^+) \frac{T \cdot (W^+ - U^+)}{\|W^+ - U^+\|_4} . \tag{4.43}$$

  Then the first face is constructed with the vertex Y^+ that minimizes the angle β between the hyper plane $T_V' M$ and the orthogonal projection P of the vector $Y^+ - U^+$ with respect to the edge formed by U^+ and W^+:

$$\cos \beta = \frac{T' \cdot P}{\|P\|_4} \quad \text{with} \quad P = Y^+ - U^+ - (W^+ - U^+) \frac{(Y^+ - U^+) \cdot (W^+ - U^+)}{\|W^+ - U^+\|_4^2} . \tag{4.44}$$

- To complete the initial simplex $\sigma_{\langle U,W,Y,X \rangle}$ the signed Delaunay distance to the constructed face $\langle U, W, Y \rangle$ is minimized.

There is also a minor modification to the bucketing technique necessary. The vertices cannot be just assigned to a uniform grid by using their position. The weight has to be taken into account. This can be done simply by assigning the vertex $V = (\mathbf{v}, w_v)$ to all boxes that are covered by a sphere with radius $\sqrt{w_v}$ representing the vertex weight w_n. In order to collect the vertices uniquely in a set $\mathcal{L}$ to find the vertex minimizing the signed Delaunay distance (Eq. 4.39) one should use a hash map to see if a vertex assigned to a boxes is already present in $\mathcal{L}$. Note, that when the weights get so large that the corresponding spheres contain a large portion of the vertex set $\mathcal{V}$ then $\mathcal{L}$ will be as large $\mathcal{V}$ and the advantage of the bucketing technique gets lost. However, this is not the case for the tissue simulation where spheres have radii of the order of their average distance.

4.2.1 Robustness of topological properties

It is an important problem in computational geometry that topological informations rely on computations with real numbers. For example the orientation primitive $O(A, B, C, D)$ uses a determinant to determine if the vertex D lies above or below the plane formed by the vertices A, B, and C. However, computers can calculate real number values only with limited precision causing uncertainties if $O(A, B, C, D) > 0$ or not. Methods to deal with that problem are required. One possible solution is to use integers instead of real numbers which is similar to introducing a very fine grid to the problem. The disadvantage is the limitation of flexibility. The application will naturally use real numbers describing the position of its entities which would have to be approximated by integers within the triangulation. Therefore, another solution has been chosen presented in the next three subsections.

In principle a third approach might have been chosen to overcome this problem. The major problem of the numerical inaccuracy is the loss of associativity, that is the result of (Eq. 4.1) and (Eq. 4.2) depends on the sequence of arguments given. Most of the algorithms presented hereafter do not need to have those functions evaluated 'exactly' in the sense that the result does not suffer from roundoff errors. As long as the result is the same on every instance the 'correctness' is not the problem and the triangulation computed might not be the correct one but one that is correct within a certain precision of numerical computation. To overcome the problem with the lost associativity one may modify the implementation to calculate (Eq. 4.1) and (Eq. 4.2) such that the sequence of vertices is alway the same respecting the change of the signs according to the argument permutation. Using the metapointer introduced in (Sec. 4.4.1) one can establish a sorting relation for vertices that could guarantee a well-defined argument sequence for any subset of vertices. This approach has not been chosen as some of the algorithms cannot be broken down to such a modification causing a certain incompatibility of the results of the different subroutines. An example is the interplay of kinetic and deletion routine (discussed below). The deletion routine uses a different type of function to compute (Eq. 4.2) (see (Eq. 4.27)) which is required for the algorithm and may cause contradictory results between the triangulations computed by the two algorithms.

4.2.2 Exact predicates

For normal (unweighted) Delaunay triangulations there exists a solution to robustly compute the sign of (Eq. 4.1) and (Eq. 4.2) [*Shewchuk*, 1997]. The source code is also available. For the use with regular triangulations, modifications had to be included to deal with the vertex weights. To explain the modifications the basic principles underlying the exact primitives [*Shewchuk*, 1997] are briefly discussed. The extensions made within this work are presented thereafter.

Arbitrary precision floating-point arithmetic   The general format of floating point numbers of computers (IEEE 754 double precision) is

$$r = (-1)^s \left(b_1 2^{-1} + b_2 2^{-2} + \cdots + m_{52} 2^{-52} \right) 2^{\alpha - 127} \quad \alpha = 0, 1, \ldots 255; \quad s = 0, 1. \tag{4.45}$$

To represent numbers x which cannot be exactly represented in the double precision format r one can use an expansion

$$x = x_n + \cdots + x_2 + x_1 \tag{4.46}$$

where each x_i is a *component* of x. These components are each represented by floating point numbers r. Additionally, they are sorted by magnitude (x_n being the largest and x_1 the smallest) and are non-overlapping. Two floating-point values x_i and x_k ($i \neq k$) are non-overlapping if the least significant nonzero bit of x_i is more significant than the most significant bit of x_k or vice versa.

In order to determine the accuracy of a result one needs to specify the roundoff errors. It is assumed that addition, subtraction, and multiplication use exact rounding that is, that results that can be stored in double precision format are exact otherwise they are rounded to the nearest floating-point value. Exact rounding operations shall be denoted by $\oplus, \ominus$, and $\otimes$ for addition, subtraction, and multiplication respectively.

To analyze roundoff errors the ulp = 'unit in the last place' is used. It is the smallest increment of a number that can be recorded internally by the machine. Therefore it depends on the value actually analyzed. In general $\epsilon = \frac{1}{2} \text{ulp}(1)$ is called the *machine epsilon* which is $\epsilon = 2^{-53}$ for the double precision format. Another variable is $\text{err}(x \odot y)$ which gives the error of a floating-point operation $\odot$ that approximates the real operation $\bullet$ (addition, subtraction, multiplication, division). Such for any basic operation it results

$$x \odot y = x \bullet y + \text{err}(x \odot y). \tag{4.47}$$

In the case of exact rounding it is guaranteed that

$$|\text{err}(x \odot y)| \le \frac{1}{2} \text{ulp}(x \odot y). \tag{4.48}$$

Note that ϵ bounds the relative error of any basic operation $\epsilon \ge |\text{err}(x \odot y) / (x \odot y)|$.

In the work of Shewchuk [*Shewchuk*, 1997] it is shown how to calculate the expansion of the result of addition, subtraction, and multiplication of two floating-point values. This has been generalized

to the three operations on expansions of floating-point values representing real numbers. In order to understand the modifications to the code necessary to calculate the orientation and orthosphere predicates, just the two required functions provided by the original code are described briefly. The underlying algorithms can be found in [*Shewchuk*, 1997].

- SCALE-EXPANSION: Multiply an expansion (Eq. 4.46) with a floating point value and calculate a new expansion such that the components are non-overlapping.

- FAST-EXPANSION-SUM: Sum up two expansion creating a new expansion with non-overlapping components.

All those functions come with a version that additionally eliminates zero components and stores the significant bits with a smaller number of components saving computer memory to store the expansions.

Error propagation and adaptivity   The hand-tuned code by Shewchuk uses four precision levels to calculate the determinants of the orientation and orthosphere primitive. The higher precision steps will be computed if the error is above a certain threshold. The first level is the normal floating point calculation without using expansions. The second level is using the first component of an expansion of the calculation of the minors of degree 3 and perform the remaining steps of the calculation of the determinant with inexact floating point operations. The error is still $O(\epsilon)$ like in the first level but is in most cases still of higher precision (discussed in detail in [*Shewchuk*, 1997]) and the computation is faster when testing for this step than incurring higher precision methods with error $O(\epsilon^2)$. Using the full expansion of the minors of degree 3 to compute the determinant followed by inexact calculations the error in level three is $O(\epsilon^2)$. The fourth and last precision level uses the full expansion of the determinant to compute its sign evaluating the determinant in the slightly different form.

$$
S(A, B, C, D, V) \stackrel{\text{def}}{=}
\begin{vmatrix}
a_x & a_y & a_z & \|\mathbf{a}\|^2 & 1 \\
b_x & b_y & b_z & \|\mathbf{b}\|^2 & 1 \\
c_x & c_y & c_z & \|\mathbf{c}\|^2 & 1 \\
d_x & d_y & d_z & \|\mathbf{d}\|^2 & 1 \\
v_x & d_y & v_z & \|\mathbf{v}\|^2 & 1
\end{vmatrix}.
\tag{4.49}
$$

Upon modifying the original code to deal with orthospheres, i.e. use vertices with weight, the generalization of the calculations required to recalculate the error bounds as well. For each of the levels the error is

$$\text{level 1:} \quad (16\epsilon + 224\epsilon^2) \otimes |A_{\text{det}}| \tag{4.50}$$

$$\text{level 2:} \quad (5\epsilon + 72\epsilon^2) \otimes |A_{\text{det}}| \tag{4.51}$$

$$\text{level 3:} \quad (3\epsilon + 8\epsilon^2) \otimes |B_{\text{det}}| \oplus (71\epsilon^2 + 1408\epsilon^3) \otimes |A_{\text{det}}| \tag{4.52}$$

with

$$
\begin{aligned}
A_{\text{det}} \quad & \{[|cd| \oplus |dc|] \otimes |b_z \ominus v_z| \oplus [|db| \oplus |bd|] \otimes |c_z \ominus v_z| \oplus [|bc| \oplus |cb|] \otimes |d_z \ominus v_z|\} \\
& \otimes \{(a_x \ominus v_x)^2 \oplus (a_y \ominus v_y)^2 \oplus (a_z \ominus v_z)^2\} \\
\oplus \quad & \{[|da| \oplus |ad|] \otimes |b_z \ominus v_z| \oplus [|cd| \oplus |dc|] \otimes |c_z \ominus v_z| \oplus [|ac| \oplus |ca|] \otimes |d_z \ominus v_z|\} \\
& \otimes \{(b_x \ominus v_x)^2 \oplus (b_y \ominus v_y)^2 \oplus (b_z \ominus v_z)^2\} \\
\oplus \quad & \{[|ab| \oplus |ba|] \otimes |b_z \ominus v_z| \oplus [|bd| \oplus |db|] \otimes |c_z \ominus v_z| \oplus [|da| \oplus |ad|] \otimes |d_z \ominus v_z|\} \\
& \otimes \{(c_x \ominus v_x)^2 \oplus (c_y \ominus v_y)^2 \oplus (c_z \ominus v_z)^2\} \\
\oplus \quad & \{[|bc| \oplus |cb|] \otimes |b_z \ominus v_z| \oplus [|ca| \oplus |ac|] \otimes |c_z \ominus v_z| \oplus [|ab| \oplus |ba|] \otimes |d_z \ominus v_z|\} \\
& \otimes \{(d_x \ominus v_x)^2 \oplus (d_y \ominus v_y)^2 \oplus (d_z \ominus v_z)^2\}
\end{aligned}
$$

using the convention $|ab| = |(a_x \ominus v_x) \otimes (b_y \ominus v_y)|$ and B_{det} being the absolute value of the result of the computation of the determinant of the second level.

For the estimate of the error bound the first few steps of the underlying calculation shall be given here. Consider the error incurred by $x = a \oplus b$ which is not larger than $\epsilon |x|$ also it is smaller than $|a + b|$. Assume $t = a + b$ represents the true value then one yields $t = x \pm \epsilon |x|$ and $t = x \pm \epsilon |t|$. Both of the error bounds are useful. When calculating the error bounds one has to take care that also the calculation of the error is done using the exact rounding operations $\oplus, \ominus, \otimes$. Any operation that is not performed using these symbols incurs an error when executed on a real world processor.

Now define

$$
\begin{aligned}
x_{11} &= a_x \ominus v_x & (4.53) \\
x_{12} &= a_y \ominus v_y & (4.54) \\
x_{13} &= a_z \ominus v_z & (4.55) \\
x_{21} &= b_x \ominus v_x & (4.56) \\
\dots & & (4.57) \\
x_{43} &= d_z \ominus v_z. & (4.58)
\end{aligned}
$$

In order to compute the determinant one develops (Eq. 4.2) after the last column. The error propagation for the first steps then read:

$$
\begin{aligned}
t_{ij} &= x_{ij} \pm \epsilon |x_{ij}| \quad \text{with } i, j = 1, 2, 3, 4 & (4.59) \\
t_{i1,k2} &= t_{i1} t_{k2} & (4.60) \\
&= (x_{i1} \pm \epsilon |x_{i1}|)(x_{k2} \pm \epsilon |x_{k2}|) & (4.61) \\
&= x_{i1} x_{k2} \pm 2\epsilon |x_{i1}| |x_{k2}| \pm \epsilon^2 |x_{i1}| |x_{k2}| & (4.62) \\
&= \underbrace{x_{i1} \otimes x_{k2}}_{x_{i,k2}} \pm \epsilon |x_{i1}| \otimes |x_{k2}| \pm (2\epsilon + \epsilon^2)(1 + \epsilon) |x_{i1}| \otimes |x_{k2}| & (4.63) \\
&= x_{i1,k2} \pm (3\epsilon + 3\epsilon^2 + \epsilon^3)) |x_{i1}| \otimes |x_{k2}| & (4.64)
\end{aligned}
$$

These are the subtractions of entries of the determinant and their products which give the 2×2 minor determinants of the first two columns in (Eq. 4.2). The second last transformation respects that the

product $x_{i1}x_{k2}$ is exact while the processors performs $x_{i1} \otimes x_{k2}$ resulting in an error $\epsilon|x_{i1}| \otimes |x_{k2}|$. Similar for the error $(2\epsilon + \epsilon^2)|x_{i1}||x_{k2}|$ resulting in an additional factor $(1 + \epsilon)$ when replacing $|x_{i1}||x_{k2}|$ by $|x_{i1}| \otimes |x_{k2}|$. The subtraction of the 2×2-minors reads:

$$
\begin{aligned}
t_{[i1,k2]} &= t_{i1,k2} - t_{k1,i2} & (4.65) \\
&= x_{i1,k2} - x_{k1,i2} \pm (3\epsilon + 3\epsilon^2 + \epsilon^3)(|x_{i1}| \otimes |x_{k2}| + |x_{k1}| \otimes |x_{i2}|) & (4.66) \\
&= \underbrace{x_{i1,k2} \ominus x_{k1,i2}}_{x_{[i1,k2]}} \pm \epsilon|x_{i1,k2} \ominus x_{k1,i2}| \pm (3\epsilon + 3\epsilon^2 + \epsilon^3)(1 + \epsilon)(|x_{i1}| \otimes |x_{k2}| \oplus |x_{k1}| \otimes |x_{i2}|) & (4.67)
\end{aligned}
$$

With

$$
|x_{i1,k2} \ominus x_{k1,i2}| \leq |x_{i1,k2} \oplus x_{k1,i2}| \leq |x_{i1}| \otimes |x_{k2}| \oplus |x_{k1}| \otimes |x_{i2}| \tag{4.68}
$$

this simplifies further to

$$
t_{[i1,k2]} = x_{[i1,k2]} \pm (4\epsilon + 6\epsilon^2 + 4\epsilon^3 + \epsilon^4)(|x_{i1}| \otimes |x_{k2}| \oplus |x_{k1}| \otimes |x_{i2}|). \tag{4.69}
$$

The following steps until the error of the full determinant are calculated following the same principles. For the final error estimate one has to take into account that the ϵ-dependent prefactor is usually not representable in double precision thus that the result has to be rounded up properly. Continuing this procedure for the full determinant including the vertex weights gives the error bounds for the three different adaptive levels:

$$
\begin{aligned}
\text{level 1:} \quad & (16\epsilon + 256\epsilon^2) \otimes |A_{\text{det}}| & (4.70) \\
\text{level 2:} \quad & (5\epsilon + 88\epsilon^2) \otimes |A_{\text{det}}| & (4.71) \\
\text{level 3:} \quad & (3\epsilon + 8\epsilon^2) \otimes |B_{\text{det}}| \oplus (71\epsilon^2 + 1664\epsilon^3) \otimes |A_{\text{det}}| & (4.72)
\end{aligned}
$$

Note, that there is some ambiguity to calculate the error bounds by using the two different estimates $t = x \pm \epsilon|x|$ and $t = x \pm \epsilon|t|$ as well as upper bound estimates for intermediate results. Thus, tighter bounds might be calculated using different error estimates in different steps. However, tighter bounds may required more complex computations such that the code performs slower even it avoids higher precision levels more often.

The additional lines of code imposed by the inclusion of vertex weights are SCALE-EXPANSION of the four 3×3 minors multiplied with the vertex weight during the level 2 and 3 adaptive steps and the five 4×4-minors for the exact step. Finally, an additional FAST-EXPANSION-SUM for adding these products is required. Both operations are the source for the enlarged error bound given above.

4.2.3 Interval arithmetics

The interval arithmetics is used to compute the numerical errors of real number computations. It allows to determine if a computation gives reliable results or not, i.e. the result of a calculation with intervals guarantees that the exact result is contained in the interval. It is mainly used in the construction algorithm (Sec. 4.3.1) and the vertex movement algorithm (Sec. 4.3.3). It avoids the need to write hand-tuned code as it has been done for (Eq. 4.1) and (Eq. 4.2). Thus, it is more flexible in its usage.

An interval is defined by

$$[a, b] = \{x \in \mathbb{R} \,|\, a \leq x \leq b\}. \tag{4.73}$$

To use it for reliable computations a and b have to be representable by double precision floating-point values. Then for any operation $\bullet$ between two intervals

$$
\begin{aligned}
[x_1, x_2] \bullet [y_1, y_2] &= \{x \bullet y \,|\, \forall x \in [x_1, x_2],\ y \in [y_1, y_2]\} \\
&= [\min(x_1 \bullet y_1, x_1 \bullet y_2, x_2 \bullet y_1, x_2 \bullet y_2), \max(x_1 \bullet y_1, x_1 \bullet y_2, x_2 \bullet y_1, x_2 \bullet y_2)]
\end{aligned}
$$

which yields to

$$[x_1, x_2] + [y_1, y_2] = [x_1 + y_1, x_2 + y_2] \tag{4.74}$$

$$[x_1, x_2] - [y_1, y_2] = [x_1 - y_2, x_2 - y_1] \tag{4.75}$$

$$[x_1, x_2] \cdot [y_1, y_2] = [\min(x_1 y_1, x_1 y_2, x_2 y_1, x_2 y_2), \max(x_1 y_1, x_1 y_2, x_2 y_1, x_2 y_2)] \tag{4.76}$$

$$[x_1, x_2] / [y_1, y_2] = [x_1, x_2] \cdot (1/[y_1, y_2]) \tag{4.77}$$

$$
\text{with} 1/[y_1, y_2] =
\begin{cases}
[1/y_2, 1/y_1] & , \quad 0 \notin [y_1, y_2] \\
[-\infty, 1/y_1] & , \quad y_2 = 0 \\
[1/y_2, \infty] & , \quad y_1 = 0 \\
[-\infty, \infty] & , \quad \text{else}
\end{cases}
\tag{4.78}
$$

for the four basic operations. The operations with real numbers r are immediately given by using the interval $r = [r, r]$. For the parts of the algorithms where interval arithmetics is recommended the BOOST library [boo] is used to perform interval arithmetics. Depending on the context the lower or upper limit of the interval is used, or it is tested if the interval contains 0.

4.2.4 The iRRAM library

The iRRAM library [*M"uller*, 2001] is used for an error-free implementation of certain calculation in the construction algorithm (Sec. 4.4.2). In contrast to the two former methods (Sec. 4.2.2) and (Sec. 4.2.3) the result does not contain only reliable information on the sign but guarantees an error-free computation of a real value. In principle, for the purpose that the iRRAM library is used in the presented algorithms, one could have chosen the same approach as for the exact predicates (Sec. 4.2.2). However, the work of Shewchuk is a big amount of hand-tuned code which is in no relation to the frequency that it is actually performed in the final implementation. Therefore, the additional work was skipped to write similar code for the algorithms in (Sec. 4.4.3) in favor of the iRRAM library which is a ready-to-use C++ implementation of the *real RAM model*. This allows the use of arbitrary real numbers with exact arithmetic. The implementation bases on representing real number by intervals with rational endpoints. All calculations are done such that the output is given with an arbitrarily chosen precision (which is of course finite). The intervals themselves are based on other packages providing multiple precision arithmetic. If the intermediate results accumulate too much errors then the calculation is repeated with a tighter precision bound and the intervals are chosen to be smaller initially. Basically, the idea can be viewed such that interval computations are used to compute the error. An increased number of bits is used to repeat the calculation if an intermediate or the final result are too imprecise, i.e. the interval exceeds the demanded error threshold.

4.2.5   Where robustness is required

The algorithms introduced in detail in the following sections make use of different strategies to achieve robustness.

- Whenever the orthosphere primitive is calculated directly the exact predicates (Sec. 4.2.2) are used. This applies to the insertion using Bowyer-Watson (Sec. 4.3.1 and Sec. 4.4.3) and the flip algorithm (Sec. 4.3.3 and Sec. (Sec. 4.4.6)).

- Interval arithmetics (Sec. 4.2.3) is used during initial construction (Sec. 4.4.2) deletion (Sec. 4.3.2 and Sec. 4.4.4), and the recovery from non-flippable configurations (Sec. 4.3.3) in order to calculate the signed Delaunay distance (Eq. 4.31). It is also used for calculating the maximum step a vertex can be displaced before applying the flip algorithm (Sec. 4.3.3).

- The iRRAM library is only used for constructing the initial simplex for the incremental construction algorithm (Sec. 4.2 paragraph "Incremental Construction - Extension to regular triangulations").

4.3   Dynamic and kinetic algorithms

This section deals with a brief discussion of methods to realize dynamic and kinetic regular triangulations. The dynamics of a regular triangulation is defined as insertion (Sec. 4.3.1) and deletion (Sec. 4.3.2) of vertices. The kinetics is originally defined as the change of the position of vertices (Sec. 4.3.3). In this work the change of the weight is included into the kinetic part of the triangulation.

4.3.1   Insertion algorithms

Two of the construction algorithms are also suitable to use them for inserting vertices in an already existing triangulation. One is the Bowyer-Watson algorithm the other the flip algorithm (Sec. 4.2). Both construction algorithms are based on an incremental insertion, that is adding a vertex to an existing regular triangulation which is obviously the same operation as inserting vertices. In contrast the incremental construction algorithm cannot be used for vertex insertion.

4.3.2   Deletion algorithms

For the deletion of vertices there exist two algorithms. In the parallelization section (Sec. 4.4.4) the algorithm that serves as basis for the parallel routine will be presented in more detail.

One of the algorithms relies on the flip algorithm [*Vigo and Pla*, 2002]. It requires that a history of flip operations is stored when a vertex is inserted into the triangulation. In previous work additional op-
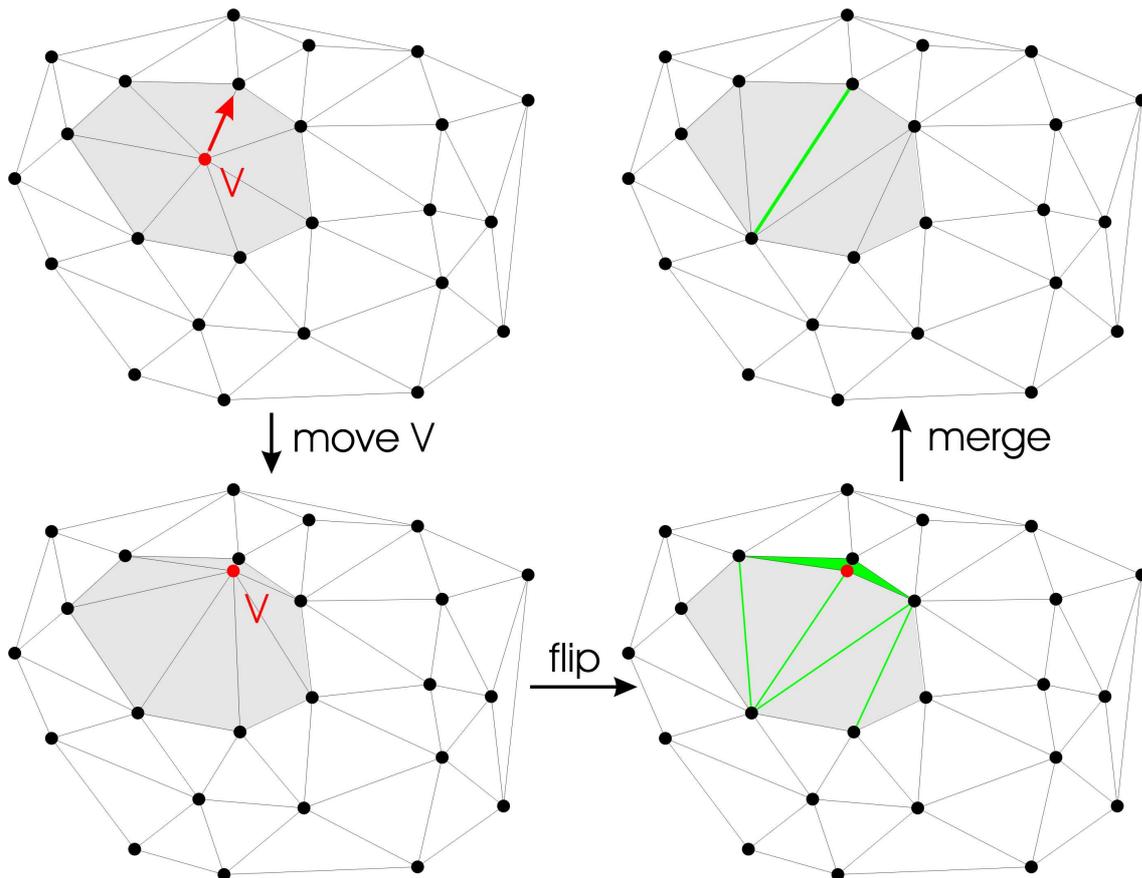
Figure 4.9: A vertex V can be deleted by moving it close to one of its neighbor simplices performing the induced flip operations. Then the two vertices are merged omitting the corresponding simplices (green) and updating the neighborship relations in the data structure.

erations permitting the deletion of vertices have been presented [*Vigo and Pla*, 2002]. This algorithm is not suitable for the purpose of this work as:

1. The construction requires the flip algorithm.

2. It conflicts with the kinetic algorithm (Sec. 4.3.3) as the whole history of flip operations needs to be stored which will get quite extensive after some time.

3. It is not suitable for parallelization as deletion has to be performed incrementally.

There exist also the possibility to use the flip algorithm in a different way to delete vertices (Fig. 4.9). One moves a vertex V_1 to be deleted close to another vertex V_2. When the vertices V_1 and V_2 are close enough their common simplices can be collapsed to faces without changing the orientation of adjacent simplices (Fig. 4.9). This possibility has not been chosen because it is inefficient for parallelization when two neighbor vertices are to be deleted. Also the complexity of the flip algorithm which might need to be called several times (to move the vertices close to each other) possibly inducing non-flippable configurations (Sec. 4.3.3) argues against using this method.

The method used in this work is related to the incremental construction (Sec. 4.2) termed *cavity filling*. All simplices that have the vertex V to be deleted as endpoint are removed from the triangu-
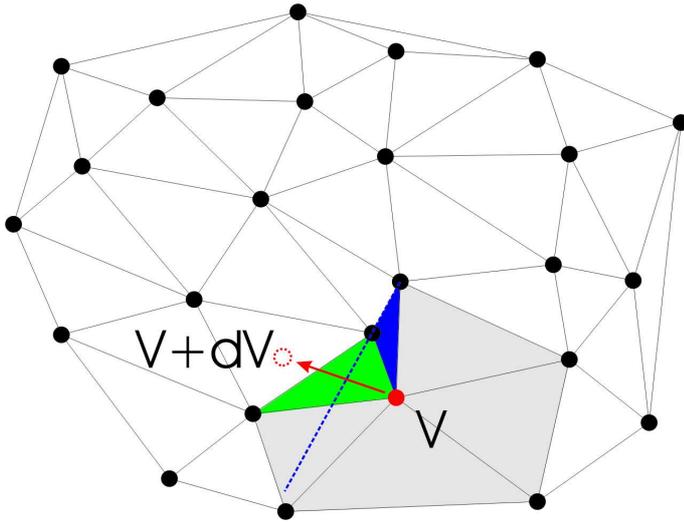
Figure 4.10: The maximum allowed vertex displacement. The vertex V is requested to be displaced to the location $V + dV$. However, doing this in one step would change the orientation of the green simplex as it penetrates the face opposite of the vertex. A stronger restriction is provided by the simplex indicated in blue. The vertex V crosses the plane of one face (blue dashed line) changing the orientation of the blue simplex. In order to prevent this the maximum displacement is calculated such that it respects the orientation of all simplices that have V as endpoint (grey triangles, blue, and green triangle).

lation. Their faces common with the surrounding adjacent simplices are stored in an AFL and the construction algorithm is called using the faces in the AFL. The triangulation of the cavity is completely similar to completing a partially constructed regular triangulation of a vertex set using the incremental construction.

A similar concept has been used before [*Devillers*, 1999]. The authors termed their method *shelling* and used the concept of convex hulls to implement the algorithm. The complexity of the algorithm is better than the one presented and used in this work and can in principle serve as a replacement without interfering with the parallelization described here (Sec. 4.4.4).

4.3.3 Kinetic algorithms

Up to now their exists only one known implementation [*Schaller and Meyer-Hermann*, 2004] for combined dynamic and kinetic regular triangulations apart from the one presented in this work. In most cases kinetic triangulations have been realized by complete new construction – when basically all vertices change their position – or by dynamic routines, i.e. deleting the vertex at the old position and inserting it at the new vertex position. The present work extents the method of using the flip algorithm for kinetic vertices. This has been realized before [*Ferrez*, 2001] and combined with triangulation dynamics [*Schaller and Meyer-Hermann*, 2004]. Another study [*Guibas and Russel*, 2004] examined the efficiency of the flip method compared to reconstruction and a dynamic realization. The major outcome is that in the case of small displacement – which is realistic for the purpose of particle simulation as in the presented work – and large particle numbers the flip algorithms succeeds the other methods in terms of performance.

Vertex movement

The kinetics of a triangulation solves only one part of the problem concerning vertex movement. There is an additional restriction that has to be applied. The flip algorithm can only work with trian-

gulations [2], i.e. simplices are not overlapping. If now a vertex moves far it can change the orientation of simplices (Fig. 4.10) leaving simplices overlapping each other. The flip algorithm cannot be applied in such situations. Therefore, a method to prevent simplex orientation changes is needed. The algorithm has been worked out before [*Schaller and Meyer-Hermann*, 2004]. The basic concept is briefly discussed in this section.

The idea is to calculate the maximal allowed displacement of a vertex V in a given direction $\hat{\mathbf{e}}$ without the simplex $\sigma_{\langle A,B,C,V \rangle}$ changing its orientation (Fig. 4.10).

$$O(A, B, C, V + \lambda \hat{\mathbf{e}}) = 0 \tag{4.79}$$

Using the linearity of the orientation function resulting from the linear properties of the underlying determinant one yields

$$\lambda = \frac{O(A, B, C, V)}{O(A, B, C, \hat{\mathbf{e}})}. \tag{4.80}$$

If the desired displacement $|\mathbf{dr}|$ is larger than the allowed λ then it is splitted into several steps. An allowed displacement is applied followed by the call of a flip algorithm. Then the allowed displacement has to be calculated again to apply the remaining displacement $\mathbf{dr} - \lambda \hat{\mathbf{e}}$. The whole procedure is iterated until the final displacement $\mathbf{dr}$ has been applied. Note, that after calculating λ for a vertex, the change must be applied instantly to the triangulation in order to determine the allowed displacement of the neighbor vertices correctly.

The calculation of the orientation function is not exact. This can cause simplices to change their orientation without indication by the orientation function. In order to prevent this interval arithmetics can be used. λ is then estimated by the lower bound of the interval. The robust orientation predicates of Shewchuk [*Shewchuk*, 1997] (Sec. 4.2.2) cannot be used as they guarantee only the sign of the orientation predicate to be exact not its absolute value which is required here.

The splitting into several movement step requires the computation of intermediate regular triangulations. It is not guaranteed that the vertices do not become redundant during the intermediate steps while they are not redundant in the final triangulation when all vertices have been displaced properly. To cope with this issue the intermediately redundant vertices will be inserted using the dynamic insertion routine. Experience shows that these events occur very rarely thus the insertion takes a negligible amount of time not hampering the performance of the kinetic routine.

The change of the vertex weight is not critical with respect to simplex orientations and is performed on all vertices before the flip routine is executed.

Recover from non-flippable situations

To keep the performance advance of the flip algorithm in three dimensions it is desired to use the simple version of the flip algorithm [*Joe*, 1989, 1991; *Lawson*, 1972] instead of the save variant to move only one vertex at once before updating the triangulation [*Edelsbrunner and Shah*, 1996].

---

[2]That it might fail due to non-flippable configurations is subject to the next section
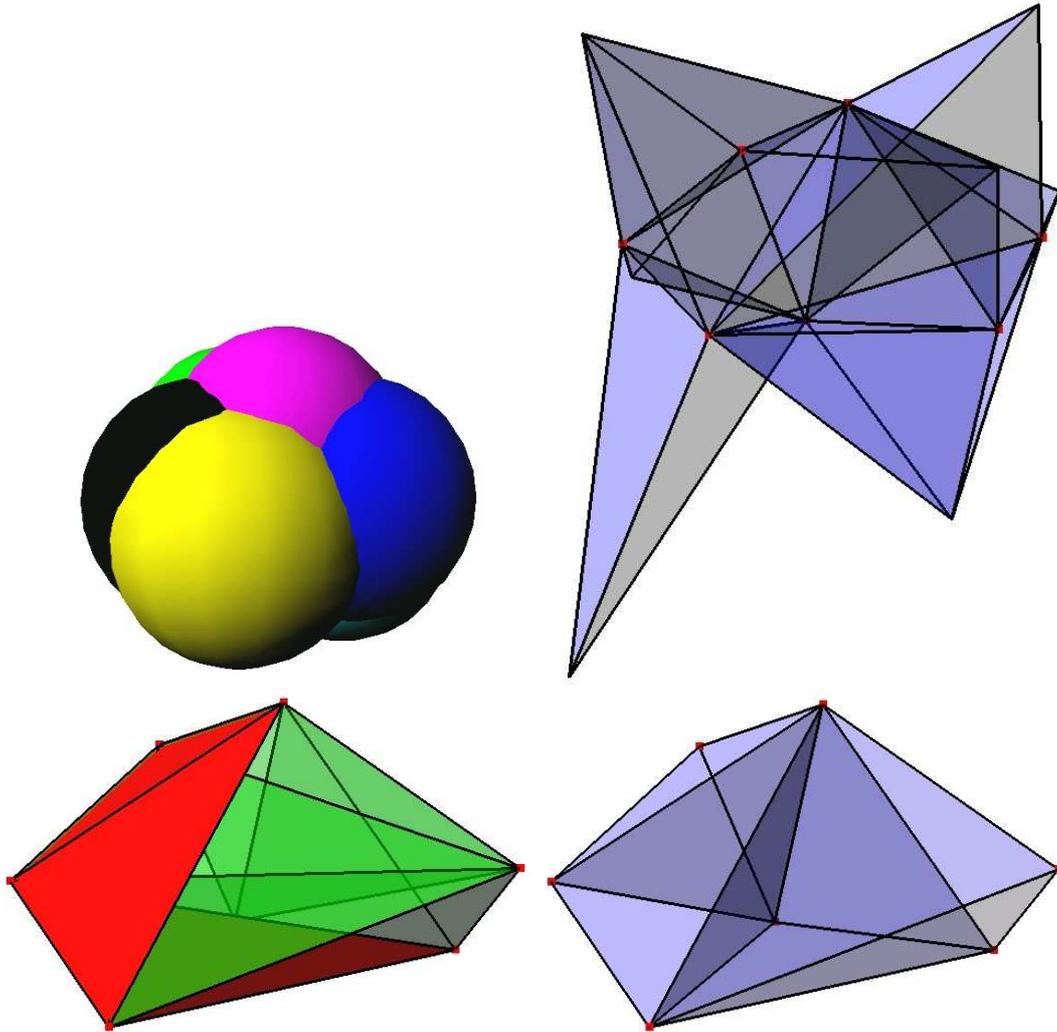
Figure 4.11: Example for a non-flippable situation. The upper left panel shows the vertices represented by colored balls. The lower left panel shows the non-regular and non-flippable configuration of simplices with red indicating the locally regular but globally non-regular and green the locally non-regular simplices. The corrected triangulation is shown in the lower right panel. The upper right panel shows the regular simplices adjacent to the non-regular triangulation that serves as anchorage for the reconstruction providing the faces for the AFL.
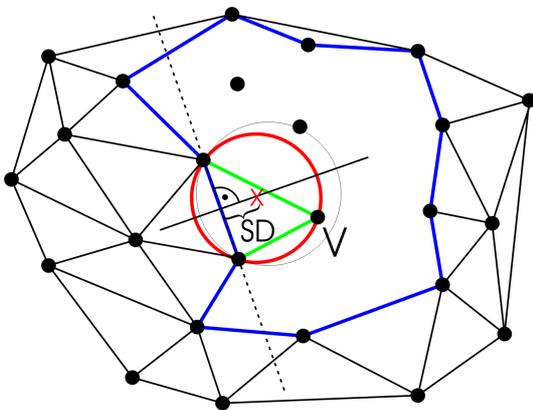
Figure 4.12: Restore the cavity formed by non-regular simplices. When all non-regular simplices resulting form a non-flippable configuration are identified they are removed creating a cavity bounded by regular simplices. The adjacent face (blue lines) are stored in an AFL and subject to the incremental construction algorithm by minimizing the signed Delaunay distance (SD) to find the vertex V that forms a regular simplex (green) with one of the faces, i.e. no vertices violate its orthosphere (red circle).
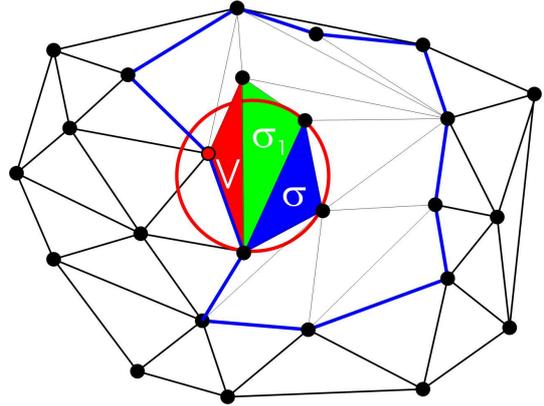
Figure 4.13: Local regular but global non-regular simplices in non-flippable configurations. For simplicity it is assumed that the shown triangulation inside the blue outlined are is non-flippable (which is never the case in 2D). Critical cases are simplices like σ (blue) which is locally regular, e.g. the green triangle σ_1, but globally non-regular as indicate by the vertex V that violates the orthosphere of σ as indicated by the red circle.

However, this can result in non-flippable configurations [*Edelsbrunner and Shah*, 1996; *Vigo and Pla*, 2002].

Definition 12 *A non-flippable configuration is defined as a subset $\mathcal{S}$ of simplices of a triangulation $\mathcal{T}$ that are locally non-regular but cannot be transformed into locally regular simplices using elementary topological transformations.*

This can be prevented by using either presorting of the operations or applying all changes of the triangulation kinetics incrementally [*Edelsbrunner and Shah*, 1996; *Vigo and Pla*, 2002]. Both methods to prevent non-flippable configurations add cost to the algorithm even if the non-flippable configuration does not occur in every instance. More important they prevent the algorithm from parallel execution as these strategies are inherently sequential. Instead a new method to recover from non-flippable configurations was innovated [*Beyer and Meyer-Hermann*, 2006].

The underlying idea is to find all non-regular simplices the flip algorithm leaves when a non-flippable configuration occurs. Those simplices are removed. The remaining cavity is bounded by faces of regular simplices which can be stored in an AFL that triangulates the cavity using the incremental construction (Fig. 4.11). This is basically the same strategy applied to the deletion of vertices with choosing just another subset of simplices to be replaced by a newly calculated set of regular simplices (Fig. 4.12).

The critical point of the method is to find all non-regular simplices (Fig. 4.13). In a naive way one may detect the non-flippable configuration by finding locally non-regular simplices and then starts to check all simplices for global regularity which is however inefficient due to its quadratic complexity, i.e. check all simplices against all vertices. The improved method used here is inspired by the incremental construction algorithm.

The existence of non-flippable configurations requires that locally non-regular simplices are present. Starting from these simplices one performs *incremental deconstruction* (Fig. 4.14). The detailed steps are as follows:

- Create a list $\mathcal{S}$ of all locally non-regular simplices.

- For all adjacent simplices $\sigma \notin \mathcal{S}$ compute the orthosphere M. Test if any vertex violates the orthosphere. If the simplex is invalid store it in $\mathcal{S}$.

```
begin incremental_deconstruction(S,V)
create uniform grid for V
AFL ← face from S
while AFL not empty do
    simplex s ← incident simplex of f ∈ AFL
    if s is non-regular for vertex v ∈ V then
        AFL ← faces of s
        V_cav ← vertices of s
    else
        F ← f
    end if
    remove f from AFL
end while
call incremental_construction(V_cav,F)
end incremental_deconstruction
```

Figure 4.14: Pseudo code for incremental deconstruction. The input are the set of locally non-regular simplices S and the set of vertices V. The output are a subset of vertices V_{cav} and a list of faces used as the AFL of the incremental reconstruction.

The second step is needed as locally regular simplices are not necessarily globally regular. Numerical experiments show that locally regular but globally non-regular occurs in most (but not all) situations of non-flippable configurations.

The detection of vertices violating the orthosphere of a simplex would in principle be a operation of linear complexity, i.e. performing the test with all vertices. Using a grid as described for the initial construction (Sec. 4.2 paragraph "Incremental Construction") can speed up the algorithm. There is also the possibility to do so without a grid, explained below.

If the regular triangulation reduces to a simple Delaunay triangulation the search for globally non-regular simplices can be improved. Instead of using an underlying grid to locate the vertices that may violate the orthosphere criterion of a simplex σ in question one can use the simplex list representing the triangulation in the following way (Fig. 4.15). First one computes the radius r_m and center $\mathbf{m}$ of the circumsphere M of the simplex σ which is – in the case of the normal Delaunay triangulation – identical to the orthosphere. Then one starts to collect all simplices σ_L in a list L which have a non-vanishing intersection with the ball b_M bounded by the sphere M, i.e. $\sigma_L \cap b_M \neq \emptyset$. All adjacent simplices σ_i $i = 1, 2, 3, 4$ of σ are automatically in the list L. To find all other simplices that intersect with b_M one proceeds in the following way. Let $\sigma_{\langle A,B,C,V \rangle} \notin L$ be a simplex adjacent to $\sigma_{\langle A,B,C,D \rangle} \in L$. First, one has to check if the vertex V lies within the sphere M, that is to use the orthosphere test (Eq. 4.2) of the vertices of the simplex σ with the vertex V and all vertex weights $w = 0$. To reduce the number of tests one can mark the vertex V as tested in order to prevent multiple calculations of (Eq. 4.2) due to the fact that vertex V is endpoint of more than one simplex. If the vertex V lies inside the circumsphere M and is not an endpoint of the simplex σ then σ is non-regular. Otherwise one has to test if the plane spanned by the vertices A, B, and C intersects the sphere M. This can be done

simply by calculating the plane distance l from the center of the sphere M by the equation

$$l = |(\mathbf{m} - \mathbf{a}) \cdot \mathbf{n}| \tag{4.81}$$

with the plane normal

$$\mathbf{n} = \frac{(\mathbf{b} - \mathbf{a}) \times (\mathbf{c} - \mathbf{a})}{\|(\mathbf{b} - \mathbf{a}) \times (\mathbf{c} - \mathbf{a})\|}. \tag{4.82}$$

If $l < r_m$ the simplex $\sigma_{\langle A,B,C,V \rangle}$ is inserted in the list $\mathcal{L}$ and the procedure starts with the next simplex $\sigma' \notin \mathcal{L}$ being adjacent to a simplex $\sigma_{\mathcal{L}} \in \mathcal{L}$. When all those simplices are found and none of their vertices lie in the circumsphere then the simplex is regular. Note, that $l < r_m$ is a sufficient but not a necessary condition to ensure that simplex $\sigma_{\langle A,B,C,V \rangle}$ intersects the sphere M. One may perform an additional test checking if the face formed by the vertices A, B, and C intersects with the projection of the sphere M in the plane spanned by A, B, and C. Let $\tilde{M}$ be the projection of the sphere M, that is a circle with center

$$\tilde{\mathbf{m}} = (\mathbf{m} - \mathbf{a}) - (\mathbf{m} - \mathbf{a}) \cdot \frac{(\mathbf{b} - \mathbf{a}) \times (\mathbf{c} - \mathbf{a})}{\|(\mathbf{b} - \mathbf{a}) \times (\mathbf{c} - \mathbf{a})\|}$$

and radius $\tilde{r}_m = \sqrt{r_m^2 - l^2}$. Let $\langle A, B \rangle$ be one edge of the triangle $\langle A, B, C \rangle$. Then with $\mathbf{u} = (\mathbf{b} - \mathbf{a}) / \|\mathbf{b} - \mathbf{a}\|$ and $\mathbf{v} = (\mathbf{c} - \mathbf{a}) / \|\mathbf{c} - \mathbf{a}\|$ one computes the normal vector

$$\tilde{\mathbf{n}} = \mathbf{v} - \mathbf{v} \cdot \mathbf{u}$$

of the edge $\langle A, B \rangle$ in the plane spanned by A, B, and C. Finally,

$$\tilde{l} = (\tilde{\mathbf{m}} - \mathbf{a}) \cdot \tilde{\mathbf{n}} \tag{4.83}$$

gives the signed distance of the projected sphere $\tilde{M}$ from the line passing through A and B. The projected sphere $\tilde{M}$ intersects the triangle $\langle A, B, C \rangle$ when

1. $\tilde{l} > 0$ for all edges

2. $\tilde{l} > 0$ for two edges and $|\tilde{l}| < \tilde{r}_m$ for the third edge

3. $\tilde{l} < 0$ for two edges and $\|\mathbf{f} - \tilde{\mathbf{m}}\| < \tilde{r}_m$ for the common vertex F of those edges.

Note, that this additional test is not necessary to detect whether the simplex σ is globally regular or not. In most cases it will not improve the efficiency of the algorithm as the gain by decreasing the amount of simplices to be tested is out-balanced by additional computations.

For regular triangulations the method presented above cannot be used in general. However, if there exists an upper bound for the weights of the vertices then an analog algorithm for the vertex search can be used. Let W be the maximal weight of all vertices and $R = \sqrt{|W|}$ be the corresponding maximum radius. Then the circumsphere M is replaced by a sphere M' with center $\mathbf{m}'$ equal to the center of the orthosphere of the simplex σ. The radius of M' is equal $r_m' = \sqrt{R + r}$ where r is the radius of the orthosphere. The above algorithm can then be used to check whether simplex σ is globally regular or not by using the sphere M' with a minor modification. An additional orthosphere test for the vertex V is necessary as V may lie within V but still does not violate the orthosphere of simplex σ. This is due to the fact that the sphere M' is used to ensure that every vertex in question is found. In contrast to the situation in the Delaunay triangulation it is not equivalent to the orthosphere test.

```
begin simplex_regular( σ )
list of simplices 𝓛
𝓛 ← σ
for all σ⟨A,B,C,V⟩ ∉ 𝓛 adjacent to σ⟨A,B,C,D⟩ ∈ 𝓛
do
  if  ‖v − m‖ < r_m  then
      return false (σ is non-regular)
  else
      l distance of plane (Eq. 4.81)
      if  l < r_m  then
        𝓛 ← σ⟨A,B,C,V⟩
      end if
  end if
end for
return true (σ is regular)
end simplex_regular
```

Figure 4.15: Pseudo code for finding vertices that are needed to test the global regularity of the simplex σ. The function returns whether σ is regular (true) or not (false). The circumsphere of the simplex σ is given by its center $\mathbf{m}$ and radius r_m.

4.4 Parallel three-dimensional dynamic and regular triangulation

This section discusses the implementation and parallelization of the algorithms which have been published in [*Beyer et al.*, 2005]. The code has been written in C++ in conjunction with the MPI library [*Message-Passing Interface Forum*, 1995] for platform-independent parallel communication. Furthermore, the BOOST library [boo] has been used for interval arithmetics, the modified predicates of Shewchuk [*Shewchuk*, 1997] (Sec. 4.2.2), the iRAMM library for exact real number arithmetic [*M"uller*, 2001] (Sec. 4.2.4), and finally the ParMetis library [*Karypis and Kumar*, 1997] for distributing data (see below).

4.4.1 Basic concepts and data structure

There are two levels of data structures: One is the local data structure the other the global data structure. The local data structure will be discussed first. It is similar to the one used in a serial implementation for most algorithms [*Schaller and Meyer-Hermann*, 2004].

The triangulation is stored as a connected simplex list. The data for a simplex is stored as pointers to its four vertices and to its four adjacent simplices. The faces of outer simplices that have no adjacent simplex are omitted. The vertices are also stored in a list. Each of the vertices has a list of pointer to simplices which have this vertex as endpoint. A list of neighbor vertices is also stored using pointers. To reduce the amount of computation there is some additional information stored in each simplex data structure. The first is that the sequence of vertex pointer arguments is such that the simplex is positively oriented upon construction, i.e. the sequence is not changed when the vertices change their
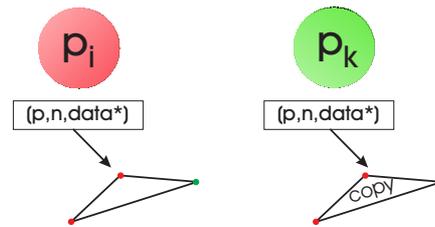
Figure 4.16: Basic MPI operations. The three basic MPI operations used in the implementation of the parallel regular triangulation. The `Send` and `Recv` pair blocks the computation at a process until the message exchange has been finished (dashed line). The non-blocking `ISend` is used to allow calculations at the process while the message is not received yet. Collective communications is virtually synchronous at all process and eventually blocks computations of processes until all of them finished the collective communication. An example for delayed messages is shown which reverses the logical order of messages arriving at the process p_k.
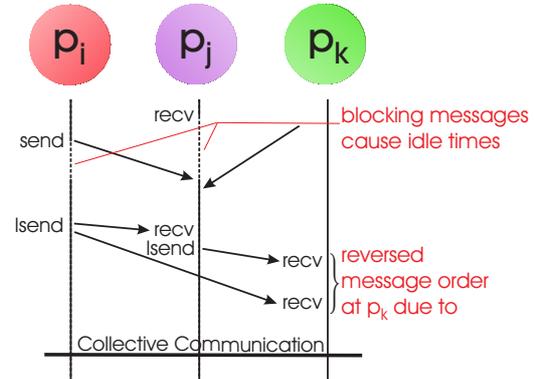
position after the simplex has been created by some routine. All routines are coded such that the simplex orientation results from combinatorial test such that (Eq. 4.1) needs to be computed only once during the initial triangulation basically omitting the need for calculating orientation determinants throughout the remaining calculations. For each pointer to a neighbor simplex the result of the last orthosphere criterion calculation is stored together with a flag indicating its last update. Depending on the subroutine which are presented below the result of a former computation can be reused without actually performing the calculation. Especially, the flip algorithm benefits from that concept as explained below. For the purpose of using the dual graph – the Voronoi tessellation – the center of the orthosphere is stored, again invoking a flag that indicates if a recomputation is needed.

The changes to the triangulation are handled differently for simplices and vertices. Simplices are only created and destroyed. Vertices keep their data structure and change properties in the case of triangulation kinetics. They are also created/removed during triangulation dynamics.

The parallel implementation is based on the Message Passing Interface (MPI) [*Message-Passing Interface Forum*, 1995]. The concept is to run the same program on different processes – which are usual different physical processors or even computers – and include code which process performs which instruction including sending or receiving data from other processes through some type of network provide by the hardware.

Short outline of MPI The basic concept of MPI is to send messages among different processes by programming which process sends a specific piece of data to some other process (Fig. 4.16). There are basically three communication modes.

1. *Collective communication* is used to exchange information for a group of processes synchronously. For the algorithms below it is not used very often but it plays a role to synchronize

global variables in the cell modeling (which will not be discussed explicitely as it is a straight-forward parallelization).

2. *Synchronous point-to-point communication* is understood in this work as a prefixed communication method in which it is known and written in the program code at which timepoint during execution a process has to send or receive data. The only unknowns are the amounts of data to be exchanged which are usually transmitted using a preceding message of fixed length.

3. The dominant communication mode is *asynchronous point-to-point communication* where a process does not know by program code when a message arrives from some process. The most important function is the function `Iprobe()` which scans for messages. It is provided by the MPI library and serves to detect and prepare the receipt of a message sent by some process. It also implies that the sending process does not know in advance when the data has arrived at the target process. The function involved in this communication method are briefly discussed in the following.

The most widely used functions in the parallel implementation of the algorithms presented in the following sections. The functions are part of the MPI library and executed independent of the main program in the sense that at any time point the processor running the program can perform a MPI function or a function of the main program similar to multitasking on a desktop PC.

- `MPI::Comm::Isend( buffer, count, type, target, tag )`: This function opens a request to send data consisting of `count` number of pieces of the type `type` which are stored in the memory at `buffer`. The data will be send to the process `target` with the message identifier `tag`.

- `MPI::Comm::Irecv( buffer, count, type, source, tag )`: This function opens a request to receive `count` number of data pieces of the type `type` which are then stored in the memory at `buffer`. The `source` gives the process that sends the message while `tag` indicates an identifier of the message.

- `MPI::Request`: This structure holds information about a communication process requested to be performed. It holds information which are the arguments of the two functions above together with the status of the message, i.e. whether a message has been sent/received.

An important problem that has to be solved for each algorithm is *consistency* to prevent *deadlocks*. Consistency implies that their are not more(less) messages sent than expected by the receiver. Moreover, the messages have to match such that the balance of messages is pointwise between processes and the tag-arguments, i.e. the message identity of the sending and receiving functions are the same. Otherwise a deadlock can be the result when a process waits for a message that has never been sent or vice versa. Also the sequence of messages must be organized properly to prevent deadlocks. An example is (see also (Fig. 4.16)): Process p_1 sends message m_1 to the process p_2. On the other side p_2 is waiting for message m_2 from process p_1. If wrongly organized, message m_2 might be sent by p_1 only when it detected that m_1 has been received. Message requests are used to prevent most of such situations as this allows to perform another task, i.e. send/receive another message, before a certain communication has been completed.

Metapointer   The concept of *metapointer* has been introduced before [*Ferrez*, 2001]. It has been extended for the presented work in a way that allows for a global data structure with distributed data architectures. A metapointer consists of a pointer to a local data structure (vertex or simplex), a process number and an index. The pair (p, n) = (process,index) serves as unique global identifier for the data. The pair is chosen in order to simplify the generation of unique indices. In the presented way a process needs only to ensure local index uniqueness to guarantee global uniqueness without invoking data exchange with other processes. In the implementation there is some storage holding a number of indices from which new indices can be generated. As soon as vertex or simplex is removed by the dynamic or kinetic routines the index is put back to the storage. The whole metapointer is a structure like this

```
metapointer{
   int p;     // the process
   int n;     // the index
   data* it;  // pointer to the data
}
```

Practically, the pair (p, n) can be merged into a single integer to save memory and still have the capability to store enough data for most applications.

The communication using metapointers between processes is organized as follows. In most cases the geometric objects and an instruction for some operation on these objects is sent to a process. Instead of sending the vertex or simplex itself only the corresponding metapointer is sent. The receiving process *translates* the metapointer into the local copy of the geometric object. This is realized by an array that contains a pointer to the copy of the corresponding object data for every metapointer. Using the process-index pair the pointer variable of the metapointer is set to the local copy of the data identified by the metapointer thus allowing local data access via the metapointer.

Concepts for parallel computing   There exist a few theoretical concepts of parallel computing (see for example `http://www.tc.cornell.edu/Services/Education/Topics/Parallel/Concepts/3.+Taxonomy.htm`) which barely fit the real-world applications. The execution model used fits best to multiple-data multiple-instruction. Data-parallelism is used by distributing the data of the triangulation across the processors. Within the subroutines there is task-parallelism while the execution of the routines is synchronized.

Data-parallelism is based on the metapointer concept. The process number of the metapointer (p, n) of a vertex is used to indicate that the vertex is *owned* by the process p. This in turn means that all application properties, and dynamics, and kinetics are handled by the process p. The metapointer indices n are exclusively generated by the process that will own the vertex. The simplices are managed exclusively by some process p if all of their endpoints belong to the process p. All other simplices are shared and can be changed by any of the processes owning the endpoints. The metapointer indices are generated by some process that generates the simplex but it can be removed (during any dynamic or kinetic routine) by another process. Usually, the generating process has to perform this change as well thus recognizing that the index can be reused. The artificial vertices needed for the flip algorithm (Sec. 4.4.6) are not owned by any process. Each process holds a copy of these vertices which will
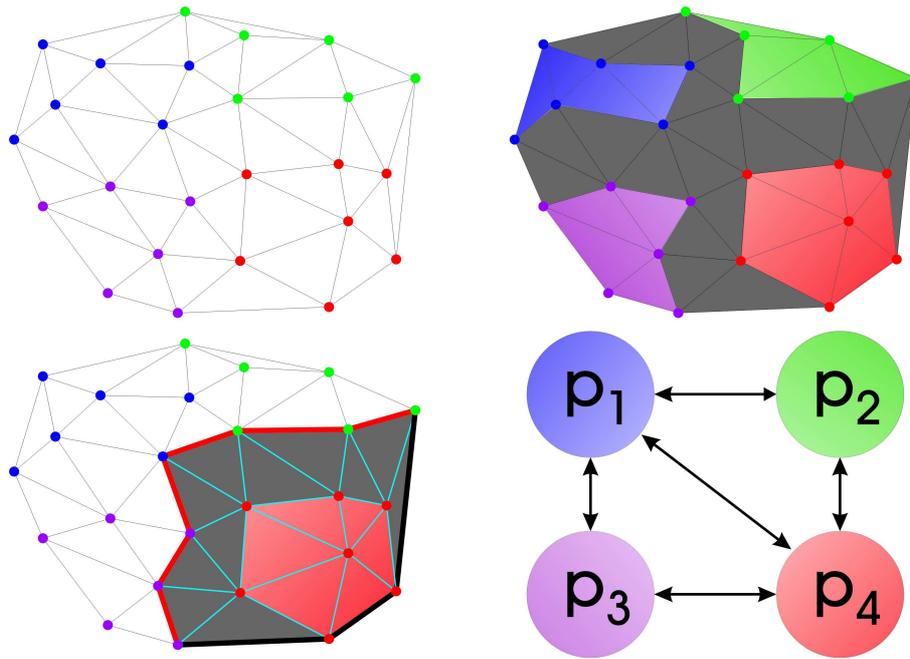
Figure 4.17: Data parallelism concept. The data parallelism is achieved by assigning each vertex uniquely to one process (colored dots). The local simplices (color shaded areas) are stored only at the process owning the corresponding vertices while boundary simplices (grey shaded) are stored as copy at each process that requires it. The resulting process topology that sets up the communication pattern is shown on the right.

never change their position. Thus it is always accessible like a global variable.

To simplify the notation vertices owned by some process are called *local vertices* (with respect to the process). If some of the vertices of a process p_i are neighbor vertices of a process p_k the vertices of p_i are called *neighbor vertices of the process p_k* and the process p_i is a *neighbor process* of p_k. Note, that the process topology results from the topology of the triangulation. This also defines the communication topology for point-to-point communication via MPI functions. In addition to its own vertices any process holds copies of all vertices of its neighbor processes. It would be sufficient to hold copies of only those vertices that are neighbor vertices in the triangulation. However, the dynamic and kinetic routine will frequently change these relations such that it would require communication to transfer the vertex data instead of its metapointer only. This is different for simplices which do not change topologically, i.e. simplices with endpoints at a process p_i alone will never be accessed by a any other process p_k. Another point is that the dynamic and kinetic routines may create or destroy process neighborships when vertices of two different processes p_i, p_j are connected which had no such connection before. This can only be detected by a common neighbor process p_k which will send a message to both processes p_i and p_j to exchange their vertices and establish point-to-point communication. The procedure is just the implementation of creating a new edge in the network of the communication topology. In basically all situations of the algorithms presented below, the changes applied to the regular triangulation implicitly contain information when two processes need to be connected. In this case both processes immediately start to exchange their vertices interrupting all other tasks until this is completed. The implementation of the algorithms ensures that the process inter-connection does not cause deadlocks despite the priority given to this operation. The principle

is the same for all dynamic and kinetic algorithms and details will not be discussed explicitly in the corresponding sections. Two processes having no longer a connection among their vertices is equivalent to not sharing simplices. To save memory and reduce the amount of communication the two processes are disconnected by simply removing the copies of the corresponding neighbor vertices. This is done after each routine has been applied once.

Similar to vertices, *boundary simplices* in the process context are defined as simplices that have vertex endpoints owned by different processes (Fig. 4.17). It is close to the former definition of outer simplices in the context of the regular triangulation in the sense that some simplices miss simplex adjacency relations. A simplex neighborship relation at a process p is missing if none of the vertices of the common face is owned by p while the simplex adjacency relation is set on all processes owning those vertices (Fig. 4.17). That simplifies most routines as this prevents access to simplices that are not represented by a local copy [3] at process p in a simple way. All simplices that are present at a process including the boundary vertices is called *domain* of the process. Thus, the intersection of two process domains gives all boundary simplices which are *shared* by these processes.

The task-parallel execution allows that different parts of the algorithms presented below can be executed concurrently. This requires that the communication is asynchronously. In most cases tasks will be transmitted among processes without the receiving process 'knowing' in advance which task or when it will be received. However, the problem of message delays is induced which will be discussed in more detail in the following paragraph.

The basic concept of all algorithms presented below is to have a while loop looking for messages and local operations. As long as local operations (insertion, deletion, etc.) are not completed and messages from neighbor processes are sending instructions the routine will continue. Concurrency (task-parallelism) is reached by performing each task concurrently giving priority to execute instructions received from neighbor processes over performing local operations. This is realized by storing messages in a local buffer in the sequence they arrive and only perform local operations when the buffer is empty. The buffer is used mainly to receive messages needed to perform a certain instruction which itself relies on other messages which are delayed (see next paragraph and the sections below). The MPI library might block the specific message that is needed when their are already too much messages that need to be received which can cause dead locks preventing the program from continuing execution. This inherit constraint of MPI is overcome by using additional message buffers in the program.

The data parallelism is not complete because simplices are shared between processes and many algorithms modify adjacent simplices such that a ownership of simplices is not adequate. Instead dynamic temporary unique *access rights* are used: simplices can be *blocked* by a process p. This usually requires that a MPI message has to be send to all other processes by the blocking process p. There are also cases that a neighbor process can deduce the access rights from local information depending on the algorithm (and discussed in more detail where this appears). In some cases a similar access right concept is needed for vertices (Sec. 4.4.5). In this case the blocking is not performed individually but on all vertices of a process p_i which are neighbor vertices of the process p_j at once.

---

[3]The copy can exist as the fourth vertex of both simplices may by owned by p. For consistency the adjacency relation is still not set.

The overall scheme of the application is organized as follows:

1. Create the initial vertex set according to the application.

2. Distribute the vertices among the processes and start the parallel incremental construction to get the initial state of the regular triangulation.

3. Compute the dynamic and kinetic changes from the application.

4. Apply the changes to the regular triangulation using the parallel dynamic and kinetic routines.

5. Iterate through 3 and 4 as required by the application.

Message delays and synchronization of asynchronous communication   The usage of point-to-point communication induces the problem that messages may not arrive in the order they are generated. This is because MPI guarantees only to preserve the message order between two processes. An example can look like the following (Fig. 4.16):

- Process p_i sends information `data1` to the processes p_j and p_k.

- p_j receives the information `data1` of p_i which induces a message `data2` to process p_k.

- In order to perform its task process p_k may require `data1` prior to `data2`. This behavior is not guaranteed by MPI so that `data2` can be the first message received by p_k.

Depending on the algorithm their are different solutions to the message ordering problem that are explained in detail in the corresponding sections.

4.4.2   Parallel construction algorithm

For the construction algorithm incremental construction has been chosen because of its capability for parallelization. The parallelization has been done before [*Cignoni et al.*, 1993; *Teng et al.*, 1993] by a divide-and-conquer approach. The extension made to this is the generalization to regular triangulations as well as the partition of the initial vertex set $\mathcal{V}$. In contrast to the former methods the partition of vertices on the different processes is done externally in order to allow it to adapt for optimal performance of the application instead of optimal performance of the initial construction. Of course the initial construction of the regular triangulation will take longer but the price has to paid only once and the flexibility of data distribution has been favored over maximum performance.

The algorithm starts with distributing all vertices to the appropriate processes. Then a common uniform grid is calculated by finding the bounding box of all vertices. The uniform grid is set up by:

1. Calculate the edge length of the grid cells $l = \sqrt[3]{\frac{\text{number of vertices}}{(x_{\max} - x_{\min})(y_{\max} - y_{\min})(z_{\max} - z_{\min})}}$

2. Generate a grid of dimension $X \times Y \times Z$ is created with $X = \lceil (x_{\max} - x_{\min})/l \rceil$, $Y = \lceil (y_{\max} - y_{\min})/l \rceil$, $Z = \lceil (z_{\max} - z_{\min})/l \rceil$. ($\lceil . \rceil$ being the ceiling function returning the next highest integer). In practice an array of the length $X * Y * Z$ is created and accessed it by a single index

```
begin incremental_construction( V )          begin find_initial_simplex()
create uniform grid                          calculate T_V M from V^+ ∈ V^+
call find_initial_simplex()                  for all D^+ ∈ V^+, D^+ ≠ V^+ do
while AFL not empty do                           if T · (D^+ − V^+) > 0 then
   face f ← f ∈ AFL                                 U^+ ← D^+
   for all vertices D ∈ V do                     end if
      if D in positive half space of f and    end for
      SD(D) < SD(V) then                       for all D^+ ∈ V^+, D^+ ≠ U^+ do
         vertex V ← D                             if (T·(D^+−U^+))/‖D^+−U^+‖_4 < (T·(W^+−U^+))/‖W^+−U^+‖_4 then
      end if                                         W^+ ← D^+
   end for                                        end if
   if V not empty then                         end for
      create simplex σ_⟨A,B,C,V⟩              T ← T − (W^+ − U^+) (T·(W^+−U^+))/‖W^+−U^+‖_4
      for all nf ∈ new faces do               T ← T / ‖T‖_4
         if nf ∉ AFL then                      Q ← W^+ − U^+
            if nf ≠ boundary face then         Q ← Q/ ‖Q‖_4
               AFL ← nf                        for all D^+ ∈ V^+, D^+ ≠ U^+, W^+ do
            end if                                P ← D^+ − U^+ − Q [(D^+ − U^+) · Q]
         else                                     P′ ← Y^+ − U^+ − Q [(Y^+ − U^+) · Q]
            remove nf from AFL                    if (T·P)/‖P‖_4 < (T·P′)/‖P′‖_4 then
         end if                                       Y^+ ← D^+
      end for                                      end if
   else                                         end for
      border of domain                         for all D ∈ V do
   end if                                         if SD(D) < SD(X) then
   remove face ⟨A, B, C⟩ from AFL                   X ← D
end while                                         end if
synchronize simplices                         end for
end incremental_construction                  create simplex σ_⟨U,W,Y,X⟩
                                              end find_initial_simplex
```

Figure 4.18: Pseudo code of initial triangulation of a set of vertices V. Only the creation of the uniform grid and the synchronization of simplices requires communication. The vertex searches are optimized using the uniform grid. See text for symbols.

I. An index function converts a grid cell with the coordinates (i, j, k) to a single index I by $I = k + Z * j + Y * Z * i$.

3. Insert all vertices (not just local vertices) on the grid. Each entry in the array of the grid gets a pointer to the vertices whose coordinates fit into the grid cell (Fig. 4.7).

The choice of assigning all vertices to the grid on all processes is costly concerning memory. It is necessary when the information which vertices are connected in the final triangulation is missing. If there is an estimate for the process topology one can reduce the uniform grid to the vertices owned by the process an the vertices of the neighbor processes thus reducing the memory overhead. Experience shows that this is not necessary as the memory costs are paid only once in the beginning of the

program. There is a strategy to reduce the memory overhead in a different way discussed in the experimental section for the implementation (Sec. 4.4.9).

The incremental construction algorithm is parallelized in a direct way. Each process generates an initial simplex. Preferably, it contains at least one of the vertices owned by the process. However, this cannot always be guaranteed for regular triangulations due to redundant vertices. This issue will be discussed under the term *construction hopping* later in this section. When the initial simplex is constructed the AFL (Sec. 4.2) is set up. There is a slight change to the faces entering the AFL. Only faces that have at least one endpoint of the constructing process are inserted.Thus, the algorithm constructs only simplices that contain at least one vertex owned by the process. However, it can happen that not all those simplices are constructed at once. This is the case if subsets of the triangulation with the vertices owned by a process are not simply connected. Then one of the vertices not being endpoint of a simplex is used to construct a new initial simplex setting up a new AFL. The whole procedure is iterated until all vertices have been connected to the triangulation. In regular triangulations redundant vertices may appear that interfere with this simple scheme. The problem and its solution is explained in the following paragraph.

After each process has finished constructing its local portion of the triangulation including the boundary simplices to neighbor processes the communication topology is set up which involves two steps. First of all the process-process neighborship relations are extracted from the vertex-vertex neighborship relations of the triangulation at each process. In the next step the boundary simplices are synchronized. Every process constructs the boundary simplices its own vertices are involved in. Consequently, those simplices get different metapointers at each process. The ambiguity is resolved by exchanging the geometry of the simplices, i.e. of which vertices they are made of, and then choose a unique metapointer out of the created ones. To choose a unique metapointer a simple scheme of *process ranking* is applied. The metapointer created by the process with the highest process number will be chosen to give the simplex its process-index pair.

Construction hopping   When the incremental construction leaves unconnected vertices there are two possible causes: The vertex *V* is redundant or part of a non-simply connected part of the triangulation. It is also possible that the initial vertex *V* selected for the initial simplex is not owned by the process. The common solution to this problem is the *construction hopping* method (Fig. 4.19).

Prior to the construction hopping a few calculations are done dependent on the situation mentioned above. In the case that a vertex is left after constructing the triangulation it will be tested using the simplex walk (Sec. 4.2). If it is within a simplex but does not violate the orthosphere it is redundant and is not considered anymore. The simplex walk can also fail as the partial triangulation at some process is usually not convex or the vertex is located outside the constructed domain. In this case construction hopping is inferred.

The basic idea is to do a simplex walk on an incomplete regular triangulation. The simplices which do not exist because they are part of the domain of a neighbor process are constructed intermediately. The method works like this

1. A face oriented towards the vertex *V* of the simplex is selected.

Figure 4.19: Construction hopping principle. The triangulation present at the process owning the red vertices cannot be completed due to a non-simply connected part of the triangulation, that is, the incremental construction algorithm stops at the face indicated by the blue line. To triangulate the part involving the rightmost red vertex the construction hopping is used similar to the simplex walk. The algorithm expands the blue face into the first simplex 1 (bright blue). This simplex will be used to find the green face that can be expanded into the green simplex with number 2. The step is repeated until a simplex is found that contains the vertex (3, red). From there on the triangulation can be completed using the normal algorithm to triangulate the area shaded in grey. Note, that the construction hopping is mostly used when the rightmost red vertex cannot be used to create an initial simplex or when it is redundant, i.e. the simplex 3 would contain this vertex in its interior and not as endpoint as shown in the scheme.
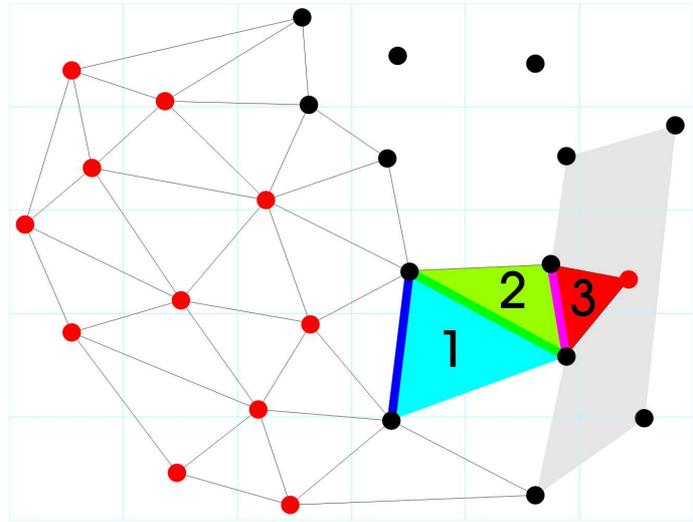
2. This face is expanded into an intermediate simplex σ using the minimization of the signed Delaunay distance like in the incremental construction (Sec. 4.2).

3. If the simplex . . .

   - . . . contains no vertex owned by the process then select a face from the simplex σ and repeat the minimization procedure.

   - . . . contains a vertex owned by the process and the simplex does not exist stop construction hopping and start the normal construction routine with the faces of σ in the AFL.

   - . . . contains a vertex owned by the process and the simplex does exist use normal simplex walk possibly followed by another construction hopping. This case never happens in the first step but occurs upon iteration.

   - . . . contains the vertex V stop construction hopping and continue with incremental construction.

   - . . . lies within the simplex then the vertex V is redundant.

Note that in the second option of point 3 it is not possible that the simplex does not exist but one of its adjacent simplices is already constructed. That is because the incremental construction algorithm never terminates before the missing simplex would have been constructed.

4.4.3   Parallel insertion algorithm

The parallel insertion algorithm bases on the Bowyer-Watson algorithm [*Bowyer*, 1981; *Chrisochoides and Sukup*, 1996a,b; *Watson*, 1981] (Sec. 4.2).

```
begin insert_vertices( ilist )          begin insert_events()
while ilist not empty do                 if simplex walk request then
  if messages received then                continue simplex walk
    call insert_events()                   if simplex walk at border then
  else                                         send simplex walk to neighbor
    vertex V ← V ∈ ilist                   else
    if simplex walk at border then           start virtual domain
      send simplex walk to neighbor        end if
    else                                 else if virtual domain vd then
      start virtual domain vd              if data structure not consistent then
      block simplices invalidated by V       receive delayed messages
      construct virtual simplices          end if
      if σ ∈ vd is shared then             expand virtual domain
        send vd to neighbor processes      if vd is complete then
      else                                     send result to initiator of vd
        turn virtual domain 'real'         else if σ ∈ vd is blocked then
      end if                                   send abort to initiator of vd
    end if                                 end if
  end if                                 else if virtual domain complete then
end while                                  turn virtual domain 'real'
end insert_vertices                        request neighbor to turn vd 'real'
                                         else if request to turn vd real then
                                           turn virtual domain 'real'
                                         else if virtual domain blocked then
                                           abort virtual domain
                                           request neighbors to unblock vd
                                         end if
                                         end insert_events
```

Figure 4.20: Pseudo code for the insertion routine. The left panel shows the local process operations. The right panel shows the processes response to received messages.

Parallel simplex walk   Each process starts a simplex walk of one of the vertices V to be inserted. When the simplex walk terminates at a boundary simplex σ of a processes domain, it will send the vertex V together with σ to the process p with the lowest process rank (which is just an arbitrary choice of different possibilities). The process p will receive the vertex V and the simplex σ and resume the simplex walk. The simplex walk stops as soon as the simplex σ_1 the vertex V lies within has been found. If the vertex V violates the orthosphere of σ_1 a parallel Bowyer-Watson is initiated. In the other case the vertex V is redundant. The process starting the Bowyer-Watson algorithm generates also a new metapointer for the vertex V thereby getting owner of the vertex. This ensures a better balancing of vertices among processes.

Parallel Bowyer-Watson   The parallel Bowyer-Watson algorithm starts with collecting all simplices whose orthospheres are violated by the vertex V in a list $\mathcal{L}$. If all simplices are local the vertex is

Figure 4.21: Two virtual domains from vertices V_1 and V_2 to be inserted. The colored areas are blocked simplices which are replaced by a star-shaped triangulation around the vertices V_1 and V_2 (bright blue lines for the domain of V_2). If the two domains are touching each other as it is shown in the sketch the resulting triangulation can be irregular as the vertex V_1 lies within the orthospheres of the one of the new simplices generated by the insertion of V_2. These situations have to be prevented by blocking the insertion of V_1 despite the virtual domains being non-overlapping.
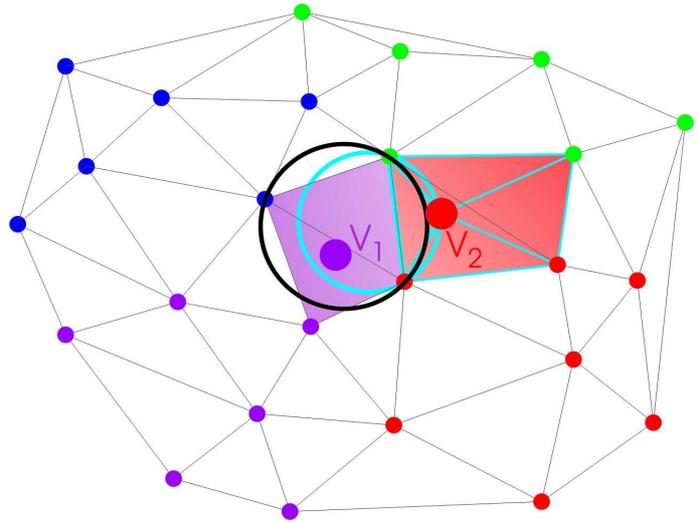
inserted like in the normal unparallelized case. Otherwise the list $\mathcal{L}$ is sent to every neighbor process p_i having shared simplices $\sigma' \in \mathcal{L}$. These processes will continue to collect simplices violated by V – *expand* $\mathcal{L}$ – until $\mathcal{L}$ is complete. Then the subset of the triangulation $\mathcal{L}$ is replaced by a star-shaped triangulation as in the usual Bowyer-Watson method.

In order to optimize the algorithm *virtual domains* are introduced. During the collection of the simplices of $\mathcal{L}$ it is possible to compute the new triangulation virtually, in the sense that the simplices of the star-shaped subset are constructed and stored in a list $\mathcal{N}^*$ but no neighborship relations are set yet (Fig. 4.21). This allows to reduce the communication overhead for the case of two processes. Call the process owning the vertex V to be inserted *active process* and the processes that share simplices in $\mathcal{L}$ *passive processes* which implies a concept similar to a master process dynamically recruiting worker processes. If there is only one passive process the usage of virtual domains allows that the passive process to turn the virtual triangulation $\mathcal{N}^*$ into a real one $\mathcal{N}$ by removing all simplices from $\mathcal{L}$ and setting up the adjacency relations for the simplices in $\mathcal{N}$. This allows the immediate use of the new triangulation by the passive process shortening the time of blocking simplices.

One of the problems to be solved is to detect when the list $\mathcal{L}$ is completed. The problem arises by the fact that the active processes p may not detect all passive processes p_i in the beginning due to two reasons: The expansion of the list $\mathcal{L}$ at the p_i contacts neighbors processes p_j not contacted by p before or that may even not be neighbor processes of p. Also it is possible that $\mathcal{L}$ is returned to p for an expansion which in turn is send back two the passive processes a second time. Thus the list $\mathcal{L}$ can be send to many processes repeatedly. The active process cannot determine a priori when the collection of simplices in $\mathcal{L}$ is complete. To solve these two things the concept of conserved *charge* $\Omega = 1$ is introduced. The idea is to let every message be accompanied by a certain fraction of Ω. At each passive process the charge is equally distributed among each message send to any neighbor process requesting the expansion of $\mathcal{L}$. The active process does the same with the difference the it is treated as sending a message to itself, i.e. when n neighbor processes are contacted Ω is split in $n + 1$ equal portions. The active process adds every fraction of Ω coming from a neighbor process until $\Omega = 1$ holds. This simple procedure ensures that every message required to collect the complete list $\mathcal{L}$ is received. If that is the case the active process sends a completion signal to all participating

processes to turn the virtual domain $\mathcal{N}^*$ into a real domain $\mathcal{N}$. In order to allow the active process to call every passive process every process expanding $\mathcal{L}$ reports back to the active process which neighbor processes it has contacted to expand $\mathcal{L}$ thus the active process 'knows' even process which may not be part of its neighbors in the process topology.

In order to keep the algorithm simple any process is will only insert one of its vertices at once. The only exception is that if the process waits for task it may try to insert a vertex locally, i.e. the insertion is only allow to complete if no boundary vertices are involve and naturally respecting the access rights as well.

Obstacles of the algorithm and their prevention   Unfortunately, the basic algorithm indicated above induces some interference between processes that need to be resolved. The most dominant obstacle is that two virtual domains overlap. To guarantee unique access to simplices they are blocked as described previously. However, this is not sufficient. To virtual domains must not have any face in common (Fig. 4.21). Consider two adjacent simplices σ_1 and σ_2 with common face $\langle A, B, C \rangle$ and two vertices V_1, V_2 to be inserted. Further let V_1 violate σ_1 but not σ_2 and vice versa for V_2. It can happen that when σ_1 is replaced by a simplex $\sigma_{\langle A,B,C,V_1 \rangle}$ that this new simplex is violated by V_2. If both vertices are allowed to be inserted concurrently the change a triangulation that was present before either of these vertices have been inserted and the list of violated simplices does not respect the insertion of the other vertex, finally creating a non-regular triangulation. This can be prevented simply by extending the access rights for simplices to the regular simplices adjacent to the virtual domain.

Due to the fact that many processes can be involved in inserting a simplex the access rights to simplices may be given inconsistently. An example is that two active processes p_1 and p_2 contact two passive processes p_1', p_2'. The access right to shared simplices at p_1' are given to p_1 and at p_2' are given to p_2. Thus both insertion procedures collide at the processes. In a naive way one may just abort the insertion of both vertices by sending a message to remove the virtual simplices and unblock all involved simplices. However, it is not guaranteed that inserting other vertices – if any – before continuing with the interfering vertices resolves the problem finally ending up in a deadlock situation. In such cases the *complaint system* is used. If a passive process reports a blocked simplex to the active process p_i or p_i itself detects a simplex blocked by some process p_k then p_i will abort the insertion and send a *complaint* to the process p_k. The process that detects the blocked simplex (either p_i or a passive process) can also identify which vertex T causes the blocking by looking up the buffer or virtual domains and transmits this *blocking vertex T* along with the complaint. The process p_k receiving the complaint can do the following

- If T is already inserted signal p_i to retry insertion.

- The vertex T has been deferred, i.e. it has been aborted before, signal p_i to retry insertion.

- The blocking vertex T is part of the active virtual domain. Check if the vertex T has been aborted, i.e. p_k is complaining to some process p_j. If p_i and p_k complaint on each others vertices, i.e. $p_j = p_i$, the higher ranking process is allowed to resume the insertion of its vertex while the other will defer the insertion of its vertex.

The abortion of the insertion process before complaining is required to reduce interference with other processes as well as ensuring that outdated data will not be used when continuing the vertex insertion. It is additionally required to remember the outcome of a received or sent complaints to deal with the rare case that two processes complain an each other about the same vertices repeatedly. This can happen due to message delays and will not be explained in detail. The solution is to check the status of the blocking vertex – by asking the responsible process – before the vertex that has been deferred will be considered for insertion again.

Synchronize vertex copies   All vertices of neighbor processes are kept as local copies to a process (Sec. 4.4.1). In line with the insertion of vertices there are vertices which are not part of the border of processes domain. Thus, all vertices are send to neighbor processes when they are inserted. To reduce the amount of communication this is only done before the next message of a virtual domain is sent or just before the algorithm terminates. It is not possible to collect all such vertices and send them in one message as the ongoing insertion of vertices might connect some of those vertices to neighbor vertices located at another process. In this case they are endpoint of simplices shared with other processes created later during the routine and therefore need to be present at the corresponding neighbor processes.

Termination of the algorithm   The termination of the algorithm is a non-trivial task due to asynchronous messages and message delays. The basic idea is to select one master process that records messages from any other process when it has completed. A process p has completed when there are no local tasks, the message buffer is empty, and all instructions from neighbor processes p_i are completed. However, this does not guarantee that no message is received by a neighbor process p_i generating new tasks at p. Thus, all processes send *local completion messages* to there neighbors if the former condition is fulfilled. If a process p is locally complete and received messages from all neighbors that they are locally complete as well, p will send a *group completion* signal to the master. When the master has received the group completion signal from all processes it will request for a confirmation of the group completion status and send the routine termination signal if the answer is positive. The confirmation is required because tasks may be send across many process as for example the parallel simplex walk may pass the whole triangulation. Thus, the the local and the group completion is not sufficient to ensure that a process p does not receive a message inducing a new task.

Even this quite complicated concept is not failsafe. It suffers from messages delays. There is a possibility that a task could slip through the termination sequence. That is when all but one process p have completed (group completed). p starts a simplex walk of a vertex V that crosses several processes. When this is the last task, process p reports its complete status to the master. The master in turn request for confirmation which can be granted if the following happens: The process p_i sends vertex V to process p_k. The latter one confirms the completion signal before receiving the vertex V as it has reached the complete status before (see above). Meanwhile p' confirms the completion signal as well as the last task – sending vertex V to $\hat{p}$ – has been finished. This induces the master to terminate the routine before the vertex V is correctly inserted, in the worst case causing an inconsistent triangulation. The solution is to count the number of vertices send to a neighbor process during

```
begin delete_vertices( dlist )              begin deletion_events()
while dlist not empty do                     if blocking requested then
   if messages received then                    if no access then
      call deletion_events()                        deny blocking
   else                                          else
      vertex V ← V ∈ dlist                          block simplex
      for all simplices σ with V ∈ σ do          end if
         if σ not blocked then                 else if unblock requested then
            block σ                               unblock simplex
         else                                  else if blocking successful then
            V → dlist                             if all simplices accessible then
            V ← V ∈ dlist                            delete vertex and fill cavity
         end if                                      send result to neighbors
      end for                                     end if
      if σ : V ∈ σ is shared then             else if access denied then
         if rank > neighbor ranks then           unblock simplices
            block σ                               send unblock request to neighbor
         else                                     V → dlist
            request neighbor to block σ           V ← V ∈ dlist
         end if                                else if result received then
      else                                        if improper deletion history then
         delete vertex and fill cavity               receive delayed messages
      end if                                     end if
   end if                                       apply received changes
end while                                    end if
end delete_vertices                          end deletion_events
```

Figure 4.22: Pseudo code for deleting vertices from a list `dlist`. The left panel shows the serial part of the code. The right panel the response of the process to messages.

simplex walks. The local completion message of a process p_i will transmit the number of simplex walk vertices received form a neighbor process p_k to the same process p_k. This one will check if p_i has received already all vertices such that the messages of p_k will not induce new tasks at p_i. Thus, only local completion message with the correct simplex walk vertex counter will be accepted else another completion message is expected. The other steps of the termination procedure remain as described above.

4.4.4 Parallel deletion algorithm

Parallel deletion is achieved by using the cavity filling method (Sec. 4.3.2). The parallel version has to ensure that the cavities of two vertices that are deleted are not created at the same time. This is achieved by a blocking procedure. A process p_i determines the cavity by collecting all simplices that have the vertex V to deleted as endpoint in a list $\mathcal{L}$. This is exactly the list of metapointers to simplices which are part of the vertex data structure. Note, that these informations are completely available at

the process p as by definition all simplices, that have a vertex V that is owned by p as endpoint, are part of the domain of the process. If necessary the list $\mathcal{L}$ of simplices is sent to all required neighbor processes which block the simplices or reject it if the simplices are already blocked. In the latter case the process p gets a message that the vertex V cannot be deleted at the moment which in turn induces p to send messages to all neighbors that have successfully blocked the simplices to free them again. The vertex will be deferred and p tries to delete another vertex. In case process p gets exclusive access rights to the simplices of $\mathcal{L}$ it removes all the simplices, stores the faces bounding the cavity in a list $\mathcal{F}$ and all neighbor vertices of V in a list $\mathcal{V}$. Those two lists are given to a routine that is basically the incremental construction routine using $\mathcal{F}$ as AFL. The difference is that the vertices are not located via a uniform grid but by a direct search in the list $\mathcal{V}$. This is suitable because the $\mathcal{V}$ has a size < 20 for most cases [4].

The new triangulation $\mathcal{L}'$ filling the cavity is send to all neighbor processes which share simplices of $\mathcal{L}'$. These processes will just create the corresponding simplices and establish the adjacency relations. The routine uses the same termination mechanism used for insertion omitting the confirmations step which is not required here.

Message delays and the deletion history   To detect message delays the deletion history is send to neighbor processes p_i immediately before a a new triangulation $\mathcal{L}'$ is sent. The history transmits all vertices of process p that have been deleted since the last time one of p's vertices that involved the processes p_i had been transmitted. This includes vertices that have been deleted without involving neighbor processes. The receiving processes p_i control if these vertices are already deleted. If not, the message buffer is searched for these vertices to find the instructions for deleting them. Thus, the correct sequence of vertex deletions is restored. To optimize the whole process the test is done only when required, i.e. there must be more than one neighbor process p_i involved. That is possible because MPI preserves the message order between two processes such that the sequence of messages to delete vertices is synchronized between each process pair.

4.4.5 Parallel vertex movement

The movement of vertices required to check for the conservation of simplex orientation (Sec. 4.3.3). This procedure has to take care of the fact that the allowed distance of movement of one vertex depends on how far other vertices were already allowed to move. The incremental change of the vertex positions according to their allowed displacement would require a serial execution but it still can be parallelized as follows:

- Incrementally change the vertex positions respecting the simplex orientation for all vertices that do not have vertex neighbors owned by other processes.

- Move the vertices V that have neighbors owned by other processes p_i if the rank of the process owning V is higher than that of all p_i connected to V.

---

[4]This holds for almost uniform vertex distributions like in biological tissue. The number can vary considerably with other vertex distributions.

```
begin move_vertices( mlist, wlist )
perform weight changes from wlist
while mlist not empty do
  for all V ∈ mlist do
    if orientation violated then
      split displacement
    else
      displace vertex
      remove vertex from mlist
    end if
  end for
  call do_flips()
end while
end move_vertices
```

Figure 4.23: The pseudo code for the kinetic algorithm moving vertices according to `mlist` and performs weight changes according to `wlist`.

- Transmit the changes of vertex positions to all neighbor processes.

- Change all vertex positions of vertices that have neighbor vertices of higher ranking processes.

This procedure reduces the serial execution to only those vertices that are connected to vertices of other processes. Moreover, due to the only pairwise process synchronization this part of the algorithm is also mostly parallel. The update of the regular triangulation which is the second part of the kinetic routine is described in the next section.

4.4.6 Parallel flip algorithm

The sequential algorithm (Sec. 4.2) is a simple search for non-regular simplices in a list of simplices: A simplex of that list that is chosen is called *active* simplex. The orthosphere criterion with its neighbor simplices (the *passive* simplices) is calculated. If a flip is necessary it will be performed, and the new simplices are stored at the end of the simplex list [*Edelsbrunner and Shah*, 1996; *Ferrez*, 2001; *Joe*, 1989; *Lawson*, 1972; *Schaller and Meyer-Hermann*, 2004]. The algorithm iterates through the list. When the end is reached the triangulation has become regular [*Edelsbrunner and Shah*, 1996]. As every valid simplex will become an active simplex at least once it is possible that the same orthosphere criterion is computed twice to check for the flip $2 \rightarrow 3$, three times for flip $3 \rightarrow 2$, and four times for flip $4 \rightarrow 1$. To prevent this overhead every result of a orthosphere criterion with a neighbor simplex is stored at both the active and passive simplices (Sec. 4.4.1).

Before the flip algorithm has been parallelized another optimization that works also with serial implementations has been done. Let $\sigma_{\langle A,B,C,D \rangle}$ be an active simplex and σ_i the corresponding passive simplices with the opposing vertices V_i.

- Check the orthosphere criterion with V_1.

```
begin do_flips()                          begin flip_events()
slist {list of simplices to check}        count message from neighbor process
flist {list of flips}                     if flip counting not up to date then
while slist not empty do                      received delayed messages
   for i = 0 until i < frequency do       end if
      if σ ∈ slist is non-regular then    if flip result then
         if all simplices accessible then    apply changes
            execute flip                  else if flip suggested then
            attach new simplices to slist    if simplices accessible then
            if flip is shared then              apply flip
               store result in flist            store result in flist
            end if                           else
         else                                  reject flip
            block simplices                 end if
            store suggested flip in flist  else if flip suggested by third then
         end if                               if simplices accessible then
      end if                                    store suggested flip in flist
   end for                                   end if
   send flist to neighbors                 else if reject suggested flip then
   call flip_events()                        unblock simplices
end while                                  end if
end do_flips                               end flip_events
```

Figure 4.24: The pseudo code for the parallel flip algorithm. The left panel shows the serial part of the algorithm while the right panel denotes the events following received messages. The term 'frequency' determines the number of simplices which are checked for the Delaunay criterion before parallel tasks are performed. The term 'suggested by third' refers to figure 4.25.
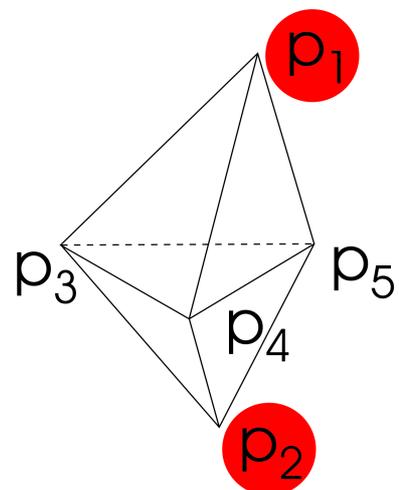
Figure 4.25: Suggestion of flips. A suggested flip that cannot be detected by the processes with access rights to either of the simplices. The flip $2 \rightarrow 3$ shall be detected. The upper simplex belongs to process p_1 and the lower one to p_2 (indicated by red shading). Both processes are not linked because they do not share any simplex (compare figure 4.17). Thus one of the processes p_3, p_4, or p_5 will detect and suggest the flip either to p_1 or p_2. The implementation assures that the flip is uniquely suggested by only one process.

- If V_1 violates $\sigma_{\langle A,B,C,D \rangle}$.

  - If two vertices V_i are equal to V_1 a flip $\mathcal{F}_{4\rightarrow 1}$ is required.

  - If one other vertex V_i is equal to V_1 a flip $\mathcal{F}_{3\rightarrow 2}$ is required.

  - If no other vertex V_i is equal to V_1 than a flip $\mathcal{F}_{2\rightarrow 3}$ can be done if $\sigma_{\langle A,B,C,D \rangle}$ and σ_1 are in a convex configuration.

- If V_1 does not violate $\sigma_{\langle A,B,C,D \rangle}$ then check V_2 doing similar combinatorial checks as for V_1 leaving out the possibilities that imply that V_1 violates $\sigma_{\langle A,B,C,D \rangle}$, i.e. $V_1 \neq V_2$.

This reduces the amount of tests for the orthosphere criterion and for convexity of two simplices taking into account that one orthosphere criterion result holds for several faces depending on the combinatorial structure of the simplices.

The parallel algorithm is based on the definition of access rights to the simplices. The basic idea is to use a relational operation of vertices. A process p has access to a simplex $\sigma_{\langle A,B,C,D \rangle}$ when p has the greatest numbers of vertices in $\sigma_{\langle A,B,C,D \rangle}$ (4, 3, or 2). If several processes have equal greatest numbers of vertices in $\sigma_{\langle A,B,C,D \rangle}$ (all 1 or all 2) the one with the 'largest' vertex (using an arbitrary 'less than' relation) gains access rights. The definition does not require any communication, i.e. any process can determine without communication which simplex is handled by which process. Consequently, blocking of simplices is now a purely local operation. Additionally, this definition of access rights has the favorable implication, that every flip affects only simplices accessible by exactly one or two processes even when four simplices are involved.

In the course of the algorithm a process checks every simplex for local regularity with or without having access rights. Any flip of accessible simplices will be performed by the process. If boundary simplices are involved the result will be stored to inform neighbor processes. This information will be exchanged regularly between the processes (fig. 4.24, left panel). Every process uses the received information to apply the flip sequence generated by the corresponding sending process to its copy of the boundary simplices until the final state is achieved. No further communication is required.

If a flip between accessible and non-accessible simplices is detected by a process p_1 the flip will be *suggested* to the other process p_2 (fig. 4.24). That process will check if this flip is possible which is the case if the simplex has not already been involved in another flip and not been used in a flip suggested by p_2 itself. All possible flips are performed immediately. To prevent deadlocks of processes suggesting each other the same flip, every flip is made unique by process ranking. It is required to perform the orthosphere test with non-accessible simplices as active simplices. That is because the simplex σ accessible by process p may be locally regular when tested by p. Due to changes of adjacent simplices a flip may be induced. There are two ways that the newly created flip configurations got detected. Either the simplex σ gets active or the newly created simplices. The flip algorithm always resolves this be testing the new simplices as they automatically become active at some point as they are stored at the end of the simplex list. However, the access right definition does not care about active and passive simplices. Thus the new simplex might be non-accessible by the process p, i.e. the orthosphere test would be never performed if p does not allow active simplices to be non-accessible by p to perform the orthosphere test.

A special case is that a flip may not be detected by the processes p_1 and p_2 owning the simplices. They may not share all the simplices or they just do not have the corresponding simplex-simplex neighborship relations (Fig. 4.25). The detecting process then suggests a flip to one of the processes p_1 and p_2. The receiving process will detect if this flip is still possible and suggest the flip to the second process like in the case of normally suggested flips (fig. 4.24, right panel).

Termination of the routine   Controlling the termination of the algorithm is widely similar to vertex deletion and insertion. As for insertion the master will request from every process a confirmation of the termination status. The final confirmation is required because a process p_i can report that it is in the finished state while a neighbor process p_k induces new non-regular simplices for the process p_i much like in the simplex walk vertices in the insertion routine.

Message delays and flip counting   The loose synchronization of the processes raises the same difficulties message ordering as in the dynamic algorithms. Similarly as for vertex deletion this is detected by the receiving process. Each group of flips exchanged with neighbor processes will be counted at the sending and receiving end. Additionally, the sending process p_1 will send the counter of all flip messages it has received from its neighbor processes p_i. The receiver p_2 will then check if all flip messages from its neighbors p_k have been received according to the counters. If not, the message will be received and the correct message order is restored. Note that the message synchronization takes place only when the messages depend on each other, i.e. only processes which are neighbors of both processes p_1 and p_2 need to be considered for delayed messages. Otherwise the basic principle 'first come, first served' is applied.

4.4.7   Error handling

Although the algorithms have to be shown to run stably with each routine called several million times an error handling system has been implemented. It can catch errors that appear in functions used as subroutines in the main algorithms discussed above. The process that detects an error throws an exception that is caught within the routines. All local tasks are aborted and all message requests are collected. A special function received messages as long as all processes reported that there are no more messages that have been sent. This bases on the guarantee of MPI point-to-point communication to be in correct order which allows to use a 'stop' signal sent to each process which guarantees that there will no further messages. If the stop signal is received from all processes the routine will be aborted and a complete re-triangulation is performed respecting the changes to the triangulation that have not been applied yet, i.e. include not-yet-inserted vertices, delete vertices, and move all vertices in their final position before triangulating.
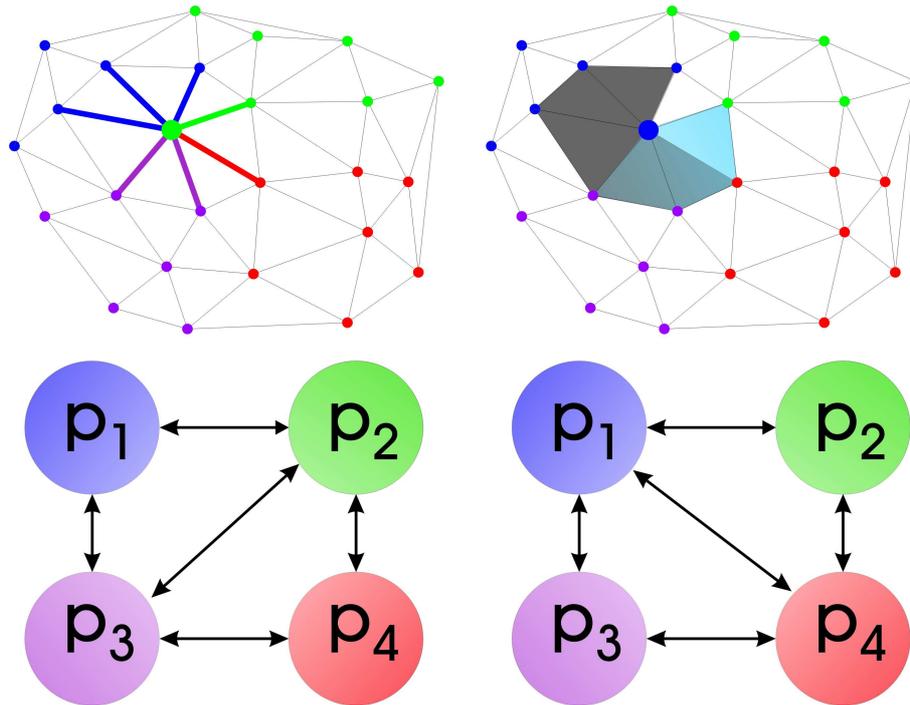
Figure 4.26: Load balancing of the regular triangulation. To optimize the data distribution among the processes the number of connections to each process is counted. Consider the vertex indicated by the large dot (upper left panel). It has three connections to the process marked by the blue color and less connection to all other processes. According to (Eq. 4.84) it is most probable that the blue process becomes the owner of the vertex as indicated in the upper right panel. This imposes some redistribution of data. The blue process need additional copies of the blue marked simplices which where formerly not connected to the process marked with the blue color. Similar the process marked with green does no longer need the copies indicated by the grey shaded and bluish grey shaded area. As a consequence the process topology also changes that is that the process p_1 (blue) and p_4 (red) become newly connected and share common simplices while p_2 (green) and p_3 (purple) get disconnected and do not need to exchange data anymore.

4.4.8 Load balancing

The distribution of the first vertices is done using the geometric partition function of the ParMetis library [*Karypis and Kumar*, 1997]. As the dynamic and kinetic routine frequently change the topology of the regular triangulation it follows that the number of shared simplices is likely to increase. This in turn increases the need for synchronization of tasks and communication, slowing down the overall performance. Dynamic load balancing is use to resolve the need for increased communication tasks.

A very simple approach inspired by the Potts-model [*Graner and Glazier*, 1992] has been chosen (Fig. 4.26). All vertices at the boundary of a processes p domain are tested for rebalancing by counting their number of vertex neighborships to vertices owned by other processes. A probability $P(p_n)$ to

assign this vertex to a neighbor process p_n is calculated by

$$\Delta\mathcal{H} \;=\; \sum_{p_n}\left\{\frac{[C(p_n)-C(p)]}{C}\right\} + \lambda\left(\frac{N_{\mathcal{V}}}{N_{\text{desired}}}\right)^2 \tag{4.84}$$

$$w(p_n) \;=\; \begin{cases} \exp[-\beta\Delta\mathcal{H}] & \Delta\mathcal{H} > 0 \\ 1 & else \end{cases} \tag{4.85}$$

$$P(p_n) \;=\; \frac{w(p_n)}{\sum_{p_n} w(p_n)} \tag{4.86}$$

with $C(p_n)$ the number of vertex-vertex-neighborships with vertices owned by process p_n and $C = \sum_{p_n} C(p_n)$. Note, that the 'volume' term, that tries to keep an optimal number N_{desired} of vertices assigned to own process, only depends on the local number of vertices. This can create a larger imbalance which has no great influence as long as the number of vertices to be re-assigned is low but comes with the favorable property that the algorithm doesn't need communication before moving the vertices.

The re-assignment of vertices is implemented such that the data structure is correctly transfered as required including the creation of new boundary simplices and their adjacency relations.

4.4.9   Results for parallel implementation

The result of the implementation have been published before [*Beyer et al.*, 2005]. The test have been performed on a SGI Origin 3800 with R12000 processors located at the Center for Information Services and High Performance Computing at the Technical University of Dresden.

Each of the algorithms was tested separately using the following protocols. The test systems were uniform vertex distributions inside a cube. Distributions with 1000 (1k), 4000 (4k), 8000 (8k), 16000 (16k), 100000 (100k), and 1000000 (1000k) vertices were used. Most of the tests were performed with usual Delaunay triangulations without vertex weights. The weight has major influence on the initial construction and is tested for the system size of 16k. The performance of the dynamic and kinetic algorithms is widely independent of the presence of vertex weights – provided the weight changes are small. The regular triangulation is tested with a uniform distribution of the vertex weights with values between 0, and 10%, 100%, or 1000% of the average vertex distance. The average vertex distance l is approximated by $l = (V_{\text{cube}}/N_{\text{vert}})^{1/3}$ with V_{cube} the volume of the cube and N_{vert} the numbers of generated vertices. Note, that redundant vertices may be included in N_{vert}. Any operation on the triangulation can change the balance of vertices distributed across the processes. In the tests shown the indicated change started with a fresh partition. Currently dynamic load balancing between the processes is left to the application.

The initial triangulation and the changes in terms of vertex positions, insertions, deletions, and displacements were generated using the pseudo-random number generator 'Scalable Parallel Random Number Generator' (SPRNG) version 1.0 [*at Florida State University*].

The tests were performed on an SGI Origin 3800 with R12000 processors located at the Centre for Information Services and High Performance Computing at the Technical University of Dresden, Ger-

operation	1k	4k	8k	16k	100k	1000k
deletion						
1%	0.02 (0.70)	0.09 (0.80)	0.16 (0.86)	0.37 (0.94)	2.5 (0.98)	26.6 (1.00)
10%	0.19 (0.88)	0.82 (0.93)	1.8 (0.97)	3.7 (0.98)	25.5 (0.99)	258 (1.00)
100%	1.7 (0.94)	8.1 (0.97)	17.6 (0.99)	36.2 (0.99)	246 (0.99)	2660 (1.00)
insertion						
10%	0.05 (0.37)	0.26 (0.72)	0.58 (0.79)	1.1 (0.75)	5.6 (0.85)	109 (0.97)
100%	0.63 (0.69)	3.1 (0.86)	6.6 (0.90)	14.3 (0.93)	89.3 (0.96)	1274 (0.99)
1000%	7.7 (0.79)	34.7 (0.90)	77.9 (0.95)	155 (0.95)	956 (0.97)	
random insertion						
10%	0.06 (0.56)	0.27 (0.74)	0.68 (0.86)	1.6 (0.91)	14.7 (0.97)	198 (0.99)
100%	0.74 (0.63)	3.2 (0.83)	7.6 (0.90)	16.6 (0.93)	156 (0.98)	2377 (0.99)
1000%	8.4 (0.75)	40.1 (0.87)	91 (0.94)	197 (0.95)	1790 (0.98)	
displacement						
10%	0.65 (0.37)	0.82 (1.6)	0.85 (3.3)	0.87 (6.7)	0.83 (24.0)	0.96 (442)
100%	0.64 (1.8)	0.84 (8.4)	17.6 (0.87)	36.4 (0.89)	175 (0.90)	
1000%	10.0 (0.37)	54.6 (0.61)	149 (0.77)	313 (0.79)	1975 (0.83)	

Table 4.1: Table of parallel efficiency for the various operations performed on the triangulation. The experiments were fitted with Amdahl's law [*Amdahl*, 1967]: $t_p = t_s [(1 - f) + f/p]$, with t_p the parallel execution time, t_s the execution time on a single processor, f the fraction of parallelizable work, and p the number of processors used. Shown are t_s (f) with t_s in seconds. Optimal scaling behavior would be $f = 1$. Data points at 1000k vertices and 1000% insertion are missing for hardware constraints.
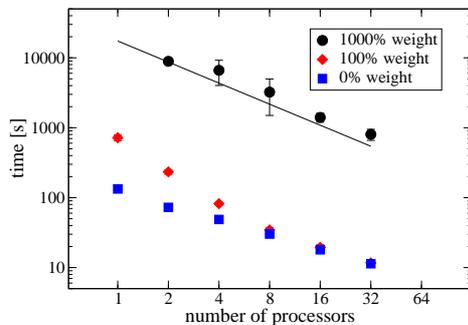
Figure 4.27: Parallel performance of the incremental construction algorithm for 16k vertices with different closed symbols denoting different vertex weights. The line indicates the slope of -1 achieved by optimal scaling for comparison. (The data for 1000% vertex weight have not been measured with 1 processor and contain less than 10 runs per data point for 2, 4, and 8 processors due to extremely long execution times.)

many. Times were recorded using `MPI::Wtime()` command from the MPI library. Error bars indicate one standard deviation out of 10 different experiments with different seeds for SPRNG [*at Florida State University*]. Data points missing in the figures have not been measured due to either large execution times on small numbers of processors, or memory constraints for large sizes, or too few vertices to be distributed efficiently on many processors.

All presented algorithms show a remarkable scaling behavior, i.e. the execution time is decreasing when more processors are used. An overview of the parallel performance is shown in (table 1) as a fit to Amdahl's law [*Amdahl*, 1967].
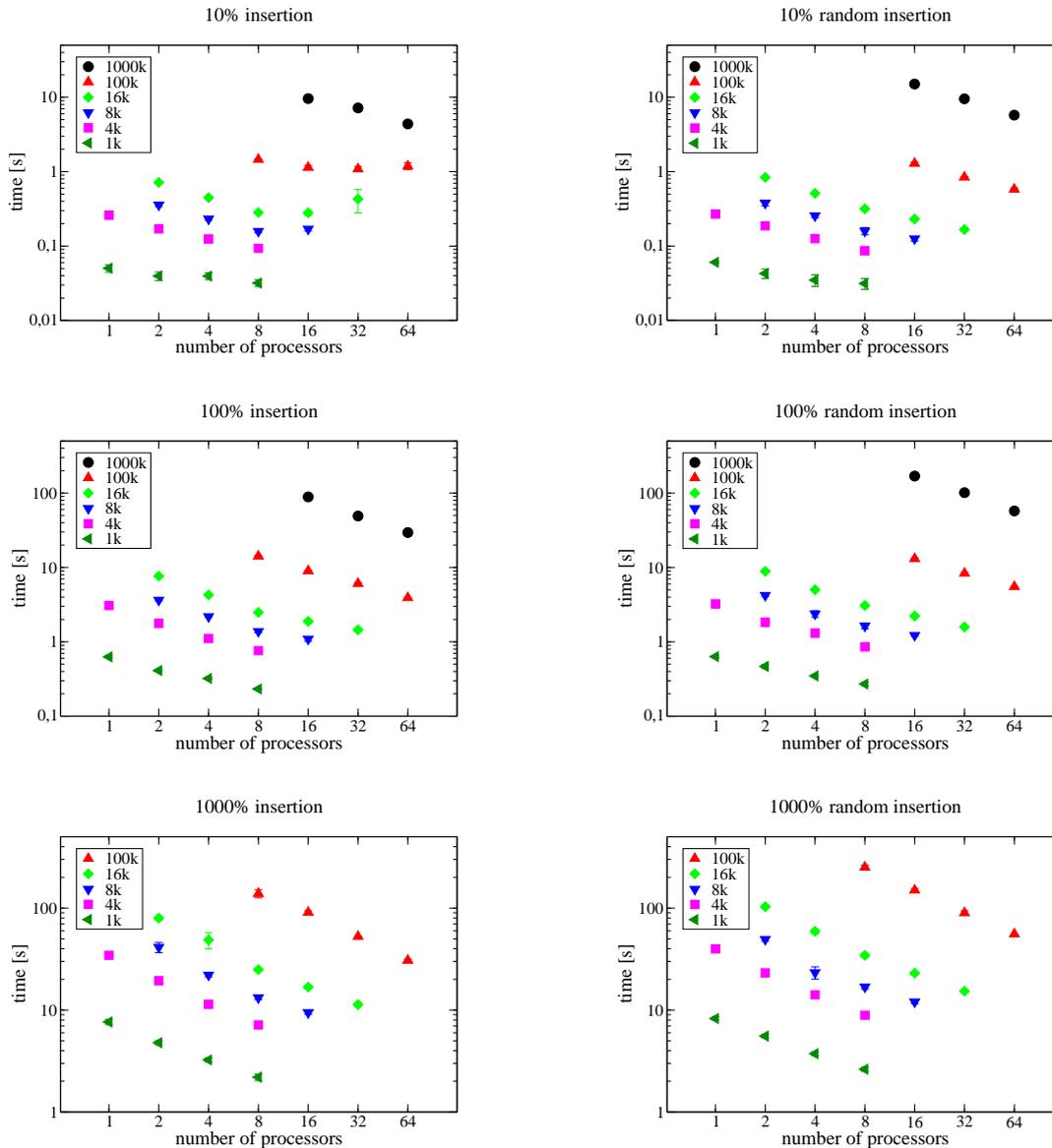
Figure 4.28: Timings of the insertion routine for inserting vertices close to a given vertex (left panels) and without providing an initial guess (right panels). The different symbols denote different initial system sizes while the different panels correspond to different fractions of inserted vertices. See text for details.

Initial construction Although the modified incremental construction algorithm exhibits a sufficient scaling behavior (Fig. 4.27), the cost for inserting a single vertex is high. The execution time of the algorithm increases dramatically when the vertex weights are large compared to the average vertex distance (Fig. 4.27). The time loss is caused by the increased numbers of vertices to be checked during face expansion.

Insertion To test the dynamical insertion of vertices initial triangulations were constructed and vertices were added in two manners: First, the new vertices were inserted close (less than the average vertex distance) to other vertices – mimicking cell division in biological tissues. This is used to pro-
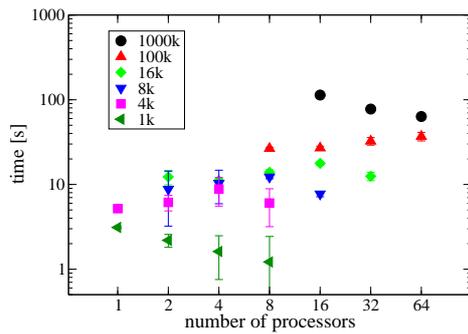
Figure 4.29: The construction times for the initial triangulation using incremental construction and concurrent Bowyer-Watson combined. The different symbols denote different system sizes. Error bars indicate one standard deviation of 100 runs. The construction times are substantially smaller as compared to a pure incremental construction (Fig. 4.27). However, the scaling behavior is destroyed. See text for details.

vide an initial guess where to start the simplex visibility walk. Second, vertices were added randomly inside the cube containing the initial vertex distribution without a guess. Three different numbers of vertices were chosen: (i) A fraction 0.1 of the initial system size (10% insertion). (ii) The vertex number was doubled (100% insertion). (iii) The 10-fold numbers of vertices of the initial triangulation was added (1000% insertion).

The parallel scaling factor of the insertion algorithm shows no significant difference between localized and random vertex insertion (Fig. 4.28) (table 1). For small system size the parallel scaling is reduced, since much of the triangulation consists of boundary simplices requiring much communication. In the case of weighted vertices the insertion times are decreasing with increasing weight (not shown). This effect is caused by an increased amount of redundant vertices. For those the algorithm stops with the completion of the simplex walk omitting the effort of the Bowyer-Watson algorithm.

Despite similar scaling behavior the timing when inserting vertices without initial guess is significantly increased for large sizes indicating the additional time required to locate the first simplex of the Bowyer-Watson algorithm by the simplex visibility walk.

Combining initial construction and insertion   As the initial construction has an unsatisfying serial performance other tests were performed in which 1000 vertices per processor were selected randomly for triangulation using the incremental construction while the remaining ones (if any) are inserted using the concurrent Bowyer-Watson algorithm. The number of vertices has to be chosen sufficiently large in order to distribute them on large numbers of processes.

The overall gain in performance by the combined initial construction is significant as long as a relevant amount of vertices are inserted with the concurrent Bowyer-Watson algorithm (see fig. 4.29 as compared to 4.27). However, the scaling behavior is destroyed. The more processors are used the more vertices are triangulated by the incremental construction algorithm and less by the concurrent Bowyer-Watson algorithm. Therefore the gain achieved by the parallel execution is counteracted by a higher fraction of vertices inserted with the slower incremental construction. The total gain in performance can also be observed when triangulating vertices with different weights. For small weights there is no significant difference to the unweighted case. For large weights the overall construction time is dominated by the slow incremental construction step at the beginning (not shown).
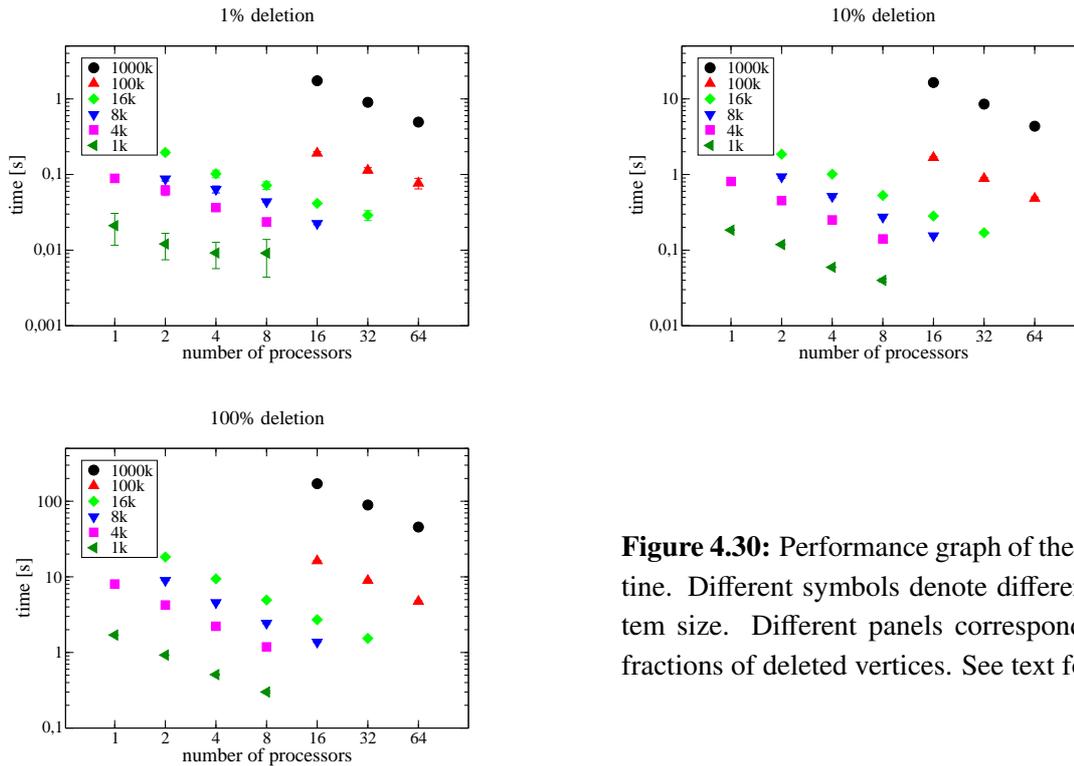
Figure 4.30: Performance graph of the deletion routine. Different symbols denote different initial system size. Different panels correspond to different fractions of deleted vertices. See text for details.

Deletion   The deletion algorithm was tested by removing a randomly chosen fraction of 1%, 10%, and 100% of the triangulated vertices. It exhibits the best scaling behavior of the algorithms presented here (table 1). Smaller gains in performance are observed for small systems and small numbers of deleted vertices (Fig. 4.30). This result reflects the greater influence of inhomogeneities of the data distribution within data-parallel algorithms. The time needed to delete all the vertices is about as large as the construction time for the triangulation (Fig. 4.29). The cause is the slow incremental construction algorithm used to fill the cavity which exceeds the time needed to locate the vertex in the triangulation with the concurrent Bowyer-Watson algorithm.

Moving vertices   In the kinetic tests all vertices have been moved by choosing every component of the displacement vector uniform randomly within a symmetric interval $[-l, l]$ with l equal 10%, 100%, or 1000% of the average distance of vertices (Fig. 4.31). For most applications the smallest displacement is realistic. The numerical experiments also support the view that larger changes in the triangulation are inefficiently solved by the flip algorithm. As mentioned before the problem of non-flippable configurations can arise when moving all vertices synchronously. Indeed, for 100% displacement this occurred quite frequently while in the case of 1000% displacement almost none of the new configurations could be achieved by the flip algorithm and the run got stuck in non-flippable configurations. When the code detects such situations, the triangulation is recomputed form scratch. Therefore the presented timings consist of the time needed for the flip algorithm until failure plus the time for a complete re-triangulation (Fig. 4.31). Thus, only displacements significantly smaller than the average vertex distance take advantage of the flip algorithm to restore the Delaunay criterion. Note that, all times shown include the time for checking the orientation of simplices before applying
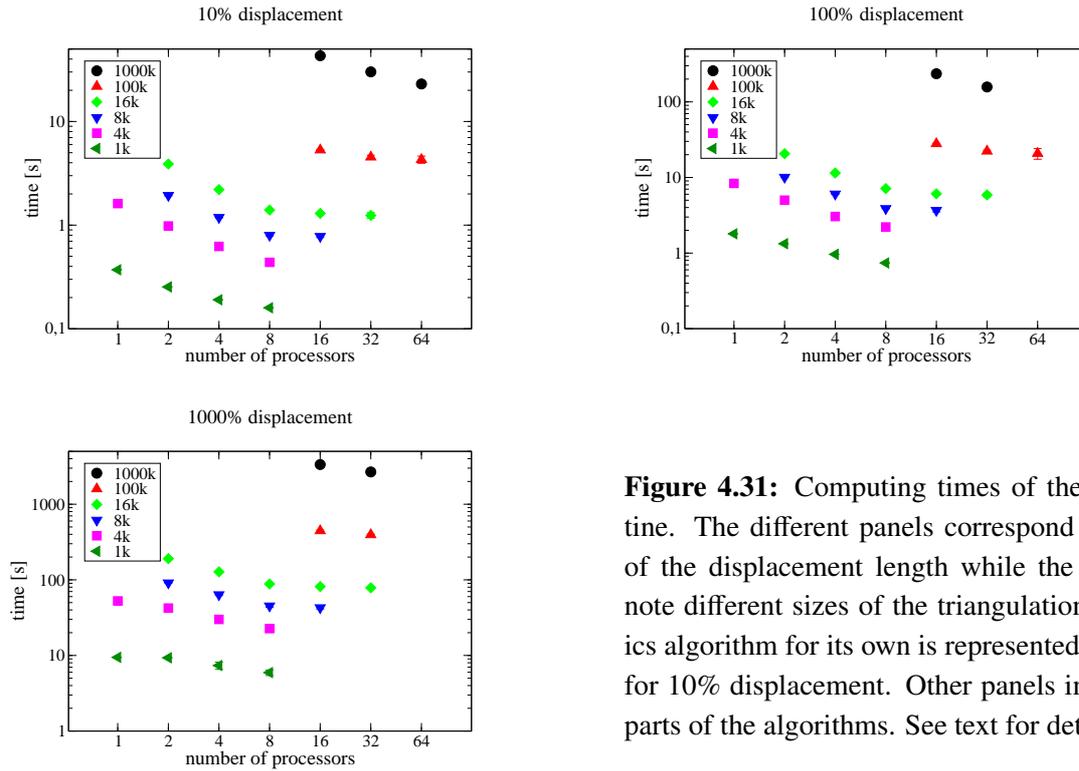
Figure 4.31: Computing times of the kinetic routine. The different panels correspond to variations of the displacement length while the symbols denote different sizes of the triangulation. The kinetics algorithm for its own is represented by the graph for 10% displacement. Other panels intermix other parts of the algorithms. See text for details.

the vertex displacements (Sec. 4.3.3) and the *a posteriori* orientation check.

4.5 *Summary of regular triangulation algorithms*

To overcome current computer hardware limits it is desirable to develop parallel algorithms for dynamic (vertex insertion and removal) and kinetic (vertex displacement) regular triangulations. Although serial algorithms exist for either dynamic or kinetic vertices [*Bowyer*, 1981; *Edelsbrunner and Shah*, 1996; *Ferrez*, 2001; *Joe*, 1989, 1991; *Lawson*, 1972; *Schaller and Meyer-Hermann*, 2004; *Vigo and Pla*, 2002; *Watson*, 1981], parallel solutions in three dimensions are limited to solutions of subproblems. To our knowledge no parallel deletion algorithms exist while vertex insertion is restricted to the Delaunay triangulation, i.e. not covering the more general regular triangulation [*Chrisochoides and Sukup*, 1996a,b]. The only parallel solution for kinetic vertices is based on shared memory architectures and limited to small displacements [*Ferrez*, 2001]. The task to generate an initial Delaunay triangulation is achieved by many parallel solutions [*Blelloch et al.*, 1999; *Cignoni et al.*, 1993; *Kolingerova and Kohout*, 2002; *Lee et al.*, 2001; *Teng et al.*, 1993], but none of these can generate regular triangulations. Additionally a part of these solutions relies on specialized architectures like shared memory, limiting portability of the algorithm and implementation code.

This work presents a parallel algorithm for the construction and maintenance of regular triangulations supporting dynamic vertices (insertion and deletion) as well as a parallel scheme for vertex kinetics (movement). The tool is appropriate for arbitrary partitions of vertices and for arbitrary vertex distributions. An important issue of the present work is to avoid a predetermined partition of the vertices

like in the projection-based algorithms [*Blelloch et al.*, 1999; *Lee et al.*, 2001]. This allows to distribute vertices according to the needs of the application, e.g. tissue simulations, rather than to an optimal partition for the triangulation itself.

Chapter 5

Cell model

In this part the underlying cell model and model concepts for describing biological tissue are presented. There are three levels of modeling which will be discussed separately including their relationship among each other. The theoretical description of biological phenomena like chemotaxis are described thereafter. This will also cover the concrete realization of chemotaxis within the three level concepts of the tissue simulations software. A parameter table with the most common parameter choices is given at the end of this chapter (Table 5.4).

5.1 Available Models for Tissue Simulations

There exist already a number of models to describe certain aspects of the formation of PLF. They will be shortly summarized and discussed in this section.

5.1.1 Models of Cell Migration

There are several models describing cell migration starting from a molecular basis. All of them do not describe the forces exerted to the environment which is the input required for the presented PLF model (Sec. 5). For instance a detailed PDE model was proposed coupling the cytomechanics of deformation and migration to described experimental results on fibroblasts including chemotaxis [*Stephanou and Tracqui*, 2002]. This approach could demonstrate how external stimuli induce morphologic instabilities leading to migration of cells. Another PDE model based on the viscoelastic description of the cytoplasm and actin polymerization dynamics has been used to compute the dependence of the cell's velocity on the adhesion to a substrate [*Gracheva and Othmer*, 2004]. The non-linear dynamics of actin polymerization has lead to several models of cell migration based on symmetry breaking in the system [*Romanovskii and Teplov*, 1995; *Sambeth and Baumgaertner*, 2001]. There exist even more sophisticated models combining several basic concepts to explain several experiments regarding cell mechanics comprehensively [*Herant et al.*, 2003].

There exists a theoretical study on indirect interaction of cells via the elastic properties of the ECM [*Bischofs et al.*, 2004; *Bischofs and Schwarz*, 2003; *Schwarz and Safran*, 2002]. The forces exerted by cells on the matrix induce a prestress which stiffens the ECM. Cells then respond to this stiffened matrix by reorienting their migration. Thus cell interaction and axis alignment is described by force dipoles. The experimental basis for this mechanism has been recently demonstrated [*Kaverina et al.*, 2002]. The tensile stress on cells induces the growth of microtubules which may act as mechanosensor for cells. Due to a lack of experimental evidence and the virtual absence of ECM fibers in the PLF system (Sec. 2.3.1) this guiding mechanism of cells does not enter the model presented in (Sec. 5).

Altogether these models contain to much unconfirmed details to form a reliable basis for a multi-cellular description as needed for the model of the PLF system. Especially the generated forces cannot be derived from most of the models. Thus a simplified approach will be used (Sec. 5.7).

5.1.2 Models for Chemotaxis

Models dealing with chemotaxis can be separated in two classes: population and single-cell modeling. The consideration of cell population models like the Keller-Segel model [*Horstmann*, 2003] and various modifications of it are not suitable to the purpose of the agent-based model. This is mostly because these models – usually partial differential equation models – absorb several microscopic effects in macroscopic variables. For instance volume exclusion is entering those models effectively only. Also the output variables like the speed of cells provides only averaged quantities hiding variables like the distribution of direction of cells which is determining the average cell speed in experiments [*Gunzer et al.*, 2004; *Miller et al.*, 2002; *Okada et al.*, 2005; *Wei et al.*, 2003]. Therefore this section concentrates on the single-cell models.

Models for chemotaxis mostly focus on the internal signaling requirement to sense spatial gradients [*Levchenko and Iglesias*, 2002]. One of the basic assumptions is that global inhibition and local excitation of the signaling cascade provides the underlying mechanism for the gradient sensing in eukaryotic cells. There is a model that investigates how a cell responds to multiple chemokines characterized by their concentrations and gradients [*Painter et al.*, 2000]. This model couples the microscopic behavior – characterized by some not yet determined function – to the population dynamics. In principle it provides the possibility to extract information on the chemotactic response of a single cell to multiple chemokines from the patterns that are observed in cell population. However, this information is not available for the cells considered in the PLF system. Thus the present PLF model cannot give more information than a direct implementation of the observed rules, i.e. the vector sum of various gradients or cross-desensitization (Sec. 5.5).

5.1.3 Models for Tissues

There exist several model types for simulating tissue with increasing microscopic complexity (reviewed in [*Drasdo*, 2003]). This section shall provide a brief overview of methods that have been developed to simulate biological tissue.

Classical approaches The most abstract level of modeling are ordinary differential equations (ODE) dealing with population dynamics. These models have no spatial resolution and treat cells by cell numbers n_i with cell interactions defined by a function f

$$\dot{n}_i(t) = f\left(t, n_i(t), \{n_j\}\right) \tag{5.1}$$

with $\{n_j\}$ denoting a set of different cell populations n_j. Adding spatial information leads to partial differential equations where effects like cell migration enter via diffusive transport ($\nabla(D(\mathbf{x})\nabla c_i(t, \mathbf{x}))$) with diffusion constant D or advective transport ($\mathbf{v} \cdot \nabla c_i(t, \mathbf{x})$) with the cell velocity $\mathbf{v}$:

$$\dot{c}_i(t, \mathbf{x}) = \nabla\left(D(\mathbf{x})\nabla c_i(t, \mathbf{x})\right) + \mathbf{v} \cdot \nabla c_i(t, \mathbf{x}) + f\left(t, \mathbf{x}, c_i(t, \mathbf{x}), \{c_j(t, \mathbf{x})\}\right). \tag{5.2}$$

The space-coordinate x can be one, two, or three-dimensional. This model type requires high cell numbers to have the cell concentrations $c_i(t, x)$ meaningful.

Lattice-based methods A more detailed description is achieved using lattice models. The first type are cellular automata models where each point of a regular lattice corresponds to one cell represented by a finite set of states $\mathcal{S}$. Empty space is treated as a special cell type. The simplest applications provide a set of rules to compute the state $\mathcal{S}_i^{(n+1)}$ at the point i at discrete time $n + 1$ from the state $\mathcal{S}_i^n$ and the states $\{\mathcal{S}_j^n\}$ of the neighbor lattice points j at time n. The neighborhood topology can be chosen very differently depending on the lattice type and dimension. Most common is the Moore-neighborhood on 2D square lattices where the four adjacent horizontal and vertical neighbor points are chosen. Other realizations of cellular automata represent cell movement more directly where a cell at some point is moved to a neighbor site based on certain rules. However, this is not that much different from the usual cellular automata. The latter model can be mapped on the state representation by changing two lattice sites at once. Extensions of these models use probabilities instead of deterministic rules or replace regular lattices by irregular ones like static Voronoi tessellations [*Kansal et al.*, 2000]. Also diffusive substance are coupled to the model in so-called hybrid cellular automata [*Beyer et al.*, 2002; *Deutsch and Dormann*, 2003; *Meyer-Hermann*, 2002] to model the effect of diffusive differentiation signals or chemotaxis.

One form of adding complexity is to represent cells by many lattice sites. A well known and often used model is the extended Potts-model [*Graner and Glazier*, 1992]. It is derived from the Ising-model known in physics. Instead of using two spins (up and down in the Ising-model) N spins equal to the number of cells – where surrounding medium is considered as one cell – are used. In this representation one spin state s corresponds to one single cell of type $\tau(s)$. This type of model incorporates discretized shapes of cells. The interaction of the cells is described analogously to the physical origin with a model energy (Hamiltonian)

$$H = \sum_{i,j;i<j} J_{\tau(s_i)\tau(s_j)}(1 - \delta_{s_i,s_j}) + \lambda \sum_s [V(s,t) - V_0(\tau(s),t)]^2. \tag{5.3}$$

Herein $J_{\tau(s_i)\tau(s_j)}$ is the surface energy of two neighboring sites i and j occupied by the cells s_i and s_j of type $\tau(s_i)$ and $\tau(s_j)$, respectively. The Kronecker-symbol is 1 if $s_i \neq s_j$ and 0 otherwise. It is used to constrain the surface energy sum to the interface between two cells. The second term is a volume constraint to have a cell s close to a target volume $V_0(\tau(s), t)$ for the corresponding cell type

$\tau(s)$. $V(s, t)$ is the volume of the cell calculated by counting all lattice site i which belong to the cell s, i.e. are in the spin state s. There have been several extensions of this model to incorporate chemotaxis [*Jiang et al.*, 1998], proliferation [*Stott et al.*, 1999], or more complex cell shape [*Merks et al.*, 2006] by adding further terms to the Hamiltonian (Eq. 5.3). Like in cellular automata a hybridization by coupling a PDE system is done, e.g. for chemotaxis. There has been one attempt to develop the continuous limit of the extended Potts-model [*Turner et al.*, 2004]. However, this has been done for 1D only and generalizations for (Eq. 5.3) are also not included.

A recent model for representing cells by many sites on a lattice is hyphasma [*Meyer-Hermann and Maini*, 2005b]. The dynamics of the cell's subunits follow a complete different scheme than the extended Potts-model. The volume of cell's is strictly conserved. The subunits are moved according to a probability p that is calculated based on the cells speed v, space resolution Δx, and cellular polarity $\mathbf{o}$

$$p = \frac{1}{\eta} \frac{\Delta t}{\Delta x} v \qquad (5.4)$$

with Δt denoting the time resolution and η a viscosity that summarizes all external and internal friction forces acting on the moving cell. The cellular polarity $\mathbf{o}$ determines to which free lattice sites the cells subunits move. An additional force – that modifies the probability p – drives the cells towards a spherical shape in order to maintain cellular integrity. The model has been used to simulate two-photon imaging data on lymphocyte migration in SLT [*Meyer-Hermann and Maini*, 2005b; *Miller et al.*, 2002]. However, the simulation has been performed with single cells moving in 2D. More complex situations like 3D and many interacting cells (especially dense tissue are still in development.

Off-Lattice methods The microscopic details of the description of cells can be increased by a continuum space representation. Instead of a composition of the cell by multiple sites of a discrete lattice one can propose the shape of the cell and add deformability [*Dallon and Othmer*, 2004; *Odell et al.*, 1981; *Palsson*, 2001; *Palsson and Othmer*, 2000]. For example ellipsoids are used [*Dallon and Othmer*, 2004; *Palsson and Othmer*, 2000]. The three axes of the ellipsoid change their length following forces exerted on the model cell. The response to these external forces are calculated according to effective viscoelastic models like the Voigt- or the Kelvin-model (see also (Fig. 5.6)). Consequently, the rotation of cells enters as additional degree of freedom. Alternatively the effect of deformable cells can be taken into account without explicitly describing the cell shape. Cell interactions in this approach are modeled by potentials [*Drasdo*, 2003; *Drasdo et al.*, 1995]. Therefor the dynamics of the system and the effective cell shape result from the interactions imposed by the potential that may depend in the inter-cell distance, the size of the cell, and other cell properties.

Another ansatz is to let the cell shape be determined by the neighbor cells like in the Voronoi method. This has been used for tissues in 2D [*Meineke et al.*, 2001] as well as for 3D [*Schaller and Meyer-Hermann*, 2005]. The Voronoi method is like an intermediate between imposing a cell shape and using potentials only. The shape of the cell results from the dynamics of the system and affects the interaction of cells which is described either by potentials or directly by forces acting on cells. However, in contrast to the first method of this paragraph the cell shape has no 'internal' dynamics, i.e. it is a only dependent on inter-cellular interactions and cell parameters. The difference to the

potential ansatz is that the potentials are dependent on the cell shapes.

A quite different approach to include cell shapes uses deformable space-filling polyhedrals [*Honda et al.*, 2004]. The dynamics of the cells is described by equations of motions for the vertices of the polyhedrals, i.e. the cell surface. Thus the faces of the polyhedrals are not of fixed shape. The major advantage is that cells are described by objects that neither overlap nor produce gaps which is the case in all other approaches discussed in this paragraph. Also the dynamics of the vertices allows to include inter-cellular and intra-cellular interactions in a comprehensive way. The major drawback of the method is that it demands a high amount of computer resources per cell thus allowing to model only rather small numbers of cells.

The model architectures with most similarities to the PLF model presented in this chapter are off-lattice models with deformable ellipsoids [*Dallon and Othmer*, 2004; *Palsson and Othmer*, 2000]. The PLF model differs in three major aspects from these models: The shape of the cells is described by a modified Voronoi cell (Sec. 5.4.1) instead of a deformable ellipsoid. The definition of a neighbor is done using a regular triangulation (Chapter 4 and this chapter) And finally, the rotational degree of freedom of a solid-like cell ellipsoid is not taken into account in the PLF model.

A model system with similarities to lymphoid tissue So far only model architectures have been presented. There is also an application to a biological system that shows a number of characteristics that can be found in the PLF system as well. The crawling slug stage of *Dictyostelium discoideum* was studied many times with various methods. Among them are hybrid cellular automata and PDE models [*Jiang et al.*, 1998; *Savill and Hogeweg*, 1997]. Other developmental stages of *Dictyostelium discoideum* were also investigated using off-lattice models [*Dallon and Othmer*, 2004; *Palsson and Othmer*, 2000]. This system shares the high motility of many cells in amoeboid motion with the PLF system in which patterns of cell types appear. In sharp contrast it lacks a stromal cell type and has a constant number of cells, i.e. does not cover the situation in which cells in a flow equilibrium form a morphological pattern.

Conclusions on existing model architectures Considering the modeling of cell migration the lack of a comprehensive theoretical model for cell migration is a drawback. The huge amount of information about the force generation and shape of cells is mostly acquired on two-dimensional substrates. Thus the link to the force pattern in loose ECM that is present in the SLT is missing. Moreover the influence of the high cell density in the tissue, where each cell has all the time contact with other migrating cells is unknown. The interplay of migrating cells in tissue has been investigated with various theoretical models. Those models – especially the off-lattice methods – will in part enter the model used to simulate the organogenesis of PLF explained in detail in this chapter.
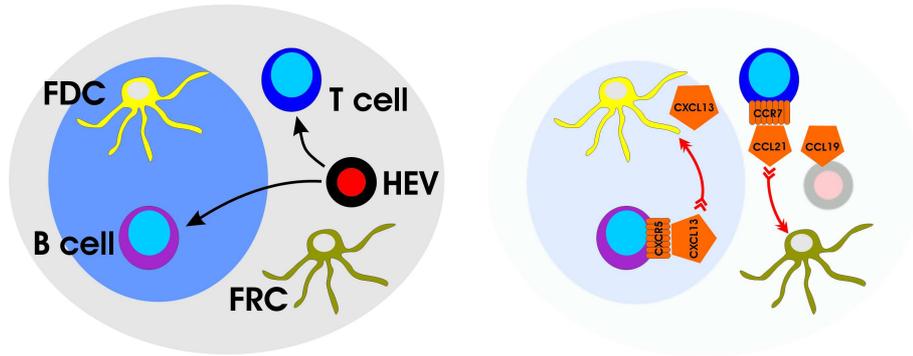
Figure 5.1: Basic interactions in the follicle. B cells and T cells enter through blood vessels. B cell migrate towards FDC in response to the chemokine CXCL13 secreted by FDC. T cell chemotax in the T zone towards CCL21 produced by FRC.

5.2   Model of the primary lymphoid follicle

This section will summarize the basic underlying concepts that will enter the model of the PLF system (Fig. 5.1). The model system is composed of two cellular components, the lymphocytes and the stromal background. The stromal cells form a network that is rather immobile (Sec. 2.2.4) and (Sec. 2.3.1). The cells of the network can produce either CCL21 associated with FRC (Sec. 2.2.4) or CXCL13 associated with FDC (Sec. 2.2.3). According to the experimental data the molecule $LT\alpha_1\beta_2$ is required to generate and maintain stromal cells in the FDC state. All other members of the TNF superfamily are summed up in this signal molecules not taking into account the different requirements for lymphotoxins and TNF-α in the different SLT assuming that the basic differentiation process is similar. Consequently, the FDC generating process is assumed to be basically the same in organogenesis and lymphneogenesis with just renamed players as discussed later (Sec. 6). Lymphocytes, as the second cellular component, enter the model system at some spots simulating HEV (Sec. 2.3.2). To allow for a complete circulation these cells require exit points. In the simulation the lymphocytes are just removed from the simulation at those specific sites accounting for the emigration of lymphocytes through ELV (Sec. 2.3.3). In contrast to the stromal background the lymphocytes are quite mobile cells which has to be included into the model properly. Additionally, B cells provide the critical $LT\alpha_1\beta_2$ signal that can be enhanced when they encounter CXCL13 as it is suggested by the positive feedback loop found in the spleen (Sec. 2.2.2). The dynamics of the various components, e.g. angiogenesis or chemokine receptor desensitization are discussed in the following sections. The results of the dynamics are subject to the next chapter (Sec. 6).

5.3   Cells as point-like particles with internal degrees of freedom

The most fundamental part of the cell model is an internal state vector ϕ of the cell's internal degrees of freedom. That includes (Fig. 5.2)

- surface receptor and ligand concentrations,

- cell cycle status,

- and internal timings.

The detailed variables used in the tissue simulation will be given in the result section together with their impact on the model outcome (Sec. 6).

A class of variables are internal event timings τ (Table 5.1). The dynamics of processes like proliferation or apoptosis are described by these variables. Depending on the external or internal states of a cell the time until a certain event occurs is determined. This can be a normally distributed time or a fixed time without fluctuations. These times are compared to an internal clock. The event that is reached first will be executed which may in turn modify the whole internal state ϕ including the event itself and other event's timings.

Another set of variables is represented by binary values β. Herewith discrete properties of cells are described. This set of variables defines the type of cell as well as subtypes of the cell. In the model there is no clear distinction between cell types and subtypes as the β defines the behavior under the influence of internal stimuli (like τ) or external stimuli, e.g. does the cell react to a certain stimulus or not. The variables ϕ include the presence or absence of receptors or ligands. In certain cases the receptor/ligand dynamics is included such that an additional continuous variable describes the receptor/ligand level (Sec. 5.5) and (Sec. 5.6).

Finally, a set of variables describes the mechanics of the cell:

- velocity

- orientation

- (target) volume

These variables couple directly to the next level of description, the contact interaction of cells, and have no influence on other internal states ϕ directly but can influence the variables ϕ of neighbor cells.
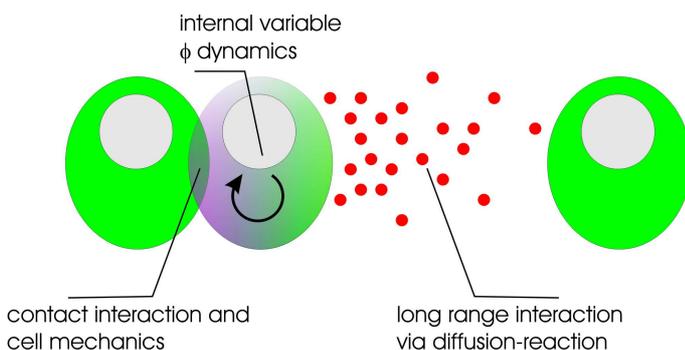
Figure 5.2: The three basic levels of cell modeling. The internal variables ϕ change the way a cells responds to external stimuli provided either by contact (level 2, mechanical interaction) or by diffusing substances (level 3).

variable	distribution	description
proliferation time	normal	time until next mitosis
life time	normal	time until the cell enters the irreversible state of apoptosis
differentiation time	none/normal	time until the next differentiation occurs, no fluctuation with external triggers
contact time	none	similar to an integrator of external contact-dependent signals
stimulus time	none	similar to contact time integrating the time the cell is exhibited to a certain stimulus (e.g. chemical signal)
persistence time	none	used for cell migration to determine when the cell enters/leaves a migration cycle (Sec. 5.5)

Table 5.1: Overview of internal timing events. No distribution indicates that no fluctuations of the variable are taken into account. Note, not all of these variables are actually used in the simulation of the PLF system.

5.3.1   Cell differentiation

The general realization of cell differentiation is derived from the change of the binary states β upon internal stimuli or external stimuli as indicated in the previous section (Sec. 5.3). Here the details specific to the model describing the PLF system are presented. One fundamental question in the PLF formation is: Where do the FDC come from? In the model this is realized via the differentiation of FRC to FDC (Fig. 5.3). This can be viewed as FDC being an 'excited' state of stromal cells. However, the FRC origin needs not to be interpreted in a strict sense. It is also possible that FRC and FDC have a common progenitor which can develop in either FRC or FDC depending on the external stimuli (see also (Sec. 6)). Experimental evidence suggests that FDC are of stromal origin (Sec. 2.2.3) supporting the direct interpretation of the FDC differentiation model outlined hereafter. Also contradictory data exist that identify non-stromal cells of hematopoietic origin FDC-precursor. It cannot be excluded that FDC are a heterogeneous cell population and that the typical properties of FDC – e.g. dendritic shape, IC trapping, CXCL13 production – are just states that can be induced on different cell types. An interesting hint for this comes form studies showing that follicular T helper cells can produce CXCL13 [*Kim et al.*, 2004a] previously thought produced exclusively by FDC.

Within the model an FRC differentiates to an FDC when the signal threshold for $LT\alpha_1\beta_2$ has been exceeded for a given time $T_{FRC\leftarrow FDC}$ (Fig. 5.3). The signal is determined by summing up all $LT\alpha_1\beta_2$ contributions from neighbor cells, i.e. surface density of $LT\alpha_1\beta_2$ times contact area. The differentiation is then instantly performed changing the internal cell states of an FRC into that of an FDC. In a similar manner FDC differentiate back to FDC after the $LT\alpha_1\beta_2$ signal is below the threshold for a given time $T_{FDC\leftarrow FRC}$ (Sec. 2.2.3) [*Bofill et al.*, 2000]. To reduce the amount of parameters and considering the lack of experimental data $T_{FRC\leftarrow FDC} = T_{FDC\leftarrow FRC}$. The presence or absence of the signal must be continuous for the time $T_{FRC\leftarrow FDC}$. If it is interrupted the time integration will start from the beginning. For instance if the $LT\alpha_1\beta_2$ signal given to an FRC drops below the threshold the signal is required to persist for the time $T_{FRC\leftarrow FDC}$ to induce FDC differentiation independent of the integrated stimulus
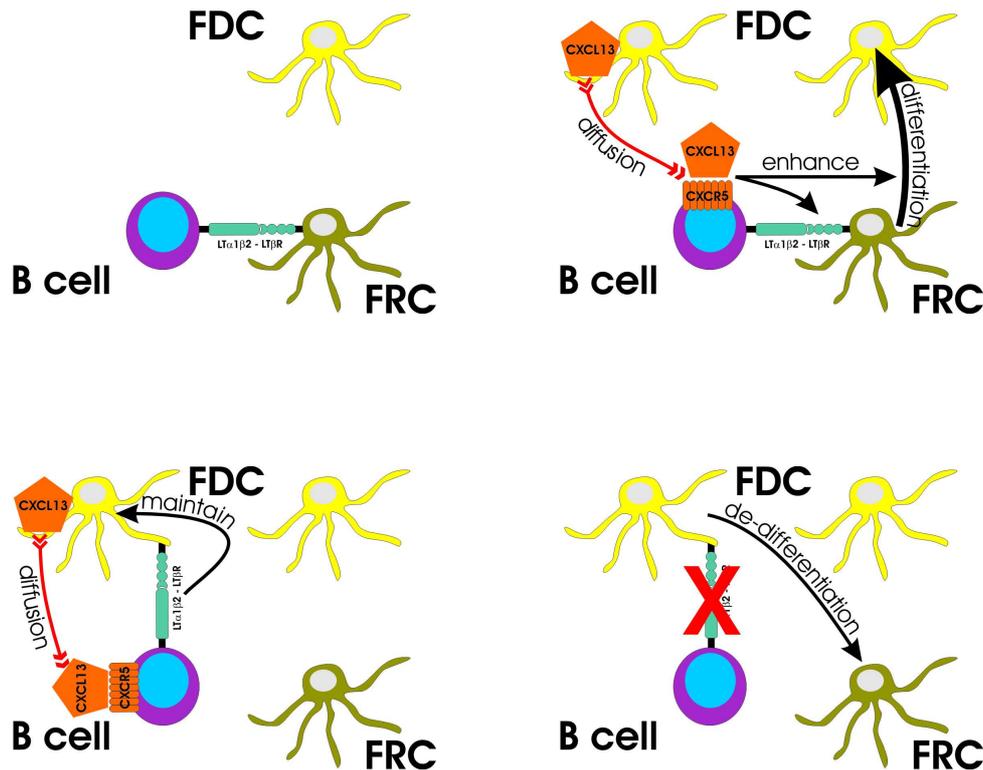
Figure 5.3: Model of FDC generation. First a sufficient $LT\alpha_1\beta_2$ signal from B cells induces the differentiation of FRC into FDC (upper left panel). These in turn produce CXCL13 which increases the $LT\alpha_1\beta_2$ level on B cells further promoting the differentiation of FRC (upper right panel). A second function of $LT\alpha_1\beta_2$ is to maintain FDC in their FDC state by constitutive signaling through B cells (lower left panel). Without this stimulus the FDC backdifferentiate to FRC (lower right panel).

before the interruption. Also the thresholds for $LT\alpha_1\beta_2$ are identical constants for FRC to FDC and FDC to FRC differentiation. The value of the thresholds and stimulus time $T_{\text{FRC}\leftarrow\text{FDC}}$ is motivated by the following arguments and supported by the numerical experiments in (Sec. 6.1). First of all the differentiation must be a slow process compared to cell migration to allow a stable situation. Second the threshold should be such that only sufficient number of cells can induce FDC/FRC differentiation. On the contrary the threshold must be low enough to ensure a high probability for the formation of a sufficient number of cells signaling together to exceed the threshold. This has to be robust against 'contamination' by other cells as it cannot be expected that the total area of cell, e.g. an FRC, can be used for signaling, i.e. the cell is totally engulfed by the signaling cell type, e.g. lymphocytes.

This simple model contains basic observations from experiments but does not cover detailed signal dynamics which by itself is yet unknown.

To account for the dynamics of the T zone during generation it is assumed that FRC develop from a chemokine-negative stromal precursor. CCL21 expression is used to characterize the T zone FRC in the model. The induction of CCL21 expression is dependent on the presence of lymphocytes or LTIC during organogenesis (Sec. 2.2.2). Similar to FDC differentiation this process is modeled as differentiation by a stimulus exceeding a certain threshold. The production of TNF-α and $LT\alpha_1\beta_2$ is considered to be critical for the differentiation of FRC precursor into FRC expressing CCL21 based

on experimental data [*Katakai et al.*, 2004b] (Sec. 2.2.4). Also unknown factors seem to play a role for the expression of CCL21 (Sec. 2.2.4). In complete analogy to the FDC generation the parameters are also set to the same value as for FDC-FRC differentiation as experimental backup is missing.

5.4 Cell mechanics and contact interaction of cells

Using an off-lattice model one has to define the cell contact separately. In contrast to lattice models where neighborhood topology, contact areas, and distances are predefined this has to be calculated from the actual cell configuration. The regular triangulation can provide the neighborhood topology from which the basic variables contact distance and area are calculated. The cell volume plays a role as volume exclusion should be respected. Also the use of cells of different size, e.g. during a growth process after cell division or differentiation, needs to be defined properly.

To incorporate cell mechanics into the model there are many sophisticated models on the single-cell level available. However, as pointed out in section 5.4.2 they are far to detailed on one side and not general enough on the other side to be useful for the purpose of this work. Therefore, the physical model of Johnson, Kendall, and Roberts for adhesive elastic spheres is used (Sec. 5.4.3).

The basic equation for cell movement is the Newtonian equation of motion in the overdamped approximation [*Dallon and Othmer*, 2004; *Schaller and Meyer-Hermann*, 2005]

$$
\begin{aligned}
m_i \ddot{\mathbf{x}}_{\mathbf{i}}(t) = & \mathbf{F}_i^{\text{drag}}\left(\dot{\mathbf{x}}_i, \{\dot{\mathbf{x}}_j\}_{\mathcal{N}_i}\right) + \mathbf{F}_i^{\text{active}}\left(\phi_i(t)\right) \\
& + \sum_{j \in \mathcal{N}_i} \mathbf{F}_{ij}^{\text{active}}\left(\phi_i(t)\right) + \sum_{j \in \mathcal{N}_i^c} \left[-\mathbf{F}_{ji}^{\text{active}}\left(\phi_j(t)\right) + \mathbf{F}_{ij}^{\text{passive}}\left(\mathbf{x}_i(t), \mathbf{x}_j(t)\right) \right] \approx 0.
\end{aligned} \tag{5.5}
$$

The single force contributions acting on cell i explained in detail in the following sections are (Fig. 5.4):

- The force generated by the cell $\mathbf{F}_i^{\text{active}}(\phi_i(t))$ acting on the ECM – which is assumed to have approximately infinite mass as the ECM is connected to the whole organism (Sec. 5.7). Thus there is no backreaction of ECM-forces included.

- Active forces $\mathbf{F}_{ij}^{\text{active}}(\phi_i(t))$ exerted to the surrounding. The set $\mathcal{N}_i$ is represented by Delaunay neighbors of the underlying regular triangulation independent whether the cell j is in contact with i or not (Sec. 5.7).

- The cell i also feels all active forces $\mathbf{F}_{ji}^{\text{active}}\left(\phi_j(t)\right)$ which are exerted on it from neighbor cells j in contact ($\mathcal{N}_i^c$) (Sec. 5.7).

- All mechanical forces $\mathbf{F}_{ij}^{\text{passive}}\left(\mathbf{x}_i(t), \mathbf{x}_j(t)\right)$ which are independent of the internal cell state, e.g. forces due to cell collision (Sec. 5.4.2). These force act only between cells $j \in \mathcal{N}_i^c$ that have contact to the cell i.

- According to the overdamped approximation the forces are counterbalanced by the drag force $\mathbf{F}_i^{\text{drag}}\left(\mathbf{v}_i, \{\mathbf{v}_j\}_{\mathcal{N}_i^c}\right)$ collecting all velocity-dependent terms including adhesion (Sec. 5.4.5).
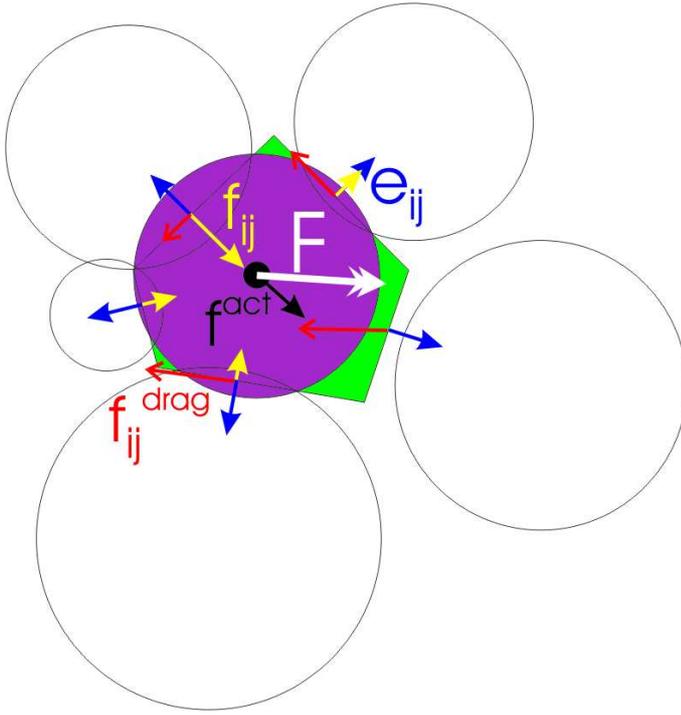
Figure 5.4: Forces acting on the model cell. The various contributions of the force $\mathbf{f}_{ij}$ (yellow arrows) acting on the contact surface with other cells along the normal directions $\mathbf{e}_{ij}$ (blue arrows) and the forces generated by the cell itself $\mathbf{f}^{\text{act}}$ (black arrow) add up to the the total force $\mathbf{F}$ (white arrow). This force is counterbalanced by the drag forces which act tangential to the contact surfaces with other cells f_{ij}^{drag} (red arrows) or against the direction of motion in the case of contact with the medium (red arrow at the right face).

The assumption of overdamped motion is indeed a very good approximation estimated the following way. A single adhesive bond can resist forces of around 1–10 pN [*Mijailovich et al.*, 2002; *Palecek et al.*, 1998; *Sagvolden et al.*, 1999]. The gravitational force of a box-shaped cell of $10\,\mu$m size with the density of water is $\sim 10\,$pN and thus can be counterbalanced by a few adhesive bonds. Estimating the highest accelerations one arrives at $10^{-5}\,\text{ms}^{-2}$ by assuming that a cell reaches a speed of $10\,\mu\text{ms}^{-1}$ within one second. That corresponds to a velocity of $600\,\mu\text{m}\,\text{min}^{-1}$ by far exceeding speeds of real cells (Sec. 3.2). Also the acceleration is by far smaller than the effect of gravitation that can already by counter-balanced be few adhesive bonds. Another estimate can be made by comparing the typical cell velocities with Stokes friction in water with viscosity $\eta = 10^{-3}\,$Pa s. The cell velocity v is then decaying like

$$v(t) = v_0 \, \exp\left\{-\frac{6\pi\eta r}{m}t\right\}. \tag{5.6}$$

Assuming a cell of radius $r = 5\,\mu$m and an initial velocity of $v_0 = 1\,\mu\text{ms}^{-1}$ the cell stops after $\frac{mv_0}{6\pi\eta r} \approx 10^{-11}$m $= 0.01\,$nm – a length scale that has no realistic meaning anymore. It is reasonable to assume that the viscosity of a medium filled with cells is higher than that of water. This clearly indicates that accelerations of cells can be safely neglected in the Newtonian equations of motion. Similar arguments can be found in [*Dallon and Othmer*, 2004; *Schaller and Meyer-Hermann*, 2005].

5.4.1 Cell contact modeling

One of the basic interactions of cells is via cell-cell contact. This brings together receptors and membrane-bound ligands signaling both to the cell interior to trigger the changes of the internal states ϕ. These interactions often depend on the number of receptor-ligand pairs. Although depending

on the system under investigation the interaction is stronger for increased interaction surfaces. The simplest approach is a linear relationship between interaction area and signal strength assuming that receptors and ligands have a constant surface density and clustering phenomena occur only within the interaction area but not over the whole cell surface. It is known for some receptors that they are not evenly distributed over the cell membrane. This could be easily incorporated by defining a polarized density [*Figge and Meyer-Hermann*, 2006]. The dynamics of receptor density would require more sophisticated models involving membrane transport models which is far beyond the scope of this work.

The basic question is how to define the interaction area a_{ij}. In a simple model the intersection area of two spheres can be used. However, when cells are at high density this over-estimates the area. The sum of the interaction surfaces exceeds the total surface of a cell. This might not be too unrealistic as the cell membrane is wrinkled and the real membrane surface area exceeds the apparent surface area [*Bongrand*, 1995]. However, experimentally this is not well defined and would introduce additional uncertainty to the model. Thus, the model is restricted to the apparent surface. Therefore, considering the dense configuration one can use the Voronoi picture of the regular triangulation. In these cases the face of the polyhedra forming the Voronoi cell can serve as realistic estimate for the interaction surface. In the case of low density cells this has the unfavorable property that the interaction areas increase with distance – clearly contradicting the real situation. Consequently, the minimum between spherical overlap and the Voronoi area is used as estimate for the interaction are between two cells [*Schaller*, 2006].

The mechanical implications of the cell contact are discussed in the next section.

5.4.2   Elastic interaction

This section concentrates on the modeling of the mechanical response of interacting cells. This implies the deformation of cells although the shape of the cell does not enter the model explicitly.

The Hertz model

The Hertz model has been derived by Heinrich Hertz in 1882 to describe the contact area and penetration depth of two elastic spheres pressed together with a given force (Fig. 5.5). With the assumption of a linear isotropic elastic media under low strain, the force $\mathbf{F}_{ij}^{\text{passive}} = F_{ij}^{\text{Hertz}} \, \hat{\mathbf{e}}_{ij}$ acting along the normal

$$\hat{\mathbf{e}}_{ij} = \frac{\mathbf{x}_j - \mathbf{x}_i}{\left\| \mathbf{x}_j - \mathbf{x}_i \right\|} \tag{5.7}$$
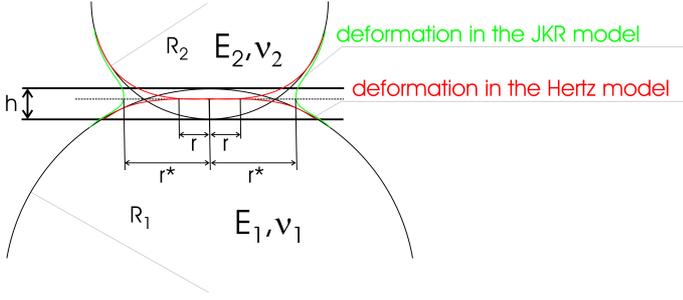
Figure 5.5: The Hertz model for elastic interactions. The deformation of two elastic spheres penetrating each other by a distance h is shown. In comparison the deformation in the presence of adhesion (JKR model (Sec. 5.4.3)) is shown. The contact plane indicated by the dashed line corresponds to the plane where the common face of the corresponding Voronoi cells of the two spheres is located.

is given by

$$F_{ij}^{\text{Hertz}}\left(\mathbf{x}_i, \mathbf{x}_j\right) = \frac{E_{ij}^*}{r_{ij}^*}\zeta_{ij}^3 \tag{5.8}$$

$$\frac{1}{E_{ij}^*} = \frac{3}{4}\left[\frac{1-\nu_i^2}{E_i} + \frac{1-\nu_j^2}{E_j}\right] \tag{5.9}$$

$$\frac{1}{r_{ij}^*} = \frac{1}{r_i} + \frac{1}{r_j} \tag{5.10}$$

with the effective elasticity E_{ij}^* calculated from the elastic constants E_i, E_j and the Poisson ratios ν_i, ν_j of the spheres (cells). The effective radius r_{ij}^* is computed from the sphere radii r_i, r_j. The contact radius ζ_{ij} is dependent on the distance of the two spheres. An alternate formulation with the penetration depth $h_{ij} = r_i + r_j - \left\|\mathbf{x}_j - \mathbf{x}_i\right\|$ yields

$$F_{ij}^{\text{Hertz}}\left(\mathbf{x}_i, \mathbf{x}_j\right) = E_{ij}^*\sqrt{r_{ij}^*}\,h_{ij}^{3/2}. \tag{5.11}$$

Thus the relation between contact radius and penetration depth is

$$\zeta_{ij} = \sqrt{r_{ij}^* h_{ij}} \tag{5.12}$$

which is different from the contact radius resulting from the intersection of two overlapping spheres. However, the Hertz-model is considered as distance-dependent interaction potential between two spherical cells, ignoring the geometrical implications for the other parts of the model depending on the contact area. This choice is motivated by the fact that the Hertz-model describes only two-body forces while the geometric contact areas in the model are derived from the Voronoi tessellation respecting the many-body property. One way to solve the inconsistency is to use the geometric contact ζ_{ij} in (Eq. 5.8). An unfavorable consequence is that the interaction between two cells can change considerably when neighbor cells change their position. This kind of many-body force is not accessible analytically and is therefore hard to study in detail. To avoid uncontrollable situations the distance-dependent description is used (see also (Sec. 5.4.3)).

Tensegrity, non-linear cell behavior and alternative mechanical models

There exist models for cell mechanics that respect the biological nature of a cell better than the Hertz-model taking into account viscous properties or the internal organization of the cell. The dominant cell models are one-dimensional effective models of continuum theory. The basic elements are an

ideal Hooke spring and the Newtonian fluid. The Hooke spring is characterized by

$$\sigma = E\,\epsilon \tag{5.13}$$

with the stress σ linear dependent on the deformation ϵ. The elasticity constant E is a material parameter. The Newtonian fluid is described by

$$\dot{\sigma} = \eta\,\dot{\epsilon} \tag{5.14}$$

where the stress σ depends on the rate of deformation $\dot{\epsilon}$ with the viscosity η as material parameter. More complex behavior is achieved by combing these two elements like an electrical circuit usually called rheological models (Fig. 5.6). One of the most popular models (e.g. see [*Bausch et al.*, 1998; *Dallon and Othmer*, 2004; *Forgacs et al.*, 1998; *Palsson and Othmer*, 2000; *Verdier*, 2003]) is the Kelvin-element which is a combination of a spring and a dashpot (described by the Newtonian fluid) resembling viscoelastic behavior. A cell is then characterized by a spring constant k and a viscosity η. Other models require usually more parameters. An extension of this type of modeling is to use it for three-dimensional deformations of ellipsoids [*Dallon and Othmer*, 2004; *Palsson*, 2001; *Palsson and Othmer*, 2000].

There are numerous experiments on cell mechanics that demonstrate non-linear mechanical behavior of cells. That includes stiffening responses (strain hardening), influence of prestress, hysteresis (e.g. references in [*Stamenovic and Ingber*, 2002]). The are several types of models trying to describe this behavior

- Open foam models consist of a network of elastic rods and predict strain hardening under compression in agreement with experimental data [*Stamenovic and Coughlin*, 1999; *Wang et al.*, 2002a].

- Structures supported by stress require prestress to maintain their structure. The tensegrity model falls into this model type [*Ingber*, 1997, 2000, 2003a,b; *Wang et al.*, 2002a, 1993, 2001a]. It consists of stressed cables which are balanced by compression-supporting rods.

- The tensed cable networks are similar to the tensegrity model [*Stamenovic and Coughlin*, 1999]. The compression force are balanced externally by the ECM and internally by the cytoplasm pressure or cytoskeletal elements. A subtype of this structures is the tensegrity model.

- The cortical membrane model treats the cell as a stressed elastic membrane enclosing the liquid cytoplasm [*Evans and Yeung*, 1989; *Stamenovic and Wang*, 2000]. Mechanical stress is balanced by the pressure of the cytoplasm. This model type seems to fit leukocytes best taking into account the low organization of their cytoskeleton.

- Percolation theory [*Forgacs*, 1995] have been considered in terms of connectivity of the cytoskeleton but have been rarely used to calculate real mechanical responses of cells. Some models based on percolation theory pointing out the importance of direct mechanical signaling to the nucleus which in turn explains in part how the mechanical properties of cells modulate the cell responses [*Forgacs*, 1995].

- Models adapted from polymer physics can quantify effects of thermodynamics of the cytoskeleton [*Forgacs*, 1995] yet they fail to describe pronounced effects of the mechanical response,
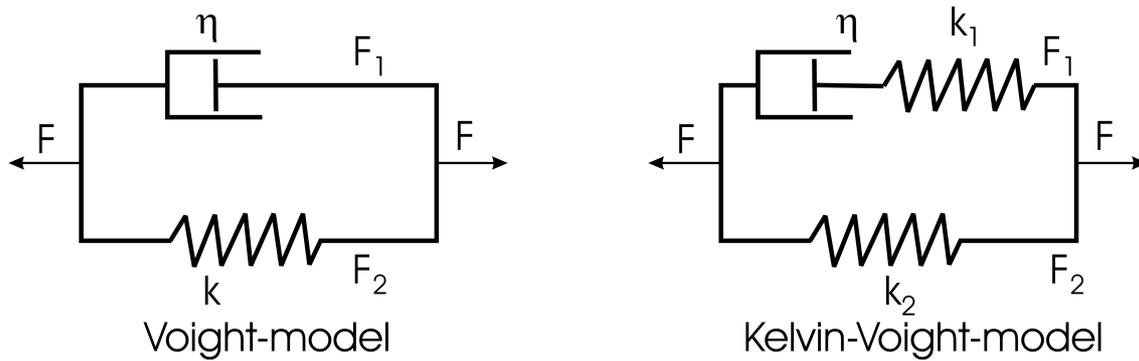
Figure 5.6: Simple viscoelastic models. The Kelvin-model is constructed by a parallel response of a spring (characterized by the spring constant k) and a dashpot (characterized by the viscosity η). The force acting on the element is splitted in two forces with F_1 providing the elastic response and F_2 proving the viscous response. Another often used model is the Kelvin-Voigt-model which has an additional spring in series with the dashpot leading to more complex viscous behavior.

    e.g. prestress [*Stamenovic and Ingber*, 2002].

- Glass-transition models are used to describe the dynamics of the cytoskeleton – which is not possible with the static structure of the first three model types [*Fabry et al.*, 2003]. These models can describe the power-law behavior of the elastic modulus and viscosity in dependence of the frequency of the mechanical stimulus.

- Other models are sol/gel transformation models [*Oster*, 1984]

The stiffening response of cells states that the stress-strain relationship increases stronger than linearly, i.e. the apparent elastic modulus $E = \sigma/\epsilon$ increases with increasing stress σ and increasing strain ϵ. This response requires that the mechanical stimulus is transfered to the cytoskeleton via the appropriate receptors and an intact network structure of all cytoskeleton components – microfilaments, microtubules, and intermediate filaments [*Wang et al.*, 1993]. For this type of behavior the tensegrity model (Fig. 5.7) has been proposed and discussed many times [*Ingber*, 1997, 2000, 2003a,b; *Wang et al.*, 2002a, 1993, 2001a]. The tensegrity model implies the existence of stress fibers to be really applicable. A generalization of this concept to the cortical shell is possible but does not introduce any new insights to the simple cortical shell model. Instead only the required computational power is increased.

The prestress of cells is of the order of $1000\,\mathrm{Pa}$ [*Griffin et al.*, 2004]. Certain experiments emphasize the importance of the prestress as well [*Pourati et al.*, 1998; *Wang et al.*, 1993]. The resulting non-uniform stress distribution has been shown by imaging the strain of intermediate filaments of the cytoskeleton demonstrating that there exist discrete foci of high strain [*Helmke et al.*, 2003; *Hu et al.*, 2003] and high stress [*Hu et al.*, 2003], respectively. There exists also a number of opposing results not observing strain hardening [*Bausch et al.*, 1999] or purely local responses [*Heidemann et al.*, 1999]. The results are summarized in (Table 5.2). Of note the experiments use different cell types used. The 'pro-prestress' fraction is using fibroblast or fibroblast-like cells while the 'contra-prestress' is often using leukocytes. It is known that leukocytes do not from stress fibers [*Friedl et al.*, 2001; *Friedl and Brocker*, 2000; *Samstag et al.*, 2003] such that tensegrity cannot be applied in its strict
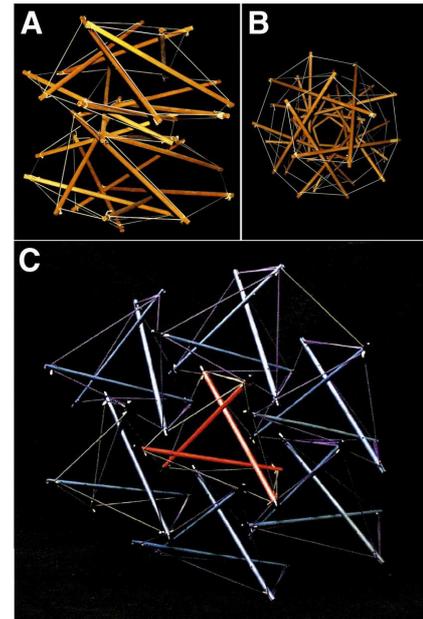
Figure 5.7: Tensegrity model for cell mechanics. A model constructed of strings and bars in side view (A) and top view (B). The name tensegrity means 'integrity by tension' which indicates that the tension provided by the strings keeps the structure in shape. The lower panel shows a model of two interconnected tensegrity structures which are supposed to represent the coupling of the mechanical response of the nucleus (red) with the response of the cell cytoskeleton (blue).
Source: `http://jcs.biologists.org/cgi/content-nw/full/116/7/1157/FIG7`

sense.

The viscoelastic properties are subject to measurements using very different methods like magnetic tweezers [*Bausch et al.*, 1999]. The typical relaxation times are 0.1–10 s [*Bausch et al.*, 1998; *Forgacs et al.*, 1998; *Pourati et al.*, 1998]. The magnetic bead twisting has also been analyzed by finite element modeling demonstrating that this method measures local properties only, i.e. whole cell responses can be quite different [*Mijailovich et al.*, 2002]. Furthermore, a specific magnetic bead twisting experiments could be related to micropipette aspiration techniques by rescaling the material parameters according to the finite element model. Instead of the fine-gridded finite element models the viscoelastic properties are usually described by one-dimensional effective models connecting elastic and viscous elements in different ways (Fig. 5.6). There are also some efforts using generalized non-linear elastic, viscous, viscoelastic, and viscoplastic theories [*Verdier*, 2003]. However, these models suffer usually from the steep increase in the number of parameters.

Much attention has been paid to study the mechanical response of cell spreading on a substrate. An example is to treat the cytoplasm and the nucleus as isotropic elastic media with different elastic moduli. The elastic media are positioned around a tensegrity structure and the whole model cell is enclosed by an elastic membrane [*McGarry and Prendergast*, 2004]. This models can describe the qualitative non-linear behavior of cells which is not really surprising considering the high number of parameters compared to the amount of available experimental data. Other tensegrity-based models investigate the response to compressive load [*Stamenovic et al.*, 1996; *Wendling et al.*, 2003, 1999], oscillatory deformations [*Tracqui and Ohayon*, 2004], viscoelasticity of the cytoskeleton [*Canadas et al.*, 2002; *Sultan et al.*, 2004], response to torque [*Laurent et al.*, 2002; *Stamenovic et al.*, 1996], and spreading of adherent cells [*Stamenovic and Coughlin*, 1999; *Tracqui and Ohayon*, 2004]. One of the results is that the Poisson ratio of tensegrity structure is not a constant but always $\nu > 0.5$ for certain structures [*Wendling et al.*, 2003, 1999]. Another result is that the cells behave softer than their structural elements, i.e. viscosity and elasticity of cells are several orders of magnitude smaller compared to the corresponding values of actin [*Canadas et al.*, 2002]. Other analyses of tensegrity

method and cell type	viscosity η [Pa s]	elasticity [Pa]	forces f [nN]	remarks and source
magnetic bead microrheometer; 3T3 fibroblasts	$2000 - 4000$	$G = 2 \cdot 10^4 - 4 \cdot 10^4$	2	no strain hardening below 2 nN [*Bausch et al.*, 1998]
magnetic tweezer, displacement field; J774 macrophages	210 ± 143	$G = 20 - 735$		no strain hardening [*Bausch et al.*, 1999]
pressure plates; chicken embryonic cells	$10^4 - 10^5$	$G = 100 - 1000$		[*Forgacs et al.*, 1998]
micropipette aspiration, atomic force microscope; erythrocytes			$14 - 27$	[*Hategan et al.*, 2003]
poking with glass needles; REF 52 fibroblasts			70	response is local [*Heidemann et al.*, 1999]
pulling cells; S180 cells + dextran		$E = 3500 \pm 1500$		JKR theory valid [*Chu et al.*, 2005]

Table 5.2: The results of different methods for measuring mechanical properties of cells. Elasticities are given as shear modulus G or Young's modulus E. Forces are either typical forces generated by cells or force applied to cells during experiment.

structures predict softening behavior of cells under certain load conditions [*Stamenovic et al.*, 1996; *Volokh et al.*, 2000]. These are not yet confirmed by experiment.

Together one can conclude that the models can explain certain behavioral characteristics of cells under mechanical stress. However, they are far too complex on one and hand and not general enough on the other hand. Most of the features of the models is tributed to the cytoskeleton. On the contrary the actin filaments in lymphocytes – the dominant cell population in the model – seem to be less organized such that a simpler model can do well enough considering the lack of experiments for this cell type.

5.4.3 Cell adhesion

The adhesion between cells is in principle mediated by any receptor-ligand pair of membrane-bound molecules [*Bongrand*, 1995; *Evans*, 1995]. However, in the literature specific adhesion molecules are discussed whose primary function is to mediate adhesion. There exist several classes of adhesion molecules:

- Cadherins: These adhesion molecules show mostly homophilic interactions. Intracellular domains are anchored to the cytoskeleton. Mostly involved in direct cell-cell adhesion.

- Integrins: Transmembrane heterodimers of α and β subunits which come in two states of affinity to their ligands. Conformational changes can trigger the high affinity state from the low-affinity state. Major ligands are extra-cellular matrix proteins like laminins and fibronectin or cellular membrane ligands like members of the immunoglobulin superfamily. Integrins are intracellu-

larly bound to cytoskeleton directly to actin or indirectly via a linker like talin.

- Selectins: Transiently expressed adhesion molecules in vertebrates consisting of a single transmembrane polypeptide. Main ligands are sialated glycans. Selectins are involved in transendothelial migration of leukocytes.

- Immunoglobulin superfamily cell adhesion molecules (IgCAM): A diverse group of adhesion molecules structurally similar to antibodies.

In the modeling there will be no distinction of these classes directly. They are converted to basic classes of the model distinguished by their function

- CELL-CELL-STRESS: Adhesion molecules that can transmit forces between the cytoskeletons of two cells thus allow to transfer tensile stress.

- CELL-CELL-FRICTION: The second class does not connect the cytoskeletons but is still mediating between two cells. When the molecules are mobile in the membrane this type of adhesion mostly generates friction forces and is not able transmit significant stress across the membrane compared to the former group.

- CELL-ECM-FRICTION: Similar to the group above but the ligand is attached to the ECM.

- CELL-ECM-STRESS: Formally, there would be a class of molecules that connects the cytoskeleton of a cell to the ECM. However, lymphocytes are not tightly bound to the ECM (Sec. 3.2). During migration the adhesion molecules involved in the attachment to the ECM are weakened such that they generate a friction behavior like the third group.

The two classes CELL-ECM-FRICTION and CELL-CELL-FRICTION are summed up in the friction terms given below (Sec. 5.4.5). All adhesion molecules of type CELL-CELL-STRESS enter the elastic response introduced in the next section (Sec. 5.4.3).

The model of Johnson, Kendall, and Roberts

To incorporate adhesion one has to keep in mind that the physical term adhesion is different from the biological use [*Bongrand*, 1995; *Evans*, 1995]. In physical terms it is a reversible process while in biology many phenomena imply active changes by the cell. The attachment of a cell to a substrate by means of adhesion requires additional forces. The forces generated by the adhesive contact are not sufficient to drive the required deformation of the cell [*Evans*, 1995]. The required additional forces can be active forces of the cell generated by the cytoskeleton or forces acting from outside on the cell for instance the experimentalist pushing the cell. On the contrary the forces required to detach the cell can be such high that the cell may break before the contact with the substrate is lost. Together describing the biological adhesion in physical terms would require at least two adhesion energies. One has also to take into account that the cell membrane has a surface that is larger than the apparent surface. This can change the number of adhesion molecules bound to the substrate, i.e. the adhesion strength can change while the apparent contact area seems to remain constant.

The Johnson-Kendall-Roberts model (JKR model) [*Johnson et al.*, 1971] is a modification of the Hertz-model (Sec. 5.4.2) to incorporate physical adhesion between two soft elastic spheres. The adhesion is described by the usual surface energy (σ_{ij}) formulation used in physics implying that adhesion is a reversible process [*Evans*, 1995]. All other parameters remain as introduced in (Sec. 5.4.2).

$$F_{ij}^{\text{JKR}}\left(\mathbf{x}_i, \mathbf{x}_j\right) = \frac{E_{ij}^*}{r_{ij}^*}\zeta_{ij}^3 + \sqrt{6\pi\sigma_{ij}E_{ij}^*\zeta_{ij}^3} \tag{5.15}$$

$$\frac{1}{E_{ij}^*} = \frac{3}{4}\left[\frac{1-v_i^2}{E_i} + \frac{1-v_j^2}{E_j}\right] \tag{5.16}$$

$$\frac{1}{r_{ij}^*} = \frac{1}{r_i} + \frac{1}{r_j} \tag{5.17}$$

The relation between the radius ζ_{ij} of the contact area and penetration depth h_{ij} is no longer like in the Hertz-model (Sec. 5.4.2) [*Schaller*, 2006; *Yang*, 2003]. However, it is still a good approximation. Therefore, the JKR-theory is reformulated in a distance-dependent manner analogously to the Hertz-case.

$$F_{ij}^{\text{JKR}}\left(\mathbf{x}_i, \mathbf{x}_j\right) \approx E_{ij}^*\sqrt{r_{ij}^*}\,h_{ij}^{3/2} - \sqrt{6\pi\sigma_{ij}E_{ij}^*r_{ij}^{*\,3/2}h_{ij}^{3/2}} \tag{5.18}$$

One should keep in mind that this approximation treats attachment and detachment symmetrically, while in reality one would expect different relations [*Schaller*, 2006; *Yang*, 2003]. This would require for each step to calculate the relative movement between each cell pair. However, it is a priori not clear which neighbor cells detach or attach. This depends on the movement of the cells calculated from the equations of motion (Eq. 5.5). Thus, an iterative procedure is needed to determine if cells are attaching or detaching and solve the equations of motion again until a consistent solution is found [*Oron and Herrmann*, 1998]. Solving the equations under this conditions is a non-trivial task. Concerning the experimental situation, i.e. the available data, this seems not to be a necessary effort.

In principle one may use the contact area a_{ij} (Sec. 5.4.1) to calculate the contact radius ζ_{ij} that enters the JKR-model. However, this his an unfavorable consequence. The JKR-model has an equilibrium contact radius (see below Eq. 5.19) respectively area for two cells in contact that defines an equilibrium distance for the two cells. If now multiple cells j surround a cell i it may be possible that all of the neighbor cells j are at a distance larger than the equilibrium distance. Thus all of the cells j would move closer to i. In a Voronoi tessellation that results in smaller contact surface a_{ij} such that the cells may be attracted to the cell i evens stronger. Finally, cell i would be compressed to zero volume which is of course unnatural. The pressure concept that is presented later (Sec. 5.4.4) could compensate this. However, a clear separation between two-cell and many-cell forces is favored such that the unphysiological multi-cell effect of the JKR-model in dependence of the cell contact area a_{ij} is avoided using the approximation by the penetration depth h_{ij}.

The equilibrium distance of cells varies in dependence of the adhesion energy σ_{ij}.

$$h_{\text{eq}} = \left[\frac{6\pi\sigma_{ij}r_{ij}^{*\,1/2}}{E_{ij}^*}\right]^{\frac{2}{3}} \tag{5.19}$$

In the many body case this implies that the equilibrium will not preserve the volume of the cells. One

can make h_{eq} independent of σ_{ij} by scaling all penetration depths to a reference penetration depth h_{ref} using a reference adhesion strength σ_{ref}

$$h \mapsto \left(\frac{\sigma_{\text{ref}}}{\sigma_{ij}} \right)^{\frac{2}{3}} h. \tag{5.20}$$

However, this changes the strength of the JKR force (Eq. 5.15) effectively changing the elasticity while preserving the adhesion. One may also include a constant offset to the penetration depth h such that all cell pairs in equilibrium have an equal real penetration depth. This requires that the offset has to be determined for each cell pair separately. For simplicity one can take advantage of the fact that adhesion is likely to play a minor role in the PLF system, i.e. the highly motile lymphocytes are not observed to adhere significantly to each other [*Gunzer et al.*, 2004; *Miller et al.*, 2003, 2002; *Okada et al.*, 2005; *Wei et al.*, 2003]. Strong adhesion occurs only between stromal cells and lymphocytes (Sec. 2.2.3). Due to the dendritic morphology of stromal cells (Sec. 2.2.3) the spherical approximation of the cell is not good thus that the volume conservation of these cells is not useful to demand for. In conclusion the imbalance of the equilibrium penetration depth between cells of different types can be safely ignored in the PLF system.

The new parameter σ_{ij} added to the Hertz-model has been investigated directly using the JKR model to fit the data. The experimental results for adhesion energies of agarose beads covered with adhesion molecules are in the range of $0.20 \pm 0.01 \, nN\mu m^{-1}$ for specific and $0.02 \pm 0.01 \, nN\mu m^{-1}$ for non-specific interaction defined via the equilibrium surface dissociation constant K_{d} of the adhesive molecules [*Moy et al.*, 1999]. This corresponds to forces of real cells of $\sim 0.1 \, \text{nN}$ and $10 \, \text{nN}$, respectively, depending also on the adhesion receptor density of the cells. Adhesive forces measured directly on cells end up in the range of $20 - 200 \, \text{nN}$ for cervical carcinoma cells taking into account all adhesive interactions between those cells [*Sagvolden et al.*, 1999]. Experimental studies also showed that the JKR-theory fits quite to the experimental [*Chu et al.*, 2005; *Moy et al.*, 1999]. Also the dependence of the surface energy on K_{d} fits to a model known as Dembo-model [*Dembo et al.*, 1988].

$$W = k_{\text{b}} T N_{\text{R}} \ln[1 + (N_{\text{L}}/K\text{D})] \tag{5.21}$$

with Boltzmann constant k_{b}, temperature T and N_{R} and N_{R} being the receptor and ligand densities, respectively.

The JKR model is rather simple considering the complexity of the internal cell structure, i.e. the cytoskeleton. Recent experiments demonstrated that JKR-theory applies surprisingly well to living cells [*Chu et al.*, 2005; *Moy et al.*, 1999]. Even more interesting disrupting the microfilaments of cytoskeleton invalidates the applicability of JKR suggesting that JKR effectively describes certain features of the mechanical behavior of the cytoskeleton. The validity of this is however restricted to contacts in the order of ten seconds. For longer contacts the cytoskeleton may be remodeled resembling plastic flow. Thus, on longer time scales the elastic behavior may get lost and the applicability of JKR to the mechanics of cells suffers.

Modification for strongly compressed cells   One problem with the JKR-model is that the force is limited when two cells are compressed such that one would completely cover the other. The missing

interaction is a kind of hard core repulsion limiting the minimal distance two cells can have. One may modify the JKR force by a term that has a very high repulsing force when the minimal distance is approached. However, this response would also induce too high cell velocities (Sec. 5.4.6). Therefore another approach has been chosen. For each cell being closer than a given minimal distance a strong but finite repulsive force is added. For many cells this results in a vector for the hard core repulsion. All components of the forces that are orthogonal to the hard core repulsion are taken into account. Thus the movement into directions without a hard core interaction is preserved. In the direction of the hard core repulsion a generic force is added such that the cell is moving with a reasonable velocity. The whole procedure is a way to displace the cell deterministically in a direction that avoids the high overlap of two cells on a time scale that is similar to the other interactions while the forces not affected by the hard core repulsion are preserved.

The feasibility can be shown by the following consideration. The solution of the model equations (Eq. 5.5) bases on the forward Euler method (Sec. 5.4.6) such that

$$\mathbf{x}_i(t + \Delta t) = \mathbf{x}_i(t) + \mathbf{v}_i(t)\Delta t \tag{5.22}$$
$$\Gamma_i \mathbf{v}_i(t) = F_i(t, x_i(t)) \tag{5.23}$$

with Γ_i being a friction matrix and $F_i(t, x_i(t))$ being the sum of all force acting on the cell i except friction (for details see (Sec. 5.4.6)). Now with a hard core repulsion acting during a short time scale $\Delta t' \ll \Delta t$ with a high velocity $\mathbf{v}_{hc}$ such that $\mathbf{v}_{hc}\Delta t' \sim \mathbf{v}_i(t)\Delta t$ one can basically separate the fast displacement $\mathbf{v}_{hc}\Delta t'$ from the remaining forces $F_i(t, x_i(t))$

$$\mathbf{x}_i(t + \Delta t') = \mathbf{x}_i(t) + (\mathbf{v}_{hc}(t) + \mathbf{v}_i(t))\Delta t' \tag{5.24}$$
$$\approx \mathbf{x}_i(t) + \mathbf{v}_{hc}(t)\Delta t' \tag{5.25}$$

because $\|\mathbf{v}_{hc}\|\Delta t' \gg \|\mathbf{v}_i\|\Delta t'$ by definition of the hard core repulsion. The choice is motivated by assuming that the hard core repulsion acts on length scales of the order of or below the spatial resolution. Now using $\Delta t - \Delta t' \approx \Delta t$ one gets the new position of cell i after the full time step Δt

$$\mathbf{x}_i(t + \Delta t) \approx \mathbf{x}_i(t + \Delta t') + \mathbf{v}_i(t)\Delta t \tag{5.26}$$
$$\mathbf{x}_i(t + \Delta t) = \mathbf{x}_i(t) + \mathbf{v}_{hc}(t)\Delta t' + \mathbf{v}_i(t)\Delta t \tag{5.27}$$

Note that this introduces an additional error as the velocity $\mathbf{v}_i$ is computed from the force at time t and not at time $t + \Delta t'$ where the position has changed according to $\mathbf{v}_{hc}(t)\Delta t'$. However, one can interpret this equation differently by assuming that the hard core repulsion acts at the end of the displacement which just introduces an error of the order of the spatial resolution to the onset of the hard core repulsion. As the choice for the hard core repulsion is set to be active at large overlaps this large overlap can be defined only with the precision of the spatial resolution. Now one can scale the hard core response $\mathbf{v}_{hc}(t)$ such that $\mathbf{v}_{hc}(t)\Delta t' = \mathbf{v}_{hc}^*(t)\Delta t$ and apply the displacement imposed by the hard core repulsion in one single timestep.

5.4.4 Pressure concept

The JKR-model defines a two cell interaction which exhibits an equilibrium distance (Eq. 5.19) mediated by the balance of surface energy and elastic repulsion. For two cells this leads to a negligible deviation of the volume attributed to the vertex and the relaxed volume of the real cell. However, cells will frequently interact with several cells such that specific situations can occur in which cells have a volume deviating considerably from the real volume without a correspondingly large relaxing force being generated. Thus, cells might remain in a highly compressed state for too long times because of the neglect of many-body interactions. The pressure of a cell is calculated by

$$p_i \;=\; K_i\left(1 - \frac{V_i}{V_i(\tau_i)}\right) \tag{5.28}$$

$$K_i \;=\; \frac{E_i}{3(1 - 2\nu_i)} \tag{5.29}$$

using a linear compression model with compressibility K_i. $V_i(\tau_i)$ is the target volume a cell i has at the internal time τ_i (Sec. 5.3). The forces resulting from the pressure are exerted between cells only adding the term

$$\mathbf{F}_{ij}^{\text{compress}} = a_{ij}(p_i - p_j)\hat{\mathbf{e}}_{ij} \tag{5.30}$$

to the passive cell forces $\mathbf{F}_{ij}^{\text{passive}}\big(\mathbf{x}_i(t), \mathbf{x}_j(t)\big)$. Such the total passive forces become

$$\mathbf{F}_{ij}^{\text{passive}}\big(\mathbf{x}_i(t), \mathbf{x}_j(t)\big) = \left\{ E_{ij}^* \sqrt{r_{ij}^*}\, h_{ij}^{3/2} - \sqrt{6\pi\sigma_{ij}E_{ij}^* r_{ij}^{*\,3/2} h_{ij}^{3/2}} + a_{ij}(p_i - p_j) \right\} \hat{\mathbf{e}}_{ij} \tag{5.31}$$

To get the actual volume the minimum from the sphere volume and the Voronoi cell volume is taken like it is done for the contact areas (Sec. 5.4.1). Note, that in this way the pressure depends on the position of all neighbor cells, i.e. the Voronoi volume, even though it is formally added to the two body force $\mathbf{F}_{ij}^{\text{passive}}\big(\mathbf{x}_i(t), \mathbf{x}_j(t)\big)$ acting between i and j.

5.4.5 Cell friction

There are two sources of friction in the model. One is the friction provided by the environment which consists mainly of water and the ECM with the latter component presumably providing the larger contribution. The second source are cell-cell contacts. The solid friction between cells can be neglected [*Bongrand*, 1995; *Evans*, 1995]. That is a result of the glycocalyx that covers the membrane of a cell and prevents direct cell membrane contact. The friction caused by lubrication is unknown but seem to be reduced by the glycocalyx as well [*Bongrand*, 1995; *Wu et al.*, 2004]. The largest contribution is assumed to be provided by the specific and unspecific cell-cell adhesion of the type CELL-CELL-FRICTION (Sec. 5.4.3). To simplify the model there will be no cell-dependence of the cell-cell-friction coefficient γ_{ij}. This parameter is completely unknown and needs to be fitted, i.e. the experimental situation does not allow to identify a cell-dependence of γ_{ij}. Concerning the purpose of the model this seems not important as the outcome is robust against variations of the friction coefficients. Therefore they are chosen to match the migration speed of cells [*Gunzer et al.*, 2004;

Miller et al., 2003, 2002; *Okada et al.*, 2005; *Wei et al.*, 2003] in a high cell density situation with sufficient precision (Appendix B) [*Beyer and Meyer-Hermann*, 2007b] .

The further underlying assumptions made to the cell friction are as follows:

- Cell-cell-friction is proportional to the interaction surface.

- CELL-CELL-FRICTION acts parallel to the cell membrane contacts.

- Normal friction is not taken into account.

For all interactions a linear velocity dependency is assumed. By calculating the Reynolds-number this seems to be reasonable choice as low Reynolds-number indicate laminar flow [*Dallon and Othmer*, 2004; *Palsson and Othmer*, 2000; *Schaller*, 2006]. Onset of turbulent flow is generally around $Re \sim 10^3$.

$$Re = \frac{\rho v r}{\eta} \sim 10^{-2} \tag{5.32}$$

with fluid density $\rho = 1\,\mathrm{g\,cm^{-3}}$ and viscosity $\eta = 10^{-3}\,\mathrm{Pa\,s}$ of water. The cell is characterized by its speed $v = 1\,\mu\mathrm{m\,min^{-1}}$ and radius $r = 10\,\mu\mathrm{m}$. Overall, a linear force-velocity relationship seems to be an excellent approximation.

The friction coefficients are assumed to take into account viscous and a part of adhesive force (Sec. 5.4.3). The viscous contribution is assumed to be a combination of the viscous-like deformation of the ECM and the cell viscosity. The later contributes when two cells slide along each other inducing a deformation of both cells and consequently a flow of their cytoplasmas. The deformation of the cytoskeleton of the cells is assumed to be mainly elastic with a minor viscous and plastic behavior. That is also the argument to ignore the cell-cell friction for normal motion as the cytoplasmatic flow is assumed to be neglected due to the symmetry in this situation. Consider a head-to-head collision of two cells. Then both cells are deformed while the cytoplasm increases its pressure but does not flow significantly. In numerical terms one does not need this contribution of friction as the additional parameter is not needed to describe the data properly (Sec. 6). This has been shown in similar models previously [*Dallon and Othmer*, 2004; *Palsson*, 2001; *Palsson and Othmer*, 2000; *Schaller and Meyer-Hermann*, 2005]. The dominant source of cell-cell friction is assumed to be caused by adhesive force between two cell membranes which acts only tangentially to the contact surface as defined by the geometry of the problem.

The component of friction between two cells i and j in contact read

$$\tilde{\mathbf{F}}_{ij}^{\mathrm{drag}}\left(\mathbf{v}_i, \mathbf{v}_j\right) = \gamma_{ij}\left\{(\mathbf{v}_j - \mathbf{v}_i) - \hat{\mathbf{e}}_{ij}\left[\hat{\mathbf{e}}_{ij} \cdot (\mathbf{v}_j - \mathbf{v}_i)\right]\right\} \tag{5.33}$$

taking into account only the tangential parts of the relative velocity between the cells. The unit vector $\hat{\mathbf{e}}_{ij}$ is the normal vector of the plane of the cell contact. The friction coefficient γ_{ij} has the dimension of a viscosity times a length scale. The choice has been such that γ_{ij} is proportional to the contact area between the cells. The total drag force is the sum of all friction forces with neighbor cell plus a term of the free surface of the cell having interaction with the surrounding medium. In contrast to the cell friction the medium interaction is assumed to have a normal component as well. The overall drag

force is then given by

$$\mathbf{F}_i^{\text{drag}}\left(\mathbf{v}_i, \{\mathbf{v}_j\}_{\mathcal{N}_i^c}\right) = -\gamma_{\text{med}}\mathbf{v}_i + \sum_{j \in \mathcal{N}_i^c} \tilde{\mathbf{F}}_{ij}^{\text{drag}} \tag{5.34}$$

$$= -\mu_{\text{medium}}(A_i^{\text{tot}} - A)\mathbf{v}_i + \sum_{j \in \mathcal{N}_i^c} \mu_{ij}a_{ij}\left\{(\mathbf{v}_j - \mathbf{v}_i) - \hat{\mathbf{e}}_{ij}\left[\hat{\mathbf{e}}_{ij} \cdot (\mathbf{v}_j - \mathbf{v}_i)\right]\right\} \tag{5.35}$$

with specific coefficients μ_{medium} and μ_{ij} (thus $\gamma_{ij} = \mu_{ij}a_{ij}$) giving the strength of friction per unit area. $A = \sum_{j \in \mathcal{N}_i^c} a_{ij}$ is the surface in contact with other cells. $A_i^{\text{tot}} = A + A_{\text{med}} = \sum_{j \in \mathcal{N}_i} a_{ij}$ is the total surface of a cell with A_{med} being the surface in contact with the medium which is calculated as the sum of the minima of the corresponding Voronoi faces and the contact face to a virtual cell of the same size at equilibrium distance.

5.4.6 Solving the equations of motion

The general solution to the ODE system (Eq. 5.5) is chosen to be forward Euler. Implicit schemes are not useful for the model as this would require to somehow compute the inverse of the regular triangulation which is simply not feasible. Already the non-linear nature of forces between two cells would make an implicit approach inefficient. The implicit approach could in principle be done using iterative schemes. However, due to the expenses computing the regular triangulation and all to body forces this is not favorable. For the same reason multi-step schemes are not the method of choice.

The forward Euler scheme is to approximate the solution $\mathbf{X}(t) = (\mathbf{x}_1(t), \dots, \mathbf{x}_i(t), \dots, \mathbf{x}_N(t))$ by

$$\mathbf{X}(t + \Delta t) \approx \mathbf{X}(t) + \Delta t \dot{\mathbf{X}}(\mathbf{t}) \tag{5.36}$$

The velocity $\dot{\mathbf{X}}(t)$ can be computed from the force

$$\mathbf{F}(t, \mathbf{X}(t)) = (\mathbf{F}_1(t, \mathbf{X}(t)), \dots, \mathbf{F}_i(t, \mathbf{X}(t)), \dots, \mathbf{F}_N(t, \mathbf{X}(t))) \tag{5.37}$$

with $\mathbf{F}_i(t, \mathbf{X}(t))$ being the sum of all non-friction forces (Eq. 5.5)

$$\mathbf{F}_i(t, \mathbf{X}(t)) = \mathbf{F}_i^{\text{active}}(\phi_i(t)) + \sum_{j \in \mathcal{N}_i} \mathbf{F}_{ij}^{\text{active}}(\phi_i(t)) + \sum_{j \in \mathcal{N}_i^c}\left[-\mathbf{F}_{ji}^{\text{active}}(\phi_j(t)) + \mathbf{F}_{ij}^{\text{passive}}(\mathbf{x}_i(t), \mathbf{x}_j(t))\right] \tag{5.38}$$

by solving the linear system

$$\Gamma(t)\dot{\mathbf{X}}(t) = \mathbf{F}(t, \mathbf{X}(t)) \tag{5.39}$$

with a sparse matrix structure for the friction matrix Γ. The sparsity comes from the sum over neighbor cells which gives only about 60 entries in each row of Γ. This number corresponds to 20 neighbor cells with three degrees of freedom, a number that results from experience and is a property of a regular triangulation with almost uniform vertex distributions [*Schaller and Meyer-Hermann*, 2004]. Solving the equation system (Eq. 5.39) can be done either by using standard linear solvers or fixpoint iteration. The standard linear solvers are implemented using the PETSc library [*Balay et al.*, 2004, 2001, 1997]. This library offers various solving schemes such as the conjugate gradient method. However, it has been found to be a more efficient approach to use a fixpoint iteration scheme [*Bronstein et al.*, 1996a]

that incorporates the specific structure of the matrix Γ. The system

$$\mathbf{V} \equiv \dot{\mathbf{X}}(t) \quad = \quad \Gamma(t)^{-1}\mathbf{F}(t, \mathbf{X}(t)) \tag{5.40}$$

is solved by using a Jacobi-like iteration. Instead of inverting the diagonal only the 'cell-diagonal' is inverted. Rewriting (Eq. 5.5) using (Eq. 5.34)

$$F \equiv F_i(t, \mathbf{X}(t)) \quad = \quad -\mathbf{F}_i^{\text{drag}}(\mathbf{V}(t)) \tag{5.41}$$

$$= \quad -\gamma_{\text{medium}}\mathbf{v}_i - \sum_{j \in \mathcal{N}_i^c} \gamma_{ij} \left\{ (\mathbf{v}_j - \mathbf{v}_i) - \hat{\mathbf{e}}_{ij} \left[\hat{\mathbf{e}}_{ij} \cdot (\mathbf{v}_j - \mathbf{v}_i) \right] \right\} \tag{5.42}$$

$$F + \underbrace{\sum_{j \in \mathcal{N}_i^c} \gamma_{ij} \left\{ \mathbf{v}_j - \hat{\mathbf{e}}_{ij} \left[\hat{\mathbf{e}}_{ij} \cdot \mathbf{v}_j \right] \right\}}_{\Gamma'\mathbf{V}} \quad = \quad \underbrace{-\gamma_{\text{medium}}\mathbf{v}_i + \sum_{j \in \mathcal{N}_i^c} \gamma_{ij} \left\{ \mathbf{v}_i - \hat{\mathbf{e}}_{ij} \left[\hat{\mathbf{e}}_{ij} \cdot \mathbf{v}_i \right] \right\}}_{\Gamma_i\mathbf{v}_i} \tag{5.43}$$

$$F + \Gamma'\mathbf{V} \quad = \quad \Gamma_i\mathbf{v}_i \tag{5.44}$$

one gets an equation that can be solved by fixpoint iterations for $\mathbf{V} = (\mathbf{v}_1, \dots, \mathbf{v}_N)$ by

$$\mathbf{v}_i^{(k+1)} \quad = \quad \Gamma_i^{-1}(F + \Gamma'\mathbf{V}^{(k)}). \tag{5.45}$$

The matrix Γ_i is a 3x3 matrix that has to be inverted once per time step for each cell i. Convergence of this fixpoint iteration can be assured if

$$\left| \bigoplus_{i=1}^{N} \Gamma_i \right| < 1 \tag{5.46}$$

which can always be achieved numerically be using proper length, time, and force scales.

Given the velocity field $\mathbf{V}$ the maximal timestep is computed by ensuring that the displacement of any cell does not exceed a space discretization threshold Δx. The discretization can be chosen to be about 10% of a cell diameter for several reasons. First, the typical scale of the JKR forces is in that order. Second, the membrane fluctuations are also in this range [*Gunzer et al.*, 2004; *Jiang et al.*, 1998; *Miller et al.*, 2003, 2002; *Okada et al.*, 2005; *Wei et al.*, 2003]. Thus, a finer spatial resolution is meaningless as long as the cell shape is not taken into account which is also the third reason not to increase the spatial resolution such that the spherical approximation of the cells shape gets meaningless.

To speed up computation, cells are updated asynchronously. If the movement is below a certain threshold forces will not be recomputed and the cell will remain in its place. However, all displacements are summed until a critical predefined threshold of $10^{-2}\Delta x$ of the space discretization Δx is reached and the cell position is changed. The basic approximation is

$$\mathbf{F}_{ij}(\mathbf{x}_1, \dots, \mathbf{x}_i + \Delta\mathbf{x}_i, \dots, \mathbf{x}_j + \Delta\mathbf{x}_j, \dots, \mathbf{x}_n) \approx \mathbf{F}_{ij}(\mathbf{x}_1, \dots, \mathbf{x}_i, \dots, \mathbf{x}_j, \dots, \mathbf{x}_n) \tag{5.47}$$

$$\tag{5.48}$$

for $\Delta\mathbf{x}_i$ and $\Delta\mathbf{x}_j$ sufficiently small compared to the typical length scales in the system which is given by the penetration depth arising from the JKR model and is typically in the order of 0.1 cell diameter. In practice the space discretization Δx is chosen to be of that size and the threshold for updating forces is 0.1 of the maximal allowed displacement imposing errors of the order Δx^2. Finally, the position of

the cell i is computed from the history of forces acting on it during previous time steps and the total displacement gets large.

5.5   Description of chemotaxis

There exist several chemokines in the PLF (Sec. 2.2.2). Mainly two are important: CXCL13 and CCL21. CXCL13 is produced by FDC and acts on B cells via the receptor CXCR5. CCL21 is produced in the T zone and attracts both, B and T cells, acting on the receptor CCR7. On B cells CXCR5 has higher levels than CCR7 making these cells more sensitive for CXCL13 than CCl21. The chemotaxis model considered in this section shall be as simple as possible and couple a freely diffusing chemokine to the receptors on the cell membrane. The migration of cells couples to the chemokine gradient by sensing the gradient periodically according to a persistence time [*Albrecht and Petty*, 1998; *Ehrengruber et al.*, 1996]. In between the direction of migration is kept constant [*Miller et al.*, 2003, 2002; *Okada et al.*, 2005; *Wei et al.*, 2003]. As a possible mechanism for the size regulation of PLF (Sec. 6.1) the desensitization of chemokine receptors is included. Support for the desensitization of the chemokine receptor CXCR5 comes from a study that investigates mice deficient for TNF-α or TNFR-I which have reduced CXCL13 expression but have slightly enhanced CXCR5 levels on B cells [*Ngo et al.*, 1999] suggesting that under normal conditions the CXCR5 surface levels are in a steady state with an increased portion of internalized receptors. The basic idea is that the cell looses sense for directionality when a certain signal derived from the chemokine input is below a threshold. In order to model the desensitization of cells to a chemokine signal a sensitivity needs to be defined that states at which point internalization is sufficient in order that a cell losses its sense for directionality.

Receptor internalization   Desensitization is achieved by internalizing the receptor R with the rate k_i (Fig. 5.8) when it is bound with the ligand c [*Neel et al.*, 2005].

$$
\begin{aligned}
\dot{R} &= -k_{on}R\,c + k_{off}R_b + k_r R^* \\
\dot{R}_b &= k_{on}R\,c - k_{off}R_b - k_i R_b \\
\dot{R}^* &= k_i R_b - k_r R^* \\
\dot{c} &= -k_{on}R\,c + k_{off}R_b
\end{aligned}
\tag{5.49}
$$

The binding of the ligand is characterized by the on and off rate constants k_{on} and k_{off} leading to the ligand-receptor complex R_b. The rate k_r describes the recycling of the internalized receptor R^* into the free membrane form R. The basic assumption is that the total receptor content $R_{tot} = R + R_b + R^*$ is conserved. This view is supported by the fact that ligand-receptor complex dissociation may be involved in the process [*Neel et al.*, 2005]. The turnover of the receptor by transcription and degradation may be considered to be in equilibrium independent of the receptor dynamics described in (Eq. 5.49). When this turnover is slow the corresponding rate terms can be neglected.

The reaction equations (Eq. 5.49) are completed by an unspecific decay κc of the chemokine and a source term Q. This describes that chemokines are inactivated and processed by all cells without reac-
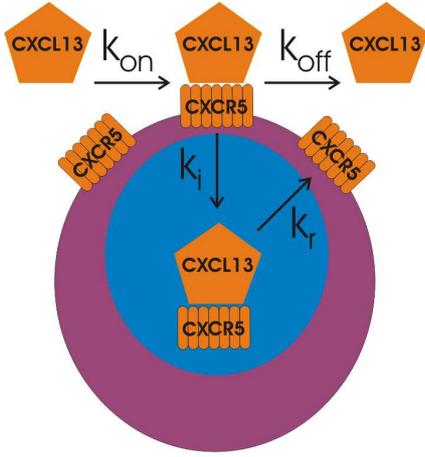
Figure 5.8: Receptor desensitization model. The chemokine CXCL13 binds with the rate constant k_{on} to its receptor CXCR5. The CXCL13-CXCR5 complex can either dissociate with the rate constant k_{off} or internalized with the rate constant k_i. The internalized complex gets recycled reexpressing the receptor CXCR5 on the surface. The recycling is characterized by the rate constant k_r

tion with the proper receptor limiting the life time of a chemokine molecule. Using the conservation of R_{tot} (omitting the redundant equation for R_b) yields

$$
\begin{aligned}
\dot{R} &= -k_{on} R c + k_{off}(R_{tot} - R - R^*) + k_r R^* \\
\dot{R}^* &= k_i(R_{tot} - R - R^*) - k_r R^* \\
\dot{c} &= -k_{on} R c + k_{off}(R_{tot} - R - R^*) - \kappa c + Q.
\end{aligned}
\tag{5.50}
$$

The system can be solved using the implicit Euler-method [*Bronstein et al.*, 1996b]. The choice has been done because of the L-stability of this method.

Definition 13 *A method is called* A-stable *if for the test problem*

$$
y' = \lambda y; \quad y(0) = y_0 \quad with \quad \mathrm{Re}(\lambda) < 0
\tag{5.51}
$$

for all step widths h and all hλ

$$
\lim_{n \to \infty} y_n = 0.
\tag{5.52}
$$

Definition 14 *A method is called* L-stable *if it is A-stable and for fixed h and* $\mathrm{Re}(\lambda) \to -\infty$

$$
\lim_{n \to \infty} y_n = 0.
\tag{5.53}
$$

L-stability is useful to treat the stiff numerical problem (Eq. 5.50), i.e. the time step is large compared to the typical time scale given by the association rate k_{on}. This results in the calculation of the equilibrium solution for long time steps.

Estimate parameters The parameters used in the ODE system (Eq. 5.50) are not known but can be estimated from data of similar systems. The dissociation constant K_d for chemokines and their receptors are measured for other chemokines then the ones used here (CCL19, CCL21, CXCL13) (Table 5.3). The values for K_d range from 0.2 nM to 5 nM [*Lin et al.*, 2004; *Pelletier et al.*, 2000; *Slimani et al.*, 2003; *Yoshida et al.*, 1998]. The only dissociation constant of a PLF chemokine is K_d for CCR7 with CCL21 which has a value of 1.6 nM [*Willimann et al.*, 1998]. Considering the range of all these values it is likely that K_d is similar for CXCL13 and CCL19. A less favorable situation

exists for the reaction rate k_{on} (k_{off} can be calculated from k_{on} for a known K_d). Only few data exists which spread over several orders of magnitude. For instance, values for the association rate k_{on} are available for CXCL12 binding to fibronectin ($2.5 \cdot 10^5 \, \mathrm{M^{-1} s^{-1}}$) [*Pelletier et al.*, 2000]. The off rate k_{off} measured for CXCL12 binding to fibronectin is $6.5 \cdot 10^{-3} \, \mathrm{s^{-1}}$ [*Pelletier et al.*, 2000].

The other two rates k_i and k_r (see (Eq. 5.50)) can be estimated from experimental data on receptor desensitization and resensitization experiments reviewed recently [*Neel et al.*, 2005]. It is assumed that all non-internalized receptors have bound its ligand which is reasonable considering that the chemoattractant concentrations in the experiment are far above K_d. The only equation that is left for the desensitization process is then (Eq. 5.50) ($R = 0$)

$$\dot{R}^* \quad = \quad k_i(R_{tot} - R^*) - k_r R^* \tag{5.54}$$

with the solution

$$R^*(t) \quad = \quad \frac{R_{tot}}{1 + k_r/k_i} \{1 - \exp\left[-(k_i + k_r)t\right]\} \tag{5.55}$$

and the internalized receptor fraction r^* at equilibrium

$$r^* = \frac{R^*(t \to \infty)}{R_{tot}} \quad = \quad \frac{1}{1 + k_r/k_i}. \tag{5.56}$$

For the resensitization process $k_i = 0$ is set and the process starts from $R^*(t = 0) = r^* R_{tot}$. In the absence of the ligand the dynamics for the internalized receptor during resensitization becomes

$$R^*(t) \quad = \quad r^* R_{tot} \exp\left[-k_r t\right]. \tag{5.57}$$

With typical values of $r^* = 0.3 \ldots 0.8$ when desensitized and typical recycling times of 60–180 minutes to get $r^* \sim 0.2$ upon resensitization [*Neel et al.*, 2005] one arrives at

$$k_r \quad = \quad 1 \cdot 10^{-4} \ldots 7 \cdot 10^{-3} \, \mathrm{s^{-1}}$$
$$k_i \quad = \quad 5 \cdot 10^{-5} \ldots 3 \cdot 10^{-2} \, \mathrm{s^{-1}}.$$

Assuming that the internalization process is not in steady state – and solving (Eq. 5.55) numerically – doesn't change the results very much compared to the experimental uncertainty. The numerical results can be shown not to be sensitive to this parameter (Sec. 6).

The receptor levels for the chemokines are not known explicitly. Form similar receptors the number of CCR7 on T cells has been estimated to be 10^5 [*Willimann et al.*, 1998] and 10^4 for B cells as indicated by the studies that find a factor 10 difference of CCR7 levels between B and T cells [*Okada et al.*, 2002].

Sensitivity of Chemotaxis   To analyze the chemotactic sensitivity of cells the assumption is made that the internalization and recycling process of the receptor are slow which is reasonable considering the typical time scale of minutes compared to a far below seconds regime of the binding process (k_r and k_i vs. k_{off}). Further it is assumed that chemical equilibrium between receptor and ligand is reached. Thus the bound receptor is given by

$$R_b = \frac{k_{on}}{k_{off}} R c = \frac{R c}{K_d} \tag{5.58}$$

k_i	$5 \cdot 10^{-5} \dots 3 \cdot 10^{-2}\,\mathrm{s}^{-1}$	[*Neel et al.*, 2005]
k_r	$1 \cdot 10^{-4} \dots 7 \cdot 10^{-3}\,\mathrm{s}^{-1}$	[*Neel et al.*, 2005]
K_d	$0.2 \dots 5\,\mathrm{nM}$	[*Lin et al.*, 2004; *Pelletier et al.*, 2000; *Slimani et al.*, 2003;
		Willimann et al., 1998; *Yoshida et al.*, 1998]
k_{on}	$2.5 \cdot 10^5 \dots 10^8\,\mathrm{M}^{-1}\mathrm{s}^{-1}$	[*Pelletier et al.*, 2000]
k_{off}	$10^{-4} \dots 1\,\mathrm{s}^{-1}$	(from K_d and k_{on})
κ	$2 \cdot 10^{-4}\,\mathrm{s}^{-1}$	[*Bar-Even et al.*, 2006]
Q	$2.5 \cdot 10^1 \dots 10^4\,\mathrm{s}^{-1}$	[*Hu*, 2004; *Vissers et al.*, 2001]
R_{tot}	$10^4–10^5$	[*Okada et al.*, 2002; *Willimann et al.*, 1998]

Table 5.3: Parameters for the constants of the equation system (Eq. 5.50).

with the equilibrium dissociation constant K_d.

Let us assume the cell determines the direction by comparing the amount of bound receptor along its membrane and can determine the direction when the difference along the steepest gradient is large enough (Fig. 5.9). In a first approximation this difference is

$$\Delta R_b = 2\frac{\Delta R\,c + R\,\Delta c}{K_d} \tag{5.59}$$

with delta denoting the *half* the difference along the cell length (see below).

Further let $R^{(1)}$ and $R^{(2)}$ be the receptor concentration at two opposite ends of a cell and $R_b^{(1)}$, $R_b^{(2)}$ be the corresponding ligand-receptor complexes such that

$$
\begin{aligned}
\gamma &= \frac{R^{(1)} + R_b^{(1)}}{R^{(2)} + R_b^{(2)}} = \frac{R + R_b + \Delta R + \Delta R_b}{R + R_b - \Delta R - \Delta R_b} \\
R &= \frac{1}{2}(R^{(1)} + R^{(2)}) \qquad \Delta R = \frac{1}{2}(R^{(1)} - R^{(2)}) \\
R_b &= \frac{1}{2}(R_b^{(1)} + R_b^{(2)}) \qquad \Delta R_b = \frac{1}{2}(R_b^{(1)} - R_b^{(2)})
\end{aligned}
\tag{5.60}
$$

with γ indicating the chemokine receptor polarization. Rewriting the last equations gives

$$\Delta R = \frac{\gamma - 1}{\gamma + 1}(R + R_b) - \Delta R_b. \tag{5.61}$$

Combining this with equation (Eq. 5.59) yields

$$\Delta R_b = \frac{2}{K_d}\left[\frac{\gamma - 1}{\gamma + 1}(R + R_b) - \Delta R_b\,c + R\,\Delta c\right]. \tag{5.62}$$

Hence, solving for ΔR_b by using $R_b = R\,c/K_d$

$$\Delta R_b = 2\left[\frac{\gamma - 1}{\gamma + 1}\frac{R\,c}{K_d} + \frac{R\Delta c}{K_d + 2c}\right] \tag{5.63}$$

which simplifies to

$$\Delta R_b = \frac{2R\Delta c}{K_d + 2c} \tag{5.64}$$
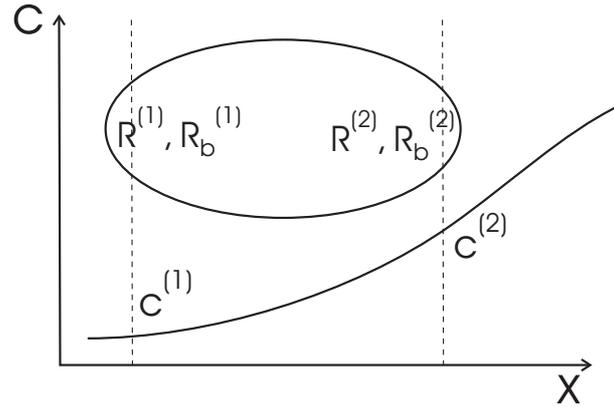
Figure 5.9: Model for chemotactic sensitivity. It is assumed that the cells compares the concentration along some axis X via the amount of bound receptor R_b at two opposing ends labeled 1 and 2.

in the case of $\gamma = 1$, i.e. without polarized receptors. In this very simple model it is assumed that the chemotactic sensitivity behaves like

$$\chi \sim \frac{\Delta R_b}{\Delta R_{\text{crit}}} \tag{5.65}$$

describing how the point-like cell responds chemotactically to the chemotactic field. Any other monotonic function $\chi(\Delta R_b)$ that describes the signaling pathway inside the cell could do the same. Qualitatively, if the concentration c is rising the sensitivity goes to zero provided the maximal gradient along the cell is of limited strength. Also in the case $c \to 0$ the sensitivity becomes zero as $\Delta c \to 0$. In the case of several chemokines c_A the sensitivity χ may behave like

$$\chi \sim \sum_A \frac{2R_A \, \Delta c_A}{K_{d,A} + 2c_A} \tag{5.66}$$

indicating a vector sum of gradients determining the cells direction like it was demonstrated for neutrophils [*Foxman et al.*, 1999]. Thus, the sensitivity from this very simple estimate depends on both concentration and gradient of the chemoattractant.

For simplicity χ is chosen as step function, i.e. if the signal ΔR_b exceeds a threshold ΔR_{crit} then the cell chooses the direction according to the chemokine otherwise a random direction is chosen. The threshold can be estimated by calculating the number of molecules of the chemokine in the vicinity of the cell. Assuming the cell to be in a box of 10 μm length, a concentration of 1 nM corresponds to 700 molecules. Taking into account that the cell occupies a large part of this volume the number of molecules that can signal to the cell is in the order of 100 molecules. Such a concentration of less than 0.1 nM (10 molecules) seems not to be realistic to allow a cell to sense the gradient of the chemokine because the term concentration looses its meaning and the stochastic fluctuations in the molecule distribution will dominate. This also corresponds nicely to the results obtained by various experiments [*Kim et al.*, 1998; *Tomhave et al.*, 1994; *Yoshida et al.*, 1998]. One may assume that the receptors of very high affinity – like fMLP receptor of neutrophils[*Albrecht and Petty*, 1998; *Tomhave et al.*, 1994] – that are able to induce chemotactic activity in a subnanomolar range work only when sensed with the temporal sensing mechanism described below. The desensitization mechanism described above may also lead to a switch from gradient sensing to temporal sensing when the receptor number is low such that even at higher concentration only few molecules can be detected because only a few free receptors are avaliable. However, this has not been incorporated into the model.

Temporal sensing It has been show that leukocytes can use a temporal sensing mechanism to determine chemotactic gradients [*Albrecht and Petty*, 1998]. This can be incorporated very directly by using an internal cell variable ϕ (Sec. 5.3) that stores the last chemokine concentration encountered by the cell and comparing it to the present concentration after the persistence time given by the experiment. If the concentration is decreasing the cell reverses its direction of motion else the direction is kept. This still can lead to Brownian-like motion in the dense cell phase. The direction of motion is influenced by collisions with other cells and the direction including deviations by collisions is reversed.

Temporal sensing can also be made in the presence of multiple chemokines. Assuming that a cell uses some kind of vector sum for the signal [*Foxman et al.*, 1999] the model weights the relative response proportional to the amount of bound receptor. Thus the internal variable stores the total amount of all bound receptors (of all chemokine receptor types) and compares it to the present state of binding after the persistence time [*Albrecht and Petty*, 1998].

Interaction with the extracellular matrix It seems that the biological activity of chemokines *in vivo*, in contrast to *in vitro*, is provided only by chemokines which are bound to glycosaminoglycans on the ECM fibers and not by the soluble substance [*Hoogewerf et al.*, 1997; *Moser et al.*, 2004; *Proudfoot et al.*, 2003; *Slimani et al.*, 2003]. In principle the ODE system (Eq. 5.50) could be extended by two equations for free binding sites on the ECM and for chemokine bound to ECM. Considering the lack of parameter knowledge for the original system (Eq. 5.50) this does not make much sense as the outcome of the extended model would be more or less arbitrary depending on the parameter set. It is also not clear a priori whether the presence of the ECM would change the gradients of the chemokine concentrations much with respect to free diffusion only. It is likely that the binding to the ECM yields a similar chemokine distribution assuming the binding site on the ECM are sufficiently numerous. Just the amount of active ligand would be reduced by a certain fraction which can be absorbed by the uncertainty of the production rate of the chemokines and other parameters. An interesting result may be expected from the fact that ECM is virtually absent from the PLF (Sec. 2.3.1). That sets the ability of CXCL13 to induce chemotaxis inside the PLF into question. Note that the different ECM distribution is not taken into account by any part of the model.

5.6 *Long range interaction of cells via reaction-diffusion*

The reaction of the chemokine with its receptor is only one part of the interaction. The description of the diffusion of the chemokines has to be included. This results in a reaction-diffusions system of the type

$$\dot{c}(\mathbf{x}, t) = \frac{\partial c(\mathbf{x}, t)}{\partial t} = D\Delta c(\mathbf{x}, t) - \kappa c(\mathbf{x}, t) + \mathrm{f}\left(c(\mathbf{x}, t), \phi\right). \tag{5.67}$$

The function $\mathrm{f}\left(c(\mathbf{x}, t), \phi\right)$ couples the internal states ϕ of the cells to the diffusion of a substance described by $c(\mathbf{x}, t)$ via some reaction. This function will be provided by coupling the ODE system (Eq. 5.49) to (Eq. 5.67) with some chemokine $c(\mathbf{x}, t)$. Note, that the diffusion is homogeneous in space.

The possibly different diffusions constants depending on the cellular content and the density of the ECM are omitted due to the lack of available experimental data. However, the inhomogeneous media formed by the tissue may cause a reaction-diffusion approach to become invalid and refinements might be necessary [*Schnell and Turner*, 2004].

The complete set of equations describing a chemokine c then reads

$$
\begin{aligned}
\dot{R} &= -k_{\text{on}}R\,c + k_{\text{off}}(R_{\text{tot}} - R - R^*) + k_{\text{r}}R^* \\
\dot{R}^* &= k_{\text{i}}(R_{\text{tot}} - R - R^*) - k_{\text{r}}R^* \\
\dot{c} &= D\triangle c - k_{\text{on}}R\,c + k_{\text{off}}(R_{\text{tot}} - R - R^*) - \kappa c + Q.
\end{aligned}
\tag{5.68}
$$

To solve systems of type (Eq. 5.67) the splitting method is used [*Karlsen and Lie*, 1999; *Tyson et al.*, 1996]. The general scheme is that the solution $c(\mathbf{x}, t)$ is approximated by

$$
c(\mathbf{x}, n\Delta t) \approx [\mathcal{R}(\Delta t) \circ \mathcal{D}(\Delta t)]^n\, c(x, 0)
\tag{5.69}
$$

with $\mathcal{R}(\Delta t)$ denoting the solution operator for the reaction part $\dot{c} = -\kappa c + \mathrm{f}(c, \phi)$ and $\mathcal{D}(\Delta t)$ the solution operator for the diffusion $\dot{c} = D\Delta c$. This method is first order accurate [*Tyson et al.*, 1996]. Both operators are provided by using implicit Euler for the reaction and the diffusion part. The choice for the implicit Euler method, despite its only linear accuracy, is justified by the property of A-stability which guarantees a decay of the numerical solution (while for example the Crank-Nicholson scheme can oscillate) [*Tyson et al.*, 1996]. This ensures that the solution converges to the steady state solution for $\Delta t \rightarrow \infty$. Due to the splitting, multi-step methods cannot be used as the intermediate results are not available. In the model used here a Delaunay boundary condition with zero concentration is applied.

Diffusion Step   An important issue is to discretize the PDE to get the solution operator $\mathcal{D}(\Delta t)$ for the diffusion step. A finite difference scheme on a regular grid has been chosen. The choice of the grid spacing has to be such that the cell can still be treated as point-like particle with respect to the solution of the chemokine distribution. A higher resolution would be useless without a detailed description of source and sink terms on the cellular level. On the other hand the volume elements of the grid should be small enough to have an approximately homogeneous solution which can be used to solve the reaction part on a node of the grid. The chosen grid spacing x is $35\,\mu$m. With a diffusion constant $D = 10\ldots100\,\mu\text{m}^2\text{s}^-$ [*Randolph et al.*, 2005] the induced time scale $\Delta x^2/4D \approx 10\,$s is comparable to the time scale of the cellular movement.

The above equation (Eq. 5.67) needs also a source term for the chemokines $c(\mathbf{x}, t)$. The sources are cells. According to the chosen grid size the cellular source are treated as point-like. The source term $q(\mathbf{x}, t)$ for a single cell is then approximated by the production rate Q of the chemokine within the volume element the cell is located in. Additionally the source term $q(\mathbf{x}, t)$ is trilinearly interpolated

on the grid nodes with grid spacing $\Delta x, \Delta y, \Delta z$ and $x \in [x_i, x_{i+1}];$ $\quad y \in [y_j, y_{j+1}];$ $\quad z \in [z_i, z_{i+1}]$

$$
\begin{aligned}
q(x_i, y_j, z_k) &= \frac{Q}{\Delta x \Delta y \Delta z} \frac{x - x_i}{\Delta x} \frac{y - y_j}{\Delta y} \frac{z - z_k}{\Delta z} \\
q(x_{i+1}, y_j, z_k) &= \frac{Q}{\Delta x \Delta y \Delta z} \frac{x_{j+1} - x}{\Delta x} \frac{y - y_j}{\Delta y} \frac{z - z_k}{\Delta z} \\
q(x_i, y_{j+1}, z_k) &= \frac{Q}{\Delta x \Delta y \Delta z} \frac{x - x_i}{\Delta x} \frac{y_{j+1} - y}{\Delta y} \frac{z - z_k}{\Delta z} \\
&\vdots \\
q(x_{i+1}, y_{j+1}, z_{k+1}) &= \frac{Q}{\Delta x \Delta y \Delta z} \frac{x_{i+1} - x}{\Delta x} \frac{y_{j+1} - y}{\Delta y} \frac{z_{k+1} - z}{\Delta z}.
\end{aligned}
\tag{5.70}
$$

The sum of all eight $q(.,.,.)$ equals the source $Q/(\Delta x \Delta y \Delta z)$. In a similar manner the concentrations of $c(\mathbf{x}, t)$ are accessed by a trilinear interpolation from the node values to calculate the reaction step involving chemokine concentration at the cell's position. An important difference to usual splitting methods is that the reaction step is not taking place on the grid. The spatial description is done according to the cell distribution with each cell acting as a node of an irregular grid overlaying the regular grid of the diffusion step. The interpolation between these two grids is done by trilinear interpolation as shown above.

Reaction Step One should keep in mind that the space where the substance diffuses is not a homogeneous 3D space but the gaps between cells. Therefore within each volume element the effective concentration entering the ODE system (Eq. 5.68) is higher corresponding to the volume fraction ζ of non-cellular space.

$$
\zeta = \frac{\text{volume of element - volume of cellular content}}{\text{volume of element}}
\tag{5.71}
$$

The influence by the complex geometry of the space available for diffusion can be governed by an effective diffusion constant which is unfortunately not known. Numerical experiments demonstrated that the outcome of the simulations is not critically dependent on these parameters allowing to use a rough estimate from related experiments [*Sen*, 2004].

There is however an additional complication. The ODE system (Eq. 5.49) describes a receptor binding reaction that is in reality taking place on a surface. Thus, the concentrations should be surface concentrations. This would require to know the reaction parameters for the 2D reaction which is not the case. Therefore the system has been described in three dimensions considering the following estimates. A real difference between the 2D and 3D case occurs if diffusion on the surface is a limiting step in the reaction otherwise one can assume that the surface concentrations behave like the bulk concentration in a thin sheet corresponding to the typical gap between the cells. The parameter used to estimate this is the Damköhler number Da [*Batsilas et al.*, 2003; *Solomon and Paul*, 2006]

$$
Da = \frac{k_{on} R_d d}{D} \sim 0.01 \ldots 0.1
\tag{5.72}
$$

with the reaction rate $k_{on} = 10^7 \, \text{M}^{-1}\text{s}^{-1}$, receptor surface concentration R_d, layer thickness $d = 250 \, \text{nm}$, and bulk diffusion constant $D = 100 \, \mu\text{m}^2\text{s}^-$. The receptor surface concentration can be estimated to be

$R = 10^5/(N_A \cdot A) = 4 \cdot 10^{-22}\,\mathrm{mol}\,\mu\mathrm{m}^{-2}$ assuming about 10^5 receptors distributed on the surface of $A = 400\,\mu\mathrm{m}^2$ (N_A is the Avogadro number; for parameter values see (Table 5.4)). This number is the ratio of the reaction timescale to the timescale of the diffusive transport. If Da is small compared to 1 then the reaction is limiting and the diffusion can be considered as homogeneous to a good approximation. This allows to use the bulk concentration for the ODE system (Eq. 5.49). Fortunately, as long as the reaction rates are fast compared to the experimentally observed rate for the internalization and recycling the general behavior of the system won't change much.

It is of importance to note that the Damköhler number Da for the chosen parameter set indicates that diffusion does not play a significant role in the desensitization model on a cellular length scale (Eq. 5.68) but this can easily change by using a different parameter set. It could be that the diffusion constant D is smaller or the reaction rate k_{on} is greater yielding $Da \gg 1$ indicating a diffusion-limited process. A meaningful test of this parameter range would require explicit modeling of a surface reaction implying a far higher spatial resolution than the model provides which treats cells as point-like particles with respect to the diffusion-reaction system. Considering the results this seems however not to have too much influence on the conclusions made in this thesis.

5.7 Modeling cell migration

This section describes the forces generated by migrating cells. The cell's choice of direction in response to a chemokine has been explained in the previous section.

The main question is where cells do exert their forces on to move through their environment. One component is the ECM the other are the neighbor cells. The ECM is considered as a background with infinite mass such that all forces exerted onto the matrix are used for propulsing the cell. Deformations or remodeling of the ECM are not covered in this work. This seems to be a reasonable assumption realizing that lymphocytes show amoeboid migration behavior which is independent of matrix metalloproteinases that remodel the ECM [*Wolf et al.*, 2003b] and the high flexibility of these cell (Sec. 3.2.1). The forces exerted directly on neighbor cells are less known. However, in the LN, expecially in the PLF, the ECM is rather sparse (Sec. 2.3.1). That leads to the conclusion that neighbor cells can serve as anchorage for lymphocyte migration.

The model for the migrative force exerted on other cells is based on the observation of constriction rings in lymphocyte migration [*de Bruyn*, 1946; *Lewis*, 1931; *Murray et al.*, 1992; *Wolf et al.*, 2003b] (Sec. 3.2.1). In the model it is assumed that a lymphocyte forms a single constriction ring which is initially generated at the leading edge of the cell. The ring is assumed to be tightly connected to the ECM and the cell is squeezing itself through the ring (Fig. 5.10). The part of cell in front of the constriction ring is assumed to exert an outwards directed pressure that is generated by contracting the posterior of the cell. Thus a cell pushes away the cells in front of itself and – dependent on the strength of adhesion – pulls on the cells on its back. The force acting on cell i by exerting active forces on a neighbor cell j reads

$$\mathbf{F}_{ij}^{\mathrm{active}}(\phi_i) = a_{ij} p_i^* \,\mathrm{sign}([\mathbf{x}_{ij} - \mathbf{x}_i^*] \cdot \mathbf{o}_i)\, \frac{\mathbf{x}_{ij} - \mathbf{x}_i^*}{\|\mathbf{x}_{ij} - \mathbf{x}_i^*\|} \qquad (5.73)$$

with the cell orientation $\mathbf{o}_i$, cell surface contact point $\mathbf{x}_{ij}$, constriction ring center $\mathbf{x}_i^*$, interaction area a_{ij} and the pressure p_i^* exerted by cell i. The force is directed as a centralized field radiating from the center of the constriction ring. For short this direction is abbreviated

$$\hat{\mathbf{n}}_{ij} \equiv \frac{\mathbf{x}_{ij} - \mathbf{x}_i^*}{\|\mathbf{x}_{ij} - \mathbf{x}_i^*\|} . \tag{5.74}$$

The total force on the cell i can be computed in the continuous limit[1] by integrating over the surface of cell with radius r_i

$$\mathbf{F}_i^{\text{propulsive}} = \sum_{j \in \mathcal{N}_i} \mathbf{F}_{ij}^{\text{active}} \to p_i^* r_i^2 \int_0^{2\pi} d\phi \int_{-1}^{+1} d(\cos\theta)\, \text{sign}([\mathbf{x}_{ij} - \mathbf{x}_i^*] \cdot \mathbf{o}_i)\, \hat{\mathbf{n}}_{ij}. \tag{5.75}$$

From the figure (Fig. 5.10) one can see that

$$\text{sign}([\mathbf{x}_{ij} - \mathbf{x}_i^*] \cdot \mathbf{o}_i) = \text{sign}(\cos\theta - \cos\theta_0) \tag{5.76}$$

holds. Splitting the integral over $\cos\theta$ in (Sec. 5.75) at $\cos\theta_0$ yields

$$\int_0^{2\pi} d\phi \int_{-1}^{+1} d(\cos\theta)\, \text{sign}(\cos\theta - \cos\theta_0)\, \hat{\mathbf{n}}_{ij} = \int_0^{2\pi} d\phi \int_{\cos\theta_0}^{+1} d(\cos\theta)\, \hat{\mathbf{n}}_{ij}$$
$$- \int_0^{2\pi} d\phi \int_{-1}^{\cos\theta_0} d(\cos\theta)\, \hat{\mathbf{n}}_{ij}. \tag{5.77}$$

The force direction $\hat{\mathbf{n}}_{ij}$ can be expressed as (Fig. 5.10)

$$\begin{aligned}
\hat{\mathbf{n}}_{ij} &= \frac{\hat{\mathbf{e}}_r - \cos\theta_0 \hat{\mathbf{e}}_z}{\|\hat{\mathbf{e}}_r - \cos\theta_0 \hat{\mathbf{e}}_z\|} \\
&= \frac{\sin\phi \sin\theta\, \hat{\mathbf{e}}_x + \cos\phi \sin\theta\, \hat{\mathbf{e}}_y + (\cos\theta - \cos\theta_0)\, \hat{\mathbf{e}}_z}{1 + 2\cos\theta_0 \cos\theta - \cos\theta_0^2}
\end{aligned} \tag{5.78}$$

where the relation $\hat{\mathbf{e}}_r = \sin\phi \sin\theta\, \hat{\mathbf{e}}_x + \cos\phi \sin\theta\, \hat{\mathbf{e}}_y + \cos\theta\, \hat{\mathbf{e}}_z$ has been used in the second equality. The integration over ϕ for the $\hat{\mathbf{e}}_x$ and $\hat{\mathbf{e}}_y$ terms vanish due to the integration over a full period of the trigonometric functions. With the term $\cos\theta_0 \hat{\mathbf{e}}_z$ being also independent of ϕ due to the cylinder symmetry of the problem the integrals simplifies to (using the short notation $\cos\theta = u$)

$$2\pi \left\{ \int_{u_0}^{+1} du \frac{u - u_0}{1 - 2u_0 u + u_0^2} - \int_{-1}^{u_0} du \frac{u - u_0}{1 - 2u_0 u + u_0^2} \right\} \hat{\mathbf{e}}_z. \tag{5.79}$$

Solving the integrals gives

$$\int_{u_0}^{+1} du \frac{u - u_0}{1 - 2u_0 u + u_0^2} - \int_{-1}^{u_0} du \frac{u - u_0}{1 - 2u_0 u + u_0^2} = 1 \tag{5.80}$$

and finally

$$\mathbf{F}_i^{\text{propulsive}} = 2\pi\, p_i^* r_i^2 \hat{\mathbf{e}}_z \tag{5.81}$$

for the total force which is independent of the position of the constriction ring. One may also use an

---

[1]In the simulation only the sum $\sum_{j \in \mathcal{N}_i}$ is computed. Therefore the geometry of the neighbor cell configuration influences the total force by approximating the cell's sphere as polyhedron according to the Voronoi cell picture.
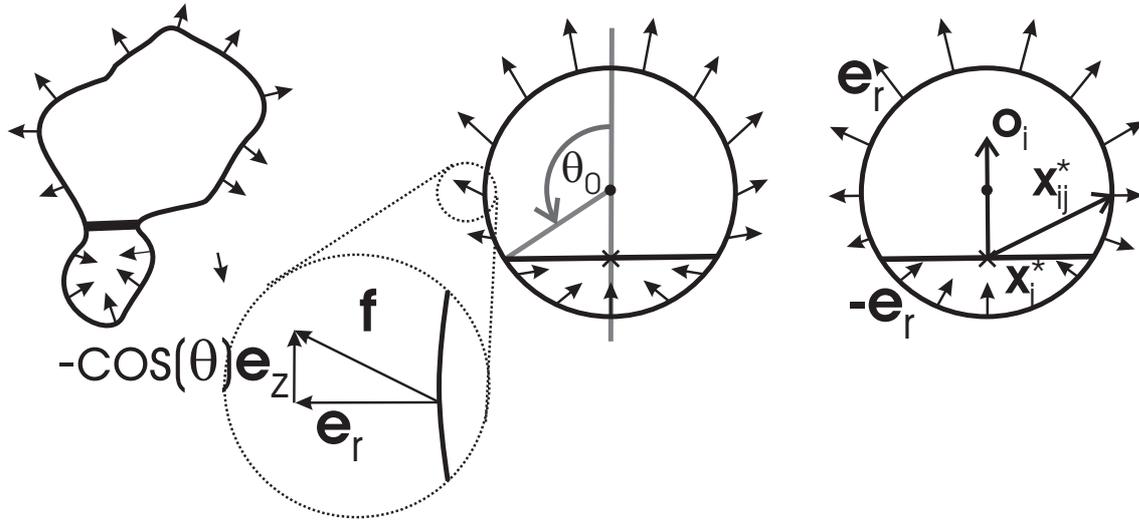
Figure 5.10: Active forces of an actively migrating lymphocyte. A realistic force distribution of a migration lymphocyte is shown in the left panel with the constriction ring (thick horizontal line) separating the area from inwards directed forces from the area with outside directed forces. Two possible models of this process mapped on spherical cell representation are shown on the right. In the middle panel the force center is located in the middle of the constriction ring. In the right panel the center of the forces is located in the center of the cell implying that the forces act perpendicular to the cell surface. In the model the spherical surface is approximated by the polyhedral shape of a Voronoi cell determined by the neighbor cells the active forces act on. The angle θ_0 determines the position of the constriction ring relative to the cell.

alternative force relation by demanding that the force on the cell surface is acting perpendicular

$$\mathbf{F}_{ij}^{\text{active}} = a_{ij} p_i^* \, \text{sign}([\mathbf{x}_{ij} - \mathbf{x}_i^*] \cdot \mathbf{o}_i) \, \hat{\mathbf{e}}_{ij} \tag{5.82}$$

which is to replace $\hat{\mathbf{n}}_{ij}$ by the face normal $\hat{\mathbf{e}}_{ij}$ and the radial unit vector $\hat{\mathbf{r}}$ in the continuous limit. Then (Eq. 5.79) changes into

$$2\pi \left\{ \int_{u_0}^{+1} du\, u - \int_{-1}^{u_0} du\, u \right\} \hat{\mathbf{e}}_z = 2\pi \, \hat{\mathbf{e}}_z \tag{5.83}$$

resulting in the constant force

$$\mathbf{F}_i^{\text{propulsive}} = 2\pi \, p_i^* r_i^2 \hat{\mathbf{e}}_z. \tag{5.84}$$

As the total force is the same in both situations none of the force models can be preferred over the other and the first version has been chosen.

Considering the experimental data the velocity during one migration cycle is not constant [*Murray et al.*, 1992]. Thus the simple model presented here does not fully cover the experimental data. One may assume that the force is proportional to the rear area of the cell which is generating the forces such that p_i^* depends on the position of the constriction ring.

5.8 Stromal cell networks and ECM

In contrast to lymphocytes stromal cells (FRC and FDC) are not moving significantly. Their mesenchymal precursors are migrating but the matured cell is embedded in the ECM also produced by the stromal cells itself. Stromal cells are connected to each other via their dendrites and ECM fibers forming a meshwork supporting and connecting stromal cells. In LN the conduit system provides an extraordinary network formation of this type where stromal cells are wrapping hollow ECM fibers (Sec. 2.2.4 and Sec. 2.3.1). The different behavior of stromal cells is described by a different 'migration'-model. It is assumed that every stromal cell is connected to all other stromal cells within a given range either via dendrites or ECM fibers. It is further assumed that the connections provide a semi-elastic mechanical framework by resisting stretching beyond a certain resting length (resulting from the initial condition) while not resisting compression below this resting length. The forces are described according to a half-open harmonic potential

$$\mathbf{f}_i^{\text{network}} = k_{\text{network}} \sum_{j \in \mathcal{N}} \Theta\left(\left|\mathbf{x}_j - \mathbf{x}_i\right| - l_{ij}\right)\left(\mathbf{x}_j - \mathbf{x}_i\right) \tag{5.85}$$

with a spring constant k_{network}, connection resting length l_{ij}, and $\Theta(.)$ being the Heaviside-step function. The whole stromal cell network is fixed to an infinite mass outside the simulation area. The differentiation of FRC to FDC and vice versa does not modify this 'migration'-model.

5.9 Simple angiogenesis and vasculogenesis model

There are quite some sophisticated models investigating which mechanisms underly the structure formation of blood vessels [*Chaplain and Anderson*, 2004; *Chaplain*, 2000; *Merks et al.*, 2006; *Namy et al.*, 2004]. In the present context the interest is not in the formation and regulation of vessels. The basic feature needed is that a certain number of vessels is present in an area dependent on the environment, e.g. the type of cells present there (Sec. 2.3.2 and Sec. 2.3.3). In addition it is not necessary to have a network of vessels as they serve only as entry and exit points for lymphocytes. Thus, the model represents vessel with a certain density of spheres of given size where cells can enter the tissue – by inserting them into the underlying regular triangulation – or leave the tissues – delete the corresponding vertex from the triangulation. Neither the internal dynamics of vessels nor the precise growth pattern is incorporated. Therefore the model generates isolated spheres representing the vessels. The model for the dynamics of HEV can be interpreted in a way that they get functional when signals from lymphocytes are provided as shown by experiments (Sec. 2.3.2).

There are no theoretical studies on the vasculogenesis of the lymphatic system. Also the experimental situation is not satisfying. Only recently there has been some efforts to find the factors regulating the growth of lymphatic vessels (Sec. 2.3.3). It seems to be widely similar to angiogenesis with slightly different factors involved. In the model lymphatic vessels are simulated in analogy to the blood vessels as spherical regions allowing cells to leave the tissue also omitting a detailed network formation dynamics.

The angiogenesis and vasculogenesis models are used to simulate a correct location of entry and exit
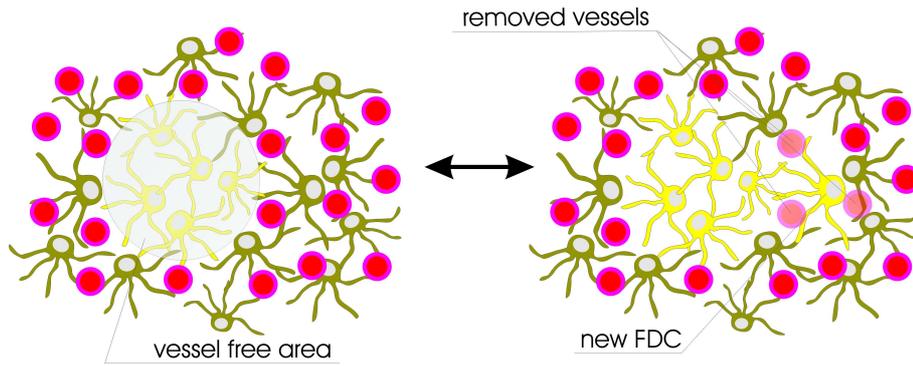
Figure 5.11: Simple angiogenesis model. The distribution of blood or lymphatic vessels correlates with the FDC-free area (left panel). For simplicity vessels are represented by a certain density of points (red disks) permitting either the entry or exits of cells. When an FRC differentiates to an FDC the vessels in this area are removed (right panel). Analogously vessels are create when an FDC differentiates back into an FRC.

points for lymphocytes in the PLF system, therefore it is correlated with the stromal background (Fig. 5.11) in a way that FDC-rich areas are free of both vessel types (Sec. 2.3.2 and Sec. 2.3.3).

5.10   Common model parameters

The cell parameters entering the model are mostly known by experiments or can be estimated by available experimental data. The references given provide the sections where the parameter is discussed in more detail including values or estimates. A few parameters are just technical values to solve the simulation and chosen to achieve suitable precision and to respect the underlying assumptions.

5.11   Summary of model idea

The model relies on three description levels. The first level determines the phenotype and biological behavior of cells. It incorporates the behavior when signals are encounter, e.g the generation of FDC when $LT\alpha_1\beta_2$ signals are provided (Sec. 2.2.2). The detailed signaling dynamics is unknown and not resolved in the model. It can be expected that this is not too important as the change of expression levels of many molecules has some quantitative effects without inducing qualitative differences (Sec. 2.2.2). The next level is the mechanical interaction of cells which includes the behavior upon cell collision and deformation. This is modeled using a rather simple approach of the JKR model. One may argue that the basic features of repulsion of cells in close contact and increase of contact surface and short-range attraction of cells upon adhesion are sufficient while the detailed behavior may not show up on the level of tissues. However, the influence of detailed mechanics has not been explored which is related to the lack of information about cell mechanics of lymphocytes in tissues. Also the required computer power can be expected to increase tremendously making it impossible to achieve a reasonable calculation time for the simulation of organogenesis with present hardware. The third and final level of the model includes the interaction of cells via diffusible substances. For the

parameter	value	remarks
maximal cell displacement Δx (Secs. 5.4.6, 5.6)	$0.6\mu m$	1/10th of B cell diameter
minimal time resolution Δt (Secs. 5.4.3, 5.4.6, 5.6)	10 s	adaptive time steps are usually 2.5 s
B cell : T cell ratio	0.4 : 0.6	[*Sacca et al.*, 1998; *Young*, 1999]
influx of cells (B + T)	0.1–2 cells s^{-1}	(Sec. 6.1.1)
diameter of simulation area	600 μm	
number of stromal cells	2500–11000	choice depends on the chosen FDC size
lymphocytes diameter (Sec. 5.4.3, Eqs. 5.15, 5.75)	$6\mu m$	[*Bornens et al.*, 1989; *Entschladen and Zanker*, 2000; *van Ewijk and van der Kwast*, 1980; *Haston and Shields*, 1984; *Thompson et al.*, 1984; *Wilkinson and Newman*, 1992]
time constant for vessel dynamics	6 h	delay time between FDC and vessel dynamics (Sec. 5.9)
vessel density	5%	volume fraction HEV and ELV (Sec. 6.2)
vessel number	5	number of vessels in the naive model (Sec. 6.1)
cell elasticity E (Eq. 5.8)	1 kPa	Table 5.2 (Sec.5.4.3)
Poisson ratio ν (Eq. 5.8)	0.4	Table 5.2 and [*Maniotis et al.*, 1997] (Sec.5.4.3)
adhesion energy σ (Eq. 5.15)	0–0.3 nN μm^{-1}	(Sec. 5.4.3)
migration force on ECM F^{active} (Eq. 5.5)	50–200 nN	(Sec. 3.2.2)
constriction ring pressure p_i^* (Eq. 5.73)	0.4 nN μm^{-2}	[*Galbraith and Sheetz*, 1999] (Sec. 5.7)
persistence time (Sec. 5.3)	120–180 s	[*Miller et al.*, 2002; *Wei et al.*, 2003]
friction coefficients	1500 nN μm^{-1} s	fitted to cell speed (Appendix B), (Table 5.2)
adhesion rupture force	100 nN	[*Burton et al.*, 1999; *Evans*, 1995; *Galbraith and Sheetz*, 1999] (Sec. 5.4.3)
onset of hard potential(Sec. 5.4.3)	100 nN	
elastic interactions of stromal cells k_{network} (Eq. 5.85)	100 nNμm^{-1}	(Sec. 5.8)
$LT\alpha_1\beta_2$ threshold on FRC	1	arbitrary unit; required to stimulate an FRC to differentiate to an FDC (Sec. 5.3.1)
low density $LT\alpha_1\beta_2$ on B cells	$0.025\,\mu m^{-2}$	unknown, equal to 5 cells in contact with stromal cell (Sec. 5.3.1) at equilibrium (h_{eq}, Eq. 5.19)
high density $LT\alpha_1\beta_2$ on B cells	$0.5\,\mu m^{-2}$	unknown, 25% of contact area at equilibrium sufficient for FDC induction (Sec. 5.3.1)
differentiation time for FDC $T_{\text{FRC}\rightarrow\text{FDC}}$	3 h	(Sec. 6.1.1, Sec. 5.3.1)
dissociation constant K_d	3 nM	(Sec. 5.5)
on-rate k_{on} (Eq. 5.49)	$10^7\,\text{M}^{-1}\text{s}^{-1}$	(Sec. 5.5)
internalization rate constant k_i (Eq. 5.49)	$5 \cdot 10^{-4}\,\text{s}^{-1}$	(Sec. 5.5)
receptor recycling rate constant k_r (Eq. 5.49)	$2 \cdot 10^{-4}\,\text{s}^{-1}$	(Sec. 5.5)
chemokine decay κ (Eq. 5.50)	$2 \cdot 10^{-4}\,\text{s}^{-1}$	[*Bar-Even et al.*, 2006]
chemokine production rate Q (Eq. 5.50)	$10^4\,\text{s}^{-1}$	(Sec. 5.5)
receptor density R_{tot} (Eq. 5.49)	10^4–10^5	(Sec. 5.5)
diffusion constant D (Eq. 5.68)	10–100 $\mu m^2\,s^{-1}$	[*Randolph et al.*, 2005]
volume fraction for diffusion ζ (Eq. 5.71)	0.03	[*Sen*, 2004]
size of diffusion grid	$1200\mu m$	
resolution of diffusion grid	35 μm	
gradient sensitivity threshold ΔR_{crit} (Sec. 5.5)	2%	concentration difference along cell diameter [*Parent and Devreotes*, 1999]

Table 5.4: The parameter used in the simulation. The equations and sections in the first column indicate where the parameter is introduced/discussed. In sections referenced in the right column indicate where the parameter value is discussed in more detail.

PLF system this is mainly the diffusion and reaction of chemokines. The reaction part is coupled to the first level of the model by the dynamics of the chemokine receptors that is modeled explicitely. The model is completed by including simple dynamics of vessels that allow cells to enter or leave the simulated tissue. The interaction of vessels is limited to this cell-flow property and interactions on level one and three. Mechanical interactions are ignored as the network property of the vessels is omitted. The model can describe all major features of PLF formation and SLT in general (Sec. 2) and perform tests to identify the relevant interactions or yet unknown interactions.

Chapter 6

Simulation Results

Simulations of primary lymphoid follicle formation have been performed using the agent-based model (Sec. 5) on top of regular triangulations (Sec. 4). The incorporated cell types are migrating B and T cells and FRC and FDC building the more or less immobile stromal background. Interactions between the cells are modeled according to the three level model of internal cell states, contact interaction, and long range interaction mediated by reaction-diffusion systems (Sec. 5.6).

The choice for an agent-based method has been made to treat single cell properties. This applies to the generation of FDC (Sec. 5.3.1) and the internalization dynamics of chemokine receptors (Sec. 5.5). The combination with a grid to describe soluble substance like chemokines allows to incorporate long-range interactions between cells and in general properties of a biological system that would be inefficiently described by an agent-based approach. The advantage and new feature of the chosen model is the explicit design to describe highly motile cells using the constriction ring model (Sec. 5.7). The model has been successfully used to describe two-photon imaging data on lymphocyte motility in SLT (Appendix B) [*Beyer and Meyer-Hermann*, 2007b; *Miller et al.*, 2002; *Okada et al.*, 2005].

The regular triangulation underlying the model architecture permits a continuous description of cell positions and motility and an efficient way to deal with frequently changing neighborhood relationships between cells. The same property is also required for the high cell fluxes resulting from the immigration end egress of lymphocytes from SLT (Sec. 2.4). In contrast, lattice-based architectures have difficulties to model fast cell migration. Either complicated rules are needed or a lattice-gas model is required [*Deutsch and Dormann*, 2003]. In both cases the parameters coupled with the modifications are not easily converted to observable quantities.

This chapter is organized as follows. First a simplistic simulation of follicle formation will be presented (Sec. 6.1) ignoring most of the dynamics and with minimal input from the microanatomy discussed previously (Sec. 2.2). The assumptions entering this reference system are provided in the next section. Changes or extensions to the reference model are given at the beginning of each section where certain subproblems of PLF formation are investigated in more detail. The second section concentrates on investigating the requirements for a stable B cell flux through SLT (Sec. 6.2). The results on the segregation of T cells and B cells forming rings as seen in many genetic deficiencies and

other manipulations of the system is discussed thereafter (Sec. 6.4). A dynamic for the T zone will be introduced here. The final section assembles all pieces of the previous simulations to a complete picture of lymphoid organogenesis and lymphneogenesis (Sec. 6.5).

6.1   Naive model of primary lymphoid follicle formation

Within a naive model a set of minimal assumptions is tested to build up a reference system. On this basis additional dynamics can be tested. This is useful to find out if a mechanism is really relevant and makes some contribution to PLF formation or if it is redundant and can be neglected in lymphoid tissue formation. In order to investigate the stability of a formed follicle a preformed network of FDC is investigated. Thereafter the dynamic formation of a PLF without FDC in the initial stage is simulated.

In summary, the minimal set of assumptions entering the model is

- fixed number of non-migrating FRC (Sec. 2.2.4),

- constant entrance of B cells and T cells via small number of HEV (Sec. 2.3.2),

- B cells and T cells use a small number of fixed ELV for egress from the SLT (Sec. 2.3.3),

- B cells and T cells leaving the SLT via ELV when $S1P_1$ levels are sufficient (Sec. 2.4.2),

- generation of FDC by B cell $LT\alpha_1\beta_2$ signaling (Sec. 2.2.2 and Sec. 5.3.1),

- replacement of FRC by generated FDC (Sec. 5.3.1),

- removal of FDC (replaced by FRC) in case of lack of $LT\alpha_1\beta_2$ stimulation (Sec. 5.3.1),

- secretion of CXCL13 by FDC (Sec. 2.2),

- secretion of CCL21 by FRC (Sec. 2.2),

- secretion of S1P by ELV (Sec. 2.4.2),

- chemotactic activity of B cells to CXCL13, CCL21 (Sec. 2.2), and S1P (Sec. 2.4.2),

- chemotactic activity of T cells to CCL21 (Sec. 2.2) and S1P (Sec. 2.4.2),

- CXCR5 and CCR7 receptors have an internalization dynamics when bound to their ligands CXCL13 and CCL21, respectively (Sec. 5.5)

- B and T cell migrate according to the constriction ring model (Sec. 5.7),

- the passive mechanical cell contacts are described by the JKR-model (Sec. 5.4.3).

In the naive model the basic assumption is that cells enter a stromal environment at some point and leave it at some other point to allow for a flow equilibrium. Thus, the second and third assumption that lymphocytes enter through a small number of HEV and leave through a small number of ELV represent the simplest version for a flux of lymphocytes (except for entering and leaving through the
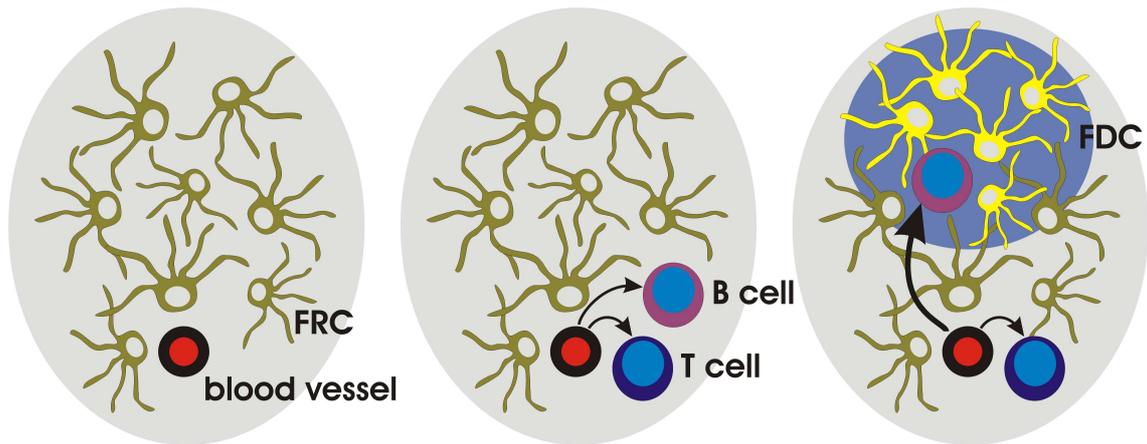
Figure 6.1: The sequence of follicle formation. The initial condition is the presence of an entry point (blood vessel) and a stromal background of FRC (left panel). The immigration of B and T cells (middle panel) leads to the generation of FDC which attracts B cells (right panel). The T cells stay in the area filled with FRC. Note that the points where B and T cells leave the tissue are not shown.

same spot). The remaining critical assumptions are all backed up by experiments and are discussed in more detail in the following sections.

Finally, the stromal environment in the simulation is bound by a capsule. This simplifies the simulation but is not absolutely required as the PLF size shall not be bounded by connective tissue. Note, that the capsule is not corresponding to one that forms around the PLF directly (Sec. 2.3.1). It is like the boundary that is formed by the encapsulation of the organ, i.e. the capsule of the LN or the epithelial tissue of the the mucosa in the case of MALT.

6.1.1 Initial formation of follicular dendritic cells

An important question is how the first FDC is generated. In various knockout experiments (Sec. 2.2.2) it has been observed that the lymphoid tissue microarchitecture can be restored by the influx of lymphocytes depending on specific experimental conditions. This suggests that the low basal levels of $LT\alpha_1\beta_2$ on lymphocytes are sufficient to induce the generation of FDC.

In order to allow low levels of $LT\alpha_1\beta_2$ per B cell to stimulate FDC properly, an aggregate of B cells around an FRC has to form that provides a total $LT\alpha_1\beta_2$ stimulus sufficient to induce the FRC differentiation to an FDC and subsequent CXCL13 production. The model replaces an FRC by an FDC in order to generate an FDC (Fig. 6.1). This can be done either by local differentiation but is also consistent with immigration of FDC which get activated and somehow lead to the depletion of nearby FRC (Sec. 2.2.3).

The onset of CXCL13 production by FDC effectively starts two separate positive feedback loops. First, more B cells are attracted raising the integrated $LT\alpha_1\beta_2$ levels sensed by the FDC and nearby FRC. Second, the positive feedback loop increases the $LT\alpha_1\beta_2$ one single B cells [*Ansel et al.*, 2000] by stimulation of CXCR5. This enhances the effects of the first loop. The CXCL13-induced $LT\alpha_1\beta_2$ level can be chosen to be proportional to the concentration of bound or internalized CXCR5

receptors. The first option gives an immediate response while the latter one includes a delay. There is no principal difference in the outcome of either variant. That is due to the fact that the delay in $LT\alpha_1\beta_2$ response of B cells is still shorter than the differentiation of FRC into FDC. Assuming that the increased levels of $LT\alpha_1\beta_2$ on CXCL13-stimulated B cells lasts longer than the average time needed to induce the FDC phenotype would however change the picture. In this case B cells usually leave the tissue before the elevated $LT\alpha_1\beta_2$ levels can take effect. One should not that the first feedback mechanism is already sufficient for PLF formation suggesting that the feedback-loop between $LT\alpha_1\beta_2$ and CXCL13 [*Ansel et al.*, 2000] is not important for generating PLF. This is also suggested by the presence of FDC in $CXCR5^{-/-}$ when B cells form a ring around the T zone but no PLF [*Voigt et al.*, 2000]. It might be that the increased $LT\alpha_1\beta_2$ levels induced by CXCL13 via the positive feedback loop are required in reconstitution experiments, i.e. the threshold for the generation of FDC may be raised after a developmental time window – a concept supported by other experiments [*Cupedo et al.*, 2004a]. Thus the positive feedback is important during lymphneogenesis but not during normal organogenesis.

In the simulation the density of stromal cells is lower than in the real tissue. That is an artifact of the modeling of stromal cells as spherical particles. In order to keep the surface of the stromal cells in the range of the real cells they are simulated as enlarged spheres with about the same surface as real stromal cells. The typical number of B cells per FDC are 20 to 100 [*Haberman and Shlomchik*, 2003; *Kosco et al.*, 1992]. The interaction surface can be estimated to $50\pi\,(6\mu m)^2 * (1/2) \approx 2800\,\mu m^2$ resulting in a stromal cell diameter of 30 μm. As the FDC are quite big they cannot be represented with the same number density as in the real system. To counterbalance the relatively low number of FDC the amount of CXCL13 produced by FDC is increased accordingly mimicking the production rate of several FDC. Similar arguments apply to FRC as source of CCL21. An effect that is also not taken into account is that the stromal network may extent when it gets filled with lymphocytes, i.e. the average distance between stromal cells is kept constant.

A critical parameter is the differentiation time of FRC into FDC $T_{\mathrm{FRC}\leftarrow\mathrm{FDC}}$. It has been chosen to be 3 hours. Experimentally the typical time may be in the order of 1 day [*van Ewijk and van der Kwast*, 1980; *Huber et al.*, 2005; *Mackay and Browning*, 1998; *Mebius et al.*, 1997] (Sec. 2.5). with the first signs of follicle formation as early as 6 hours [*van Ewijk and van der Kwast*, 1980]. However, for the simulations the exact value is not important as long as the typical time is well separated from the time for the other process which act on scales from 1–15 minutes (migration and receptor dynamics). Thus, the short differentiation time is chosen to speed up the simulation.

6.1.2   Inflow of lymphocytes

The entry of lymphocytes through HEV is simulated by generating new cells at fixed spots that represent the HEV. The influx of lymphocytes is chosen to be constant and is derived from the following estimate (see also (Sec. 2.4)). The typical size of a PLF is in the order of several 100 μm implying a typical B cell number of few thousand cells for 100 μm diameter to $\sim 3 \cdot 10^4$ cells for 200 μm diameter in the case of a dense packing of spherical B cells that have a diameter of about 6 μm. The flow through 1 gram LN containing $2 \cdot 10^9$ cells is in the order of $3 \cdot 10^7$ per hour [*Young*, 1999]. It

can be assumed that 25% of the cells are B cells within the PLF according to the fraction of B cells among the inflowing immune cells [*Sacca et al.*, 1998; *Young*, 1999]. The typical number of B cells per follicle leads to about $0.25 \cdot 2 \cdot 10^9 / 3 \cdot 10^4$ follicles per gram LN tissue. For influx of B cells into one follicle one gets $0.25 \cdot 3 \cdot 10^7 \text{cells hr}^{-1} / (0.25 \cdot 2 \cdot 10^9 / 3 \cdot 10^4) \approx 0.1 \, \text{cell s}^{-1}$. Considering the total travel time of lymphocytes through a large LN of sheep of 24 hours one may assume that the B cells reside about one third of the time in the follicle, i.e. 8 hours. For a typical follicle of 300 μm diameter a dense packing of B lymphocytes implies that about $3 \cdot 10^4$ B cells are in the PLF at any time point. The typical cell flow through the follicle is then $3 \cdot 10^4$ cells/8hr $\approx 1 \, \text{cell s}^{-1}$.

6.1.3 Lymphocyte egress from the lymphoid tissue

The efflux of B cells is assumed to be regulated by two mechanisms. There is a minimum time the cells spend in the lymphoid tissue which is regulated by the the resensitization of the S1P receptor $S1P_1$. The receptor dynamics generates transit times of about 2–3 hours (Sec. 2.4.2). This corresponds nicely to the measured minimal transit time for lymphocytes [*Pellas and Weiss*, 1990a,b; *Srikusalanukul et al.*, 2002; *Young*, 1999]. The $S1P_1$ mechanism is also assumed to regulate the T cell traffic. However, experiments with lymphocytes overexpressing $S1P_1$ challenge this view as those cells can still be found in SLT albeit at slightly changed locations [*Lo et al.*, 2005]. Probably additional mechanisms are involved in regulating the minimal transit time of lymphocytes.

A hint for a possible additional mechanism that regulates the lymphocyte efflux from SLT comes from the effects of IFNα on lymphocyte egress from lymphoid tissues [*Hein and Supersaxo*, 1988; *Kalaaji et al.*, 1988]. Increased IFNα levels reduce the amount of lymphocytes in the ELV, i.e. it is reducing the outflux of lymphocytes from SLT. A possible explanation for this effect might be the observation that IFNα can increase the chemotaxis of B cells [*Badr et al.*, 2005] (Sec. 3.3) thus trapping them in the B cell area by an enhanced response to CXCL13. This motivates the assumption that B cells in the follicle have an additional mechanism regulating their time spent in the tissue via the desensitization of CXCR5. Taking into account the chemotactic effects of S1P the balanced chemotactic response of B cells towards S1P and CXCL13 is regulating the retention time. The basic idea is that once B cells are able to respond to S1P they can get attracted to the ELV. As long as they have high CXCR5 levels this is prevented by the stronger attraction to the follicle following the CXCL13 produced by the FDC. The high levels of CXCL13 that are present in the follicle will lead to the subsequent internalization of the CXCR5 receptor and consequently to a decreased sensitivity of B cells to CXCL13. Thus, after the B cells spent a certain time in the follicle they will tend to follow the S1P gradient finally exiting the tissue by transmigrating through the ELV. Note, that the $S1P_1$ resensitization dynamics imposes a minimal size of the follicle in the order of 'time for $S1P_1$ resensitization * cell influx' which is already about $10^3 \ldots 10^4$ cells depending on the influx.

The internalized $S1P_1$ regulating the minimal transit time of lymphocytes is caused by the internalization of the receptor due to high levels of S1P in the blood stream (Sec. 2.4.2). The resensitization is simulated without taking into account the S1P concentration in the tissue in contrast to the more detailed model for the chemokines CXCL13 and CCL21 in which Eq. 5.55 is used. Without the knowledge about the S1P concentrations one can assume two regimes which are related to the

chemotactic sensitivity [*Dorsam et al.*, 2003]. In the first regime the S1P concentration is rather high such that within a certain distance from the ELV (source of S1P) S1P cannot act a chemoattractant, i.e. the optimal chemotactic sensitivity of the cell is far below that concentration. This has the effect that the cells close to the S1P source exhibit non-directed motility. In the second regime the S1P concentration is low enough to permit chemotaxis close to the source as well but consequently has a shorter range. The simulation results presented below demonstrate that the first regime gives more realistic results. The reason is that the chemokines CXCL13 and CCL21 needed to shape the PLF are easily dominated by the S1P response in the second regime (see below).

6.1.4   Non-lymphocyte populations in organogenesis

During the organogenesis of LN and PP lymphocyte populations are largely absent. The corresponding hematopoietic cells are LTIC and later DC. From the experimental data discussed in (Sec. 2.5) it seems that LTIC play the same role in development as B cells in the spleen while DC behave similar to T cells with respect to their localization. Therefore, throughout the simulation one can interprete B cells as LTIC and T cells as DC, respectively if the simulation is applied to the organogenesis of LN and MALT. For the spleen and lymphneogenesis B and T cells remain the major players. However, on should note that the migration data will change as it is known that DC migrate significantly slower than T cells [*Gunzer et al.*, 2000; *Miller et al.*, 2004] and there is no migration data available for LTIC.

6.1.5   Results

The results of the simulation demonstrate that a flow equilibrium is established. Putting in the experimental data for the simulation parameters (Table 5.4) one achieves reasonable follicle sizes although they are usually in the range of small follicles (Table 2.1). Analyzing the results in detail reveals certain interesting aspects.

Location of PLF formation   The relative geometric position of HEV and efferent vessels influences the position and shape of the generated PLF. The detailed geometry in relation to the boundaries of the simulation area also has some influence. However, the impact of the boundary is minor such that the position of the HEV has been kept fixed during the simulations. For small distances between HEV and ELV of ~100 μm the follicle forms a sphere around the ELV (Fig. 6.2 and Fig. 6.4) due to the chemoattraction mediated by S1P. The position of the follicle is stable as even the presence of a preformed FDC network would not determine the position of the PLF. The distribution of the chemokine CXCL13 that is leading B cells to the follicle develops from a rather simplex peak-distribution (Fig. 6.3, 0 min) to a more complex pattern (Fig. 6.3) which is the effect of the CXCR5 internalization dynamics and the dynamics of the FDC. This will be investigated in more detail in the next two paragraphs.

T cells are engulfing the follicle crescent-shaped. Occasionally, the T zone is completely surrounding the follicle (Fig. 6.4). The T cells do not need to cross the B cell follicle in order to reach the ELV.
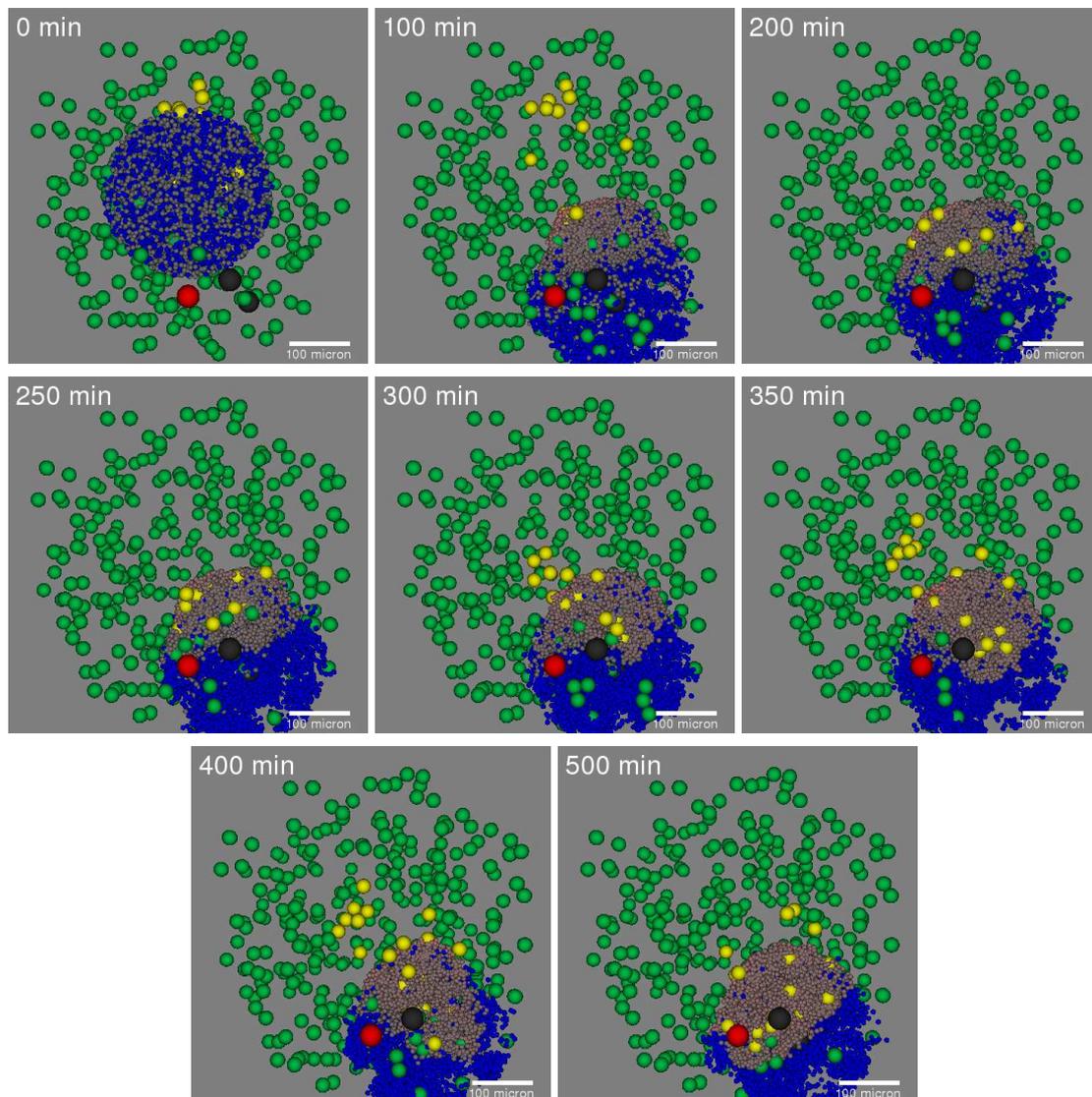
Figure 6.2: Generation of a follicle starting with an unsorted lymphocyte pool. A number of FDC are pre-formed at the initial stage together with a few thousand T and B cells. The follicle forms around the ELV. However, a few of the initial FDC are dragged with the B cells moving in response to S1P towards the ELV and are slowly released and repositioned in the stromal network (not shown here). The remnant of the initial configuration is an orientation of the PLF in the direction of the initial FDC (see 500 min). This is however not significant (Fig. 6.4). Note, that at all time steps the internalization level of CXCR5 is low on all B cells indicated by the grey color (high levels would appear pale red, compare to (Fig. 6.6)). (3D slice projection; light grey to pale red: B cells with increasing internalization levels of CXCR5, dark blue: T cells, green: FRC, yellow: FDC, red: HEV, dark grey: ELV)
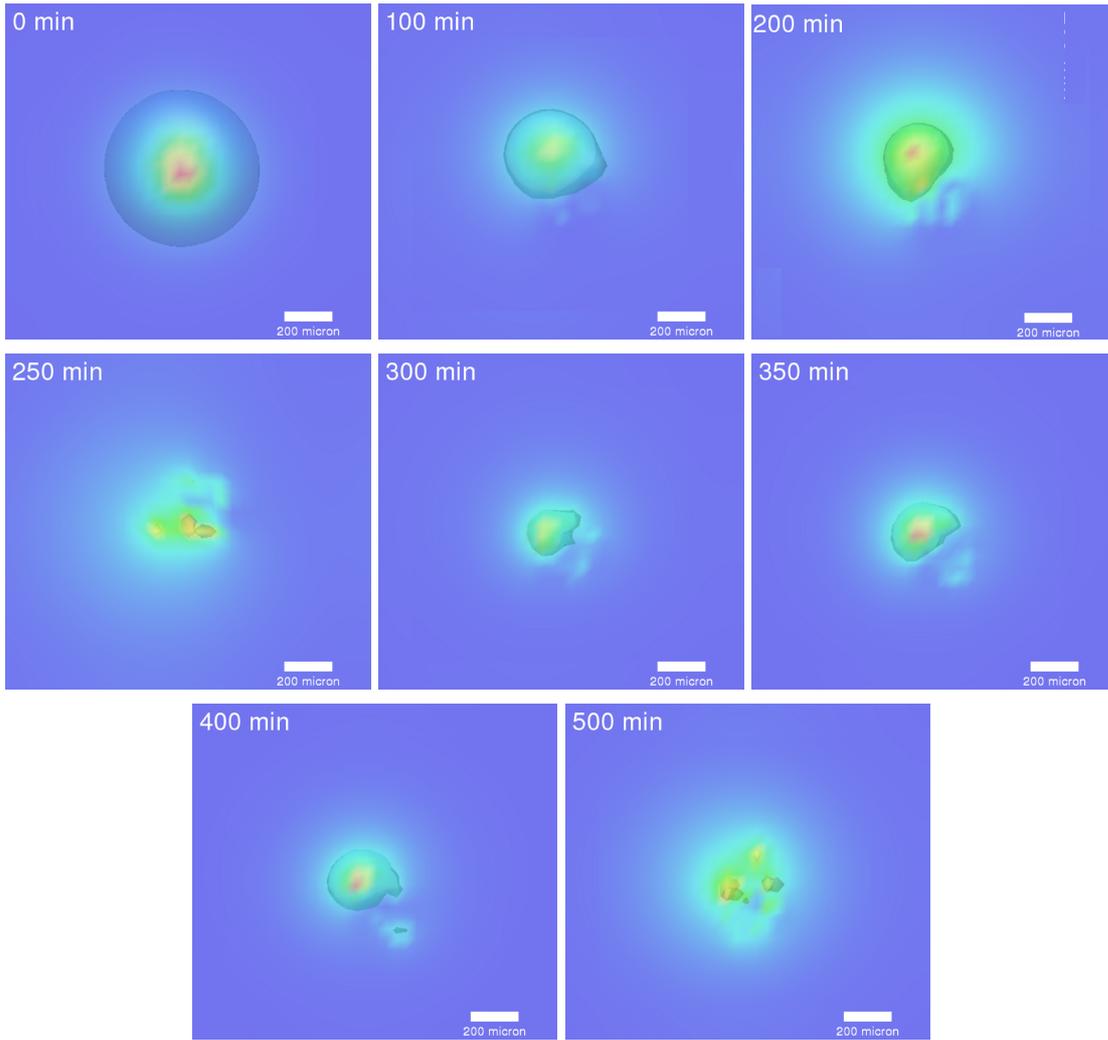
Figure 6.3: The CXCL13 concentration corresponding to (Fig. 6.2). (color code: relative concentration increasing from blue to green to yellow to red, absolute concentrations change between the panels)
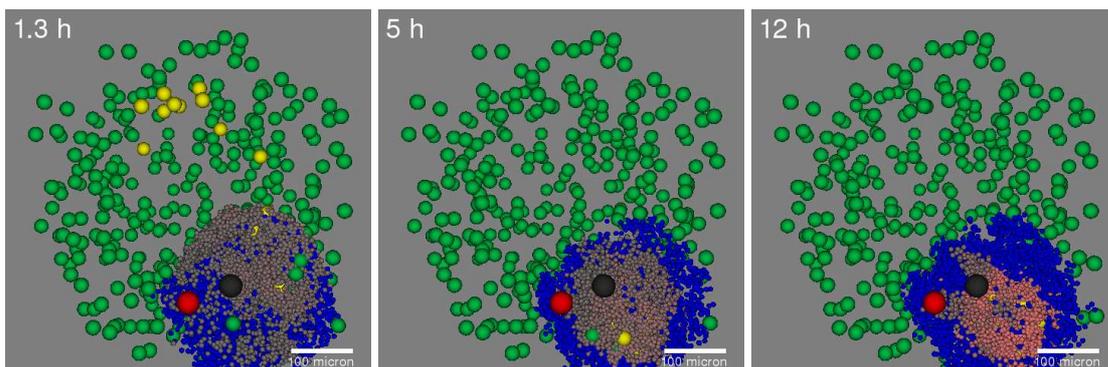
Figure 6.4: A follicle that is completely surrounded by T cells. Initial conditions are as in (Fig. 6.2). This effect is mostly dependent on the T cell number. With abundant T cell numbers they flow around the follicle. With lower numbers T cells remain together at one side of the follicle. Note, that in the rightmost panel the internalization of CXCR5 by B cells is very strong (small red balls) correlating with the recent generation of FDC in the follicle. (3D slice projection; light grey to pale red: B cells with increasing internalization levels of CXCR5, dark blue: T cells, green: FRC, yellow: FDC, red: HEV, dark grey: ELV)
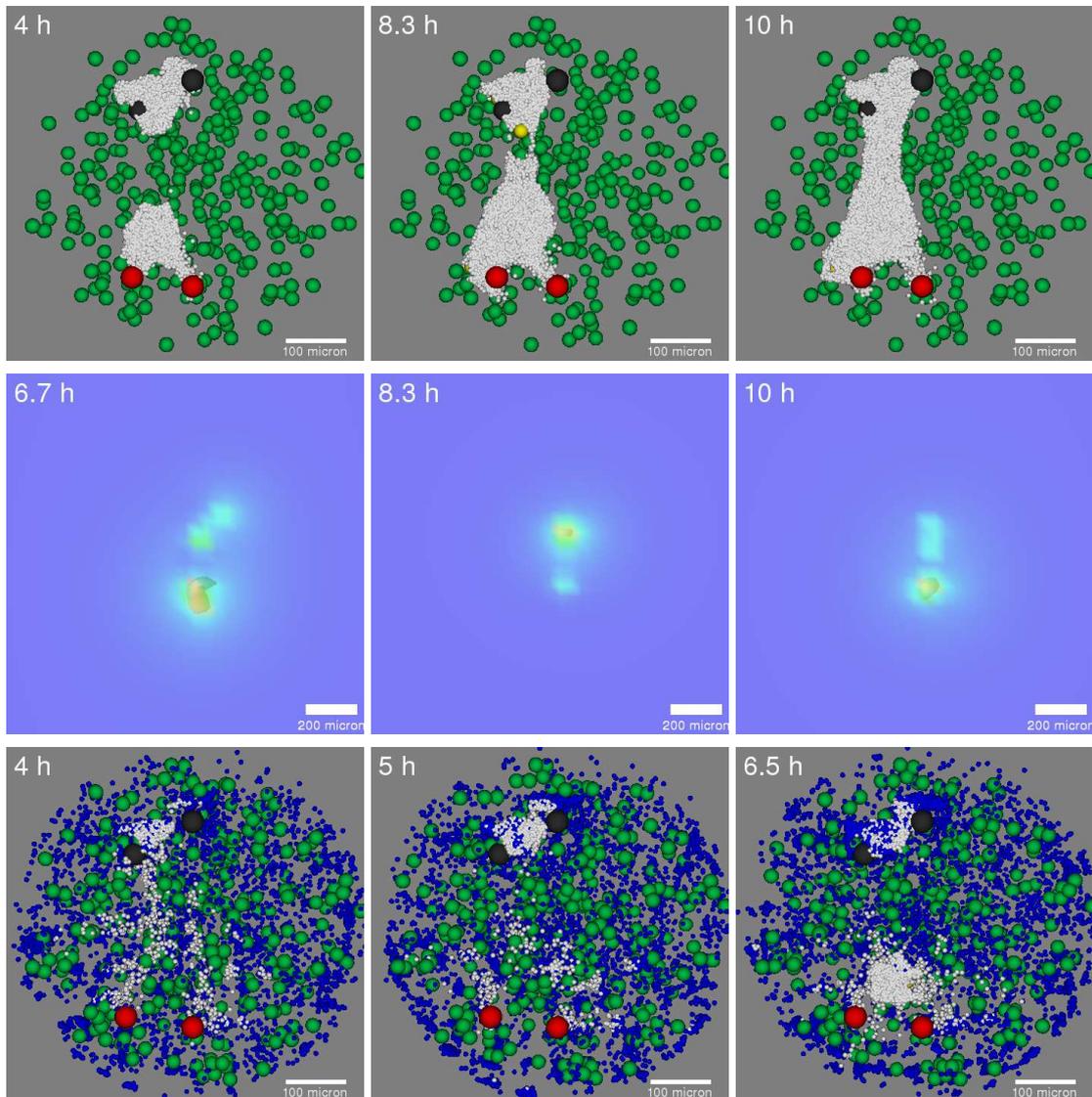
Figure 6.5: Formation of two B cell aggregates when the distance between ELV and HEV is large. The situation is not stable because as the aggregate around the HEV grows it makes contact with the second aggregate forming a bridge across B cells are flowing towards the ELV (upper series). The internalization process leads to the disruption of the bridge by lowering the CXCL13 concentration in this area leading to the dominance of one of the two aggregation centers (3 panels in the middle). The presence of T cells does prevent this to a certain extent (last series). (3D slice projection; white: B cells, dark blue: T cells, green: FRC, yellow: FDC, red: HEV, dark grey: ELV; most FDC are hidden between the B cells in this example; color code for concentration plots: relative concentration increasing from blue to green to yellow to red, absolute concentrations change between the panels)

At least one of these vessels is always located close to the T zone. This can be understood simply by considering the hypothetical situation that all ELV would be located inside the follicle. Then numerous T cells accumulate and – by random migration towards the follicle – reach a high density at some of the vessels. In the following the B cell density can get low enough to loose the maintenance signal for FDC and consequently the CXCL13 source close to this ELV. The asymmetry of the B cell distribution with respect to the ELV is preserved by the higher CCL21 concentrations close to the B cell-free lymphatic vessel compared to all other vessel. Thus the vicinity of the B cell-low ELV preferentially attracts T cells while the areas around the other ELV remain close to FDC and attract B cells.

For large distances between HEV and ELV the follicle forms in between those two vessel types. The PLF is elongated towards the ELV and shows a slow displacement in the direction of the efferent lymphatic vessels. Frequently, two follicles are formed around HEV and ELV. Cells are exchanged between these two follicles with the flow from the HEV-located follicle towards the one located around the ELV (Fig. 6.5). The two follicles around HEV and ELV get sometimes connected by a bridge of B cells. This bridge is influenced by the CXCR5 internalization dynamics. There are two peaks in the CXCL13 concentration – one for each FDC network. The internalization of CXCR5 lowers the CXCL13 concentration of the follicle close to the HEV (because of the high influx of B cells with full CXCR5 expression). The FDC network around the ELV still provides a strong CXCL13 gradient attracting the B cells around the HEV. That establishes a bridge between the follicles. The bridge disappears when the B cells approaching the PLF located around the ELV by lowering the CXCL13 concentration between the follicles. The B that moved to the ELV lower the CXCL13 concentration due to the CXCR5 internalization dynamics. The CXCL13 concentration around the HEV can recover due to low B cell numbers. Essentially the situation is the inverse to the situation before the formation of the bridge. Now B cells form a bridge to migrate from the ELV follicle towards the HEV follicle and the whole cycle can start again. Note, that the effective flux of B cells is directed to the ELV, i.e. the flux of the second B cell bridge pointing towards the HEV transports on average lower numbers of B cells. Of note, T cells can prevent these processes to a certain extent by effectively lowering the B cell density between the follicles. This keeps the CXCL13 concentration between the follicles rather high and permits a stable – but lower – flux between the follicles directed from the HEV to the ELV.

Internalization dynamics   The internalization of the CXCL13 receptor CXCR5 shows some interesting behavior. In Fig. 6.6 it can be seen that the population of B cells is synchronized with respect to the internalization levels of CXCR5. Moreover the CXCR5 internalization levels are cycling aperiodically between phases of low and high internalization, i.e. high and low chemotactic sensitivity for CXCL13. The cycling occurs due to fluctuations in the FDC generation. Whenever a new FDC is generate by a sufficient $LT\alpha_1\beta_2$ stimulus the amount of CXCL13 per B cell is increasing such that CXCR5 is internalized stronger. The decreased sensitivity for CXCL13 leads to a dominance of S1P chemotaxis of B cells causing them to leave the SLT faster. The reduced number of B cells is not able to provide sufficient $LT\alpha_1\beta_2$ maintenance signals for all FDC such that some FDC de-differentiate back to FRC. This reduces the level of CXCL13 and consequently B cells remain more sensitive for CXCL13 due to decreased CXCR5 internalization levels and the B cell outflux is reduced.
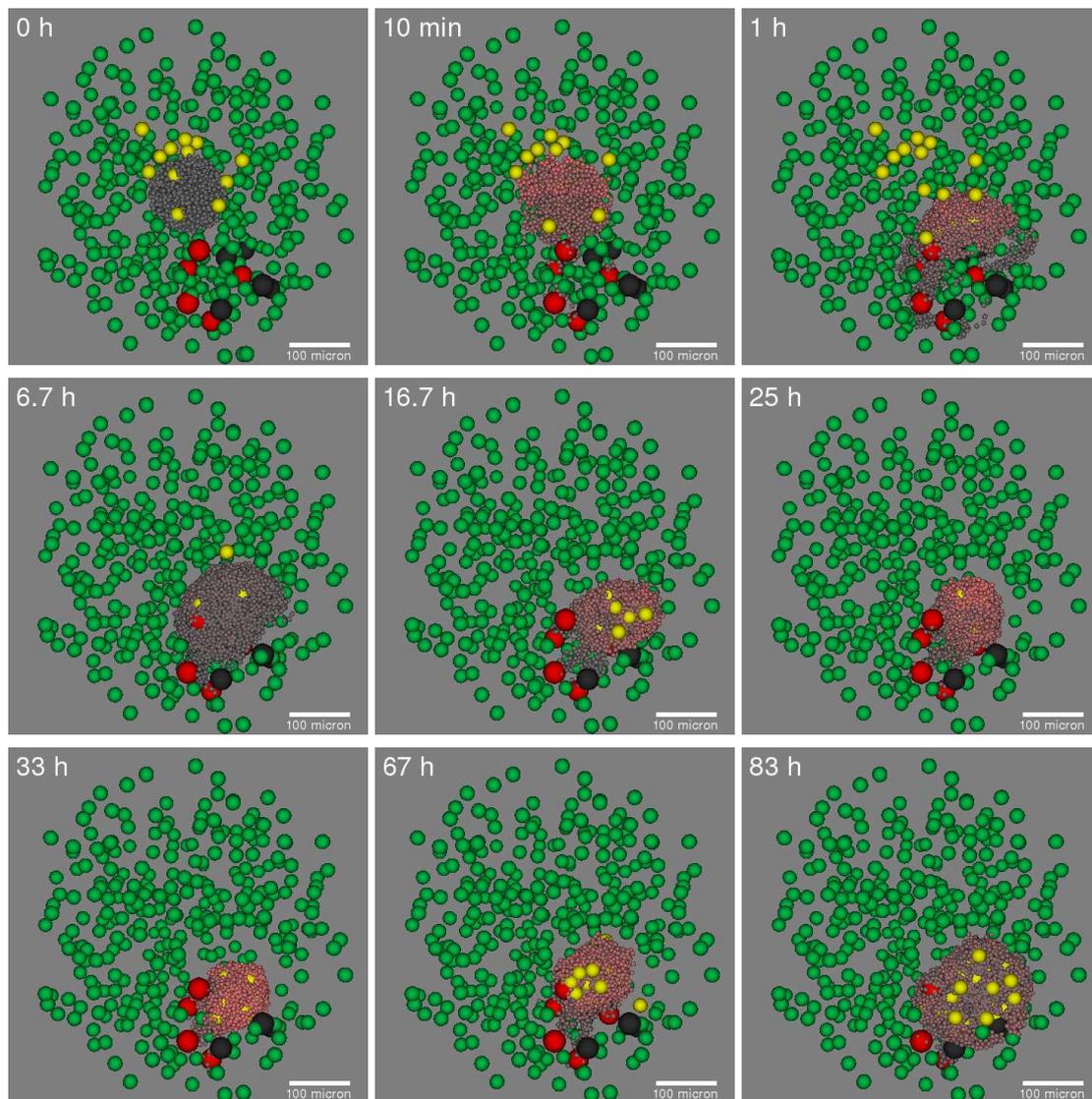
Figure 6.6: Naive model of follicle formation without T cells. The simulation starts with 5000 B cells that are initially sensitive for CXCL13 (small light grey balls). An FDC network has been preformed (0 h). The CXCL13 levels secreted by the FDC lead to a rapid internalization of the CXCR5 receptor (pale red color of B cells) while the B cells approach the FDC network (10 min). Newly inflowing cells from the HEV are initially grey and stain deeper red when CXCR5 is internalized as the cells chemotax towards the FDC (1 h). The asymmetry of the B cell distribution leads to a translocation of the FDC network by generating new FDC close to the vessels while FDC of the initial network backdifferentiate to FRC without the maintaining $LT\alpha_1\beta_2$ signal of the B cells (6.7 h). Of note, the B cells resensitize during this process due to the lack of a sufficient CXCL13 source. This increases the cell outflux effectively reducing the B cell number such that the relative amount of CXCL13 per B cell is sufficient for CXCR5 internalization (16.7 h). The process of B cell sensitization and re-sensitization can cycle aperiodically (25 – 83 h).

The location of the PLF is close to the ELV. Without a preformed FDC network the follicle grows immediately around the ELV and the remaining dynamics is the same (not shown). (3D slice projection; light grey to pale red: B cells with increasing internalization levels of CXCR5, green: FRC, yellow: FDC, red: HEV, dark grey: ELV)
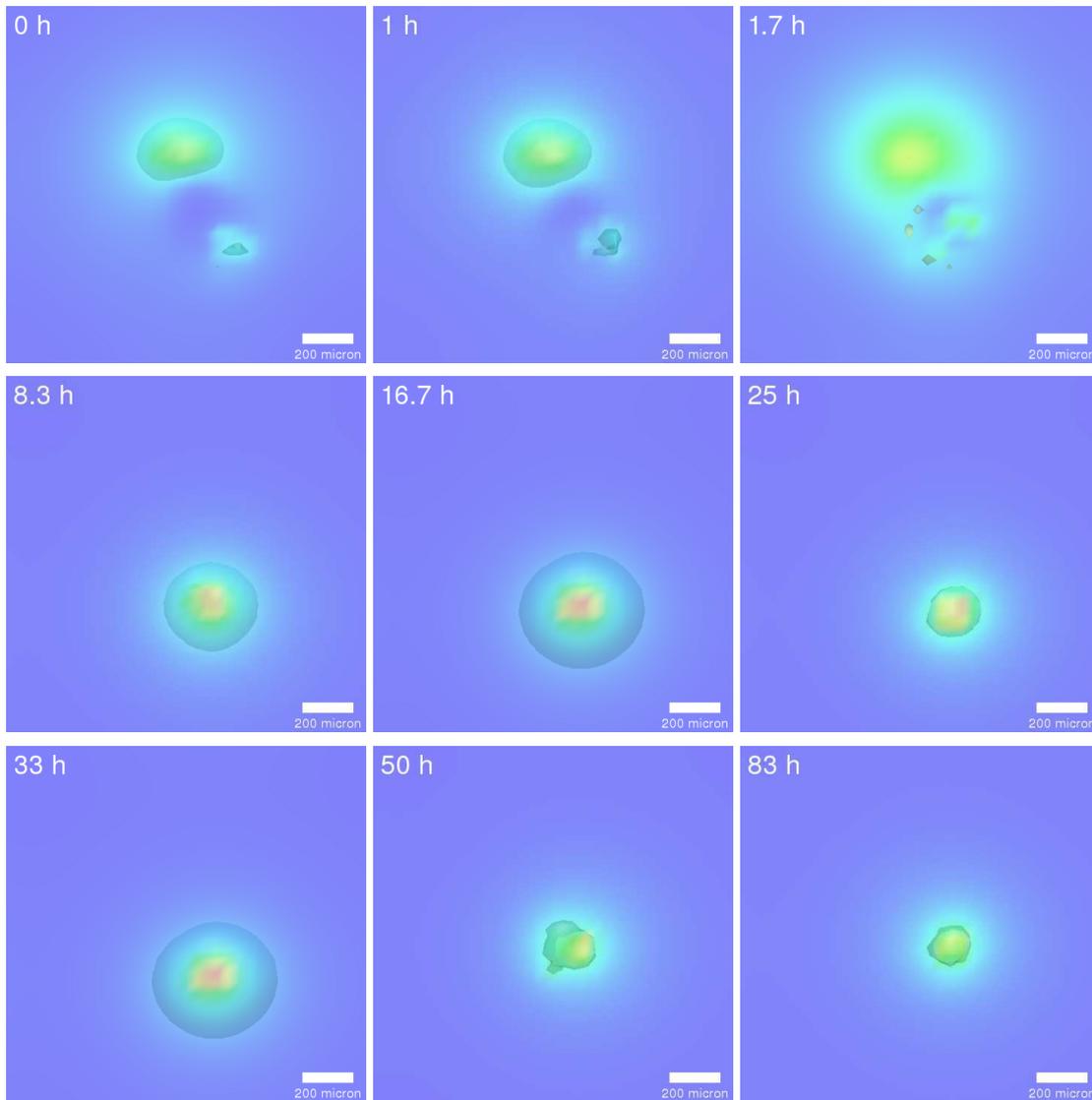
Figure 6.7: The CXCL13 concentration during the follicle formation in the simulation shown in (Fig. 6.6). In the initial picture the CXCL13 concentration is a result of the stationary diffusion solution and the onset of the internalization process (0 h). This leaves the peak concentration in the lower right corner while there is a markedly decrease in CXCL13 concentration in between (0 h). This is the position of the B cells that internalize CXCR5 and thus lower the concentration of CXCL13. The initial peak diffuses away (1.7 h vs. 8.3 h). The total concentration of CXCL13 decreases in the center when FDC backdifferentiate and B cell internalize the remaining CXCL13. The generation of new FDC can be clearly seen by generating a new peak concentration on the right (which is only accidently at the same place like the source-less concentration peak at 0 h). The cycling behavior of the follicle (Fig. 6.6) is indicated by the color changes from 8.3 to 83 h. (color code: relative concentration increasing from blue to green to yellow to red, absolute concentrations change between the panels).
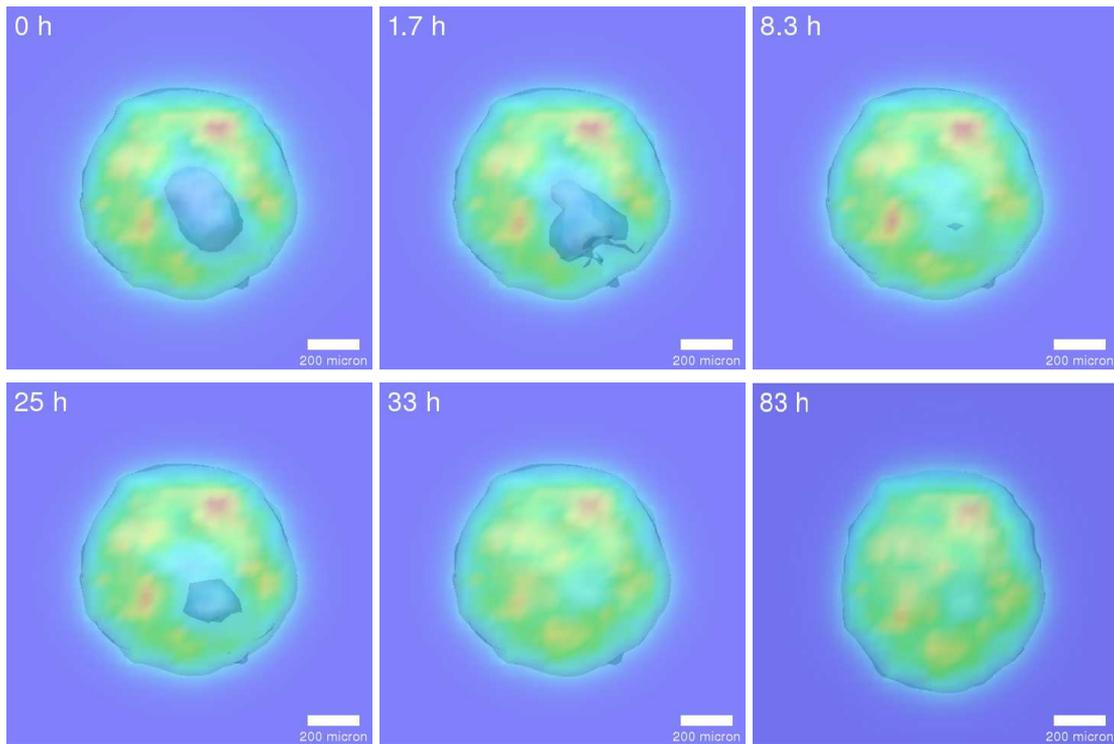
Figure 6.8: The CCL21 distribution corresponding to the simulation shown in (Fig. 6.6). The location of the B cells can be identified by the blue colored cavity indicating a low concentration. The cycling in the B cell number can be seen by the occasional size changes of the cavity (e.g. 8.3 h, 25 h, and 33 h).(color code: relative concentration increasing from blue to green to yellow to red, absolute concentrations change between the panels).

Increased B cell numbers lead to further reduction of CXCR5 internalization per B cell and an even stronger increase of B cell numbers until new FDC are generated starting the cycle from the beginning. The apparent synchronization of the CXCR5 internalization levels during the cycle is mediated by CXCL13 itself. Diffusion of CXCL13 prevents the presence of strong gradients such that the CXCL13 concentration tends to get homogeneous inside the PLF. This leads to the recycling of CXCR5 when CXCL13 levels are low, almost independent of the receptor state before, and to internalization when the concentrations are high.

Another effect of the CXCR5 internalization is the uptake of CXCL13 (Fig. 6.7). The CXCR5 internalization dynamics leads to reduced CXCL13 thus that the gradients of the chemokine can be locally inverted. This is indicated by the seemingly second source of CXCL13 that shows up as CXCL13 peak in the lower right corner of Fig. 6.7, top row. Note, that in Fig. 6.6 (0 h) the B cells and the FDC network do not have exactly the same center. Thus the majority of the B cells is located outside the highest production and concentration of CXCL13. This creates the asymmetry that shows up as double-peak structure in the CXCL13 concentration. Over time the CXCL13 concentration can rise again because most of the CXCR5 has been internalized (Fig. 6.7, 1.7 h) and most of the B cells already followed S1P towards the EVL (Fig. 6.7, 1 h). Later when the preformed FDC network has been lost and new FDC are created around the ELV the CXCL13 concentration shows a single peak because FDC and B cells are forming around the same center – the ELV. Thus the CXCR5 internaliza-

tion decreases the CXCL13 concentration in a symmetric manner preserving the peak shape (Fig. 6.7, 8.3-83 h). However, the absolute concentration keeps changing as discussed previously (Fig. 6.6, 6.7-83h).

The internalization dynamics has also the consequence that the areas with high cell densities show lowered concentrations of the chemokine CCL21 (Fig. 6.8). This leads to an attraction away from the aggregation area (central blue areas in Fig. 6.8). In the naive follicle model this chemotactic response is counter-balanced by the attraction mediated by S1P such that the T cells remain close to the follicle (Fig. 6.2 and Fig. 6.4). Experimental evidence shows that CCL21 does not lead to the internalization of CCR7 [*Bardi et al.*, 2001]. This may in part explain why CCL21 is 100-fold more abundant in the T zone compared to CCL19 [*Luther et al.*, 2002]. However, one should keep in mind that cells are more sensitive to CCL19 compared to CCL21 [*Kim et al.*, 1998; *Willimann et al.*, 1998] such that the internalization dynamics assumed in the simulation is related to CCL19. The simulation does not distinguish between those two chemokines because they act on the same receptor CCR7.

Switching off S1P chemotaxis and CXCR5 internalization induced shape instability   In order to understand the dynamics of the system without the S1P response, S1P chemotaxis is switched off. The follicle cannot be stabilized with a fixed size because the efflux of cells due to random migration towards the ELV is always too low (not shown). Thus, the dynamics under zero flux conditions has been investigated, i.e a fixed number of B cells interacting with the stromal background. This identifies the synchronous cycling behavior of CXCR5 internalization levels as a source of instability for the PLF system (Fig. 6.9). In the full system described above this instability is counterbalanced by S1P providing an additional chemotactic attractor for B cells. The reason for the generated instability is that the cells which are exposed to a high CXCL13 concentration have raised $LT\alpha_1\beta_2$ levels (according to the positive feedback loop [*Ansel et al.*, 2000]) enabling them to stimulate FRC to FDC differentiation and maintenance very easily. At the same time the high chemokine concentrations lead to the internalization of CXCR5 promoting random migration of the B cells. Thus, the B cells leave the aggregate and induce FDC in the vicinity of the aggregate effectively deforming the FDC network and consequently the CXCL13 source distribution. Each new CXCL13 source leads to the redistribution of the B cells which finally (due to their fixed number) reduces the maintenance signal for some FDC that now differentiate back into an FRC. This dynamics leads to frequent shape changes and instability of the PLF system based on the CXCL13 internalization dynamics (Fig. 6.9). Note, that whether the CXCL13 concentration nor the B cell location in the previous simulations (Fig. 6.6 and Fig. 6.7) showed this instability. This is the effect of S1P that guarantees the shape of the aggregate independent of CXCR5 internalization. Instead of the shape instability the cycling behavior of CXCR5 internalization and B cell numbers appears (former paragraph).

Formation of follicles by random B cell aggregation   To study the efficiency of initiating the first FDC out of a network of FRC, a fixed number of B cells are allowed to migrate freely within the stromal background. The response to S1P is switched off in order to have no chemoattraction to the ELV. The initial migration pattern is free diffusion as there is no source of CXCL13 that could attract B cells. This still leads to the random aggregation of a sufficient number of B cells around one FRC
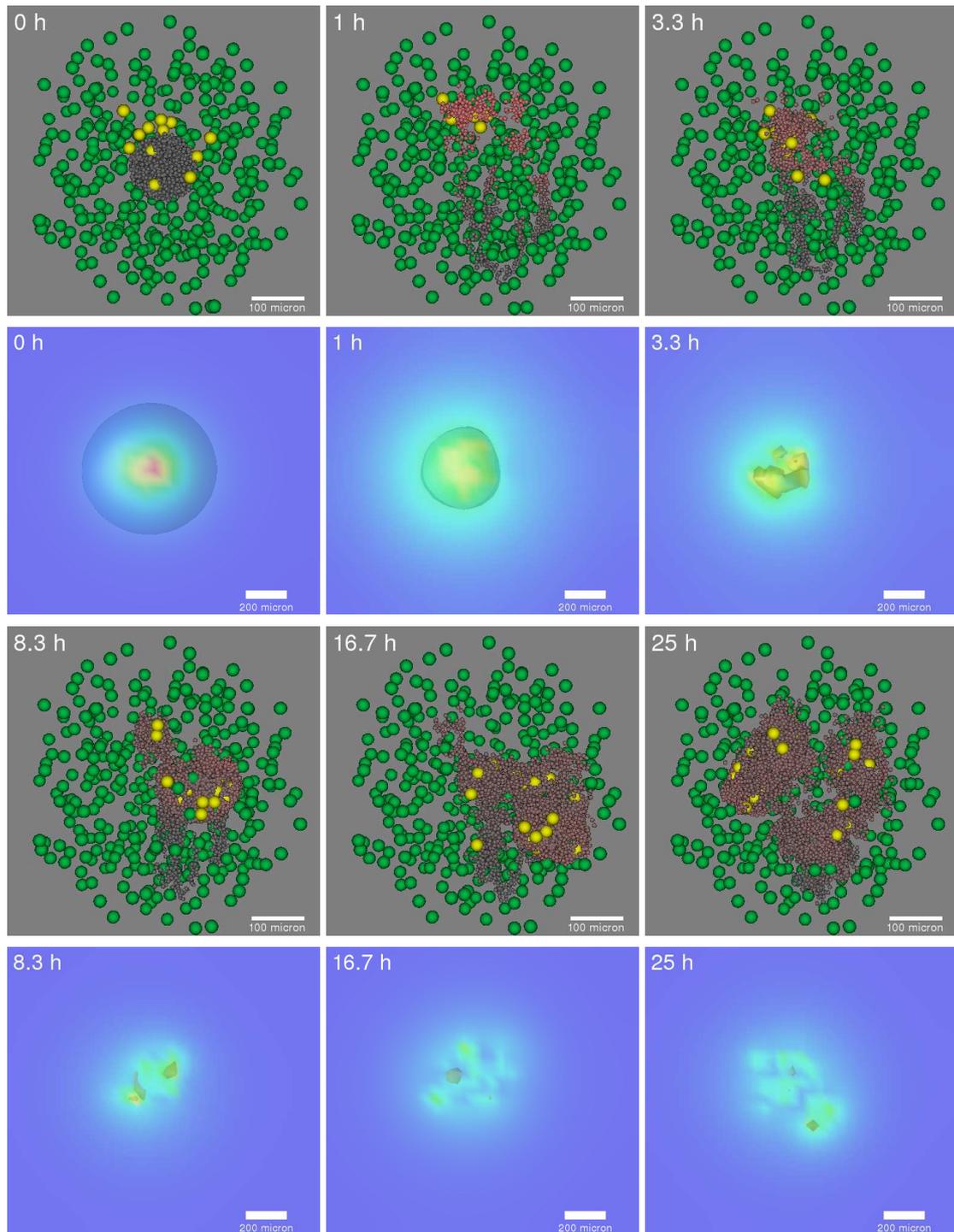
Figure 6.9: PLF dynamics without S1P chemotaxis and ELV, no influx and a preformed FDC network. This shows the instability of the system caused by the internalization process leading to rapid shape changes in the system despite the presence of a preformed FDC network. The CXCL13 distribution shows the corresponding changes, e.g. locally inverted gradients and multiple peaks. Furthermore, it demonstrates that CXCR5 internalization leads to cycling behavior by CXCL13 uptake (Fig. 6.6 and Fig. 6.7). Note, that the instability is not dependent on the preformed network (compare to Fig. 6.11). (3D slice projection; light grey to pale red: B cells with increasing internalization levels of CXCR5, green: FRC, yellow: FDC; color code for concentration plots: relative concentration increasing from blue to green to yellow to red, absolute concentrations change between the panels))
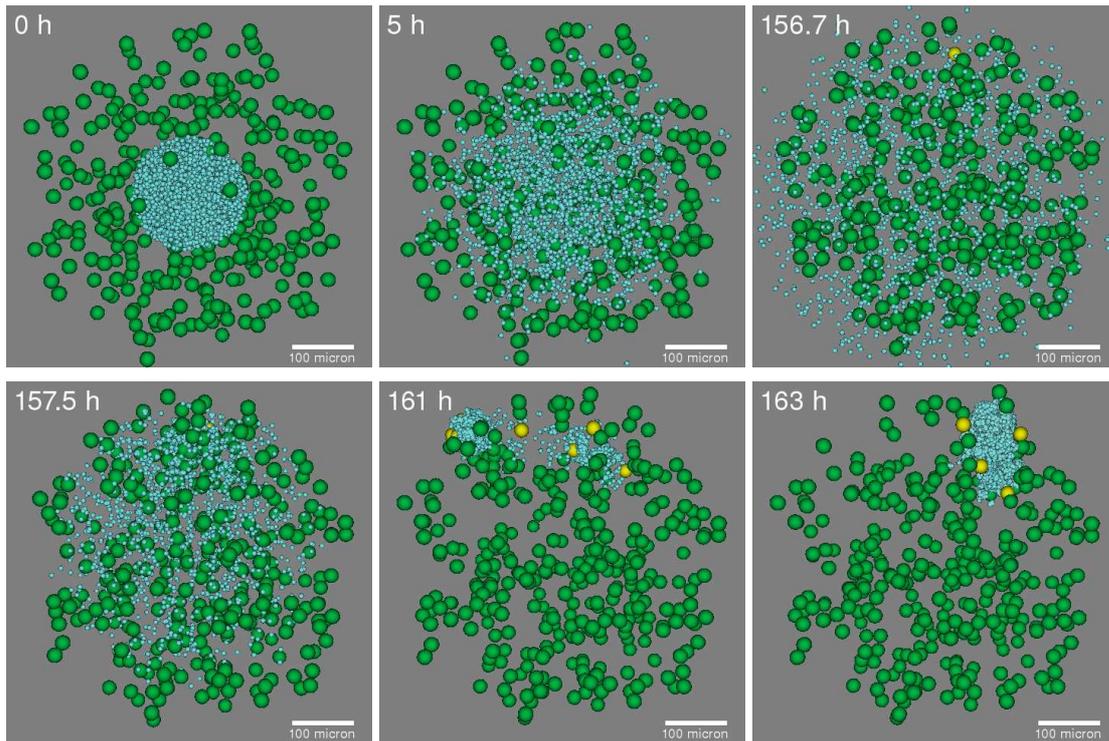
Figure 6.10: Formation of follicles by random aggregation of B cells. Influx and efflux of cells is not present in this simulation. S1P chemotaxis is shut off. Randomly forming B cell aggregates are sufficient to induce FDC, i.e. there can be B cell density fluctuations that are large and last long enough to provide the required $LT\alpha_1\beta_2$ stimulus. As soon as one FDC is generated all B cells are attracted and induce the differentiation of nearby FRC into FDC. It can also happen that a second follicle is generated depending on the aggregation speed and cell density in the system. The second follicle moves out of plane in the last panel due to the instability induced by the internalization as discussed before (Fig. 6.9). The critical parameters for the probability of generating the follicle are the B cell density (5000 B cells in this simulation) and the stimulation time required to induce a first FDC. (3D slice projection; bright blue: B cells, green: FRC, yellow: FDC
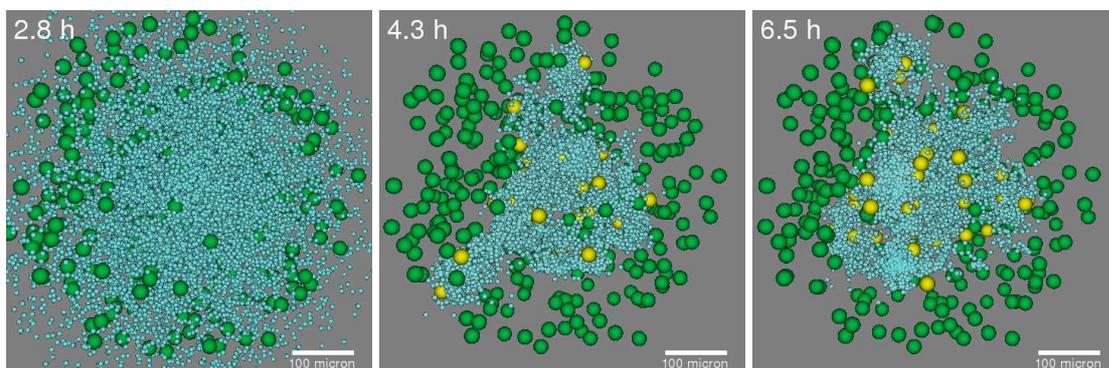
Figure 6.11: The same simulation as in Fig. 6.10 with a larger constant number of $3 \cdot 10^4$ B cells. The larger number of B cells makes the internalization-induced instability visible. Comparison with (Fig. 6.9) shows that the instability does not correlate with the presence of a preformed FDC network. (3D slice projection; bright blue: B cells, green: FRC, yellow: FDC, red: HEV, dark grey: ELV)

inducing the formation of a follicle by rapidly attracting all B cells within range (Fig. 6.10). The resulting follicle is usually not stable according to the results presented in the former paragraph. This is clearly visible when the number of B cells is increased (Fig. 6.11). The increased B cell number also demonstrates nicely that the generation of the first FDC is dependent on the density of B cells as can be seen by comparing the times when the first FDC is generated, i.e. 156.7 h vs. 4.3 h (Fig. 6.10 and Fig. 6.11). In both simulations B cells are weakly CCL21 responsive. Due to the almost homogeneous distribution of the source the CCL21 concentration is more or less constant and does not induce the aggregation of B cells. This can also be seen by the bright blue color of the B cells that shows that the CCR7 is rapidly internalized, thus the B cells are virtually insensitive to CCL21. A CCL21 sensitive cell would appear grey according the chosen visualization in Fig. 6.10 and Fig. 6.11. The cycling behavior that can be seen in the CXCL13 dynamics is not present because of the low concentration of the CCR7 receptor compared to the CCL21 sources such that the presence of B cells does not modify the CCL21 concentration significantly leaving it always at high concentrations (compared to (Fig. 6.8)).

The final conclusion is that the desensitization mechanism does not play a significant role in the regulation of the PLF size. The major effect regulating the PLF size in the naive model is that the efflux is regulated by the time a S1P resensitized cell needs to approach the ELV. This time is increased by the presence of the B cell aggregate forming the follicle. However, the chemotaxis attracting B cells towards the center of the follicle helps to increase the egress of the lymphocytes. This is in contrast to the expectation that the desensitization for CXCL13 regulates the B cell egress (Sec. 6.1.3) The internalization of B cells was introduced to allow B cells to respond to S1P, leave the follicle, and enter the ELV but in the simulation CXCL13 is supporting S1P to guide B cells close to exit spots. This effect is exclusively related to the position of the ELV inside the PLF. Therefore additional mechanism are required, especially a dynamics that keeps lymphatic vessels and PLF separated.

6.2 Efferent vessel dynamics

The microanatomy of SLT shows that the ELV are surrounding the PLF and are absent from the inside of the PLF (Sec. 2.3.3). This is in marked contrast to the naive model that forms PLF preferably containing efferent lymphatics. In principle there might be two solutions.

1. The ELV preform a hollow structure in which the PLF is formed during development.

2. The formation of the PLF induces remodeling of the lymphatic endothelium such that the follicular area is spared out.

There are several experiments that can decide about these two options. First, lymphatic vessels in knockout mice lacking PLF (Sec. 2.2.2) can be observed. If the lymphatics forms the same hollow structures seen in the normal tissue then the lymphatic vascularization would determine the position and size of the PLF. The absence of these structures however is not conclusive and could indicate that the precise formation of ELV directly depends on $LT\alpha_1\beta_2$ or TNF-α. But one still may favor the second interpretation as long as the overall lymphatic structure has not been reported to be abnormal elsewhere in the body. The effect of TNF-α and $LT\alpha_1\beta_2$ on blood endothelial cells (BEC) is primarily the expression of adhesion molecules [*von Andrian and Mempel*, 2003; *Cupedo et al.*, 2004c; *Drayton et al.*, 2003; *Rennert et al.*, 1997] while a reorganization of the vessel structure has not been reported so far. Second, the blocking of the $LT\alpha_1\beta_2$ signal via LTβR-Ig may induce the remodeling of the efferent lymphatics such that the PLF are vanishing and replaced by ELV. Similar to the knockout experiment this would favor the second concept but cannot rule out the first one, as a direct effect of $LT\alpha_1\beta_2$ on LEC cannot be excluded.

The direct observation of lymphatic endothelium development predicts opposite time sequences for the two concepts: The formation of PLF after remodeling of the lymphatics for the first case and vice versa for the second. However, if the changes occur together such that the increase of PLF size and the lymphatic network formation parallel each other the observation is not decisive again. Possibly the best experiment is the investigation of ectopic GC formation (Sec. 2.6) and artificial lymphneogenesis (Sec. 2.5.4). In both cases it can be assumed that the ELV are not a priori forming a follicle-supporting structure. The observation of lymphatic endothelium surrounding the newly formed follicles supports the notion that FDC generation can induce remodeling of efferent vasculature. In unorganized lymphoid tissue-like infiltrates arising in the course of ectopic expression of certain members of the TNF superfamily or chemokines (Sec. 2.5.4) the efferent lymphatics should appear as a homogeneous network. The vessels should reorganize when an Ag-challenge induces the proper lymphoid tissue structure (Sec. 2.5.4), i.e. the lymphatic endothelium has to vanish in the follicle area.

The working hypothesis is based on the observation that lymphneogenesis generates follicles with the typical PLF size independent from the precise location. Thus, it is assumed that the lymphatic networks are dynamically remodeled during PLF formation. An important aspect is that the ELV dynamics acts as a global inhibitor. When the follicle grows the surface of the lymphatic vessel network available for the B cells to leave the follicle increases. Thus the increase in the follicle size should lead to an increased efflux. Consequently, a decrease in B cell number decreases the efflux which should result in a stable follicle size.

The changes with respect to the naive model (Sec. 6.1) are:

- ELV are initially distributed throughout the stromal network,

- ELV disappear in the vicinity of newly generated FDC,

- ELV reappear when FDC differentiate back to FRC.

6.2.1 Realization of lymphatic vessel remodeling

A realization of the efferent lymphatic reorganization following PLF formation could be that the lymphocytes are pushing the vessels away. However, this raises the question why the vessels are pushed away by migrating lymphocytes in the B zone but not in the T zone. From the variations in the morphology of the sinus lining of follicles (Sec. 2.3.3) it seems more plausible that the lymphatic vascularization is remodeled by lymphangiogenesis-like processes creating and also disintegrating vessels. A recent report investigating the dynamics of T cells in the LN indicates that at least T cells can pass lymphatic endothelium in both directions quite well [*Wei et al.*, 2005] suggesting that lymphocytes cannot apply mechanical pressure on the vessels. This implies that the remodeling occurs by a restructuring on the cellular level and not just by mechanical deformation. Experimentally, the analysis of the time required for ELV remodeling can decide about the mechanism because mechanical responses occur practically without delay with respect to the lymphocyte location. The time for the restructuring by lymphangiogenesis can be estimated from the fact that the blood vessel network in LN is remodeled on a time scale of 24 hours during inflammation [*Herman et al.*, 1972]. This time is comparable to the FRC to FDC differentiation time [*van Ewijk and van der Kwast*, 1980; *Huber et al.*, 2005; *Mackay and Browning*, 1998; *Mebius et al.*, 1997] (Sec. 2.5) thus in the model the timescale for lymphangiogenic processes is chosen to be of the order of the differentiation of FRC and FDC. This is consistent with the chosen time scale separation of cell migration and FDC-FRC dynamics (Sec. 6.1.1). The details of the model explained below fit better to the remodeling of the efferent lymphatic vessels by creating and destruction of vessels. In principle it is compatible with the mechanical translocation if the delay time of the vessel dynamics is set to zero. However, the increased density of lymphatic vascularization around the follicle due to the compression of a mechanically deformed network is not taken into account properly by this description.

Coupling lymphangiogenesis to the formation of follicular dendritic cells   The coupling of FDC and dynamic ELV is realized such that whenever an FDC is appearing the lymphatic vessels in the vicinity are removed with a certain time delay. Analogously, the backdifferentiation of an FDC into an FRC is followed by the creation of ELV. It is reasonable to assume that the remodeling is orchestrated by the exchange of chemicals inducing behavioral changes of the LEC. This induces time delays of at least several hours as discussed in the former paragraph. A candidate for the regulation of the lymphatic endothelium dynamics is the ECM. The reticular fibers are sparse in the PLF (Sec. 2.3.1). Their absence is possibly causing the disintegration of lymphatic vessels in the B zone. There exists experimental evidence that CXCL13 can modulate angiogenesis [*Spinetti et al.*, 2001] and may be involved in restructuring ELV as well. Also the expression of MMP by FDC [*Braun et al.*, 2004]

may be involved in the absence of ECM and ELV in the PLF. Consequently, the generation of ECM components by FRC may provide the ground for LEC to extent the network in the FRC-covered area, i.e. the T zone. The growth factors VEGF-C and/or VEGF-D that are required additionally can be provided from cells like macrophages (a minor SLT population, macrophages can transdifferentiate into LEC [*Kerjaschki*, 2005]) or DC (Sec. 2.3.3) both of which can be found in the T zone [*von Andrian and Mempel*, 2003]. The relationship between ECM and ELV dynamics may be visible in the developing follicle of sheep. The gradual destruction of the reticular network during the size increase of PLF in sheep LN [*Halleraker et al.*, 1994] may be accompanied by a gradual loss of lymphatic vascularization in this area further promoting the size increase of the PLF. However, the described scenario still needs experimental validation by the direct observation of ELV during LN development.

An interesting experiment would be to investigate the ELV dynamics in the absence of VEGF-D. This lymphatic vascular growth factor has been shown to be not absolutely required for normal lymphatics in tissue [*Baldwin et al.*, 2005] but may play some role upon dynamic remodeling [*Aurora et al.*, 2005]. The absence of VEGF-D may cause a different ELV distribution in SLT that provides insight into the regulation of LEC during PLF development.

6.2.2   Failure of stable follicle formation

The introduction of the ELV dynamics into the PLF model destabilizes the follicle formation and leads to infinite growth of PLF (Fig. 6.12).

The first step to understand the instability of the PLF is to clarify how B cells leave the tissue in the configuration of ELV outside the PLF. There is some mechanism required to override the CXCL13 chemotaxis that keeps the B cells in the follicle. It is proposed that this mechanism is the desensitization of the chemokine receptor CXCR5 (Sec. 6.1.3). With the decreased response for CXCL13 the B cells can start to respond chemotactically to S1P (Sec. 2.4.2). However, experiments indicate that S1P is not relevant for lymphocyte chemotaxis *in vivo* [*Wei et al.*, 2005]. Yet, B cells still can reach the periphery by random migration when the directed response to CXCR5 is shut off by receptor desensitization. Morphologically, the response to S1P can be estimated such that it does not disturb the border of the follicle. However, this cannot be provided in absolute numbers relevant for experiments as neither the receptor levels and S1P concentration nor the chemotactic sensitivies are known. It should be noted that S1P chemotaxis is not required for the egress of B cells in contrast to the naive model (Sec. 6.1.5). The efflux of B cells by randomly finding an ELV is sufficiently high while in the case of naive follicle formation it was not because of the different geometry of the problem.

The second important step to understand the PLF instability is the generation of FDC. When B cells reach the periphery of the follicle they still can induce FDC by their surface levels of LT$\alpha_1\beta_2$. This is independent of the mechanism of LT$\alpha_1\beta_2$ induction on the B cells. Even without the elevated LT$\alpha_1\beta_2$ expression induced by the stimulation of CXCR5-levels LT$\alpha_1\beta_2$ is still sufficient when more than one B cell is present. The generation of FDC leads to the exclusion of efferent lymphatics in this area (with or without time delay). This increases the distance the B cells have to migrate in order
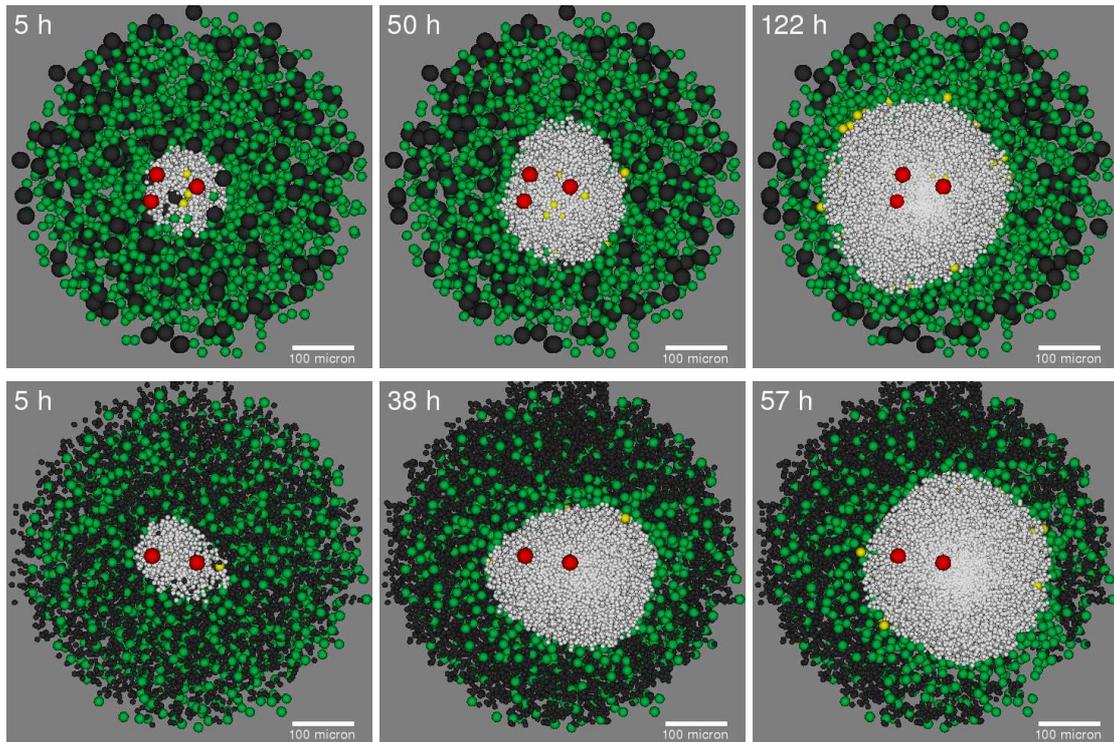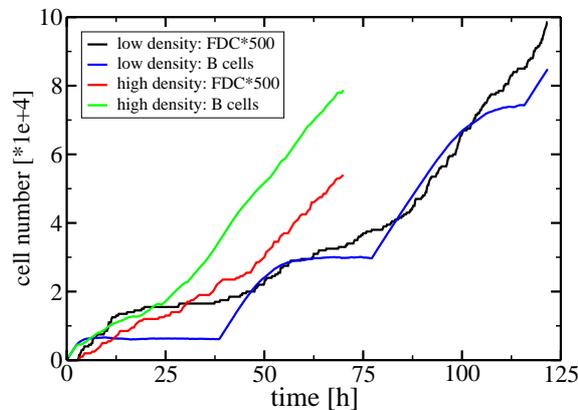
Figure 6.12: Instability of the PLF formation with ELV dynamics. The location of the follicle is determined by the central position of the HEV. The ELV dynamics cannot stabilize the system. The effect is independent of the density of the ELV (compare the upper and lower sequence of Figures with low and high density, respectively. The limiting factor for the follicle growth is mainly the influx of B cells as shown by the number of cells at each time point (diagram). In the case of low density there exist metastable states in which the B cell number is almost constant while the number of FDC is growing. The FDC network reaches the ELV and pushes them away which then leads to increased B cell numbers due to the decreased outflux of B cells. (3D slice projection; white: B cells, green: FRC, yellow: FDC, red: HEV, dark grey: ELV)

to leave the follicle. The longer migration path in turn implies that the B cells have more time to resensitize for CXCR5 and they are more likely to return to the follicle before leaving the tissue. All these steps together generate a feedback loop between increasing the FDC network and pushing away the efferent lymphatics leading to the growth of the follicle.

The instability imposed by the internalization dynamics (Fig. 6.9) adds to the effect of the dynamic ELV. The desensitization by receptor internalization implies that CXCL13 is degraded by the lymphocytes. When more B cells are arriving they will 'use up' the CXCL13 and decrease its concentration such that the desensitization is reduced preventing the cells from leaving the follicle. However, the remaining CXCL13 levels are still sufficient to induce chemotaxis (in agreement with *in vitro* observations [*Luther et al.*, 2002]). On the long run B cells induce new FDC either by basal $LT\alpha_1\beta_2$ levels or CXCR5-stimulated increased $LT\alpha_1\beta_2$ levels. Due to the delay in the production of CXCL13 the average desensitization of B cells remains low. Therefore the additional FDC do not increase the outflux and the follicle continues to grow. Therefore the cause for the growth instability of the PLF is that the FRC - FDC differentiation is slow compared to the desensitization mechanism amplifying fluctuations in the B cell flux. Thus any equilibrium generated with this mechanism is unstable. In principle a desensitization mechanism that does not involve CXCL13 degradation could solve this problem. For example the binding of the chemokines to the ECM [*Hoogewerf et al.*, 1997; *Moser et al.*, 2004; *Pelletier et al.*, 2000; *Proudfoot et al.*, 2003; *Weissenbach et al.*, 2004] may prevent CXCL13 internalization, i.e. the signaling structure of each CXCR5 receptor could be inactivated but the receptor would remain on the cell surface. This is in contradiction to the results showing varying CXCR5 levels (Sec. 2.5.2). Also the stability of the PLF size regulation will not be restored as the destabilizing effect of the ELV dynamics remains.

In all the destabilizing mechanism discussed above, the changes in the B cell efflux are amplified by the fact that the larger the follicle gets the longer the average distance the B cells have to migrate to leave the follicle adding another feedback to the destabilizing mechanisms. The increased average time the B cell spend in the follicle lead to a decreased B cell efflux. In addition the desensitization mechanism is most efficient in the center of the follicle where the CXCL13 concentration is highest. Thus, the cells most likely have to travel the maximal distance while they can resensitize for CXCL13 on their way to the periphery due to the decreasing chemokine concentration.

In conclusion the reason for the instability induced by the ELV dynamics is that when B cells approach the lymphatic vessels they are still able to induce the differentiation of FRC into FDC. Several effects related to the cell migration amplify the instability by decreasing the effective B cell efflux. Thus the follicle keeps growing.

6.2.3 Morphologic results

Multiple follicles   Under zero flux conditions with a constant B cell number multiple follicles can be generated (Fig. 6.13). In contrast to the simulations presented above (Sec. 6.2) B cells respond to S1P chemotactically. This prevents that all B cells respond chemotactic to the first FDC, i.e. from a certain distance on S1P dominates the CXCL13 response. Thus not all B cells are attracted to the
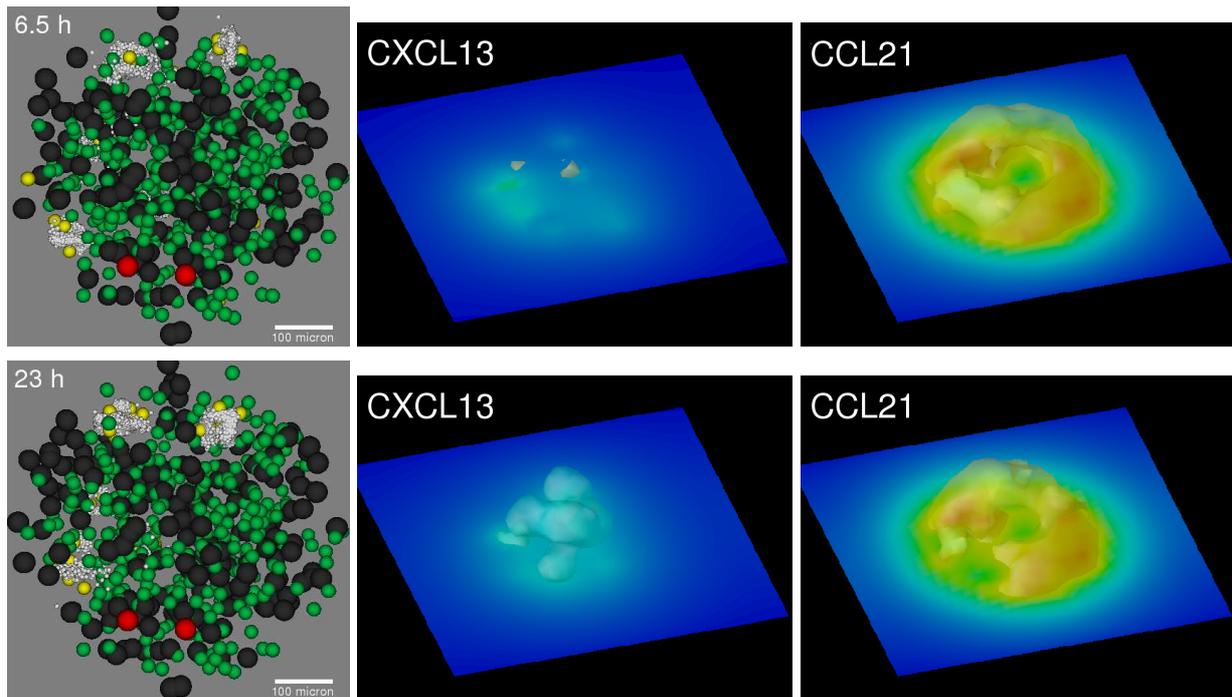
Figure 6.13: Generation of multiple follicles under zero flux conditions. The projections of the chemotactic fields indicate the location of the follicles by the presence of cavities in the CCL21 distribution and corresponding peaks in the CXCL13 distribution. (3D slice projection; white: B cells, green: FRC, yellow: FDC, red: HEV, dark grey: ELV)

first forming PLF and multiple follicles can form whenever sufficiently large B cell aggregates form locally.

Localization of PLF The site of follicle formation is changed in the model with ELV dynamics. The preferred site of formation are the HEV now (Fig. 6.14) compared to the ELV in the former configuration without ELV dynamics (Sec. 6.1). The cells migrate randomly due to shallow gradients of S1P and CCL21 although the response to the latter can be generally neglected due to the internalization of CCR7. Thus, the highest density of the cells is close to their source leading to a high probability of initiating a differentiation of an FRC into the FDC state.

The T zone is not densely occupied with T cells because of the flat concentration profile of CCL21 and S1P, i.e no aggregation center exists. Thus the T cells distribute homogeneously throughout the T zone. This, on one hand, can be considered as an simulation artifact as in normal tissue the space around the stromal cells is not empty. On the other hand as long as no migration barrier exists in the real tissue – like basal membranes – the free space in the simulation can be considered to be filled by some cell and the migration of T cells is basically not affected. The same discussion applies to B cells when FDC generation is suppressed (e.g. like in $LT\alpha_1\beta_2^{-/-}$ animals) (left panel in fig. 6.15). In contrast to the naive model the ELV do not provide an aggregation center such that B cells spread in the simulation area if no follicle can be formed.

Interestingly, providing an aggregation center by a preformed FDC network the follicle can remain at
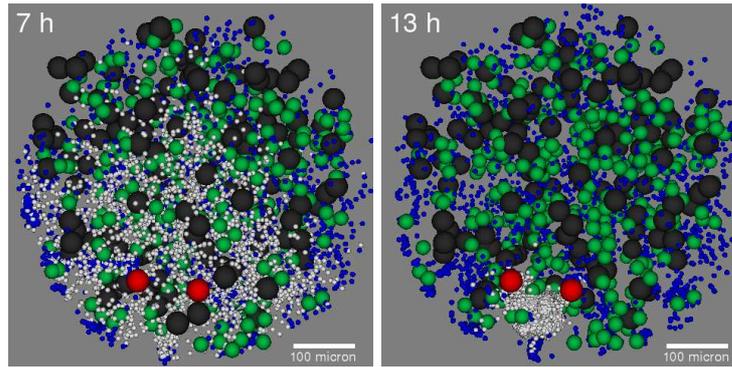
Figure 6.14: Free PLF formation with ELV dynamics. The follicle is located around the HEV despite the diffusion like pattern before FDC generation. The probability for forming a sufficiently large B cell aggregate to induce the first FDC is highest close to the source of the cells. The T cell distribution is a result of flat S1P and CCL21 distributions determined by the almost homogeneous distribution of the two chemoattractant sources (ELV and FRC, respectively). (3D slice projection; white: B cells, dark blue: T cells, green: FRC, yellow: FDC, red: HEV, dark grey: ELV)

its position (not accounting for the growth instability) while another follicle forms around the HEV almost merging with the first one (middle panel in fig. 6.15). The presence of T cells can prevent the formation of this second follicle (right panel in fig. 6.15). The influx of T cell decreases the probability of forming a B cell aggregate – and finally FDC – around the HEV when the follicle is preformed at a sufficient distance. Without a preformed FDC network the PLF again forms around the HEV (not shown).

The effects of the homogeneous distribution of S1P sources lead to the conclusion that S1P chemotaxis can be omitted. S1P leads to a diffuse border of follicles due to the S1P chemotaxis interfering with the response to CXCL13 (middle and right panel in fig. 6.15). In contrast the B cell response to CCL21 cannot be responsible for the ruffled border because it is down-regulated by CCR7 internalization. The ruffled border is also not a result of CXCR5 internalization. Switching off CXCR5 internalization does not create a sharp follicular border (not shown). In Like previously discussed the diffuse appearance is due to the chemotactic interaction of S1P with the chemokine CXCL13.
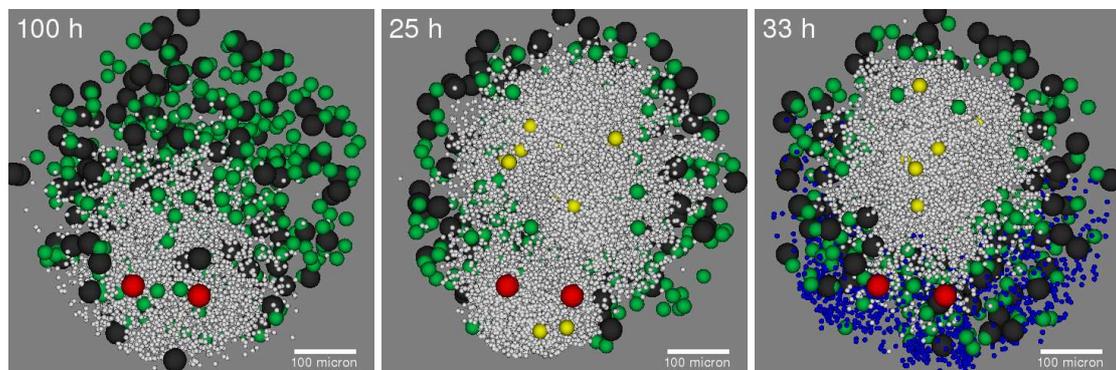
Figure 6.15: B cell flux in a network of ELV. FDC generation is suppressed in the left panel. The homogeneous distribution of S1P sources prevents the formation of B cell aggregates resulting in a diffuse distribution leading to the conclusion that in this regime S1P chemotaxis can be omitted. FDC formation is not suppressed in the second panel and PLF are forming. S1P chemotaxis interfers with the response to CXCL13 and leads to a ruffled follicle border. Actually two follicles are forming: one in the center and one close to the HEV. However, they appear merged due to the ruffled borders but there are clearly two separated FDC networks. In the right panel T cells are entering through the EHV. An almost follicle like structure appears that is separated from a scattered distribution of T cells. Again the ruffled border of the follicle is a result of S1P chemotaxis. (3D slice projection; white: B cells, dark blue: T cells, green: FRC, yellow: FDC, red: HEV, dark grey: ELV)

6.3   B cell homeostasis

The dynamics of efferent lymphatic vessels failed to create stable follicles. However, at each time point the morphology of the follicles appeared widely normal, especially when S1P is not chemotactic. A spherical structure of B cells with FDC inside and the ELV distributed around are present. The PLF may form around the HEV, however few HEV within PLF have been reported (e.g. [*Azzali*, 2003; *Azzali et al.*, 2002; *Bhalla et al.*, 1981; *Herman et al.*, 1972]).

The major problem when comparing to the naive model (Sec. 6.1.5) is that the B cell efflux is not stable in the case of dynamic ELV. The responsible process is that the B cells approaching the ELV can stimulate FRC to become FDC which pushes away the vessels. This may be due to the parameters of the dynamics. A reduced retention time that B cells spend between leaving the follicle and finding an ELV to exit from the tissue may improve the situation. The conclusion from the results of the former section (Sec. 6.2.2) is that S1P chemotaxis is not sufficient to do so but perturbs the border of the follicle. Additionally, the retention time of the B cells close to the follicle periphery is enlarged by the counter-balancing chemotaxis in response to CXCL13 due to resensitized CXCR5 such that the CXCR5 desensitization is not able to solve the problem. Also, an increase in the delay of the efferent lymphatic dynamics with respect to the FDC-FRC dynamics cannot be used to stabilize the size of the PLF. The generation of the FDC deterministically shifts the vessels away independent of how long it takes. The fact that the low levels of $LT\alpha_1\beta_2$ are able to induce FDC demonstrate that these FDC can be maintained by constitutive $LT\alpha_1\beta_2$ signals.

The remaining parameter to stabilize the follicle formation with ELV dynamics is the density of the ELV. When the density of the ELV is increased the B cells are not required to spend a long time on the periphery preventing first the resensitization of CXCR5 and subsequent attraction to the center of the follicle via CXCL13. Also the duration of the FDC-inducing $LT\alpha_1\beta_2$ signal of a single B cells is reduced. To test the effect of a changed ELV density, first a preformed static FDC network (located away from the HEV) is exposed to a constant B cell influx. The size of the follicle is determined by the density of the efferent lymphatics. However it turns out that the dependence on the density is weak above a threshold density.

The following assumptions are different from the naive model (Sec. 6.1):

- ELV are initially everywhere but in the FDC network,

- ELV are varied in size and density,

- the FDC dynamics is switched off, i.e. a static preformed FDC network is used,

- receptor internalization is switched off to suppress shape instabilities (Fig. 6.9),

- T cells are not taken into account,

- a negative regulation of FDC generation will be introduced.

Evaporation experiment   A follicle is simulated under zero influx conditions. The FDC network is static and B cells move under the chemotactic influence of CXCL13 only. In this case the B cells form
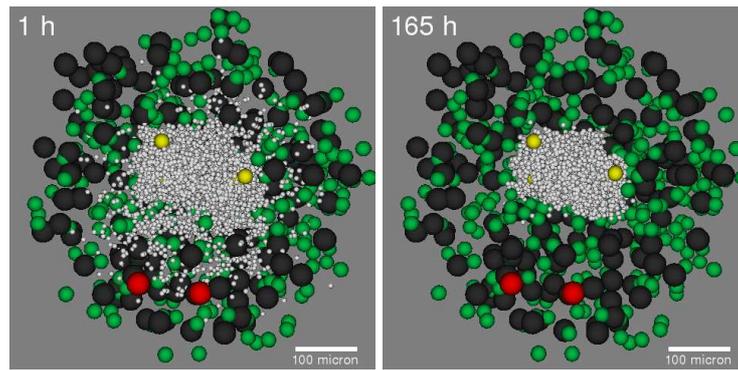
Figure 6.16: Evaporation of a follicle. The FDC network is static and located away from the HEV. There is no B cell influx through HEV but efflux of cells via ELV is permitted. The system reaches a state where cell are almost equilibrated thus cells are leaving very slowly. The internalization of CXCR5 is active but the cells can leave the follicular area by random motion. (3D slice projection; white: B cells, green: FRC, yellow: FDC, red: HEV, dark grey: ELV)

an aggregate that is stable for a very long time (Fig. 6.16). The reason is that the random migration of B cells after desensitization is limited before the recycling of the receptor restores the CXCL13 sensitivity. Without newly inflowing cells, B cells seem to have a stabilized migration cycling pattern. The cell in the center of the aggregate are desensitized strongly and start their random motion through the shell of less desensitized B cells. In this area the CXCL13 concentration is low enough in order to allow reexpression of CXCR5 on the surface and the B cells are attracted towards the center. The resensitized B cells from the outer area can move towards the center occupying the free space of the cells that moved out recently by random migration. Of note, this is not a stable flow pattern of a deterministic cell exchange. It is only an average result of the processes acting on each B cell.

The evaporation experiment changes when the response to S1P is switched on. This leads to a rapid exit of all B cells. That is in part due to the shorter time for CXCR5 desensitized B cells to leave the follicle under the guidance of chemotaxis. The time is linear dependent on the distance traveled in contrast to random migration which has a quadratic dependence on the follicle radius. With the migration parameters known from experiment [*Miller et al.*, 2002] and a follicle of 100 μm radius these times can be estimated to be 15 minutes and > 12 hours, respectively. It can be clearly seen that a B cell has sufficient time to resensitize before reaching the follicle border in the case of random migration such that B cells are likely to return to the follicle before they approach a lymphatic vessel while this is not the case with S1P chemotaxis.

Stable B cell numbers with constant B cell influx   Using preformed FDC networks exposed to a constant influx of B cells one can determine the influence of the ELV density on the B cell efflux. In order to do so the ELV are made effectively smaller allowing to vary the density of the representing exit 'balls' smoothly ((Fig. 6.17) compared to (Fig. 6.18)). The result of the simulations is that the density of the vessels is of low importance as soon as a threshold density is reached (see below).

The threshold for the ELV density can be estimated as follows: The motility coefficient of B cells is $D = 12\,\mu\text{m}^2\,\text{min}^{-1}$ [*Miller et al.*, 2002]. The mean free path a cell has to travel in order to find an

ELV is about $\rho^{-1/3}$ with ρ being the vessel density. The estimated time for a randomly migrating cell to travel this distance is proportional to $\rho^{-2/3}/D$. There should be sufficient of those vessels around the follicle to compensate an influx of 10 cells per minute (Sec. 6.1.2). Assuming homogeneous B cell distribution with density ρ_B the efflux of B cells is $V\rho_B D\rho^{2/3}$ with V being the volume of a shell surrounding the follicle harboring the ELV. This volume can be described as a spherical shell with inner radius $r = 100\,\mu m$ and thickness d. The thickness is at least of the average distance between ELV, i.e. $d \geq \rho^{-1/3}$. The density of B cells can not exceed a dense packing $\rho_B = 1/V_B = 0.003\,\mu m^{-3}$ with the cell volume V_B. Then one yields $4\pi d\,r^2\rho_B D\rho^{2/3} = 4\pi r^2 \rho_B D\rho \leq 10\,\text{cells min}^{-1}$ resulting in a vessel density of $\rho \geq 10^{-5}\,\mu m^{-3}$ which corresponds to one vessel within a box of about $45\,\mu m$ length. In practice the density shall be slightly higher to have a thinner shell of B cells which is not densely packed with B cells (but probably contains other cell types).

In either case – high or low ELV density – the B cell density is high in a shell surrounding the FDC network. There are enough spots for the B cells to use the exit points but they may not be used due to the S1P dynamics. $S1P_1$ has been downregulated when B cells enter the tissue and needs time to be reexpressed. In the simulation it has been assumed that high $S1P_1$ levels are needed to allow the cells to exit the tissue (Sec. 6.1.3). Thus these B cells contribute to the shell surrounding the static FDC network. If the $S1P_1$-constraint for B cell exit would be omitted the cells could not reach the follicle as they have to pass a network of ELV leading to their exit before approaching to the follicle.

An experiment that determines when and where the B cells leave the lymphoid tissue could reveal if the premature exit of B cells occurs with significant rates. If this is the case many B cells would enter the tissue and leave without ever entering a follicle. That raises the question how S1P and $S1P_1$ could be involved in the exit of lymphocytes from lymphoid tissue [*Wei et al.*, 2005]. The effect of $S1P_1$ might be that S1P-sensitive cells do not respond to chemokines by a cross-desensitization process (Sec. 3.3) induced by the high S1P levels in the vessel. Thus lymphocytes with down-regulated S1P can pass the vessels following chemotactic gradients. The cross-desensitization interpretation is consistent with the results of $S1P_1$ overexpression on B cells in which the overexpression caused the cells to stay outside splenic follicles [*Lo et al.*, 2005]. However, the $S1P_1$ overexpression does not explain why those B cells do not enter the ELV in the T zone, leaving open the question how the entrance to the lymphatic system is regulated in detail.

Stability of PLF shape   Using a static FDC network one can again identify the CXCR5 internalization instability (Sec. 6.1). As in previous simulations the change of the CXCL13 concentration deforms the B cell aggregate (Fig. 6.19, compare to sharp PLF borders in Fig. 6.17). In contrast to the situation presented beforehand (Fig. 6.9) the FDC network is kept fixed thus that the instability is not enhanced by the dynamics of the CXCL13 sources. A major difference to the naive model without fluxes and S1P chemotaxis (Sec. 6.1.5, third paragraph) is that a B cell flux is permitted. Which is possible with the changed ELV location as the efflux of B cells remains efficient despite the absence of S1P chemotaxis. This is due to the frequent location of B cells close to the ELV which was not possible in the naive model (Fig. 6.9). In the naive model the cells are required to use S1P chemotaxis to migrate to the few localized ELV. Thus it can be concluded that the instability of the internalization dynamics is not an artifact of the constant B cell numbers.
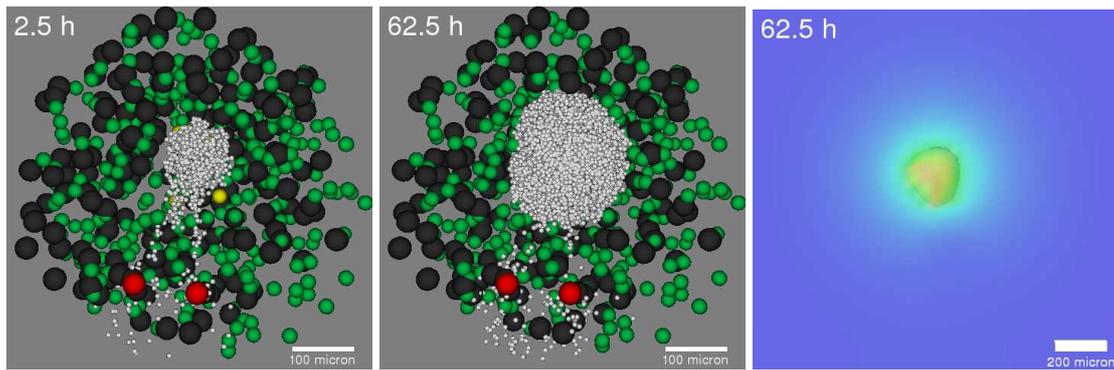
Figure 6.17: B cell homeostasis with fixed FDC network. The follicle is sharply delineated. It is important to note that the B cell follicle extents beyond the area where FDC are located (FDC at 62.5 h are the same as at timepoint 2.5 h). Comparing this with the CXCL13 distribution the B cells extent to an area where the concentration of CXCL13 is low and the border is defined by the sensitivity threshold towards CXCL13. (3D slice projection; white: B cells, dark blue: T cells, green: FRC, yellow: FDC, red: HEV, dark grey: ELV; color code for concentration plot: relative concentration increasing from blue to green to yellow to red)
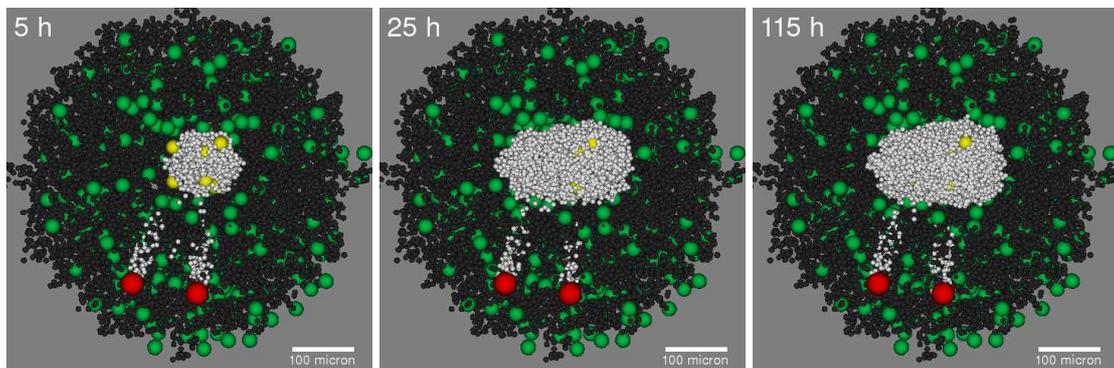
Figure 6.18: B cell homeostasis with fixed FDC network and increased ELV density. Compared to Fig. 6.17 the density of ELV has been increased. The size of the ELV has been decreased in order to allow for high density of non-overlapping vessels (represented by spheres). The high density of exit points does not change the overall picture of Fig. 6.17.(3D slice projection; white: B cells, dark blue: T cells, green: FRC, yellow: FDC, red: HEV, dark grey: ELV)

6.3.1 Negative regulation of FDC generation

The instability of the follicle formation and the disturbed morphology by concurrently acting chemokines suggests that additional factors regulate the FDC differentiation. All mechanisms that have been proposed in the previous sections to limit the follicle size have been shown to be insufficient. The desensitization of CXCR5 on B cells is not working because it causes itself an instability in the aggregation of B cells. The dynamic ELV fails as it is a source of the growth instability. B cells generate FDC close to the PLF leading to ELV remodeling effectively pushing the vessels away. As indicated by the microanatomy (Sec. 2.3.3) the B cells can leave the PLF only on the surface of the follicle. Thus the stabilizing mechanism has to work in a way that either has to stop the creation of new FDC on the follicle surface or that the ELV are not remodeled when the PLF has reached a certain size. The latter mechanism is not significantly different from the former one. A negatively regulated
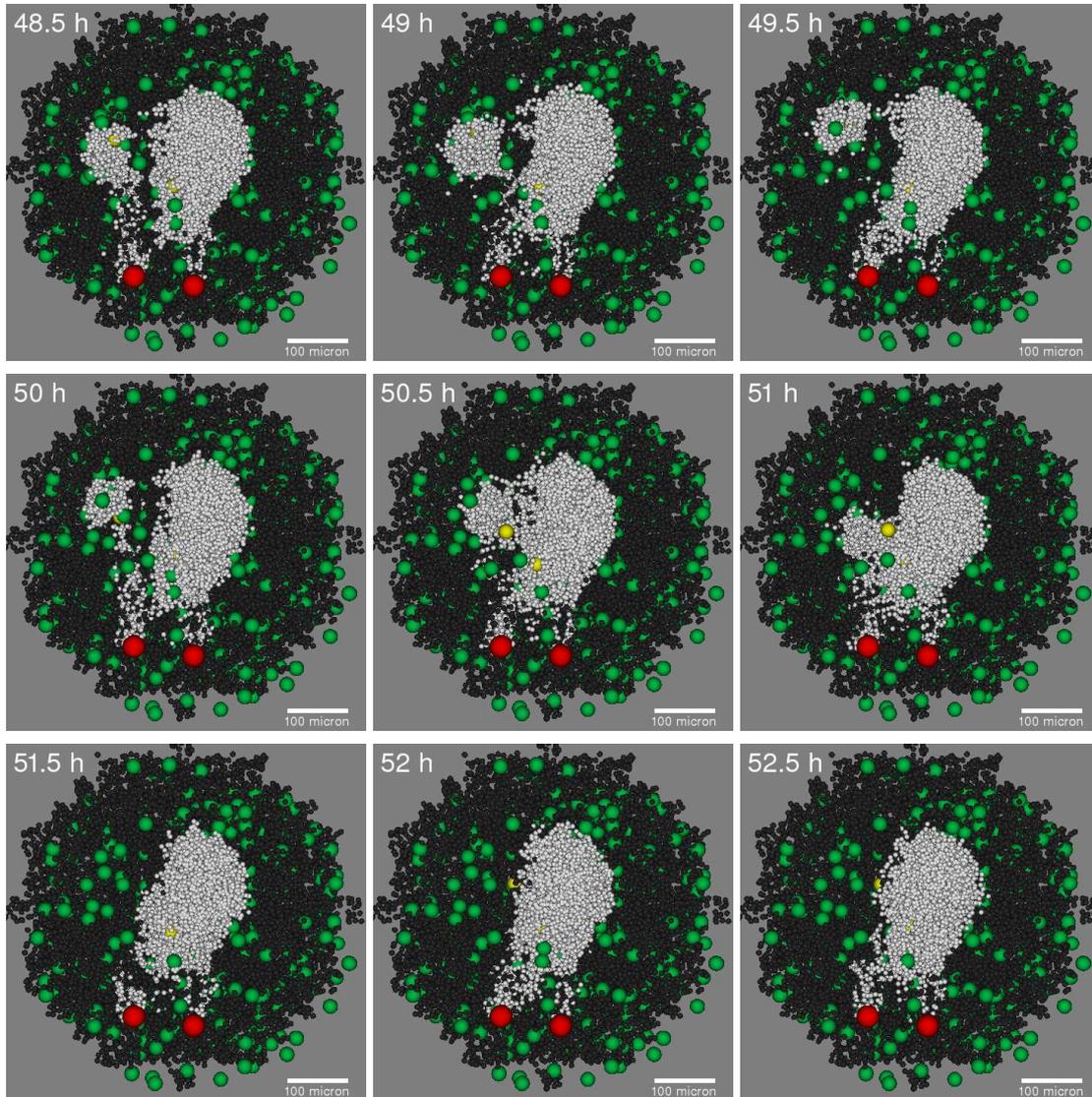
Figure 6.19: Like in the case with the static ELV the internalization process destabilizes the follicle shape, even in the case where the FDC network is of fixed size. A dynamics of the FDC would enhance the instability. It is important to note that the presence of ELV cannot counter-balance this instability due to the fact that S1P-insensitive cells are not permitted to use the exit routes. One can conclude that the desensitization of CXCR5 on B cells in the PLF will not only play no role but more stronger contradicts a stable shape of PLF. (3D slice projection; white: B cells, green: FRC, yellow: FDC, red: HEV, dark grey: ELV)
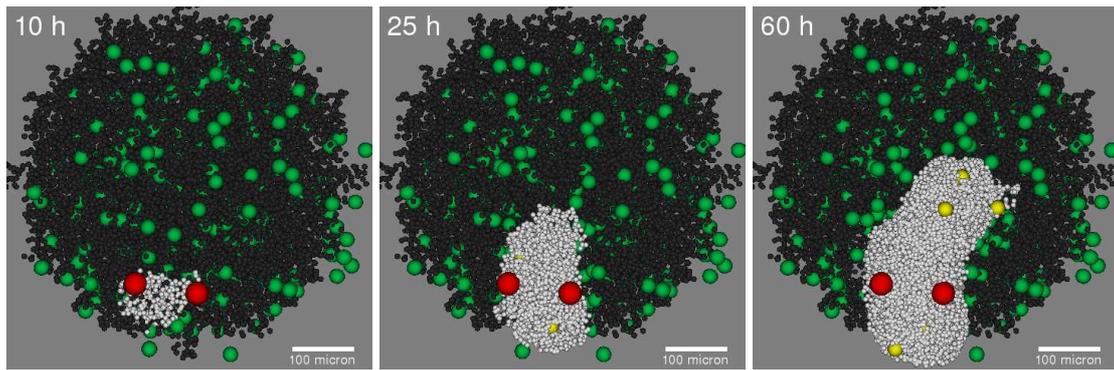
Figure 6.20: Dynamic PLF formation in dense efferent lymphatic networks. The FDC network is dynamic with a negative regulation of FDC generation. The follicle forms around the HEV as expected from previous simulations (Fig. 6.5 and Fig. 6.5). If however, like in the shown case, B cells chemotax towards CCL21 the follicle may elongate towards the center of the stromal network. (3D slice projection; white: B cells, dark blue: T cells, green: FRC, yellow: FDC, red: HEV, dark grey: ELV)

ELV dynamics implies that FDC can be created between the ELV such that the PLF stops growing due to an enhanced B cell efflux in the surface shell of the follicle. Finally, FDC are also negatively regulated indirectly by the ELV causing the decrease of B cells that can provide $LT\alpha_1\beta_2$. However, the coexistence of ELV and FDC networks seems to be ruled out by the found microanatomy of the PLF (Sec. 2.3.3).

Besides an indirect effect mediated by the lymphatic vessels, a negative regulation of FDC differentiation can in principle be mediated by two qualitatively different mechanisms. First, the lack of some signal prevents the generation of new FDC, i.e. a signal that keep FRC in an 'I can differentiate to an FDC' state gets lowered below a threshold. Note, that the negative regulation must not affect existing FDC and does not induce their backdifferentiation to FRC. A possible candidate for a negatively regulating factor could be the ECM as it gets degraded in the follicle (Sec. 2.3.1). However, the ECM is denser at the follicle border questioning this at the same moment. Also the ECM can only serve as short ranged signal – much below the follicle size – while the size regulation of the follicle demands an accumulating and therefore diffusive signal type.

The second possibility is that FDC produce some substance that prevents the differentiation of FRC into FDC. This substance has to accumulate and must not affect present FDC. As before the signal must be diffusive. The simulations show that this type of signal can regulate the size of the follicle with preformed networks and dynamically evolving FDC networks (see Fig. 6.20 and below). Also the lack of a T zone related signal stabilizes the follicle growth. The major argument against this option is that the presence of the signal would then depend on the boundary conditions of the lymphoid tissue. Follicles close to some border could not be generated because the signal would be low already in this region which contrasts the location of PLF in LN (e.g. Fig 2.4).

Letting the FDC network evolve dynamically one can observe a follicle generated close to the HEV (Fig. 6.20). The follicle shape however is not spherical. One reason is CCL21. The follicle elongates towards the center of the simulation area because the generation of FDC leads to an inhomogeneous distribution of FRC, i.e. CCL21 sources, that generates a peak of CCL21 close to the center of the
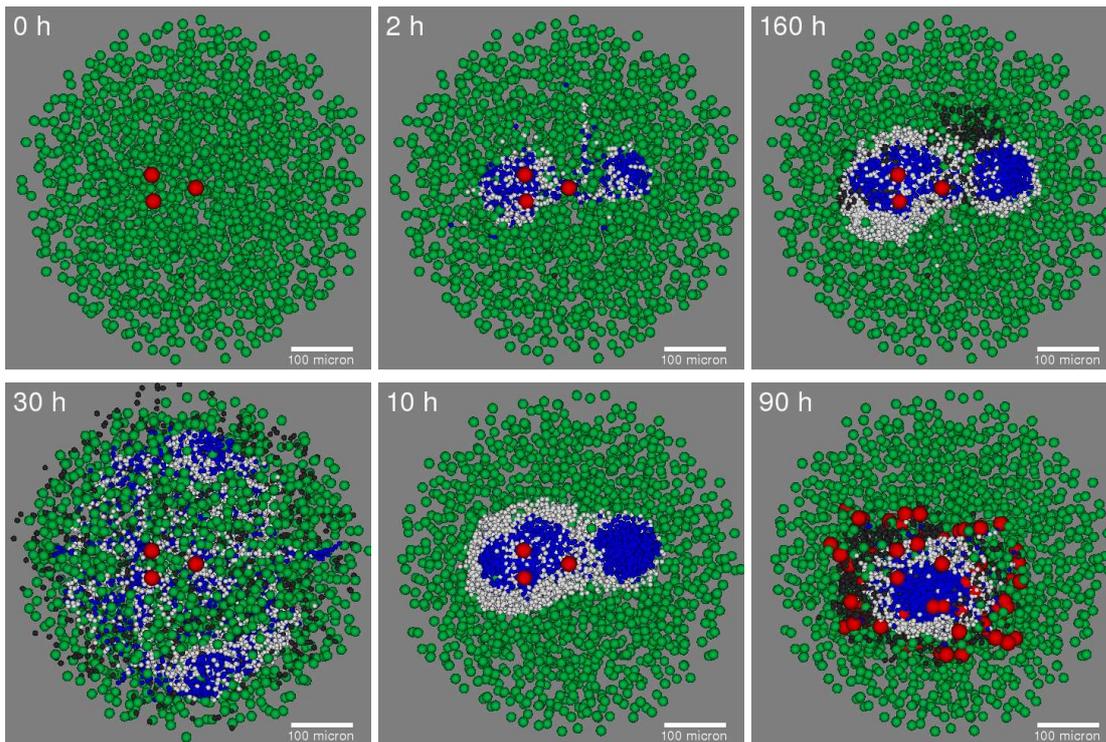
Figure 6.21: Simulating a LT$\alpha_1\beta_2^{-/-}$ experiment by setting the B cell LT$\alpha_1\beta_2$ level to zero results in the typical ring formation seen in experiment (Sec. 2.2.2). The first row shows the ring formation with dynamic FRC, ELV and static HEV. The leftmost panel in the second row shows the situation if FRC are preformed. Cells spread in the stromal network and there are no signs of ring formation. The two right panels in the second row show the ring formation with dynamics HEV. The two B cell rings formed initially merge into a single ring. (3D slice projection; white: B cells, dark blue: T cells, green: FRC, red: HEV, dark grey: ELV)

simulation area. A similar effect can be mediated by chemotactically active S1P although it causes a diffuse boundary in addition (not shown). Thus, without chemokine receptor internalization the follicle shape is a result of the induction of FDC, i.e. CXCL13 sources, and the superposition with the CCL21 gradient. With internalization of CCR7 the follicle remains spherical provided that S1P is not chemotactically active (not shown). If, in addition, CXCR5 is internalized the diffuse and unstable follicle shape reappears (not shown) similar to the case of the static FDC network (Fig. 6.19).

6.4   B cell rings in LT-deficiencies

In knockout experiments the SLT develop with disturbed structures. In many of these cases B and T cells separate without the formation of PLF and FDC networks (Sec. 2.2.2). Instead the B cells form a ring (or shell in three dimensions) around the T zone. Occasionally, isolated FDC and/or low CXCL13 expression have been reported (Sec. 2.2.2). Also during organogenesis the formation of this ring is an intermediate step that seems to occur in all lymphoid tissues (Sec. 2.5). The observation that the ring formation occurs in the absence of CXCL13 and CXCR5 indicates that the ring structure is independent of chemotaxis of the B cell towards a populations residing in the ring. Moreover even in
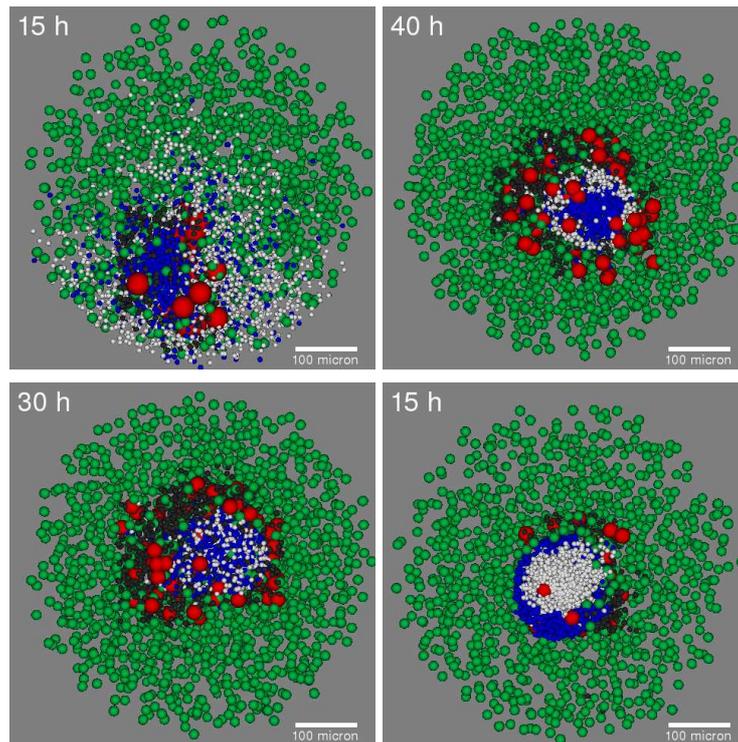
Figure 6.22: Identification of the critical parameter determining the B cell ring formation. Detailed evaluation of the critical parameter shows that the different strength of migration forces of B and T cells leads to the separation. In order to keep the B cells close to the T zone the low CCR7 expression by B cells [*Kim et al.*, 1998; *Yoshida et al.*, 1998] has to be taken into account. Without it B cells just diffuse in the T cell-free area (upper left panel). With exchanged CCR7 expression levels, i.e. B cells more sensitive than T cells, the ring remains normal (upper right panel). Keeping all parameters equal between B and T cells but use differential adhesion (Sec. 5.4.3) cannot create a ring structure (lower left panel). Exchanging the active force parameters (Sec. 5.7) of B and T cells the ring can be inverted (lower right panel). (3D slice projection; white: B cells, dark blue: T cells, green: FRC, red: HEV, dark grey: ELV)

wildtype animals the process seems independent of CXCL13 as demonstrated recently [*Cupedo et al.*, 2004b]. However, the authors concluded that another chemotactic factor should be responsible for the ring formation. It will be shown here that no additional guidance factors are needed to understand the ring formation.

In summary the following changes to the naive model (Sec. 6.1) have been done:

- chemotaxis to S1P is switched off,

- internalization of chemokine receptors is switched off,

- initially, the simulation starts with a network of stromal cells, that do not secrete chemokines,

- B and T cells can stimulate stromal cells to differentiate to FRC (T zone dynamics),

- stimulation of B cells is not possible, i.e. a B cell $LT\alpha_1\beta_2^{-/-}$ knockout is simulated,

- ELV are dynamic and positively correlated with FRC,

- HEV have a dynamics similar to ELV, however a few HEV are present initially.

The choice for the dynamics of HEV follows consistency arguments. It is known that HEV are rarely found in PLF (Sec. 2.3.2). It has not been considered a major problem previously as the HEV are not strictly excluded from follicles (e.g. [*Azzali*, 2003; *Azzali et al.*, 2002; *Bhalla et al.*, 1981; *Herman et al.*, 1972]). However, the ELV dynamics applied to HEV will ensure that HEV are everywhere in the T zone [*Azzali and Arcari*, 2000; *Azzali et al.*, 2002; *Belisle and Sainte-Marie*, 1990; *Bhalla et al.*, 1981; *Ekino et al.*, 1979; *Herman et al.*, 1972; *Sainte-Marie et al.*, 1984] while in the previous simulations the HEV are localized in a small area (Sec. 6.1). This small area is still needed as there is a requirement to have some influx of lymphocytes to start the simulation. However, the HEV in the simulation might be unspecialized blood vessels at the beginning of organogenesis or lymphneogenesis.

Mechanisms behind B cell ring formation   The basic idea is that the ring is formed because T cells aggregate due to the strong chemotactic response to CCL21. B cells are known to respond to CCL21 as well [*Kim et al.*, 1998; *Yoshida et al.*, 1998]. The assumptions made in this section can indeed generate a B cell ring (Fig. 6.21).

The ring formation requires that the T zone defined by CCL21 expression is as large or slightly smaller than the area occupied by the T cells, i.e. the size of the CCL21-expressing tissue matches the number of T cells (which depends on the influx of T cells). If the area was larger T cells would spread throughout the area homogeneously and B cells would accumulate in between instead of forming a ring (Fig.6.21, lower left panel). This implies that during organogenesis – when T cells are not yet present (Sec. 2.5) – the size of the T zone is regulated by the size of a migrating, most likely non-stromal population. A similar notion holds for the generation of HEV that can only be found in the T zone. However, few initial HEV are sufficient and dynamic HEV do not change the ring formation picture drastically (Fig.6.21, two right panels in lower row). A hint to resolve the T zone size is the possibility that many cytokines like CCL19, CCL21, IL-4, IL-7, and IL-15 can stimulate $LT\alpha_1\beta_2$ on T cells *in vitro* [*Cyster*, 2005; *Luther et al.*, 2002; *Tumanov et al.*, 2003]. The fact that *in vitro* T cell increase their $LT\alpha_1\beta_2$ levels strongly when stimulated with only 0.1 nM of CCL19 or 1 nM of CCL21 makes it feasible to assume that T cells carry $LT\alpha_1\beta_2$ on their surface when they are located in the T zone. In contrast at least 10 nM CXCL13 are needed to upregulate $LT\alpha_1\beta_2$ on B cells [*Luther et al.*, 2002]. The $LT\alpha_1\beta_2$-CXCL13 feedback loop [*Ansel et al.*, 2000] claimed to be important for the PLF should have a counterpart in the T zone via $LT\alpha_1\beta_2$-CCL21. However, $LT\alpha_1\beta_2$ levels on naive T cells do not increase when entering the T zone of spleen or LN [*Luther et al.*, 2002]. This may be due to inhibitory effects of high levels of CCL21 in the tissue ($\sim 1\,\mu$M) [*Luther et al.*, 2002] which have not been tested yet *in vitro*.

In principle the adhesive properties of a certain area could also mediate aggregation of T cells. However, *in situ* imaging [*Miller et al.*, 2003, 2002; *Okada et al.*, 2005; *Wei et al.*, 2003] demonstrates that T cells remain very motile in the LN. The only possibility for adhesion that seems compatible with these observations is that the T zone is confining the T cell movement by providing a preferred substrate for migration. This is basically the same concept as the confinement of T cell migration by CCL21. It has to be regulated such that the T zone – this time defined by the corresponding adhe-

sion molecule – is adapted to the size of the T cell population else the T cells would again spread in preformed but to large area.

By variation of the simulation parameters one can identify the major determinant of B cell ring formation (Fig. 6.22). In agreement with experiment the CCL21 response of B cells is relevant (Fig.6.22, upper left panel). Note, that the internalization of CCR7 and the chemotaxis to S1P have been switched off. However, provided that both cells respond to CCL21 the relevant mechanism lies in the different mechanical response of both cell types. T cells produce stronger migration forces because these cells are faster [*Miller et al.*, 2003, 2002; *Okada et al.*, 2005; *Wei et al.*, 2003]. Thus the T cells are accumulating in the T zone and 'squeezing' out the B cells. This can be demonstrated by exchanging the mechanical migration parameters of B and T cells while keeping every other property (e.g. the internal dynamics, surface properties, and chemokine receptors). The T cells form a ring around a central B zone (Fig. 6.22 lower right panel). The ring is wider than before which is due to the higher ratio of T cells in the cell influx compared to B cells. Different CCR7 levels (Fig. 6.22 upper right panel) or adhesion properties (Fig. 6.22 lower left panel) are not responsible for the ring formation

Dynamic T zone   The final conclusions drawn from the results of this section are that the T zone of SLT contains a positive feedback loop similar to the one proposed for the PLF [*Ansel et al.*, 2000]. As in the case for B cell-FDC interaction (Sec. 6.1) there are actually two feedback loops: One is the increase of a signal (like $LT\alpha_1\beta_2$) by the accumulation of T cells with low levels of the signal. The second one is the increase of the signaling on single T cells by stimulation via CCL21. Thus it is assumed that the properties of the stromal compartment of the T zone depend on the presence and constitutive signals of the lymphocytes. This interaction has to be active at least during organogenesis. However, blocking experiments with $LT\alpha_1\beta_2$-Ig lead to the disruption of the BP-3$^+$ network in the spleen in the course of 1 week [*Ngo et al.*, 1999]. Similar conclusions were drawn from genetic analysis of $LT\alpha^{-/-}$, $LT\beta^{-/-}$, and TNF-$\alpha^{-/-}$ mice [*Shakhov and Nedospasov*, 2001] and the distribution of the FRC marker ER-TR7 [*Kuprash et al.*, 2002]. Another marker for T zone stroma – gp38 – shows a similar $LT\alpha_1\beta_2$-dependency [*Ngo et al.*, 2001]. These experiments indicate that the T zone has a similar flexibility like the B zone of lymphoid tissue and adapts to its lymphocyte content. This explains how varying numbers of T cells are harbored in these tissues. For example the stromal compartment of the LN T zone in *nude* mice and rat [*Sainte-Marie et al.*, 1984] – where T cells are almost absent – needs to be remodeled. As T cells are almost absent in these mice the T zone has to decrease in size after the time window in which the LTIC has generated the proper T zone stroma (Sec. 2.5.2). Similarly, when T cell deficient mice are reconstituted with wildtype bone marrow or splenocytes [*Gonzalez et al.*, 1998] the T zones appear in these cases. That suggests already that the T zone is also dynamic although it might be that the typical time scale is longer than for the formation of the B zone. The *in vitro* experiments [*Katakai et al.*, 2004b] concerning the dependence of the FRC network formation on the presence of lymphocytes are strongly supporting this interpretation. These experiments fail however to explain why $LT\alpha_1\beta_2$ has more severe effects on T zone stromal network formation than TNF-α as in the experiment TNF-α and $LT\alpha_3$ are strictly required while this seems not the be case in the knockout-systems (Sec. 2.2.2). In contrast to these data the expression of CCL21 seems to be independent on constitutive $LT\alpha_1\beta_2$ [*Ngo et al.*, 2001] while others report a minor effect on B cell/T cell segregation on long term blocking of $LT\alpha_1\beta_2$ [*Fu and Chaplin*, 1999]. This may

be the reason why the *in vitro* administration of TNF-α and LT$\alpha_1\beta_2$ failed to induce CCL21 in cell cultures of FRC [*Katakai et al.*, 2004b]. In knockout mice however CCL21 depends on LT$\alpha_1\beta_2$ but not TNF-α [*Shakhov and Nedospasov*, 2001]. One explanation for the inconsistency of the dependency of CCL21 expression on LT$\alpha_1\beta_2$ may be that the dynamics of the T zone appears on a longer time scale than that of the FDC. It is possible that the nature of the CCL21 expression in the T zone is not a change of state of the cell as proposed for the FDC but a real differentiation process that involves the recruitment of CCL21 expressing stromal cells from a mesenchymal population. Once a cell reached the CCL21-expressing state it remains in it for its life time and the slow turnover in blocking experiments represents the failure of recruiting new cells into the CCL21-expressing population while the CCL21-positive population dies out slowly, i.e. no back differentiation exits (as it has been proposed for the FDC). Thus it can be assumed that the FRC population reaches homeostasis by a balance of cell growth or recruitment and cell death.

Ring-shaped B zones as natural precursor of follicles   A recent study on the SLT structure in the nurse shark revealed their morphology [*Rumfelt et al.*, 2002]. As these animals are the evolutionary oldest vertebrate branch that is known to have an AIS their SLT structure is of special interest. It has been shown that the B cells form a ring around the T zone in the splenic white pulp. The 3D study showed that the B cells form a complete shell surrounding the T zone. This demonstrates that the ring formation is a natural step in SLT development that seems to be based on conserved evolutionary morphogenesis.

Cortex localization of follicles   The ring formation naturally explains the cortical localization of PLF. In order to work it requires that the stromal compartment of the T zone defined by the chemokine expression is established before the induction of FDC. Naturally, this might be explained by assuming that FRC are precursors of FDC or the stromal network constitutes the necessary background for the immigration of FDC precursor. Thus, an attraction to the cortex is not needed in contrast to an interpretation given previously [*Cupedo et al.*, 2004b].

6.5   *Lymphoid tissue genesis*

The subject of this section is the generation of lymphoid tissue on a stromal background without prestructures. The full dynamics implies the reorganization of lymphatic vessels, the stromal structure in terms of CCL21-expressing FRC and CXCL13-expressing FDC, and the reorganization of blood vessels which is mainly the generation of HEV. The initial condition is a stromal network without chemokine expressing cells and few blood vessels that allow the immigration of lymphocytes. For the result it is not important whether or not ELV are initially present. If they are not present, the generation of ELV is coupled with FRC thus creating a lymphatic network in the developing T zone. Note, that in the simulations in this section the stromal cells are smaller than before (Sec. 6.1, Sec. 6.2, and Sec. 6.3). The thresholds for their stimulation signals (e.g. LT$\alpha_1\beta_2$) has been adopted accordingly. As the previous sections demonstrated that the higher number of B cells can aggregate around an FRC

and induce differentiation into FDC it is sufficient to allow for a lower number of B cells. This has the advantage that the density of stromal cells is now closer to the real case (compare to (Sec. 6.1)). As in the previous simulations the internalization dynamics has been shown to induce a unstable border of the follicles (Sec. 6.3) the simulations are done without internalization dynamics. Similarly, the chemotaxis to S1P is not active as suggest by previous simulations (Sec. 6.2.2) and recent experiments [*Wei et al.*, 2005].

In summary the following assumptions enter the complete SLT formation model:

- fixed number of non-migrating stromal cells that secrete no chemokines,

- small number of initial HEV,

- no initial ELV,

- constant entrance of B cells and T cells via dynamic HEV (Sec. 2.3.2),

- B cells and T cells use dynamic ELV for egress from the SLT (Sec. 2.3.3),

- B cells and T cells leaving the SLT via ELV when $S1P_1$ levels are sufficient (Sec. 2.4.2),

- stromal cells differentiate to FRC upon lymphocyte contact

- generation of FDC by B cell $LT\alpha_1\beta_2$ signaling (Sec. 2.2.2 and Sec. 5.3.1),

- replacement of FRC by generated FDC (Sec. 5.3.1),

- removal of FDC (replaced by FRC) in case of lack of $LT\alpha_1\beta_2$ stimulation (Sec. 5.3.1),

- ELV are dynamic and positively correlated with FRC,

- ELV are negatively correlated with FDC,

- HEV have a dynamics identical to ELV,

- secretion of CXCL13 by FDC (Sec. 2.2),

- secretion of CCL21 by FRC (Sec. 2.2),

- secretion of S1P by ELV (Sec. 2.4.2),

- chemotactic activity of B cells to CXCL13, CCL21 (Sec. 2.2),

- chemotactic activity of T cells to CCL21 (Sec. 2.2),

- no CXCR5 or CCR7 receptors internalization,

- no S1P chemotaxis of lymphocytes,

- B and T cell migrate according to the constriction ring model (Sec. 5.7)

- the passive mechanical cell contacts are described by the JKR-model (Sec. 5.4.3).

6.5.1 Results

With the full follicle dynamics the simulation of the developing PLF shows all details found in experimental situations (Fig. 6.23). Initially the B cells form a ring zone around a developing T zone in which HEV are formed as well. The CCL21 response of B cells is not absolutely required but prevents a diffuse B cell ring. The ring would vanish in a bounded system that keeps the cells at high density by mechanical constraints which might be the case in the LN (Sec. 2.1.4) but probably not in the spleen due to a loose mechanical separation of red and white pulp (Sec. 2.1.3) . After about 24 hours a follicle is created which harbors all B cells. The vessels systems need some time to equilibrate such that the cell numbers stabilize (Fig. 6.24). The PLF is accompanied by a T zone adjacent to it harboring the HEV and ELV. The density of ELV can be relatively small. Quite frequently two T zones are formed (Fig. 6.25). This is similar to the morphology reported for PLF in PP (references in (Sec. 2.5.1)).

With increased influx of cells two follicles are created intermediately (Fig. 6.26). They merge however, because the negative regulation does not stabilize the small follicle size such that the random fluctuations in the shape and follicle growth lead to the appearance of one single follicle. The gap in between the T zone and the follicle is a result of a low threshold to induce CCL21 expression and consequently the generation of ELV and HEV. The low threshold allows that an aggregate of very few cells can initiated an HEV by cells diffusing away from the T zone. This leads to rapid extension of the CCL21 producing zone with peaks in the center of the stromal network while the position of the follicle remains unaffected. The initial condition of having HEV at the periphery of the stromal network makes the gap visible. Otherwise the follicle would also form in the center together with the T zone. This points out that the initiation of stromal properties due to lymphocyte contact is critical and should not become to strong. In the case of FDC generation even a negative regulation is required to create stable PLF (Sec. 6.3).

Effect of migration parameters on the SLT formation   A change in the migration parameters of the lymphocytes can have effects on the SLT formation. The forces – including friction – are changed such that the migration speed of the lymphocytes is kept constant where possible. Mainly the relative contribution of active (Sec. 5.7) and passive forces (Sec. 5.4.3) acting on cells is changed. For comparison the active forces of T and B cells have been chosen to be similar (such that they have equal speed) to identify the effect of the different forces of the lymphocytes. The intermediary ring phase then vanishes (Fig. 6.27) as shown previously (Sec. 6.4). However, the final outcome – the PLF with adjacent T zone – is indistinguishable form the normal situation (Fig. 6.23). This is true even if the migration parameter are exchanged such that B cells are now faster than T cells and the ring inverts (Fig. 6.28 and Sec. 6.4). The SLT at the end of the simulation shows no signs of the change in the migration parameters.

If now the passive forces are lowered the ring phase can also vanish (not shown) because of the increased average contact surface between stromal cells and lymphocytes. Thus small lymphocyte aggregates already induce FDC which happens before the B cell ring can form. As the parameter for the $LT\alpha_1\beta_2$ stimulation has been derived to fit together with a certain set of migration parame-
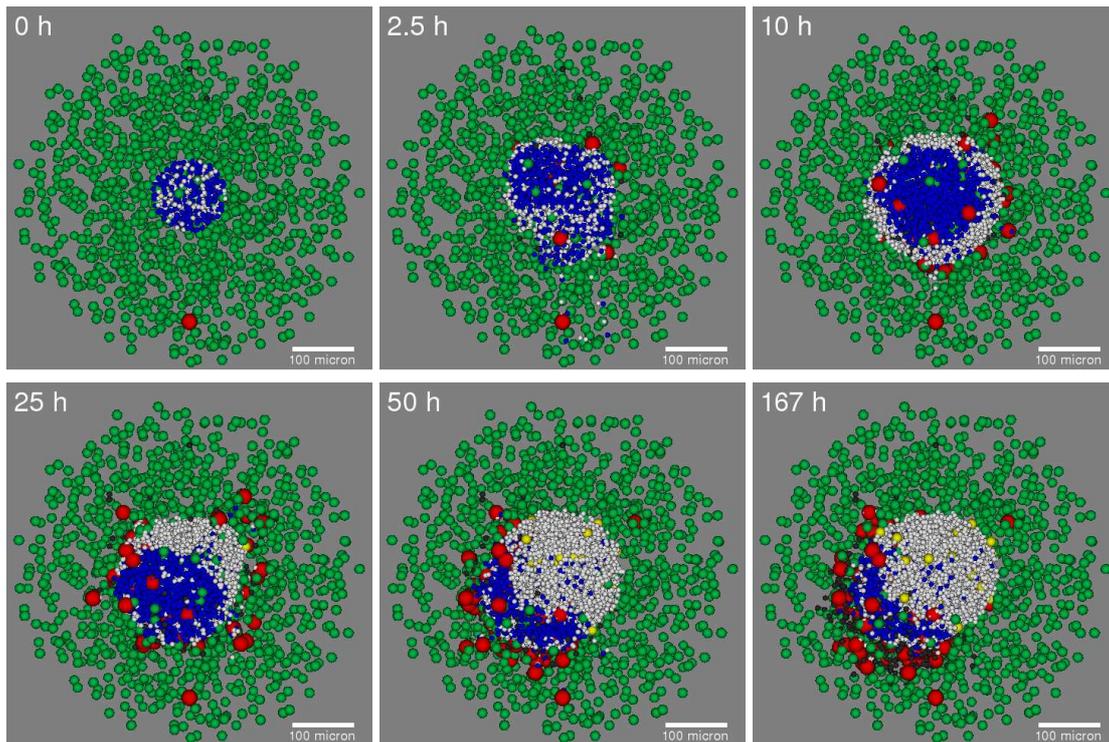
Figure 6.23: Full follicle formation dynamics. HEV and ELV are dynamic. Also the CCL21 expression by FRC is dynamically regulated by T and B cells. During tissue genesis the ring pattern appears intermediately (15 h). Soon after that one single follicle forms and the T cells resort themselves into a T zone. The absence of ELV and HEV at the top right border of the PLF is a result of the FDC and the FRC dynamics. There are no T cells that could recruit FRC from the stromal compartment. At the same time the generation of FDC disrupts any vessel that had been created in this area previously. (3D slice projection; white: B cells, dark blue: T cells, green: FRC, yellow: FDC, red: HEV, dark grey: ELV)

ters (Table 5.4) it can be stated that $LT\alpha_1\beta_2$ stimulation and migration behavior are not completely independent parameters. If the elastic interaction was stronger the active forces, the ring would form but the follicle would be missing. There would not be sufficient contact surface between B cells and stromal cells to initiate FDC such that the system would get trapped in the intermediary ring phase (not shown).

6.5.2 Reconstitution of SCID mice

The experiments that identify structures resembling preformed PLF in the spleen and LN of SCID mice [*Gonzalez et al.*, 1998] may be a remnant of normal organogenesis involving LTIC. These structures are normally not found as the virtual absence of lymphocytes in SCID mice does not permit to label B and T zones by B220 and CD3, respectively. The absence of typical FDC marker might be a result of very immature FDC. The earliest FDC marker CNA.42 [*Kasajima-Akatsuka and Maeda*, 2006] could be used in experiments to detect the immature FDC. From the presence of follicular-like prestructures in SCID mice one can conclude that an aggregating factor is present – most likely CXCL13. This may explain why short-term reconstitution of SCID mice with wildtype lymphocytes
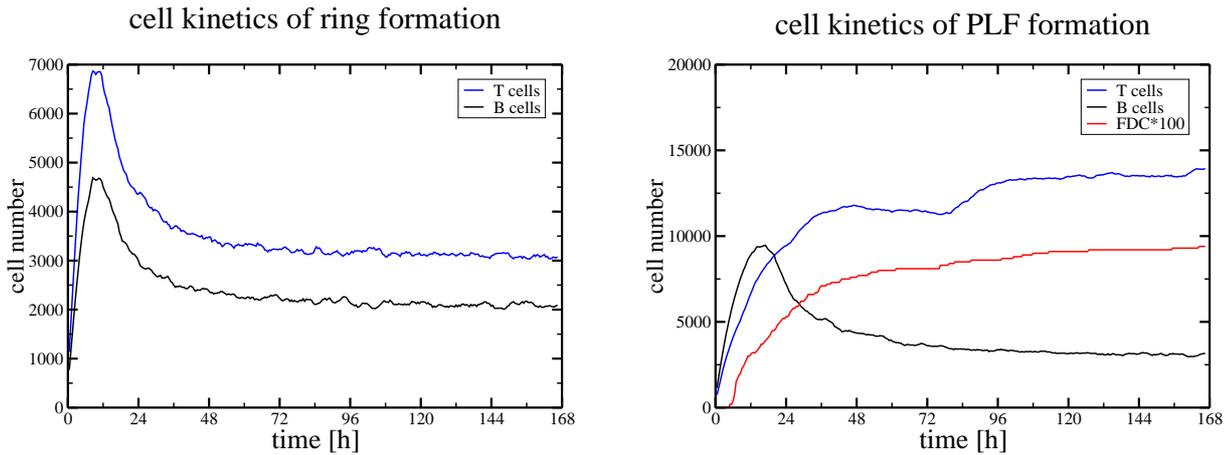
Figure 6.24: Comparison of kinetics of T and B cells when follicles are formed or not. The left panel (corresponding to a $LT\alpha_1\beta_2^{-/-}$ animal) shows that the number of B cells approaches a low flow equilibrium. The number is higher when a PLF is present. The initial rise in the cell numbers is due to the dynamics of ELV with a typical time constant of 6 hours. The peak is not relevant for the outcome of the simulations as preformed lymphatic vessels system does prevent the peak and slightly delays the follicle formation but does not influence the final result (not shown).
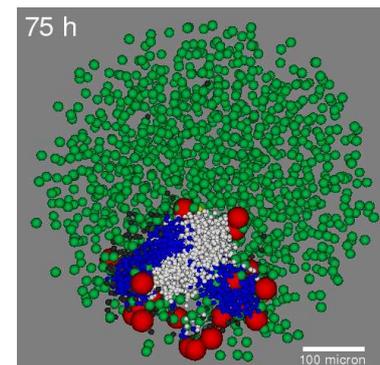
Figure 6.25: Formation of two T zones. The setup is identical to Fig. 6.23 except for a different position of the initial HEV. Two T zones are formed next to a PLF . (3D slice projection; white: B cells, dark blue: T cells, green: FRC, yellow: FDC, red: HEV, dark grey: ELV)

show a normal segregation of B and T cells [*Gonzalez et al.*, 1998]. The segregation can be prevented by blocking the $LT\alpha_1\beta_2$-pathway prior to the lymphocyte reconstitution. Considering the data about organogenesis (Sec. 2.5) one may assume that LTIC may provide the $LT\alpha_1\beta_2$ signal. These cells have been found in the spleen and LN of SCID mice [*Mebius et al.*, 1997]. The conclusion is that the lymphoid follicle organization can happen with exchangeable players using the same basic mechanism. The detailed requirements are:

1. A stromal cell type that can be induced to produce CXCL13 upon stimulation by lymphotoxins ($LT\alpha_1\beta_2$, $LT\alpha_3$, and possibly TNF-α).

2. A CXCR5-positive hematopoietic cell type that expresses some lymphotoxin, either constitutively or induced by molecules such as CXCL13, IL-7, or TRANCE.
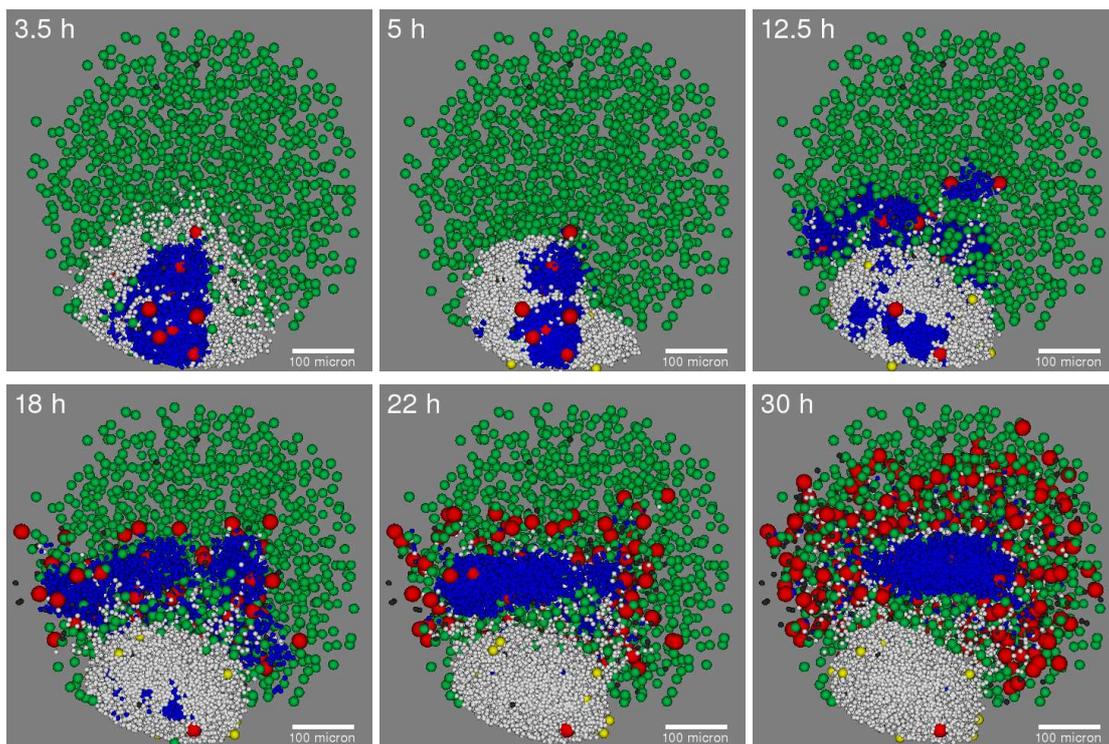
Figure 6.26: Full follicle formation dynamics. The gap between T and B zone is a result of a low threshold to induce CCL21 expression (and HEV generation consequently). This allows that an aggregate of very few cells can initiate CCL21-expressing FRC. Thus small number of lymphocytes that randomly migrate away from the T zone can generate new FRC outside the T zone. HEV are created at the new FRC stabilizing the stimulation of new FRC in the vicinity due to the influx of lymphocytes. That leads to rapid extension of the CCL21 producing zone which peaks in the center of the stromal network while the position of the follicle remains unaffected by this process. (3D slice projection; white: B cells, dark blue: T cells, green: FRC, yellow: FDC, red: HEV, dark grey: ELV)
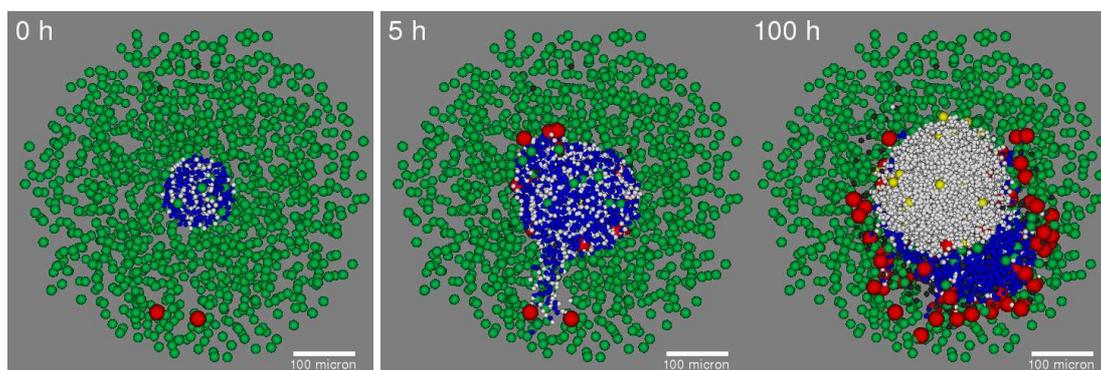
Figure 6.27: The simulation of Fig. 6.23 with changed migration parameters. B and T cells have equal speeds. The follicle forms in the center of the area. No intermediary ring is formed while the asymptotic PLF formation is preserved. (3D slice projection; white: B cells, dark blue: T cells, green: FRC, yellow: FDC, red: HEV, dark grey: ELV)
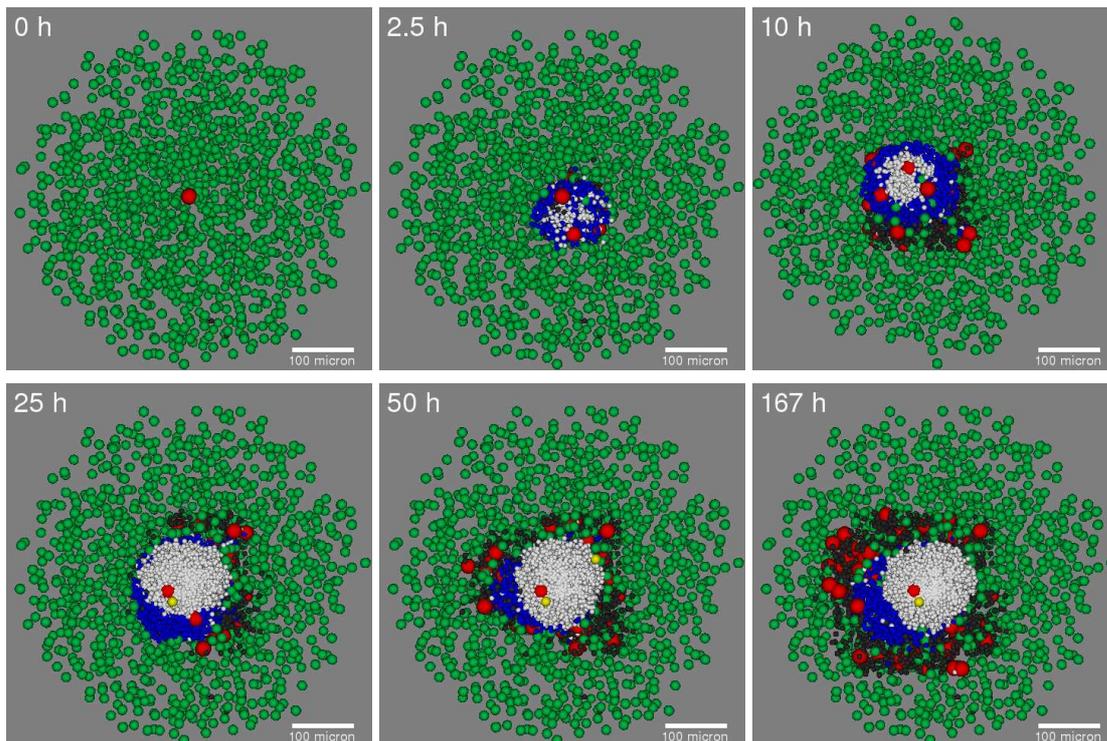
Figure 6.28: The simulation of Fig. 6.23 with exchanged migration parameters. During tissue genesis a T cell ring appears intermediately (10 h) as shown in previous results (Fig. 6.22). A PLF is still formed such that the final state is rather independent of the biomechanics of the lymphocyte migration (compare to Fig. 6.23. (3D slice projection; white: B cells, dark blue: T cells, green: FRC, yellow: FDC, red: HEV, dark grey: ELV)

Chapter 7

Summary and discussion

A model to study the formation of primary lymphoid follicles has been developed. The architecture of the simulation tool is agent-based and relies on a regular triangulation in order to deal with a continuous representation of cell positions and sizes. The regular triangulation provides information about the neighborhood topology and possible cell interactions. The dual of the regular triangulation – the Voronoi tessellation – gives information of other geometric parameters like cell volume and cell contact areas. In order to cope with the large number of cells and the frequent changes of cell numbers and relative cell positions, new algorithms to calculate dynamic and kinetic regular triangulations on parallel computer architectures have been developed and implemented using the Message Passing Interface (MPI) [*Message-Passing Interface Forum*, 1995]. Cells are modeled as elastic, interacting spheres with an internal cell dynamics that determine the phenotype of a cell. The model incorporates:

- cell differentiation

- contact interactions leading to changed internal cell dynamics

- mechanical behavior of cells

- forces generated by migrating cells

- reaction-diffusion systems to describe chemotaxis

The model has been extended by a phenomenological angio- and lymphangiogenesis model to cover the full dynamics of SLT organogenesis.

Comprehensive model of secondary lymphoid tissue organogenesis   There are no prestructures required to simulate the organization of SLT. Thus, the characteristic SLT morphology that has a typical length scale of hundreds of micrometers is a result of the cellular interactions between stromal cells, lymphocytes, and blood and lymphatic vessels with the help of mediating diffusing signal molecules.

The overall picture of SLT organogenesis that is derived from the simulations is as follows. There are two classes of cells which are realized differently in the lymphoid organs and experimental conditions.

One class is the lymphocyte-like class which is made of LTIC and DC in developing LN and PP and of B and T cells in the spleen. The second class is the stromal background of FRC which – according to the hypothesis used in this work – can be 'excited' into a CXCL13-producing FDC state. This state requires the presence of a $LT\alpha_1\beta_2$ signal during a sufficient time for FDC-state induction and the constitutive presence for FDC maintenance. The $LT\alpha_1\beta_2$ signal itself may be substituted by related molecules depending on the tissue in which the PLF is generated (Sec. 2.2.2). Note, that the definition of FDC is solely based on the CXCL13 production property (and being a stromal cell type). The common markers used to detect FDC are likely to be the result of further maturation [*Gonzalez et al.*, 1998; *Kasajima-Akatsuka and Maeda*, 2006] corresponding to a more 'excited' state (Sec. 2.2.3).

The influx of the lymphocyte class of cells first induce the production of CCL21 that leads to the separation of LTIC and DC or B and T cells, respectively. A ring of the first cell type forms around the second cell type in each pair of interacting cells. This requires only a different response to CCL21 which is not mediated by different levels of CCR7 receptors but by a different mechanical behavior. The generation of FDC in the ring breaks the symmetry leading to the formation of discrete follicles. Their size is determined by the negative regulation of FDC generation. The negative regulation is required to stabilize the size of the follicle, thus, to prevent B cell aggregates to increase existing PLF. The fact that in experiment CXCL13 sources appear at random in the B cell ring prior to follicle formation [*Cupedo et al.*, 2004b] supports the symmetry breaking picture drawn here. The negative regulation is not yet reflected in experiment.

In the simulations performed the T cell number in the T zone is smaller than in real systems, maybe except for PP. This is a tribute to the computing times. There is no reason that higher T cell numbers change the picture significantly. Tests with a twofold increase indeed double the size of the T-Zone (not shown). Moreover the frequent generation of two T zones may no longer occur as sufficient number of T cells are likely to lead to a merged T zone (Sec. 6.1.5).

Negative regulation of FDC   The negative regulation is mediated by an FDC-correlated signal. The negative regulation can explain why the follicles are of more or less the same size in all organisms and organs having lymphoid follicles. Also the separation of B cells into distinct follicles can be explained by the negative regulation. The simulations require that the negative regulation signal is diffusive while it is not determined which source is responsible. If autocrine or paracrine mechanisms are acting cannot be determined from the theoretical description. FDC themselves may produce the negatively regulating signal. Also B cells located in the follicle may be stimulated to secrete the corresponding signal molecule. A possible candidate for a molecule that is involved in the negative regulation of PLF growth is CD137 [*Sun et al.*, 2005]. It has been shown that T cells co-stimulated with CD137 can decrease FDC numbers in the follicle and the absence of T cells protects the FDC networks indicating that only CD137 on T cells is relevant for the (additional) suppression of FDC networks. Of note, FDC express CD137 on their surface [*Lindstedt et al.*, 2003; *Pauly et al.*, 2002]. Further evidence is provided by the suppression of auto-immune GC reactions by anti-CD137 antibodies [*Foell et al.*, 2003]. Within the context of the work this can be interpreted as the inability to form FDC networks by excessive negative regulation via CD137. From that perspective it would be interesting to know whether FRC express CD137 as well which would support the notion of a negative regulation of FRC

to FDC differentiation. In the hypothesized scenario the T cells in the T zone stimulated by the CD137 on the surface of the FRC produce a signal that inhibits the differentiation process of the FRC. The important question remains how this signal relates to the follicle size and if it exists, how it may work in T cell deficient mice. A correlation with T cells is supported by the observation that the follicle size increases in athymic rat which lack the majority of T cells [*Sainte-Marie et al.*, 1984] although other sources for the relevant factor must exist in order to limit PLF size in the absence of T cells. The view of the negative regulation is challenged by the observation that a CTLA-4 knockout mouse leads to significantly increased GC [*Walker et al.*, 2003]. This may indicate that the size regulation of the FDC network is differently regulated in GC compared to PLF and/or that there exists a signal threshold up to which the negative regulation proposed in this work is efficient. In the latter case $LT\alpha_1\beta_2$-overexpression on B cells is likely to lead to enlarged PLF.

A regulation mechanism that has not been studied extensively is the control of the influx of lymphocytes. It is possible that CXCL13 which is transported along the conduit appearing on the HEV [*Nolte et al.*, 2003] regulates the influx of B cells. In that context the desensitization by CXCR5 internalization would reduce the CXCL13 levels that are able to reach the HEV when high B cell numbers are present and consequently limit the influx of B cells. On the contrary it has been shown that in LN the response to CCL21 is equally important while CXCL13 dominates in the PP [*Cyster*, 2005; *Muller et al.*, 2003; *Okada et al.*, 2002]. Thus this mechanism would not be sufficient as the CXCL13-independent influx found in experiment of cells leads to the unstable PLF formation scenarios described in this thesis.

Generation of first FDC   The initial formation of the FDC by a random B cell aggregate of sufficient size may not be absolutely required. During development the LTIC show higher levels of $LT\alpha_1\beta_2$ which is induced by IL-7 or TRANCE (Sec. 2.5). This immediately raises the question which cell provides the initial signal in restoration experiments with $LT\alpha_1\beta_2$ or TNF-α knockouts (Sec. 2.2.2)? The answer may be that some of the B cells are Ag-activated and serve as nucleation center for the induction of FDC networks. This view is supported by the observation that ectopic lymphoid follicles seem to be exclusively SLF, i.e. contain a GC, while PLF are not observed (Sec. 2.6). The ectopic formation of PLF is only present in ectopic expression of lymphotoxins or chemokines (Sec. 2.5.4). The observation that the subdermal injection of LTIC derived from newborn mice are able to stimulate lymphoid tissue neogenesis in young but not in adult mice [*Cupedo et al.*, 2004a] supports the view of higher $LT\alpha_1\beta_2$ on LTIC. This interpretation of the experiment implies that the IL-7 or TRANCE induced $LT\alpha_1\beta_2$-levels on the LTIC are rapidly downregulated upon transfer in the IL-7 and TRANCE low environment of adult mice [*Cupedo et al.*, 2004a]. The unorganized infiltrates caused by the LTIC-injection in adult mice can be structured when an inflammation is induced that restores the proper $LT\alpha_1\beta_2$-levels. A repetition of this experiment providing IL-7 or TRANCE to the adult mouse may lead to a proper ectopic lymphoid tissue formation without the necessity to induce an inflammation. More support for the idea of an $LT\alpha_1\beta_2$ threshold for FDC induction – and probably also for FDC maintenance – comes from the observation that disrupting the afferent vessels to LN leads to the loss of organization in the LN [*von Andrian and Mempel*, 2003; *Hendriks and Eestermans*, 1983]. Without afferent lymph the major route for Ag to enter the LN is cut off. The LN organization can be in part restored by inducing an immune reaction directly in the LN [*von Andrian*

and Mempel, 2003; *Hendriks and Eestermans*, 1983]. Similarly, the organization of the paracortex is correlated with exposure to Ag [*Belisle and Sainte-Marie*, 1981e]. Under the assumption that some cells are required to initiate PLF formation either by Ag exposure or cytokine stimuli, the picture drawn by the simulation changes slightly as even few cells can initiate the first FDC while in the presented simulation several B cells need to aggregate. However, the later stages of the simulation are not affected by high $LT\alpha_1\beta_2$-levels on B cells. The negative regulation is still required in order to prevent that these $LT\alpha_1\beta_2$ nucleation centers induce FDC at random locations. When the positive feedback loop [*Ansel et al.*, 2000] is acting under these conditions the instabilities due to internalization (see Sec. 6.1.5) remain if one assumes that the CXCR5 induced $LT\alpha_1\beta_2$-levels on B cells need some time to downregulate (in the order of 1 hour). Under these circumstances the deformed B cell aggregates can induce new FDC without nucleation centers. A strong separation of the time scale of FDC differentiation and CXCR5-induced $LT\alpha_1\beta_2$ levels however will prevent this, i.e. that the CXCL13-induced high $LT\alpha_1\beta_2$ levels decay much faster compared to the time needed to induce the FDC phenotype. When the B cells would then need Ag to provide a sufficient amount of $LT\alpha_1\beta_2$ for FDC induction – random B cell aggregates are not sufficient to do so – the instabilities of the B cell chemotaxis would not generate new FDC, thus the FDC network itself remains stable.

The relevance of the positive feedback loop between CXCL13 and $LT\alpha_1\beta_2$ [*Ansel et al.*, 2000] is set in question by the presented simulations. Its significance is also questioned by experiments with ectopic CXCL13 expression [*Luther et al.*, 2000]. There B cells accumulate following the CXCL13 gradient but no FDC can be found. The high levels of $LT\alpha_1\beta_2$ that should be induced by CXCL13 are not able to induce FDC although it has been shown that ectopic expression of $LT\alpha_1\beta_2$ directly can induce FDC [*Kim et al.*, 2004b]. Thus from the point of view of this work the positive feedback loop that couples the levels of $LT\alpha_1\beta_2$ on B cells to the cells exposure to CXCL13 is not necessary to understand PLF formation. Assuming the additional stimulation of $LT\alpha_1\beta_2$ is required to initiate the first FDC (as discussed in the former paragraph) than the feedback loop [*Ansel et al.*, 2000] may indeed be required to maintain the PLF. However, according to the simulation, it is still not required to initiate follicle formation. Even with the assumption of an additional stimulation of $LT\alpha_1\beta_2$, the results of the challenging experiments [*Kim et al.*, 2004b; *Luther et al.*, 2000] cannot be resolved.

Dynamics of blood vessels and lymphatic endothelium   An important result of this study is that the generation of ELV and HEV play an important role in the process of PLF formation and the basic correlation of 'FDC = no vessels' is sufficient to understand this process. It may be speculated that the signal that disintegrates or prevents the vessel formation in the follicle serves as negative regulation for the FDC generation as well. The dynamics of the ELV shall be interpreted strictly as remodeling process with creation and destruction of vessels. The HEV dynamics needs not to be interpreted in the sense of angiogenesis but may be related to the change of the endothelium to a 'high' endothelium due to $LT\alpha_1\beta_2$ signals (Sec. 2.3.2). Experimentally, the HEV dynamics is likely to be really angiogenic as it has been found in PP [*Hashi et al.*, 2001]. An homogeneous distribution of HEV gets remodeled to spare out the developing follicles according to the staining pattern of MAdCAM. The fact that in early developmental stages blood and lymphatic endothelial cells show MAdCAM expression the observed pattern may be also valid for ELV. The view of adaptive vessel remodeling for lymphoid tissues is supported by the appearance of HEV in the vicinity of $LT\alpha_1\beta_2$-induced ectopic lymphoid follicles

[*Kratz et al.*, 1996]. Also the redistribution of blood vessel during an immune response provides evidence for the importance of dynamic HEV [*Herman et al.*, 1972].

The effect of the vessel dynamics acting together with the negative regulation is that the B cell follicle has two zones. The inner part of the PLF contains FDC and B cells and is free of ELV and HEV. The second zone is a small rim in which B cells and vessels are present while FDC are missing. This defines more precisely why and how B cells occupy a larger area than the FDC network.

A test for the phenomenology of the proposed vessel dynamics can be done by blocking $LT\alpha_1\beta_2$ in wildtype mice or reconstitute them with bone marrow from $LT\alpha_1\beta_2^{-/-}$. The disruption of the PLF shall be followed by the presence of vessels in these areas. When using anti-angiogenic factors during the experiment, the gaps in the vessels network due to the PLF should be preserved when the PLF disappear. Another indication can be provided by the ring found in certain $LT\alpha_1\beta_2$-deficiencies (Sec. 2.2.2) which should be devoid of ELV (HEV are shown to depend already on $LT\alpha_1\beta_2$ themselves (Sec. 2.3.2)).

An indirect indicator that the dynamics of ELV occurs is the expression of transglutaminase immediately at the border of PLF [*Thomazy et al.*, 2003]. Transglutaminase is involved in the modification of the ECM and is expressed strongly on the lymphatic endothelial cells close to the PLF. This may indicate the dynamics not only of the ECM but also of the lymphatic endothelial cells themselves. One may speculate that IL-6 or TNF-α, both of which are known to induce transglutaminase [*Thomazy et al.*, 2003] and are increased in the PLF (Sec. 2.2.2), are involved in the lymphangiogenesis processes correlated with the formation of PLF.

The observation of angiogenesis and lymphangiogenesis during airway infections being dependent on B cells [*Aurora et al.*, 2005] may be related to the vessel dynamics process used in the simulations. It seems that VEGF-D is involved in this process [*Aurora et al.*, 2005]. The relation of VEGF-D to its cellular sources is not clear such that the angiogenic effect may be directly related to B cells. This is supported by the stimulation of VEGF by c-Myc$^+$ B cells in lymphomas [*Ruddell et al.*, 2003]. In conclusion, B cells may directly influence the ELV and HEV when forming a follicle by expressing or at least modulating factors regulating vessel growth. Also the effect of B cells may be indirect by promoting CXCL13 expression, whereas CXCL13 is known to modulate angiogenic factors [*Spinetti et al.*, 2001]. Another candidate for the source of growth factors for the vessels are the DC in the T zone [*Hamrah et al.*, 2003]. As T cells and DC both uses CCR7 to localize in the T zone it may be that DC are more important for structuring the T zone. The coupling of vessels to lymphocyte occupied but FDC free areas could be realized directly as DC occupied areas that promote vessels growth. This however does not change the outcome of the simulation because as soon as FDC form the DC would be replaced by B cells. Thus the VEGF will no longer be present and consequently blood vessels and ELV are not maintained. The reduced number of DC in $LT\alpha^{-/-}$[*Ngo et al.*, 1999; *Wang et al.*, 2002a] may influence the vessel structure in SLT and may serve as experimental indicator for the contribution of DC to angio- and lymphangiogenesis in SLT.

The effect of TNF-α to upregulate VEGF-C [*Hamrah et al.*, 2003; *Kerjaschki*, 2005] suggests that T cells remain correlated to the vessel dynamics in the T zone via their TNF-α levels. Similar B cells are known to express TNF-α. Thus lymphocytes may, in the presence of the mediating DC, influence

angio- and lymphangiogenesis. The function of efferent vessel to guide the egress of lymphocytes seems to depend on S1P [*Cyster*, 2005; *Lo et al.*, 2005; *Matloubian et al.*, 2004; *Sallusto and Mackay*, 2004] which itself is also influenced by TNF-α [*Rosen and Goetzl*, 2005] suggesting that TNF-α is not only involved in modulating the FDC/FRC phenotype when shaping the SLT but also in the structure of the supporting vessel systems.

An experiment to decide about the DC influence on SLT vessel formation would be a mouse with VEGF$^{-/-}$ DC. A direct test for the vessel dynamics model would be to provide anti-angiogenic factors to LT$\alpha_1\beta_2$$^{-/-}$ or similar knockouts prior to reconstitution by wildtype lymphocytes or bone marrow. The follicles that form should be much smaller than usual (due to increased cell efflux) and contain both vessel types.

The fact that HEV take the role of ELV in pigs [*Binns and Licence*, 1990] strongly suggests that the angiogenesis and lymphangiogenesis in the context of PLF formation is based on the same principle. Like in the simulation it is likely that the anti-correlation between FDC and vessels uses the same molecular mechanism. The interesting fact that the LN structure of pigs is in general inverted [*Spalding and Heath*, 1989] is likely to be correlated with the different behavior of lymphocytes to leave the lymphoid tissue via the HEV [*Binns and Licence*, 1990]. In this system it is favorable that the simulation treats the development of both vessel types similarly such that one can immediately conclude from the simulation that the HEV is participating in the regulation of the PLF size. They are part of the outer rim of the PLF in which B cells and vessel but no FDC are present. There, the HEV can act as exit sites for B cell egress. However, even in pigs the ELV show the same microanatomy as for the other species (Sec. 2.3.3) but it remains unclear what the purpose of these ELV is. Probably the transport of DC and Ag [*von Andrian and Mempel*, 2003] is still provided by the ELV in pigs.

Related secondary lymphoid tissue structures   The results drawn for the PLF may also be relevant for the deep cortical unit [*Belisle and Sainte-Marie*, 1981a,b,c,d,e, 1990; *Belisle et al.*, 1982; *Sainte-Marie et al.*, 1981]. The fact that an area filled with lymphocytes is bounded by a zone that contains lymphocytes, ECM-fibers, efferent lymphatic and blood vessels reproduces almost all basic features of the PLF structure. The regulation of the size of the deep cortical unit which is also basically constant in all mammalian species [*Belisle and Sainte-Marie*, 1981a] may also be a result of a corresponding negative regulation. This is supported by the observation that the developmental steps of the deep cortical unit are similar to the ones of the PLF [*Belisle and Sainte-Marie*, 1981e]. The unit starts from an area that is homogeneously filled with ECM and stromal cells but is low on lymphocytes. Within 1 day this area show the first signs of restructuring into deep cortical units. The location of the units is correlated with the entry points of the afferent vessels of the LN [*Belisle and Sainte-Marie*, 1981c,e]. Over two weeks the deep cortical units enlarge to their mature size and the ELV are established at the end of this development. This may indicate that the units are formed in the beginning with a low efflux of cells that helps to increase the size of the deep cortical unit. One may speculate that the slightly increased size of PLF in LN reported for mice lacking most T cells [*Sainte-Marie et al.*, 1984] are due to an underdeveloped efferent lymphatic vessel system that is observed in these animals [*Sainte-Marie et al.*, 1984] (an interpretation different from the negative regulation by CD137 discussed above). The question remains if there is a cell type that takes the role of the FDC

in the PLF. It is unlikely that FRC play this role as they are found in association with ECM fibers (Sec. 2.3.1) which are not present in the center of the deep cortical unit.

Ring structure in secondary lymphoid tissue   The ring formation of B cells around the T zone in certain TNF-α- or lymphotoxin-deficient animals (Table 2.2) or as intermediate structure during development (Sec. 2.5) can be related to the different response of B and T cells towards CCL21 and especially their different mechanical response. More precisely, the stronger migration of forces of T cells compared to B cells, which leads to faster T cell migration, are the major determinant of the separation of B and T cells in the ring phase of development. Neither differential adhesion [*Steinberg*, 1970] nor additional chemokines [*Cupedo et al.*, 2004b] are required. Moreover the patterns seen in mice with ectopic chemokine expression are explained by the results of the simulations. The ectopic expression of CCL19 or CCL21 induces the typical ring structure [*Luther et al.*, 2002]. However, when CXCL13 is ectopically expressed the ring structure is inverted with T cells forming a ring around a B cell aggregate [*Luther et al.*, 2000] suggesting that the different response to CXCL13 is sufficient, or more general a different chemokine response is sufficient for the separation of two cell types into a ring structure. A similar observation holds for CCR7$^{-/-}$ and the *plt/plt* mutant strain in which cases the B/T segregation is missing in LN but T cells form ring around the PLF in the PP [*Muller et al.*, 2003]. The special structure of LN of pigs with PLF in the center of the LN and the T zone at the periphery [*Spalding and Heath*, 1989] is an interesting case to study ring formation. Unfortunately, no reports on the intermediate stage of LN organogenesis in pigs are known. The simulation results suggest that the intermediate ring picture may be inverted in pigs which would keep the T cells at the periphery to build up the T zone there. This predicts that B cells migrate faster in pig LN than T cells which seems rather unlikely. Another possibility is that not only CCL21 is acting during LN organogenesis but other factors such that the situation in pigs may be closer to formation of tertiary lymphoid tissue by ectopic CXCL13 expression [*Luther et al.*, 2000].

The inverted ring picture upon ectopic CXCL13 expression [*Luther et al.*, 2002] – T cells around B cell aggregates – questions the outcome of this work that the ring formation depends on a different mechanical response of the cells if they both react to the same chemoattractant. This implies that in the inverted ring case the T cells are not responsive to CXCL13 but must be attracted by another secondary factor.

The proposed mechanism for B cell ring formation cannot rule out the existence of additional factors attracting B cells towards the cortex. Likely candidates are the other chemotactic factors IL-6 and IL-15 that are produced by FDC [*Clark et al.*, 1992; *Huber et al.*, 2005; *Husson et al.*, 2000; *Kim et al.*, 1994; *Nieto et al.*, 1997; *Park and Choi*, 2005; *Weissenbach et al.*, 2004]. It seems however more plausible that the attraction, if existent, correlates with the afferent vessels in LN or the specialized epithelium covering MALT. The guiding factors may be antigens or complement factors which can serve as chemoattractors for B cells [*Komai-Koma et al.*, 1997; *Ottonello et al.*, 1999]. The additional attraction may also act in the LN of pigs as the usually cortex located structures appear in the center of those LN [*Spalding and Heath*, 1989].

Real chemotaxis in secondary lymphoid tissues   In all simulations B cells are attracted towards the follicle chemotactically. This at first sight is in contradiction to the experiments [*Miller et al.*, 2003, 2002; *Okada et al.*, 2005; *Wei et al.*, 2003]. Two-photon imaging experiments could not identify a directed motion of naive lymphocytes. Instead a random pattern inside the compartments have been observed. The motility coefficient for B cells has been determined to be $D = 12\,\mu m^2\,min^{-1}$. In order to travel a distance of $100\,\mu m$ the cell would take roughly 14 hours. This is unrealistically high as the typical distance of a HEV to the next follicle can be easily larger [*Gretz et al.*, 1997]. Whether B cells leave the SLT before they reach the follicle, as discussed for the S1P resensitization previously (Sec. 6.3), or B cells exit from HEV only close to the follicle border remains to be determined. The exit of lymphocyte from HEV close to the follicular border is known to happen for the PP [*Muller et al.*, 2003] while there seems to be no preferential entry site for B cells in the LN [*van Ewijk and van der Kwast*, 1980]. The random motion of T cells within the T zone and B cells within the PLF may be just a result of the rather flat chemokine distribution in these areas as it is found in the simulations. Such chemotaxis-guided cell motility occurs only at the interface of B and T zone. In the case of large follicles the random motion inside the compartment becomes more obvious.

The simulations suggest that the internalization dynamics of chemokine receptors does not play a significant role. It can even lead to a destabilization of the follicle which has to be counter-balanced by some other mechanism. A direct test of the impact of internalization dynamics on the follicle could be provided by the administration of IFN-α which has been shown to enhance chemotaxis by increasing the receptors levels [*Badr et al.*, 2005]. It is most likely that the effect is mediated by increased recycling or decreased internalization of the receptor-ligand process. If internalization plays a significant role in the PLF formation IFN-α should increase the size of the follicle. This would imply that the internalization process is to a certain extent contributing to the size regulation.

Considering the instability found in this work, the CXCL13 production rate shall be sufficiently high to counterbalance the instability reduced by CXCR5 internalization. Alternatively, the internalization process could work differently than used throughout the thesis. The basic difference that need to be made is that chemokines that are bound to GAG on the ECM (Sec. 3.3) cannot be internalized together with the receptor. In detail that requires that the receptor CXCR5 unbinds from the GAG-immobilized CXCL13 prior to internalization. Also, CXCL13 needs to be bound to the FDC directly as the ECM in the follicular are is virtually absent (Sec. 2.3.1). Yet, the binding properties of CXCL13 (or related chemokines) with GAG, ECM components, or FDC are unknown such that a reliable investigation is not possible at the moment.

Outlook   The multiscale agent-based model resulting from an interdisciplinary approach of physics, informatics, and biology is able to simulate the development of PLF and the adjacent T zone. In general it is capable to simulate tissues that contain fast migrating cells and/or cells in a flow equilibrium. For example the remodeling process in the bone [*Garcia-Aznar et al.*, 2005] is a possible application of the model architecture.

The natural extension of the present PLF model and another application of the architecture is the germinal center reaction [*Beyer et al.*, 2002; *MacLennan*, 1994; *Meyer-Hermann and Beyer*, 2003; *Meyer-Hermann et al.*, 2001, 2006; *Meyer-Hermann and Maini*, 2005a]. The agent-based approach

allows to track the fate of every single B cell clone in the germinal center and generate geneanologic trees of the B cell populations. Moreover the model is ideal to describe the high motility of germinal center B cells [*Allen et al.*, 2007; *Schwickert et al.*, 2007].

The modular design of the model architecture permits a straightforward extension to other specific biological system. In most cases the behavior of cells will change. In the multiscale agent-based approach of this work only the internal dynamics of cells need to be adapted while the equations describing contact and long-range interaction remain unchanged. In a similar manner improved experimental and/or theoretical data on the mechanical cell interactions can be a easily included into the model without touching the specific properties of a certain biological system, e.g. the PLF. Thus, it is possible to investigate the impact of biomechanics on a system as it was demonstrated for the B cell ring formation.

Independent of the tissue model the algorithms and the code of the regular triangulation can be used for any kind of particle simulation with contact interactions. The major advantage of the code that was developed during this thesis is that it provides every operation that can be applied to a regular triangulation: inserting, removing, and displacing vertices. In addition it is the only code that deal with non-flippable configurations of simplices which allows an efficient parallel performance of the flip algorithm. Together with the parallel algorithms for the other operations the code allows to simulate a large number of objects on parallel computer systems.

To conclude, the presented model architecture is a step to investigate complex interactions of biological systems with high numbers of cells. Starting from known molecular and cellular interactions, changes on the morphology of tissues can help to get insights into yet unknown molecular or cellular mechanisms. Simulations can help to design and guide experiments to test mechanisms that are identified by theoretical considerations of biological systems.

Appendix A

Simulation validation

A.1   Test the regular triangulation

In order to test the triangulation the orthosphere criterion has been checked explicitely for the resulting triangulation. For small triangulations (less then 10000 vertices) the global orthosphere test has been performed for each simplex while for larger ones only the local criterion has been checked. Additionally, the data structure has been checked for consistency by cross-checking all bidirectional relationships like:

- If vertex *A* is neighbor of *B* then *A* has to be a neighbor of *B*.

- If vertex *A* is neighbor of *B* then there exists at least one simplex that is common between *A* and *B*.

- If a simplex σ has the vertex *A* as endpoint then σ is stored in the simplex list of *A*.

- If a simplex contains the vertices *A* and *B* then *A* and *B* are neighbors.

- If simplex σ_1 is adjacent to simplex σ_2 then σ_2 is adjacent to σ_1.

Finally, the program has been check for memory errors by applying the memory debugger Valgrind to different test runs of the program.

A.2   Test the model

A.2.1   Diffusion and reaction

The solution of the diffusion equation has been checked by comparing it to analytical stationary solutions first. Second, the time-dependent solution has been checked for by providing a time-dependent solution and calculate the corresponding source terms over time. Than this source distribution has been put into the code to recalculate the starting solution.

The reaction terms have been compared to manually computed results for the implicit Euler method. Analytical results can be obtained by setting various rates of (Eq. 5.49) to zero and compare it to the reaction terms computed by the program. Finally, the limiting behavior against large or small concentrations has been checked.

A.2.2 Mechanical model

The correct computations of the forces have each been checked manually by comparing the computed results with the results computed by hand. The solution of the linear system (Sec. 5.4.6) has been cross-checked by computing the difference between the drag force (Eq. 5.34) explicitely from the velocity field of the cells. The sum of all forces has been shown to be zero for all cells with the relative precision requested from the solution method (PETSc or fixpoint iteration (Sec. 5.4.6)).

The step size chosen for the model has been checked by comparing the analytical solution of the JKR model for two cells with the analytical solution as it has been done previously [*Schaller*, 2006].

A.2.3 Internal cell states

The internal cell states have been checked directly by manually comparing conditions and the induced changes in the internal times τ with the given parameters.

Appendix B

Fitting biomechanical parameters

The active forces exerted by lymphocytes to the ECM ($F_i^{\text{active}}(\phi_i)$, Eq. 5.5) and to other cells (p_i^*, (Eq. 5.73)) are not known explicitly (there are just estimates based on experiments of other cell types [*Balaban et al.*, 2001; *Burton et al.*, 1999; *Galbraith and Sheetz*, 1999; *Schwarz et al.*, 2002]). The same applies to the friction parameters (μ_i and μ_{medium}, (Eq. 5.34)). For simplicity it is assumed that $\mu_i = \mu_{\text{medium}}$ for all lymphocytes. As the known average speed is essentially determined by the ratio of active forces and the friction parameters only 2 parameters per cell type remain unknown. These can be determined from the measured speed distributions for B and T cells within SLT [*Miller et al.*, 2002; *Okada et al.*, 2005]. A reduced cell system with a constant number of lymphocytes that respond to a chemotactic point source is used. The cell constituents are either B or T cells only or an even mix of both cell types.

The parameters for the JKR-forces are relatively well known. The parameters entering (Eq. 5.15) are the elasticity of lymphocytes is $E_i = 1kPa$ [*Bausch et al.*, 1999, 1998; *Chu et al.*, 2005; *Forgacs et al.*, 1998], the Poisson number $\nu_i = 0.4$ [*Hategan et al.*, 2003; *Maniotis et al.*, 1997], and the surface energy $\sigma_{ij} = 0 - -0.3\text{nN}\,\mu\text{m}^{-1}$ [*Moy et al.*, 1999; *Verdier*, 2003]. Thus the elastic cell interactions can serve as reference forces limiting the reasonable range of friction parameters. Therefore the fit to the speed distribution was performed with two qualitatively different friction regimes. In the low friction regime ($\mu_i = \mu_{\text{medium}} = 150\,\text{nN}\,\mu\text{m}^{-2}\,s$) the active forces that are required to produce the correct speed distribution are of the same order as the JKR forces. In this regime it turns out that the mode of measuring the cell speed becomes crucial: The speed distribution of the real system was measured on the basis of the average displacement over an interval of $\Delta T = 10 - -15\,\text{s}$ [*Miller et al.*, 2002; *Okada et al.*, 2005]. These data are reproduced and compared to the simulation results in the two upper panels of FIG. B.1. Using a faster sampling with $\Delta T = 1\,\text{s}$ the speed distribution becomes different and exhibits the influence of JKR forces that lead to fluctuations at rather high speed (FIG. B.1 middle panel). The JKR forces dominantly lead to reversed or perpendicular motion of cells with respect to their migration axis when cells collide due to active movement. Thus the net-displacement by JKR forces during $\Delta T = 15\,\text{s}$ is rather small and does only show up at lower speeds in the resulting distribution when longer sampling intervals are used.

In the second regime with high friction ($\mu_i = \mu_{\text{medium}} = 1500\,\text{nN}\,\mu\text{m}^{-2}\,s$) (Fig. B.1) the average speed
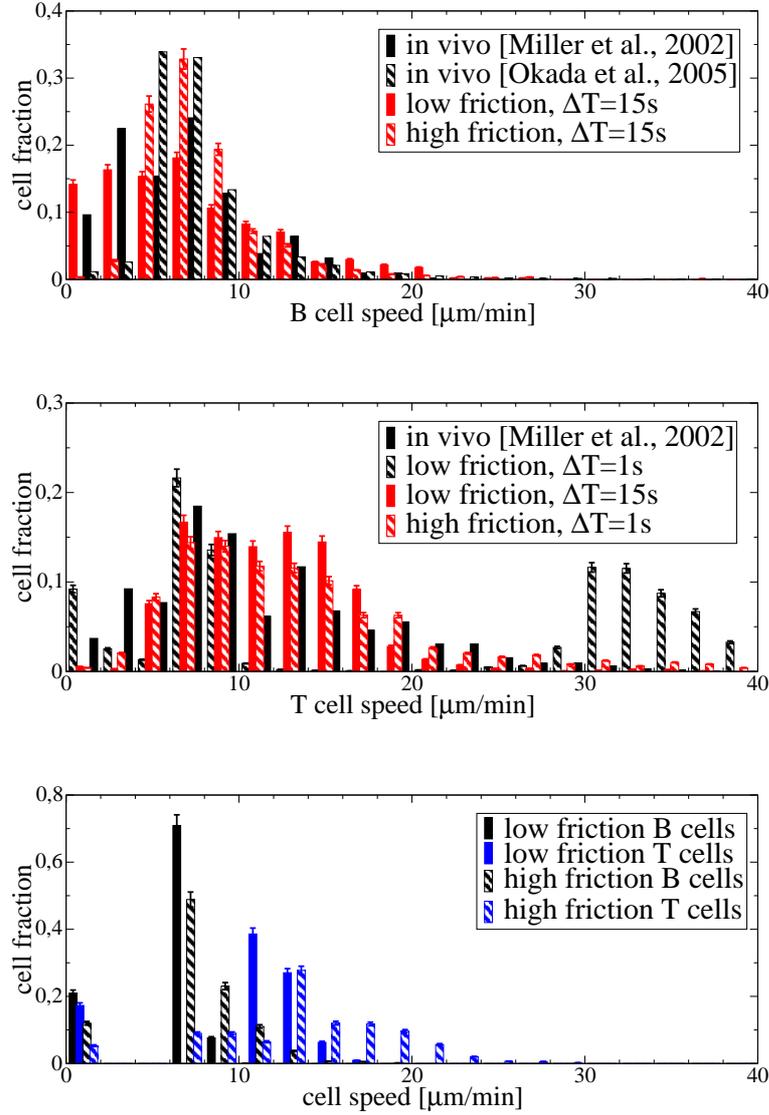
Figure B.1: Comparison of experimental and simulated cell speed distributions. Each bin represents a 2 μm min^{-1} speed interval. For clear visibility the bins are placed around the centers of the speed intervals. The upper panel shows the B cell speed distribution at low ($F_{\text{Bcell}}^{\text{act}} = 18 \pm 3$ nN, $p_{\text{Bcell}}^* = 0.04 \pm 0.01$ nN μm^{-2}) and high friction ($F_{\text{Bcell}}^{\text{act}} = 120 \pm 20$ nN, $p_{\text{Bcell}}^* = 1.7 \pm 0.05$ nN μm^{-2}) compared to two experimental data sets. The middle panel shows the speed distribution of T cells. The way of determining the speed distribution is crucial in the case of the low friction ($F_{\text{Tcell}}^{\text{act}} = 22 \pm 3$ nN, $p_{\text{Tcell}}^* = 0.06 \pm 0.02$ nN μm^{-2}). With a high sampling rate ($\Delta T = 1$ s) the distribution has a contribution at high speeds ($> 30 \mu$m min^{-1}) that is not seen using a larger sampling interval ($\Delta T = 15$ s). For comparison the high friction regime ($F_{\text{Tcell}}^{\text{act}} = 240 \pm 35$ nN, $p_{\text{Tcell}}^* = 3.7 \pm 1.1$ nN μm^{-2}) is also shown (in that case the speed distributions with $\Delta T = 1$ s and $\Delta T = 15$ s are virtually indistinguishable). When the inter-cellular active forces are omitted ($p_{\text{Tcell}}^* = p_{\text{Bcell}}^* = 0$ (Eq. 5.73)) the speed distributions show rather sharp peaks (lower panel, sampling interval $\Delta T = 15$ s).

with $\Delta T = 1$ s and $\Delta T = 15$ s match each other (not shown). The resulting speed distribution usually fit better to the experimental ones, in particular, because low speed contributions now are shifted to the peak resulting in a sharper speed distribution . Although the active forces are higher than measured experimentally [*Balaban et al.*, 2001; *Burton et al.*, 1999; *Schwarz et al.*, 2002] the parameter set is computationally favorable as the high speed fluctuations are missing. This allows for larger time steps in the simulation. Moreover the components of the speed distribution in the low speed range are smaller as the active forces can more easily overcome the JKR forces such that cells are less likely to be immobilized in an cellular environment of high density.

The effect of active forces F_{ij}^{active} (Eq. 5.73) resulting from the constriction ring model is relevant to the speed distribution. Without these active inter-cellular forces the speed distribution shows only sharp peaks (Fig. B.1) lower panel). Also when the speed distribution of each lymphocyte subset is fitted using a homogeneous cell aggregate the peaks in the speed distribution tend to be sharper than in experiment. This could be compensated with larger active cell interaction forces F_{ij}^{active} which however produces the wrong speed distribution when B and T cells interact which each other (not shown).

The motion of cells can also be characterized using a motility coefficient that is similar to diffusion coefficient in Brownian motion. However, it is not just a result of physical contacts with the environment but also involves intrinsic features of cell migration. The motility coefficient D_{cell} is influenced by the cell's speed v and the mean free path length [*Dickinson and Tranquillo*, 1993]. In cells the latter one is determined by the persistence time T_{p} during which the cell maintains its polarized structured fixing the direction of force exertion and therefore the direction of motion [*Meyer-Hermann and Maini*, 2005b; *Miller et al.*, 2003, 2002; *Okada et al.*, 2005; *Wei et al.*, 2003].

$$D_{\text{cell}} = \frac{1}{3}v^2 T_{\text{p}} \tag{B.1}$$

Thus the persistence time is a parameter describing the migration of cells independently of force generation.

Conclusions The constriction ring model takes into account lateral force generation by actively migrating cells which are ignored in other force-based models that consider only the generated net force [*Dallon and Othmer*, 2004; *Palsson and Othmer*, 2000]. It is shown that the cell interaction due to the exchange of active forces is the major determinant of the width of the speed distributions. Thus this interaction might be interpreted as a Brownian motion-like fluctuation of the cell speed also it is deterministic. The parameter coupled with the constriction ring is the pressure the pressure p_i^* (Eq. 5.73). The force $F_i^{\text{active}}(\phi_i)$ exerted to the extra-cellular matrix may be either generated by the integrated pressure of the constriction ring model directly exerted to the matrix or by the filopodia dynamics of the classical three-step migration model (reviewed in [*Lauffenburger and Horwitz*, 1996; *Mitchison and Cramer*, 1996]). Recent data demonstrates that both migration modes act in lymphocytes [*Yoshida and Soldati*, 2006] although the contribution of the constriction ring is greater during chemotactic responses of migrating lymphocytes [*Friedl et al.*, 2001; *Friedl and Brocker*, 2000; *Yoshida and Soldati*, 2006]. Especially, the characteristic time of the cytoskeleton dynamics of the ring coincides nicely with the persistence time [*Paluch et al.*, 2005; *Yoshida and Soldati*, 2006]. The persistence time, the

time interval during which the direction of active forces is constant, is likely to be an intrinsic feature of the underlying cytoskeleton dynamics [*Cunningham*, 1995; *Keller and Eggli*, 1998; *Paluch et al.*, 2005, 2006; *Yoshida and Soldati*, 2006].

Appendix C

Using ellipsoidal cells

The general idea is to introduce a non-spherical cell by changing the interaction potentials. The simplest case is to use rotational ellipsoids introducing an additional shape parameter denoting the length of the cell. When the elongation is not to large the regular triangulation will not change too much such that the neighborhood relationships can be computed from the case of spherical cells. However, the contact distances and areas do no longer correspond to the dual Voronoi tessellation. Instead they are computed directly for the cells that are in the neighborhood as defined by the triangulation. Additionally, the contact force has to be adapted. The introduction of an axis implies that the torque acting on cells has to be respected. However, it is not clear if cells act as rigid bodies when exposed to torque but may adapt their direction actively, i.e. by restructuring their cytoskeleton. To account for this the torque acting on a cell may reorient it but is assumed that the reorientation of the cells does not generate torque to its environment (like friction forces for example) such that the rotational velocities of cells are uncoupled and the rotation change $\Delta \omega$ can be compute simply via

$$\Delta \omega_i = \dot{\omega}_i \Delta t = \frac{1}{\gamma_{\text{rot}}} \mathbf{M}_i \tag{C.1}$$

for each cell i with $\mathbf{M}_i$ being the torque.

The modification of the interaction potential can be done analogously to the simulations in particle physics. One should not that the distance between two ellipsoid cannot be computed directly in general. Instead numerical approaches or approximations can be performed. One simplification is to define the interaction strength by the overlap of two stretched Gaussians representing the ellipsoids giving a indirect measure [*Cleaver et al.*, 1996]. However, this generates some unphysical behavior [*Everaers and Ejtehadi*, 2003; *Perram et al.*, 1996]. The approach that is presented here will use a numerical scheme that reduces automatically to the Voronoi description when reduced to spherical particles. It is based on the idea to define the contact point of two ellipsoids by rescaling them introduced by Perram and Wertheim [*Perram and Wertheim*, 1985]. The contact function is based on the definition of

$$s_{ij}(\lambda) = 4\lambda(1-\lambda)\mathbf{r}_{ij} Y^{-1}(\lambda)\mathbf{r}_{ij} \tag{C.2}$$

with the center distance $\mathbf{r}_{ij} = \mathbf{r}_j - \mathbf{r}_i$ and the matrix

$$Y(\lambda) = \lambda A_i^{-1} * (1 - \lambda)A_j^{-1} \tag{C.3}$$

involving the matrices A that describe the ellipsoids. These matrices define the ellipsoids by

$$1 = \mathbf{x}^{\mathrm{T}} A \mathbf{x}. \tag{C.4}$$

The function (Eq. C.2) is maximized with respect to the parameter λ and the contact function is defined as

$$P_{ij} = \left\{ \max s_{ij}(\lambda) \,|\, \lambda \in [0, 1] \right\}. \tag{C.5}$$

Note that the Gay-Berne potential is an approximation to this function by setting $\lambda = 1/2$ which is the its value for the case of two spheres [*Perram et al.*, 1996]. Practically, (Eq. C.5) can be evaluated using the Newton-algorithm with only few iterations [*Donve et al.*, 2005]. With this definition it holds

$$P_{ij} = \begin{cases} < 1, & \text{overlapping} \\ = 1, & \text{externally tangent} \\ > 1, & \text{no contact} \end{cases} \tag{C.6}$$

and the point of contact is

$$\mathbf{r}_C = \mathbf{r}_i + (1 - \lambda_m)A_i^{-1}Y(\lambda_m)^{-1}\mathbf{r}_{ij} = \mathbf{r}_j - \lambda_m A_j^{-1}Y(\lambda_m)^{-1}\mathbf{r}_{ij} \tag{C.7}$$

with λ_m maximizing $s_{ij}(\lambda)$. The vector $\mathbf{n} = Y(\lambda_m)^{-1}\mathbf{r}_{ij}$ is parallel to the normal in the contact point. The function (Eq. C.5) is however not a distance but it can be converted to distance-like function by using

$$h_{\mathrm{ij}} = s_0 \sqrt{P_{ij}} \tag{C.8}$$

as replacement for the penetration depth in the JKR model (Eq. 5.15), i.e. as the contact is defined by scaling the interaction potential is scaled accordingly. Hereby $s_0^2 = b_i^2 + b_j^2$ with the b being the short half axes of the two ellipsoids. Additionally, one has to deal with the radii in the JKR force (Eq. 5.15). The natural choice is to use the radii of the spheres of curvature at the contact point of the two ellipsoids. The curvature of the ellipsoid in the point $\mathbf{x} = (x, y, z)$ is given by

$$R_i = a_i b_i c_i \left(\frac{x^2}{a_i^4} + \frac{y^2}{b_i^4} + \frac{z^2}{c_i^4} \right) \tag{C.9}$$

using the normal form with the three half axes a_i, b_i, c_i. Using the matrix form this can be written as (respecting that A_i is symmetric)

$$R_i = a_i b_i c_i \mathbf{x}^{\mathrm{T}} A_i A_i \mathbf{x}. \tag{C.10}$$

The point where the curvature is taken is related to the normal in the contact point which shall be parallel to the normal in the corresponding point on the ellipsoidal surface

$$\mathbf{A}_i \mathbf{x} \sim \mathbf{n} \tag{C.11}$$

taking care of the correct sign of $\mathbf{A}_i \mathbf{x}$ pointing into the direction of the second ellipsoid. With some

simple algebra one arrives at

$$\mathbf{A}_i \mathbf{x} = \frac{\mathbf{n}}{\sqrt{\mathbf{n}^T A_i \mathbf{n}}} \tag{C.12}$$

This changes the expression for the curvature to

$$R_i = a_i b_i c_i \frac{\mathbf{n}^T \mathbf{n}}{\mathbf{n}^T A_i \mathbf{n}}. \tag{C.13}$$

Finally, to derive the force and the torques one needs the potential of the JKR model which can be computed by integrating (Eq. 5.15)

$$V^{\mathrm{JKR}} = \frac{2}{5} h_{ij}^{5/2} K R^{1/2} - \frac{4}{7} h_{ij}^{7/4} \sqrt{6\pi K R^{1/2} \sigma_{ij}} \tag{C.14}$$

$$\frac{1}{K} \equiv \frac{1}{E_{ij}^*} = \frac{3}{4} \left[\frac{1 - v_i^2}{E_i} + \frac{1 - v_j^2}{E_j} \right] \tag{C.15}$$

$$R = \frac{1}{R_{ij}^*} = \frac{1}{R_i} + \frac{1}{R_j} \tag{C.16}$$

Using the contact definition by Perram and Wertheim the curvature dependent factor K reads

$$K = \frac{\mathbf{n}^T A_i \mathbf{n} + \mathbf{n}^T A_j \mathbf{n}}{\mathbf{n}^T \mathbf{n}} \tag{C.17}$$

$$= \frac{\mathbf{n}^T [A_i + A_j] \mathbf{n}}{\mathbf{n}^T \mathbf{n}}. \tag{C.18}$$

Following [*Allen and Germano*, 2002] one can compute the force acting between the cells i and j modeled as ellipsoids by

$$f_{ij} = -\frac{\partial V^{\mathrm{JKR}}}{\partial \mathbf{r}_{ij}} = -\frac{\partial V^{\mathrm{JKR}}}{\partial h_{ij}} \frac{\partial h_{ij}}{\partial \mathbf{r}_{ij}} - \frac{\partial V^{\mathrm{JKR}}}{\partial R} \frac{\partial R}{\partial \mathbf{r}_{ij}}. \tag{C.19}$$

One has to take into account that λ_m is implicitly dependent on the distance vector $\mathbf{r}_{ij}$ as well. The derivatives of λ_m can be computed by taking the implicit derivative of $dP_{ij}(\lambda_m)/d\lambda_m = 0$ such that

$$\frac{\partial \lambda_m}{\partial \mathbf{r}_{ij}} = -\left[\frac{\partial^2 P_{ij}}{\partial \lambda_m^2} \right]^{-1} \frac{\partial P_{ij}}{\partial \mathbf{r}_{ij}} \tag{C.20}$$

Then the single contributions read

$$\frac{\partial V^{\mathrm{JKR}}}{\partial h_{ij}} = h_{ij}^{3/2} K R^{1/2} - h_{ij}^{3/4} \sqrt{6\pi K R^{1/2} \sigma_{ij}} \tag{C.21}$$

$$\frac{\partial V^{\mathrm{JKR}}}{\partial R} = \frac{1}{5} h_{ij}^{5/2} K R^{-1/2} - \frac{1}{7} h_{ij}^{7/4} \sqrt{6\pi K R^{-3/2} \sigma_{ij}} \tag{C.22}$$

$$\frac{\partial h_{ij}}{\partial \mathbf{r}_{ij}} = -\frac{s_0}{2P_{ij}} \lambda_m (1 - \lambda_m) \mathbf{n} \tag{C.23}$$

$$\frac{\partial R}{\partial \mathbf{r}_{ij}} = 2\lambda_m (1 - \lambda_m) Y^{-1} \mathbf{W} + 2XY^{-1} \tilde{\mathbf{W}} \tag{C.24}$$

with

$$W = \frac{1}{\lambda_m(1 - \lambda_m)\mathbf{n}^T\mathbf{n}} \left[(A_i^{-1} + A_j^{-1}) - \frac{\mathbf{n}^T(A_i^{-1} + A_j^{-1})\mathbf{n}}{\mathbf{n}^T\mathbf{n}} \right] \mathbf{n},$$

(C.25)

$$\tilde{W} = \left[-\lambda_m^2 A_i^{-1} + (1 - \lambda_m)^2 A_j^{-1} \right] \mathbf{n}$$

(C.26)

and

$$X = \frac{W^T Y^{-1} \tilde{W}}{\mathbf{n}^T[-\lambda_m^2 A_i^{-1} + (1 - \lambda_m)^2 A_j^{-1}]^{-1}\mathbf{n}}$$

(C.27)

For the torques one has to compute

$$\mathbf{m}_i = - \sum_{\alpha=1,2,3} \hat{\mathbf{a}}_\alpha \times \frac{\partial V^{JKR}}{\partial \hat{\mathbf{a}}_\alpha}$$

(C.28)

$$\mathbf{m}_j = - \sum_{\beta=1,2,3} \hat{\mathbf{b}}_\alpha \times \frac{\partial V^{JKR}}{\partial \hat{\mathbf{b}}_\beta}$$

(C.29)

with the axis vectors of the ellipsoids

$$A_i = \sum_{\alpha=1,2,3} a_\alpha^2 \hat{\mathbf{a}}_\alpha \otimes \hat{\mathbf{a}}_\alpha$$

(C.30)

$$A_j = \sum_{\beta=1,2,3} b_\beta^2 \hat{\mathbf{b}}_\alpha \otimes \hat{\mathbf{b}}_\alpha.$$

(C.31)

Performing the derivatives and reducing the equation to rotational ellipsoids with the principal axis $\hat{\mathbf{u}}_i$ and $\hat{\mathbf{u}}_j$, respectively, one yields

$$
\begin{aligned}
\mathbf{m}_i \quad = \quad & 2\frac{(A_i\mathbf{n}) \times \mathbf{n}}{\mathbf{n}^T\mathbf{n}} - 2\lambda_m^2(1 - \lambda_m)\left[(A_i^{-1}\mathbf{n}) \times (Y^{-1}W) + (A_i^{-1}Y^{-1}W) \times \mathbf{n} \right] \\
& - X\left\{ \lambda_m \left[(A_i^{-1}Y^{-1}\tilde{W} \times \mathbf{n} + (A_i^{-1}\mathbf{n}) \times (Y^{-1}\tilde{W}) \right] + \lambda_m^2(A_i^{-1}\mathbf{n}) \times \mathbf{n} \right\} \\
& + (\mathbf{r}_i - \mathbf{r}_C) \times \mathbf{n}
\end{aligned}
$$

(C.32)

$$
\begin{aligned}
\mathbf{m}_j \quad = \quad & 2\frac{(A_j\mathbf{n}) \times \mathbf{n}}{\mathbf{n}^T\mathbf{n}} - 2\lambda_m(1 - \lambda_m)^2 \left[(A_j^{-1}\mathbf{n}) \times (Y^{-1}W) + (A_j^{-1}Y^{-1}W) \times \mathbf{n} \right] \\
& - X\left\{ (1 - \lambda_m) \left[(A_j^{-1}Y^{-1}\tilde{W} \times \mathbf{n} + (A_j^{-1}\mathbf{n}) \times (Y^{-1}\tilde{W}) \right] - (1 - \lambda_m)^2(A_j^{-1}\mathbf{n}) \times \mathbf{n} \right\} \\
& - (\mathbf{r}_j - \mathbf{r}_C) \times \mathbf{n}
\end{aligned}
$$

(C.33)

with the last term being the curvature-independent contribution of the JKR potential. Again derivatives of λ_m are necessary and are treated similar to (Eq. C.20).

The ellipsoid representation of cells has been implemented and tested. The test were performed by controlling the conservation law

$$\mathbf{r}_{ij} \times \mathbf{f}_{ij} + \mathbf{m}_i + \mathbf{m}_j = 0.$$

(C.34)

Also the limiting cases were the ellipsoids are spherical have been checked for correctness. Additionally, the special cases of configurations with parallel or perpendicular ellipsoid principal axis have been used to check for the correct implementation. However, the ellipsoid representation has not

been used as the required time and spatial resolution increase demanding more computational power. This is mainly caused by the stiffer mechanical response of the cells at their tips due to the small radius of curvature increasing the effective elasticity.

Abbreviations

Abbreviations of terms used in this study

Ag	antigen
AIS	adaptive immune system
BCR	B cell receptor
BEC	blood endothelial cell
DC	dendritic cell
ELV	efferent lymphatic vessel
FDC	follicular dendritic cell
FRC	fibroblastic reticular cell
GALT	gut-associated lymphoid tissue
GC	germinal center
HEV	high endothelial venule
Ig	immunoglobulin
IIS	innate immune system
ILF	isolated lymphoid follicles
IS	immune system
LEC	lymphatic endothelial cell
LF	lymphoid follicle (primary or secondary)
LN	lymph node
MALT	mucosa-associated lymphoid tissue
MLN	mesenteric lymph node
NALT	nasal-associated lymphoid tissue
PLF	primary lymphoid follicle
PP	Peyer's patch
SLF	secondary lymphoid follicle
SLT	secondary lymphoid tissues
TCR	T cell receptor

Abbreviations and alternative names for molecules

short name	full name and alternative name(s)
BP-3	name is derived from name of corresponding gene of a glycosylated glycosyl-phosphatidylinositol-linked molecule; new designation CD157, also known as bone marrow stromal cell antigen-1 (BST-1)
CCL19	systematic name for a member of the CC-chemokine family (L for ligand); also known as macrophage inflammatory protein 3β (MIP-3β), EBI-1-Ligand Chemokine (ELC, EBI=Epstein-Barr Virus-Induced)
CCL21	systematic name for a member of the CC-chemokine family (L for ligand); also known as secondary lymphoid-tissue chemokine (SLC)
CCR7	CC-Chemokine receptor 7, chemokine receptor for CCL19 and CCL21; also known as CD197
CR	complement receptor
CR1	complement receptor 1, binds to C1q, C3b and C4b; new designation CD35
CR2	complement receptor 2, binds to C3d; new designation CD21
CXCL13	systematic name for a member of the CXC-chemokine family (L for ligand), also known as B cell homing chemokine (BLC), B cell attracting chemokine (BCA)
CXCR5	CXC-Chemokine receptor 5, receptor for CXCL13; also known as Burkitt's lymphoma receptor-1 (blr-1), CD185
FDC-M1	marker for follicular dendritic cells
FDC-M2	marker for follicular dendritic cells, presumably identical to the complement component C4
ICAM-1	intercellular adhesion molecule-1; new designation CD54
IFN-γ	interferon-γ
IL	interleukin
LFA-1	lymphocyte function-associated antigen-1; new designation CD11a
LIGHT	acronym is derived from homologous to **l**ymphotoxins, **i**nducible expression, competes with HSV **g**lycoprotein D for **H**VEM, a receptor expressed on **T** cells (HSV=herpes simplex virus, HVEM=herpes virus entry mediator), member of the TNF superfamily; new designation TNFSF14 (TNF ligand superfamily member 14)
LTα	lymphotoxin α monomer, new designation TNFSF1 (TNF ligand superfamily member 1), old name TNF-β
LTβ	lymphotoxin β monomer, new designation TNFSF3 (TNF ligand superfamily member 3)
LTα_3	lymphotoxin α homotrimer
LT$\alpha_1\beta_2$	lymphotoxin heterotrimer composed of one α and two β subunits
LTβR	receptor for LT$\alpha_1\beta_2$
MAdCAM	mucosal addressin cell adhesion molecule
MMP	matrix metalloproteinase
PNAd	peripheral lymph node addressin
TG	transglutaminase

TNF-α tumor necrosis factor; often the simpler synonym TNF is used, new designation TN-FSF2 (TNF ligand superfamily member 2)

TNFR-I   TNF receptor I; also known as CD120a, old name is p55

TNFR-II   TNF receptor II; also known as CD120b, old name is p75

TRANCE   TNF-related activation induced cytokine; also known as receptor activator of NF-κB ligand (RANKL), new designation TNFSF11 (TNF ligand superfamily member 11)

VCAM-1   vascular cellular adhesion molecule-1; new designation CD106

VEGF   vascular endothelial growth factor

VEGFR-3   vascular endothelial growth factor receptor-3

WP1   monoclonal antibody against stromal cells

List of Figures

The figures in this thesis have been created on a Linux operating system using the programs **XmGrace** [xmg] for graphs, **IBM Data Explorer** [dx] for the colour-coded visualization of density plots and the calculation of isosurfaces, and **POVRay** [pov] or **VRMLview** [vrm] for rendering colour-coded representations of cells. Drawings were created using the Windows-based **CorelDraw** graphics package [cor].

List of Tables

Acknowledgments

Bibliography

Boost Library. URL http://www.boost.org.

CorelDraw 10. Corel Corporation. URL http://www.corel.com.

OpenDX IBM Visualization Data Explorer. Visualization and Imagery Solutions Inc. URL http://www.opendx.org.

POV-Ray - The Persistence of View Raytracer. Persistence of Vision Team and Persistence of Vision Raytracer Pty. Ltd. URL http://www.povray.org.

VRMLview. System in Motion AS. URL http://www.sim.no.

Xmgrace. Grace Development Team. URL http://plasma-gate.weizmann.ac.il/Grace/.

Albrecht, E. and Petty, H. R., 1998. Cellular memory: neutrophil orientation reverses during temporally decreasing chemoattractant concentrations. *Proc. Natl. Acad. Sci. U.S.A.*, **95**(9):5039–44.

Alexandre-Pires, G., Pais, D., and Esperanca Pina, J. A., 2003. Intermediary spleen microvasculature in canis familiaris- morphological evidences of a closed and open type. *Anat. Histol. Embryol.*, **32**(5):263–70.

Allen, C. D., Ansel, K. M., Low, C., Lesley, R., Tamamura, H., Fujii, N., and Cyster, J. G., 2004. Germinal center dark and light zone organization is mediated by CXCR4 and CXCR5. *Nat. Immunol.*, **5**(9):943–52.

Allen, C. D., Okada, T., Tang, H. L., and Cyster, J. G., 2007. Imaging of germinal center selection events during affinity maturation. *Science*, **315**(5811):528–31.

Allen, M. and Germano, G., 2002. Rigid body potentials, forces and torques. Departmental Technical Report CSC-64, Centre for Scientific Computing, University of Warwick.

Amdahl, G. M., 1967. Validity of the single processor approach to achieving large scale computing capabilities. In *AFIPS Conf. Proc.*

von Andrian, U. H. and Mempel, T. R., 2003. Homing and cellular traffic in lymph nodes. *Nat. Rev. Immunol.*, **3**(11):867–78.

Ansel, K. M., McHeyzer-Williams, L. J., Ngo, V. N., McHeyzer-Williams, M. G., and Cyster, J. G., 1999. In vivo-activated CD4 T cells upregulate CXC chemokine receptor 5 and reprogram their response to lymphoid chemokines. *J. Exp. Med.*, **190**(8):1123–34.

Ansel, K. M., Ngo, V. N., Hyman, P. L., Luther, S. A., Forster, R., Sedgwick, J. D., Browning, J. L., Lipp, M., and Cyster, J. G., 2000. A chemokine-driven positive feedback loop organizes lymphoid follicles. *Nature*, **406**(6793):309–14.

Arai, H., Monteclaro, F. S., Tsou, C. L., Franci, C., and Charo, I. F., 1997. Dissociation of chemotaxis from agonist-induced receptor internalization in a lymphocyte cell line transfected with CCR2B. Evidence that directed migration does not require rapid modulation of signaling at the receptor level. *J. Biol. Chem.*, **272**(40):25037–42.

Armengol, M. P., Juan, M., Lucas-Martin, A., Fernandez-Figueras, M. T., Jaraquemada, D., Gallart, T., and Pujol-Borrell, R., 2001. Thyroid autoimmune disease: demonstration of thyroid antigen-specific B cells and recombination-activating gene expression in chemokine-containing active intrathyroidal germinal centers. *Am. J. Pathol.*, **159**(3):861–73.

Asano, T., Edahiro, M., Imai, H., and Iri, M., 1985. Practical use of bucketing techniques in computational geometry. In G. T. Toussaint (ed.), *Computational Geometry*. Elsevier.

Aurenhammer, F., 1987. Power diagram: properties, algorithms and applications. *SIAM J.*, **16**(1):78–96.

Aurenhammer, F., 1991. Voronoi diagram – a survey of a fundamental geometric data structure. *ACM Computing Survey*, **23**(3):345–405.

Aurora, A. B., Baluk, P., Zhang, D., Sidhu, S. S., Dolganov, G. M., Basbaum, C., McDonald, D. M., and Killeen, N., 2005. Immune complex-dependent remodeling of the airway vasculature in response to a chronic bacterial infection. *J. Immunol.*, **175**(10):6319–26.

Azzali, G., 2003. Structure, lymphatic vascularization and lymphocyte migration in mucosa-associated lymphoid tissue. *Immunol. Rev.*, **195**:178–89.

Azzali, G. and Arcari, M. L., 2000. Ultrastructural and three dimensional aspects of the lymphatic vessels of the absorbing peripheral lymphatic apparatus in Peyer's patches of the rabbit. *Anat. Rec.*, **258**(1):71–9.

Azzali, G., Vitale, M., and Arcari, M. L., 2002. Ultrastructure of absorbing peripheral lymphatic vessel (ALPA) in guinea pig Peyer's patches. *Microvasc. Res.*, **64**(2):289–301.

Badr, G., Borhis, G., Treton, D., and Richard, Y., 2005. IFNα enhances human B-cell chemotaxis by modulating ligand-induced chemokine receptor signaling and internalization. *Int. Immunol.*, **17**(4):459–67.

Bairati, A., Amante, L., Petris, S. D., and Benvenuto, S., 1964. Studies on the ultrastructure of the lymph nodes. 1. The reticular network. *Z. Zellforsch.*, **63**:644–72.

Balaban, N. Q., Schwarz, U. S., Riveline, D., Goichberg, P., Tzur, G., Sabanay, I., Mahalu, D., Safran, S., Bershadsky, A., Addadi, L., and Geiger, B., 2001. Force and focal adhesion assembly: a close relationship studied using elastic micropatterned substrates. *Nature Cell Biol.*, **3**:466–472.

Balay, S., Buschelman, K., Eijkhout, V., Gropp, W. D., Kaushik, D., Knepley, M. G., McInnes, L. C., Smith, B. F., and Zhang, H., 2004. PETSc users manual. Technical Report ANL-95/11 - Revision 2.1.5, Argonne National Laboratory.

Balay, S., Buschelman, K., Gropp, W. D., Kaushik, D., Knepley, M. G., McInnes, L. C., Smith, B. F., and Zhang, H., 2001. PETSc Web page. URL http://www.mcs.anl.gov/petsc.

Balay, S., Gropp, W. D., McInnes, L. C., and Smith, B. F., 1997. Efficient management of parallelism in object oriented numerical software libraries. In E. Arge, A. M. Bruaset, and H. P. Langtangen (eds.), *Modern Software Tools in Scientific Computing*, pp. 163–202. Birkhäuser Press.

Baldwin, M. E., Halford, M. M., Roufail, S., Williams, R. A., Hibbs, M. L., Grail, D., Kubo, H., Stacker, S. A., and Achen, M. G., 2005. Vascular endothelial growth factor D is dispensable for development of the lymphatic system. *Mol. Cell. Biol.*, **25**(6):2441–9.

Balogh, P., Aydar, Y., Tew, J. G., and Szakal, A. K., 2001. Ontogeny of the follicular dendritic cell phenotype and function in the postnatal murine spleen. *Cell. Immunol.*, **214**(1):45–53.

Balogh, P., Aydar, Y., Tew, J. G., and Szakal, A. K., 2002. Appearance and phenotype of murine follicular dendritic cells expressing VCAM-1. *Anat. Rec.*, **268**(2):160–8.

Balogh, P., Horvath, G., and Szakal, A. K., 2004. Immunoarchitecture of distinct reticular fibroblastic domains in the white pulp of mouse spleen. *J. Histochem. Cytochem.*, **52**(10):1287–98.

Banchereau, J. and Steinman, R. M., 1998. Dendritic cells and the control of immunity. *Nature*, **392**(6673):245–52.

Bar-Even, A., Paulsson, J., Maheshri, N., Carmi, M., O'Shea, E., Pilpel, Y., and Barkai, N., 2006. Noise in protein expression scales with natural protein abundance. *Nat. Genet.*, **38**:636–43.

Bardi, G., Lipp, M., Baggiolini, M., and Loetscher, P., 2001. The T cell chemokine receptor CCR7 is internalized on stimulation with ELC, but not with SLC. *Eur. J. Immunol.*, **31**(11):3291–7.

Batsilas, L., Berezhkovskii, A. M., and Shvartsman, S. Y., 2003. Stochastic model of autocrine and paracrine signals in cell culture assays. *Biophys. J.*, **85**(6):3659–65.

Bausch, A. R., Moller, W., and Sackmann, E., 1999. Measurement of local viscoelasticity and forces in living cells by magnetic tweezers. *Biophys. J.*, **76**(1 Pt 1):573–9.

Bausch, A. R., Ziemann, F., Boulbitch, A. A., Jacobson, K., and Sackmann, E., 1998. Local measurements of viscoelastic parameters of adherent cell surfaces by magnetic bead microrheometry. *Biophys. J.*, **75**(4):2038–49.

Belisle, C. and Sainte-Marie, G., 1981a. Topography of the deep cortex of the lymph nodes of various mammalian species. *Anat. Rec.*, **201**(3):553–61.

Belisle, C. and Sainte-Marie, G., 1981b. Tridimensional study of the deep cortex of the rat lymph node. I: Topography of the deep cortex. *Anat. Rec.*, **199**(1):45–59.

Belisle, C. and Sainte-Marie, G., 1981c. Tridimensional study of the deep cortex of the rat lymph node. II: Relation of deep cortex units to afferent lymphatic vessels. *Anat. Rec.*, **199**(1):61–72.

Belisle, C. and Sainte-Marie, G., 1981d. Tridimensional study of the deep cortex of the rat lymph node. III. Morphology of the deep cortex units. *Anat. Rec.*, **199**(2):213–26.

Belisle, C. and Sainte-Marie, G., 1981e. Tridimensional study of the deep cortex of the rat lymph node. V: Postnatal development of the deep cortex units. *Anat. Rec.*, **200**(2):207–20.

Belisle, C. and Sainte-Marie, G., 1990. Blood vascular network of the rat lymph node: tridimensional studies by light and scanning electron microscopy. *Am. J. Anat.*, **189**(2):111–26.

Belisle, C., Sainte-Marie, G., and Peng, F. S., 1982. Tridimensional study of the deep cortex of the rat lymph node. VI. The deep cortex units of the germ-free rat. *Am. J. Anat.*, **107**(1):70–8.

Belz, G. T., 1998. Intercellular and lymphatic pathways associated with tonsils of the soft palate in young pigs. *Anat. Embryol. (Berl)*, **197**(4):331–40.

Belz, G. T. and Heath, T. J., 1995. Intercellular and lymphatic pathways of the canine palatine tonsils. *J. Anat.*, **187 (Pt1)**:93–105.

Bernardini, G., Hedrick, J., Sozzani, S., Luini, W., Spinetti, G., Weiss, M., Menon, S., Zlotnik, A., Mantovani, A., Santoni, A., and Napolitano, M., 1998. Identification of the CC chemokines TARC and macrophage inflammatory protein-1 beta as novel functional ligands for the CCR8 receptor. *Eur. J. Immunol.*, **28**(2):582–8.

Beutler, B., 2004. Innate immunity: an overview. *Mol. Immunol.*, **40**(12):845–59.

Beyer, T. and Meyer-Hermann, M., 2006. The treatment of non-flippable configurations in three dimensional regular triangulations. *WSEAS Trans. Syst.*, **5**(5):1100–7.

Beyer, T. and Meyer-Hermann, M., 2007a. Mechanisms of organogenesis of primary lymphoid follicles. *preprint at http://arxiv.org/q-bio/0611058*.

Beyer, T. and Meyer-Hermann, M., 2007b. Modeling emergent tissue organization involving high-speed migrating cells in a flow equilibrium. *preprint at http://arxiv.org/q-bio/0611057*.

Beyer, T., Meyer-Hermann, M., and Soff, G., 2002. A possible role of chemotaxis in germinal center formation. *Inter. Immunol.*, **14**(12):1369–81.

Beyer, T., Schaller, G., Deutsch, A., and Meyer-Hermann, M., 2005. Parallel dynamic and kinetic regular triangulation in three dimensions. *Comput. Phys. Commun.*, **172**(2):86–108.

Bhalla, D. K., Murakami, T., and Owen, R. L., 1981. Microcirculation of intestinal lymphoid follicles in rat Peyer's patches. *Gastroenterology*, **81**(3):481–91.

Binns, R. M. and Licence, S. T., 1990. Exit of recirculating lymphocytes from lymph nodes is directed by specific exit signals. *Eur. J. Immunol.*, **20**(2):449–52.

Bischofs, I. B., Safran, S. A., and Schwarz, U. S., 2004. Elastic interactions of active cells with soft materials. *Phys. Rev. E*, **69**(2 Pt 1):021911.

Bischofs, I. B. and Schwarz, U. S., 2003. Cell organization in soft media due to active mechanosensing. *Proc. Natl. Acad. Sci. U.S.A.*, **100**(16):9274–9.

Blelloch, G. E., Hardwick, J. C., Miller, G. L., and Talmor, D., 1999. Design and implementation of a practical parallel Delaunay algorithm. *Algorithmica*, **24**(3):243–69.

Bleul, C. C., Schultze, J. L., and Springer, T. A., 1998. B lymphocyte chemotaxis regulated in association with microanatomic localization, differentiation state, and B cell receptor engagement. *J. Exp. Med.*, **187**(5):753–62.

Bofill, M., Akbar, A. N., and Amlot, P. L., 2000. Follicular dendritic cells share a membrane-bound protein with fibroblasts. *J. Pathol.*, **191**(2):217–26.

Bongrand, P., 1995. Adhesion of cells. In R. Lipowsky and E. Sackmann (eds.), *Handbook of Biological Physics. Volume I*, pp. 755–803. Elsevier Science B.V.

Bornens, M., Paintrand, M., and Celati, C., 1989. The cortical microfilament system of lymphoblasts displays a periodic oscillatory activity in the absence of microtubules: implications for cell polarity. *J. Cell Biol.*, **109**(3):1071–83.

Bowyer, A., 1981. Computing Dirichlet tesselations. *Comput. J.*, **24**(2):162–66.

Brachtel, E. F., Washiyama, M., Johnson, G. D., Tenner-Racz, K., Racz, P., and MacLennan, I. C., 1996. Differences in the germinal centres of palatine tonsils and lymph nodes. *Scand. J. Immunol.*, **43**(3):239–47.

Braun, A., Takemura, S., Vallejo, A. N., Goronzy, J. J., and Weyand, C. M., 2004. Lymphotoxin beta-mediated stimulation of synoviocytes in rheumatoid arthritis. *Arthritis Rheum.*, **50**(7):2140–50.

Breitfeld, D., Ohl, L., Kremmer, E., Ellwart, J., Sallusto, F., Lipp, M., and Forster, R., 2000. Follicular B helper T cells express CXC chemokine receptor 5, localize to B cell follicles, and support immunoglobulin production. *J. Exp. Med.*, **192**(11):1545–52.

Bromley, S. K., Thomas, S. Y., and Luster, A. D., 2005. Chemokine receptor CCR7 guides T cell exit from peripheral tissues and entry into afferent lymphatics. *Nat. Immunol.*, **6**(9):895–901.

Bronstein, I. N., Semendjajew, K. A., Grosche, G., Ziegler, V., and Ziegler, D., 1996a. *Teubner-Taschenbuch der Mathematik*. B. G. Teubner Verlagsgesellschaft Leipzig.

Bronstein, I. N., Semendjajew, K. A., Grosche, G., Ziegler, V., and Ziegler, D., 1996b. *Teubner-Taschenbuch der Mathematik*. B. G. Teubner Verlagsgesellschaft Leipzig.

Brown, K. Q., 1979. Voronoi diagrams form convex hulls. *Inf. Process. Lett.*, **9**(5):223–8.

Brown, M. J., Hallam, J. A., Liu, Y., Yamada, K. M., and Shaw, S., 2001. Cutting edge: integration of human T lymphocyte cytoskeleton by the cytolinker plectin. *J. Immunol.*, **167**(2):641–5.

de Bruyn, P. P. H., 1946. The amoeboid movement of the mammalian leukocyte in tissue culture. *Anat. Rec.*, **95**(2):177–91.

Burton, K., Park, J. H., and Taylor, D. L., 1999. Keratocytes generate traction forces in two phases. *Mol. Biol. Cell*, **10**(11):3745–69.

Canadas, P., Laurent, V. M., Oddou, C., Isabey, D., and Wendling, S., 2002. A cellular tensegrity model to analyse the structural viscoelasticity of the cytoskeleton. *J. Theor. Biol.*, **218**(2):155–73.

Casamayor-Palleja, M., Mondiere, P., Verschelde, C., Bella, C., and Defrance, T., 2002. BCR ligation reprograms B cells for migration to the T zone and B-cell follicle sequentially. *Blood*, **99**(6):1913–21.

Castanos-Velez, E., Biberfeld, P., and Patarroyo, M., 1995. Extracellular matrix proteins and integrin receptors in reactive and non-reactive lymph nodes. *Immunology*, **86**(2):270–8.

Chang, K. C., Huang, X., Medeiros, L. J., and Jones, D., 2003. Germinal centre-like versus undifferentiated stromal immunophenotypes in follicular lymphoma. *J. Pathol.*, **201**(3):404–12.

Chaplain, M. and Anderson, A., 2004. Mathematical modelling of tumour-induced angiogenesis: network growth and structure. *Cancer Treat. Res.*, **117**:51–75.

Chaplain, M. A., 2000. Mathematical modelling of angiogenesis. *J. Neurooncol.*, **50**(1-2):37–51.

Chen, L. T. and Weiss, L., 1972. Electron microscopy of the red pulp of human spleen. *Am. J. Anat.*, **134**(4):425–57.

Chrisochoides, N. and Sukup, F., 1996a. Task parallel implementation of the Bowyer-Watson algorithm. Technical Report CTC96TR235, Cornell Theory Center.

Chrisochoides, N. and Sukup, F., 1996b. Task parallel implementation of the Bowyer-Watson algorithm. Technical Report CTC96TR235, Cornell Theory Center.

Chu, Y. S., Dufour, S., Thiery, J. P., Perez, E., and Pincet, F., 2005. Johnson-Kendall-Roberts theory applied to living cells. *Phys. Rev. Lett.*, **94**(2):028102.

Cignoni, P., Montani, C., Pereo, R., and Scopino, R., 1993. Parallel 3D Delaunay triangulation. *Computer Graphics Forum*, **12**(3):129–42.

Clark, E. A., Grabstein, K. H., and Shu, G. L., 1992. Cultured human follicular dendritic cells. Growth characteristics and interactions with B lymphocytes. *J. Immunol.*, **148**(11):3327–35.

Clark, S., 1962. The reticulum of lymph nodes in mice studied with the electron microscope. *Am. J. Anat.*, **110**:217–58.

Cleaver, D. J., Care, C. M., Allen, M. P., and Neal, M. P., 1996. Extension and generalization of the Gay-Berne potential. *Phys. Rev. E*, **54**(1):559–567.

Condeelis, J. and Segall, J. E., 2003. Intravital imaging of cell movement in tumours. *Nat. Rev. Cancer*, **3**(12):921–30.

Corcione, A., Ottonello, L., Tortolina, G., Tasso, P., Ghiotto, F., Airoldi, I., Taborelli, G., Malavasi, F., Dallegri, F., and Pistoia, V., 1997. Recombinant tumor necrosis factor enhances the locomotion of memory and naive B lymphocytes from human tonsils through the selective engagement of the type II receptor. *Blood*, **90**(11):4493–501.

Crivellato, E. and Mallardi, F., 1997. Stromal cell organisation in the mouse lymph node. A light and electron microscopic investigation using the zinc iodide-osmium technique. *J. Anat.*, **190 (Pt 1)**:85–92.

Crivellato, E., Vacca, A., and Ribatti, D., 2004. Setting the stage: an anatomist's view of the immune system. *Trends Immunol.*, **25**(4):210–7.

Cruikshank, W. W., Center, D. M., Nisar, N., Wu, M., Natke, B., Theodore, A. C., and Kornfeld, H., 1994. Molecular and functional analysis of a lymphocyte chemoattractant factor: association of biologic function with CD4 expression. *Proc. Natl. Acad. Sci. U.S.A.*, **91**(11):5109–13.

Cunningham, C. C., 1995. Actin polymerization and intracellular solvent flow in cell surface blebbing. *J. Cell Biol.*, **129**(6):1589–99.

Cupedo, T., Jansen, W., Kraal, G., and Mebius, R. E., 2004a. Induction of secondary and tertiary lymphoid structures in the skin. *Immunity*, **21**(5):655–67.

Cupedo, T., Lund, F. E., Ngo, V. N., Randall, T. D., Jansen, W., Greuter, M. J., de Waal-Malefyt, R., Kraal, G., Cyster, J. G., and Mebius, R. E., 2004b. Initiation of cellular organization in lymph nodes is regulated by non-B cell-derived signals and is not dependent on CXC chemokine ligand 13. *J. Immunol.*, **173**(8):4889–96.

Cupedo, T., Vondenhoff, M. F., Heeregrave, E. J., De Weerd, A. E., Jansen, W., Jackson, D. G., Kraal, G., and Mebius, R. E., 2004c. Presumptive lymph node organizers are differentially represented in developing mesenteric and peripheral nodes. *J. Immunol.*, **173**(5):2968–75.

Cyster, J. G., 1999. Chemokines and cell migration in secondary lymphoid organs. *Science*, **286**(5447):2098–102.

Cyster, J. G., 2005. Chemokines, sphingosine-1-phosphate, and cell migration in secondary lymphoid organs. *Annu. Rev. Immunol.*, **23**:127–59.

Cyster, J. G., Ansel, K. M., Reif, K., Ekland, E. H., Hyman, P. L., Tang, H. L., Luther, S. A., and Ngo, V. N., 2000. Follicular stromal cells and lymphocyte homing to follicles. *Immunol. Rev.*, **176**:181–93.

Dallon, J. C. and Othmer, H. G., 2004. How cellular movement determines the collective force generated by the Dictyostelium discoideum slug. *J. Theor. Biol.*, **231**(2):203–22.

Dasso, J. F., Obiakor, H., Bach, H., Anderson, A. O., and Mage, R. G., 2000. A morphological and immunohistological study of the human and rabbit appendix for comparison with the avian bursa. *Dev. Comp. Immunol.*, **24**(8):797–814.

Debes, G. F., Arnold, C. N., Young, A. J., Krautwald, S., Lipp, M., Hay, J. B., and Butcher, E. C., 2005. Chemokine receptor CCR7 required for T lymphocyte exit from peripheral tissues. *Nat. Immunol.*, **6**(9):889–94.

Dembo, M., Torney, D. C., Saxman, K., and Hammer, D., 1988. The reaction-limited kinetics of membrane-to-surface adhesion and detachment. *Proc. R. Soc. Lond. B*, **234**(1274):55–83.

Deutsch, A. and Dormann, S., 2003. *Cellular Automaton Modeling of Biological Pattern Formation*. Birkhäuser, Basel, 1st edition.

Devillers, O., 1999. On deletion in Delaunay triangulations. In *Symposium on Computational Geometry*, pp. 181–88. URL http://citeseer.ist.psu.edu/devillers99deletion.html.

Dickinson, R. B. and Tranquillo, R. T., 1993. Optimal estimation of cell movement indices from the statistical analysis of cell tracking data. *Am. Inst. Chem. Eng. J.* , **39**(12):1995–2010.

Donve, A., Torquato, S., and Stillinger, F., 2005. Neighbor list collision-driven molecular dynamics simulation for nonspherical hard particles: II. applications to ellipses and ellipsoids. *J. Comput. Phys.*, **202**(2):765–93.

Dorsam, G., Graeler, M. H., Seroogy, C., Kong, Y., Voice, J. K., and Goetzl, E. J., 2003. Transduction of multiple effects of sphingosine 1-phosphate (S1P) on T cell functions by the S1P1 G protein-coupled receptor. *J. Immunol.*, **171**(7):3500–7.

Downey, H., 1922. The structure and origin of the lymph sinuses of mammalian lymph nodes and their relations to endothelium and reticulum. *Haematologica*, **3**:431–68.

Drasdo, D., 2003. *Polymer and cell dynamics: multiscale modeling and numerical simulations*, chapter On selected individual-based approaches to the dynamics in multicellular systems, pp. 169–204. Birkhäuser, Basel.

Drasdo, D., Kree, R., and McCaskill, J. S., 1995. Monte carlo approach to tissue-cell populations. *Phys. Rev. E*, **52**(6):6635–57.

Drayton, D. L., Ying, X., Lee, J., Lesslauer, W., and Ruddle, N. H., 2003. Ectopic LT alpha beta directs lymphoid organ neogenesis with concomitant expression of peripheral node addressin and a HEV-restricted sulfotransferase. *J. Exp. Med.*, **197**(9):1153–63.

Drinker, C. K., Wislocki, G. B., and Field, M. E., 1933. The structure of the sinuses in the lymph nodes. *Anat. Rec.*, **56**(3):261–273.

Du Pasquier, L., 2005. Meeting the demand for innate and adaptive immunities during evolution. *Scand. J. Immunol.*, **62 Suppl 1**:39–48.

Dubois, B., Massacrier, C., and Caux, C., 2001. Selective attraction of naive and memory B cells by dendritic cells. *J. Leukoc. Biol.*, **70**(4):633–41.

Eason, D. D., Cannon, J. P., Haire, R. N., Rast, J. P., Ostrov, D. A., and Litman, G. W., 2004. Mechanisms of antigen receptor evolution. *Semin. Immunol.*, **16**(4):215–26.

Edelsbrunner, H. and Shah, N. R., 1996. Incremental topological flipping works for regular triangulations. *Algorithmica*, **15**(3):223–41.

Ehrengruber, M. U., Deranleau, D. A., and Coates, T. D., 1996. Shape oscillations of human neutrophil leukocytes: characterization and relationship to cell motility. *J. Exp. Biol.*, **199**(4):741–7.

Ekino, S., Matsuno, K., and Kotani, M., 1979. Distribution and role of lymph vessels of the bursa Fabricii. *Lymphology*, **12**(4):247–52.

Endres, R., Alimzhanov, M. B., Plitz, T., Futterer, A., Kosco-Vilbois, M. H., Nedospasov, S. A., Rajewsky, K., and Pfeffer, K., 1999. Mature follicular dendritic cell networks depend on expression of lymphotoxin beta receptor by radioresistant stromal cells and of lymphotoxin beta and tumor necrosis factor by B cells. *J. Exp. Med.*, **189**(1):159–68.

Entschladen, F., Gunzer, M., Scheuffele, C. M., Niggemann, B., and Zanker, K. S., 2000. T lymphocytes and neutrophil granulocytes differ in regulatory signaling and migratory dynamics with regard to spontaneous locomotion and chemotaxis. *Cell Immunol.*, **199**(2):104–14.

Entschladen, F. and Zanker, K. S., 2000. Locomotion of tumor cells: a molecular comparison to migrating pre- and postmitotic leukocytes. *J. Cancer Res. Clin. Oncol.*, **126**(12):671–81.

Estes, J. D., Keele, B. F., Tenner-Racz, K., Racz, P., Redd, M. A., Thacker, T. C., Jiang, Y., Lloyd, M. J., Gartner, S., and Burton, G. F., 2002. Follicular dendritic cell-mediated up-regulation of CXCR4 expression on CD4 T cells and HIV pathogenesis. *J. Immunol.*, **169**(5):2313–22.

Evans, E., 1995. Physical actions in biological adhesion. In R. Lipowsky and E. Sackmann (eds.), *Handbook of Biological Physics. Volume I*, pp. 723–753. Elsevier Science B.V.

Evans, E. and Yeung, A., 1989. Apparent viscosity and cortical tension of blood granulocytes determined by micropipet aspiration. *Biophys. J.*, **56**(1):151–60.

Everaers, R. and Ejtehadi, M. R., 2003. Interaction potentials for soft and hard ellipsoids. *Phys. Rev. E*, **67**(4 Pt 1):041710.

van Ewijk, W. and van der Kwast, T. H., 1980. Migration of B lymphocytes in lymphoid organs of lethally irradiated, thymocyte-reconstituted mice. *Cell. Tissue Res.*, **212**(3):497–508.

van Ewijk, W. and Nieuwenhuis, P., 1985. Compartments, domains and migration pathways of lymphoid cells in the splenic pulp. *Experientia*, **41**(2):199–208.

Fabry, B., Maksym, G. N., Butler, J. P., Glogauer, M., Navajas, D., Taback, N. A., Millet, E. J., and Fredberg, J. J., 2003. Time scale and other invariants of integrative mechanical behavior in living cellsa. *Phys. Rev. E*, **68**:041914.

Fan, L., Reilly, C. R., Luo, Y., Dorf, M. E., and Lo, D., 2000. Cutting edge: ectopic expression of the chemokine TCA4/SLC is sufficient to trigger lymphoid neogenesis. *J. Immunol.*, **164**(8):3955–9.

Ferguson, A. R., Youd, M. E., and Corley, R. B., 2004. Marginal zone B cells transport and deposit IgM-containing immune complexes onto follicular dendritic cells. *Int. Immunol.*, **16**(10):1411–22.

Ferrez, J.-A., 2001. *Dynamic triangulations for efficient 3D simulation of granular materials*. Ph.D. thesis, Ecole Polytechnique Federal de Lausanne.

Figge, M. T. and Meyer-Hermann, M., 2006. Geometrically repatterned immunological synapses uncover formation mechanisms. *PLoS Comput. Biol.*, **2**(11):e171.

Fillatreau, S. and Gray, D., 2003. T cell accumulation in B cell follicles is regulated by dendritic cells and is independent of B cell activation. *J. Exp. Med.*, **197**(2):195–206.

Finke, D., 2005. Fate and function of lymphoid tissue inducer cells. *Curr. Opin. Immunol.*, **17**(2):144–50.

at Florida State University, C. S. Scalable Parallel Pseudo Random Number Generator Library. URL `http://sprng.cs.fsu.edu`.

Foell, J., Strahotin, S., O'Neil, S. P., McCausland, M. M., Suwyn, C., Haber, M., Chander, P. N., Bapat, A. S., Yan, X. J., Chiorazzi, N., Hoffmann, M. K., and Mittler, R. S., 2003. CD137 costimulatory T cell receptor engagement reverses acute disease in lupus-prone NZB x NZW F1 mice. *J. Clin. Invest.*, **111**(10):1505–18.

Forgacs, G., 1995. On the possible role of cytoskeletal filamentous networks in intracellular signaling: an approach based on percolation. *J. Cell Sci.*, **108**:2131–43.

Forgacs, G., Foty, R. A., Shafrir, Y., and Steinberg, M. S., 1998. Viscoelastic properties of living embryonic tissues: a quantitative study. *Biophys. J.*, **74**(5):2227–34.

Forster, R., Mattis, A. E., Kremmer, E., Wolf, E., Brem, G., and Lipp, M., 1996. A putative chemokine receptor, BLR1, directs B cell migration to defined lymphoid organs and specific anatomic compartments of the spleen. *Cell*, **87**(6):1037–47.

Foxman, E. F., Kunkel, E. J., and Butcher, E. C., 1999. Integrating conflicting chemotactic signals. The role of memory in leukocyte navigation. *J. Cell. Biol.*, **147**(3):577–88.

Franitza, S., Hershkoviz, R., Kam, N., Lichtenstein, N., Vaday, G. G., Alon, R., and Lider, O., 2000. TNF-α associated with extracellular matrix fibronectin provides a stop signal for chemotactically migrating T cells. *J. Immunol.*, **165**(5):2738–47.

Friedl, P., Borgmann, S., and Brocker, E. B., 2001. Amoeboid leukocyte crawling through extracellular matrix: lessons from the Dictyostelium paradigm of cell movement. *J. Leukoc. Biol.*, **70**(4):491–509.

Friedl, P. and Brocker, E. B., 2000. The biology of cell locomotion within three-dimensional extracellular matrix. *Cell Mol. Life Sci.*, **57**(1):41–64.

Fu, Y. X. and Chaplin, D. D., 1999. Development and maturation of secondary lymphoid tissues. *Annu. Rev. Immunol.*, **17**:399–433.

Fu, Y. X., Huang, G., Wang, Y., and Chaplin, D. D., 1998. B lymphocytes induce the formation of follicular dendritic cell clusters in a lymphotoxin α-dependent fashion. *J. Exp. Med.*, **187**(7):1009–18.

Fu, Y. X., Molina, H., Matsumoto, M., Huang, G., Min, J., and Chaplin, D. D., 1997. Lymphotoxin-alpha (LTalpha) supports development of splenic follicular structure that is required for IgG responses. *J. Exp. Med.*, **185**(12):2111–20.

Fukuyama, S., Hiroi, T., Yokota, Y., Rennert, P. D., Yanagita, M., Kinoshita, N., Terawaki, S., Shikina, T., Yamamoto, M., Kurono, Y., and Kiyono, H., 2002. Initiation of NALT organogenesis is independent of the IL-7R, LTβR, and NIK signaling pathways but requires the Id2 gene and CD3(-)CD4(+)CD45(+) cells. *Immunity*, **17**(1):31–40.

Galbraith, C. G. and Sheetz, M. P., 1998. Forces on adhesive contacts affect cell function. *Curr. Opin. Cell Biol.*, **10**(5):566–71.

Galbraith, C. G. and Sheetz, M. P., 1999. Keratocytes pull with similar forces on their dorsal and ventral surfaces. *J. Cell. Biol.*, **147**(6):1313–24.

Gallego, M., del Cacho, E., Lopez-Bernad, F., and Bascuas, J. A., 1997. Identification of avian dendritic cells in the spleen using a monoclonal antibody specific for chicken follicular dendritic cells. *Anat. Rec.*, **249**(1):81–5.

Garcia-Aznar, J. M., Rueberg, T., and Doblare, M., 2005. A bone remodelling model coupling micro-damage growth and repair by 3D BMU-activity. *Biomech. Model Mechanobiol.*, **4**(2-3):147–67.

Garrafa, E., Alessandri, G., Benetti, A., Turetta, D., Corradi, A., Cantoni, A. M., Cervi, E., Bonardelli, S., Parati, E., Giulini, S. M., Ensoli, B., and Caruso, A., 2006. Isolation and characterization of lymphatic microvascular endothelial cells from human tonsils. *J. Cell. Physiol.*, **207**(1):107–13.

Garside, P., Ingulli, E., Merica, R. R., Johnson, J. G., Noelle, R. J., and Jenkins, M. K., 1998. Visualization of specific B and T lymphocyte interactions in the lymph node. *Science*, **281**(5373):96–9.

Gommerman, J. L., Mackay, F., Donskoy, E., Meier, W., Martin, P., and Browning, J. L., 2002. Manipulation of lymphoid microenvironments in nonhuman primates by an inhibitor of the lymphotoxin pathway. *J. Clin. Invest.*, **110**(9):1359–69.

Gonzalez, M., Mackay, F., Browning, J. L., Kosco-Vilbois, M. H., and Noelle, R. J., 1998. The sequential role of lymphotoxin and B cells in the development of splenic follicles. *J. Exp. Med.*, **187**(7):997–1007.

Gracheva, M. E. and Othmer, H. G., 2004. A continuum model of motility in ameboid cells. *Bull. Math. Biol.*, **66**(1):167–93.

Graner, F. and Glazier, J. A., 1992. Simulation of biological cell sorting using a two-dimensional extended Potts model. *Phys. Rev. Lett.*, **69**(13):2013–2016.

Grayson, M. H., Hotchkiss, R. S., Karl, I. E., Holtzman, M. J., and Chaplin, D. D., 2003. Intravital microscopy comparing T lymphocyte trafficking to the spleen and the mesenteric lymph node. *Am. J. Physiol. Heart Circ. Physiol.*, **284**(6):H2213–26.

Grell, M., Douni, E., Wajant, H., Lohden, M., Clauss, M., Maxeiner, B., Georgopoulos, S., Lesslauer, W., Kollias, G., Pfizenmaier, K., and Scheurich, P., 1995. The transmembrane form of tumor necrosis factor is the prime activating ligand of the 80 kDa tumor necrosis factor receptor. *Cell*, **83**(5):793–802.

Gretz, J. E., Anderson, A. O., and Shaw, S., 1997. Cords, channels, corridors and conduits: critical architectural elements facilitating cell interactions in the lymph node cortex. *Immunol. Rev.*, **156**:11–24.

Gretz, J. E., Kaldjian, E. P., Anderson, A. O., and Shaw, S., 1996. Sophisticated strategies for information encounter in the lymph node: the reticular network as a conduit of soluble information and a highway for cell traffic. *J. Immunol.*, **157**(2):495–9.

Gretz, J. E., Norbury, C. C., Anderson, A. O., Proudfoot, A. E., and Shaw, S., 2000. Lymph-borne chemokines and other low molecular weight molecules reach high endothelial venules via specialized conduits while a functional barrier limits access to the lymphocyte microenvironments in lymph node cortex. *J. Exp. Med.*, **192**(10):1425–40.

Griebel, P. J. and Hein, W. R., 1996. Expanding the role of Peyer's patches in B-cell ontogeny. *Immunol. Today*, **17**(1):30–9.

Griffin, M. A., Engler, A. J., Barber, T. A., Healy, K. E., Sweeney, H. L., and Discher, D. E., 2004. Patterning, prestress, and peeling dynamics of myocytes. *Biophys. J.*, **86**(2):1209–22.

Guibas, L. and Russel, D., 2004. An empirical comparison of techniques for updating Delaunay triangulations. In *Proceedings of the twentieth annual symposium on Computational geometry*, pp. 170–9. ACM Press New York, NY, USA.

Gunn, M. D., Ngo, V. N., Ansel, K. M., Ekland, E. H., Cyster, J. G., and Williams, L. T., 1998. A B-cell-homing chemokine made in lymphoid follicles activates Burkitt's lymphoma receptor-1. *Nature*, **391**(6669):799–803.

Gunzer, M., Friedl, P., Niggemann, B., Brocker, E. B., Kampgen, E., and Zanker, K. S., 2000. Migration of dendritic cells within 3-D collagen lattices is dependent on tissue origin, state of maturation, and matrix structure and is maintained by proinflammatory cytokines. *J. Leukoc. Biol.*, **67**(5):622–9.

Gunzer, M., Weishaupt, C., Hillmer, A., Basoglu, Y., Friedl, P., Dittmar, K. E., Kolanus, W., Varga, G., and Grabbe, S., 2004. A spectrum of biophysical interaction modes between T cells and different antigen-presenting cells during priming in 3-D collagen and in vivo. *Blood*, **104**(9):2801–9.

Guyader, H. L. and Hyver, C., 1997. Periodic activity of the cortical cytoskeleton of the lymphoblast: modelling by a reaction-diffusion system. *C R Acad. Sci. III*, **320**(1):59–65.

Haberman, A. M. and Shlomchik, M. J., 2003. Reassessing the function of immune-complex retention by follicular dendritic cells. *Nat. Rev. Immunol.*, **3**(9):757–64.

Halleraker, M., Press, C. M., and Landsverk, T., 1994. Development and cell phenotypes in primary follicles of foetal sheep lymph nodes. *Cell. Tissue Res.*, **275**(1):51–62.

Hamrah, P., Chen, L., Zhang, Q., and Dana, M. R., 2003. Novel expression of vascular endothelial growth factor receptor (VEGFR)-3 and VEGF-c on corneal dendritic cells. *Am. J. Pathol.*, **163**(1):57–68.

Hashi, H., Yoshida, H., Honda, K., Fraser, S., Kubo, H., Awane, M., Takabayashi, A., Nakano, H., Yamaoka, Y., and Nishikawa, S., 2001. Compartmentalization of Peyer's patch anlagen before lymphocyte entry. *J. Immunol.*, **166**(6):3702–9.

Haston, W. S. and Shields, J. M., 1984. Contraction waves in lymphocyte locomotion. *J. Cell Sci.*, **68**:227–41.

Hategan, A., Law, R., Kahn, S., and Discher, D. E., 2003. Adhesively-tensed cell membranes: lysis kinetics and atomic force microscopy probing. *Biophys. J.*, **85**(4):2746–59.

Heidemann, S. R., Kaech, S., Buxbaum, R. E., and Matus, A., 1999. Direct observations of the mechanical behaviors of the cytoskeleton in living fibroblasts. *J. Cell Biol.*, **145**(1):109–22.

Hein, W. R. and Supersaxo, A., 1988. Effect of interferon-alpha-2a on the output of recirculating lymphocytes from single lymph nodes. *Immunology*, **64**(3):469–74.

Heit, B., Tavener, S., Raharjo, E., and Kubes, P., 2002. An intracellular signaling hierarchy determines direction of migration in opposing chemotactic gradients. *J. Cell. Biol.*, **159**(1):91–102.

Helfand, B. T., Chang, L., and Goldman, R. D., 2003. The dynamic and motile properties of intermediate filaments. *Annu. Rev. Cell. Dev. Biol.*, **19**:445–67.

Helmke, B. P., Rosen, A. B., and Davies, P. F., 2003. Mapping mechanical strain of an endogenous cytoskeletal network in living endothelial cells. *Biophys. J.*, **84**(4):2691–9.

Hendriks, H. R. and Eestermans, I. L., 1983. Disappearance and reappearance of high endothelial venules and immigrating lymphocytes in lymph nodes deprived of afferent lymphatic vessels: a possible regulatory role of macrophages in lymphocyte migration. *Eur. J. Immunol.*, **13**(8):663–9.

Herant, M., Marganski, W. A., and Dembo, M., 2003. The mechanics of neutrophils: synthetic modeling of three experiments. *Biophys. J.*, **84**(5):3389–413.

Herman, P. G., Yamamoto, I., and Mellins, H. Z., 1972. Blood microcirculation in the lymph node during the primary immune response. *J. Exp. Med.*, **136**(4):697–714.

Hjelmstrom, P., 2001. Lymphoid neogenesis: de novo formation of lymphoid tissue in chronic inflammation through expression of homing chemokines. *J. Leukoc. Biol.*, **69**(3):331–9.

Honda, H., Tanemura, M., and Nagai, T., 2004. A three-dimensional vertex dynamics cell model of space-filling polyhedra simulating cell behavior in a cell aggregate. *J. Theor. Biol.*, **226**(4):439–53.

Honda, K., Nakano, H., Yoshida, H., Nishikawa, S., Rennert, P., Ikuta, K., Tamechika, M., Yamaguchi, K., Fukumoto, T., Chiba, T., and Nishikawa, S. I., 2001. Molecular basis for hematopoietic/mesenchymal interaction during initiation of Peyer's patch organogenesis. *J. Exp. Med.*, **193**(5):621–30.

Hong, Y. K., Shin, J. W., and Detmar, M., 2004. Development of the lymphatic vascular system: a mystery unravels. *Dev. Dyn.*, **231**(3):462–73.

Hoogewerf, A. J., Kuschert, G. S., Proudfoot, A. E., Borlat, F., Clark-Lewis, I., Power, C. A., and Wells, T. N., 1997. Glycosaminoglycans mediate cell surface oligomerization of chemokines. *Biochemistry*, **36**(44):13570–8.

Horstmann, D., 2003. From 1970 until present: The Keller-Segel model in chemotaxis and its consequences I. *Jahresbericht DMV*, **105**(3):103–65.

Hu, S., Chen, J., Fabry, B., Numaguchi, Y., Gouldstone, A., Ingber, D. E., Fredberg, J. J., Butler, J. P., and Wang, N., 2003. Intracellular stress tomography reveals stress focusing and structural anisotropy in cytoskeleton of living cells. *Am. J. Physiol. Cell Physiol.*, **285**(5):C1082–90.

Hu, W.-S., 2004. Stoichiometry and kinetics of cell growth and product formation. URL http://hugroup.cems.umn.edu/Cell_Technology/cd-rom/Stoichiometry%20and%20Kinetics/Stoichiometry%20and%20Cell%20Kinetics.pdf.

Huber, C., Thielen, C., Seeger, H., Schwarz, P., Montrasio, F., Wilson, M. R., Heinen, E., Fu, Y. X., Miele, G., and Aguzzi, A., 2005. Lymphotoxin-beta receptor-dependent genes in lymph node and follicular dendritic cell transcriptomes. *J. Immunol.*, **174**(9):5526–36.

Husson, H., Lugli, S. M., Ghia, P., Cardoso, A., Roth, A., Brohmi, K., Carideo, E. G., Choi, Y. S., Browning, J., and Freedman, A. S., 2000. Functional effects of TNF and lymphotoxin $\alpha 1\beta 2$ on FDC-like cells. *Cell Immunol.*, **203**(2):134–43.

Iglic, A., Veranic, P., Batista, U., and Kralj-Iglic, V., 2001. Theoretical analysis of shape transformation of V-79 cells after treatment with cytochalasin B. *J. Biomech.*, **34**(6):765–72.

Ingber, D. E., 1997. Tensegrity: the architectural basis of cellular mechanotransduction. *Annu. Rev. Physiol.*, **59**:575–99.

Ingber, D. E., 2000. Opposing views on tensegrity as a structural framework for understanding cell mechanics. *J. Appl. Physiol.*, **89**(4):1663–70.

Ingber, D. E., 2003a. Tensegrity I. Cell structure and hierarchical systems biology. *J. Cell Sci.*, **116**(Pt 7):1157–73.

Ingber, D. E., 2003b. Tensegrity II. How structural networks influence cellular information processing networks. *J. Cell Sci.*, **116**(Pt 8):1397–408.

Irjala, H., Johansson, E. L., Grenman, R., Alanen, K., Salmi, M., and Jalkanen, S., 2001. Mannose receptor is a novel ligand for L-selectin and mediates lymphocyte binding to lymphatic endothelium. *J. Exp. Med.*, **194**(8):1033–42.

Janeway, C. A. and Travers, P., 1997. *Immunologie*. Spektrum, Akad. Verl., 2nd edition.

Jiang, Y., Levine, H., and Glazier, J., 1998. Possible cooperation of differential adhesion and chemotaxis in mound formation of Dictyostelium. *Biophys. J.*, **75**(6):2615–25.

Joe, B., 1989. Three dimensional triangulations from local transformations. *SIAM J. Sci. Stat. Comput.*, **10**:718–41.

Joe, B., 1991. Construction of three-dimensional Delaunay triangulations using local transformations. *Computer Aided Geometric Design*, **8**:123–42.

Johnson, K., Kendall, K., and Roberts, A., 1971. Surface energy and the contact of elastic solids. *Proc. R. Soc. London A*, **324**(1558):303–13.

Kalaaji, A. N., Abernethy, N. J., McCullough, K., and Hay, J. B., 1988. Recombinant bovine interferon-alpha i 1 inhibits the migration of lymphocytes from lymph nodes but not into lymph nodes. *Reg. Immunol.*, **1**(1):56–61.

Kaldjian, E. P., Gretz, J. E., Anderson, A. O., Shi, Y., and Shaw, S., 2001. Spatial and molecular organization of lymph node T cell cortex: a labyrinthine cavity bounded by an epithelium-like monolayer of fibroblastic reticular cells anchored to basement membrane-like extracellular matrix. *Int. Immunol.*, **13**(10):1243–53.

Kang, Y. M., Zhang, X., Wagner, U. G., Yang, H., Beckenbaugh, R. D., Kurtin, P. J., Goronzy, J. J., and Weyand, C. M., 2002. CD8 T cells are required for the formation of ectopic germinal centers in rheumatoid synovitis. *J. Exp. Med.*, **195**(10):1325–36.

Kansal, A. R., Torquato, S., Harsh GR, I. V., Chiocca, E. A., and Deisboeck, T. S., 2000. Simulated brain tumor growth dynamics using a three-dimensional cellular automaton. *J. Theor. Biol.*, **203**(4):367–82.

Kapasi, Z. F., Qin, D., Kerr, W. G., Kosco-Vilbois, M. H., Shultz, L. D., Tew, J. G., and Szakal, A. K., 1998. Follicular dendritic cell (FDC) precursors in primary lymphoid tissues. *J. Immunol.*, **160**(3):1078–84.

Karlsen, K. H. and Lie, K.-A., 1999. An unconditionally stable splitting scheme for a class of nonlinear parabolic equations. *IMA J. Num. Anal.*, **19**:609–35.

Karypis, G. and Kumar, V., 1997. A coarse-grain parallel formulation of a multilevel k-way graph partitioning algorithm. In *Eighth SIAM Conference on Parallel Processing for Scientific Computing*.

Kasahara, M., Suzuki, T., and Pasquier, L. D., 2004. On the origins of the adaptive immune system: novel insights from invertebrates and cold-blooded vertebrates. *Trends Immunol.*, **25**(2):105–11.

Kasajima-Akatsuka, N. and Maeda, K., 2006. Development, maturation and subsequent activation of follicular dendritic cells (FDC): immunohisto-chemical observation of human fetal and adult lymph nodes. *Histochem. Cell. Biol.*, **126**(2):261–73.

Kaser, A., Dunzendorfer, S., Offner, F. A., Ludwiczek, O., Enrich, B., Koch, R. O., Cruikshank, W. W., Wiedermann, C. J., and Tilg, H., 2000. B lymphocyte-derived IL-16 attracts dendritic cells and Th cells. *J. Immunol.*, **165**(5):2474–80.

Kaser, A., Dunzendorfer, S., Offner, F. A., Ryan, T., Schwabegger, A., Cruikshank, W. W., Wiedermann, C. J., and Tilg, H., 1999. A role for IL-16 in the cross-talk between dendritic cells and T cells. *J. Immunol.*, **163**(6):3232–8.

Katakai, T., Hara, T., Lee, J. H., Gonda, H., Sugai, M., and Shimizu, A., 2004a. A novel reticular stromal structure in lymph node cortex: an immuno-platform for interactions among dendritic cells, T cells and B cells. *Int. Immunol.*, **16**(8):1133–42.

Katakai, T., Hara, T., Sugai, M., Gonda, H., and Shimizu, A., 2003. Th1-biased tertiary lymphoid tissue supported by CXC chemokine ligand 13-producing stromal network in chronic lesions of autoimmune gastritis. *J. Immunol.*, **171**(8):4359–68.

Katakai, T., Hara, T., Sugai, M., Gonda, H., and Shimizu, A., 2004b. Lymph node fibroblastic reticular cells construct the stromal reticulum via contact with lymphocytes. *J. Exp. Med.*, **200**(6):783–95.

Kaverina, I., Krylyshkina, O., Beningo, K., Anderson, K., Wang, Y. L., and Small, J. V., 2002. Tensile stress stimulates microtubule outgrowth in living cells. *J. Cell Sci.*, **115**(Pt 11):2283–91.

Keller, H. and Eggli, P., 1998. Protrusive activity, cytoplasmic compartmentalization, and restriction rings in locomoting blebbing Walker carcinosar-coma cells are related to detachment of cortical actin from the plasma membrane. *Cell Motil. Cytoskeleton*, **41**(2):181–93.

Kerjaschki, D., 2005. The crucial role of macrophages in lymphangiogenesis. *J. Clin. Invest.*, **115**(9):2316–9.

Killich, T., Plath, P. J., Wei, X., Bultmann, H., Rensing, L., and Vicker, M. G., 1993. The locomotion, shape and pseudopodial dynamics of unstimulated Dictyostelium cells are not random. *J. Cell Sci.*, **106** (Pt 4):1005–13.

Kim, C. H., 2005. The greater chemotactic network for lymphocyte trafficking: chemokines and beyond. *Curr. Opin. Hematol.*, **12**(4):298–304.

Kim, C. H., Lim, H. W., Kim, J. R., Rott, L., Hillsamer, P., and Butcher, E. C., 2004a. Unique gene expression program of human germinal center T helper cells. *Blood*, **104**(7):1952–60.

Kim, C. H., Pelus, L. M., White, J. R., Applebaum, E., Johanson, K., and Broxmeyer, H. E., 1998. CKβ-11/macrophage inflammatory protein-3β/EBI1-ligand chemokine is an efficacious chemoattractant for T and B cells. *J. Immunol.*, **160**(5):2418–24.

Kim, D., Mebius, R. E., MacMicking, J. D., Jung, S., Cupedo, T., Castellanos, Y., Rho, J., Wong, B. R., Josien, R., Kim, N., Rennert, P. D., and Choi, Y., 2000. Regulation of peripheral lymph node genesis by the tumor necrosis factor family member TRANCE. *J. Exp. Med.*, **192**(10):1467–78.

Kim, H. J., Kammertoens, T., Janke, M., Schmetzer, O., Qin, Z., Berek, C., and Blankenstein, T., 2004b. Establishment of early lymphoid organ infrastructure in transplanted tumors mediated by local production of lymphotoxin alpha and in the combined absence of functional B and T cells. *J. Immunol.*, **172**(7):4037–47.

Kim, H. S., Zhang, X., and Choi, Y. S., 1994. Activation and proliferation of follicular dendritic cell-like cells by activated T lymphocytes. *J. Immunol.*, **153**(7):2951–61.

Kolingerova, I. and Kohout, J., 2002. Optimistic parallel Delaunay triangulation. *The Visual Computer*, **18**(6):511–29.

Komai-Koma, M., Donachie, A. M., and Wilkinson, P. C., 1997. Antigen-specific chemotaxis of B cells. *Immunology*, **91**(4):579–85.

Kosco, M. H., Pflugfelder, E., and Gray, D., 1992. Follicular dendritic cell-dependent adhesion and proliferation of B cells in vitro. *J. Immunol.*, **148**(8):2331–9.

Kosco, M. H., Szakal, A. K., and Tew, J. G., 1988. In vivo obtained antigen presented by germinal center B cells to T cells in vitro. *J. Immunol.*, **140**(2):354–60.

Kosco-Vilbois, M. H., 2003. Are follicular dendritic cells really good for nothing? *Nat. Rev. Immunol.*, **3**(9):764–9.

Kratz, A., Campos-Neto, A., Hanson, M. S., and Ruddle, N. H., 1996. Chronic inflammation caused by lymphotoxin is lymphoid neogenesis. *J. Exp. Med.*, **183**(4):1461–72.

Kumar, P. and Timoney, J. F., 2006. Histology, immunohistochemistry and ultrastructure of the tonsil of the soft palate of the horse. *Anat. Histol. Embryol.*, **35**(1):1–6.

Kuprash, D. V., Alimzhanov, M. B., Tumanov, A. V., Grivennikov, S. I., Shakhov, A. N., Drutskaya, L. N., Marino, M. W., Turetskaya, R. L., Anderson, A. O., Rajewsky, K., Pfeffer, K., and Nedospasov, S. A., 2002. Redundancy in tumor necrosis factor (TNF) and lymphotoxin (LT) signaling in vivo: mice with inactivation of the entire TNF/lt locus versus single-knockout mice. *Mol. Cell. Biol.*, **22**(24):8626–34.

Kuprash, D. V., Tumanov, A. V., Liepinsh, D. J., Koroleva, E. P., Drutskaya, M. S., Kruglov, A. A., Shakhov, A. N., Southon, E., Murphy, W. J., Tessarollo, L., Grivennikov, S. I., and Nedospasov, S. A., 2005. Novel tumor necrosis factor-knockout mice that lack Peyer's patches. *Eur. J. Immunol.*, **35**(5):1592–600.

Lane, P. J., Gaspal, F. M., and Kim, M. Y., 2005. Two sides of a cellular coin: CD4(+)CD3- cells regulate memory responses and lymph-node organization. *Nat. Rev. Immunol.*, **5**(8):655–60.

Lanning, D. K., Rhee, K. J., and Knight, K. L., 2005. Intestinal bacteria and development of the B-lymphocyte repertoire. *Trends Immunol.*, **26**(8):419–25.

Larsson, A. and Warfvinge, G., 1998. Immunohistochemistry of 'tertiary lymphoid follicles' in oral amalgam-associated lichenoid lesions. *Oral. Dis.*, **4**(3):187–93.

Lauffenburger, D. A. and Horwitz, A. F., 1996. Cell migration: a physically integrated molecular process. *Cell*, **84**(3):359–69.

Laurent, V. M., Canadas, P., Fodil, R., Planus, E., Asnacios, A., Wendling, S., and Isabey, D., 2002. Tensegrity behaviour of cortical and cytosolic cytoskeletal components in twisted living adherent cells. *Acta Biotheor.*, **50**(4):331–56.

Lawson, C. L., 1972. Generation of a triangular grid with applications to contour plotting. Technical report, Memo 299, Jet Propulsion Laboratory, Pasadena, California.

Lee, S., Choi, K., Ahn, H., Song, K., Choe, J., and Lee, I., 2005. Tuj1 (class III beta-tubulin) expression suggests dynamic redistribution of follicular dendritic cells in lymphoid tissue. *Eur. J. Cell Biol.*, **84**(2-3):453–9.

Lee, S., Park, C.-I., and Park, C.-M., 2001. An improved parallel algorithm for Delaunay triangulation on distributed memory parallel computers. *Parallel Processing Lett.*, **11**(2 & 3):341–52.

Legler, D. F., Loetscher, M., Roos, R. S., Clark-Lewis, I., Baggiolini, M., and Moser, B., 1998. B cell-attracting chemokine 1, a human CXC chemokine expressed in lymphoid tissues, selectively attracts B lymphocytes via BLR1/CXCR5. *J. Exp. Med.*, **187**(4):655–60.

Levchenko, A. and Iglesias, P. A., 2002. Models of eukaryotic gradient sensing: application to chemotaxis of amoebae and neutrophils. *Biophys. J.*, **82**(1 Pt 1):50–63.

Lewis, W., 1931. Locomotion of lymphocytes. *Bull. Johns Hopkins Hosp.*, **49**:29–36.

Liakka, K. A. and Autio-Harmainen, H. I., 1992. Distribution of the extracellular matrix proteins tenascin, fibronectin, and vitronectin in fetal, infant, and adult human spleens. *J. Histochem. Cytochem.*, **40**(8):1203–10.

Lin, F., Nguyen, C. M., Wang, S. J., Saadi, W., Gross, S. P., and Jeon, N. L., 2004. Effective neutrophil chemotaxis is strongly influenced by mean IL-8 concentration. *Biochem. Biophys. Res. Commun.*, **319**(2):576–81.

Lindhout, E., van Eijk, M., van Pel, M., Lindeman, J., Dinant, H. J., and de Groot, C., 1999. Fibroblast-like synoviocytes from rheumatoid arthritis patients have intrinsic properties of follicular dendritic cells. *J. Immunol.*, **162**(10):5949–56.

Lindstedt, M., Johansson-Lindbom, B., and Borrebaeck, C. A., 2003. Expression of CD137 (4-1BB) on human follicular dendritic cells. *Scand. J. Immunol.*, **57**(4):305–10.

Liu, Y. J. and Arpin, C., 1997. Germinal center development. *Immunol. Rev.*, **156**:111–26.

Liu, Y. J., Grouard, G., de Bouteiller, O., and Banchereau, J., 1996. Follicular dendritic cells and germinal centers. *Int. Rev. Cytol.*, **166**:139–79.

Liu, Y. J., Zhang, J., Lane, P. J., Chan, E. Y., and MacLennan, I. C., 1991. Sites of specific B cell activation in primary and secondary responses to T cell-dependent and T cell-independent antigens. *Eur. J. Immunol.*, **21**(12):2951–62.

Lo, C. G., Xu, Y., Proia, R. L., and Cyster, J. G., 2005. Cyclical modulation of sphingosine-1-phosphate receptor 1 surface expression during lymphocyte recirculation and relationship to lymphoid organ transit. *J. Exp. Med.*, **201**(2):291–301.

Luther, S. A., Ansel, K. M., and Cyster, J. G., 2003. Overlapping roles of CXCL13, interleukin 7 receptor alpha, and CCR7 ligands in lymph node development. *J. Exp. Med.*, **197**(9):1191–8.

Luther, S. A., Bidgol, A., Hargreaves, D. C., Schmidt, A., Xu, Y., Paniyadi, J., Matloubian, M., and Cyster, J. G., 2002. Differing activities of homeostatic chemokines CCL19, CCL21, and CXCL12 in lymphocyte and dendritic cell recruitment and lymphoid neogenesis. *J. Immunol.*, **169**(1):424–33.

Luther, S. A., Lopez, T., Bai, W., Hanahan, D., and Cyster, J. G., 2000. BLC expression in pancreatic islets causes B cell recruitment and lymphotoxin-dependent lymphoid neogenesis. *Immunity*, **12**(5):471–81.

Maatta, M., Salo, S., Tasanen, K., Soini, Y., Liakka, A., Bruckner-Tuderman, L., and Autio-Harmainen, H., 2004. Distribution of basement membrane anchoring molecules in normal and transformed endometrium: altered expression of laminin gamma2 chain and collagen type XVII in endometrial adenocarcinomas. *J. Mol. Histol.*, **35**(8-9):715–22.

Mackay, F. and Browning, J. L., 1998. Turning off follicular dendritic cells. *Nature*, **395**(6697):26–7.

MacLennan, I. C., 1994. Germinal centers. *Annu. Rev. Immunol.*, **12**:117–39.

Magalhaes, R., Stiehl, P., Morawietz, L., Berek, C., and Krenn, V., 2002. Morphological and molecular pathology of the B cell response in synovitis of rheumatoid arthritis. *Virchows Arch.*, **441**(5):415–27.

Magliozzi, R., Columba-Cabezas, S., Serafini, B., and Aloisi, F., 2004. Intracerebral expression of CXCL13 and BAFF is accompanied by formation of lymphoid follicle-like structures in the meninges of mice with relapsing experimental autoimmune encephalomyelitis. *J. Neuroimmunol.*, **148**(1-2):11–23.

Makala, L. H., Kamada, T., Nishikawa, Y., Nagasawa, H., Igarashi, I., Fujisaki, K., Suzuki, N., Mikami, T., Haverson, K., Bailey, M., Stokes, C. R., and Bland, P. W., 2000. Ontogeny of pig discrete Peyer's patches: distribution and morphometric analysis. *Pathobiology*, **68**(6):275–82.

Makala, L. H., Suzuki, N., and Nagasawa, H., 2002-2003. Peyer's patches: organized lymphoid structures for the induction of mucosal immune responses in the intestine. *Pathobiology*, **70**(2):55–68.

Makinen, T., Veikkola, T., Mustjoki, S., Karpanen, T., Catimel, B., Nice, E. C., Wise, L., Mercer, A., Kowalski, H., Kerjaschki, D., Stacker, S. A., Achen, M. G., and Alitalo, K., 2001. Isolated lymphatic endothelial cells transduce growth, survival and migratory signals via the vegf-c/d receptor vegfr-3. *EMBO J.*, **20**(17):4762–73.

Mandik-Nayak, L., Huang, G., Sheehan, K. C., Erikson, J., and Chaplin, D. D., 2001. Signaling through TNF receptor p55 in TNF-α-deficient mice alters the CXCL13/CCL19/CCL21 ratio in the spleen and induces maturation and migration of anergic B cells into the B cell follicle. *J. Immunol.*, **167**(4):1920–8.

Maniotis, A. J., Chen, C. S., and Ingber, D. E., 1997. Demonstration of mechanical connections between integrins, cytoskeletal filaments, and nucleoplasm that stabilize nuclear structure. *Proc. Natl. Acad. Sci. U.S.A.*, **94**(3):849–54.

Manzo, A., Paoletti, S., Carulli, M., Blades, M. C., Barone, F., Yanni, G., Fitzgerald, O., Bresnihan, B., Caporali, R., Montecucco, C., Uguccioni, M., and Pitzalis, C., 2005. Systematic microanatomical analysis of CXCL13 and CCL21 in situ production and progressive lymphoid organization in rheumatoid synovitis. *Eur. J. Immunol.*, **35**(5):1347–59.

Matloubian, M., Lo, C. G., Cinamon, G., Lesneski, M. J., Xu, Y., Brinkmann, V., Allende, M. L., Proia, R. L., and Cyster, J. G., 2004. Lymphocyte egress from thymus and peripheral lymphoid organs is dependent on S1P receptor 1. *Nature*, **427**(6972):355–60.

Matsumoto, M., Fu, Y. X., Molina, H., Huang, G., Kim, J., Thomas, D. A., Nahm, M. H., and Chaplin, D. D., 1997. Distinct roles of lymphotoxin alpha and the type I tumor necrosis factor (TNF) receptor in the establishment of follicular dendritic cells from non-bone marrow-derived cells. *J. Exp. Med.*, **186**(12):1997–2004.

Matsumoto, M., Lo, S. F., Carruthers, C. J., Min, J., Mariathasan, S., Huang, G., Plas, D. R., Martin, S. M., Geha, R. S., Nahm, M. H., and Chaplin, D. D., 1996. Affinity maturation without germinal centres in lymphotoxin-alpha-deficient mice. *Nature*, **382**(6590):462–6.

McDonald, K. G., McDonough, J. S., and Newberry, R. D., 2005. Adaptive immune responses are dispensable for isolated lymphoid follicle formation: antigen-naive, lymphotoxin-sufficient B lymphocytes drive the formation of mature isolated lymphoid follicles. *J. Immunol.*, **174**(9):5720–8.

McGarry, J. and Prendergast, P., 2004. A three-dimensional finite element model of an adherent eukaryotic cell. *Eur. Cell. Mat.*, **7**:27–34.

McHeyzer-Williams, L. J., Driver, D. J., and McHeyzer-Williams, M. G., 2001. Germinal center reaction. *Curr. Opin. Hematol.*, **8**(1):52–9.

Mebius, R. E., Miyamoto, T., Christensen, J., Domen, J., Cupedo, T., Weissman, I. L., and Akashi, K., 2001. The fetal liver counterpart of adult common lymphoid progenitors gives rise to all lymphoid lineages, CD45+CD4+CD3- cells, as well as macrophages. *J. Immunol.*, **166**(11):6593–601.

Mebius, R. E., Rennert, P., and Weissman, I. L., 1997. Developing lymph nodes collect CD4+CD3- LTβ+ cells that can differentiate to APC, NK cells, and follicular cells but not T or B cells. *Immunity*, **7**(4):493–504.

Meineke, F. A., Potten, C. S., and Loeffler, M., 2001. Cell migration and organization in the intestinal crypt using a lattice-free model. *Cell Prolif.*, **34**(4):253–66.

Meinhardt, H., 1982. *Models of biological pattern formation*. Academic Press, London.

Mempel, T. R., Henrickson, S. E., and Von Andrian, U. H., 2004. T-cell priming by dendritic cells in lymph nodes occurs in three distinct phases. *Nature*, **427**(6970):154–9.

Merks, R. M., Brodsky, S. V., Goligorksy, M. S., Newman, S. A., and Glazier, J. A., 2006. Cell elongation is key to in silico replication of in vitro vasculogenesis and subsequent remodeling. *Dev. Biol.*, **289**(1):44–54.

Message-Passing Interface Forum, 1995. *MPI: A Message–Passing Interface Standard*. University of Tennessee, Knoxville, Tennessee. URL ftp://ftp.mcs.anl.gov/pub/mpi/mpi-1.jun95/mpi-report.ps.

Meyer-Hermann, M., 2002. A mathematical model for the germinal center morphology and affinity maturation. *J. Theor. Biol.*, **216**(3):273–300.

Meyer-Hermann, M. and Beyer, T., 2003. Conclusions from two model concepts on germinal center dynamics and morphology. *Dev. Immunol.*, **9**(4):203–14.

Meyer-Hermann, M., Deutsch, A., and Or-Guil, M., 2001. Recycling probability and dynamical properties of germinal center reactions. *J. Theor. Biol.*, **210**(3):265–85.

Meyer-Hermann, M., Maini, P. K., and Iber, D., 2006. An analysis of b cell selection mechanisms in germinal centers. *Math. Med. Biol.*, **23**:255–77.

Meyer-Hermann, M. E. and Maini, P. K., 2005a. Back to "one-way" germinal centers. *J. Immunol.*, **174**(5):2489–93.

Meyer-Hermann, M. E. and Maini, P. K., 2005b. Interpreting two-photon imaging data of lymphocyte motility. *Phys. Rev. E*, **71**(6 Pt 1):061912.

Mijailovich, S. M., Kojic, M., Zivkovic, M., Fabry, B., and Fredberg, J. J., 2002. A finite element model of cell deformation during magnetic bead twisting. *J. Appl. Physiol.*, **93**(4):1429–36.

Miller, M. J., Hejazi, A. S., Wei, S. H., Cahalan, M. D., and Parker, I., 2004. T cell repertoire scanning is promoted by dynamic dendritic cell behavior and random T cell motility in the lymph node. *Proc. Natl. Acad. Sci. U.S.A.*, **101**(4):998–1003.

Miller, M. J., Wei, S. H., Cahalan, M. D., and Parker, I., 2003. Autonomous T cell trafficking examined in vivo with intravital two-photon microscopy. *Proc. Natl. Acad. Sci. U.S.A.*, **100**(5):2604–9.

Miller, M. J., Wei, S. H., Parker, I., and Cahalan, M. D., 2002. Two-photon imaging of lymphocyte motility and antigen response in intact lymph node. *Science*, **296**(5574):1869–73.

Mitchison, T. J. and Cramer, L. P., 1996. Actin-based cell motility and cell locomotion. *Cell*, **84**(3):371–9.

Moe, R., 1963. Fine structure of the reticulum and sinuses of lymph nodes. *Am. J. Anat.*, **112**:313–35.

Moser, B. and Loetscher, P., 2001. Lymphocyte traffic control by chemokines. *Nat. Immunol.*, **2**(2):123–8.

Moser, B., Wolf, M., Walz, A., and Loetscher, P., 2004. Chemokines: multiple levels of leukocyte migration control. *Trends Immunol.*, **25**(2):75–84.

Moy, V. T., Jiao, Y., Hillmann, T., Lehmann, H., and Sano, T., 1999. Adhesion energy of receptor-mediated interaction measured by elastic deformation. *Biophys. J.*, **76**(3):1632–8.

Mücke, E. P., 1998. A Robust Implementation for three-dimensional Delaunay Triangulations. *International Journal of Computational Geometry and Applications*, **8**(2):255–76.

Muller, G., Hopken, U. E., and Lipp, M., 2003. The impact of CCR7 and CXCR5 on lymphoid organ development and systemic immunity. *Immunol. Rev.*, **195**:117–35.

M"uller, N. T., 2001. The iRRAM library: Exact arithmetic in C++. In *Selected Papers from the 4th International Workshop on Computability and Complexity in Analysis*, pp. 222–52. Springer-Verlag.

Murray, J., Vawter-Hugart, H., Voss, E., and Soll, D. R., 1992. Three-dimensional motility cycle in leukocytes. *Cell. Motil. Cytoskeleton*, **22**(3):211–23.

Namy, P., Ohayon, J., and Tracqui, P., 2004. Critical conditions for pattern formation and in vitro tubulogenesis driven by cellular traction fields. *J. Theor. Biol.*, **227**(1):103–20.

Neel, N. F., Schutyser, E., Sai, J., Fan, G. H., and Richmond, A., 2005. Chemokine receptor internalization and intracellular trafficking. *Cytokine Growth Factor Rev.*, **16**(6):637–58.

Ng, C. P., Helm, C. L., and Swartz, M. A., 2004. Interstitial flow differentially stimulates blood and lymphatic endothelial cell morphogenesis in vitro. *Microvasc. Res.*, **68**(3):258–64.

Ngo, V. N., Cornall, R. J., and Cyster, J. G., 2001. Splenic T zone development is B cell dependent. *J. Exp. Med.*, **194**(11):1649–60.

Ngo, V. N., Korner, H., Gunn, M. D., Schmidt, K. N., Riminton, D. S., Cooper, M. D., Browning, J. L., Sedgwick, J. D., and Cyster, J. G., 1999. Lymphotoxin α/β and tumor necrosis factor are required for stromal cell expression of homing chemokines in B and T cell areas of the spleen. *J. Exp. Med.*, **189**(2):403–12.

Ngo, V. N., Tang, H. L., and Cyster, J. G., 1998. Epstein-Barr virus-induced molecule 1 ligand chemokine is expressed by dendritic cells in lymphoid tissues and strongly attracts naive T cells and activated B cells. *J. Exp. Med.*, **188**(1):181–91.

Nibbs, R. J., Kriehuber, E., Ponath, P. D., Parent, D., Qin, S., Campbell, J. D., Henderson, A., Kerjaschki, D., Maurer, D., Graham, G. J., and Rot, A., 2001. The beta-chemokine receptor d6 is expressed by lymphatic endothelium and a subset of vascular tumors. *Am. J. Pathol.*, **158**(3):867–77.

Nicander, L., Halleraker, M., and Landsverk, T., 1991. Ontogeny of reticular cells in the ileal Peyer's patch of sheep and goats. *Am. J. Anat.*, **191**(3):237–49.

van Nierop, K. and de Groot, C., 2002. Human follicular dendritic cells: function, origin and development. *Semin. Immunol.*, **14**(4):251–7.

Nieto, M., Frade, J. M., Sancho, D., Mellado, M., Martinez-A, C., and Sanchez-Madrid, F., 1997. Polarization of chemokine receptors to the leading edge during lymphocyte chemotaxis. *J. Exp. Med.*, **186**(1):153–8.

Niggemann, B., , Joseph, J., Weidt, C., Lang, K., Zaenker, K. S., and Entschladen, F., 2004. Tumor cell locomotion: differential dynamics of spontaneous and induced migration in a 3D collagen matrix. *Exp. Cell Res.*, **298**(1):178–87.

Nishikawa, S., Honda, K., Vieira, P., and Yoshida, H., 2003. Organogenesis of peripheral lymphoid organs. *Immunol. Rev.*, **195**:72–80.

Nolte, M. A., Belien, J. A., Schadee-Eestermans, I., Jansen, W., Unger, W. W., van Rooijen, N., Kraal, G., and Mebius, R. E., 2003. A conduit system distributes chemokines and small blood-borne molecules through the splenic white pulp. *J. Exp. Med.*, **198**(3):505–12.

Odell, G. M., Oster, G., Alberch, P., and Burnside, B., 1981. The mechanical basis of morphogenesis. I. Epithelial folding and invagination. *Dev. Biol.*, **85**(2):446–62.

Ogata, T., Yamakawa, M., Imai, Y., and Takahashi, T., 1996. Follicular dendritic cells adhere to fibronectin and laminin fibers via their respective receptors. *Blood*, **88**(8):2995–3003.

Ohtani, O., Kikuta, A., Ohtsuka, A., and Murakami, T., 1991. Organization of the reticular network of rabbit Peyer's patches. *Anat. Rec.*, **229**(2):251–8.

Ohtani, O., Ohtani, Y., Carati, C. J., and Gannon, B. J., 2003. Fluid and cellular pathways of rat lymph nodes in relation to lymphatic labyrinths and Aquaporin-1 expression. *Arch. Histol. Cytol.*, **66**(3):261–72.

Ohtani, O., Ohtsuka, A., and Owen, R. L., 1986. Three-dimensional organization of the lymphatics in the rabbit appendix. A scanning electron and light microscopic study. *Gastroenterology*, **91**(4):947–55.

Ohtsuka, A., Piazza, A. J., Ermak, T. H., and Owen, R. L., 1992. Correlation of extracellular matrix components with the cytoarchitecture of mouse Peyer's patches. *Cell Tissue Res.*, **269**(3):403–10.

Okabe, A., Boots, B., Sugihara, K., and Chiu, S. N., 2000. *Spatial tessellations: Concepts and applications of Voronoi diagrams.* Probability and Statistics. Wiley, NYC, $2^n d$ edition.

Okada, T., Miller, M. J., Parker, I., Krummel, M. F., Neighbors, M., Hartley, S. B., O'Garra, A., Cahalan, M. D., and Cyster, J. G., 2005. Antigen-engaged B cells undergo chemotaxis toward the T zone and form motile conjugates with helper T cells. *PLoS. Biol.*, **3**(6):e150.

Okada, T., Ngo, V. N., Ekland, E. H., Forster, R., Lipp, M., Littman, D. R., and Cyster, J. G., 2002. Chemokine requirements for B cell entry to lymph nodes and Peyer's patches. *J. Exp. Med.*, **196**(1):65–75.

Olah, I. and Glick, B., 1979. Structure of the germinal centers in the chicken caecal tonsil: light and electron microscopic and autoradiographic studies. *Poult. Sci.*, **58**(1):195–210.

Oliver, T., Dembo, M., and Jacobson, K., 1999. Separation of propulsive and adhesive traction stresses in locomoting keratocytes. *J. Cell Biol.*, **145**(3):589–604.

Oron, G. and Herrmann, H., 1998. Exact calculation of force networks in granular piles. *Phys. Rev. E*, **58**:2079–2089.

Oster, G. F., 1984. On the crawling of cells. *J. Embryol. Exp. Morphol.*, **83 Suppl**:329–64.

Ottonello, L., Corcione, A., Tortolina, G., Airoldi, I., Albesiano, E., Favre, A., D'Agostino, R., Malavasi, F., Pistoia, V., and Dallegri, F., 1999. rC5a directs the in vitro migration of human memory and naive tonsillar B lymphocytes: implications for B cell trafficking in secondary lymphoid tissues. *J. Immunol.*, **162**(11):6510–7.

Pabst, O., Herbrand, H., Worbs, T., Friedrichsen, M., Yan, S., Hoffmann, M. W., Korner, H., Bernhardt, G., Pabst, R., and Forster, R., 2005. Cryptopatches and isolated lymphoid follicles: dynamic lymphoid tissues dispensable for the generation of intraepithelial lymphocytes. *Eur. J. Immunol.*, **35**(1):98–107.

Painter, K. J., Maini, P. K., and Othmer, H. G., 2000. Development and applications of a model for cellular response to multiple chemotactic cues. *J. Math. Biol.*, **41**(4):285–314.

Paiva, D. D., Morais, J. C., Pilotto, J., Veloso, V., Duarte, F., and Lenzi, H. L., 1996. Spectrum of morphologic changes of lymph nodes in HIV infection. *Mem. Inst. Oswaldo Cruz*, **91**(3):371–9.

Palecek, S. P., Huttenlocher, A., Horwitz, A. F., and Lauffenburger, D. A., 1998. Physical and biochemical regulation of integrin release during rear detachment of migrating cells. *J. Cell Sci.*, **111** (Pt 7):929–40.

Palsson, E., 2001. A three-dimensional model of cell movement in multicellular systems. *Future Gen. Comp. Sys.*, **17**:835–852.

Palsson, E. and Othmer, H. G., 2000. A model for individual and collective cell movement in Dictyostelium discoideum. *Proc. Natl. Acad. Sci. U.S.A.*, **97**(19):10448–53.

Paluch, E., Piel, M., Prost, J., Bornens, M., and Sykes, C., 2005. Cortical actomyosin breakage triggers shape oscillations in cells and cell fragments. *Biophys. J.*, **89**(1):724–33.

Paluch, E., Sykes, C., Prost, J., and Bornens, M., 2006. Dynamic modes of the cortical actomyosin gel during cell locomotion and division. *Trends Cell Biol.*, **16**(1):5–10.

Parent, C. A. and Devreotes, P. N., 1999. A cell's sense of direction. *Science*, **284**(5415):765–70.

Park, C. S. and Choi, Y. S., 2005. How do follicular dendritic cells interact intimately with B cells in the germinal centre? *Immunology*, **114**(1):2–10.

Park, C. S., Yoon, S. O., Armitage, R. J., and Choi, Y. S., 2004. Follicular dendritic cells produce IL-15 that enhances germinal center B cell proliferation in membrane-bound form. *J. Immunol.*, **173**(11):6676–83.

Pasparakis, M., Alexopoulou, L., Grell, M., Pfizenmaier, K., Bluethmann, H., and Kollias, G., 1997. Peyer's patch organogenesis is intact yet formation of B lymphocyte follicles is defective in peripheral lymphoid organs of mice deficient for tumor necrosis factor and its 55-kDa receptor. *Proc. Natl. Acad. Sci. U.S.A.*, **94**(12):6319–23.

Pasparakis, M., Kousteni, S., Peschon, J., and Kollias, G., 2000. Tumor necrosis factor and the p55TNF receptor are required for optimal development of the marginal sinus and for migration of follicular dendritic cell precursors into splenic follicles. *Cell. Immunol.*, **201**(1):33–41.

Pauly, S., Broll, K., Wittmann, M., Giegerich, G., and Schwarz, H., 2002. CD137 is expressed by follicular dendritic cells and costimulates B lymphocyte activation in germinal centers. *J. Leukoc. Biol.*, **72**(1):35–42.

Pellas, T. C. and Weiss, L., 1990a. Deep splenic lymphatic vessels in the mouse: a route of splenic exit for recirculating lymphocytes. *Am. J. Anat.*, **187**(4):347–54.

Pellas, T. C. and Weiss, L., 1990b. Migration pathways of recirculating murine B cells and CD4+ and CD8+ T lymphocytes. *Am. J. Anat.*, **187**(4):355–73.

Pelletier, A. J., van der Laan, L. J., Hildbrand, P., Siani, M. A., Thompson, D. A., Dawson, P. E., Torbett, B. E., and Salomon, D. R., 2000. Presentation of chemokine SDF-1 alpha by fibronectin mediates directed migration of T cells. *Blood*, **96**(8):2682–90.

Perram, J. and Wertheim, M., 1985. Statistical mechanics of hard ellipsoids. I. Overlap algorithm and the contact function. *J. Comput. Phys.*, **58**:409–16.

Perram, J. W., Rasmussen, J., Praestgaard, E., and Lebowitz, J. L., 1996. Ellipsoid contact potential: Theory and relation to overlap potentials. *Phys. Rev. E*, **54**(6):6565–6572.

Pierini, L. M., Lawson, M. A., Eddy, R. J., Hendey, B., and Maxfield, F. R., 2000. Oriented endocytic recycling of alpha5beta1 in motile neutrophils. *Blood*, **95**(8):2471–80.

Pillai, S., Cariappa, A., and Moran, S. T., 2005. Marginal zone B cells. *Annu. Rev. Immunol.*, **23**:161–96.

Ploemen, J. P., Ravesloot, W. T., and van Esch, E., 2003. The incidence of thymic B lymphoid follicles in healthy beagle dogs. *Toxicol. Pathol.*, **31**(2):214–9.

Pourati, J., Maniotis, A., Spiegel, D., Schaffer, J. L., Butler, J. P., Fredberg, J. J., Ingber, D. E., Stamenovic, D., and Wang, N., 1998. Is cytoskeletal tension a major determinant of cell deformability in adherent endothelial cells? *Am. J. Physiol.*, **274**(5 Pt 1):C1283–9.

Prevo, R., Banerji, S., Ferguson, D. J., Clasper, S., and Jackson, D. G., 2001. Mouse LYVE-1 is an endocytic receptor for hyaluronan in lymphatic endothelium. *J. Biol. Chem.*, **276**(22):19420–30.

Proudfoot, A. E., Handel, T. M., Johnson, Z., Lau, E. K., LiWang, P., Clark-Lewis, I., Borlat, F., Wells, T. N., and Kosco-Vilbois, M. H., 2003. Glycosaminoglycan binding and oligomerization are essential for the in vivo activity of certain chemokines. *Proc. Natl. Acad. Sci. U.S.A.*, **100**(4):1885–90.

Randolph, D. A., Huang, G., Carruthers, C. J., Bromley, L. E., and Chaplin, D. D., 1999. The role of CCR7 in TH1 and TH2 cell localization and delivery of B cell help in vivo. *Science*, **286**(5447):2159–62.

Randolph, G. J., Angeli, V., and Swartz, M. A., 2005. Dendritic-cell trafficking to lymph nodes through lymphatic vessels. *Nat. Rev. Immunol.*, **5**(8):617–28.

Rangel-Moreno, J., Moyron-Quiroz, J., Kusser, K., Hartson, L., Nakano, H., and Randall, T. D., 2005. Role of CXC chemokine ligand 13, CC chemokine ligand (CCL) 19, and CCL21 in the organization and function of nasal-associated lymphoid tissue. *J. Immunol.*, **175**(8):4904–13.

Ratner, S., Sherrod, W. S., and Lichlyter, D., 1997. Microtubule retraction into the uropod and its role in T cell polarization and motility. *J. Immunol.*, **159**(3):1063–7.

Reif, K., Ekland, E. H., Ohl, L., Nakano, H., Lipp, M., Forster, R., and Cyster, J. G., 2002. Balanced responsiveness to chemoattractants from adjacent zones determines B-cell position. *Nature*, **416**(6876):94–9.

Rennert, P. D., Browning, J. L., and Hochman, P. S., 1997. Selective disruption of lymphotoxin ligands reveals a novel set of mucosal lymph nodes and unique effects on lymph node cellular organization. *Int. Immunol.*, **9**(11):1627–39.

Rey, M., Vicente-Manzanares, M., Viedma, F., Yanez-Mo, M., Urzainqui, A., Barreiro, O., Vazquez, J., and Sanchez-Madrid, F., 2002. Cutting edge: association of the motor protein nonmuscle myosin heavy chain-IIA with the C terminus of the chemokine receptor CXCR4 in T lymphocytes. *J. Immunol.*, **169**(10):5410–4.

Rinehart, J., 1930. Reticulum. Its origin. The occurrence of reticulum fibrils in capillary endothelium. A new method of demonstration. I. The finer capillary bed. *Am. J. Path.*, **6**:525–39.

Romanovskii, Y. M. and Teplov, V. A., 1995. The physical base of cell movement. The mechanisms of self-organisation of amoeboid motility. *Physics-Uspekhi*, **38**(5):521–543.

Romppanen, T., 1981. A morphometrical method for analyzing germinal centers in the chicken spleen. *Acta Pathol. Microbiol. Scand. C*, **89**(4):263–8.

Rosen, H. and Goetzl, E. J., 2005. Sphingosine 1-phosphate and its receptors: an autocrine and paracrine network. *Nat. Rev. Immunol.*, **5**(7):560–70.

Roy, M. P., Kim, C. H., and Butcher, E. C., 2002. Cytokine control of memory B cell homing machinery. *J. Immunol.*, **169**(4):1676–82.

Ruddell, A., Mezquita, P., Brandvold, K. A., Farr, A., and Iritani, B. M., 2003. B lymphocyte-specific c-Myc expression stimulates early and functional expansion of the vasculature and lymphatics during lymphomagenesis. *Am. J. Pathol.*, **163**(6):2233–45.

Rumfelt, L. L., McKinney, E. C., Taylor, E., and Flajnik, M. F., 2002. The development of primary and secondary lymphoid tissues in the nurse shark Ginglymostoma cirratum: B-cell zones precede dendritic cell immigration and T-cell zone formation during ontogeny of the spleen. *Scand. J. Immunol.*, **56**(2):130–48.

Sacca, R., Cuff, C. A., Lesslauer, W., and Ruddle, N. H., 1998. Differential activities of secreted lymphotoxin-alpha3 and membrane lymphotoxin-alpha1beta2 in lymphotoxin-induced inflammation: critical role of TNF receptor 1 signaling. *J. Immunol.*, **160**(1):485–91.

Sagvolden, G., Giaever, I., Pettersen, E. O., and Feder, J., 1999. Cell adhesion force microscopy. *Proc. Natl. Acad. Sci. U.S.A.*, **96**:471–476.

Sahai, E. and Marshall, C. J., 2003. Differing modes of tumour cell invasion have distinct requirements for Rho/ROCK signalling and extracellular proteolysis. *Nat. Cell Biol.*, **5**(8):711–9.

Sainte-Marie, G., Peng, F. S., and Belisle, C., 1981. Tridimensional study of the deep cortex of the rat lymph node. IV. Differential labelling of the deep cortex units with 3H-uridine. *Anat. Rec.*, **199**(2):227–37.

Sainte-Marie, G., Peng, F. S., and Pritchard, D., 1984. Tridimensional study of the deep cortex of the rat lymph node: VIII. The deep cortex units of the athymic nude rat. *Anat. Rec.*, **209**(1):95–104.

Sallusto, F. and Mackay, C. R., 2004. Chemoattractants and their receptors in homeostasis and inflammation. *Curr. Opin. Immunol.*, **16**(6):724–31.

Sambeth, R. and Baumgaertner, A., 2001. Autocatalytic polymerization generates persistent random walk of crawling cells. *Phys. Rev. Lett.*, **86**(22):5196–9.

Samstag, Y., Eibert, S. M., Klemke, M., and Wabnitz, G. H., 2003. Actin cytoskeletal dynamics in T lymphocyte activation and migration. *J. Leukoc. Biol.*, **73**(1):30–48.

Satoh, T., Takeda, R., Oikawa, H., and Satodate, R., 1997. Immunohistochemical and structural characteristics of the reticular framework of the white pulp and marginal zone in the human spleen. *Anat. Rec.*, **249**(4):486–94.

Savill, N. J. and Hogeweg, P., 1997. Modelling Morphogenesis: From Single Cells to Crawling Slugs. *J. Theor. Biol.*, **184**:229–235.

Schaller, G., 2006. *On selected numerical approaches to Cellular Tissue*. Ph.D. thesis, Johann Wolfgang Goethe-University Frankfurt Main.

Schaller, G. and Meyer-Hermann, M., 2004. Kinetic and dynamic Delaunay tetrahedralizations in three dimensions. *Comput. Phys. Commun.*, **162**:9–23.

Schaller, G. and Meyer-Hermann, M., 2005. Multicellular tumor spheroid in an off-lattice voronoi-delaunay cell model. *Phys. Rev. E.*, **71**(5 Pt 1):051910.

Schaniel, C., Pardali, E., Sallusto, F., Speletas, M., Ruedl, C., Shimizu, T., Seidl, T., Andersson, J., Melchers, F., Rolink, A. G., and Sideras, P., 1998. Activated murine B lymphocytes and dendritic cells produce a novel CC chemokine which acts selectively on activated T cells. *J. Exp. Med.*, **188**(3):451–63.

Schmidt, E. E., MacDonald, I. C., and Groom, A. C., 1985. Microcirculation in mouse spleen (nonsinusal) studied by means of corrosion casts. *J. Morphol.*, **186**:17–29.

Schmidt, E. E., MacDonald, I. C., and Groom, A. C., 1988. Microcirculatory pathways in normal human spleen, demonstrated by scanning electron microscopy of corrosion casts. *Am. J. Anat.*, **181**(3):253–66.

Schnell, S. and Turner, T. E., 2004. Reaction kinetics in intracellular environments with macromolecular crowding: simulations and rate laws. *Prog. Biophys. Mol. Biol.*, **85**(2-3):235–60.

Schwab, S. R., Pereira, J. P., Matloubian, M., Xu, Y., Huang, Y., and Cyster, J. G., 2005. Lymphocyte sequestration through S1p lyase inhibition and disruption of S1p gradients. *Science*, **309**(5741):1735–9.

Schwarz, U. S., Balaban, N. Q., Riveline, D., Bershadsky, A., Geiger, B., and Safran, S. A., 2002. Calculation of forces at focal adhesions from elastic substrate data: the effect of localized force and the need for regularization. *Biophys. J.*, **83**(3):1380–94.

Schwarz, U. S. and Safran, S. A., 2002. Elastic interactions of cells. *Phys. Rev. Lett.*, **88**(4):048102.

Schwickert, T. A., Lindquist, R. L., Shakhar, G., Livshits, G., Skokos, D., Kosco-Vilbois, M. H., Dustin, M. L., and Nussenzweig, M. C., 2007. In vivo imaging of germinal centres reveals a dynamic open structure. *Nature*, **446**(7131):83–7.

Seabrook, T., Au, B., Dickstein, J., Zhang, X., Ristevski, B., and Hay, J. B., 1999. The traffic of resting lymphocytes through delayed hypersensitivity and chronic inflammatory lesions: a dynamic equilibrium. *Semin. Immunol.*, **11**(2):115–23.

Sen, P., 2004. Diffusion and tissue microstructure. *J. Physics: Condensed Matter*, **16**(44):S5213–S5220. URL http://stacks.iop.org/0953-8984/16/S5213.

Serrador, J. M., Nieto, M., and Sanchez-Madrid, F., 1999. Cytoskeletal rearrangement during migration and activation of T lymphocytes. *Trends Cell. Biol.*, **9**(6):228–33.

Shakhov, A. N., Lyakhov, I. G., Tumanov, A. V., Rubtsov, A. V., Drutskaya, L. N., Marino, M. W., and Nedospasov, S. A., 2000. Gene profiling approach in the analysis of lymphotoxin and TNF deficiencies. *J. Leukoc. Biol.*, **68**(1):151–7.

Shakhov, A. N. and Nedospasov, S. A., 2001. Expression profiling in knockout mice: lymphotoxin versus tumor necrosis factor in the maintenance of splenic microarchitecture. *Cytokine Growth Factor Rev.*, **12**(1):107–19.

Shewchuk, J. R., 1997. Adaptive precision floating-point arithmetic and fast robust geometric predicates. *Discrete and Computational Geometry*, **18**(2):305–63.

Shi, K., Hayashida, K., Kaneko, M., Hashimoto, J., Tomita, T., Lipsky, P. E., Yoshikawa, H., and Ochi, T., 2001. Lymphoid chemokine B cell-attracting chemokine-1 (CXCL13) is expressed in germinal center of ectopic lymphoid follicles within the synovium of chronic arthritis patients. *J. Immunol.*, **166**(1):650–5.

Sixt, M., Kanazawa, N., Selg, M., Samson, T., Roos, G., Reinhardt, D. P., Pabst, R., Lutz, M. B., and Sorokin, L., 2005. The conduit system transports soluble antigens from the afferent lymph to resident dendritic cells in the T cell area of the lymph node. *Immunity*, **22**(1):19–29.

Slimani, H., Charnaux, N., Mbemba, E., Saffar, L., Vassy, R., Vita, C., and Gattegno, L., 2003. Binding of the CC-chemokine RANTES to syndecan-1 and syndecan-4 expressed on HeLa cells. *Glycobiology*, **13**(9):623–34.

Smith-Franklin, B. A., Keele, B. F., Tew, J. G., Gartner, S., Szakal, A. K., Estes, J. D., Thacker, T. C., and Burton, G. F., 2002. Follicular dendritic cells and the persistence of HIV infectivity: the role of antibodies and Fcγ receptors. *J. Immunol.*, **168**(5):2408–14.

Solomon, J. E. and Paul, M. R., 2006. The kinetics of analyte capture on nanoscale sensors. *Biophys. J.*, **90**(5):1842–52.

Spalding, H. J. and Heath, T. J., 1989. Fine structure of lymph pathways in nodes from the superficial inguinal lymph centre in the pig. *J. Anat.*, **166**:43–54.

Spinetti, G., Camarda, G., Bernardini, G., Romano Di Peppe, S., Capogrossi, M. C., and Napolitano, M., 2001. The chemokine CXCL13 (BCA-1) inhibits FGF-2 effects on endothelial cells. *Biochem. Biophys. Res. Commun.*, **289**(1):19–24.

Srikusalanukul, W., De Bruyne, F., and McCullagh, P., 2002. An application of linear output error modelling for studying lymphocyte migration in peripheral lymphoid tissues. *Australas. Phys. Eng. Sci. Med.*, **25**(3):132–8.

Stamenovic, D. and Coughlin, M. F., 1999. The role of prestress and architecture of the cytoskeleton and deformability of cytoskeletal filaments in mechanics of adherent cells: a quantitative analysis. *J. Theor. Biol.*, **201**(1):63–74.

Stamenovic, D., Fredberg, J. J., Wang, N., Butler, J. P., and Ingber, D. E., 1996. A microstructural approach to cytoskeletal mechanics based on tensegrity. *J. Theor. Biol.*, **181**(2):125–36.

Stamenovic, D. and Ingber, D. E., 2002. Models of cytoskeletal mechanics of adherent cells. *Biomech. Model Mechanobiol.*, **1**(1):95–108.

Stamenovic, D. and Wang, N., 2000. Engineering approaches to cytoskeletal mechanicss. *J. Appl. Physiol.*, **89**:2085–90.

Steinberg, M., 1970. Does differential adhesion govern self-assembly processes in histogenesis? equilibrium configurations and the emergence of a hierarchy among populations of embryonic cells. *J. Exp. Zool.*, **173**(4):395–433.

Stephanou, A. and Tracqui, P., 2002. Cytomechanics of cell deformations and migration: from models to experiments. *C. R. Biol.*, **325**(4):295–308.

Steward, G., 1973. *Introduction to Matrix Computations.* Academic Press, New York.

Stoll, S., Delon, J., Brotz, T. M., and Germain, R. N., 2002. Dynamic imaging of T cell-dendritic cell interactions in lymph nodes. *Science*, **296**(5574):1873–6.

Stott, E. L., Britton, N. F., Glazier, J. A., and Zajac, M., 1999. Stochastic simulation of benign avascular tumour growth using the Potts model. *Math. Comp. Modelling*, **30**:183–198.

Suematsu, S. and Watanabe, T., 2004. Generation of a synthetic lymphoid tissue-like organoid in mice. *Nat. Biotechnol.*, **22**(12):1539–45.

Sultan, C., Stamenovic, D., and Ingber, D. E., 2004. A computational tensegrity model predicts dynamic rheological behaviors in living cells. *Ann. Biomed. Eng.*, **32**(4):520–30.

Sun, Y., Blink, S. E., Chen, J. H., and Fu, Y. X., 2005. Regulation of follicular dendritic cell networks by activated T cells: the role of CD137 signaling. *J. Immunol.*, **175**(2):884–90.

Suzuki, A., Yamakawa, M., and Tsukamoto, M., 2001. The adhesion molecules, l-selectin and sialyl lewis x, relate to the formation of the follicular dendritic cell-lymphocyte cluster in the mantle zone. *Immunol. Lett.*, **79**(3):181–7.

Szakal, A. K., Gieringer, R. L., Kosco, M. H., and Tew, J. G., 1985. Isolated follicular dendritic cells: cytochemical antigen localization, Nomarski, SEM, and TEM morphology. *J. Immunol.*, **134**(3):1349–59.

Szakal, A. K., Kosco, M. H., and Tew, J. G., 1988. A novel in vivo follicular dendritic cell-dependent iccosome-mediated mechanism for delivery of antigen to antigen-processing cells. *J. Immunol.*, **140**(2):341–53.

Takemura, S., Braun, A., Crowson, C., Kurtin, P. J., Cofield, R. H., O'Fallon, W. M., Goronzy, J. J., and Weyand, C. M., 2001. Lymphoid neogenesis in rheumatoid synovitis. *J. Immunol.*, **167**(2):1072–80.

Tammela, T., Petrova, T. V., and Alitalo, K., 2005. Molecular lymphangiogenesis: new players. *Trends Cell. Biol.*, **15**(8):434–41.

Tarlinton, D., 1998. Germinal centers: form and function. *Curr. Opin. Immunol.*, **10**(3):245–51.

Teng, Y. A., Sullivan, F., Beichl, I., and Puppo, E., 1993. A data-parallel algorithm for three-dimensional delaunay triangulation and its implementation. In *Proceedings of Supercomputing*, pp. 112–21.

Thomazy, V. A., Vega, F., Medeiros, L. J., Davies, P. J., and Jones, D., 2003. Phenotypic modulation of the stromal reticular network in normal and neoplastic lymph nodes: tissue transglutaminase reveals coordinate regulation of multiple cell types. *Am. J. Pathol.*, **163**(1):165–74.

Thompson, C. B., Scher, I., Schaefer, M. E., Lindsten, T., Finkelman, F. D., and Mond, J. J., 1984. Size-dependent B lymphocyte subpopulations: relationship of cell volume to surface phenotype, cell cycle, proliferative response, and requirements for antibody production to TNP-Ficoll and TNP-BA. *J. Immunol.*, **133**(5):2333–42.

Tkachuk, M., Bolliger, S., Ryffel, B., Pluschke, G., Banks, T. A., Herren, S., Gisler, R. H., and Kosco-Vilbois, M. H., 1998. Crucial role of tumor necrosis factor receptor 1 expression on nonhematopoietic cells for B cell localization within the splenic white pulp. *J. Exp. Med.*, **187**(4):469–77.

Tomhave, E. D., Richardson, R. M., Didsbury, J. R., Menard, L., Snyderman, R., and Ali, H., 1994. Cross-desensitization of receptors for peptide chemoattractants. Characterization of a new form of leukocyte regulation. *J. Immunol.*, **153**(7):3267–75.

Tracqui, P. and Ohayon, J., 2004. Transmission of mechanical stresses within the cytoskeleton of adherent cells: a theoretical analysis based on a multi-component cell model. *Acta Biotheor.*, **52**(4):323–41.

Tsunoda, R., Bosseloir, A., Onozaki, K., Heinen, E., Miyake, K., Okamura, H., Suzuki, K., Fujita, T., Simar, L. J., and Sugai, N., 1997. Human follicular dendritic cells in vitro and follicular dendritic-cell-like cells. *Cell Tissue Res.*, **288**(2):381–9.

Tsunoda, R., Nakayama, M., Heinen, E., Miyake, K., Suzuki, K., Sugai, N., and Kojima, M., 1992. Emperipolesis of lymphoid cells by human follicular dendritic cells in vitro. *Virchows Arch. B*, **62**(2):69–78.

Tsunoda, T., Yamakawa, M., and Takahashi, T., 1999. Differential expression of Ca(2+)-binding proteins on follicular dendritic cells in non-neoplastic and neoplastic lymphoid follicles. *Am. J. Pathol.*, **155**(3):805–14.

Tumanov, A., Kuprash, D., Lagarkova, M., Grivennikov, S., Abe, K., Shakhov, A., Drutskaya, L., Stewart, C., Chervonsky, A., and Nedospasov, S., 2002. Distinct role of surface lymphotoxin expressed by B cells in the organization of secondary lymphoid tissues. *Immunity*, **17**(3):239–50.

Tumanov, A. V., Grivennikov, S. I., Shakhov, A. N., Rybtsov, S. A., Koroleva, E. P., Takeda, J., Nedospasov, S. A., and Kuprash, D. V., 2003. Dissecting the role of lymphotoxin in lymphoid organs by conditional targeting. *Immunol Rev*, **195**:106–16.

Turner, S., Sherratt, J. A., Painter, K. J., and Savill, N. J., 2004. From a discrete to a continuous model of biological cell movement. *Phys. Rev. E*, **69**(2):021910.

Tyson, R., Stern, L., and LeVeque, R., 1996. Fractional step methods applied to a chemotaxis model. URL `ftp://amath.washington.edu/pub/rjl/papers/rt-lgs-rjl:chemotaxis.ps.Z`.

Uchida, K. S., Kitanishi-Yumura, T., and Yumura, S., 2003. Myosin II contributes to the posterior contraction and the anterior extension during the retraction phase in migrating Dictyostelium cells. *J. Cell Sci.*, **116**(1):51–60.

Ushiki, T., Ohtani, O., and Abe, K., 1995. Scanning electron microscopic studies of reticular framework in the rat mesenteric lymph node. *Anat. Rec.*, **241**(1):113–22.

Van Drenth, C., Jenkins, A., Ledwich, L., Ryan, T. C., Mashikian, M. V., Brazer, W., Center, D. M., and Cruikshank, W. W., 2000. Desensitization of CXC chemokine receptor 4, mediated by IL-16/CD4, is independent of p56lck enzymatic activity. *J. Immunol.*, **165**(11):6356–63.

Verdier, C., 2003. Rheological properties of living materials. From cells to tissues. *J. Theo. Med.*, **5**(2):67–91.

Vicente-Manzanares, M. and Sanchez-Madrid, F., 2004. Role of the cytoskeleton during leukocyte responses. *Nat. Rev. Immunol.*, **4**(2):110–22.

Vicker, M. G., 2002a. Eukaryotic cell locomotion depends on the propagation of self-organized reaction-diffusion waves and oscillations of actin filament assembly. *Exp. Cell Res.*, **275**(1):54–66.

Vicker, M. G., 2002b. F-actin assembly in Dictyostelium cell locomotion and shape oscillations propagates as a self-organized reaction-diffusion wave. *FEBS Lett.*, **510**(1-2):5–9.

Vigo, M. and Pla, N., 2002. Regular triangulations of dynamic sets of points. *CAGD*, **19**(2):127–49.

Vissers, J. L., Hartgers, F. C., Lindhout, E., Figdor, C. G., and Adema, G. J., 2001. BLC (CXCL13) is expressed by different dendritic cell subsets in vitro and in vivo. *Eur. J. Immunol.*, **31**(5):1544–9.

Voigt, I., Camacho, S. A., de Boer, B. A., Lipp, M., Forster, R., and Berek, C., 2000. CXCR5-deficient mice develop functional germinal centers in the splenic T cell zone. *Eur. J. Immunol.*, **30**(2):560–7.

Volokh, K. Y., Vilnay, O., and Belsky, M., 2000. Tensegrity architecture explains linear stiffening and predicts softening of living cells. *J. Biomech.*, **33**(12):1543–9.

Wagner, U. G., Kurtin, P. J., Wahner, A., Brackertz, M., Berry, D. J., Goronzy, J. J., and Weyand, C. M., 1998. The role of CD8+ CD40L+ T cells in the formation of germinal centers in rheumatoid synovitis. *J. Immunol.*, **161**(11):6390–7.

Walker, L. S., Wiggett, H. E., Gaspal, F. M., Raykundalia, C. R., Goodall, M. D., Toellner, K. M., and Lane, P. J., 2003. Established T cell-driven germinal center B cell proliferation is independent of CD28 signaling but is tightly regulated through CTLA-4. *J. Immunol.*, **170**(1):91–8.

Wang, J., Foster, A., Chin, R., Yu, P., Sun, Y., Wang, Y., Pfeffer, K., and Fu, Y. X., 2002a. The complementation of lymphotoxin deficiency with LIGHT, a newly discovered TNF family member, for the restoration of secondary lymphoid structure and function. *Eur. J. Immunol.*, **32**(7):1969–79.

Wang, N., Butler, J. P., and Ingber, D. E., 1993. Mechanotransduction across the cell surface and through the cytoskeleton. *Science*, **260**(5111):1124–7.

Wang, N., Naruse, K., Stamenovic, D., Fredberg, J. J., Mijailovich, S. M., Tolic-Norrelykke, I. M., Polte, T., Mannix, R., and Ingber, D. E., 2001a. Mechanical behavior in living cells consistent with the tensegrity model. *Proc. Natl. Acad. Sci. U.S.A.*, **98**(14):7765–70.

Wang, N., Tolic-Norrelykke, I. M., Chen, J., Mijailovich, S. M., Butler, J. P., Fredberg, J. J., and Stamenovic, D., 2002b. Cell prestress. I. Stiffness and prestress are closely associated in adherent contractile cells. *Am. J. Physiol.*, **282**(3):C606–16.

Wang, Y., Wang, J., Sun, Y., Wu, Q., and Fu, Y. X., 2001b. Complementary effects of TNF and lymphotoxin on the formation of germinal center and follicular dendritic cells. *J. Immunol.*, **166**(1):330–7.

Watson, D. F., 1981. Computing the n-dimensional Delaunay tessellation with application to Voronoi polytopes. *Comput. J.*, **24**(2):167–72.

Webb, D. J., Parsons, J. T., and Horwitz, A. F., 2002. Adhesion assembly, disassembly and turnover in migrating cells – over and over and over again. *Nat. Cell Biol.*, **4**(4):E97–100.

Wei, S. H., Parker, I., Miller, M. J., and Cahalan, M. D., 2003. A stochastic view of lymphocyte motility and trafficking within the lymph node. *Immunol. Rev.*, **195**:136–59.

Wei, S. H., Rosen, H., Matheu, M. P., Sanna, M. G., Wang, S. K., Jo, E., Wong, C. H., Parker, I., and Cahalan, M. D., 2005. Sphingosine 1-phosphate type 1 receptor agonism inhibits transendothelial migration of medullary T cells to lymphatic sinuses. *Nat. Immunol.*, **6**(12):1228–35.

Weissenbach, M., Clahsen, T., Weber, C., Spitzer, D., Wirth, D., Vestweber, D., Heinrich, P. C., and Schaper, F., 2004. Interleukin-6 is a direct mediator of T cell migration. *Eur. J. Immunol.*, **34**(10):2895–906.

Wendling, S., Canadas, P., and Chabrand, P., 2003. Toward a generalised tensegrity model describing the mechanical behaviour of the cytoskeleton structure. *Comput. Methods Biomech. Biomed. Engin.*, **6**(1):45–52.

Wendling, S., Oddou, C., and Isabey, D., 1999. Stiffening response of a cellular tensegrity model. *J. Theor. Biol.*, **196**(3):309–25.

Weyand, C. M., Goronzy, J. J., Takemura, S., and Kurtin, P. J., 2000. Cell-cell interactions in synovitis. Interactions between T cells and B cells in rheumatoid arthritis. *Arthritis Res.*, **2**(6):457–63.

Weyand, C. M., Kurtin, P. J., and Goronzy, J. J., 2001. Ectopic lymphoid organogenesis: a fast track for autoimmunity. *Am. J. Pathol.*, **159**(3):787–93.

Wilkinson, P. C. and Newman, I., 1992. Identification of IL-8 as a locomotor attractant for activated human lymphocytes in mononuclear cell cultures with anti-CD3 or purified protein derivative of Mycobacterium tuberculosis. *J. Immunol.*, **149**(8):2689–94.

Willimann, K., Legler, D. F., Loetscher, M., Roos, R. S., Delgado, M. B., Clark-Lewis, I., Baggiolini, M., and Moser, B., 1998. The chemokine SLC is expressed in T cell areas of lymph nodes and mucosal lymphoid tissues and attracts activated T cells via CCR7. *Eur. J. Immunol.*, **28**(6):2025–34.

Wolf, K., Mazo, I., Leung, H., Engelke, K., von Andrian, U. H., Deryugina, E. I., Strongin, A. Y., Brocker, E. B., and Friedl, P., 2003a. Compensation mechanism in tumor cell migration: mesenchymal-amoeboid transition after blocking of pericellular proteolysis. *J. Cell Biol.*, **160**(2):267–77.

Wolf, K., Muller, R., Borgmann, S., Brocker, E. B., and Friedl, P., 2003b. Amoeboid shape change and contact guidance: T-lymphocyte crawling through fibrillar collagen is independent of matrix remodeling by MMPs and other proteases. *Blood*, **102**(9):3262–9.

Wu, Q., Andreopoulos, Y., and Weinbaum, S., 2004. From red cells to snowboarding: a new concept for a train track. *Phys. Rev. Lett.*, **93**(19):194501.

Yamada, K., Yamakawa, M., Imai, Y., and Tsukamoto, M., 1997. Expression of cytokine receptors on follicular dendritic cells. *Blood*, **90**(12):4832–41.

Yamaguchi, K. and Schoefl, G. I., 1983. Blood vessels of the Peyer's patch in the mouse: III. High-endothelium venules. *Anat. Rec.*, **206**(4):419–38.

Yamanaka, T., Helgeland, L., Farstad, I. N., Fukushima, H., Midtvedt, T., and Brandtzaeg, P., 2003. Microbial colonization drives lymphocyte accumulation and differentiation in the follicle-associated epithelium of Peyer's patches. *J. Immunol.*, **170**(2):816–22.

Yamanaka, T., Straumfors, A., Morton, H., Fausa, O., Brandtzaeg, P., and Farstad, I., 2001. M cell pockets of human Peyer's patches are specialized extensions of germinal centers. *Eur. J. Immunol.*, **31**(1):107–17.

Yang, F., 2003. Load-displacement relation in adhesion measurement. *J. Phys. D*, **36**(19):2417–20.

Yasuda, M., Kajiwara, E., Ekino, S., Taura, Y., Hirota, Y., Horiuchi, H., Matsuda, H., and Furusawa, S., 2003. Immunobiology of chicken germinal center: I. Changes in surface Ig class expression in the chicken splenic germinal center after antigenic stimulation. *Dev. Comp. Immunol.*, **27**(2):159–66.

Yasuda, M., Taura, Y., Yokomizo, Y., and Ekino, S., 1998. A comparative study of germinal center: fowls and mammals. *Comp. Immunol. Microbiol. Infect. Dis.*, **21**(3):179–89.

Ying, X., Chan, K., Shenoy, P., Hill, M., and Ruddle, N. H., 2005. Lymphotoxin plays a crucial role in the development and function of nasal-associated lymphoid tissue through regulation of chemokines and peripheral node addressin. *Am. J. Pathol.*, **166**(1):135–46.

Yopp, A. C., Ochando, J. C., Mao, M., Ledgerwood, L., Ding, Y., and Bromberg, J. S., 2005. Sphingosine 1-phosphate receptors regulate chemokine-driven transendothelial migration of lymph node but not splenic T cells. *J. Immunol.*, **175**(5):2913–24.

Yoshida, H., Honda, K., Shinkura, R., Adachi, S., Nishikawa, S., Maki, K., Ikuta, K., and Nishikawa, S. I., 1999. IL-7 receptor α+ CD3(-) cells in the embryonic intestine induces the organizing center of Peyer's patches. *Int. Immunol.*, **11**(5):643–55.

Yoshida, H., Naito, A., Inoue, J., Satoh, M., Santee-Cooper, S. M., Ware, C. F., Togawa, A., Nishikawa, S., and Nishikawa, S., 2002. Different cytokines induce surface lymphotoxin-$\alpha\beta$ on IL-7 receptor-α cells that differentially engender lymph nodes and Peyer's patches. *Immunity*, **17**(6):823–33.

Yoshida, K. and Soldati, T., 2006. Dissection of amoeboid movement into two mechanically distinct modes. *J. Cell. Sci.*, **119**(Pt 18):3833–44.

Yoshida, R., Nagira, M., Kitaura, M., Imagawa, N., Imai, T., and Yoshie, O., 1998. Secondary lymphoid-tissue chemokine is a functional ligand for the CC chemokine receptor CCR7. *J. Biol. Chem.*, **273**(12):7118–22.

Young, A. J., 1999. The physiology of lymphocyte migration through the single lymph node in vivo. *Semin. Immunol.*, **11**(2):73–83.

Young, A. J., Marston, W. L., and Dudler, L., 2000. Subset-specific regulation of the lymphatic exit of recirculating lymphocytes in vivo. *J. Immunol.*, **165**(6):3168–74.

Zhu, C., Bao, G., and Wang, N., 2000. Cell Mechanics: Mechanical Response, Cell Adhesion, and Molecular Deformation. *Annu. Rev. Biomed. Eng.*, **2**:189–226.

Zon, L. I., 1995. Developmental biology of hematopoiesis. *Blood*, **86**(8):2876–91.

Publications

Articles

T. Beyer and M. Meyer-Hermann (2008). Mechanisms of organogenesis of primary lymphoid follicles. *Inter. Immunol.*, **20**(4):615–23.

T. Beyer and M. Meyer-Hermann (2007). Modeling emergent tissue organization involving high-speed migrating cells in a flow equilibrium. *Phys. Rev. E*, **76**(2 Pt 1):021929.

T. Beyer and M. Meyer-Hermann (2006). The treatment of non-flippable configurations in three dimensional regular triangulations. *WSEAS Trans. Syst.*, **5**(5):1100–7.

J. Galle, G. Aust, G. Schaller, T. Beyer, D. Drasdo (2006). Individual cell-based models of the spatio-temporal organization of multicellular systems - achievements and limitations. *Cytometry Pt. A*, **69A**(7), 704–10.

T. Beyer, G. Schaller, A. Deutsch, and M. Meyer-Hermann (2005). Parallel dynamic and kinetic regular triangulation in three dimensions. *Comput. Phys. Commun.*, **172**(2):86–108.

M. Meyer-Hermann and T. Beyer (2004). The type of seeder cells determines the efficiency of germinal center reactions. *Bull. Math. Biol.*, **66**(1):125–41.

M. Meyer-Hermann and T. Beyer (2003). Conclusions from two model concepts on germinal center dynamics and morphology. *Develop. Immunol.*, **9**(4):203–14.

T. Beyer, M. Meyer-Hermann, and G. Soff (2002). A possible role of chemotaxis in germinal center formation. *Inter. Immunol.*, **14**(12):1369–81.

Conference Contributions

T. Beyer and M. Meyer-Hermann (2007). B cells in secondary lymphoid tissue organogenesis. Presentation and Poster at *5th B cell Forum*, Bad Bevensen/Germany.

T. Beyer (2006). Recover from non-flippable configurations in parallel approaches to three dimensional kinetic regular triangulations. Presentation at *8th WSEAS International Conference (ACMOS'06)*, Prague/Czech Republic.

T. Beyer (2005). Self-organization of primary follicles of germinal centers. Presentation at *European conference on Mathematical and Theoretical Biology 2005*, Dresden/Germany.

T. Beyer, M. Meyer-Hermann, and G. Soff (2002). Possible role of chemotaxis in germinal center formation. Poster at *14th international conference on lymphatic tissues and germinal centres in immune reactions*, Groningen/Netherlands.

Curriculum Vitae

Research experience

10/2006 - 05/2007	System administrator at the Center for Scientific Computing of the Johann Wolfgang Goethe University of Frankfurt, Germany.
since 01/2005	PhD student of the Johann Wolfgang Goethe University of Frankfurt, Germany at the Frankfurt Institute for Advanced Studies. Receiver of a studentship of the Frankfurt International School for Sciences.
07/2004 - 12/2004	Guest Scientist at the Interdisciplinary Center for Bioinformatics at the University of Leipzig, Germany. Mechanistic simulation of cell migration based upon parallel kinetic Delaunay triangulations.
10/2003 - 06/2004	PhD student at the Institute for Theoretical Physics at the Dresden University of Technology, Germany.
02/2003 - 09/2003	Guest Scientist at the Center for High Performance Computing at the Dresden University of Technology, Germany. Design and Implementation of parallel algorithms for dynamic and kinetic Delaunay triangulations.

Education

10/1997 - 11/2002	Study of physics at the Dresden University of Technology, Germany. Diploma thesis about Dynamische Strukturbildung in Keimzentren (Dynamical Pattern Formation in Germinal Centers). Graduation with diploma in physics with grade 1.15.
08/1992 - 06/1996	Secondary school in Dresden, Germany.
09/1984 - 06/1992	First school in Dresden, Germany.

Work experience during studies

07/2001 - 06/2002   Student assistant at the Institute for Polymer Research in Dresden, Germany. Work in the area of the DFG-funded project Schmelzspinnen von PEEK-Garnen mit feintitrigen Filamenten (Melt spinning of PEEK yarns with fine-spun filaments).

10/1997 - 06/2001   Student assistant at the Institute for Polymer Research in Dresden, Germany. Work in the area of the DFG-funded project Schmelzspinnen vernetzbarer thermoplastischer Elastomere mittels Zweischneckenextruder (Melt spinning of network forming thermoplastic elastomeres using two-shaft screw extruder).